THE UNIVERSITY
of ADELAIDE

3D Bioprinting of Advanced Bioinks for Tissue Engineering Applications

By

Hadi Rastin

Supervisors:

Professor Dusan Losic

Dr. Tran Thanh Tung

A thesis is submitted for the degree of

Doctor of Philosophy

In

School of Chemical Engineering and Advanced Materials

The University of Adelaide, Australia

April 2021

Summary

Organ transplantation would be the first option for those whose tissues/organs have been extremely injured. However, the growing gap between the number of organ donors and receivers has resulted in the long waiting list for organ transplantation. Regenerative medicine has emerged as a promising approach to tackle the crisis associated with organ shortage by employing the principle of engineering and biology. The regenerative medicine aims to support and accelerate the regeneration of defective tissue/organs through combining cells, scaffolds, and growth factors. Among various biofabrication methods, tremendous attention has been devoted to the recently emerged three-dimensional (3D) bioprinting technology for the fabrication of functional tissue-engineered scaffold loaded with cells due to its ability to assemble complex structures with meticulous control over the entire fabrication process. It is a computer-assisted technology that enables the direct fabrication of complex 3D constructs usually layers upon layers fashion according to a pre-designed structure. The 3D bioprinting concept was borrowed from 3D printing technology that has been primarily exploited in fabrication industries as a rapid prototyping technology. Harnessing the 3D printing technology in the generation of personalized implants, tissue-engineered scaffolds, drug delivery devices, tissue models has opened up a new avenue for the biofabrication methods. For bioprinting application, an ideal bioink should possess a set of desirable properties including biodegradability, biocompatibility, providing mechanical strength and rheological properties, and closely mimicking the native tissue microenvironment. The selection of materials to be used as bioinks remains the main bottleneck in the realization of 3D bioprinting technology. This thesis aims to develop novel bioinks to address the challenges associated with current bioinks by employing polymers and nanomaterials. The specific objectives of this thesis are organized into seven chapters that will be presented in the form of a collection of the published papers which are the results of the research. In addition, a literature review has been provided to establish the background of this research. Overall, the main contributions of this thesis to the 3D bioprinting field are as follows:

➢ Development of a novel bioink composed of methylcellulose/gelatin-methacryloyl (MC/GelMA) hydrogel with high shape integrity and improved biological stability (paper 1).

➢ Extending the usage territory of MXene nanosheets to the 3D bioprinting field owing to its favorable features (paper 2).

- ➢ Addressing the poor electrical conductivity of current bioinks by employing poly(3,4-ethylenedioxythiophene):poly(styrenesulfonate) (PEDOT:PSS) conductive polymer for neural tissue engineering (paper 3).
- ➢ Development of bioink with potent antibacterial activity toward Gram-positive (*S. aureus*) and Gram-negative (*P. aeruginosa*) bacterial, while supporting the cellular functions (paper 4).

Declaration

I certify that this work contains no material which has been accepted for the award of any other degree or diploma in my name in any university or other tertiary institution and, to the best of my knowledge and belief, contains no material previously published or written by another person, except where due reference has been made in the text. In addition, I certify that no part of this work will, in the future, be used in a submission in my name for any other degree or diploma in any university or other tertiary institution without the prior approval of the University of Adelaide and where applicable, any partner institution responsible for the joint award of this degree.

The author acknowledges that copyright of published works contained within this thesis resides with the copyright holders of those works. I give permission for the digital version of my thesis to be made available on the web, via the University's digital research repository, the Library Search and also through web search engines, unless permission has been granted by the University to restrict access for a period of time.

Hadi Rastin

Date: March 30, 2021

Acknowledgment

I would like to express my sincere appreciation to the following people and organizations, without whom this thesis would have not been possible.

i. My principal supervisor **Professor Dusan Losic** for his valuable support, inspiration, and outstanding leadership throughout my Ph.D. journey. I have been so fortunate to be a member of a professional research group, where I have received significant support during stressful situations during my Ph.D. journey. His unwavering enthusiasm for discovering novel ideas always kept me constantly motivated for research. If it were not for him, I may not have discovered my desire for conducting research. It is difficult for me to express my sincere appreciation in few sentences to my supervisors.

ii. My appreciation also extends to my co-supervisor **Dr. Tran Tung** for his highly precious advice, support, and assistance. His advice has been always so beneficial for me during my Ph.D. study.

iii. I also would like to thank the Adelaide microscopy, School of Chemical Engineering and Advanced Materials, and School of Petroleum Engineering for providing the support and facilities to proceed with this research.

iv. I would like to appreciate **Professor Gerald Atkins**, director of the Centre for Orthopaedic and Trauma Research at Adelaide Health and Medical Sciences (AHMS), for his generous support and advice. My special thanks go to **Dr. Renee T. Ormsby**, who expertly helped me to proceed with the biological study despite her busy schedule.

v. I would like to express my high appreciation to **Professor Jingxiu Bi** and **Dr. Bingyang Zhang** at the School of Chemical Engineering and Advanced Materials for providing support and advice, without whom I was unable to complete my thesis.

vi. I would like to express my deepest appreciation to **Professor Sarah Vreugde** and **Dr. Mahnaz Ramezanpour** at Basil Hetzel Institute (BHI) for Translational Health Research, who have the Personal generosity of both helped me to have an enjoyable time at BHI.

Finally, I am indebted to my family and I would like to express my immense love and gratitude to my beloved father, mother, sister, and brothers for their never-ending support, inspiration, strength, and love.

Hadi Rastin

Publications

This Ph.D. thesis is submitted as a "thesis by publication" in accordance to the "Specifications for Thesis 2020" of The University of Adelaide. This thesis contains the following list of publications that resulted from my Ph.D. candidature. The outcomes generated during my PhD candidature include 8 published, accepted for publication or under reviewed journal articles (5 first-authored; 3 co-authored), 4 manuscripts under final preparation, 3 conference/workshop presentations and 5 awards.

List of journal publications (first author):

1. **Rastin H**, Ormsby RT, Atkins GJ, Losic D. 3D Bioprinting of Methylcellulose/Gelatin-Methacryloyl (MC/GelMA) Bioink with High Shape Integrity. ACS Applied Bio Materials. 2020;3(3):1815-1826. **DOI:10.1021/acsabm.0c00169**

2. **Rastin H**, Zhang B, Mazinani A, Hassan K, Bi J, Tung TT, Losic D. 3D bioprinting of cell-laden electroconductive MXene nanocomposite bioinks. Nanoscale. 2020;12(30):16069-16080. **Featured in journal cover, Recognized as a part of a most popular collection papers during 2020 in the Nanoscale journal. DOI: 10.1039/D0NR02581J**

3. **Rastin H**, Zhang B, Bi J, Hassan K, Tung TT, Losic D. 3D printing of cell-laden electroconductive bioinks for tissue engineering applications. Journal of Materials Chemistry B. 2020;8(27):5862-5876. **Featured in journal cover, Recognized as a part of most popular and most cited collection papers during 2020 in the Journal of Materials Chemistry B. DOI: 10.1039/D0TB00627K,**

4. **Rastin H,** Ramezanpour M, Hassan K, Mazinani A, Tung TT, Vreugde S, Losic D. 3D Bioprinting of a Cell-laden Antibacterial Polysaccharide Hydrogel Composite. Carbohydrate Polymers. 2021:117989. **DOI: 10.1016/j.carbpol.2021.117989**

5. **Rastin H**, Mansouri N, Hassan K, Mazinani A, Ramezanpour M, Yap P, Yu L, Tran TT, Vreugde S, Losic D. Converging 2D Nanomaterials and 3D Bioprinting Technology: State-of-the-Art, Challenges and Potential Outlook in Biomedical Applications, Advanced Materials, under review.

List of journal papers from collaboration (co-author):

6. Hassan K, Nine M.J, Tung TT, Stanley N, Yap P.L, **Rastin H**, Yu L, Losic D. Functional inks and extrusion-based 3D printing of 2D materials: a review of current research and applications. Nanoscale. 2020;12(37):19007-19042. **DOI: 10.1039/D0NR04933F**

7. Hassan K, Tung TT, Stanley N, Yap P.L, Farivar F, **Rastin H**, Nine M.J, Losic D. Graphene ink for 3D extrusion micro printing of chemo-resistive sensing devices for volatile organic compound detection, Nanoscale. 2021;13(37):5356-5368. **DOI: 10.1039/D1NR00150G**

8. Hassan K, **Rastin H,** Yap P.L, Tung TT, Stanley N, Losic D. Bio-inspired fractal designed VOC sensors for smart packaging application, Applied Materials Today, Under Review

List of journal papers (in final preparations):

1. Shaheer Maher, **Rastin H**, Vreugde S, Losic D. Engineered titanium implants for localized drug delivery of gallium, Under preparation

2. Shaheer Maher, **Rastin H**, Vreugde S, Losic D. Nanoengineered titania nanotube arrays for drug delivery, Under preparation.

3. Mazinani A, Nine M.J, Lee J, Tikhomirova A, **Rastin H**, Tung TT, Ghomashchi R, Kidd S, Losic D. The Improved antibacterial activity of titania PEO coatings by addition of multilayer 2D antimicrobial flakes through the simple drop-casting method, Under preparation

4. Mazinani A, Nine M.J, Lee J, **Rastin H**, Losic D. Engineering nanostructured titania surfaces with tuneable and mixed topography by combined plasma electrolytic oxidation (PEO) and hydrothermal process, Under preparation

List of conference/workshop presentations:

1. **Rastin H,** Tung TT, Losic D. MXene nanocomposite bioink, Third ARC Graphene Research Hub Workshop, 2021 (**Oral presentation**), **People's Choice Award.**

2. **Rastin H,** Tran D, Losic D. 3D bioprinting of self-supporting Methylcellulose/GelMA bioink with enhanced biological stability, First ARC Graphene Research Hub Workshop, 2019 (**Poster presentation**)

3. **Rastin H,** Tran D, Losic D. 3D printing of shear-thinning and printable Nano-engineered Gelatin/Laponite/Graphene hydrogels, First Australian-Europe Graphene Workshop, 2018 (**Poster presentation**)

List of awards:

1. **Certificate of Best Oral Presentation People's Choice Awards** at Third ARC Graphene Hub Workshop, 26 March 2021, Adelaide, Australia.

2. Published a paper selected as a part of a **most popular collection papers during 2020 in the Nanoscale journal.**

3. Published a research paper recognized as a part of **most popular and most cited collection papers during 2020 in the Journal of Materials Chemistry B.**

4. **Ph.D. Scholarship -** Adelaide Postgraduate Award (2017), Australia

5. **Two journal covers** featured in the "Nanoscale" journal and "Journal of Materials Chemistry B journal"

Featured cover article: Vol. 12, Issue 30, 2020, Nanoscale:
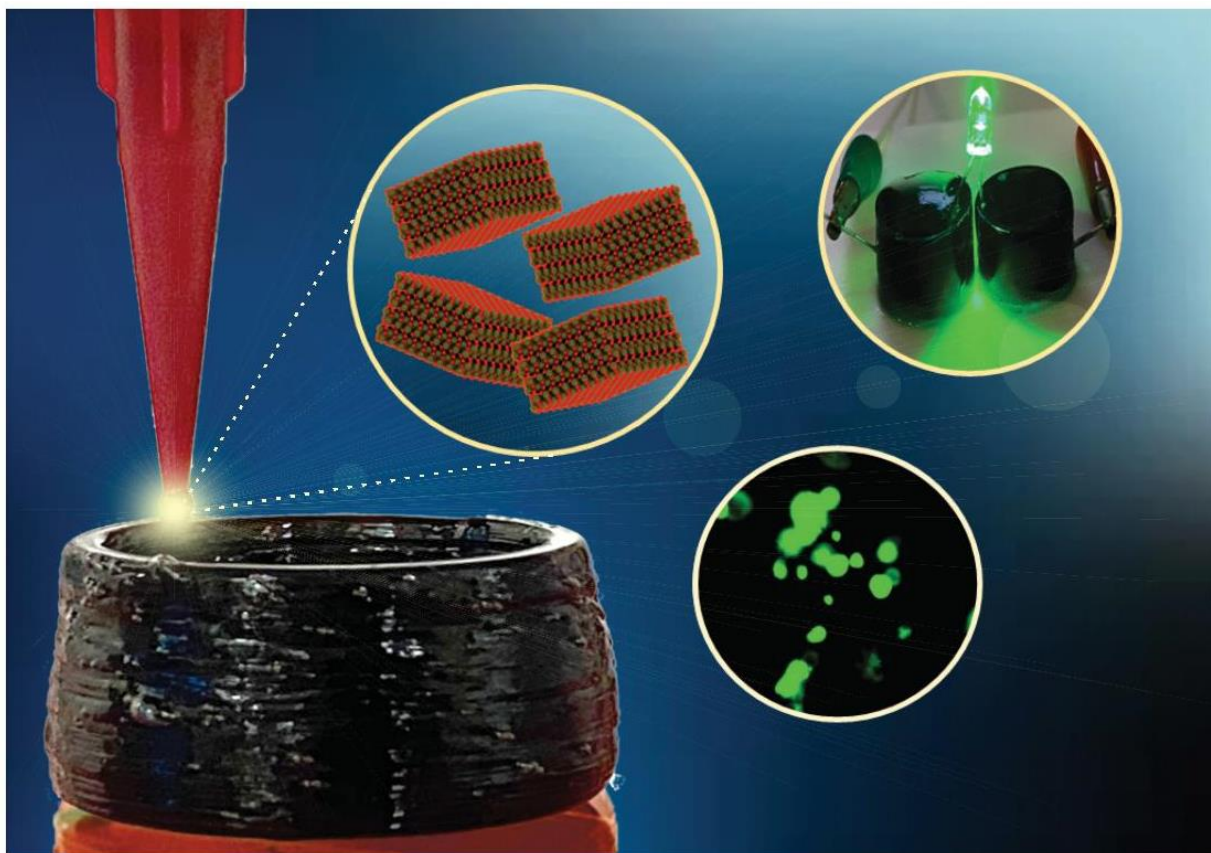
Showcasing research from Prof. Dusan Losic's group at the School of Chemical Engineering and Advanced Materials, The University of Adelaide, Adelaide, Australia.

3D bioprinting of cell-laden electroconductive MXene nanocomposite bioinks

A new electroconductive cell-laden bioink composed of Ti_3C_2 MXene nanosheets dispersed homogeneously within Hyaluronic acid/Alginate (HA/Alg) hydrogel has been introduced that displayed excellent rheological properties, allowing the fabrication of multilayered 3D structures with high resolution and shape retention. The introduction of Ti_3C_2 MXene nanosheets within the HA/Alg hydrogel endows the electrical conductivity to the ink, addressing the poor electrical conductivity of current bioinks that mismatch with physico-chemical properties of tissue.

As featured in:

See Dusan Losic *et al.*, *Nanoscale*, 2020, **12**, 16069.

ROYAL SOCIETY OF CHEMISTRY

rsc.li/nanoscale

Registered charity number: 207890

Featured cover article: Vol. 8, Issue 27, 2020, Journal of Materials Chemistry B:

ROYAL SOCIETY
OF CHEMISTRY
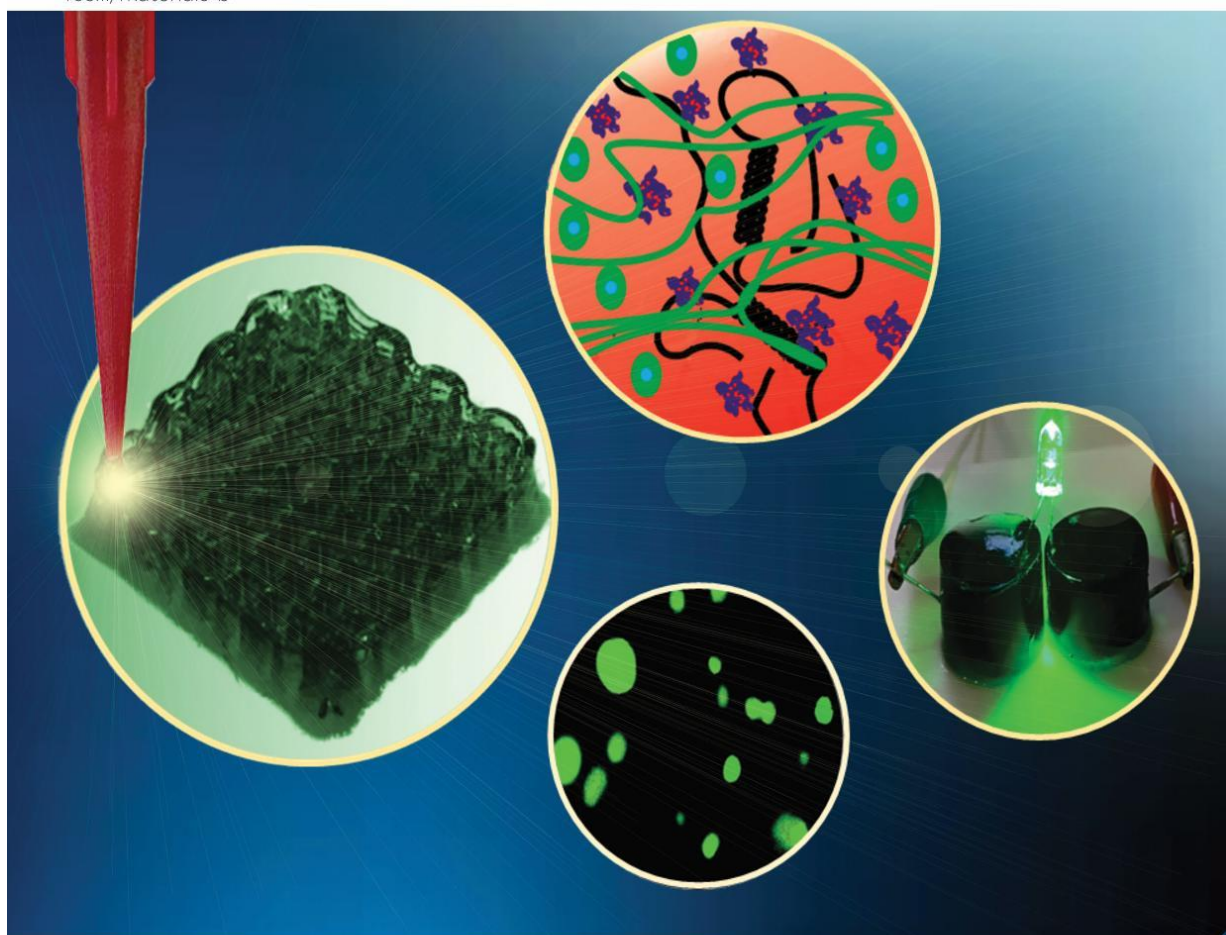
PAPER
Dusan Losic *et al.*
3D printing of cell-laden electroconductive bioinks for tissue
engineering applications

Indexed in
Medline!

Abbreviation

Description	Notation
Drop-on-demand	DOD
Extracellular matrix	ECM
Gelatin methacryloyl	GelMA
Graphene oxide	GO
Hexagonal boron nitride	hBN
High-resolution transmission electron microscopy	HRTEM
Interpenetrating networks	IPNs
kappa-carrageenan	κCA
Laser-induced forward transfer	LIFT
Magnetic Resonance Imaging	MRI
Methylcellulose	MC
N-acryloyl glycinamide	NAGA
Nanoengineered ionic-covalent entanglement	NICE
Poly(ethylene glycol) diacrylate	PEGDA
Poly(ethylene glycol)-dithiothreitol	PEGDTT
Poly(ε-caprolactone)	PCL
Poly(lactic-co-glycolic acid)	PLGA
Polyethylene glycol	PEG
Polyvinyl alcohol	PVA
Reduced graphene oxide	rGO
Silver	Ag
Strontium-containing hydroxyapatite	SrHA
Ultraviolet	UV
β-tricalcium phosphate	β-TCP
poly(3,4-ethylenedioxythiophene):poly(styrenesulfonate)	PEDOT:PSS
Hyaluronic acid	HA
Alginate	Alg
Gallium	Ga^{+3}
human mesenchymal stem cell behavior	hMSC
Nanomaterials	NMs
mannuronic acid	M
L-guluronic acid	G

Contents

List of Figures

This page is left blank intentionally

Chapter 1 Page 1

Introduction and motivation

I n this chapter, a summary of this multi-disciplinary thesis is provided with a special focus on the significance of this research to the field. This chapter first discusses the crisis of tissue/organ shortages that remains a life-threatening challenging matter that was the main motivation of this thesis. Then, challenges associated with current bioinks have recognized, allowing us to define the aims of this thesis.

1.1 Abstract

A variety of biofabrication methods such as solvent casting, gas forming, membrane lamination, salt leaching, and fiber binding have been introduced in the regenerative medicine. However, these conventional biofabrication methods suffer from serious limitations such as the inability to replicate the complicated microenvironment of native tissues. Recently, three-dimensional (3D) bioprinting has emerged as a revolutionary biofabrication method, offering the unprecedented capability to deposit cells at the desired location to construct a complex structure with superior resolution. 3D bioprinting allows rapid patterning of living and non-living biological materials through robotic dispensing of bioink into a tissue-like architecture. Thus, tremendous efforts have been devoted to the development of 3D bioprinting techniques to achieve functional tissue/organ with matched properties to the actual organs. The primary aim of this thesis is to develop novel cell-laden bioinks for tissue engineering applications using the extrusion-based 3D bioprinting technique.

1.2 Research motivation

The crisis of tissue/organ shortages remains a life-threatening challenging matter due to the unbalanced bomber of organ donors and receivers [1]. The current approach relies on the donated tissue/organ that encounters the challenges associated with the possible immunological rejection of the donated organ and shortage of organs [2]. According to the statistics shown in **Figure 1.1**, the waiting list has experienced a significant expansion over the last decades, while the organ donors available cannot fulfill this demand. This leads to the increasing waiting time for those who require critical organs on transplant lists. While 79 people revive critical organs every day, 18 people die waiting for organs that could save their lives [2].
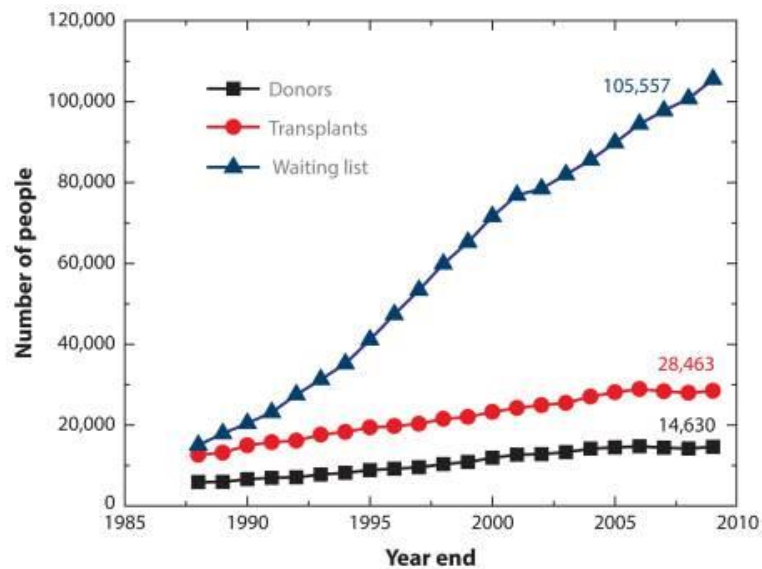
Figure 1.1. The statistics of the number of organ donors, transplantation, and waiting list [2]. Reproduced with permission [2]. Copyright (2014) Annual Reviews.

Tissue engineering has emerged as a promising alternative approach to regenerate and replace the damaged organs from the patient's cells [3]. Tissue engineering is identified as an interdisciplinary field of research that integrates the principle of engineering and biology to fabricate functional tissue-like structures (**Figure 1.2**) [4]. Tissue engineering has been successfully employed to build a variety of organs and tissues with different organizations and functionalities such as kidney [5], tendon [6], and cornea [7] to blood vessels [8] and the heart [9]. Tissue engineering uses the combination of cells and biomaterials in which cells are seeded onto or into the scaffold [4]. The scaffold support cell to grow and generate extracellular matrix before implantation. In addition, tissue engineering has exhibited high potentials in scientific researches owing to the capability of the fabrication of in vitro models that could be used for the assessment of drug candidates and novel treatments [10]. From the economic point of view, the cost for the assessment of a drug candidate is over one billion dollars with an average drug development timeline of 10 years [4]. Despite these high expenses and long screening time, the high failure rate for candidate drugs adds to the difficulty. This is because the 2D cell monocultures used in preclinical studies cannot replicate closely the behavior of target tissue. Fabrication of laboratory-grown 3D may replicate closely the whole spectrum of characteristics of native tissue [11].
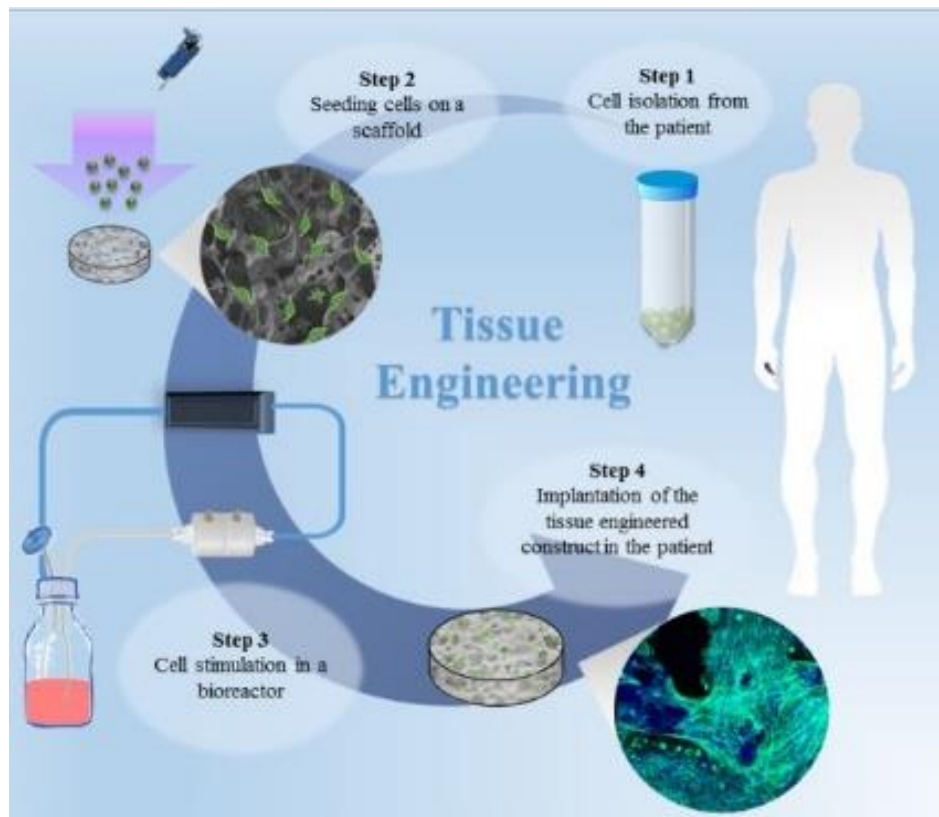
Figure 1.2. The workflow of tissue engineering for the regeneration of a tissue/organ. Accordingly, cells are harvested from the patients, followed by seeding onto or into the 3D scaffold and let them grow and produce the ECM before implantation in a bioreactor [4]. Reproduced with permission [4]. Copyright (2017) Frontiers.

Biofabrication refers to the techniques that allow the fabrication of scaffolds in an automated manner with precise hierarchical architecture [2]. The biofabrication techniques aim to generate a functional tissue-like structure that resembles closely endogenous tissues. Considering the critical role of biofabrication method in the tissue engineering strategy, a variety of biofabrication methods have been developed to achieve better control over the fabrication of the complex heterogeneous nature of endogenous cells, tissues, and organs [12]. Particulate leaching, freeze-drying, electrospinning, and microengineering are typical examples of conventional biofabrication methods that can create 3D scaffolds. Although these conventional biofabrication methods can mimic a certain degree of native tissue microenvironment, they have some serious limitations such as poor reproducibility and versatility in their fabrication procedures that limit their applications [2]. For example, all the above-mentioned techniques require post cell-seeding procedure that proved to be challenging [2]. Recently, the 3D bioprinting technique has revolutionized the biofabrication field that offers enhanced control over the fabrication of cell-laden 3D networks [13]. 3D bioprinting allows the fabrication of 3D

structure through the layer-by-layer deposition of materials in the pre-designed location [14]. 3D bioprinting has the advantage of high reproducibility due to the nature of the automated printing process. There has been tremendous effort focused on the development of 3D bioprinting techniques over the last decades as demonstrated by the number of publications in this field (**Figure 1.3 a**) [15]. 3D bioprinting has been extensively investigated for the fabrication of various tissue/organs for specifically tissue engineering application (**Figure 1.3 b**). Although 3D bioprinting is still in its preliminary stages, it has exhibited tremendous promise in a variety of biomedical application including drug discovery, high throughput screening, cancer models, smart implants, etc. (**Figure 1.3 c**).
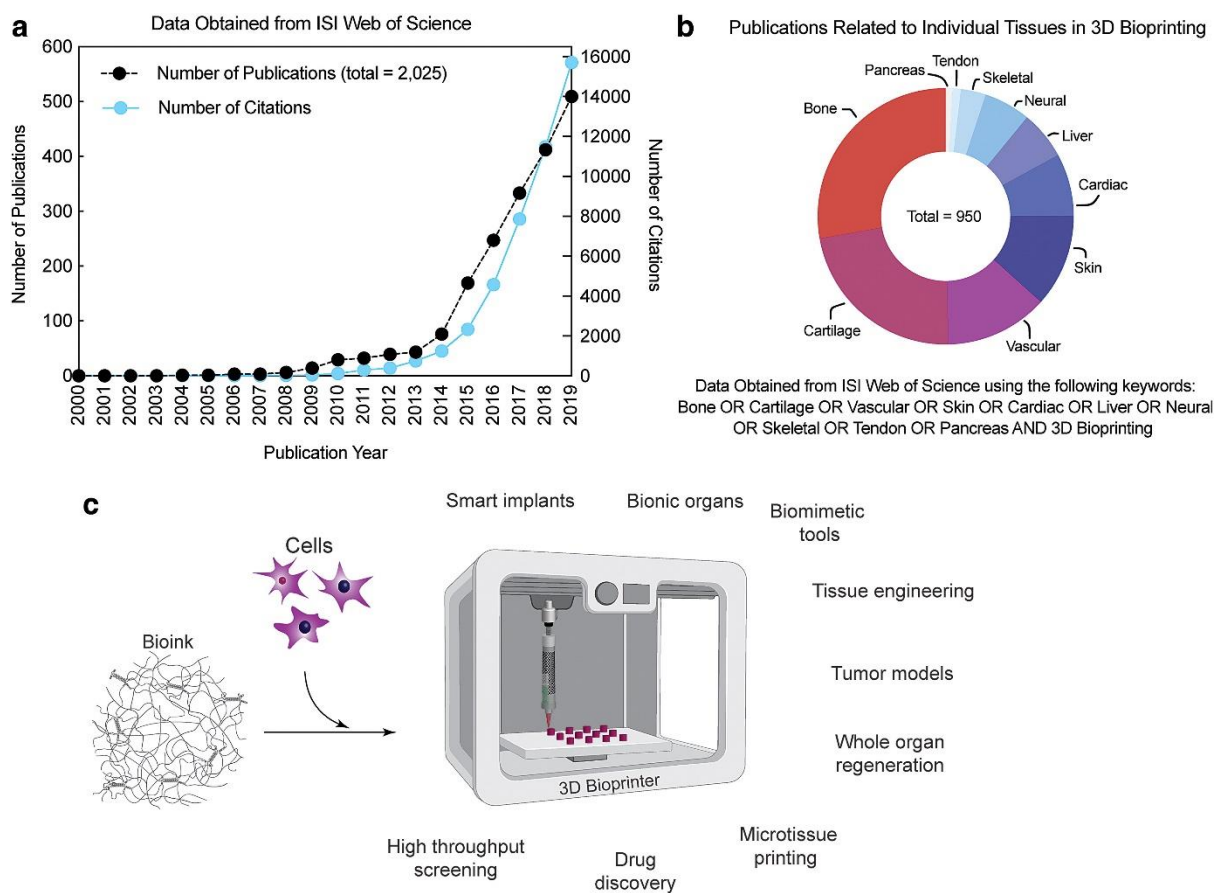
Figure 1.3. (a) Schematic illustration of trends in the 3D bioprinting field, showing the rising number of publication related to 3D bioprinting according to the data extracted from ISI Web of Science using "3D bioprinting." (b) The number of a publication focused on certain tissue engineering using the 3D bioprinting biofabrication method. (c) Potential application of 3D bioprinting in biomedical applications [15]. Reproduced with permission [15]. Copyright (2020) liebertpub.

1.3 Knowledge gaps

According to the comprehensive literature review in Chapter 2, certain challenges associated with the 3D bioprinting field have been recognized. The current bioinks suffer from serious limitations that deserved to be addressed as outlined here briefly:

- Lack of ideal printable bioinks with high shape fidelity and improved biological stability.
- A limited selection of biomaterials that have been employed in the design of bioinks.
- Poor electrical conductivity of current bioinks due to the inherent properties of polymers used in bioinks. Electroconductive bioinks facilitate the uniform distribution of electrical cues to encapsulated cells within 3D printed structure, improving the signaling between cells.
- Lack of a bioink with inherent antibacterial activity to eliminate the risks associated with bacterial infections while supporting tissue regeneration.

1.4 Research aims and questions

The primary aim of this thesis is to develop novel cell-laden bioinks for tissue engineering applications using the extrusion-based 3D bioprinting technique. An ideal bioink should provide both printability and biocompatibility requirements and mimic closely the physio-chemical properties of the native tissue microenvironment. This research generally attempts to design novel bioinks with improved performance. From the recognized knowledge gaps in the 3D bioprinting field, the following research aims were developed:

- **Aim 1**: To design a cell-laden bioink with long-term biological stability and excellent printability by employing photo-crosslinkable hydrogels.
- **Aim 2**: To explore the potential use of Ti_3C_2 MXene nanosheets in the design of bioinks for tissue engineering applications.
- **Aim 3**: To address the poor electrical conductivity of current bioinks by employing (3,4-ethylenedioxythiophene):poly(styrenesulfonate) (PEDOT:PSS) conducting polymers.
- **Aim 4**: To eliminate the risk of bacterial infection at the lesion site for skin tissue engineering.

This thesis attempts to address the following questions in separate chapters:

- **Question 1:** How to improve the biological stability of the methylcellulose-based bioinks in the biological condition without compensating for the printability of methylcellulose?
- **Question 2:** How does MXene affect the ultimate properties of the bioink in terms of mechanical strength, printability, electrical conductivity, and biocompatibility?

➢ **Question 3**: How do tune the electrical conductivity of a bioink by employing conducting polymers?

➢ **Question 4**: How the gallium-crosslinked hydrogels can protect the bioink against bacterial infection?

1.5 Hypothesis

To address the above-mentioned aims and questions, the following hypothesis is made:

1) Gelatin methacrylol with permanent crosslinking ability under UV irradiation allows the long-term stability of 3D printed structure in the biological media.

2) MXene nanosheets have exhibited a reinforcement effect on the hydrogel composites. In addition, it possesses high electrical conductivity that is expected to endow the bioink with high electrical conductivity.

3) Conducting polymers have been widely used in tissue engineering applications due to their excellent biocompatibility and excellent electrical conductivity. Therefore, it is hypothesized that the addition of PEDOT:PSS can impart electrical conductivity to the bioink.

4) Gallium-based compounds have demonstrated potent antibacterial activity toward a broad range of gram-negative and gram-positive bacteria while demonstrating acceptable toxicity toward normal cells. Therefore, I hypothesized the use of gallium in the bioink formulation can eliminate the risk of bacterial infection at the lesion site.

1.6 Thesis outline

This Ph.D. thesis is organized into seven chapters; introduction, literature review, four chapters adapted from the publications, and finally a chapter of conclusions and suggested future research works. A summary of each chapter is given below.

Chapter 1: Introduction introduces tissue engineering as the promising alternative approach to tackle the unbalanced number of organ donors and receivers. This chapter also highlights the promise of 3D bioprinting in addressing the challenges associated with conventional biofabrication methods. Finally, this chapter discusses the motivation of this research, and current main research gaps, and subsequent research aims.

Chapter 2: Literature review provides a comprehensive overview of the challenges associated with the design of advanced bioinks for extrusion-based 3D bioprinting mode. This chapter begins with the definition of bioink and different modes of 3D bioprinting, followed by the main characteristics of bioink. Next, the chapter summarizes the strategies have

employed to overcome the challenges associated with single-component bioinks. Knowledge gaps are highlighted at the end of this chapter.

The main contribution of this chapter is to provide a compressive literature review regarding the current bioinks and highlight the knowledge gap in this area.

Chapter 3: Development of a bioink with high stability is the first results chapter of this thesis, where a bioink with high shape integrity is introduced. This bioink took advantage of the printability of methylcellulose (MC) and the permanent photo-cross-linking of Gelatin-Methacryloyl (GelMA) under UV irradiation. This chapter begins with the extensive characterization of bioink in terms of degradation kinetics, the swelling ratio, mechanical behavior, and morphological features. Following this, the chapter provides a comprehensive rheological characterization of bioink in terms of shear-thinning, self-healing, yield stress, time, and temperature sweep. Finally, the viability of human primary osteoblasts encapsulated within the MC/GelMA hydrogel was evaluated to confirm the biocompatibility of prepared bioinks and their ability to be used for practical 3D bioprinting applications.

The main contribution of this chapter is to address the poor and quick dissociation of MC-based bioinks by employing a permanent photocrosslinking method. This bioink demonstrated long-term stability in the biological media without significant dissociation. In addition, this bioink demonstrated better printing resolution and shape integrity compared to the pristine MC bioink.

Chapter 4: Employing MXene nanosheets in the 3D bioprinting is the second results chapter of this thesis, where the development of a nanoengineered bioink composed of 2D Ti_3C_2 MXene nanosheets dispersed within the hyaluronic acid/alginate (HA/Alg) hydrogel for extrusion-based 3D bioprinting is presented. In this chapter, the bioink properties are specifically formulated to achieve the synergistic effect between HA/Alg and 2D Ti_3C_2 MXene nanosheets, in which the highly thixotropic behavior of HA/Alg provides excellent printability and Ti_3C_2 MXene nanosheets improve the mechanical, rheological, electrical conductivity of the bioink. Herein, the effect of MXene dosages on the key properties of the prepared MXene HA/Alg bioink is evaluated. Next, the printability of the optimized bioink was fully investigated using rheological measurements followed by the printing of multilayered complex 3D structures to demonstrate its printing performance. Finally, the *in vitro* biocompatibility of the MXene nanocomposite ink was characterized by the LIVE/DEAD cell assay in the bulk and bioprinted structures.

The main contribution of this chapter is to introduce a nanocomposite bioink with adjustable mechanical, rheological, and electrical properties. This MXene nanocomposite bioink also have demonstrated high biocompatibility as evidenced by the high viability of encapsulated cell within both bulk hydrogel and 3D bioprinted structures. These results suggest the potential application of the developed MXene nanocomposite bioink in tissue engineering.

Chapter 5: Development of an electroconductive bioink is the third results chapter of this thesis, where the key challenges in the development of cell-laden electroconductive bioinks for extrusion-based 3D printing are addressed. The bioink is composed of PEDOT:PSS conductive polymer that dispersed homogeneously within highly thixotropic hydrogels and imparts high electrical conductivity to the bioink. It was demonstrated that the bioink can print 3D stable multilayered structures with high shape fidelity and resolution without the need for the added complexity of support baths or UV radiation.

The main original contribution of this chapter is to address the challenges associated with the poor electrical conductivity of current bioinks. The electrical conductivity of the developed bioink can be adjusted upon the change in the PEDOT:PSS dosage.

Chapter 6: Development of an antibacterial bioink is the fourth results chapter of this thesis, where a cell-laden bioink with potent antibacterial activity for skin tissue engineering applications is introduced to address the challenges associated with a bacterial infection. This challenging matter has been fulfilled by the use of gallium in the formulation of the bioink that plays dual functions; (i) First, it stabilizes the hydrogel network through the formation of ionic crosslinking with Alg chains. (ii) Second, it endows the hydrogel with potent antibacterial activity toward both gram-negative and gram-positive bacteria. Taken together the excellent printability, potent antibacterial activity, and high cytocompatibility makes it a potential candidate for skin regenerative medicine.

The main original contribution in this chapter is to introduce a novel bioink with potent antibacterial activity against both gram-negative and gram-positive bacteria while supporting cellular functions.

Chapter 7: Conclusion and Future directions first provide the summary of this thesis by highlighting the main findings obtained from the results. Next, this chapter discusses the possible future directions for perusing this work.

1.7 Format

The thesis entitled" 3D Bioprinting of Advanced Bioinks for Tissue Engineering Applications" has been prepared as a portfolio of the publications based on the requirements of The University of Adelaide. The printed and online versions of this thesis are identical.

1.8 References

[1]   a) L. G. Griffith, G. Naughton, *science* **2002**, 295, 1009; b) V. Mironov, T. Boland, T. Trusk, G. Forgacs, R. R. Markwald, *TRENDS in Biotechnology* **2003**, 21, 157.

[2]   P. Bajaj, R. M. Schweller, A. Khademhosseini, J. L. West, R. Bashir, *Annual Review of Biomedical Engineering* **2014**, 16, 247.

[3]   a) P. Sharma, P. Kumar, R. Sharma, V. D. Bhatt, P. Dhot, *Journal of medicine and life* **2019**, 12, 225; b) A. Haleem, M. Javaid, R. H. Khan, R. Suman, *Journal of clinical orthopaedics and trauma* **2020**, 11, S118.

[4]   S. Caddeo, M. Boffito, S. Sartori, *Frontiers in Bioengineering and Biotechnology* **2017**, 5.

[5]   a) K. H. Moon, I. K. Ko, J. J. Yoo, A. Atala, *Methods* **2016**, 99, 112; b) J. S. Uzarski, Y. Xia, J. C. Belmonte, J. A. Wertheim, *Current opinion in nephrology and hypertension* **2014**, 23, 399.

[6]   a) J. T. Shearn, K. R. Kinneberg, N. A. Dyment, M. T. Galloway, K. Kenter, C. Wylie, D. L. Butler, *Journal of musculoskeletal & neuronal interactions* **2011**, 11, 163; b) W. L. Lim, L. L. Liau, M. H. Ng, S. R. Chowdhury, J. X. Law, *Tissue engineering and regenerative medicine* **2019**, 16, 549.

[7]   a) R. N. Palchesko, S. D. Carrasquilla, A. W. Feinberg, *Advanced healthcare materials* **2018**, 7, 1701434; b) F. N. Syed-Picard, Y. Du, A. J. Hertsenberg, R. Palchesko, M. L. Funderburgh, A. W. Feinberg, J. L. Funderburgh, *Journal of tissue engineering and regenerative medicine* **2018**, 12, 59.

[8]   M. Baguneid, A. Seifalian, H. Salacinski, D. Murray, G. Hamilton, M. Walker, *British Journal of Surgery* **2006**, 93, 282.

[9]   J. Kluin, H. Talacua, A. I. Smits, M. Y. Emmert, M. C. Brugmans, E. S. Fioretta, P. E. Dijkman, S. H. Söntjens, R. Duijvelshoff, S. Dekker, *Biomaterials* **2017**, 125, 101.

[10]   D. P. Pacheco, N. S. Vargas, S. Visentin, P. Petrini, *Biomaterials Science* **2021**, 9, 70.

[11]   Y. K. Kurokawa, S. C. George, *Advanced drug delivery reviews* **2016**, 96, 225.

[12]   a) J. Malda, J. Visser, F. P. Melchels, T. Jüngst, W. E. Hennink, W. J. Dhert, J. Groll, D. W. Hutmacher, *Advanced materials* **2013**, 25, 5011; b) J. Groll, T. Boland, T. Blunk, J. A. Burdick, D.-W. Cho, P. D. Dalton, B. Derby, G. Forgacs, Q. Li, V. A. Mironov, *Biofabrication* **2016**, 8, 013001.

[13]   S. Ostrovidov, S. Salehi, M. Costantini, K. Suthiwanich, M. Ebrahimi, R. B. Sadeghian, T. Fujie, X. Shi, S. Cannata, C. Gargioli, *Small* **2019**, 15, 1805530.

[14]   B. K. Gu, D. J. Choi, S. J. Park, Y.-J. Kim, C.-H. Kim, *Cutting-Edge Enabling Technologies for Regenerative Medicine* **2018**, 15.

[15]   K. A. Deo, K. A. Singh, C. W. Peak, D. L. Alge, A. K. Gaharwar, *Tissue Engineering Part A* **2020**, 26, 318.

Chapter 2

Literature review

fter introducing the significance of 3D bioprinting technology in the previous
chapter, an overview of the challenges associated with the design of ideal bioinks
for extrusion-based 3D bioprinting mode is discussed in the second chapter. First,
the terminology of bioink and different mode of 3D bioprinting is provided,
followed by an introduction of hydrogels as the dominant biomaterials in the formulation of
bioinks. Next, the key characteristics of hydrogel required for 3D bioprinting applications are
discussed in detail. As the main focus of this chapter, the opposing behavior of printability and
biocompatibility of bioink were discussed through the definition of biofabrication window. As
single-component bioink cannot fulfill all required characteristics of bioink, advanced bioink
is introduced as the next generation of bioinks. Next, the current gaps in the design of an ideal
bioink are recognized that are considered as the aims of this thesis.

The outcome of this chapter is a submitted manuscript to the "Advanced Materials" journal as
follows:

" **Rastin H**, Mansouri N, Hassan K, Mazinani A, Ramezanpour M, Yap P, Yu L, Thanh Tran,
Vreugde S, Losic D, Converging 2D Nanomaterials and 3D Bioprinting Technology: State-of-
the-Art, Challenges and Potential Outlook in Biomedical Applications, Advanced Materials,
under review".

2.1 Abstract

This chapter will first define the basic of 3D bioprinting technology such as steps involved in the 3D printing process, terminology of bioink, and different modes of 3D printing technology. Next, after briefly introducing the hydrogels as the prime biomaterial candidates in the design of bioinks, This chapter will specifically focus on the requirements of ideal bioinks. This chapter will then move on to discuss why the conventional bioinks fail to fulfill the critical criteria of an ideal bioink through the definition of biofabrication window. Finally, this chapter deliberately elaborate on the different strategies that have been exploited to obtain printable bioinks without compromising the biocompatibility requirement for tissue engineering application.

2.2 The bioprinting steps

3D printing is a computer-aided fabrication method in which materials deposit in a layer-by-layer pattern to obtain a solid 3D structure. This process follows three sequential main steps; pre-bioprinting, bioprinting, and post-bioprinting maturation stages (**Figure 2.1**) [1]. In the pre-bioprinting step, the accurate 3D models of the target tissue are designed via CAD/CAM (computer-aided manufacture) software, followed by breaking into 2D layers for a 3D bioprinter. Next, appropriate material and cell sources are selected according to the target tissue. In the bioprinting step, the bioink prints the pre-designed 3D structure through the layer-by-layer deposition of bioink. Finally, in the post-bioprinting maturation stage, the printed construct allows maturing in a bioreactor.
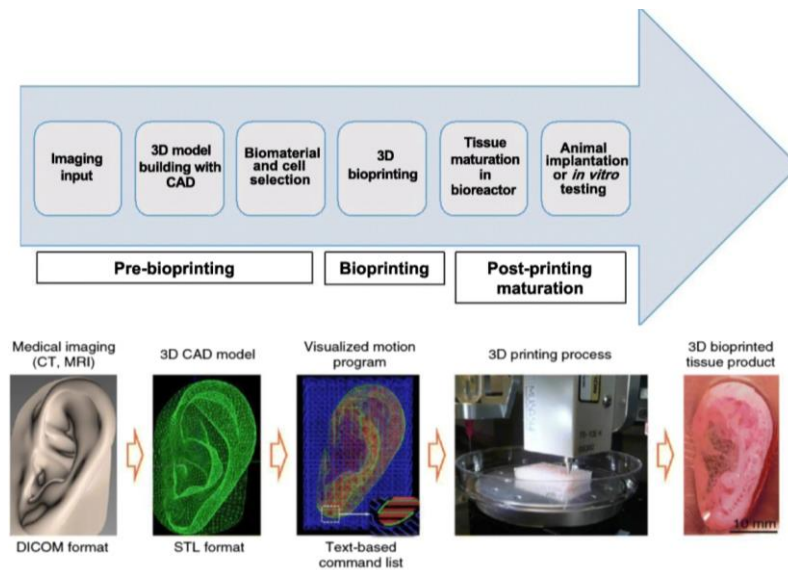
Figure 2.1. The flow diagram of steps involved in the bioprinting process [1]. Reproduced with permission [1]. Copyright (2019) Burns & Trauma.

2.3 Terminology of bioink and biomaterial ink

When it comes to bioprinting technology, it is necessary to clarify the basic definition of "bioinks" and its distinction from "biomaterial inks". As proposed by Groll et al. [2], irrespective of the type of bioprinting technology, bioinks can be defined as a formulation that must contain cells as a mandatory component before the printing process (**Figure 2.2 a**), while biomaterial ink does not directly mix with cells, and cells are seeded on the scaffold once printed (**Figure 2.2 c**). As an example of the bioink formulation, Dubbin et al. [3], developed a bioink composed of modified alginate with proline-rich peptides and a recombinant protein with the complementary peptide-binding domain. The resulting weak binding between two complementary peptide domains prevents the sedimentation of encapsulated cells (**Figure 2.2 b**). On the other hand, as an example of biomaterial ink, Liu et al. [4] printed out poly(ε-caprolactone) (PCL)/ Strontium-containing hydroxyapatite (SrHA) biomaterial ink first, after which seeded bone marrow-derived mesenchymal stem cells (BMSCs) on the scaffolds (**Figure 2.2 d**).

In the context of 3D bioprinting technology, the common biomaterials can be divided into two main groups [5]: (a) hard biomaterials such as ceramics, bioglass, and synthetic polymers that generally need high temperature or toxic solvents to be printed that makes them inappropriate for cell encapsulation. According to the above-mentioned definitions, these materials fall into the biomaterial ink category. (b) Soft biomaterials such as hydrogels are the

commonly used materials in 3D bioprinting for cell encapsulation due to their high water uptake capacity [6]. Therefore, soft biomaterials can be used in bioinks or biomaterial ink formulations. According to these definitions, bioprinting technology can be divided into two main categories based on whether or not they incorporate living cells: (i) acellular bioprinting techniques that print biomaterial inks and (ii) cellular bioprinting techniques that prints bioinks [5]. To fabricate a 3D living architecture, viable cells can directly deposit with bioinks by using cellular bioprinting techniques, which deliver some advantages. For example, the post-cell seeding procedure is avoided when using bioinks, which is a challenge for researchers. On the other hand, acellular bioprinting techniques deliver some advantages as well for tissue regeneration applications rather than cellular bioprinting techniques [7]. For example, a variety of 3D printing techniques with specific conditions (e.g. higher temperatures, chemicals, and other harsh environments) and biomaterials can be employed for the fabrications of implants or tissue [8].
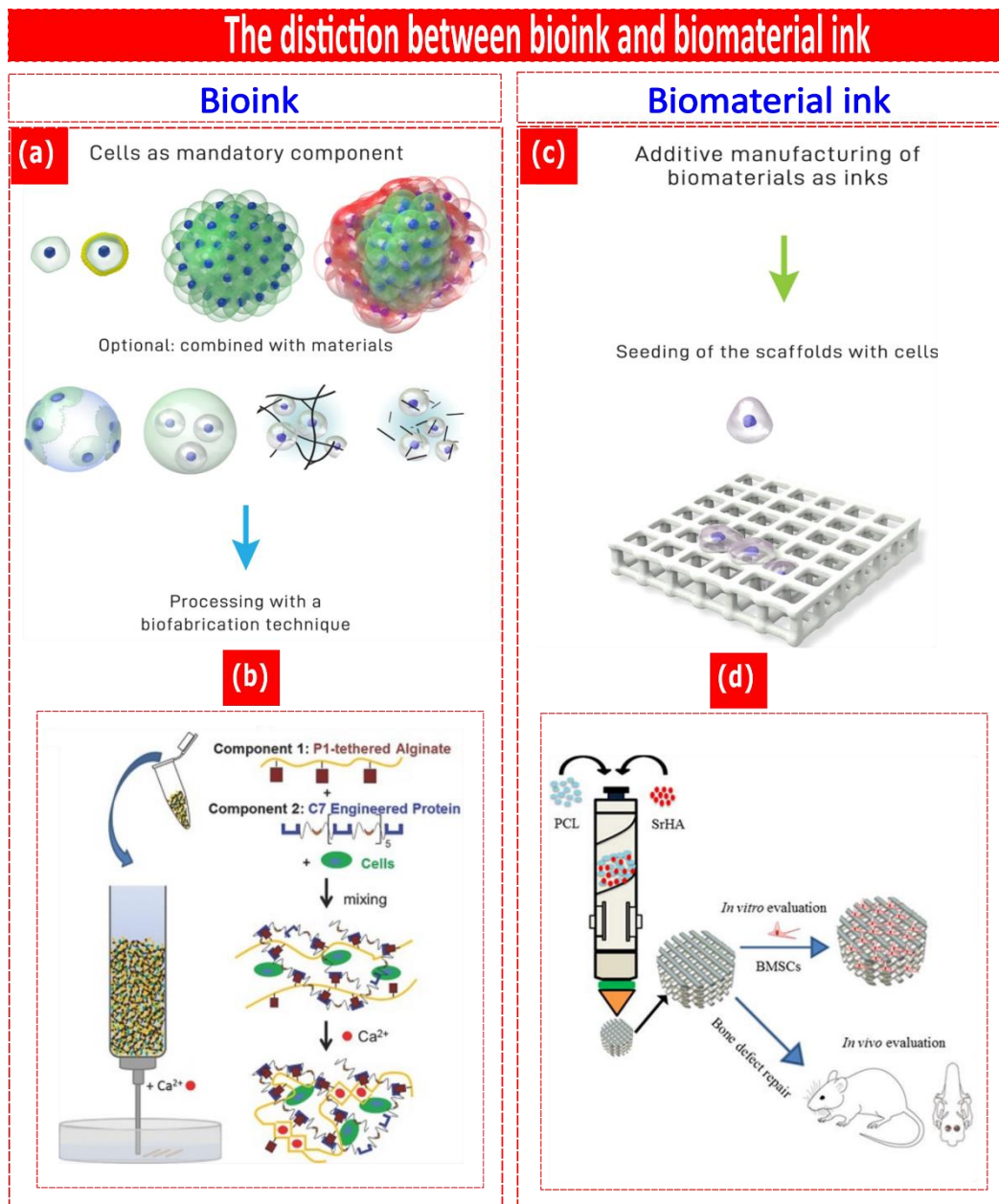
Figure 2.2. The distinction between a bioink (left) and biomaterial ink (right). (a) In the case of bioink, cells are regarded as the mandatory component of the printing formulation [2]. Reproduced with permission from ref. [2], Copyright (2018) IOPSCIENCE. (b) An example of bioink composed of modified alginate with proline-rich peptide (P1) and a recombinant protein (C7), in which NIH 3T3 cells or hASCs were encapsulated within the hydrogel [3]. Reproduced with permission from ref. [3], Copyright (2016) Wiley-VCH. (c) In the case of biomaterial ink, cells are not part of printing formulation and are just seeded after the printing process [2]. (d) An example of biomaterial ink composed of PCL and SrHA. 3D structures were

printed first, after which BMSCs were grown on the scaffold [4]. Reproduced with permission from ref. [4], Copyright (2019), Elsevier.

2.4 Different modes of 3D bioprinting technologies

Extrusion [9], inkjet [10], laser-assisted printing [11], and stereolithography [12] are the dominating modes of 3D bioprinting technology based on the working condition of bioprinting technology. These technologies have specific inherent advantages and disadvantages, which need to be carefully considered to select the best printing technology for targeted technology. These include the viscosity of ink, printing speed, resolution, cell density, and cost. Most importantly, the functions of living cells/organ architectures are also affected by the variation of available bioprinting technologies [13]. **Figure 2.3** presents schematically these printing technologies along with the advantages and disadvantages of these methods considering throughput (speed), required viscosity range, acceptable cell viability, and overall material loading. The key performances of these methods are summarized in the following section [14].

Common modes of 3D bioprinting technologies

Extrusion Bioprinting

- Ability to print high viscose inks,
- High cell density,
- Moderate cost
- Slow printing speed
- Risk of cell membrane damage
- Low printing resolution
- Occurrence of nozzle blockage

Inkjet Bioprinting

- High resolution
- Fast print speed
- Inexpensive
- Low cell destiny
- Required post-crosslinking which can potentially damage cell
- Settling of encapsulated cells
- Inability to print high viscose ink

Laser-assisted Bioprinting

Laser Pulse

Energy-absorbing layer

Bioink layer

Substrate

- High resolution
- Ability to print ink with viscosity of up to 300 mPa.s
- High cell density
- Avoided nozzle blockage matter
- Expensive
- Long printing speed
- Risk of contamination by metallic residues
- Risk of cell damage due to the heat shock

Stereolithography

Laser Pulse

Substrate

Bioink reservoir

- Inexpensive
- High resolution
- Fast print speed
- High cell density
- Avoided nozzle blockage matter
- Required large amount of bioink
- Risk of cell damage during crosslinking
- Inability to print 3D structures with horizontal gradients

Figure 2.3. Most common fabrication techniques have been used within bioprinting along with their key features.

2.4.1 Extrusion- based bioprinting mode

In the early 2000s, extrusion-based bioprinting technology was first introduced, which gained more attention among all bioprinting technologies in the fabrication of complex tissue/organs [15]. Extrusion-based bioprinter functions quite similarly to fused deposition modeling in terms of the printing process but dispensing cell-laden hydrogels, in which the bioink is pushed out through a nozzle [9]. Despite other bioprinting modes that dispense small droplets, an extrusion-based bioprinter pushes bioink filament through a nozzle in a continuous process by application of either pneumatic or mechanical forces [16]. Extrusion-based bioprinter enables the fabrication of 3D architectures by stacking 2D patterns in a layer-by-layer manner.

A notable advantage of micro-extrusion bioprinting mode is the ability to obtain high cell density similar to physiologically relevant tissues [6, 14]. In addition, 3D extrusion-based bioprinting mode has shown promise in the printing of a broad spectrum of biomaterials with viscosities ranging from 30 mPa/s up to 6×10^7 mPa/s [17]. While high-viscose bioinks can provide better printability and structural integrity, the low-viscose bioink is more beneficial for maintaining cellular functions [14, 18]. Therefore, often, researchers attempt to exploit advanced bioinks with shear-thinning behavior to fulfill both printability and biocompatibility simultaneously [19]. Shear-thinning behavior allows easy extrusion of materials along the nozzle as the viscosity of bioink drops in response to an increase in the shear rate in the nozzle [20]. Once ink exits the nozzle, the viscosity returns to its initial value and provides enough mechanical strength for subsequent layers. The high viscosity of bioink provides the initial structural integrity without the need for rapid post-crosslinking in contrast to other bioprinting modes. In addition, owing to its inherent high printing speed, this mode permits the fabrication of anatomically-relevant size tissues [21]. Taken together, extrusion-based bioprinting has become the most widespread mode, allowing the construction of anatomically-relevant size tissues within a reasonable processing time.

One of the main advantages of extrusion-based bioprinter is the ability to add an extra syringe, which realizes the printing of multiple bioinks loaded with various cell types [22]. This is highly valuable for the fabrication of complex tissue with multiple cell types and microenvironments. For example, Ozbolat et al. [23] fabricated an extrusion-based 'multi-arm bioprinter', allowing printing of multi-material within a lower time frame, while being capable to process multiple cell types simultaneously. These capabilities empower the extrusion-based printer to generate complex architectures. Lately, Liu et al. [24] proposed a swift continuous multi-material extrusion-based bioprinter, which is capable to print up to seven various kinds of bioinks without the need for switching of printing nozzles (**Figure 2.4**). The extrusion printer consists of a multi-channel, whereas each channel is connected to its bioink reservoir. The dedicated printer software is used to open the valve of each channel to diffuse various bioinks at the anticipated moment by a print head system. The benefit of this methodology is the negligible absence of an opening gap between the switching processes. As a testing procedure, they printed a range of complex 3D architectures from multi-layer cubes consisting of 2/3 various bioinks shaped as human organ structures from multiple bioinks.

One common drawback of extrusion-based bioprinter is the risk of cell membrane damage during printing, which decreases the cell viability compared to other modes [13, 21b, 25]. The mechanical shear stress inflicted on cells during printing proved to have a detrimental effect on cellular viability as well as cellular functions [25]. Although the reduction in cell viability can be diminished by using lower printing speed or larger nozzle size, it would result in a longer processing time or loss of printing resolution. Compared to other bioprinting modes, inferior printing resolution of extrusion-based bioprinting is another major drawback of this mode [26]. In addition, the blockage of the nozzle is a potential challenge in extrusion-based bioprinter once high viscose bioink is printed [14, 27].

Figure 2.4. 3D bioprinted architectures through swift continuous multi-material extrusion-based bioprinting. (a) Dual-layered cuboid block, (b) triple-layered cuboid block, (c-e) blood-vessel like constructs of dual, triple, and quadruple materials, respectively, (f) seven material-containing pyramid, (g-h) continuous segments of seven different bioinks in three- and ten-layered blocks, (i) separately printed organ-like constructs from multiple bioinks, (j-n) side views of constructs in ('i') to show 3D nature; (j) brain, (k) lung vascular, (l) kidney, (m) left atrium (heart), (n) bladder/prostate [24]. Reproduced with permission from ref. [24], Copyright (2016) Wiley-VCH.

2.4.2 Inkjet-based bioprinting mode

With superior features of inkjet bioprinting such as low cost, fast process, noncontact mode, and high resolution, extensive interest has been drawn to inkjet-based bioprinting to fabricate 3D tissue-like constructs [10]. According to its basic working process, inkjet-based bioprinting mode prints a controlled volume of discrete droplets on the printing substrate by applying external forces behind a nozzle [28]. Like extrusion-based bioprinting technology, this mode can also print different cell types [29] and materials [30] simultaneously once equipped with multiple nozzles. Inkjet-based bioprinting has demonstrated excellence in the fabrication of small-scale tissues due to its high resolution.

Inkjet bioprinting including continuous-inkjet, drop-on-demand (DOD) inkjet, and electrodynamic inkjet are more popular forms of direct bioprinting techniques [15]. In the case of continuous inkjet printing, bioink is stored in a chamber and subsequently extruded through a nozzle. This extruded stream via a nozzle breaks up into droplets owing to the Rayleigh-Plateau instability [31]. On the other hand, the DOD inkjet technique creates droplets by using thermal/piezoelectric actuators, and/or electrostatic forces, which make this technique more preferable than continuous inkjet bioprinting. Moreover, its low cost, high resolution (20–100 µm) along with the diffusion of numerous materials via multiple nozzles make this technique more advantageous. However, the DOD technique has some drawbacks as well such as selectivity of low viscous materials, longer processing time, and weak mechanical characteristics of printed patterns [7]. The third subdivision of inkjet bioprinting is electrohydrodynamic bioprinting, which exercises an electric field to drag the droplet through the orifice of the nozzle [32]. The ability to use a small diameter orifice with high concentrated bioinks uplifts this technique rather than other inkjet techniques [31].

A common drawback of inkjet-based bioprinting mode is the difficulty in the printing of high-viscose bioinks [33]. This mode is only able to print bioinks with low viscosity (<15 m.Pa/s), which requires immediate post-crosslinking by ionic [34], thermal [35], photo [36], and pH [37] crosslinking strategies to stabilize the printed structure. Post-crosslinking strategies are usually associated with excessive chemical modifications of bioink components before printing or using products or conditions that might be toxic to the cells, which can potentially deteriorate cell viability [38]. In addition, to fulfill the viscosity requirement, bioink cannot encapsulate high cell density because loading high cell density increases the viscosity and subsequently results in the blockage of the nozzle [39]. These limitations prevent its usage in the fabrication

of large-scale tissue/organs with high mechanical strength. Another drawback of inkjet-based bioprinting mode is the settling of encapsulated cells on the lower position of cartilage once transferred to the syringe, resulting from the low viscosity of the bioink [40]. Settling of cells not only results in the heterogeneous distribution of cells, but also increases the viscosity of ink placed in the lower position of cartilage and subsequently leads to the blockage of the nozzle.

The potential application of inkjet-bioprinting mode in the fabrication of functional tissues has been demonstrated by many researchers, as reviewed comprehensively elsewhere [41]. For example, Sanjana et al. [33c] demonstrated neuron adhesive patterns as a basal podium and other patterns adopting PEG (cell-repulsive material) as well as collagen/poly-D-lysine mixture (cell adhesive material) by using inkjet bioprinting technology. In addition, by using this technology, Xu et al. [42] fabricated fibrin-based 3D scaffolds, which were used to construct a 3D neural network. Later, Lee et al. [37] demonstrated artificial neural tissue fabricated by printed murine neural stem cells (NSCs) contained fibrin gel and characterized the properties of the fibrin gel on the endurance of the murine NSCs.

2.4.3 Laser-assisted bioprinting mode

Laser-induced forward transfer (LIFT) printing, also known as laser-assisted bioprinting, was first adapted for cell bioprinting in 1999 [43]. The LIFT system consists of three major parts: (i) pulsed laser sources usually work with ultraviolet (UV) or near-UV wavelengths, (ii) a donor slide (ribbon) that comprised an energy-absorbing layer (Au/Ti) on the top that responds to the stimulation of laser source and cell-containing bioink that dangled on the bottom of donor layer, (iii) a collector substrate that receives the printed material [44]. In a typical working process of LIFT bioprinting, a laser pulse focuses on the small region of the absorbing layer, where locally evaporates the absorbing layer and therefore generates a high-pressure bubble at the interface of bioink and absorbing layer. This high-pressure bubble puts pressure on the bioink to propel towards the collector substrate followed by crosslinking [44a, 45]. The resolution of LIFT and associated droplet size generally depends on the array of factors such as the thickness and viscosity of bioink, the laser pulse energy, the air gap between the donor and receiver slides, the surface tension, and the hydrophilicity of the substrate [11b, 46].

The advantages of the LIFT bioprinting mode stem from its nozzle-free working process [10a, 47]. For example, the nozzle clogging problem is avoided in LIFT bioprinting whereas other bioprinting modes often encounter nozzle clogging during printing. Moreover,

the nozzle-free process of LIFT mode avoids mechanical shear stress that cells experienced along the nozzle in other printing modes, which results in higher cell viability [44b, 48]. In addition, LIFT bioprinting can print low-to-medium viscose bioink, which broaden its usage to print a wide range of bioinks compared to inkjet-based mode. This mode also can deposit high cell density 10^8 cells/mL with high resolution by adjusting the printing parameters [11b, 49].

Despite its superior properties compared to other bioprinting techniques, there is a disadvantage as well [6a]. First, the common drawback of LIFT bioprinting mode is its long processing time, hampering the fabrication of large-scale tissue [50]. Second, the adaptation of the LIFT printing parameters is a complex process for users. Third, although the cost of the LIFT system has experienced a rapid decline, it is still a considerably expensive system compared to other bioprinting modes. Fourth, evaporation of laser-absorbing layer once irradiated by laser might leave a trace of metallic residues, imposing the risk of contamination. To address this issue, it is suggested to replace the metallic laser-absorbing layer with a non-metallic laser-absorbing layer [51]. Fifth, the laser might damage the cells due to the thermal shock [52]. Given these limitations, LIFT bioprinting is less popular compared to other printing modes.

An elaborate example of influencing parameters of LIFT bioprinting technology on skin cells (fibroblasts, keratinocytes) and human mesenchymal stem cells (hMSC) was reported [53]. They applied this printing technique on these cells because of their high potential in the regeneration of human skin as well as a possible application of stem cell therapy. They demonstrated the influence of the LIFT technique on cells by characterizing the cell's survival rate, proliferation, and apoptotic activity by monitoring for several days. It was found that both cell types remain viable during the printing procedure as the survival rate was reported 98% ± 1% for skin cells and 90% ± 10% for hMSC. In addition, no increases in apoptosis or DNA fragmentation were detected for both cell types after applied for the printing procedure. They showed in their study that, the LIFT technique can be considered as a suitable technology for computer-controlled positioning of numerous cell types and a capable tool for tissue engineering.

2.4.4 Stereolithography mode

Apart from the bioprinting methods above, stereolithography is a more remarkable bioprinting technique that uses light for the crosslinking of light-sensitive bioinks in a layer-by-layer manner [54]. In this technique, a laser/digital light projector is used over a bath of light-

sensitive bioinks to create a single printing plane [44a]. Next, the printing stage moves downward, allowing the new bioink solution to cover the printed layer and then the new layer projected on the top of the previous layer. Therefore, the printer head only needs to move in a unidirectional plane, which provides high resolution (90%) printing patterns [55]. In addition, irrespective of the complexity of the pattern, the printing time for each layer is the same because the whole pattern is projected over the printing plane, which makes this mode relatively easy to control the printing process [56].

Despite all these advantages, there are some limitations associated with the stereolithography mode, which restricted its biomedical applications [26, 57]. First, although the stereolithography printer is an inexpensive system, the need for a large amount of bioink solution imposes an additional cost. Second, the harmful nature of the UV-based cross-linking method and the risk of toxicity of photo-initiators residuals are challenges for the stereolithography users [58]. Third, UV usually involves an excessive post-crosslinking process to remove the trapped inks within the products [57]. Fourth, suitable bioinks with desired biocompatibility and biodegradable for stereolithography are lacking. However, significant progress has been made recently in the development of light-sensitive polymers suitable for stereolithography printing [12a]. Fifth, stereolithography is not compatible with the fabrications of 3D structures with horizontal gradients.

Stereolithography has been exploited for the fabrication of microfluidic architectures for organ-on-chip platforms by using transparent biocompatible polymers [59]. Since stereolithography eradicates the necessity of costly molds as well as has the benefit of swift prototyping, stereolithography-based microfluidic architecture may lead to competent commercialization of organ-on-chip platforms [60].

2.5 Hydrogels

Hydrogels are a 3D network of hydrophilic macromolecules that can absorb and preserve a large amount of water without dissolution in a swollen state [61]. The high swelling ratio of hydrogels provides an aqueous 3D microenvironment similar to that of the natural ECM for encapsulated cells [62]. Hydrogels have been widely investigated in the design of cell-laden bioinks for 3D bioprinting technologies due to their high water uptake capacity, tuneable mechanical properties, biocompatibility, and biodegradability [63]. Recent progress in the synthesis of hydrogels facilitates meticulous control over the physicochemical properties of hydrogels that make them the prime candidate for 3D printing technology [64].

Hydrogels convert from solution state to gel-like structure upon crosslinking by physical or chemical crosslinking that can be either permanent or reversible depending on the nature of the crosslinking method [65]. The physical crosslinking mechanism generally relies on the inherent chemical structure of the polymers that form a 3D network through molecular entanglements, ionic interaction, hydrogen bonding, and hydrophobic forces [66]. Despite the simplicity of this crosslinking method, it suffers from poor control over the hydrogel network [67]. By contrast, chemical-crosslinked hydrogels are generally achieved through the permanent covalent linking of separate macromolecular chains [68]. The chemical crosslinking method provides more stable and tune-able 3D networks compared to the physically crosslinked hydrogels.

According to the source, hydrogels can be alternatively divided into two major classes [69]: (1) natural hydrogels (collagen, gelatin, Hyaluronic acid, alginate , etc.), and (2) synthetic hydrogels (Polyethylene glycol, poly(lactic-glycolic)acid (PLGA), Pluronic, etc.). The two classes of hydrogels possess certain advantages and disadvantages that deserved to be considered once designing for the target application [70]. For example, natural-derived hydrogels have the advantage of better biocompatibility that can closely replicate the ECM, while synthetic-derived hydrogels provide better tune-ability over the ultimate properties of the hydrogel network [69].

2.5.1 Natural hydrogels

Gelatin, methylcellulose, alginate, hyaluronic acid, kappa-carrageenan are typical examples of natural hydrogel that have been widely employed in the design of bioink formulation [69]. Hydrogel with natural origin can be sub-categorized into two main distinct groups; protein-based materials and polysaccharide-based materials.

2.5.1.1 Protein-based materials

Gelatin is an example of protein-based hydrogels that derives from denaturing the triple-helical conformation of collagen [71]. It is a soluble biopolymer in warm aqueous solutions that undergoes sol-to-gel transition at lower temperatures. Gelatin hydrogels have been extensively explored in a variety of biomedical applications such as drug delivery, tissue engineering, and wound dressing owing to the set of favorable characteristics [71]. For example, Gelatin proved to promote cell adhesion and proliferation due to the presence of Arginine-Glycine-Aspartic acid (RGD) motif along its backbone [72]. Compared to collagen, gelatin has exhibited relatively lower immunogenicity with higher water uptake capacity [73]. In addition,

gelatin carries different functional groups along its backbone that facilitate the chemical modification of gelatin for the target applications. Gelatin-methacryloyl (GelMA), a commonly used derivative of gelatin, has been extensively investigated in the design of bioink for 3D bioprinting technology owing to its photo-crosslinking ability and inherent biocompatibility [74]. GelMA can be obtained from the reaction of gelatin and methacrylic anhydride in phosphate buffer (pH = 7.4) solution at 50 °C, in which the reactive amines are substituted with methacryloyl moieties (**Figure 2.5**) [75].
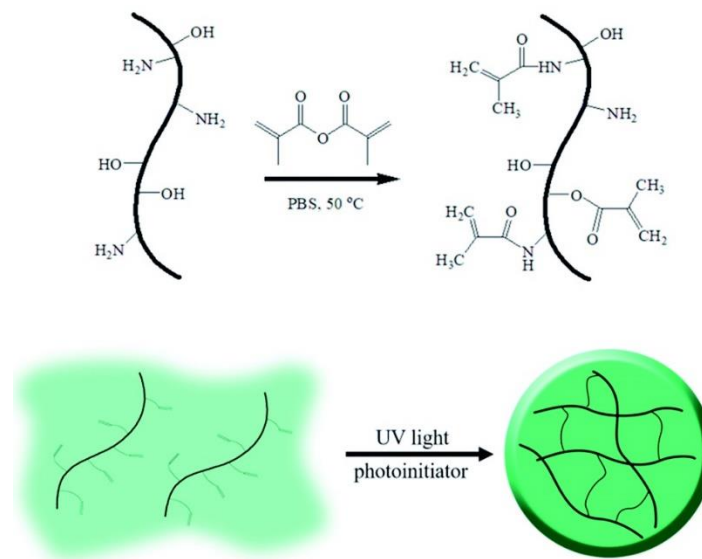
Figure 2.5. Synthesis of GelMA through the reaction of gelatin and methacrylate anhydride. Irradiation of UV light enables the fabrication of 3D network [75]. Reproduced with permission from ref. [75], Copyright (2019) Royal Society of Chemistry.

2.5.1.2 Polysaccharide-based materials

Alginate (Alg) is a well-known copolymer polysaccharide that has widely exploited in bioprinting technology due to the set of favorable features such as biocompatibility, biodegradability, tuneable characteristics, hydrophilicity, porosity, and ionic crosslinking [76]. It is composed of mannuronic acid (M) and L-guluronic acid (G) units in different ratios, forming brittle hydrogel upon the introduction of multivalent cations. This results in the linking of separate alginate chains through the formation of an "egg-box" 3D network [77] (**Figure 2.6**). However, alginate hydrogel comes with some drawbacks. For example, it dissociates in the biological media over time due to the ion-exchange processes that disrupt the physical crosslinking of alginate chains with crosslinker. In addition, alginate hydrogel

suffers from the lack of cell-adhesion domains and the risk of inflammation associated with the release of calcium ions [78].
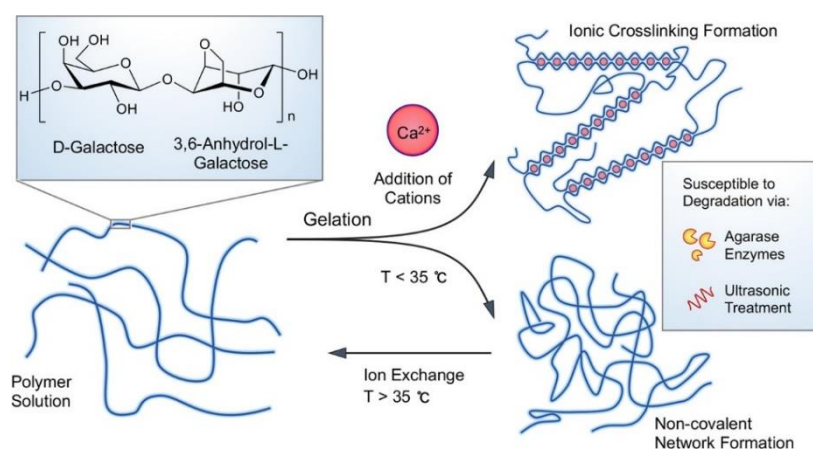
Figure 2.6. Schematic illustration of alginate chemical structure. Alginate undergoes a sol-to-gel transition once exposed to divalent cations through the formation of egg-box like 3D network [78]. Reproduced with permission from ref. [78], Copyright (2019) American Chemical Society.

Methylcellulose (MC) is a water-soluble biopolymer isolated from cellulose by partial substitution of hydroxyl groups with methoxy groups [79] and shows sol-gel transition around 37 °C, which is related to the change from a hydrophilic to a hydrophobic nature [80]. It was shown that single-component MC hydrogel could be easily printed at 21°C with more than 80% cell viability, while rough strands containing voids were observed at lower or higher temperatures [81]. Despite the suitable properties of MC for 3D bioprinting, the lack of a post-crosslinking method causes dissociation of MC in biological media. Given this, MC has been used as a printable component in combination with other polymers, which act as viscosity-enhancing agents. In the multi-component MC-based hydrogel for a 3D bioprinting application, a blend of alginate/MC bioink has been introduced, in which alginate serves as a post-crosslinking agent in the presence of calcium chloride solution [82]. Moreover, treatment of alginate/MC with trisodium citrate as a chelating agent improved the adhesion between printed layers resulting in better stackability.

Kappa-Carrageenan (κCA) is a negatively charged sulfonated polysaccharide, obtained from red algae, which is widely used as a thickening agent in the pharmaceutical and food industry[83]. It exhibits stiff gel behavior once undergoes gelation in the presence of potassium ions, which offers enough mechanical strength for supporting cells [84]. Moreover, from the rheological point of view, κCA possesses shear-thinning behavior and can be a promising

candidate in 3D bioprinting applications [21a, 85]. Given this, κCA has been blended with multiple biomaterials to generate shear-thinning bioink for extrusion-based 3D bioprinting. Accordingly, bioinks composed of κCA are benefited by good cell viability and attachment.

Hyaluronic acid (HA) is a non-sulfated glycosaminoglycan, composed of alternating glucuronic acid and N-acetyl-glucosamine saccharides that exist in the natural ECM [86]. HA hydrogel forms a viscose hydrogel with shear-thinning behavior once dissolved in water, suitable for 3D bioprinting applications [87]. HA hydrogels have the advantage of inherent bioactivity and promoting cell growth, proliferation, and differentiation. Although HA hydrogels have exhibited high cell viability and favorable tissue integration, it suffers from the poor cell adhesion and quick dissociation in biological media. Given this, it is typically functionalized by different functional groups such as methacrylate or thiol [88].

2.5.2 Synthetic hydrogels

Synthetic hydrogels are benefited by better control over mechanical strength, relatively easy processing, and chemical modifications [70]. This class of hydrogels can address the challenges associated with natural hydrogels in 3D bioprinting. However, immune reaction, high chances of infection, and the effect of degradation by-products are the drawbacks of synthetic hydrogels [89]. To overcome these challenges, synthetic hydrogels are typically modified with cell adhesion peptides or blend with other natural-derived hydrogels [90].

2.6 Key design characteristics of bioink

Lack of ideal bioink remains a challenging matter in the translation of 3D bioprinting technology to clinical applications. Recent studies reveal that the ideal bioink should meet specific chemical and physicochemical requirements to provide a cell-friendly microenvironment for the encapsulated cells during and after the printing process [70]. Here, the key characteristics of hydrogel required for 3D bioprinting applications are discussed in detail.

2.6.1 Rheological properties

Rheology is a powerful tool to quantify the flow behavior of the hydrogel under external stress [19b, 91]. Rheological studies reflect the flow behavior of the bioink at different stages of the printing process. Literature has demonstrated that the rheological characteristics of cell-laden bioink strongly impact the function of encapsulated functions such as spreading, proliferation, and differentiation [92]. Thus, meticulous tuning of the rheological behavior of a bioink is critical to a successful 3D bioprinting process. In an extrusion-based 3D bioprinting

process, bioink passes through a thin nozzle by applying mechanical pressure behind the syringe. The application of high shear stress along the nozzle might be detrimental to the viability of encapsulated cells, thus shear-thinning hydrogels with quick recoverability are advantageous to the 3D bioprinting process [93]. Overall, rheological behavior governs the printability of inks, which deserves careful modulation to attain high resolution.

2.6.1.1 Viscosity

The viscosity of bioink determines the shape fidelity of bioink once printed and directly impacts the fate of encapsulated cells [17c]. Inks with high viscosity benefit from better shape integrity with the ability to print taller constructs [91b, 94]. However, blockage of the nozzle is more likely to happen when printing high viscose inks, which can disrupt the printing process. Additionally, inks with higher viscosity deliver high shear stress to the encapsulated cells during the printing process that can potentially diminish the cell viability and directly change the cell's functions such as proliferation, expression of genes, and proteins [17b, 25, 95]. In contrast, the relatively low viscosity of hydrogels results in poor control over the shape retention of hydrogel once printed, while provides a better microenvironment for cell proliferation, migration, and tissue formation. In addition, the viscosity of bioink determines the shapes of the ink once expelled from the nozzle. Relatively low viscosity bioink form droplet at the needle tip, while the bioink high viscosity forms continuous filament shape.

2.6.1.2 Shear-thinning behavior

Bioink experiences a high shear rate once extruded along the nozzle that might deteriorate the viability of encapsulated cells. Thus, shear-thinning hydrogels have been widely exploited in the design of bioink due to their ability to alleviate the application of shear stresses on cells once extruded along the nozzle [93]. The viscosity of shear-thinning hydrogels drops upon increasing the shear rate, thus shield the encapsulated cells from disruption as well as smooth extrusion along the nozzle. Recent studies reveal that the inclusion of laponite into ink formulation allows the modulation of the rheological properties (**Figure 2.7**) [21a, 85b, 96]. Accordingly, the addition of laponite to κCA endow thixotropic behavior to the ink as evidenced by the decrease in the viscosity upon increasing shear rate (**Figure 2.7 b**). This is recognized as the pre-requisite feature for the successful printing of complex 3D structures. In addition, cell viability depends on the duration and level of shear stress during extrusion, thus careful consideration should be taken to adjust the printing parameters (pressure, temperature, printing speed, nozzle diameter) [17b, 25, 95]. Power-law model ($\eta = K\gamma^{n-1}$) is the most commonly

used model to quantify the shear-thinning behavior of the hydrogels under external stress, where η denotes the viscosity, γ is the shear rate, n is the flow index and K is the consistency index. In the case of fluid with Newtonian behavior, the power-law index is one, while the power-law index is lower than one for fluid with shear-thinning behavior. As seen in **Figure 2.7 b**, the power-law index is lower than one for all prepared formulations, showing the shear-thinning behavior of the bioink.

2.6.1.3 Recoverability

Once the extruded material exit the nozzle, the quick and high structural recovery is critical to avoid spreading of the printed stands on the printing stage [97]. Thus, in addition to shear-thinning behavior, material-forming bioink should exhibit a quick transition from fluid-like behavior to a solid-like state and recover its rheological properties after removing the stress. To quantify the extent of recoverability of the bioink, two approaches have been widely employed [98]. First, changes in the storage (G') and loss modulus (G'') of the material-forming bioinks are monitored upon series of repetitive low and high strain in an oscillation mode. In the second method, bioink undergoes a high shear rate for a short time, and recovery of the viscosity is considered as the recoverability of the bioink [99]. This method simulates the deformation of the bioink experienced during the printing process. **Figure 2.7 c** presents the recoverability of the laponite/κCA bioink over applying alternating low and high strains. Accordingly, the incorporation of laponite imparts high recoverability to the bioink [21a].
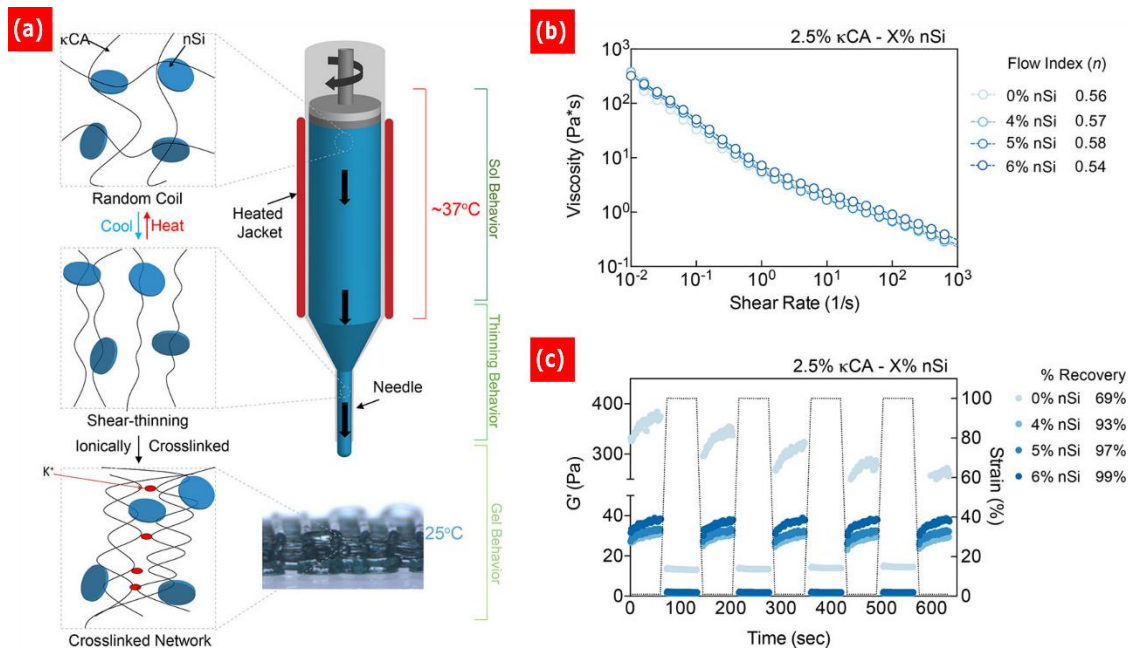
Figure 2.7. (a) A schematic illustration of laponite/κCA's bioink during different stages of 3D printing process. (b) The shear rate sweep test confirms the shear-thinning behavior of the Laponite/κCA bioink. The power-law model index is lower than one for all prepared formulations. (c) The recoverability of the bioink over applying alternating low and high strains [21a]. Reproduced with permission from ref. [21a], Copyright (2017) American Chemical Society.

2.6.1.4 Yield stress

Bioinks should exhibit sol-like behavior during extrusion with low viscosity to protect cells from the application of high shear stress. Once printed, bioink should display solid-like behavior with high self-supporting behavior to prevent the collapse and spreading to the neighboring [19b]. To examine these opposing rheological behavior of hydrogel, it is critical to monitor the storage and loss modulus of the hydrogel via oscillatory rheology. The G' reflects the elastic shape retention of hydrogel while G'' is associated with the viscous flow. In addition to the G', yield stress reflects the shape retention behavior of the hydrogel. Yield stress is defined as the minimum force required to put on fluid for initiation of flowing [100]. Thus, bioinks should overcome the yield stress to initiate flowing along the nozzle. Both G' and yield stress depend on the hydrogel network, the molecular weight of the polymer, and degree of physical entanglement within the network. In other words, the G' and yield stress dictates whether the printed structure collapse or remaining intact after the printing process. Higher yields stress of bioink means better shape integrity of the printed construct, however, it equals higher required pressure for extrusion of the material. **Figure 2.8** presents the changes in the

G' and G'' values over shear sweep, indicating the yield stress point shift toward lower values upon addition of laponite to the κCA [21a].
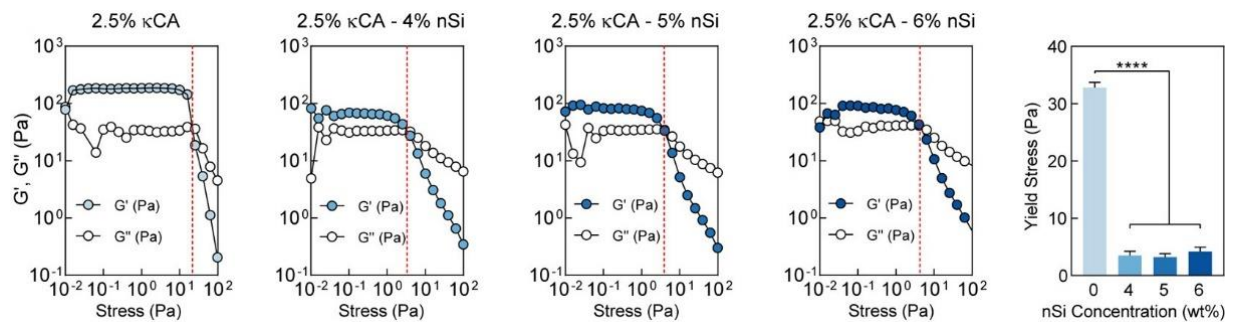
Figure 2.8. Monitoring the variation of G' and G'' over shear stress sweep to obtain the yield stress. Accordingly, yield stress decreased upon addition of Laponite to the κCA [21a]. Reproduced with permission from ref. [21a], Copyright (2017) American Chemical Society.

2.6.2 Electrical properties of bioinks

The electroconductive scaffold has been enormously exploited in tissue engineering [101], drug delivery [102], and biosensing [103]. Electroconductive scaffolds can replicate the electrical properties of the target tissue, enabling the stimulation of the cells for improvements in their growth, differentiation, and migration [104]. Current bioinks usually consist of polymers with a poor electrical conductivity that restricts their application in the regeneration of excitable tissues [105]. The development of conductive bioink has been investigated to attain materials with close similarity to the native tissue microenvironment for tissue engineering application [106]. Attributed to the high electrical conductivity of some NMs, the integration of NMs into the insulating polymers, even at a very low concentration, is found to impart improved electrical conductivity to the inks [104]. Due to the outstanding electrical conductivity of graphene, recent studies have attempted to develop new electroconductive bioinks for nerve, muscle, and cardiovascular tissue engineering. For example, Jakus et al. [104b] fabricated graphene-based composite scaffolds using an extrusion-based 3D printer with excellent biocompatibility, robustness, and electrical conductivity (more than 800 S/m), as shown in **Figure 2.9**. The potential effect of this conductive graphene scaffold was investigated on human mesenchymal stem cell behavior (hMSC) for neural tissue engineering applications. It was demonstrated that graphene-based scaffolds supported hMSC attachment, viability, and proliferation. Moreover, the printed scaffolds (with a diameter of 4 mm) induced neurogenic differentiation with noticeable upregulated glial and neuronal gene expressions. *In vivo*

experiments validated excellent biocompatibility without any inflammatory response over 30 days in a mouse model as well as the capability of the prepared scaffolds for surgical handling which holds great potential for electrogenic tissue regeneration. In other work, the 3D printing technique was integrated with microfluidic spinning to fabricate 3D GO scaffolds with tunable fiber diameter and structure [107]. Then, the hydrothermal reduction was used to obtain conductive rGO microfibrous scaffolds. The prepared 3D graphene-based scaffolds with excellent electrical properties demonstrated suitable biocompatibility on SH-SY5Y cells. However, cells grown on GO scaffolds showed better cell attachment and proliferation compared to those of rGO. Moreover, the conductive rGO scaffolds successfully induced the cell alignment along the fiber axis, which could be effective in tissue engineering of the central nervous system and myocardial repair. In another study, graphene was incorporated into Poly(trimethylene Carbonate) to improve the mechanical and electrical properties of the scaffold [108]. The 3D-printed conductive scaffold with enhanced tensile strength accelerated adipose-derived mesenchymal stem cell (MSC) proliferation and upregulated osteogenic markers. The excellent biocompatibility and processability of the composite 3D scaffolds make them a promising material for biomedical applications. Moreover, applying electrical stimulation on cell-loaded scaffolds showed an enhancement in Col I and ALP gene expressions.
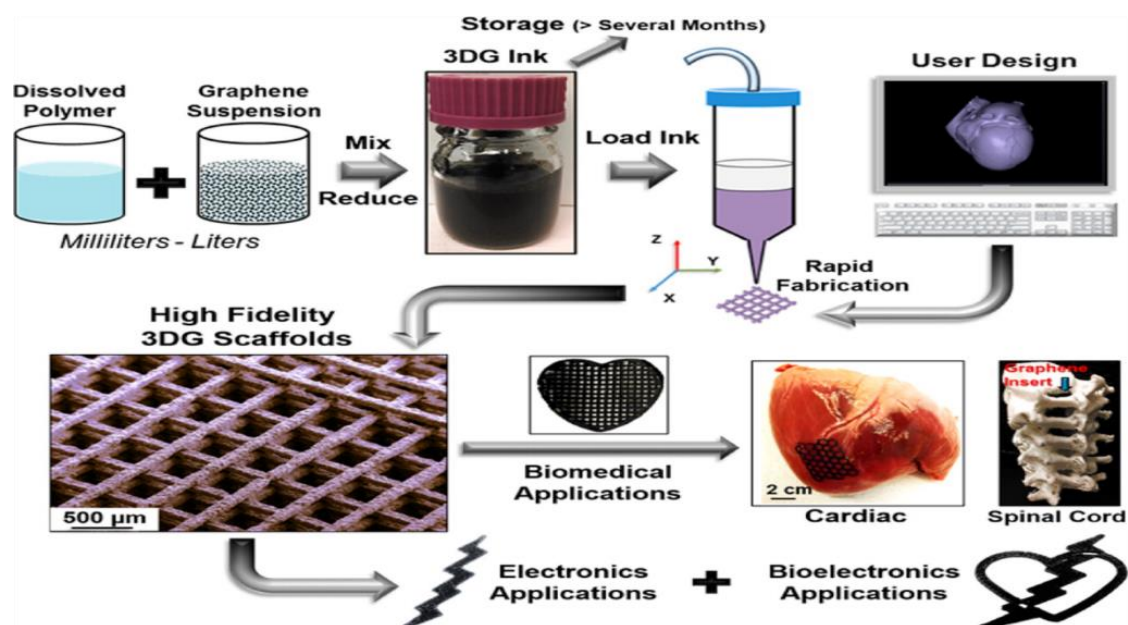
Figure 2.9. Impart the electrical conductivity into the biomaterial ink using graphene nanosheets. The simple physical blending of graphene and elastomer solution enables to print

3D structures suitable for tissue engineering and bioelectronics applications [104b]. Reproduced with permission from ref. [104b], Copyright (2015) American Chemical Society.

2.6.3 Antibacterial activity

Despite aseptic procedures during the implantation, the risk of bacterial infection at the implantation site remains a prominent challenge to the field [109]. The antibacterial activity can be endowed to a hydrogel by the encapsulation of antibiotics in the hydrogel network [110]. However, the antibacterial activity of the materials is likely to disappear after the full release of antibiotics [111]. In addition, resistance towards conventional antibiotics is another concerning issue that urgently calls for more alternative antibacterial materials [112]. Thus, designing implants with inherent antibacterial properties is highly in demand and valuable to avoid implant rejection [109b, 113]. NMs with inherent antibacterial properties are the focus of many researchers, revealing their exceptional antibacterial performance resulting from their intrinsic physicochemical characteristics [114]. For example, Zhang *et al.* [115] coated the 3D printed β-TCP bioceramic scaffolds with silver (Ag)/GO (named as Ag@GO) particles to confer the antibacterial activity to the scaffold. The scaffolds exhibited improved osteogenic differentiation of rabbit bone marrow stromal cells evidenced by the higher ALP activity and the expression of bone-related genes. In addition, the scaffold exhibited potent antibacterial activity against *E. coli* thanks to the released of silver ions. In another study [116], it was shown that incorporation of GO into PCL biomaterials ink improves the antibacterial activity of scaffold significantly in a concentration and time-dependent manner. Accordingly, around 80% of adherent *S. epidermidis and E. coli* bacteria on the printed scaffold were found dead after 24 hours of exposure at 7.5 wt.% of GO (**Figure 2.10**).
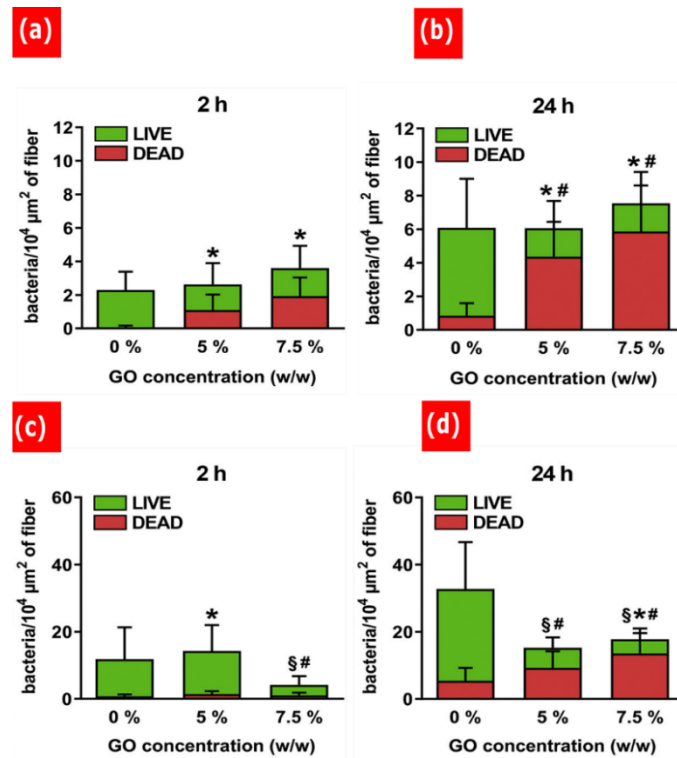
Figure 2.10. Improve the antibacterial activity of PCL biomaterial ink upon addition of GO. Percentage of live and dead *S. epidermidis* (a, b) and *E. coli* (c,d) bacteria adhered to the PCL scaffolds after 2 h and 24 h incubation [116]. Reproduced with permission from ref. [116], Copyright (2020) Elsevier.

2.6.4 Enhanced tissue formation

To replace the injured tissue with a functional scaffold, it is critical to provide an appropriate microenvironment for cell survival and growth [101a, 117]. According to the previous reports, graphene family materials have shown the prospective potential to regenerate and recover bone, neural, cardiac, cartilage, and liver tissues with the aim of future clinical applications [118]. Thus, many researchers attempt to develop graphene-containing inks to improve the cellar functions for tissue regeneration purposes. For example, Zhou et al. [119] prepared a photo-crosslinkable PEGDA-GelMA ink loaded with various concentrations of GO that were printed using stereolithography-based bioprinters (**Figure 2.11**). The prepared biocompatible were assessed for cartilage tissue engineering applications, showing that human bone marrow mesenchymal stem cell proliferation rate increased upon addition of GO, with the highest rate in 0.1 mg/mL of GO. This is attributed to the higher level of protein absorption on the scaffold surface caused by GO nanosheets. In another study conducted by Cheng et al. [120], it was demonstrated that the GO-embedded collagen/chitosan bioink blocked the

Rank/Rankl/OPG pathway and subsequently regenerated the cartilage. In another study [121], it was demonstrated that the addition of GO nanosheets into the formulation of alginate-based bioink not only contributes to the printability but also endows osteogenic differentiation due to the higher absorption of osteogenic inducers on GO nanosheets. In addition, it can enhance the viability MSCs in an oxidative stress environment, thanks to the antioxidant property of the GO and scavenging reactive oxygen species (ROS).
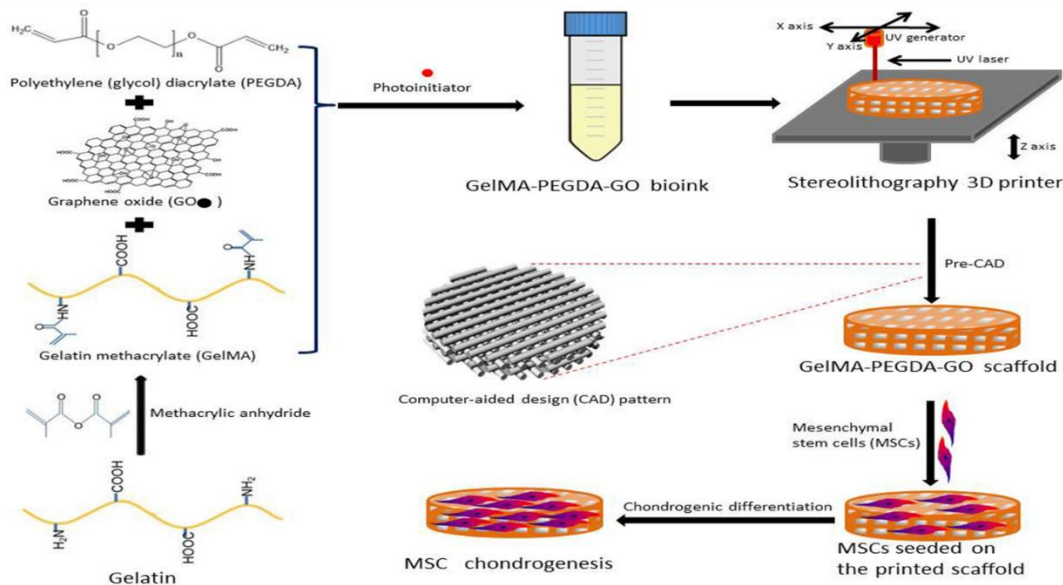
Figure 2.11. Enhanced chondrogenic differentiation of hMSCs upon addition of GO into PEGDA-GelMA biomaterial ink [119]. Reproduced with permission from ref. [119], Copyright (2017) Elsevier.

2.6.5 Mechanical strength

Engineering the mechanical properties of inks that can replicate the native tissue is found to be consistently challenging to the field as their performance relies significantly on their mechanical properties [14, 122]. Thus, designing advanced bioinks with adjustable mechanical properties is of great interest to facilitate the regeneration of functional tissue [14]. Given this, Guiney et al. [123] have developed high content hBN-embedded PLGA ink where the mechanical and thermal properties of the ink were tunable upon the change in the content of HBN (**Figure 2.12**). The 3D printed structures exhibited high flexibility as can be cut, folded, or rolled immediately after printing without collapsing. The tensile testing results show that the elongation to failure of 3D printed structure increases upon increasing the hBH till 60 vol.% then experienced a significant drop (**Figure 2.12**). In addition, evaluations of cytocompatibility of the scaffold show the high viability and proliferation of hMSCs on scaffolds over four

weeks. Similar enforcement effects of HBN have also been reported elsewhere that incorporated into the Polyvinyl Alcohol/Bacterial Cellulose biomaterial ink [124]. More recently, the *in vitro* effectiveness of HBN-containing ink on bone tissue regeneration was investigated and showed that the even small addition of exfoliated HBN into PLA favored the attachment, proliferation, and differentiation of cells with osteogenic potential [125]. They reported that printed PLA/hBN scaffolds have a higher rate of cell attachment and proliferation compared to pristine PLA scaffolds. In addition, the evaluation of mineralization activity of pristine PLA and PLA/hBN scaffold shows that the latter has a significantly higher amount of calcium deposition after three weeks.
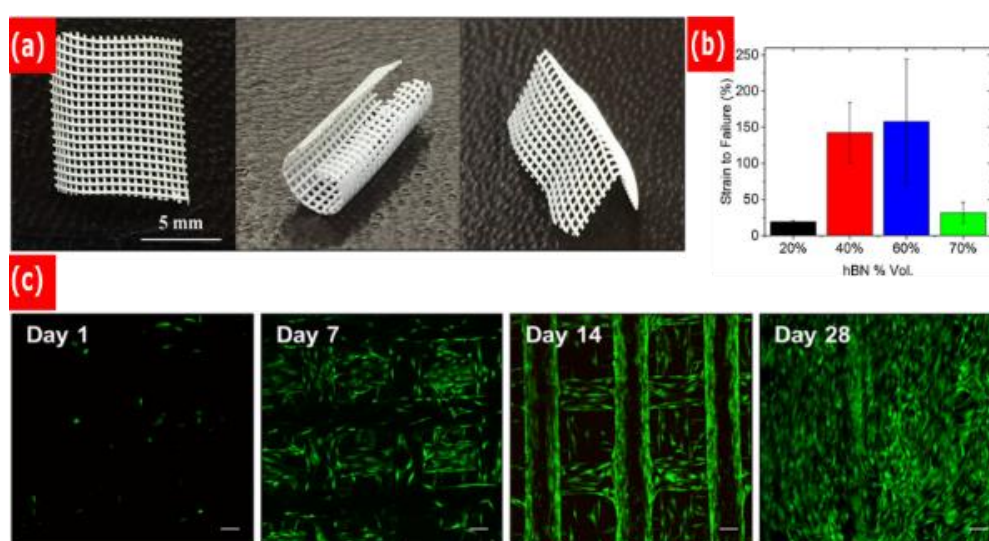
Figure 2.12. Enhanced flexibility of the 3D printed biomaterial ink upon addition of hBN. (a) Images taken from 3D printed 40% vol hBN. (b) Strain to failure results of 3D printed structure with varying amounts of hBN. (c) Cytocompatibility of hMSCs seeded on the 40% volume hBN scaffold at different time intervals [123]. Reproduced with permission from ref. [123], Copyright (2018) American Chemical Society.

2.6.6 Durability

After printing, the bioinks should support the long-term stability of 3D printed structure in the physiological media [64, 94b, 126]. In general, conventional hydrogels suffer from poor mechanical properties, making them unsuitable for certain tissues that possess a higher toughness [38]. The mechanical properties of hydrogels are generally regulated by the manipulation of the monomer and crosslinker concentrations [38]. The crosslinking procedure plays a crucial role in determining the mechanical and physicochemical properties of 3D

printed construct and subsequently matters for the regulation of cellular activity [76a]. Hydrogel bioink can be crosslinked in a variety of ways depending on the nature of the polymer and the existing functional groups [127] [128]. Physical and chemical crosslinking methods are the two most commonly used crosslinking methods, however, both may be combined to achieve advantageous properties [129]. Physical cross-linking occurs when polymer chains interact non-covalently and reversibly. For example, with the addition of divalent cations such as calcium, barium, and strontium to alginates, strong hydrogels can be formed via the coordination of divalent cations through two adjacent G-blocks [130]. Despite this, chemical cross-linking refers to the formation of an irreversible covalent bond between polymer chains[38]. The photo-crosslinking approach, for instance, is the most commonly used chemical crosslinking technique in the 3D bioprinting of methacrylated hydrogels like GelMA and PEGDA [9d, 131]. Photo-crosslinking can take place either during or after extrusion, in which the photoinitiator is exposed to light to initiate the reaction [132]. DNA undergoes changes when exposed to UV radiation, as evidenced by numerous studies, thus, many researchers have investigated photoinitiators that absorb near-UV or visible light wavelengths [133]. Hydrogels that are crosslinked through physical methods are typically softer than those that are crosslinked chemically. Although soft matrices appear to have better cell viability than stiffer systems, shape fidelity is relatively inferior [38].

2.7 Biofabrication window

The primary aim of 3D bioprinting is to fabricate a functional tissue-like structure that can replicate the complexity of the extracellular matrix of the native tissue microenvironment. In such a 3D printed scaffold, the cell-matrix interaction facilities matrix remodeling and extracellular matrix (ECM) synthesis. The rational design of bioink can provide a suitable microenvironment to control the cellular functions including adhesion, migration, proliferation, and differentiation [97]. Thus, the design of a bioink with suitable properties is the primary step for 3D bioprinting. As mentioned, hydrogels possess a set of desirable properties including cytocompatibility, tuneable rheological behavior, quick gelation kinetics, high water uptake capacity, and porosity that makes them an excellent candidate for the design of bioink [134]. In terms of biocompatibility, naturally-derived hydrogels can provide more cell-friendly microenvironments due to the presence of cell-adhesion domain along their chemical structure, whereas the synthetically-derived hydrogels have poor cell-binding sites [70]. On the other hand, bioink composed of synthetically-derived hydrogels can print 3D structures with higher shape

fidelity compared to the naturally-derived hydrogels. Convectional bioinks generally are composed of single component natural or synthetic hydrogels that suffer from poor biocompatibility or printability [18]. However, the single-component hydrogel is not able to fulfill all required properties for the design of an ideal bioink for extrusion-based 3D bioprinting technology. The biofabrication window shows the opposing relationship between printability and cytocompatibility of cells within the 3D printed structure (**Figure 2.13**). Accordingly, the properties that can improve the cytocompatibility of bioink, usually deteriorate the printability [18]. For example, increasing the hydrogel concentration can typically provide higher shape fidelity while such hydrogel network is not appropriate for cell survival and migration [135]. To achieve an ideal bioink, it is necessary to meet these opposing requirements by developing advanced bioinks. Several strategies have been employed to achieve advanced bioinks with both printability and cellular compatibility simultaneously [18].
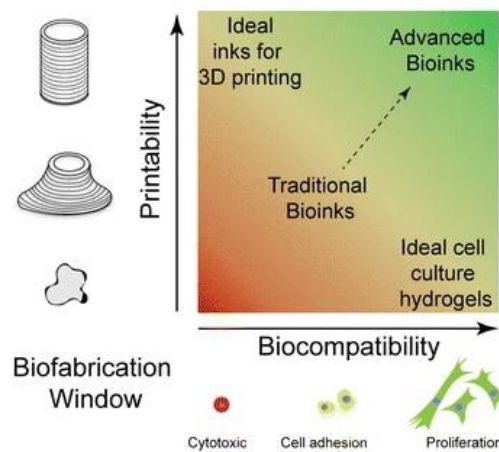
Figure 2.13. The biofabrication window for the design of advanced bioink to meet both printability and biocompatibility simultaneously [18]. Reproduced with permission from ref. [18], Copyright (2016) Springer.

2.7.1 Assessment of Printability

Bioink development requires a rigorous evaluation of printability. While "printability" is frequently mentioned in biofabrication publications, there is no definitive agreement on the definition of what "printable" material is [136]. According to Gillispie et al, printability is "the ability of a material, when subjected to a certain set of printing conditions, to be printed in a way which results in printing outcomes which are desirable for a given application" [137]. In light of this, evaluation is often conducted according to various aspects of printing, thereby making ink comparison challenging [138]. When it comes to extrusion-based bioprinting,

printability encompasses a number of dimensions, including extrudability, filament formation, and shape integrity. Shape fidelity, also often referred to as print accuracy, is used to quantify the difference between the printed construct and the original computer graphic. Bioinks with poor shape integrity may move to neighbouring areas and may collapse as more layers are added to the geometries. Due to the inability of the bioink to maintain the fiber integrity, pores may be compromised. Paxton et al.[19b] have suggested a two-step approach for the evaluation of printiability of bioink in extrusion-based bioprinting. In the first step, a manual material dispensing procedure was used to initially screen the material's probability based on filament formation, layer stacking, and merging layers after dispensing. As a consequence, this step provided a fairly thorough evaluation of the printing abilities of a material, since it covered three of the most important bioink properties: yield stress, shear thinning and recovery after dispensing. These criteria are then evaluated via rheological evaluations as the second step.

2.7.2 Effect of printing process on cellular functions

A good understanding of bioink-cell interactions and how the cells might be stimulated by the bioink is an essential step in the development of bioink. It is also crucial to measure the effects of shear forces and degradation products on cellular processes [139]. As encapsulated cells within bioink pass through the thin nozzle, they suffer from shear forces that can adversely affect their viability, adhesion, and proliferation[140]. Shear stress was demonstrated to have a significant impact on cell phenotype and functionality. As an example, articular chondrocytes can undergo significant morphological and metabolic changes at 1 Pa shear stress [141], while human mesenchymal stem cells (hMSCs) can tolerate shear stresses up to $1 * 10\text{-}5$ Pa without changing messenger RNA expressions of osteocalcin, Runx2, and alkaline phosphataste[142]. Along with the cellular viability, it is necessary to monitor the cellular functions such as adhesion, proliferation, and/or differentiation. As the cells proliferate in the bioink, they begin to deposit ECM, which is mainly composed of proteins, glycoproteins, and proteoglycans [143]. Thus, examining the deposited matrix and measuring the protein content can provide further insight into how cells behave within bioink.

Researchers have shown that the printing pressure behind the nozzle has a much greater impact on cell viability than the diameter of the nozzle. At higher pressure behind the nozzle, shear stress rises exponentially which results in an exponential drop in the percentage of living cells [17b]. The geometry of the needle also affects cell viability besides its diameter and extrusion pressure. Compared to cylindrical needles, conical needles are advantageous since

they require lower printing pressure. Thus, tapered needles require less pressure compared to cylinder needles to achieve the same flow rate [144]. The printing pressure determines the printing speed and in turn has a direct effect on cell viability. Generally, higher printing speeds result in lower cell viability due to a higher extrusion pressure [145]. Therefore, it is necessary to optimize the printing speed to minimize the negative effects of shear stress on cell viability.

2.8 Advanced bioink

Since single-component hydrogel cannot satisfy all requirements for the rational design of bioink, multiple strategies have been employed to obtain advanced bioinks to overcome the challenges associated with conventional bioinks. Generally, advanced bioink can be classified into four major groups: multi-material, interpenetrating networks, nanocomposites, and supramolecular bioinks that will be discussed in detail below (**Figure 2.14**) [18].
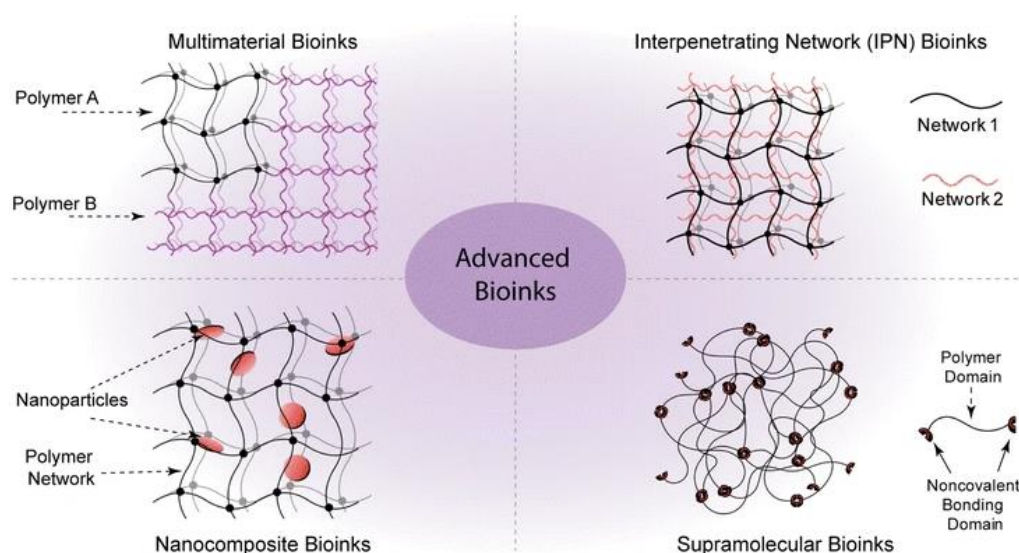
Figure 2.14. Classification of advanced bioinks into four main groups including multi-material, interpenetrating networks, nanocomposites, and supramolecular bioinks [18]. Reproduced with permission from ref. [18], Copyright (2016) Springer.

2.8.1 Multi-materials bioinks

Multi-material hydrogels have been widely explored for the design of advanced bioinks to address the drawbacks of single-component hydrogels [146]. In this strategy, blends of two (or more) polymer hydrogels are prepared to address the drawback of the other constituent hydrogel. For example, alginate forms a stable hydrogel through ionic crosslinking when exposed to divalent ions, however, the poor biocompatibility and low viscosity of alginate limit its application in the design of bioink [147]. To overcome this challenging matter, different

naturally-derived hydrogels such as gelatin have been mixed with alginate [94a]. Employing a similar strategy, Duan et al [148]. proposed a multi-material bioink based on methacrylated hyaluronic acid (Me-HA)/GelMA hydrogel for the fabrication of heart valve conduits. GelMA suffers from poor printability due to the low viscosity at low concentrations. It was demonstrated that the addition of Me-HA resulted in higher viscosity and subsequently higher printing resolution. Elsewhere, Rutz et al [146b]. proposed a multi-material bioink based on GelMA and PEG, as shown in **Figure 2.15**. They found that the pre-crosslinking of GelMA bioink with PEG crosslinker allows the tuning of the rheology and degradation behavior of the bioink. This bioink has the advantage of higher structural integrity resulted from the pre-crosslinking of strategy.
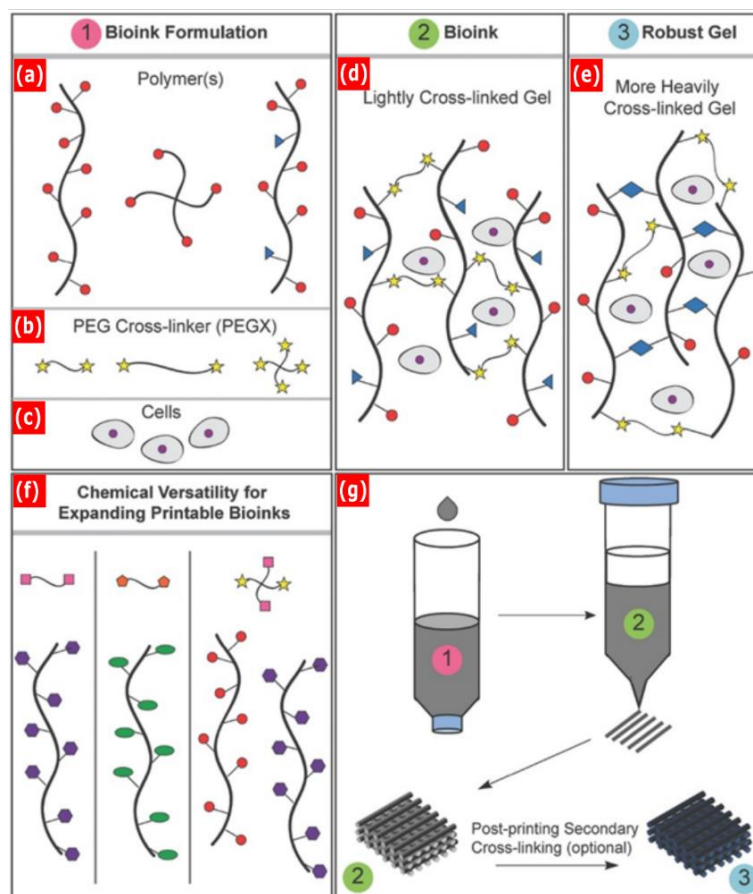
Figure 2.15. Multi-material bioink based on GelMA and PEG. (a) The chemical structure of polymers can be linear, branched, or multifunctional. (b) PEG serves as the crosslinker of polymers. The ultimate properties of bioink are tunable by varying the length and functional groups of PEG. (c) Cells can be encapsulated in the pre-crosslinked bioink. (d) Pre-crosslinking of GelMA with PEG. (e) Post-crosslinking of bioink to improve the structural integrity of the printed structure. (f) The crosslinker and polymers can carry a variety of functional groups. (g)

steps involved in the 3D printing of GelMA/PEG bioink [146b]. Reproduced with permission from ref. [146b], Copyright (2015) Wiley-VCH.

2.8.2 Interpenetrating networks (IPNs) bioinks

Compared to multi-materials bioinks, IPNs consist of two separate networks that crosslinked individually with the different crosslinking methods. Generally, the first network is flexible and soft while the second network is brittle polymers [18]. IPNs were found to exhibit superior mechanical strength compared to the single component networks of either of its constituent hydrogels. For example, In a series of promising works, a nanoengineered ionic-covalent entanglement (NICE) bioink has been introduced for the fabrication of mechanically stiff and elastomeric 3D structures (**Figure 2.16**) [21b, 85b, 149]. The NICE synthesized by the addition of GelMA into the laponite-κCA hydrogel, which overcomes the lack of cell-adhesion domain site, rapid dissociation in a physiological environment, and poor mechanical properties of laponite-κCA bioink. The synergy of ionic-covalent entanglement and nano-reinforcement provides a printable hydrogel with a cell-friendly microenvironment suitable for bone bioprinting. The NICE bioink exhibited excellent performance in terms of printability, mechanical properties, and osteoinductivity, allowing the fabrication of cellularized structures [21b, 85b]. For example, several scaffolds with various shapes were fabricated for craniomaxillofacial bone defects to showcase the capability of NICE bioinks for bone tissue engineering [21b]. It was found that the NICE bioink induced deposition of osteo-related mineralized extracellular matrix and improved endochondral differentiation of encapsulated hMSCs in a growth factor-free environment. In addition, the changes in gene expression of hMSC once exposed to laponite were investigated by RNA whole-transcriptome sequencing under 2D culture conditions. Accordingly, significant changes were recorded in the level of 4629 genes expression, especially the genes involved in the endochondral differentiation (*COL1A21, SMAD1/4/5/7, and SOX9)*, osteoblast development (TGF-β2 and the TGF-β2), and bone morphogenic protein signaling pathway (*BMP1*, *BMP4*, and *BMP2K*) were found to be upregulated due to the nanosilicate treatment. Elsewhere, Hong et al. printed out NICE hydrogels composed of poly(ethylene glycol) diacrylate (PEGDA)/alginate/laponite hydrogels. Ionic crosslinking of alginate resulted in the enhanced fracture strength of hydrogel from ~200 J/m^2 to over 1500 J/m^2. Moreover, the permanent chemical crosslinking of PEGDA preserve the structural integrity of printed structure upon application of stress.
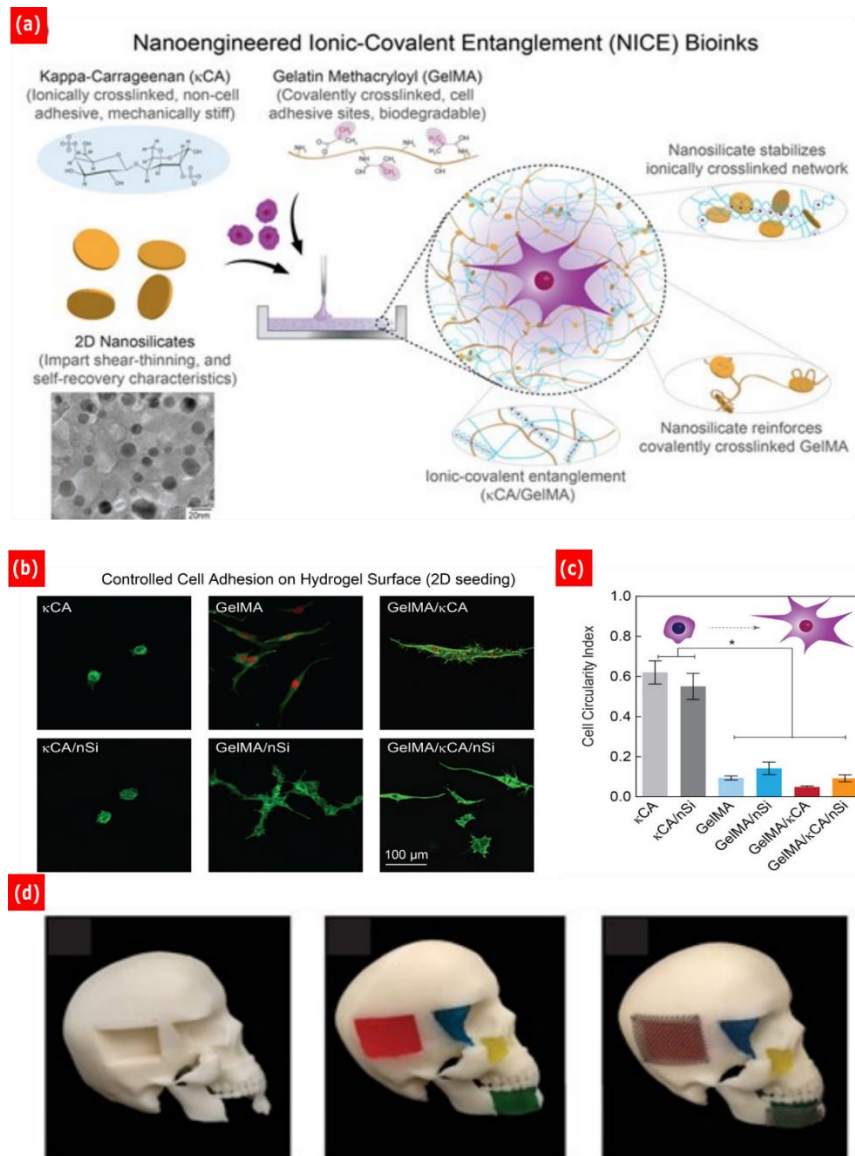
Figure 2.16. NICE bioink composed of laponite, GelMA, and κCA designed for bone tissue engineering with improved printability, bioactivity, and tuneable degradation [21b, 85b]. (a) schematic illustration of the synthesis of cell-laden NICE bioink [85b]. Reproduced with permission from ref. [85b], Copyright (2018) American Society . (b) Improved the cell adhesion on the NICE bioink upon addition of GelMA into the Laponite-κCA hydrogel [85b]. (c) The extent of cell spreading of circularity index, showing the higher elongation of cells after addition of GelMA [85b]. (d) The fabrication of several scaffolds for the craniomaxillofacial bone defects to showcase the capability of NICE bioinks for bone tissue engineering [21b]. Reproduced with permission from ref. [21b] , Copyright (2020) American Chemical Society.

2.8.3 Nanocomposites bioinks

Polymeric hydrogels have been widely studied in the bioink formulation owing to their biocompatibility, rheological properties, and easy processing [62-63, 150]. However, polymeric materials generally suffer from arrays of limitations such as insufficient bioactivity, weak mechanical properties, and poor electrical conductivity, which hamper their application in the context of 3D bioprinting [13, 18, 78]. Integration of NMs and 3D bioprinting appeared as a feasible approach to address the limitation of polymeric inks and creates an opportunity to attain advanced bioinks with unprecedented properties.

From the variety of NMs that have been exploited in the 3D bioprinting context, laponite nanoparticles are the main focus of researches to attain advanced inks [151]. This broad utility of laponite in 3D bioprinting is mainly attributed to its excellent rheological behavior, which is considered a superior benefit compared to the other 2D NMs [21a, 152]. Laponite is a synthetic nanoclay made up of layers of magnesium atoms between silicon atoms bonded with sodium atoms with the chemical formula of $Na^{+0.7}[(Si_8 Mg_{5.5}Li_{0.3}) O_{20} (OH)_4]^{-0.7}$ [153]. Laponite particle is a disk-shaped crystal with a thickness of 1 nm and diameter of about 25-30 nm which has positive and negative charges distributed on the rim and surfaces, respectively [154]. Laponite was found to significantly improve the printability of bioink as it can form hydrogel with highly thixotropic behavior in an aqueous solution thereby enabling the fabrication of 3D structures [21a, 152]. Laponite forms a "house-of-cards" structure once dissolved in an aqueous solution above 2 wt.% concentrations resulting from its dual electrostatic characteristic [154]. This structure imparts shear-thinning behavior and high recoverability to the hydrogel solution. Shear-thinning behavior is recognized as the pre-requisite characteristic for 3D bioprinting, which means the ink's viscosity drops at high shear rates that subsequently lead to higher cell viability, printing resolution, and shape fidelity of the 3D constructs [13, 20, 155]. Therefore, the inclusion of laponite into the bioink formulation can endow shear-thinning behavior to the ink to meet the criteria for extrusion-based 3D bioprinting [21a, 151c, 156]. Numerous researches have investigated the rheological properties of laponite, especially its ability to modulate the rheological properties of natural [21a, 99, 157], and synthetic polymers [151c] for 3D bioprinting applications. For example, single-component kappa-carrageenan (κCA) hydrogel suffers from poor printability as it forms an irregular filament once extruded out of the nozzle [21a]. The inclusion of laponite into κCA hydrogel allows the facile extrusion of ink along the nozzle and fabrication of physiologically relevant-scale tissue with spatial accuracy and good mechanical strength [21a] (**Figure 2.17a**). Another interesting characteristic of laponite is its ability to

improve the bioactivity of the scaffold for bone and cartilage tissue engineering [156, 158]. Cell-laden bioinks with bioactive properties are highly valuable for translation of the 3D bioprinting to preclinical models [21b, 151d, 159]. Accordingly, several studies have evaluated the bioactive properties of laponite in bone and cartilage tissue engineering [160]. Laponite was found to dissociate within the lysosome and release a variety of elements including sodium, magnesium, and lithium below pH=9 [161]. These elements with inherent bioactivity promote the osteogenic [156, 162], and chondrogenic [163] differentiation of the cells following the degradation of laponite. For example, a nanocomposite bioink was synthesized upon addition of laponite into photo-crosslinkable monomer (N-acryloyl glycinamide) (NAGA) [164], as shown in **Figure 2.17 b-d**. It was demonstrated that sustainable release of bioactive ions (Mg^{2+} and Si^{4+}) as degradation byproducts of laponite from laponite/N-acryloyl glycinamide bioink induces osteogenic differentiation of primary rat osteoblast (ROB) cells *in vitro*, which significantly contribute to the facile regeneration of new bone in tibia defects of rats *in vivo*. In addition, several studies conducted on the performance of the NICE bioinks proved that the use of laponite facilitates the deposition of a cartilage/osteoid-like matrix of GAGs, collagen, and proteoglycans during the initial few weeks of culture [21b, 85b, 149].
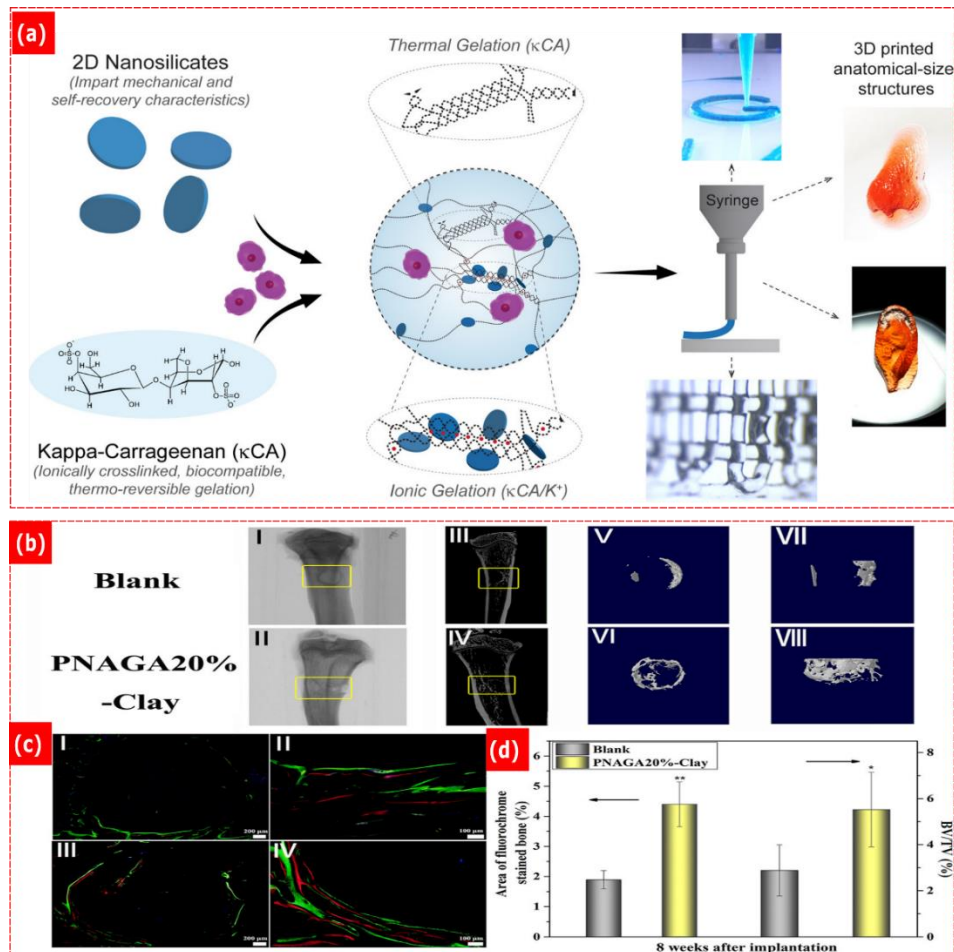
Figure 2.17. Improving the printability of κCA upon the adhesion of laponite. Laponite with intrinsic thixotropic behavior was introduced in the single-component κCA hydrogel to modify its rheological behavior [21a]. Reproduced with permission from ref. [21a], Copyright (2017) American Chemical Society. (b-d) Enhanced bone regeneration of the scaffold. The sustainable release of laponite biodegradation products improved the bone regeneration rate. (b) Evaluation of the efficiency of the implanted blank and PNAGA20%-Clay bioink in terms of new bone formation via micro-CT (b(I) and b(II)), micro-CT reconstruction images (b(III) and b(IV)), and reconstructed 3D models (b(V)-b(VIII)) of the new bones. (c) Fluorescent labeling assay of blank (c(I) and c(II)) and PNAGA20%-Clay (c(III) and c(IV)). Three different colors including yellow, red, and green represent tetracycline hydrochloride, alizarin red S, and calcein labeling, respectively. (d) Comparison of the percentage of the fluorescent labeling area of bone and new bone volume/total volume (BV/TV) ratio for blank and PNAGA20%-Clay 8 weeks after surgery [164]. Reproduced with permission from ref. [164], Copyright (2017) American Chemical Society.

2.8.4 Supramolecular networks

In supramolecular hydrogels, polymer networks are formed by non-covalent interaction, keeping the hydrogel shape fidelity [18]. Covalent interaction break irreversibly once goes under high shear rate, while the reversible nature of non-covalent interaction results in re-joining of non-covalent interaction after dissipation of energy [165]. Highley et al [166]. prepared a HA-based supramolecular hydrogel using host-guest interaction between Ada and cyclodextrine molecules which were located along polymer chains. This supramolecular bioink quickly forms a stable hydrogel resulting from the guest-host interaction (**Figure 2.18**). In addition, the bioink has exhibited shear-thinning behavior which facilitates the bioprinting process and provides enough mechanical stability exactly after the extrusion. The ultimate properties of the bioink can be tuned by varying the degree of conjugation of host and guest moieties on the polymer backbone.
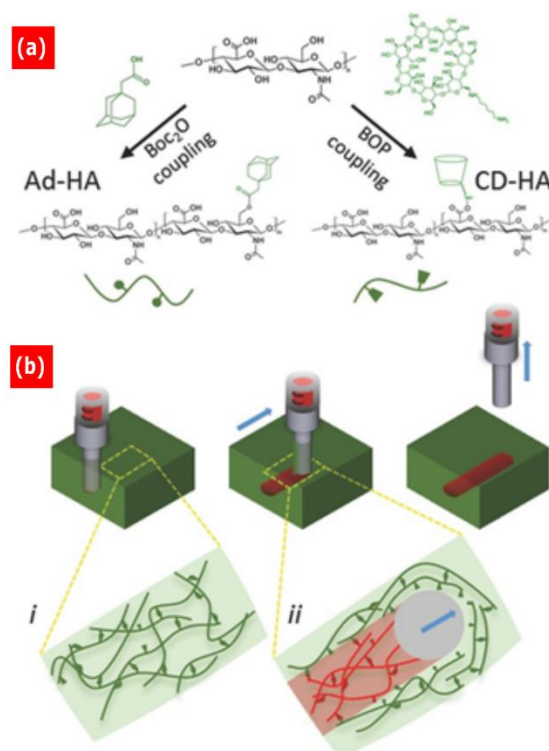
Figure 2.18. Supramolecular HA bioink modified with adamantane (Ad, guest) and β-cyclodextrin (CD, host). (a) Modification of HA backbone with Ad and β-CD. (b) Printing of supramolecular ink (red) into a supramolecular support bath (green) [166]. Reproduced with permission from ref. [166], Copyright (2015) Wiley-VCH.

Hybridization of deoxyribonucleic acid (DNA) strands also provides supramolecular hydrogel, displaying shear thinning properties that make them suitable biomaterial for the 3D

bioprinting process [167]. DNA has been employed to synthesize supramolecular hydrogels owing to its set of exciting properties such as base-pairing characteristics, structural rigidity, and minimal toxicity [168]. For example, Li et al [169]. synthesized a DNA-based supramolecular bioinks composed of a polypeptide that carrying DNA strands (Bioink A) and a complementary DNA crosslinker (Bioink B), as shown in **Figure 2.19**. The hybridization between two complementary DNA strands resulted in the quick formation of hydrogel with high structural integrity. It was observed that prepared hydrogel possesses remarkable properties such as self-healing properties, high mechanical strength, biocompatibility, biodegradability, and permeability.
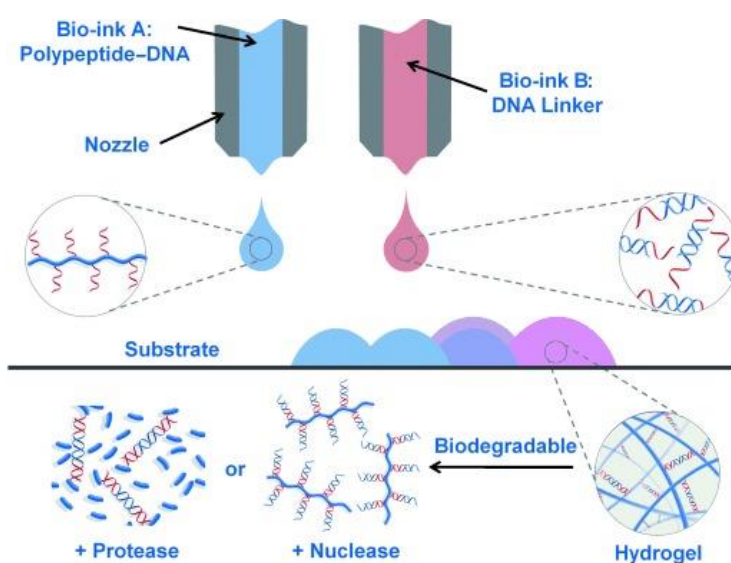
Figure 2.19. Supramolecular bioink based on DNA hybridization that composed of a polypeptide carrying DNA strands (Bioink A) and a complementary DNA linker. The quick hybridization of DNA strands enables the structural stability of hydrogel on the substrate [169]. Reproduced with permission from ref. [169], Copyright (2015) Wiley-VCH.

2.9 Knowledge gaps in the development of advanced bioinks

The literature review summarized here highlighted the need to develop advanced bioinks to overcome the challenges associated with conventional bioinks. Accordingly, several knowledge gaps are identified that deserved to be explored:

1) Lack of MC-based bioink with high printability and biocompatibility that can remain stable in biological media for long-term use.
2) A very limited number of nanoengineered bioink despite the remarkable properties of nanomaterials.

3) Lack of ideal bioink with adjustable electrical conductivity for neural tissue engineering.

4) Lack of bioink with inherent antibacterial activity to overcome the challenges associated with bacterial infections in skin tissue engineering.

2.10 Conclusion

Chapter 2 highlights the recent progress in the emergence of hydrogels in 3D bioprinting technology, with a special focus on the main attributes of hydrogels in the design of an ideal bioink. By taking advantage of the advanced bioink strategies, conventional inks can be equipped with added functionality to overcome the challenges associated with the current bioinks. This Ph.D. thesis aims to step towards addressing the current challenges in 3D bioprinting technology by developing advanced bioinks with enhanced performance.

2.11 Reference

[1]   M. Varkey, D. O. Visscher, P. P. M. van Zuijlen, A. Atala, J. J. Yoo, *Burns & Trauma* **2019**, 7, 4.

[2]   J. Groll, J. A. Burdick, D. W. Cho, B. Derby, M. Gelinsky, S. C. Heilshorn, T. Jüngst, J. Malda, V. A. Mironov, K. Nakayama, A. Ovsianikov, W. Sun, S. Takeuchi, J. J. Yoo, T. B. F. Woodfield, *Biofabrication* **2018**, 11, 013001.

[3]   K. Dubbin, Y. Hori, K. K. Lewis, S. C. Heilshorn, *Advanced Healthcare Materials* **2016**, 5, 2488.

[4]   D. Liu, W. Nie, D. Li, W. Wang, L. Zheng, J. Zhang, J. Zhang, C. Peng, X. Mo, C. He, *Chemical Engineering Journal* **2019**, 362, 269.

[5]   H. Cui, M. Nowicki, J. P. Fisher, L. G. Zhang, *Advanced healthcare materials* **2017**, 6, 1601118.

[6]   a) T. H. Jovic, G. Kungwengwe, A. C. Mills, I. S. Whitaker, *Frontiers in Mechanical Engineering* **2019**, 5; b) P. S. Gungor-Ozkerim, I. Inci, Y. S. Zhang, A. Khademhosseini, M. R. Dokmeci, *Biomaterials Science* **2018**, 6, 915.

[7]   Y.-J. Seol, H.-W. Kang, S. J. Lee, A. Atala, J. J. Yoo, *European Journal of Cardio-Thoracic Surgery* **2014**, 46, 342.

[8]   R. Lozano, L. Stevens, B. C. Thompson, K. J. Gilmore, R. Gorkin III, E. M. Stewart, M. in het Panhuis, M. Romero-Ortega, G. G. Wallace, *Biomaterials* **2015**, 67, 264.

[9]   a) K. Zhu, N. Chen, X. Liu, X. Mu, W. Zhang, C. Wang, Y. S. Zhang, *Macromolecular Bioscience* **2018**, 18, 1800127; b) W. Liu, Z. Zhong, N. Hu, Y. Zhou, L. Maggio, A. K. Miri, A. Fragasso, X. Jin, A. Khademhosseini, Y. S. Zhang, *Biofabrication* **2018**, 10, 024102; c) K. Markstedt, A. Mantas, I. Tournier, H. Martínez Ávila, D. Hägg, P. Gatenholm, *Biomacromolecules* **2015**, 16, 1489; d) J. Yin, M. Yan, Y. Wang, J. Fu, H. Suo, *ACS applied materials & interfaces* **2018**, 10, 6849.

[10]   a) A. M. Compaan, K. Christensen, Y. Huang, *ACS Biomaterials Science & Engineering* **2017**, 3, 1519; b) L. H. Solis, Y. Ayala, S. Portillo, A. Varela-Ramirez, R. Aguilera, T. Boland, *Biofabrication* **2019**, 11, 045005; c) C. Xu, W. Chai, Y. Huang, R. R. Markwald, *Biotechnology and Bioengineering* **2012**, 109, 3152.

[11]   a) J. A. Barron, P. Wu, H. D. Ladouceur, B. R. Ringeisen, *Biomedical Microdevices* **2004**, 6, 139; b) B. Guillotin, A. Souquet, S. Catros, M. Duocastella, B. Pippenger, S. Bellance, R. Bareille, M. Rémy, L. Bordenave, J. Amédée, *Biomaterials* **2010**, 31, 7250; c) V. Keriquel, H. Oliveira, M. Rémy, S. Ziane, S. Delmond, B. Rousseau, S. Rey, S. Catros, J. Amédée, F. Guillemot, *Scientific reports* **2017**, 7, 1.

[12]   a) Z. Wang, R. Abdulla, B. Parker, R. Samanipour, S. Ghosh, K. Kim, *Biofabrication* **2015**, 7, 045009; b) Z. Wang, H. Kumar, Z. Tian, X. Jin, J. F. Holzman, F. Menard, K. Kim, *ACS applied materials & interfaces* **2018**, 10, 26859; c) R. Raman, R. Bashir, in *Essentials of 3D Biofabrication and Translation*, Elsevier **2015**, p. 89.

[13]   J. Malda, J. Visser, F. P. Melchels, T. Jüngst, W. E. Hennink, W. J. Dhert, J. Groll, D. W. Hutmacher, *Advanced materials* **2013**, 25, 5011.

[14]   K. Hölzl, S. Lin, L. Tytgat, S. Van Vlierberghe, L. Gu, A. Ovsianikov, *Biofabrication* **2016**, 8, 032002.

[15]   W. Peng, D. Unutmaz, I. T. Ozbolat, *Trends in biotechnology* **2016**, 34, 722.

[16]   I. T. Ozbolat, M. Hospodiuk, *Biomaterials* **2016**, 76, 321.

[17]   a) C. C. Chang, E. D. Boland, S. K. Williams, J. B. Hoying, *Journal of Biomedical Materials Research Part B: Applied Biomaterials* **2011**, 98B, 160; b) K. Nair, M. Gandhi, S. Khalil, K. C. Yan, M. Marcolongo, K. Barbee, W. Sun, *Biotechnology Journal* **2009**, 4, 1168; c) F. P. Melchels, W. J. Dhert, D. W. Hutmacher, J. Malda, *Journal of Materials Chemistry B* **2014**, 2, 2282; d) M. Hospodiuk, M. Dey, D. Sosnoski, I. T. Ozbolat, *Biotechnology Advances* **2017**, 35, 217.

[18]   D. Chimene, K. K. Lennox, R. R. Kaunas, A. K. Gaharwar, *Annals of biomedical engineering* **2016**, 44, 2090.

[19]   a) P. T. Smith, A. Basu, A. Saha, A. Nelson, *Polymer* **2018**; b) N. Paxton, W. Smolan, T. Böck, F. Melchels, J. Groll, T. Jungst, *Biofabrication* **2017**, 9, 044107.

[20]   L. Ouyang, C. B. Highley, C. B. Rodell, W. Sun, J. A. Burdick, *ACS Biomaterials Science & Engineering* **2016**, 2, 1743.

[21]   a) S. A. Wilson, L. M. Cross, C. W. Peak, A. K. Gaharwar, *ACS applied materials & interfaces* **2017**, 9, 43449; b) D. Chimene, L. Miller, L. M. Cross, M. K. Jaiswal, I. Singh, A. K. Gaharwar, *ACS Applied Materials & Interfaces* **2020**, 12, 15976.

[22]   a) I. T. Ozbolat, H. Chen, Y. Yu, *Robotics and Computer-Integrated Manufacturing* **2014**, 30, 295; b) R. Attalla, E. Puersten, N. Jain, P. R. Selvaganapathy, *Biofabrication* **2018**, 11, 015012; c) L. Ruiz-Cantu, A. Gleadall, C. Faris, J. Segal, K. Shakesheff, J. Yang, *Materials Science and Engineering: C* **2020**, 109, 110578.

[23]   I. T. Ozbolat, H. Chen, Y. Yu, *Robotics and Computer-Integrated Manufacturing* **2014**, 30, 295.

[24]   W. Liu, Y. S. Zhang, M. A. Heinrich, F. De Ferrari, H. L. Jang, S. M. Bakht, M. M. Alvarez, J. Yang, Y. C. Li, G. Trujillo-de Santiago, *Advanced Materials* **2017**, 29, 1604630.

[25]   *Tissue Engineering Part A* **2008**, 14, 41.

[26]   J. Li, M. Chen, X. Fan, H. Zhou, *J Transl Med* **2016**, 14, 271.

[27]   I. N. Aguilar, L. J. Smith, D. J. Olivos, T.-M. G. Chu, M. A. Kacena, D. R. Wagner, *Bioprinting* **2019**, 15, e00048.

[28]   a) M. Nakamura, A. Kobayashi, F. Takagi, A. Watanabe, Y. Hiruma, K. Ohuchi, Y. Iwasaki, M. Horie, I. Morita, S. Takatani, *Tissue engineering* **2005**, 11, 1658; b) T. Boland, T. Xu, B. Damon, X. Cui, *Biotechnology Journal: Healthcare Nutrition Technology* **2006**, 1, 910.

[29]   T. Xu, W. Zhao, J.-M. Zhu, M. Z. Albanna, J. J. Yoo, A. Atala, *Biomaterials* **2013**, 34, 130.

[30]   R. Zimmermann, C. Hentschel, F. Schrön, D. Moedder, T. Büttner, P. Atallah, T. Wegener, T. Gehring, S. Howitz, U. Freudenberg, C. Werner, *Biofabrication* **2019**, 11, 045008.

[31]   H. Gudapati, M. Dey, I. Ozbolat, *Biomaterials* **2016**, 102, 20.

[32]   a) M. S. Onses, E. Sutanto, P. M. Ferreira, A. G. Alleyne, J. A. Rogers, *Small* **2015**, 11, 4237; b) S. N. Jayasinghe, A. N. Qureshi, P. A. Eagles, *Small* **2006**, 2, 216.

[33]   a) Z. Zheng, D. Eglin, M. Alini, G. R. Richards, L. Qin, Y. Lai, *Engineering* **2020**, DOI: https://doi.org/10.1016/j.eng.2020.05.021; b) B. K. Gu, D. J. Choi, S. J. Park, M. S. Kim, C. M. Kang, C.-H. Kim, *Biomaterials research* **2016**, 20, 12; c) N. E. Sanjana, S. B. Fuller, *Journal of neuroscience methods* **2004**, 136, 151.

[34]   a) L. Gasperini, D. Maniglio, A. Motta, C. Migliaresi, *Tissue engineering part C: Methods* **2015**, 21, 123; b) C. Xu, W. Chai, Y. Huang, R. R. Markwald, *Biotechnology and bioengineering* **2012**, 109, 3152.

[35]   A. Blaeser, D. F. Duarte Campos, M. Weber, S. Neuss, B. Theek, H. Fischer, W. Jahnen-Dechent, *BioResearch open access* **2013**, 2, 374.

[36]   a) *Tissue Engineering Part A* **2012**, 18, 1304; b) U. A. Gurkan, R. El Assal, S. E. Yildiz, Y. Sung, A. J. Trachtenberg, W. P. Kuo, U. Demirci, *Molecular Pharmaceutics* **2014**, 11, 2151.

[37]   Y.-B. Lee, S. Polio, W. Lee, G. Dai, L. Menon, R. S. Carroll, S.-S. Yoo, *Experimental Neurology* **2010**, 223, 645.

[38]   A. GhavamiNejad, N. Ashammakhi, X. Y. Wu, A. Khademhosseini, *Small* **2020**, 16, 2002931.

[39]   G. Gao, T. Yonezawa, K. Hubbell, G. Dai, X. Cui, *Biotechnology Journal* **2015**, 10, 1568.

[40]   a) C. J. Ferris, K. J. Gilmore, S. Beirne, D. McCallum, G. G. Wallace, M. in het Panhuis, *Biomaterials Science* **2013**, 1, 224; b) M. E. Pepper, V. Seshadri, T. C. Burg, K. J. L. Burg, R. E. Groff, *Biofabrication* **2012**, 4, 011001.

[41]   X. Li, B. Liu, B. Pei, J. Chen, D. Zhou, J. Peng, X. Zhang, W. Jia, T. Xu, *Chemical Reviews* **2020**, 120, 10793.

[42]   T. Xu, C. A. Gregory, P. Molnar, X. Cui, S. Jalota, S. B. Bhaduri, T. Boland, *Biomaterials* **2006**, 27, 3580.

[43]   a) D. J. Odde, M. J. Renn, *Trends in biotechnology* **1999**, 17, 385; b) J. A. Barron, B. R. Ringeisen, H. Kim, B. J. Spargo, D. B. Chrisey, *Thin Solid Films* **2004**, 453, 383.

[44]   a) C. Mandrycky, Z. Wang, K. Kim, D.-H. Kim, *Biotechnology Advances* **2016**, 34, 422; b) F. Guillemot, A. Souquet, S. Catros, B. Guillotin, J. Lopez, M. Faucon, B. Pippenger, R. Bareille, M. Rémy, S. Bellance, P. Chabassier, J. C. Fricain, J. Amédée, *Acta Biomaterialia* **2010**, 6, 2494.

[45]   S. Michael, H. Sorg, C.-T. Peck, L. Koch, A. Deiwick, B. Chichkov, P. M. Vogt, K. Reimers, *PloS one* **2013**, 8, e57741.

[46]   S. Catros, B. Guillotin, M. Bačáková, J.-C. Fricain, F. Guillemot, *Applied Surface Science* **2011**, 257, 5142.

[47]   F. Guillemot, A. Souquet, S. Catros, B. Guillotin, *Nanomedicine* **2010**, 5, 507.

[48]   a) D. Hakobyan, C. Médina, N. Dusserre, M.-L. Stachowicz, C. Handschin, J.-C. Fricain, J. Guillermet-Guibert, H. Oliveira, *Biofabrication* **2020**, 12, 035001; b) M. Ali, E. Pages, A. Ducom, A. Fontaine, F. Guillemot, *Biofabrication* **2014**, 6, 045001.

[49]   M. A. Heinrich, W. Liu, A. Jimenez, J. Yang, A. Akpek, X. Liu, Q. Pi, X. Mu, N. Hu, R. M. Schiffelers, *Small* **2019**, 15, 1805510.

[50]   N. Poomathi, S. Singh, C. Prakash, V. Patil Rajkumar, P. T. Perumal, A. Barathi Veluchamy, K. Balasubramanian Kalpattu, S. Ramakrishna, N. U. Maheshwari, *Rapid Prototyping Journal* **2019**, 25, 496.

[51]   J. T. Huh, J. J. Yoo, A. Atala, S. J. Lee, in *Principles of Tissue Engineering (Fifth Edition)*, DOI: https://doi.org/10.1016/B978-0-12-818422-6.00076-9 (Eds: R. Lanza, R. Langer, J. P. Vacanti, A. Atala), Academic Press **2020**, p. 1391.

[52]   a) B. Hopp, T. Smausz, G. Szabó, L. Kolozsvari, A. Nogradi, D. Kafetzopoulos, C. Fotakis, *Optical Engineering* **2012**, 51, 014302; b) H. Gudapati, J. Yan, Y. Huang, D. B. Chrisey, *Biofabrication* **2014**, 6, 035022.

[53]   L. Koch, S. Kuhn, H. Sorg, M. Gruene, S. Schlie, R. Gaebel, B. Polchow, K. Reimers, S. Stoelting, N. Ma, *Tissue Engineering Part C: Methods* **2010**, 16, 847.

[54]   a) Z. Yue, X. Liu, P. T. Coates, G. G. Wallace, *Current opinion in organ transplantation* **2016**, 21, 467; b) R. Raman, R. Bashir, in *Essentials of 3D Biofabrication and Translation*, DOI: https://doi.org/10.1016/B978-0-12-800972-7.00006-2 (Eds: A. Atala, J. J. Yoo), Academic Press, Boston **2015**, p. 89.

[55]   a) S. Zakeri, M. Vippola, E. Levänen, *Additive Manufacturing* **2020**, 35, 101177; b) F. P. Melchels, K. Bertoldi, R. Gabbrielli, A. H. Velders, J. Feijen, D. W. Grijpma, *Biomaterials* **2010**, 31, 6909.

[56]   a) J.-W. Choi, R. Wicker, S.-H. Lee, K.-H. Choi, C.-S. Ha, I. Chung, *Journal of Materials Processing Technology* **2009**, 209, 5494; b) T. Chartier, A. Badev, Y. Abouliatim, P. Lebaudy, L. Lecamp, *Journal of the European Ceramic Society* **2012**, 32, 1625.

[57]   F. P. W. Melchels, J. Feijen, D. W. Grijpma, *Biomaterials* **2010**, 31, 6121.

[58]   R. P. Sinha, D.-P. Häder, *Photochemical & Photobiological Sciences* **2002**, 1, 225.

[59]   a) A. K. Au, W. Lee, A. Folch, *Lab on a Chip* **2014**, 14, 1294; b) R. Zhang, N. B. Larsen, *Lab on a Chip* **2017**, 17, 4273.

[60]   a) S. Knowlton, B. Yenilmez, S. Tasoglu, *Trends in Biotechnology* **2016**, 34, 685; b) A. P. Kuo, N. Bhattacharjee, Y. S. Lee, K. Castro, Y. T. Kim, A. Folch, *Advanced materials technologies* **2019**, 4, 1800395.

[61]   Y. S. Zhang, A. Khademhosseini, *Science* **2017**, 356.

[62]   H. Li, C. Tan, L. Li, *Materials & Design* **2018**, 159, 20.

[63]   J. M. Unagolla, A. C. Jayasuriya, *Applied Materials Today* **2020**, 18, 100479.

[64]   S. Heid, A. R. Boccaccini, *Acta Biomaterialia* **2020**, 113, 1.

[65]   K. Varaprasad, G. M. Raghavendra, T. Jayaramudu, M. M. Yallapu, R. Sadiku, *Materials Science and Engineering: C* **2017**, 79, 958.

[66]   W. Hu, Z. Wang, Y. Xiao, S. Zhang, J. Wang, *Biomaterials science* **2019**, 7, 843.

[67]   M. Mahinroosta, Z. J. Farsangi, A. Allahverdi, Z. Shakoori, *Materials today chemistry* **2018**, 8, 42.

[68]   E. Caló, V. V. Khutoryanskiy, *European Polymer Journal* **2015**, 65, 252.

[69]   M. C. Catoira, L. Fusaro, D. Di Francesco, M. Ramella, F. Boccafoschi, *Journal of Materials Science: Materials in Medicine* **2019**, 30, 115.

[70]   J. Li, C. Wu, P. K. Chu, M. Gelinsky, *Materials Science and Engineering: R: Reports* **2020**, 140, 100543.

[71]   P. Jaipan, A. Nguyen, R. J. Narayan, *MRS Communications* **2017**, 7, 416.

[72]   K. Su, C. Wang, *Biotechnology letters* **2015**, 37, 2139.

[73]   A. I. Van Den Bulcke, B. Bogdanov, N. De Rooze, E. H. Schacht, M. Cornelissen, H. Berghmans, *Biomacromolecules* **2000**, 1, 31.

[74]   K. Yue, G. Trujillo-de Santiago, M. M. Alvarez, A. Tamayol, N. Annabi, A. Khademhosseini, *Biomaterials* **2015**, 73, 254.

[75]   Z. Dong, Q. Yuan, K. Huang, W. Xu, G. Liu, Z. Gu, *RSC Advances* **2019**, 9, 17737.

[76]   a) F. E. Freeman, D. J. Kelly, *Scientific Reports* **2017**, 7, 17042; b) E. Axpe, M. L. Oyen, *International journal of molecular sciences* **2016**, 17, 1976; c) M. D. Giuseppe,

N. Law, B. Webb, R. A. Macrae, L. J. Liew, T. B. Sercombe, R. J. Dilley, B. J. Doyle, *Journal of the Mechanical Behavior of Biomedical Materials* **2018**, 79, 150.

[77]   a) J. Lewicki, J. Bergman, C. Kerins, O. Hermanson, *Bioprinting* **2019**, 16, e00053; b) M. Alruwaili, J. A. Lopez, K. McCarthy, E. G. Reynaud, B. J. Rodriguez, *Bio-Design and Manufacturing* **2019**, 2, 172.

[78]   M. L. Bedell, A. M. Navara, Y. Du, S. Zhang, A. G. Mikos, *Chemical Reviews* **2020**.

[79]   N. Contessi, L. Altomare, A. Filipponi, S. Farè, *Materials Letters* **2017**, 207, 157.

[80]   C. Chang, L. Zhang, *Carbohydrate polymers* **2011**, 84, 40.

[81]   N. Contessi Negrini, L. Bonetti, L. Contili, S. Farè, *Bioprinting* **2018**, 10, e00024.

[82]   K. Schütz, A. M. Placht, B. Paul, S. Brüggemeier, M. Gelinsky, A. Lode, *Journal of tissue engineering and regenerative medicine* **2017**, 11, 1574.

[83]   a) S. Liu, L. Li, *ACS applied materials & interfaces* **2016**, 8, 29749; b) Y. Yuguchi, H. Urakawa, K. Kajiwara, *Food Hydrocolloids* **2003**, 17, 481.

[84]   a) S. Liu, W. L. Chan, L. Li, *Macromolecules* **2015**, 48, 7649; b) S. M. Mihaila, A. K. Gaharwar, R. L. Reis, A. P. Marques, M. E. Gomes, A. Khademhosseini, *Advanced healthcare materials* **2013**, 2, 895.

[85]   a) S. Liu, S. Huang, L. Li, *Journal of Rheology* **2016**, 60, 203; b) D. Chimene, C. W. Peak, J. L. Gentry, J. K. Carrow, L. M. Cross, E. Mondragon, G. B. Cardoso, R. Kaunas, A. K. Gaharwar, *ACS applied materials & interfaces* **2018**, 10, 9957.

[86]   a) S. H. Park, J. Y. Seo, J. Y. Park, Y. B. Ji, K. Kim, H. S. Choi, S. Choi, J. H. Kim, B. H. Min, M. S. Kim, *NPG Asia Materials* **2019**, 11, 1; b) M. F. Graça, S. P. Miguel, C. S. Cabral, I. J. Correia, *Carbohydrate Polymers* **2020**, 116364.

[87]   a) M. T. Poldervaart, B. Goversen, M. De Ruijter, A. Abbadessa, F. P. Melchels, F. C. Öner, W. J. Dhert, T. Vermonden, J. Alblas, *PLoS One* **2017**, 12, e0177628; b) I. Noh, N. Kim, H. N. Tran, J. Lee, C. Lee, *Biomaterials research* **2019**, 23, 1.

[88]   H. Si, T. Xing, Y. Ding, H. Zhang, R. Yin, W. Zhang, *Polymers* **2019**, 11, 1584.

[89]   I. Donderwinkel, J. C. M. van Hest, N. R. Cameron, *Polymer Chemistry* **2017**, 8, 4451.

[90]   L. Valot, J. Martinez, A. Mehdi, G. Subra, *Chemical Society Reviews* **2019**, 48, 4049.

[91]   a) W. Schuurman, P. A. Levett, M. W. Pot, P. R. van Weeren, W. J. Dhert, D. W. Hutmacher, F. P. Melchels, T. J. Klein, J. Malda, *Macromolecular bioscience* **2013**, 13, 551; b) J. M. Townsend, E. C. Beck, S. H. Gehrke, C. J. Berkland, M. S. Detamore, *Progress in Polymer Science* **2019**, 91, 126.

[92]   a) M. Chopin-Doroteo, E. A. Mandujano-Tinoco, E. Krötzsch, *Biochimica et Biophysica Acta (BBA) - General Subjects* **2021**, 1865, 129782; b) O. Chaudhuri, L. Gu, D. Klumpers, M. Darnell, S. A. Bencherif, J. C. Weaver, N. Huebsch, H.-p. Lee, E. Lippens, G. N. Duda, D. J. Mooney, *Nature Materials* **2016**, 15, 326.

[93]   a) Y. Chen, X. Xiong, X. Liu, R. Cui, C. Wang, G. Zhao, W. Zhi, M. Lu, K. Duan, J. Weng, *Journal of Materials Chemistry B* **2020**, 8, 5500; b) A. Parak, P. Pradeep, L. C. du Toit, P. Kumar, Y. E. Choonara, V. Pillay, *Drug discovery today* **2019**, 24, 198.

[94]   a) J. H. Chung, S. Naficy, Z. Yue, R. Kapsa, A. Quigley, S. E. Moulton, G. G. Wallace, *Biomaterials Science* **2013**, 1, 763; b) H. Rastin, R. T. Ormsby, G. J. Atkins, D. Losic, *ACS Applied Bio Materials* **2020**, 3, 1815.

[95]   Y. Zhao, Y. Li, S. Mao, W. Sun, R. Yao, *Biofabrication* **2015**, 7, 045002.

[96]   M. Mehrali, A. Thakur, C. P. Pennisi, S. Talebian, A. Arpanaei, M. Nikkhah, A. Dolatshahi-Pirouz, *Advanced Materials* **2017**, 29, 1603612.

[97]   K. A. Deo, K. A. Singh, C. W. Peak, D. L. Alge, A. K. Gaharwar, *Tissue Engineering Part A* **2020**, 26, 318.

[98]   P. A. Amorim, M. A. d'Ávila, R. Anand, P. Moldenaers, P. Van Puyvelde, V. Bloemen, *Bioprinting* **2021**, 22, e00129.

[99]   J. L. Dávila, M. A. d'Ávila, *The International Journal of Advanced Manufacturing Technology* **2019**, 101, 675.

[100] E. A. Kiyotake, A. W. Douglas, E. E. Thomas, S. L. Nimmo, M. S. Detamore, *Acta Biomaterialia* **2019**, 95, 176.

[101] a) L. Ghasemi-Mobarakeh, M. P. Prabhakaran, M. Morshed, M. H. Nasr-Esfahani, H. Baharvand, S. Kiani, S. S. Al-Deyab, S. Ramakrishna, *Journal of Tissue Engineering and Regenerative Medicine* **2011**, 5, e17; b) N. Li, Q. Zhang, S. Gao, Q. Song, R. Huang, L. Wang, L. Liu, J. Dai, M. Tang, G. Cheng, *Scientific Reports* **2013**, 3, 1604; c) B. Guo, P. X. Ma, *Biomacromolecules* **2018**, 19, 1764.

[102] a) N. Zanjanizadeh Ezazi, M.-A. Shahbazi, Y. V. Shatalin, E. Nadal, E. Mäkilä, J. Salonen, M. Kemell, A. Correia, J. Hirvonen, H. A. Santos, *International Journal of Pharmaceutics* **2018**, 536, 241; b) G. L. Mario Cheong, K. S. Lim, A. Jakubowicz, P. J. Martens, L. A. Poole-Warren, R. A. Green, *Acta Biomaterialia* **2014**, 10, 1216.

[103] a) K. Cysewska, J. Karczewski, P. Jasiński, *Measurement Science and Technology* **2017**, 28, 074004; b) R. Ravichandran, J. G. Martinez, E. W. H. Jager, J. Phopase, A. P. F. Turner, *ACS Applied Materials & Interfaces* **2018**, 10, 16244.

[104] a) H. Rastin, B. Zhang, A. Mazinani, K. Hassan, J. Bi, T. T. Tung, D. Losic, *Nanoscale* **2020**; b) A. E. Jakus, E. B. Secor, A. L. Rutz, S. W. Jordan, M. C. Hersam, R. N. Shah, *ACS Nano* **2015**, 9, 4636.

[105] S.-J. Lee, W. Zhu, M. Nowicki, G. Lee, D. N. Heo, J. Kim, Y. Y. Zuo, L. G. Zhang, *Journal of Neural Engineering* **2018**, 15, 016018.

[106] a) T. Distler, A. R. Boccaccini, *Acta biomaterialia* **2020**, 101, 1; b) S. S. Athukorala, T. S. Tran, R. Balu, V. K. Truong, J. Chapman, N. K. Dutta, N. Roy Choudhury, *Polymers* **2021**, 13, 474.

[107] H. Qing, Y. Ji, W. Li, G. Zhao, Q. Yang, X. Zhang, Z. Luo, T. J. Lu, G. Jin, F. Xu, *ACS Applied Materials & Interfaces* **2020**, 12, 2049.

[108] S. Sayyar, M. Bjorninen, S. Haimi, S. Miettinen, K. Gilmore, D. Grijpma, G. Wallace, *ACS Applied Materials & Interfaces* **2016**, 8, 31916.

[109] a) L. Zhao, P. K. Chu, Y. Zhang, Z. Wu, *Journal of Biomedical Materials Research Part B: Applied Biomaterials* **2009**, 91, 470; b) S. Li, S. Dong, W. Xu, S. Tu, L. Yan, C. Zhao, J. Ding, X. Chen, *Advanced science* **2018**, 5, 1700527.

[110] J. Hoque, B. Bhattacharjee, R. G. Prakash, K. Paramanandham, J. Haldar, *Biomacromolecules* **2018**, 19, 267.

[111] M. C. Giano, Z. Ibrahim, S. H. Medina, K. A. Sarhane, J. M. Christensen, Y. Yamada, G. Brandacher, J. P. Schneider, *Nature communications* **2014**, 5, 1.

[112] a) S. Wang, H. Zheng, L. Zhou, F. Cheng, Z. Liu, H. Zhang, L. Wang, Q. Zhang, *Nano Letters* **2020**, 20, 5149; b) Y. Zhong, H. Xiao, F. Seidi, Y. Jin, *Biomacromolecules* **2020**, 21, 2983.

[113] D. Campoccia, L. Montanaro, C. R. Arciola, *Biomaterials* **2006**, 27, 2331.

[114] a) L. Mei, S. Zhu, W. Yin, C. Chen, G. Nie, Z. Gu, Y. Zhao, *Theranostics* **2020**, 10, 757; b) Q. Wu, M. Liang, S. Zhang, X. Liu, F. Wang, *Nanoscale* **2018**, 10, 10428.

[115] Y. Zhang, D. Zhai, M. Xu, Q. Yao, H. Zhu, J. Chang, C. Wu, *Biofabrication* **2017**, 9, 025037.

[116] S. F. Melo, S. C. Neves, A. T. Pereira, I. Borges, P. L. Granja, F. D. Magalhães, I. C. Gonçalves, *Materials Science and Engineering: C* **2020**, 109, 110537.

[117] E. S. Place, J. H. George, C. K. Williams, M. M. Stevens, *Chemical Society Reviews* **2009**, 38, 1139.

[118] a) C. Gardin, A. Piattelli, B. Zavan, *Trends in Biotechnology* **2016**, 34, 435; b) S. R. Shin, Y.-C. Li, H. L. Jang, P. Khoshakhlagh, M. Akbari, A. Nasajpour, Y. S. Zhang, A.

Tamayol, A. Khademhosseini, *Advanced Drug Delivery Reviews* **2016**, 105, 255; c) S. Kumar, K. Chatterjee, *ACS applied materials & interfaces* **2016**, 8, 26431.

[119]   X. Zhou, M. Nowicki, H. Cui, W. Zhu, X. Fang, S. Miao, S.-J. Lee, M. Keidar, L. G. Zhang, *Carbon* **2017**, 116, 615.

[120]   Z. Cheng, B. Landish, Z. Chi, C. Nannan, D. Jingyu, L. Sen, L. Xiangjin, *Materials Science and Engineering: C* **2018**, 82, 244.

[121]   G. Choe, S. Oh, J. M. Seok, S. A. Park, J. Y. Lee, *Nanoscale* **2019**, 11, 23275.

[122]   a) A. L. Rutz, E. S. Gargus, K. E. Hyland, P. L. Lewis, A. Setty, W. R. Burghardt, R. N. Shah, *Acta Biomaterialia* **2019**, 99, 121; b) J. Jang, T. G. Kim, B. S. Kim, S.-W. Kim, S.-M. Kwon, D.-W. Cho, *Acta Biomaterialia* **2016**, 33, 88.

[123]   L. M. Guiney, N. D. Mansukhani, A. E. Jakus, S. G. Wallace, R. N. Shah, M. C. Hersam, *Nano letters* **2018**, 18, 3488.

[124]   D. Aki, S. Ulag, S. Unal, M. Sengor, N. Ekren, C.-C. Lin, H. Yılmazer, C. B. Ustundag, D. M. Kalaskar, O. Gunduz, *Materials & Design* **2020**, 196, 109094.

[125]   H. Belaid, S. Nagarajan, C. Barou, V. Huon, J. Bares, S. Balme, P. Miele, D. Cornu, V. Cavaillès, C. Teyssier, *ACS Applied Bio Materials* **2020**, 3, 1865.

[126]   G. Turnbull, J. Clarke, F. Picard, P. Riches, L. Jia, F. Han, B. Li, W. Shu, *Bioactive Materials* **2018**, 3, 278.

[127]   D. Petta, A. Armiento, D. Grijpma, M. Alini, D. Eglin, M. D'Este, *Biofabrication* **2018**, 10, 044104.

[128]   L. Ouyang, *Study on Microextrusion-based 3D Bioprinting and Bioink Crosslinking Mechanisms*, Springer, **2019**.

[129]   J. Y. Shin, Y. H. Yeo, J. E. Jeong, S. A. Park, W. H. Park, *Carbohydrate polymers* **2020**, 238, 116192.

[130]   H. Rastin, M. Ramezanpour, K. Hassan, A. Mazinani, T. T. Tung, S. Vreugde, D. Losic, *Carbohydrate Polymers* **2021**, DOI: https://doi.org/10.1016/j.carbpol.2021.117989117989.

[131]   J. Koffler, W. Zhu, X. Qu, O. Platoshyn, J. N. Dulin, J. Brock, L. Graham, P. Lu, J. Sakamoto, M. Marsala, S. Chen, M. H. Tuszynski, *Nature Medicine* **2019**, 25, 263.

[132]   L. E. Bertassoni, J. C. Cardoso, V. Manoharan, A. L. Cristino, N. S. Bhise, W. A. Araujo, P. Zorlutuna, N. E. Vrana, A. M. Ghaemmaghami, M. R. Dokmeci, A. Khademhosseini, *Biofabrication* **2014**, 6, 024105.

[133]   I. Noshadi, S. Hong, K. E. Sullivan, E. S. Sani, R. Portillo-Lara, A. Tamayol, S. R. Shin, A. E. Gao, W. L. Stoppel, L. D. Black III, *Biomaterials science* **2017**, 5, 2093.

[134]   S. V. Murphy, A. Atala, *Nature biotechnology* **2014**, 32, 773.

[135]   a) A. J. Engler, S. Sen, H. L. Sweeney, D. E. Discher, *Cell* **2006**, 126, 677; b) F. Guilak, D. M. Cohen, B. T. Estes, J. M. Gimble, W. Liedtke, C. S. Chen, *Cell Stem Cell* **2009**, 5, 17.

[136]   Z. Zhang, Y. Jin, J. Yin, C. Xu, R. Xiong, K. Christensen, B. R. Ringeisen, D. B. Chrisey, Y. Huang, *Applied Physics Reviews* **2018**, 5, 041304.

[137]   G. Gillispie, P. Prim, J. Copus, J. Fisher, A. G. Mikos, J. J. Yoo, A. Atala, S. J. Lee, *Biofabrication* **2020**, 12, 022003.

[138]   A. Schwab, R. Levato, M. D'Este, S. Piluso, D. Eglin, J. Malda, *Chemical Reviews* **2020**, 120, 11028.

[139]   *Tissue Engineering Part A* **2020**, 26, 318.

[140]   a) A. Blaeser, D. F. Duarte Campos, U. Puster, W. Richtering, M. M. Stevens, H. Fischer, *Advanced healthcare materials* **2016**, 5, 326; b) W. Sun, B. Starly, A. C. Daly, J. A. Burdick, J. Groll, G. Skeldon, W. Shu, Y. Sakai, M. Shinohara, M. Nishikawa, J. Jang, D.-W. Cho, M. Nie, S. Takeuchi, S. Ostrovidov, A. Khademhosseini, R. D. Kamm, V. Mironov, L. Moroni, I. T. Ozbolat, *Biofabrication* **2020**, 12, 022002.

[141] R. L. Smith, D. R. Carter, D. J. Schurman, *Clinical Orthopaedics and Related Research (1976-2007)* **2004**, 427, S89.

[142] F. Zhao, R. Chella, T. Ma, *Biotechnology and bioengineering* **2007**, 96, 584.

[143] D. E. Discher, P. Janmey, Y.-l. Wang, *Science* **2005**, 310, 1139.

[144] M. Li, X. Tian, D. J. Schreyer, X. Chen, *Biotechnology Progress* **2011**, 27, 1777.

[145] P. Bianchi, G. Petit, J.-C. M. Monbaliu, *Reaction Chemistry & Engineering* **2020**, 5, 1224.

[146] a) K. Jakab, C. Norotte, F. Marga, K. Murphy, G. Vunjak-Novakovic, G. Forgacs, *Biofabrication* **2010**, 2, 022001; b) A. L. Rutz, K. E. Hyland, A. E. Jakus, W. R. Burghardt, R. N. Shah, *Advanced Materials* **2015**, 27, 1607; c) H.-W. Kang, S. J. Lee, I. K. Ko, C. Kengla, J. J. Yoo, A. Atala, *Nature Biotechnology* **2016**, 34, 312.

[147] J. A. Rowley, G. Madlambayan, D. J. Mooney, *Biomaterials* **1999**, 20, 45.

[148] B. Duan, E. Kapetanovic, L. A. Hockaday, J. T. Butcher, *Acta Biomaterialia* **2014**, 10, 1836.

[149] C. Sears, E. Mondragon, Z. I. Richards, N. Sears, D. Chimene, E. P. McNeill, C. A. Gregory, A. K. Gaharwar, R. Kaunas, *Advanced Healthcare Materials* **2020**, 9, 1901580.

[150] J. M. Lee, W. Y. Yeong, *Advanced healthcare materials* **2016**, 5, 2856.

[151] a) S. Hong, D. Sycks, H. F. Chan, S. Lin, G. P. Lopez, F. Guilak, K. W. Leong, X. Zhao, *Advanced materials* **2015**, 27, 4035; b) T. Cebe, N. Ahuja, F. Monte, K. Awad, K. Vyavhare, P. Aswath, J. Huang, M. Brotto, V. Varanasi, *Journal of Materials Research* **2020**, 35, 58; c) C. W. Peak, J. Stein, K. A. Gold, A. K. Gaharwar, *Langmuir* **2018**, 34, 917; d) A. Nadernezhad, O. S. Caliskan, F. Topuz, F. Afghah, B. Erman, B. Koc, *ACS Applied Bio Materials* **2019**, 2, 796.

[152] a) Y. M. Joshi, G. R. K. Reddy, A. L. Kulkarni, N. Kumar, R. P. Chhabra, *Proceedings of the Royal Society A: Mathematical, Physical and Engineering Sciences* **2008**, 464, 469; b) J. L. Dávila, M. A. d'Ávila, *Carbohydrate polymers* **2017**, 157, 1.

[153] D. W. Thompson, J. T. Butterworth, *Journal of Colloid and Interface Science* **1992**, 151, 236.

[154] B. Ruzicka, E. Zaccarelli, *Soft Matter* **2011**, 7, 1268.

[155] C. B. Highley, C. B. Rodell, J. A. Burdick, *Advanced Materials* **2015**, 27, 5075.

[156] G. Cidonio, C. R. Alcala-Orozco, K. S. Lim, M. Glinka, I. Mutreja, Y.-H. Kim, J. I. Dawson, T. B. Woodfield, R. O. Oreffo, *Biofabrication* **2019**, 11, 035027.

[157] G. Lokhande, J. K. Carrow, T. Thakur, J. R. Xavier, M. Parani, K. J. Bayless, A. K. Gaharwar, *Acta Biomaterialia* **2018**, 70, 35.

[158] B. Liu, J. Li, X. Lei, P. Cheng, Y. Song, Y. Gao, J. Hu, C. Wang, S. Zhang, D. Li, H. Wu, H. Sang, L. Bi, G. Pei, *Materials Science and Engineering: C* **2020**, 112, 110905.

[159] Y. Chen, X. Xiong, X. Liu, R. Cui, C. Wang, G. Zhao, W. Zhi, M. Lu, K. Duan, J. Weng, S. Qu, J. Ge, *Journal of Materials Chemistry B* **2020**, 8, 5500.

[160] a) D. Su, L. Jiang, X. Chen, J. Dong, Z. Shao, *ACS Applied Materials & Interfaces* **2016**, 8, 9619; b) Y. Liu, H. Meng, S. Konst, R. Sarmiento, R. Rajachar, B. P. Lee, *ACS Applied Materials & Interfaces* **2014**, 6, 16982; c) A. K. Gaharwar, P. J. Schexnailder, B. P. Kline, G. Schmidt, *Acta Biomaterialia* **2011**, 7, 568.

[161] a) H. Tomás, C. S. Alves, J. Rodrigues, *Nanomedicine: Nanotechnology, Biology and Medicine* **2018**, 14, 2407; b) D. Chimene, D. L. Alge, A. K. Gaharwar, *Advanced Materials* **2015**, 27, 7261.

[162] S. Wang, R. Castro, X. An, C. Song, Y. Luo, M. Shen, H. Tomás, M. Zhu, X. Shi, *Journal of Materials Chemistry* **2012**, 22, 23357.

[163] a) C. Boyer, L. Figueiredo, R. Pace, J. Lesoeur, T. Rouillon, C. L. Visage, J.-F. Tassin, P. Weiss, J. Guicheux, G. Rethore, *Acta Biomaterialia* **2018**, 65, 112; b) X. Xie, X. Li,

T. Zhou, T. Zhang, J. Liao, in *Cartilage Regeneration*, DOI: 10.1007/978-3-319-51617-2_5 (Ed: Y. Lin), Springer International Publishing, Cham **2017**, p. 77.

[164]   X. Zhai, Y. Ma, C. Hou, F. Gao, Y. Zhang, C. Ruan, H. Pan, W. W. Lu, W. Liu, *ACS Biomaterials Science & Engineering* **2017**, 3, 1109.

[165]   H. Jian, M. Wang, Q. Dong, J. Li, A. Wang, X. Li, P. Ren, S. Bai, *ACS applied materials & interfaces* **2019**, 11, 46419.

[166]   C. B. Highley, C. B. Rodell, J. A. Burdick, *Advanced Materials* **2015**, 27, 5075.

[167]   M. M. Stanton, J. Samitier, S. Sánchez, *Lab on a Chip* **2015**, 15, 3111.

[168]   J. Müller, A. C. Jäkel, D. Schwarz, L. Aufinger, F. C. Simmel, *Small* **2020**, 16, 2001815.

[169]   C. Li, A. Faulkner-Jones, A. R. Dun, J. Jin, P. Chen, Y. Xing, Z. Yang, Z. Li, W. Shu, D. Liu, R. R. Duncan, *Angewandte Chemie International Edition* **2015**, 54, 3957.

2.12 Outcome of this chapter

The outcome of this chapter is a submitted manuscript to the "Advanced Materials" journal as follows:

" **Rastin H**, Mansouri N, Hassan K, Mazinani A, Ramezanpour M, Yap P, Yu L, Thanh Tran, Vreugde S, Losic D, **Converging 2D Nanomaterials and 3D Bioprinting Technology: State-of-the-Art, Challenges and Potential Outlook in Biomedical Applications**, Advanced Materials, under review".

This paper provides a comprehensive review on the integration of 2D nanomaterials and 3D bioprinting. The main contributions of the 2D nanomaterials in the design of bioinks are categorized into six main classes as follows; 1) reinforcement effect, 2) delivery of bioactive molecules, 3) improved electrical conductivity, 4) enhanced tissue formation, 5) photothermal effect, 6) and stronger antibacterial properties.

Statement of Authorship

Title of Paper	Converging 2D Nanomaterials and 3D Bioprinting Technology: State-of-the-Art, Challenges and Potential Outlook in Biomedical Applications
Publication Status	☐ Published ☐ Accepted for Publication ☑ Submitted for Publication ☐ Unpublished and Unsubmitted work written in manuscript style
Publication Details	Rastin H, Mansouri N, Hassan K, Mazinani A, Ramezanpour M, Yap P, Yu L, Thanh Tran, Vreugde S, Losic D. Converging 2D Nanomaterials and 3D Bioprinting Technology: State-of-the-Art, Challenges and Potential Outlook in Biomedical Applications, Advanced Materials, under review

Principal Author

Name of Principal Author (Candidate)	Hadi Rastin
Contribution to the Paper	Conceptualization, Structure of manuscript, Original Draft.
Overall percentage (%)	70%
Certification:	This paper reports on original research I conducted during the period of my Higher Degree by Research candidature and is not subject to any obligations or contractual agreements with a third party that would constrain its inclusion in this thesis. I am the primary author of this paper.
Signature		Date	20/04/2021

Co-Author Contributions

By signing the Statement of Authorship, each author certifies that:

    i.   the candidate's stated contribution to the publication is accurate (as detailed above);

    ii.   permission is granted for the candidate in include the publication in the thesis; and

    iii.   the sum of all co-author contributions is equal to 100% less the candidate's stated contribution.

Name of Co-Author	Prof. Dusan Losic
Contribution to the Paper	Conceptualization, Resources, Funding Acquisition, Re-view&Editing, Supervision, submission
Signature		Date	20/04/2021

Name of Co-Author	Dr. Tran Thanh Tung
Contribution to the Paper	C-supervision, Review & Editing.
Signature		Date	20/04/2021

Please cut and paste additional co-author panels here as required.

Name of Co-Author	Arash Mazinani		
Contribution to the Paper	Review & Editing, Selected investigation		
Signature		Date	20/04/2021

Name of Co-Author	Kamrul Hassan		
Contribution to the Paper	Review & Editing, Selected investigation		
Signature		Date	20/04/2021

Name of Co-Author	Sarah Vreugde		
Contribution to the Paper	Re-view&Editing		
Signature		Date	20/04/2021

Name of Co-Author	Mahnaz Ramezanpour		
Contribution to the Paper	Re-view&Editing		
Signature		Date	20/04/2021

Name of Co-Author	Pei Lay Yap		
Contribution to the Paper	Selected investigation, Re-view&Editing		
Signature		Date	20/04/2021

Name of Co-Author	Le Yu		
Contribution to the Paper	Review & Editing, Selected investigation		
Signature		Date	20/04/2021

Name of Co-Author	Negar Mansouri		
Contribution to the Paper	Selected investigation, Review & Editing.		
Signature	*Negar Mansouri*	Date	20/04/2021

Converging 2D Nanomaterials and 3D Bioprinting Technology:

State-of-the-Art, Challenges and Potential Outlook in Biomedical Applications

Hadi Rastin [a,b], Negar Mansouri [a,c], Kamrul Hassan [a,b], Arash Mazinani [a,b], Mahnaz Ramezanpour [d], Pei Lay Yap [a,b], Le Yu [a,b], Tran Thanh Tung [a,b], Sarah Vreugde [d], Dusan Losic [a,b]*

[a] School of Chemical Engineering and Advanced Materials, The University of Adelaide, South Australia 5005 Australia

[b] ARC Research Hub for Graphene Enabled Industry Transformation, The University of Adelaide, South Australia 5005 Australia

[c] School of electrical and electronic engineering, The University of Adelaide, South Australia 5005, Australia

[d] Department of Surgery-Otolaryngology Head and Neck Surgery, The University of Adelaide, Woodville South, Australia

Corresponding author: Professor Dusan Losic

E-mail address: dusan.losic@adelaide.edu.au

1

Abstract:

Three-dimensional (3D) bioprinting allows rapid patterning of living and non-living biological materials through robotic dispensing of bioink into a tissue-like architecture. The development of next-generation of bioinks aims to fabricate anatomical size 3D scaffold with high printability and biocompatibility, which match the physicochemical properties of the native tissues. Along with the progress in 3D bioprinting, two-dimensional nanomaterials (2D NMs) proved to be emerging frontiers in the development of advanced materials owing to their extraordinary properties. Harnessing the properties of 2D NMs in 3D bioprinting technologies can revolutionize the development of bioinks by endowing new functionalities to the current bioinks. Despite multiple published reviews on the advancements of 3D bioprinting technology using nanomaterials, there is still a gap in the review considering the added value of 2D NMS in the design of bioinks.

In this review article, in the first instance, the main contributions of 2D NMS in 3D bioprinting technologies were categorized into six main classes: 1) reinforcement effect, 2) delivery of bioactive molecules, 3) improved the electrical conductivity, 4) enhanced tissue formation, 5) photothermal effect, 6) and stronger antibacterial properties. Second, the recent advances in the use of each certain 2D NMs ((1) Graphene, (2) nanosilicate, (3) black phosphorus, (4) MXene, (5) transition metal dichalcogenides, (6) hexagonal boron nitride, and (7) metal-organic frameworks) in 3D bioprinting technology were critically summarized and evaluated thoroughly. Third, the role of physicochemical properties of 2D NMSs on their cytotoxicity is uncovered, with several representative examples of each studied 2D NMs. Finally, current challenges, opportunities, and outlook for the development of nanocomposite bioinks are discussed thoroughly. This review paper also aims to provide a comprehensive

2

summary and applicable recommendations for the design of next-generation 2D NM-based inks in 3D bioprinting technology. This review paper would be of great interest to the broad range of experienced and young researchers including biomedical engineers, biologists, material scientists, and chemical engineers.

3

Table of Contents

4

5

1. Introduction

Two-dimensional nanomaterials (2D NMs) refer to the class of materials characterized with their atomic thickness in one dimension, while the other two dimensions are beyond nanoscale [1]. 2D NMs exhibit unprecedented characteristics arising from their thinness, which cause 2D NMs to exceed their 3D counterparts in various ways [2]. Intensive global interest in 2D NMs began after the isolation of single-layer graphene nanosheets from graphite via mechanical stripping in 2004 [3]. Graphene is made up of single-layer carbon atoms connected in the hexagonal arrangement that demonstrates extraordinary properties such as high thermal and electrical conductivity, large specific surface area, excellent optical transparency, and high mechanical strength [4]. These extraordinary properties of 2D graphene have inspired scientists and researchers to explore additional graphene-analogous 2D NMs. This search has led to the discovery of dozens of 2D NMs over the last two decades and many other 2D NMs still yet to be discovered [5]. (1) Graphene-related materials [6], (2) nanosilicate [7], (3) black phosphorus (BP) [1c, 8], (4) MXene [9] (5) transition metal dichalcogenides (TMDs) [10], (6) hexagonal boron nitride (hBN) [11], and (7) metal–organic frameworks (MOF) [12] are among the most widely-explored 2D NMs in various technological applications due to their promising physicochemical properties. These 2D NMs possess a layered structure with strong in-plane covalent bonds and weak Van der Waals forces between layers[1b]. Although 2D NMs shares similarity in their planar nanostructure, they possess highly diverse properties due to their unique chemical composition and atomic arrangement [1a, 1b, 5]. As an emerging class of materials, 2D NMs also offer promising merits for a variety of biomedical applications such as drug delivery [13], biosensing [14], cancer therapy [15], and regenerative medicine [5, 16]. However, despite the significant advances that have been made in the synthesis and exploring the fundamental

6

properties of 2D NMs, the potential usage of 2D NMs for biomedical applications that need macroscopic structures has not been fully realized. Considering that the ultimate performance of macroscopic materials relies on both the nature of comprising materials and the fabrication methods, it is of utmost importance to assemble 2D NMs into macroscopic structures in a controlled manner.

Tremendous attention has been devoted to the recently emerged 3D bioprinting technology for the fabrication of functional tissue-engineered scaffold loaded with cells due to its ability to assemble complex structures with meticulous control over the entire fabrication process [17]. It is a computer-assisted technology that enables the direct fabrication of complex 3D constructs usually layer upon layer fashion according to a pre-designed structure. In fact, this 3D bioprinting concept was borrowed from 3D printing technology that has been primarily exploited in fabrication industries as a rapid prototyping technology [18]. Harnessing the 3D printing technology in the generation of personalized implants [19], tissue-engineered scaffolds [20], drug delivery devices [21], tissue models [22] have opened up a new avenue for the biofabrication methods. For bioprinting application, an ideal (bio)ink should possess a set of desirable properties including biodegradability, biocompatibility, providing mechanical strength and rheological properties, and closely mimicking the native tissue microenvironment [17b, 23]. The selection of materials to be used as bioinks remains the main bottleneck in the realization of 3D bioprinting technology.

The integration of 2D NMs and 3D printing has led to the development of advanced bioinks with added functionality, which is unattainable with conventional biomaterials [24]. The urgent need for the design of multi-functional inks with superior performance has been the main incentive for researchers to exploit 2D NMs in the design of inks (**Figure 1**). Although many

7

review papers have been published on the application of 2D NMs in biomedical applications [1c, 5, 7, 25], most have overlooked the 3D bioprinting technology. So far, a little effort has been devoted to providing a critical review of various types of 2D NMs focus on 3D bioprinting technology. Recently, a few review papers have been published that include the application of 2D NMs in electronic devices and sensors by using 3D printing applications [26]. However, the biomedical applications and the works that has been carried out by employing different 2D NMs in 3D bioprinting. Have not been addressed to date. In view of the extraordinary properties of 2D NMs and significant advances in the 3D bioprinting technology, it is timely to summarize and critically evaluate the performance of 2D nanocomposite bioinks in biomedical applications. In this review article, we provide a comprehensive literature review, which would be useful for material scientists, molecular biologists, and biomedical engineers. This review paper has been organized as follows:

- *Section 2* outlines the main state-of-the-art 3D bioprinting modalities and provide a comprehensive comparison between different techniques. To address the question 'which 3D bioprinting mode for certain ink?' is the chief goal of this section, with special stress on extrusion-based printing as the mainstream in the current printing field.

- *Section 3* briefly summarizes and compares the 2D NMs synthesis approaches including bottom-up and top-down techniques. Without digging into excessive details as they can be accessed in the plethora of literature [27], only the principle of each technique is emphasized.

- *Section 4* categorizes the contributions of 2D NMs in the inks' formulations into six classes as follows: 1) reinforcement effect, 2) delivery of bioactive molecules, 3) improved the electrical conductivity, 4) enhanced tissue formation, 5) photothermal effect, 6) and

8

stronger antibacterial properties. Next, the added values of each studied 2D NMs in the design of inks are discussed separately (*section 5*).

- Along with the rapidly growing potential biomedical applications of 2D NMs, it is of utmost importance to prudently evaluate the biocompatibility of 2D NMs in-depth to optimize their physicochemical properties for a specific application. However, research on 2D NMs is still at the preliminary stage and an in-depth understanding of their biological effects and subsequently their biocompatibility and nanotoxicological profiles are still lacking. Thus, *section 6* outlines vital issues in the cytotoxicity assessment of 2D NMs including cellular uptake mechanisms of 2D NMs, intracellular trafficking of 2D NMs, possible toxicity origins of 2D NMs, employed methodologies in the toxicity evaluations of 2D NMs, and the role of physicochemical properties of 2D NMs on the cytotoxicity. Finally, some representative examples regarding the cytotoxicity of each studied 2D NMs are provided separately.

- And finally, the currently unsolved challenges and future perspectives towards 2D NMs-based bioinks are discussed thoroughly, which provides a clear roadmap for the next-generation of bioinks (*sections 7 and 8*).

9
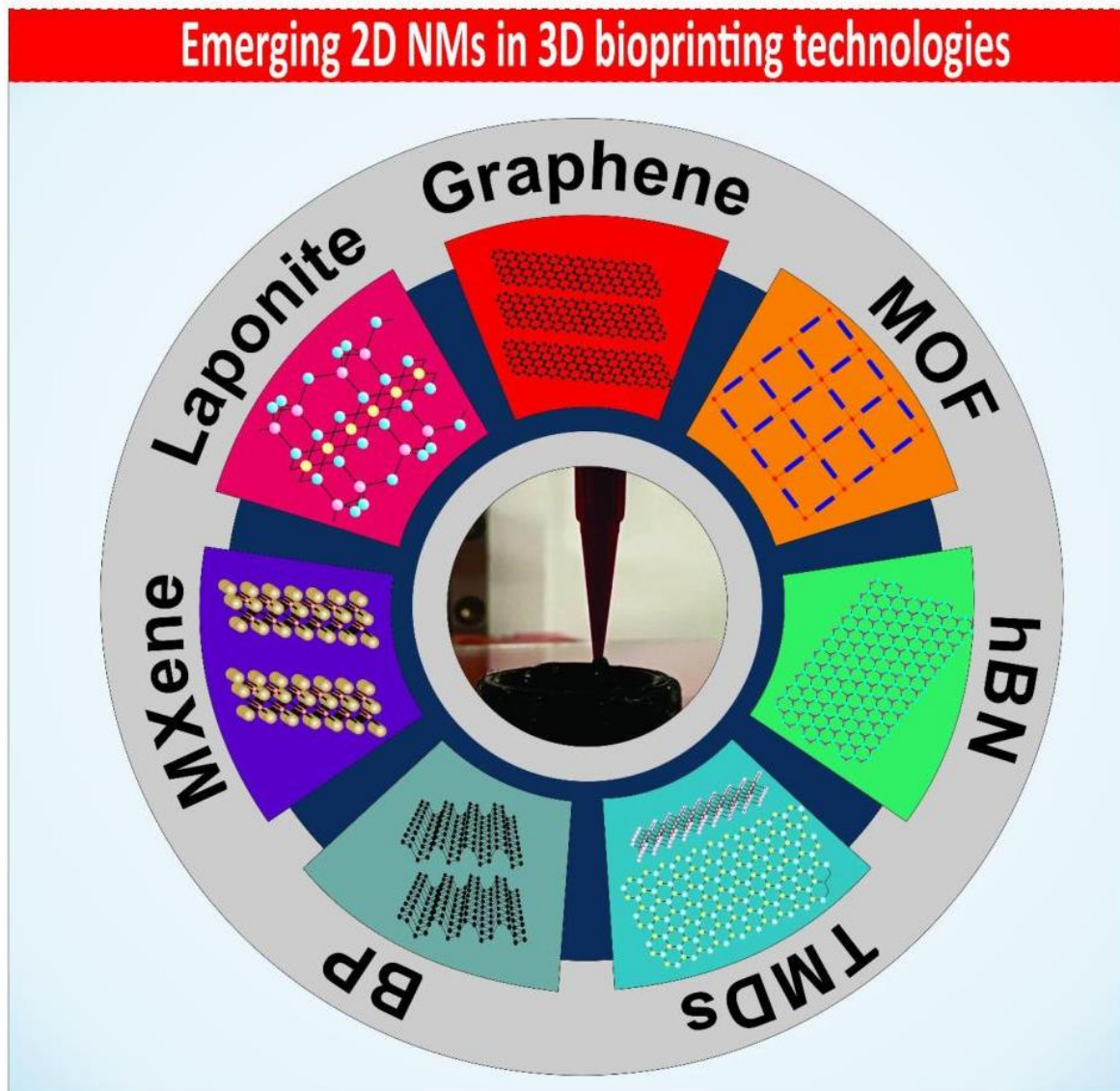
Figure 1. Schematic illustrations of the existing 2D NMs that have been applied in 3D bioprinting technology.

2. 3D bioprinting technologies

Fabrication of tissue-like models with precise control over the biological elements has been benefited from the advancement of 3D bioprinting technologies. When it comes to bioprinting technology, it is necessary to clarify the basic definition of "bioinks" and its distinction from "biomaterial inks". As proposed by Groll et al. [28], irrespective of the type of

10

bioprinting technology, bioinks can be defined as a formulation that must contain cells as a mandatory component before the printing process (**Figure 2 a**), while biomaterial ink does not directly mix with cells, and cells are seeded on the scaffold once printed (**Figure 2 b**). As an example of the bioink formulation, Dubbin et al. [29], developed a bioink composed of modified alginate with proline-rich peptides and a recombinant protein with the complementary peptide-binding domain. The resulting weak binding between two complementary peptide domains prevents the sedimentation of encapsulated cells (**Figure 2 a**). On the other hand, as an example of biomaterial ink, Liu et al. [30] printed out poly(ε-caprolactone) (PCL)/ Strontium-containing hydroxyapatite (SrHA) biomaterial ink first, after which seeded bone marrow-derived mesenchymal stem cells (BMSCs) on the scaffolds (**Figure 2 b**).

In the context of 3D bioprinting technology, the common biomaterials can be divided into two main groups [17b]: (a) hard biomaterials such as ceramics, bioglass, and synthetic polymers that generally need high temperature or toxic solvents to be printed that makes them inappropriate for cell encapsulation. According to the above-mentioned definitions, these materials fall into the biomaterial ink category. (b) Soft biomaterials such as hydrogels are the commonly used materials in 3D bioprinting for cell-encapsulation due to their high water uptake capacity [31]. Therefore, soft biomaterials can be used in bioinks or biomaterial ink formulations. According to these definitions, bioprinting technology can be divided into two main categories based on whether or not they incorporate living cells: (i) acellular bioprinting techniques that print biomaterial inks and (ii) cellular bioprinting techniques that prints bioinks [17b]. To fabricate a 3D living architecture, viable cells can directly deposit with bioinks by using cellular bioprinting techniques, which deliver some advantages. For example, the post-cell seeding procedure is avoided when using bioinks, which is a challenge for researchers. On the

11

other hand, acellular bioprinting techniques deliver some advantages as well for tissue regeneration applications rather than cellular bioprinting techniques [32]. For example, a variety of 3D printing techniques with specific conditions (e.g. higher temperatures, chemicals, and other harsh environments) and biomaterials can be employed for the fabrications of implants or tissue [33].

12
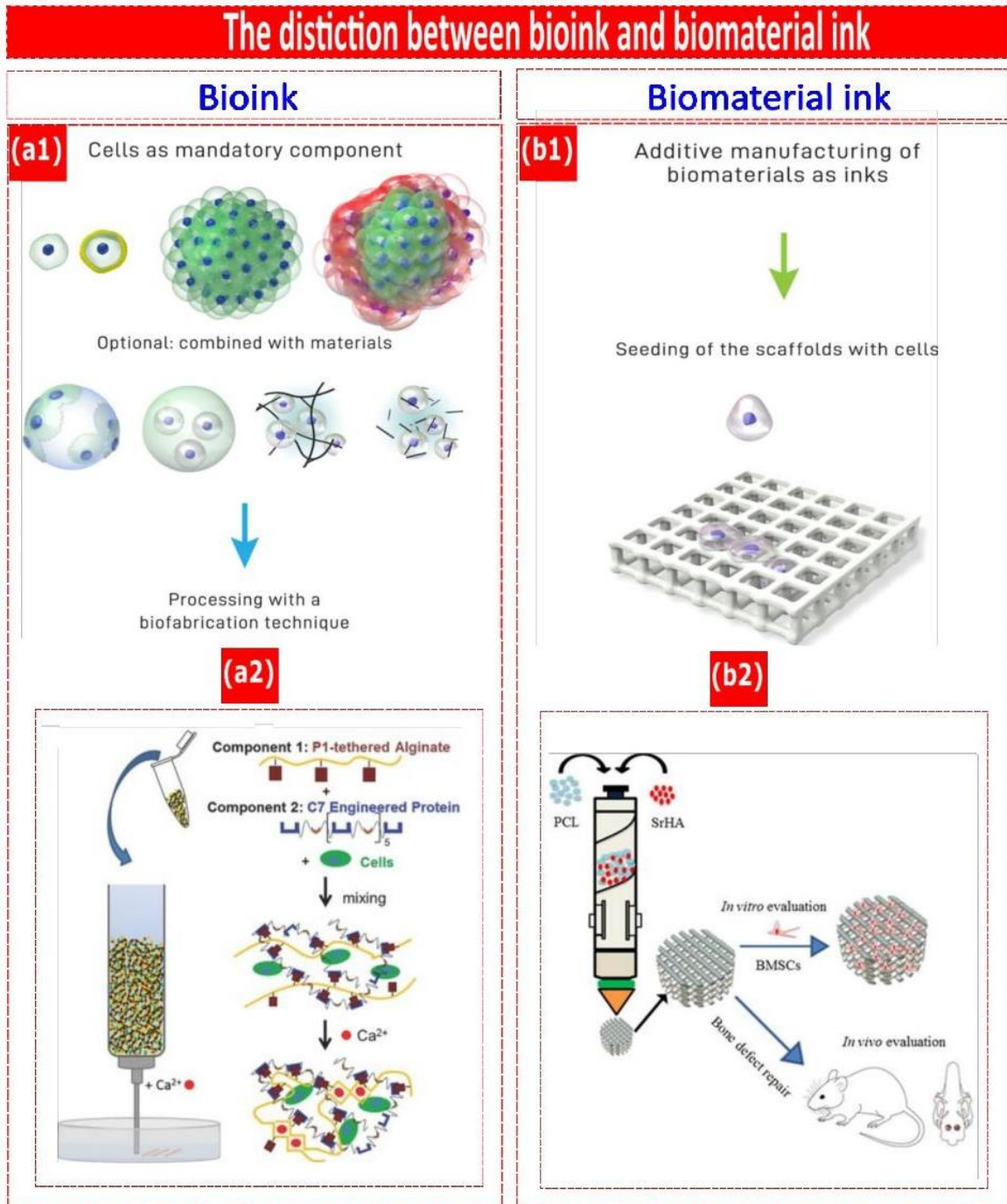
Figure 2. The distinction between a bioink (left) and biomaterial ink (right). (a1) In the

case of bioink, cells are regarded as the mandatory component of the printing formulation [28].

Reproduced with permission from ref. [28], Copyright (2018) IOPSCIENCE. (a2) An example of

bioink composed of modified alginate with proline-rich peptide (P1) and a recombinant

13

protein (C7), in which NIH 3T3 cells or hASCs were encapsulated within the hydrogel [29]. Reproduced with permission from ref. [29], Copyright (2016) Wiley-VCH. (b1) In the case of biomaterial ink, cells are not part of printing formulation and are just seeded after the printing process [28]. (b2) An example of biomaterial ink composed of PCL and SrHA. 3D structures were printed first, after which BMSCs were grown on the scaffold [30]. Reproduced with permission from ref. [30], Copyright (2019), Elsevier.

Inkjet [34], extrusion [35], laser-assisted printing [36], and stereolithography [37] are the dominating modes of 3D bioprinting technology based on the working condition of bioprinting technology. These technologies have specific inherent advantages and disadvantages, which need to be carefully considered to select the best printing technology for targeted technology. These include the viscosity of ink, printing speed, resolution, cell density, and cost. Most importantly, the functions of living cells/organ architectures are also affected by the variation of available bioprinting technologies [38]. **Figure 3** presents schematically these printing technologies along with the advantages and disadvantages of these methods considering throughput (speed), required viscosity range, acceptable cell viability, and overall material loading. The key performances of these methods are summarized in the following section [39].

14

Common modes of 3D bioprinting technologies

Extrusion Bioprinting

- Ability to print high viscose inks,
- High cell density,
- Moderate cost
- Slow printing speed
- Risk of cell membrane damage
- Low printing resolution
- Occurrence of nozzle blockage

Inkjet Bioprinting

- High resolution
- Fast print speed
- Inexpensive
- Low cell destiny
- Required post-crosslinking which can potentially damage cell
- Settling of encapsulated cells
- Inability to print high viscose ink

Laser-assisted Bioprinting

Laser Pulse

Energy-absorbing layer

Bioink layer

Substrate

- High resolution
- Ability to print ink with viscosity of up to 300 mPa.s
- High cell density
- Avoided nozzle blockage matter
- Expensive
- Long printing speed
- Risk of contamination by metallic residues
- Risk of cell damage due to the heat shock

Stereolithography

Laser Pulse

Substrate

Bioink reservoir

- Inexpensive
- High resolution
- Fast print speed
- High cell density
- Avoided nozzle blockage matter
- Required large amount of bioink
- Risk of cell damage during crosslinking
- Inability to print 3D structures with horizontal gradients

Figure 3. Most common fabrication techniques are used within bioprinting along with their key features.

2.1. Extrusion- based bioprinting mode

In the early 2000s, extrusion-based bioprinting technology was first introduced, which gained more attention among all bioprinting technologies in the fabrication of complex

15

tissue/organs [40]. Extrusion-based bioprinter functions quite similarly to fused deposition modeling in terms of the printing process but dispensing cell-laden hydrogels, in which the bioink is pushed out through a nozzle [35]. Despite other bioprinting modes that dispense small droplets, an extrusion-based bioprinter pushes bioink filament through a nozzle in a continuous process by application of either pneumatic or mechanical forces [41]. Extrusion-based bioprinter enables the fabrication of 3D architectures by stacking 2D patterns in a layer-by-layer manner.

A notable advantage of micro-extrusion bioprinting mode is the ability to obtain high cell density similar to physiologically relevant tissues [31, 39]. In addition, 3D extrusion-based bioprinting mode has shown promise in the printing of a broad spectrum of biomaterials with viscosities ranging from 30 mPa/s up to 6×10^7 mPa/s [19a, 42]. While high-viscose bioinks can provide better printability and structural integrity, the low-viscose bioink is more beneficial for maintaining cellular functions [39, 43]. Therefore, often, researchers attempt to exploit advanced bioinks with shear-thinning behavior to fulfill both printability and biocompatibility simultaneously [44]. Shear-thinning behavior allows easy extrusion of materials along the nozzle as the viscosity of bioink drops in response to an increase in the shear rate in the nozzle [45]. Once ink exits the nozzle, the viscosity returns to its initial value and provides enough mechanical strength for subsequent layers. The high viscosity of bioink provides the initial structural integrity without the need for rapid post-crosslinking in contrast to other bioprinting modes. In addition, owing to its inherent high printing speed, this mode permits the fabrication of anatomically-relevant size tissues [46]. Taken together, extrusion-based bioprinting has become the most widespread mode, allowing the construction of anatomically-relevant size tissues within a reasonable processing time.

16

One of the main advantages of extrusion-based bioprinter is the ability to add an extra syringe, which realizes the printing of multiple bioinks loaded with various cell types [47]. This is highly valuable for the fabrication of complex tissue with multiple cell types and microenvironments. For example, Ozbolat et al. [48] fabricated an extrusion-based 'multi-arm bioprinter', allowing printing of multi-material within a lower time frame, while being capable to process multiple cell types simultaneously. These capabilities empower the extrusion-based printer to generate complex architectures. Lately, Liu et al. [49] proposed a swift continuous multi-material extrusion-based bioprinter, which is capable to print up to seven various kinds of bioinks without the need for switching of printing nozzles (**Figure 4**). The extrusion printer consists of a multi-channel, whereas each channel is connected to its bioink reservoir. The dedicated printer software is used to open the valve of each channel to diffuse various bioinks at the anticipated moment by a print head system. The benefit of this methodology is the negligible absence of an opening gap between the switching processes. As a testing procedure, they printed a range of complex 3D architectures from multi-layer cubes consisting of 2/3 various bioinks shaped as human organ structures from multiple bioinks.

One common drawback of extrusion-based bioprinter is the risk of cell membrane damage during printing, which decrease the cell viability compared to other modes [38, 46b, 50]. The mechanical shear stress inflicted on cells during printing proved to have a detrimental effect on the cellular viability as well as cellular functions [50]. Although the reduction in cell viability can be diminished by using lower printing speed or larger nozzle size, it would result in a longer processing time or loss of printing resolution. Compared to other bioprinting modes, inferior printing resolution of extrusion-based bioprinting is another major drawback of this

17

mode [51]. In addition, the blockage of the nozzle is a potential challenge in extrusion-based bioprinter once high viscose bioink is printed [39, 52].

Figure 4. 3D bioprinted architectures through swift continuous multi-material extrusion-based bioprinting [49]. (a) Dual-layered cuboid block, (b) triple-layered cuboid block, (c-e) blood-vessel like constructs of dual, triple, and quadruple materials, respectively, (f) seven material-containing pyramid, (g-h) continuous segments of seven different bioinks in three- and ten-layered blocks, (i) separately printed organ-like constructs from multiple bioinks, (j-n) side views of constructs in ('i') to show 3D nature; (j) brain, (k) lung vascular, (l) kidney, (m) left atrium (heart), (n) bladder/prostate. Reproduced with permission from ref. [49], Copyright (2016) Wiley-VCH.

2.2. Inkjet-based bioprinting mode

With superior features of inkjet bioprinting such as low cost, fast process, noncontact mode, and high resolution, extensive interest has been drawn to inkjet-based bioprinting to fabricate 3D tissue-like constructs [34]. According to its basic working process, inkjet-based bioprinting mode prints a controlled volume of discrete droplets on the printing substrate by applying external forces behind a nozzle [53]. Like extrusion-based bioprinting technology, this mode can also print different cell types [54] and materials [55] simultaneously once equipped with multiple nozzles. Inkjet-based bioprinting has demonstrated excellence in the fabrication of small-scale tissues due to its high resolution.

Inkjet bioprinting including continuous-inkjet, drop-on-demand (DOD) inkjet, and electrodynamic inkjet are more popular forms of direct bioprinting techniques [40]. In the case of continuous inkjet printing, bioink is stored in a chamber and subsequently extruded through a nozzle. This extruded stream via a nozzle breaks up into droplets owing to the Rayleigh-Plateau instability [56]. On the other hand, the DOD inkjet technique creates droplets by using thermal/piezoelectric actuators, and/or electrostatic forces, which make this technique more preferable than continuous inkjet bioprinting. Moreover, its low cost, high resolution (20–100 µm) along with the diffusion of numerous materials via multiple nozzles make this technique more advantageous. However, the DOD technique has some drawbacks as well such as selectivity of low viscous materials, longer processing time, and weak mechanical characteristics of printed patterns [32]. The third subdivision of inkjet bioprinting is electrohydrodynamic bioprinting, which exercises an electric field to drag the droplet through the orifice of the nozzle [57]. The ability to use a small diameter orifice with high concentrated bioinks uplifts this technique rather than other inkjet techniques [56].

19

A common drawback of inkjet-based bioprinting mode is the difficulty in the printing of high-viscose bioinks [58]. This mode is only able to print bioinks with low viscosity (<15 m.Pa/s), which requires immediate post-crosslinking by ionic [59], thermal [60], photo [61], and pH [62] crosslinking strategies to stabilize the printed structure. Post-crosslinking strategies are usually associated with excessive chemical modifications of bioink components before printing or using products or conditions that might be toxic to the cells, which can potentially deteriorate the cell viability [63]. In addition, to fulfill the viscosity requirement, bioink cannot encapsulate high cell density because loading high cell density increases the viscosity and subsequently results in the blockage of the nozzle [64]. These limitations prevent its usage in the fabrication of large-scale tissue/organs with high mechanical strength. Another drawback of inkjet-based bioprinting mode is the settling of encapsulated cells on the lower position of cartilage once transferred to the syringe, resulting from the low viscosity of the bioink [65]. Settling of cells not only results in the heterogeneous distribution of cells, but also increases the viscosity of ink placed in the lower position of cartilage and subsequently leads to the blockage of the nozzle.

The potential application of inkjet-bioprinting mode in the fabrication of functional tissues has been demonstrated by many researchers, as reviewed comprehensively elsewhere [66]. For example, Sanjana et al. [58c] demonstrated neuron adhesive patterns as a basal podium and other patterns adopting PEG (cell-repulsive material) as well as collagen/poly-D-lysine mixture (cell adhesive material) by using inkjet bioprinting technology. In addition, by using this technology, Xu et al. [67] fabricated fibrin-based 3D scaffolds, which were used to construct a 3D neural network. Later, Lee et al. [62] demonstrated artificial neural tissue fabricated by printed murine neural stem cells (NSCs) contained fibrin gel and characterized the properties of the fibrin gel on the endurance of the murine NSCs.

20

2.3. Laser-assisted bioprinting mode

Laser-induced forward transfer (LIFT) printing, also known as laser-assisted bioprinting, was first adapted for cell bioprinting in 1999 [68]. The LIFT system consists of three major parts: (i) pulsed laser sources usually work with ultraviolet (UV) or near-UV wavelengths, (ii) a donor slide (ribbon) that comprised an energy-absorbing layer (Au/Ti) on the top that responds to the stimulation of laser source and cell-containing bioink that dangled on the bottom of donor layer, (iii) a collector substrate that receives the printed material [69]. In a typical working process of LIFT bioprinting, a laser pulse focuses on the small region of the absorbing layer, where locally evaporates the absorbing layer and therefore generates a high-pressure bubble at the interface of bioink and absorbing layer. This high-pressure bubble puts pressure on the bioink to propel towards the collector substrate followed by crosslinking [69a, 70]. The resolution of LIFT and associated droplet size generally depends on the array of factors such as the thickness and viscosity of bioink, the laser pulse energy, the air gap between the donor and receiver slides, the surface tension, and the hydrophilicity of the substrate [36b, 71].

The advantages of the LIFT bioprinting mode stem from its nozzle-free working process [34a, 72]. For example, the nozzle clogging problem is avoided in LIFT bioprinting whereas other bioprinting modes often encounter nozzle clogging during printing. Moreover, the nozzle-free process of LIFT mode avoids mechanical shear stress that cells experienced along the nozzle in other printing modes, which results in higher cell viability [69b, 73]. In addition, LIFT bioprinting can print low-to-medium viscose bioink, which broaden its usage to print a wide range of bioinks compared to inkjet-based mode. This mode also can deposit high cell density 10^8 cells/mL with high resolution by adjusting the printing parameters [36b, 74].

Despite its superior properties compared to other bioprinting techniques, there is a disadvantage as well [31a]. First, the common drawback of LIFT bioprinting mode is its long processing time, hampering the fabrication of large-scale tissue [75]. Second, the adaptation of the LIFT printing parameters is a complex process for users. Third, although the cost of the LIFT system has experienced a rapid decline, it is still a considerably expensive system compared to other bioprinting modes. Fourth, evaporation of laser-absorbing layer once irradiated by laser might leave a trace of metallic residues, imposing the risk of contamination. To address this issue, it is suggested to replace the metallic laser-absorbing layer with a non-metallic laser-absorbing layer [76]. Fifth, the laser might damage the cells due to the thermal shock [77]. Given these limitations, LIFT bioprinting is less popular compared to other printing modes.

An elaborate example of influencing parameters of LIFT bioprinting technology on skin cells (fibroblasts, keratinocytes) and human mesenchymal stem cells (hMSC) was reported [78]. They applied this printing technique on these cells because of their high potential in the regeneration of human skin as well as a possible application of stem cell therapy. They demonstrated the influence of the LIFT technique on cells by characterizing the cell's survival rate, proliferation, and apoptotic activity by monitoring for several days. It was found that both cell types remain viable during the printing procedure as the survival rate was reported 98%±1% for skin cells and 90%±10% for hMSC. In addition, no increases in apoptosis or DNA fragmentation were detected for both cell types after applied for the printing procedure. They showed in their study that, the LIFT technique can be considered as a suitable technology for computer-controlled positioning of numerous cell types and a capable tool for tissue engineering.

22

2.4. Stereolithography mode

Apart from the bioprinting methods above, stereolithography is a more remarkable bioprinting technique that uses light for the crosslinking of light-sensitive bioinks in a layer-by-layer manner [79]. In this technique, a laser/digital light projector is used over a bath of light-sensitive bioinks to create a single printing plane [69a]. Next, the printing stage moves downward, allowing the new bioink solution to cover the printed layer and then the new layer projected on the top of the previous layer. Therefore, the printer head only needs to move in a unidirectional plane, which provides high resolution (90%) printing patterns [80]. In addition, irrespective of the complexity of the pattern, the printing time for each layer is the same because the whole pattern is projected over the printing plane, which makes this mode relatively easy to control the printing process [81].

Despite all these advantages, there are some limitations associated with the stereolithography mode, which restricted its biomedical applications [51, 82]. First, although the stereolithography printer is an inexpensive system, the need for a large amount of bioink solution imposes an additional cost. Second, the harmful nature of the UV-based cross-linking method and the risk of toxicity of photo-initiators residuals are challenges for the stereolithography users [83]. Third, UV usually involves an excessive post-crosslinking process to remove the trapped inks within the products [82]. Fourth, suitable bioinks with desired biocompatibility and biodegradable for stereolithography are lacking. However, significant progress has been made recently in the development of light-sensitive polymers suitable for stereolithography printing [37a]. Fifth, stereolithography is not compatible with the fabrications of 3D structures with horizontal gradients.

23

stereolithography has been exploited for the fabrication of microfluidic architectures for organ-on-chip platforms by using transparent biocompatible polymers [84]. Since stereolithography eradicates the necessity of costly molds as well as has the benefit of swift prototyping, stereolithography-based microfluidic architecture may lead to competent commercialization of organ-on-chip platforms [85].

3. Synthesis of 2D NMs

With remarkable properties and growing applications explored in 2D NMs recently, it is necessary to develop effective synthetic methods for the manipulation of high quality and scalable 2D NMs with defined properties in terms of the number of layers, lateral size, and functionalization. To achieve nanofabrication of 2D NMs, two key approaches, namely, bottom-up or top-down strategies, have been explored (**Figure 5**) [27a, 86]. Both approaches have their strengths and limitations depending on the application of the final 2D NMs [87]. The bottom-up approach is capable of fabricating NMs with a more uniform chemical composition, fewer defects, and a more ordered structure. While a top-down strategy usually gives rise to a lower cost and high yield of 2D NMs accompanied by the downside of creating more defects within the structure of the 2D NMs as well as the tendency to generate lower quality of 2D NMs compared to the bottom-up approach [88]. Due to the extensive studies available in the literature, in this section, only the main synthesis approaches of 2D NMs are covered in this section. However, the interested reader can find more detailed and comprehensive information on various synthesis methods in the cited papers or other literature [27b, 88-89].

24
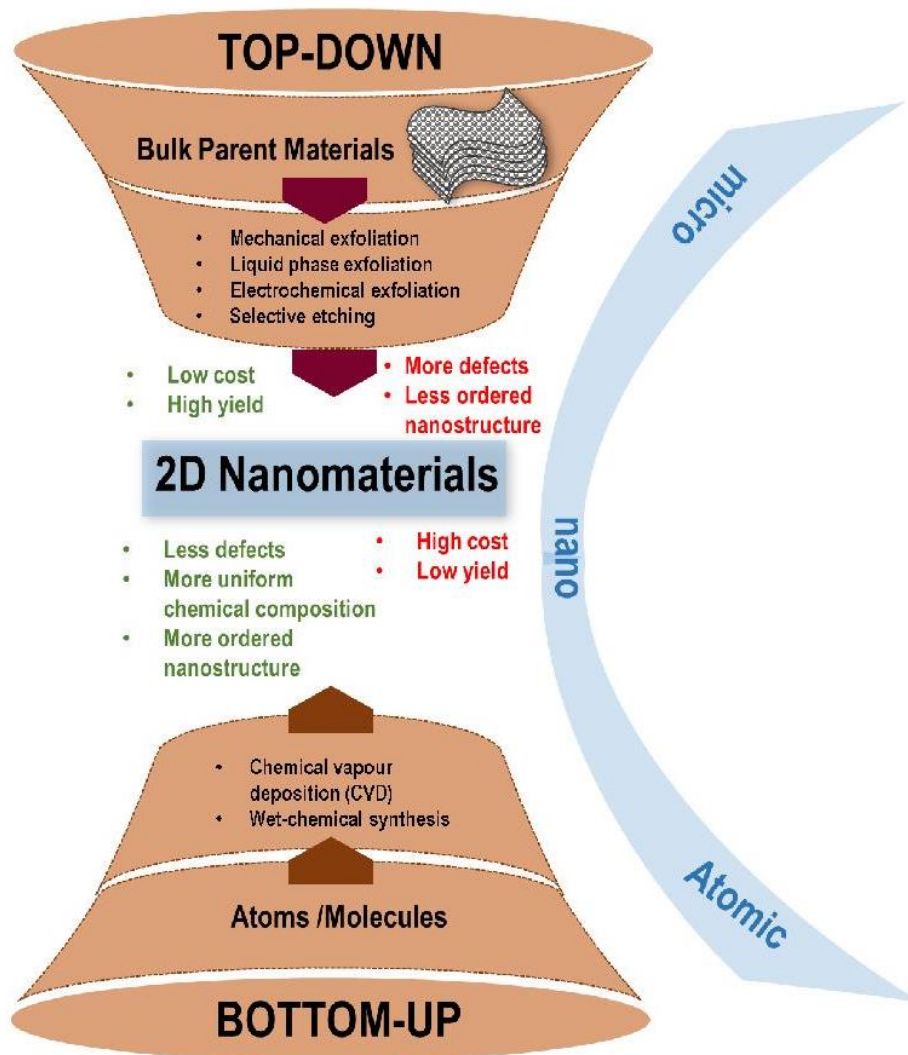
Figure 5. Overview synthesis of 2D NMs through top-down and bottom-up approaches.

3.1. Top-down approach

The top-down approach essentially involves breaking down bulk parent materials from stacked multilayers into single or few layers sheets with atomic-scaled thickness in a reverse engineering fashion [5]. This approach applies external driving forces to break the van der Waals forces that hold the crystalline layers of 2D NMs together. Mechanical exfoliation, liquid-phase

25

exfoliation, ion intercalation, and selective etching are among the popular top-down strategies used to prepare 2D NMs [5, 86a].

3.1.1. Mechanical exfoliation

Mechanical exfoliation has been broadly used to synthesize 2D NMs since the successful exfoliation of graphite into single-layer graphene by Novoselov and Geim [3, 90]. This method can be regarded as a direct, versatile, and low-cost strategy that preserves the crystal structure and properties with fewer defects being introduced to the pristine 2D NMs. However, this technique is limited to large scale production [91]. A simple procedure as illustrated in **Figure 6 a** shows the use of mechanical force to exfoliate single-layer graphene with Scotch tape [90a].

3.1.2. Liquid-phase exfoliation

Exfoliation of 2D NMs through liquid-phase approach can be considered as the most popularly adopted method to prepare 2D NMs owing to its advantages including flexibility, low cost, and high yield[92]. Numerous exfoliating agents such as ionic liquids, organic solvents, and surfactants are used to 'peel' the bulk parent 2D NMs into their corresponding nanosheets for enhanced stabilization of nanosheets in the solution [86a, 88]. Often, this method is assisted by mechanical stirring or sonication for effective exfoliation of the 2D NMs. Ultrasonic exfoliation is a versatile approach to improve the scalable liquid-phase exfoliation of 2D NMs at a low cost [90a, 91]. Taking laponite (a type of clay mineral) as an example (**Figure 6 b**), the electrostatic forces between the negatively charged layer and interlayer cations must be overcome to delaminate the laponite layer into the exfoliated clay nanoplatelets. This exfoliation technique is usually performed by manipulating parameters such as sonication time, initial material concentration, adding surfactants, or a suitable solvent to attain single or few layers of 2D NMs

26

[90a, 93]. Nevertheless, this technique fails to provide high purity single layer 2D NMs due to the remaining impurities from solvents or surfactants [91].

3.1.3. Electrochemical exfoliation

Electrochemical exfoliation involves the application of an electric driving force to insert foreign molecules or ions within the interlayer spacing of 2 D bulk parent materials [94]. It offers several merits such as large yield, high efficiency, low cost, simple instrumentation, scale-up capability, and eco-friendly approach to recycling the use of electrolytes for the exfoliation of 2D NMs with desired thickness and crystal structures [94a]. For example, layered bulk 2D NMs including graphite, MoS_2, WS_2, TiS_2, and ZrS_2 were effectively exfoliated through a controllable electrochemical lithiation process. Lithium intercalation into the bulk material can be controlled during the discharge process in an electrochemical cell as illustrated in **Figure 6 c**. Single-layer 2D nanosheets were achieved after subsequent ultrasonication and exfoliation of these intercalated compounds in a certain solvent (e.g., water and ethanol) [95].

3.1.4. Selective Etching

Selective etching is a sort of promising topochemical synthesis for making 2D NMs by introducing a guest species into a host structure that leads to significant structural modifications to the host [96]. This approach has been primarily used for the preparation of 2D NMs, especially MXene [97]. Unlike graphene layers, which are stacked together by weak van der Waals forces, fabrication of MXene through mechanical exfoliation is impossible due to the strong metallic bonds between M and A layers [98]. In this case, MXene as represented by $M_{n+1}AX_n$, where M is a transition metal (e.g. Sc, Ti, Zr, Cr, Mo, etc); X stands for carbon and/or nitrogen; while T_x denotes the surface terminations such as O, OH, F, etc and A is mostly from

27

group 13 and 14 elements in the periodic table, (e.g., Al) can be selectively etched from their parent MAX phases [96a]. Therefore, selective etching is required to break the M-A bonds that appear to be weaker than M-X bonds using etchant solutions that can be categorized into two groups: aqueous hydrofluoric acid (HF) and in situ HF-forming etchants (mixing of metal fluoride with an acid and ammonium hydrogen bifluoride) [96a, 99]. This approach has been firstly reported by Alhabeb et al. [99] that successfully prepared Ti_3C_2 MXene through selective etching of silicon from titanium silicon carbide, a common MAX phase, using a combined etching solution of HF and an oxidant (H_2O_2 or $(NH_4)_2S_2O_8$ or HNO_3 or $KMnO_4$ or $FeCl_3$).

Synthesis of 2D NMs: top-down approach

(a) Mechanical exfoliation

Single-layer graphene

1 μm

(b) Liquid phase exfoliation

Ions intercalate/exchange → Exfoliation

Intercalated ions: Na$^+$, alkylammonium ions etc.

Exfoliation → Purification

Exfoliating agent: Polymeric species

(c) Electrochemical exfoliation

Layered bulk material

1 →

Load
e$^-$

Li foil
Anode   Li$^+$ ions   Cathode

2 ↓

Li-intercalated compound

3 ←

Isolated 2D nanosheets

(d) Selective etching

Ti$_3$SiC$_2$ (MAX phase)   Ti$_3$C$_2$ (MXene)

Ti
Si
C

HF + oxidant

Selective etching of Si   Delamination

80 mL
60
40

Figure 6. Synthesis of 2D NMs by the top-down approach. (a) Mechanical exfoliation of single-layer graphene using scotch tape [90a]. Reproduced with permission from ref. [90a], Copyright (2015) Royal Society of Chemistry. (b) Liquid-phase exfoliation for ions intercalation of clay minerals and polymeric species [93]. Reproduced with permission from ref. [93], Copyright (2015) Royal Society of Chemistry. (c) Electrochemical lithiation for the fabrication of 2D nanosheets from layered bulk material [95]. Reproduced with permission from ref. [95], Copyright (2011) Wiley-VCH. (d) Synthesis of MXene by selective etching of silicon from layered MAX phase (Ti_3SiC_2) using etching solution comprising HF and an oxidant (H_2O_2 or $(NH_4)_2S_2O_8$ or HNO_3 or $KMnO_4$ or $FeCl_3$ [99]. Reproduced with permission from ref. [99], Copyright (2018) Wiley-VCH.

3.2. Bottom-up approach

The bottom-up approach, on the other hand, involves the construction of 2D NMs from molecular precursors to single or few-layer thin nanosheets which require high accuracy in the structural assembly with complicated and expensive preparation steps. One of the frequently critical challenges faced in this approach is the difficulty to transfer the fabricated 2D NM onto target substrates [94a]. Chemical Vapor Deposition (CVD) and wet chemical synthesis are the common methods explored under this approach.

3.2.1. Chemical vapor deposition

CVD is broadly applied to prepare high quality and purity 2D NMs with controlled morphology and composition based on the formation of thin films on a substrate [100]. This technique is often used to grow 2D NMs such as graphene and MoS_2 nanosheets with large surface areas, lower defects, and controllable thickness [89b, 101]. However, this technique is

30

limited by several drawbacks including identifying suitable substrate for growing the 2D NMs, recovering the final 2D NMs from the substrate, high temperature, and high vacuum conditions [86a]. For instance, large-scaled, layer-controlled (1-3 layers as shown in **Figure 7 a**) and large area MoS_2 films can be fabricated through CVD by treating the surfaces of SiO_2 substrates with oxygen plasma process (**Figure 7 a**). This work also confirmed the successful preparation of single-crystalline monolayer of MoS_2 film as well as the growth of bi- and tri-layer MoS_2 films by varying the oxygen plasma duration [102].

3.2.2. Wet chemical synthesis

Wet chemical synthesis is a direct synthesis of 2D NMs that takes place in the solution phase assisted by surfactants or polymers with advantages such as solution processibility, high yield, and massive production [103]. Although this technique is restricted by disadvantages including difficulty to achieve single layer nanosheets and the necessity of using surfactants, it is widely accepted for the fabrication of non-layer structured ultrathin 2D NMs such as metals, metal chalcogenides, and metal oxides [103a]. Wet chemical synthesis can be further broken down into template synthesis, hydro- or solvothermal synthesis, self-assembly, and soft colloidal synthesis [104]. A one-step bottom-up solvothermal route was successfully developed to prepare BP nanosheets with excellent stability directly using white phosphorus as a raw material in ethylenediamine system. According to Tian et al. [105], solvent and temperature are two vital synthesis parameters that dictated the formation of BP nanosheets and their thickness. As illustrated in **Figure 7 b**, BP nanosheets in the range of 2-9 layers have been successfully produced through this facile, scalable, and low-cost bottom-up synthesis approach.

31

32

Synthesis of 2D NMs: bottom-up approach

(a1) Chemical vapor deposition

S, O, Mo, MoO₃, MoS₂

Trilayer, Bilayer, Monolayer, Plasma treatment period, SiO₂

(a2) 80 µm, SiO₂, MoS₂
(a3) 80 µm, MoS₂, SiO₂
(a4) 80 µm, MoS₂, SiO₂

(a5) 1 µm, ~0.65 nm, SiO₂, MoS₂
(a6) 1 µm, ~1.4 nm, SiO₂, MoS₂
(a7) 1 µm, ~2.2 nm, SiO₂, MoS₂

(b1) Wet chemical synthesis
P₄, EN/P₄, 60-140 °C Solvothermal, washing dry, BP

(b2) 200 nm
(b3) 2 nm, BP (020) D=0.507 nm

(b4) ~20 L, 10 L
(b5) Height (nm), position 4: ~4.921 nm (9 L), position 3: ~4.038 nm (7 L), position 2: ~1.569 nm (2 L), position 1: ~1.352 nm (2 L), Distance (µm)

33

Figure 7. Synthesis of 2D NMs by the bottom-up approach. (a1) Schematic diagram of the layer-controlled CVD growth of large-area MoS_2 films after the surface plasma treatment. Optical images of uniform (a2) mono, (a3) bi, and (a4) trilayer MoS_2 films. Corresponding AFM images of the marked areas of the (a5) mono, (a6) bi, and (a7) trilayer MoS_2 films [102]. Reproduced with permission from ref. [102], Copyright (2015) Royal Society of Chemistry. (b1) Schematic diagram of the wet chemical synthesis of BP nanosheets. (b2) TEM image of the BP nanosheets. (b3) HRTEM image corresponding to b2. Lattice image of a BP flake shows d spacing of the (020) plane of orthorhombic BP. (b4) AFM image of BP flakes with an estimated number of layer numbers indicated. [Scale bar (thick white line): 0.2 µm.] (b5) Line scans performed along the numbered lines shown in b4. Layer numbers are identified based on their thickness. (Scale bar: 1 nm.) The BP nanosheets analyzed here were prepared at 100 °C [105]. Reproduced with permission from ref. [105], Copyright (2018) PNAS.

4. Main contributions of 2D NMs in 3D bioprinting

Polymeric hydrogels have been widely studied in the bioink formulation owing to their biocompatibility, rheological properties, and easy processing [106]. However, polymeric materials generally suffer from arrays of limitations such as insufficient bioactivity, weak mechanical properties, and poor electrical conductivity, which hamper their application in the context of 3D bioprinting [17a, 38, 43]. Integration of 2D NMs and 3D bioprinting appeared as a feasible approach to address the limitation of polymeric inks and creates an opportunity to attain advanced bioinks with unprecedented properties. This section addresses the question regarding the added values with the incorporation of 2D NMs into the 3D bioprinting technology. The contributions of 2D NMs in 3D bioprinting technology are discussed based on six main scopes including reinforcement effect, delivery of bioactive molecules, improved

34

electrical conductivity, enhanced tissue formation, photothermal effect, and antibacterial properties, as summarized in **Figure 8**.

4.1. Reinforcement effect

Rheological behavior governs the printability of inks, which deserves careful modulation to attain high resolution [44b, 107]. Inks with high viscosity benefit from better shape integrity with the ability to print taller constructs [107b, 108]. However, blockage of the nozzle is more likely to happen when printing high viscose inks, which can disrupt the printing process. Additionally, inks with higher viscosity deliver high shear stress to the encapsulated cells during the printing process that can potentially diminish the cell viability and directly change the cell's functions such as proliferation, expression of genes and proteins [42b, 50, 109]. In contrast, the relatively low viscosity of hydrogels results in poor control over the shape retention of hydrogel once printed. Recent studies reveal that the inclusion of 2D laponite NM into ink formulation allows the modulation of the rheological properties [46a, 110]. Accordingly, the addition of laponite to Gelatin methacryloyl (GelMA) endow thixotropic behavior to the ink as evidenced by the decrease in the viscosity upon increasing shear rate. This is recognized as the pre-requisite feature for the successful printing of complex 3D structures. In addition, cell viability depends on the duration and level of shear stress during extrusion, thus careful consideration should be taken to adjust the printing parameters (pressure, temperature, printing speed, nozzle diameter) [42b, 50, 109].

After printing, the bioinks should support the long-term stability of 3D printed structure in the physiological media [108b, 111]. Engineering the mechanical properties of inks that can replicate the native tissue is found to be consistently challenging to the field as their performance relies significantly on their mechanical properties [39, 112]. Thus, designing

35

advanced bioinks with adjustable mechanical properties is of great interest to facilitate the regeneration of functional tissue [39]. Several approaches have been developed to reinforce the mechanical properties of inks such as interpenetrating networks (IPNs), nanocomposites, supramolecular bioinks, and thermoplastic reinforcement [43]. Harnessing the reinforcement ability of 2D NMs is found to be a powerful tool in the fabrication of 3D structures with desirable mechanical properties [113]. On the other hand, hydrophilic hydrogels can absorb a great amount of water and swell in physiological media, which dramatically increases the shape and size of the printed structures [113c]. The inclusion of 2D NMs has been reported to limit the swelling ratio of printed hydrogels apart from keeping the shape integrity of the printed constructs [114].

4.2. Delivery of bioactive molecules

High surface area, high rate of cellular uptake, and low cytotoxicity of 2D NMs offer an attractive platform to be used as a carrier for drugs and therapeutic macromolecules [1c, 13a, 115]. This unique feature of 2D NMs has been taken advantage in the development of some inks by adding new functionality to current bioinks [116]. It should be highlighted that some 2D NMs cannot be used directly as drug carriers due to their physiological instabilities and the lack of stimuli-responsive, thus surface functionalization appears to be an effective strategy to address this issue [13a, 117].

4.3. Improved electrical conductivity

Current bioinks usually consist of polymers with a poor electrical conductivity that restricts their application in the regeneration of excitable tissues [118]. Attributed to the high electrical conductivity of some 2D NMs, the integration of 2D NMs into the insulating polymers, even at

36

a very low concentration, is found to impart improved electrical conductivity to the inks [113c, 119]. The electroconductive scaffold has been enormously exploited in tissue engineering [120], drug delivery [121], and biosensing [122]. Electroconductive scaffolds can replicate the electrical properties of the target tissue, enabling the stimulation of the cells for improvements in their growth, differentiation, and migration [113c, 119].

4.4. Enhanced tissue formation

To replace the injured tissue with a functional scaffold, it is critical to provide an appropriate microenvironment for cells survival and growth [120a, 123]. Recent finding revealed that active interaction between cells and 2D NMs can improve the cellular functions in terms of attachment, spreading, proliferation, cell signaling, and differentiation [124]. In this sense, a variety of inks containing 2D NMs have been developed to take advantage of this capability of 2D NMs in the formulation of inks with unique properties [46b, 110a, 113b, 125].

4.5. Photothermal effect

Cancer remains a challenging target in modern medicine that puts a huge financial burden on individual and society especially with and growth of an aging global population [126]. Chemo- or radiotherapy is one of the common methods applied for the cancer treatment. However, these methods suffer from ineffectiveness in some of cases and may induce serious side effects. Photothermal therapy (PTT) has emerged as a minimally invasive therapeutic strategy to ablate the tumor tissue by conversion of the absorbed near-infrared (NIR) laser light into heat energy [15a, 127]. Deep tissue penetration and minimal invasiveness to the surrounding healthy tissue are the key advantages of the PTT compared to conventional radiotherapy or chemotherapy. A variety of 2D NMs with high photothermal-conversion capacity in the NIR

region has been explored as a PTT agent *in vivo* cancer therapy resulting from their excellent plasmonic properties [1a, 128]. 2D NMs have some merits compared to the other NMs with different dimensionality in the PTT application. First, the optical properties of 2D can be easily modulated by changing the number of their layers or decorating metals on their surface [129]. Second, large surface area of 2D NMs allows loading of therapeutic drugs for synergized therapy [130].

On the other hand, entire or particular part of cancerous tissue is removed during tumor resection. However, tumor resection-induced defects can results in the severe dysfunction of the tissue/organ and adversely impact a patient's life quality. Therefore, it is critical to move forward by incorporating the bifunctional scaffold with high photothermal-conversion efficiency for treating tumor tissue as well as tissue regeneration capacity to recover the surgical resection [131]. To meet both the PTT and tissue engineering aims, it is essential to design smart inks with high sensitivity to the NIR light that can be used to effectively ablate tumor sites and to help tissue regeneration [132]. Over recent years, the application of 2D NMs with photo-thermal responsiveness in 3D bioprinting with the goal of cancer therapy and tissue regeneration has been increased [131b].

4.6. Stronger antibacterial properties

Despite aseptic procedures during the implantation, the risk of bacterial infection at the implantation site remains a prominent challenge to the field [133]. The antibacterial activity can be endowed to a hydrogel by the encapsulation of antibiotics in the hydrogel network [134]. However, the antibacterial activity of the materials is likely to disappear after the full release of antibiotics [135]. In addition, resistance towards conventional antibiotics is another concerning issue that urgently calls for more alternative antibacterial materials [136]. Thus,

designing implants with inherent antibacterial properties is highly in demand and valubale to avoid implant rejection [133b, 137]. 2D NMs with inherent antibacterial properties are the focus of many researchers, revealing their exceptional antibacterial performance resulting from their intrinsic physicochemical characteristics [138]. Unlike the conventional antibiotics, antibacterial properties of 2D NMs are less likely to begin bacterial resistance due to their high uptake rate, low toxicity, and several antibacterial mechanism activities. In addition, the large surface area and flexibility for functionalization of 2D NMs facilitate the interaction of bacteria and 2D NMs give rise to stronger antibacterial activity. Additionally, lower concentrations of the 2D NMs are required for antibacterial activity compared to traditional antibiotics [139].

39

Figure 8. Main contributions of 2D NMs in 3D bioprinting. (a) reinforcement effect [140]. Reproduced with permission from ref. [140], Copyright (2015) American Chemical Society. (b) delivery of bioactive molecules [141]. Reproduced with permission from ref. [141], Copyright (2018) Elsevier. (c) Improved the electrical conductivity [119]. Reproduced with permission from ref. [119], Copyright (2015) American Chemical Society. (d) Enhanced tissue formation [142]. Reproduced with permission from ref. [142], Copyright (2017) American Chemical Society. (e) Photothermal effect [143]. Reproduced with permission from ref. [143], Copyright (2020) Wiley-

40

VCH. (f) And stronger antibacterial properties [144]. Reproduced with permission from ref. [144], Copyright (2018) American Chemical Society.

5. Ink formulations of 2D NMs for bioprinting

The following sub-sections outline the representative examples of each studied 2D NMs in 3D bioprinting applications.

5.1. Graphene-based nanocomposite inks

Graphene is a single layer of carbon where atoms are packed by covalent sp^2 bonds in a hexagonal honeycomb network [145]. Graphene is the world's first and most well-known 2D NMs which has resulted in a major development in science and technology and offers a wealth of promising applications [146]. Graphene's lateral size can be tuned from few tens of nanometers to hundred of micrometers while its thickness ranging from monolayer (e.g., 0.34 nm) to several sheets (e.g., 1 nm) [147]. The unprecedented properties of graphene such as high specific surface area, antibacterial properties, low cytotoxicity, suitable biocompatibility, versatile chemistry, high mechanical strength, and excellent electrical properties have encouraged researchers to extensively exploit graphene derivatives in biomedical applications such as biosensors, drug/gene delivery, antibacterial agents, bioimaging, tissue engineering and regenerative medicine [16a, 146, 148]. Among all graphene-based NMs, graphene oxide (GO) and reduced graphene oxide (rGO) hold great potentials in designing appealing materials for biotechnology [7].

Along with the increasing interests in graphene NMs in a variety of biomedical fields, several studies have targeted to explore the usage of graphene in 3D bioprinting technology [113b, 125a, 149]. According to the previous reports, graphene family materials have shown the

41

prospective potential to regenerate and recover bone, neural, cardiac, cartilage, and liver tissues with the aim of future clinical applications [6, 150]. Thus, many researchers attempt to develop graphene-containing inks to improve the cellar functions for tissue regeneration purposes. For example, Zhou et al. [113b] prepared a photo-crosslinkable PEGDA-GelMA ink loaded with various concentrations of GO that were printed using stereolithography-based bioprinters (**Figure 9 a**). The prepared biocompatible were assessed for cartilage tissue engineering applications, showing that human bone marrow mesenchymal stem cells (MSCs) proliferation rate increased upon addition of GO, with the highest rate in 0.1 mg/mL of GO. This is attributed to the higher level of protein absorption on the scaffold surface caused by GO nanosheets. In another study conducted by Cheng et al. [125a], it was demonstrated that the GO-embedded collagen/chitosan bioink blocked the Rank/Rankl/OPG pathway and subsequently regenerated the cartilage. In another study [149a], it was demonstrated that the addition of GO nanosheets into the formulation of alginate-based bioink not only contributes to the printability but also endows osteogenic differentiation due to the higher absorption of osteogenic inducers on GO nanosheets. In addition, it can enhance the viability MSCs in an oxidative stress environment, thanks to the antioxidant property of the GO and scavenging reactive oxygen species (ROS).

The inclusion of graphene into the ink formulation promotes the thixotropic behavior of the ink that enables obtaining better printing resolution [149b]. For example, a recent study showed that the incorporation of GO into a bioconjugated hydrogel can improve the printability and cell proliferation of the scaffold for cartilage tissue regeneration (**Figure 9 b**) [149b]. In order to meet cartilage extracellular matrix specifications, the hydrogel ink consists of a photo-crosslinkable alginate with gelatin and chondroitin, simply coded as AGC. The long

42

recovery time of pristine ACG ink has led to the spreading of the printed strands to the adjacent area, while the addition of a small amount of GO significantly reduced the recovery time, allowing the printing of thin strands without collapsing. This is due to the physical and chemical interaction of GO with biopolymeric chains that improved the stability of the strands. The improved printability and processability of bioconjugated scaffolds have boosted cytocompatibility and chondroinductive capacity, which are effective for cartilage tissue engineering applications.

Due to the outstanding electrical conductivity of graphene, recent studies have attempted to develop new electroconductive bioinks for nerve, muscle, and cardiovascular tissue engineering. For example, Jakus et al. [119] fabricated graphene-based composite scaffolds using an extrusion-based 3D printer with excellent biocompatibility, robustness, and electrical conductivity (more than 800 S/m), as shown in **Figure 9 c**. The potential effect of this conductive graphene scaffold was investigated on human mesenchymal stem cell behavior (hMSC) for neural tissue engineering applications. It was demonstrated that graphene-based scaffolds supported hMSC attachment, viability, and proliferation. Moreover, the printed scaffolds (with a diameter of 4 mm) induced neurogenic differentiation with noticeable upregulated glial and neuronal gene expressions. *In vivo* experiments validated excellent biocompatibility without any inflammatory response over 30 days in a mouse model as well as the capability of the prepared scaffolds for surgical handling which holds great potential for electrogenic tissue regeneration. In other work, the 3D printing technique was integrated with microfluidic spinning to fabricate 3D GO scaffolds with tunable fiber diameter and structure [151]. Then, the hydrothermal reduction was used to obtain conductive rGO microfibrous scaffolds. The prepared 3D graphene-based scaffolds with excellent electrical properties demonstrated

suitable biocompatibility on SH-SY5Y cells. However, cells grown on GO scaffolds showed better cell attachment and proliferation compared to those of rGO. Moreover, the conductive rGO scaffolds successfully induced the cell alignment along the fiber axis, which could be effective in tissue engineering of the central nervous system and myocardial repair. In another study, graphene was incorporated into Poly(trimethylene Carbonate) to improve the mechanical and electrical properties of the scaffold [152]. The 3D-printed conductive scaffold with enhanced tensile strength accelerated adipose-derived mesenchymal stem cell (MSC) proliferation and upregulated osteogenic markers. The excellent biocompatibility and processability of the composite 3D scaffolds make them a promising material for biomedical applications. Moreover, applying electrical stimulation on cell-loaded scaffolds showed an enhancement in Col I and ALP gene expressions.

In addition to providing bioactivity, graphene family has been exploited for their antibacterial properties [153]. Specifically, tissue-engineered bone scaffolds with potent antibacterial activity are highly valuable to the field. For example, Zhang et al. [154] coated the 3D printed β-TCP bioceramic scaffolds with silver (Ag)/GO (named as Ag@GO) particles to confer the antibacterial activity to the scaffold. The scaffolds exhibited improved osteogenic differentiation of rabbit bone marrow stromal cells evidenced by the higher ALP activity and the expression of bone-related genes. In addition, the scaffold exhibited potent antibacterial activity against *E. coli* thanks to the released of silver ions. In another study [155], it was shown that incorporation of GO into PCL biomaterials ink improves the antibacterial activity of scaffold significantly in a concentration and time-dependent manner. Accordingly, around 80% of adherent *S. epidermidis and E. coli* bacteria on the printed scaffold were found dead after 24 hours of exposure at 7.5 wt.% of GO (**Figure 9 d**).

Furthermore, graphene-based NMs are being considered for photothermal therapy owing to their high photothermal conversion efficiency and cytocompatibility [156]. For example, GO-tricalcium phosphate (GO-TCP) scaffolds combined photothermal therapy and bone regeneration [131b]. This scaffold was fabricated using a 3D printing technique with various concentrations of GO, NIR power density, and surface modifications to investigate its potential in osteogenic differentiation of rabbit bone mesenchymal stem cells (rBMSCs) and repairing rabbit bone defects. The effective photothermal effect of the fabricated GO-TCP scaffolds showed more than 90% of osteosarcoma cell death once exposed to NIR, while no photothermal effect was detected for the pristine β-TCP scaffolds. In addition, the prepared scaffolds exhibited enhanced osteogenic differentiation, bone-related gene expression, and bone regeneration capability, showing the capability of the scaffold in the enhancement of bone regeneration. The outstanding properties of the prepared scaffolds can be ascribed to the incorporation of GO which contributed to killing tumor cells and stimulating bone regeneration.

Possessing the remarkable reinforcement effect of the graphene family on the mechanical strength of hydrogels [157] makes GO a suitable candidate to be used in the design of the inks' formulation. For example, Nosrati et al. [158] printed out reduced GO/hydroxyapatite/Gelatin scaffolds, proved the excellent reinforcement effect of graphene on mechanical properties of the hydrogel. The reinforcement effect of graphene NMs has been also reported in other inks [149b].

Overall, the remarkable physical and biological properties of graphene NMs hold promise in the design of inks for different purposes [159]. The inclusion of graphene nanomaterial family into the inks' formulation and harnessing its characteristics have led to the development of

45

new inks with added functionality. Other graphene-based nanocomposite bioinks are summarized in **Table 1**. Although extensive studies have been conducted in the formulation of graphene nanocomposite bioinks owing to the excellent biocompatibility, electrical, mechanical, and antibacterial properties of graphene NMs, more efforts and researches are required for the transition to the clinical application.
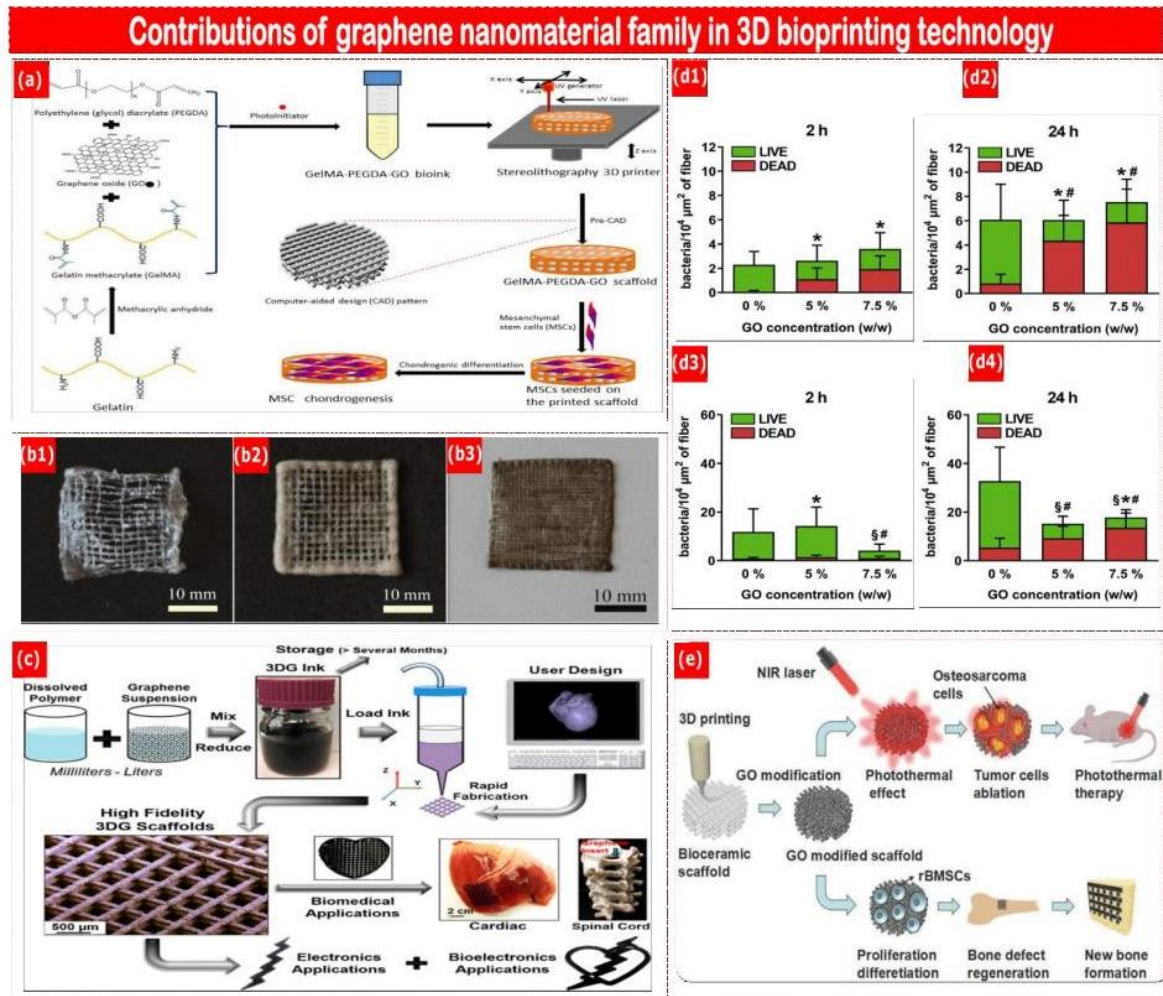
Figure 9. Contributions of graphene nanomaterial family in 3D bioprinting.(a) Enhanced chondrogenic differentiation of hMSCs upon addition of GO into PEGDA-GelMA biomaterial ink [113b]. Reproduced with permission from ref. [113b], Copyright (2017) Elsevier. (b1-b3) Improved the printability of the AGC ink upon increasing the concentrations of GO. Digital images taken from

46

the lyophilized AGC ink with (b1) 0.0 mg/mL, (b2) 0.1 mg/mL, and (b3) 1 mg/mL content of GO [149b]. Reproduced with permission from ref. [149b], Copyright (2020) American Chemical Society. (c) Impart the electrical conductivity into the biomaterial ink. The simple physical blending of graphene and elastomer solution enables to print 3D structures suitable for tissue engineering and bioelectronics applications [119]. Reproduced with permission from ref. [119], Copyright (2015) American Chemical Society. (d1-d4) improve the antibacterial activity of PCL biomaterial ink. Percentage of live and dead S. epidermidis (d1, d2) and E. coli (d3,d4) bacteria adhered to the PCL scaffolds after 2 h and 24 h incubation [155]. Reproduced with permission from ref. [155], Copyright (2020) Elsevier. (e) Photothermal conversion effect for ablation of tumor cells. 3D printing of biomaterial ink composed of GO and TCP, which demonstrate both photothermal effects for tumor therapy and bone regeneration [131b]. Reproduced with permission from ref. [131b], Copyright (2016) Wiley-VCH.

5.2. Nanosilicate-based nanocomposite inks

From the variety of 2D NMs that have been exploited in the 3D bioprinting context, laponite nanoparticles are the main focus of researches to attain advanced inks [160]. This broad utility of laponite in 3D bioprinting is mainly attributed to its excellent rheological behavior, which is considered a superior benefit compared to the other 2D NMs [46a, 161]. Laponite is a synthetic nanoclay made up of layers of magnesium atoms between silicon atoms bonded with sodium atoms with the chemical formula of $Na^{+0.7}[(Si_8 Mg_{5.5}Li_{0.3}) O_{20} (OH)_4]^{-0.7}$ [162]. Laponite particle is a disk-shaped crystal with a thickness of 1 nm and diameter of about 25-30 nm which has positive and negative charges distributed on the rim and surfaces, respectively [163].

Laponite was found to significantly improve the printability of bioink as it can form hydrogel with highly thixotropic behavior in an aqueous solution thereby enabling the fabrication of 3D

47

structures [46a, 161]. Laponite forms a "house-of-cards" structure once dissolved in an aqueous solution above 2 wt.% concentrations resulting from its dual electrostatic characteristic [163]. This structure imparts shear-thinning behavior and high recoverability to the hydrogel solution. Shear-thinning behavior is recognized as the pre-requisite characteristic for 3D bioprinting, which means the ink's viscosity drops at high shear rates that subsequently leads to higher cell viability, printing resolution, and shape fidelity of the 3D constructs [38, 45, 164]. Therefore, the inclusion of laponite into the bioink formulation can endow shear-thinning behavior to the ink to meet the criteria for extrusion-based 3D bioprinting [46a, 160c, 165]. Numerous researches have investigated the rheological properties of laponite, especially its ability to modulate the rheological properties of natural [46a, 141, 166] and synthetic polymers [160c] for 3D bioprinting applications. For example, single-component kappa-carrageenan (κCA) hydrogel suffers from poor printability as it forms irregular filament once extruded out of the nozzle [46a]. The inclusion of laponite into κCA hydrogel allows the facile extrusion of ink along the nozzle and fabrication of physiologically-relevant-scale tissue with spatial accuracy and good mechanical strength [46a] (**Figure 10 a**).

Another interesting characteristic of laponite is its ability to improve the bioactivity of the scaffold for bone and cartilage tissue engineering [165, 167]. Cell-laden bioinks with bioactive properties are highly valuable for translation of the 3D bioprinting to preclinical models [46b, 160d, 168]. Accordingly, several studies have evaluated the bioactive properties of laponite in bone and cartilage tissue engineering [124e, 169]. Laponite was found to dissociate within the lysosome and release a variety of elements including sodium, magnesium, and lithium below pH=9 [7, 170]. These elements with inherent bioactivity promote the osteogenic [165, 171] and chondrogenic [172] differentiation of the cells following the degradation of laponite. For

48

example, a nanocomposite bioink was synthesized upon addition of laponite into photo-crosslinkable monomer (N-acryloyl glycinamide) (NAGA) [142], as shown in **Figure 10 b**. It was demonstrated that sustainable release of bioactive ions (Mg^{2+} and Si^{4+}) as degradation byproducts of laponite from laponite/N-acryloyl glycinamide bioink induces osteogenic differentiation of primary rat osteoblast (ROB) cells *in vitro*, which significantly contribute to the facile regeneration of new bone in tibia defects of rats *in vivo*. In addition, several studies conducted on the performance of the NICE bioinks proved that the use of laponite facilitates the deposition of a cartilage/osteoid-like matrix of GAGs, collagen, and proteoglycans during the initial few weeks of culture [46b, 110a, 125b].

In addition to improving the rheological properties and bioactivity of the ink, laponite has been exploited as a therapeutic delivery vehicle due to its favorable properties including sustainable release, high loading efficiency, bioactivity, and hydrophilicity [173]. High surface area and dual charged characteristics facilitate the absorption of a wide range of proteins and therapeutics onto the laponite surface through electrostatic interaction and hydrogel bonding [173a, 174]. Recently, several researches have taken advantage of the high loading capacity of laponite and shown that the laponite-containing inks deliver loaded substance in a prolonged manner to cells, which can be used to regulate the cell's behavior [116, 165]. For example, Cidonio et al. [116a] developed a bioink made of laponite and GelMA. Accordingly, the inclusion of laponite into the formulation not only improved the printability, but also promoted the bioactivity of the bioink as evidenced by the higher rate of proliferation and osteogenic differentiation of HBMSCs. In addition, *ex vivo* implantation of prepared bioink in a chick chorioallantoic membrane model showed that VEGF-loaded laponite-GelMA results in the higher integration and vascularization compared to the VEGF-loaded GelMA scaffold. This is

49

attributed to the ability of laponite in absorption and prolonged delivery of the drugs. Elsewhere, the inclusion of laponite within the methylcellulose-alginate hydrogel was found to allows the 3D bioprinting of the complex 3D structures with high shape fidelity while preserving high cell viability (**Figure 10 c**) [116a, 175]. Casted alginate hydrogel and 3D printed acellular laponite-methylcellulose-alginate (3-3-3 wt.%) scaffolds with and without BMP-2 protein were implanted subcutaneously into MF-1 mice [116a]. It was found that the BMP-2 loaded scaffolds have a higher extent of mineralization compared to BMP-2 free scaffolds for both casted and printed scaffolds (**Figure 10 c1**). In addition, the histological analysis depicted the collagenous tissue penetrating the printed constructs and extensive mineralization formation in the case of BMP-2 loaded samples compared to the drug-free samples (**Figure 10 c2**). In terms of bone volume and average bone density, the inclusion of laponite improved the bone volume and bone density in both drug-free and loaded scaffolds (**Figure 10 c3**). Moreover, the drug-loaded 3-3-3 scaffold showed a higher level of bone density compared to drug-free casted control scaffolds (**Figure 10 c4**). Very recently, a bioink composed of poly(ethylene glycol)-dithiothreitol (PEGDTT)/laponite loaded with therapeutic proteins was formulated to direct cell migration in a 3D printed structure [116b]. Control over the degradation kinetics of bioink and subsequently the release of therapeutic proteins can be realized by changing the ratio of PEG:PEGDTT and nanosilicates concentration.

In a series of promising works, a nanoengineered ionic-covalent entanglement (NICE) bioink has been introduced for the fabrication of mechanically stiff and elastomeric 3D structures (**Figure 10 d**) [46b, 110a, 125b]. The NICE synthesized by the addition of GelMA into laponite-κCA hydrogel, which overcome the lack of cell-adhesion domain site, rapid dissociation in a physiological environment, and poor mechanical properties of laponite-κCA

bioink. GelMA has been widely recognized for its appropriate biological properties with the ability to mimic the native extracellular matrix (ECM) [176]. Due to the presence of cell attachment domain and matrix metalloproteinase responsive peptide motifs along GelMA backbone, GelMA was found to be a promising tissue-engineered scaffold [177]. However, GelMA suffers from poor printability due to the low viscosity at a biological temperature [178]. The synergy of ionic-covalent entanglement and nano-reinforcement provides a printable hydrogel with a cell-friendly microenvironment suitable for bone bioprinting. The NICE bioink exhibited excellent performance in terms of printability, mechanical properties, and osteoinductivity, allowing the fabrication of cellularized structures [46b, 110a]. For example, several scaffolds with various shapes were fabricated for craniomaxillofacial bone defects to showcase the capability of NICE bioinks for bone tissue engineering [46b]. It was found that the NICE bioink induced deposition of osteo-related mineralized extracellular matrix and improved endochondral differentiation of encapsulated human mesenchymal stem cells (hMSCs) in growth factor-free environment. In addition, the changes in gene expression of hMSC once exposed to laponite were investigated by RNA whole-transcriptome sequencing under 2D culture conditions. Accordingly, significant changes were recorded in the level of 4629 genes expression, especially the genes involved in the endochondral differentiation (*COL1A21, SMAD1/4/5/7, and SOX9*), osteoblast development (TGF-β2 and the TGF-β2), and bone morphogenic protein signaling pathway (*BMP1, BMP4*, and *BMP2K*) were founbd to be upregulated due to the nanosilicate treatment.

Overall, extensive efforts have been devoted to exploring the biomedical applications of laponite in a variety of fields including tissue engineering, drug delivery, controlled cell fate, and hemostatic agents [170, 174]. This broad range of utility stems from its excellent physical and

51

biological properties. The sustainable release of bioactive ions resulted from its biodegradation product induces an appropriate microenvironment to enhance osteogenesis activity [170]. In addition, possessing inherent dual charge characteristics hold the tremendous promise to interact with different molecules which results in transportation and sustained release of drugs, biochemical factors, and nanoparticles. Another intriguing feature of laponite is its high thixotropic behavior resulted from the formation of a house-of-cards structure. The growing interest in the biomedical applications of Laponite along with its promising performance in 3D printing technology highlighted the need for translational research on the laponite-based bioinks for clinical applications.

52
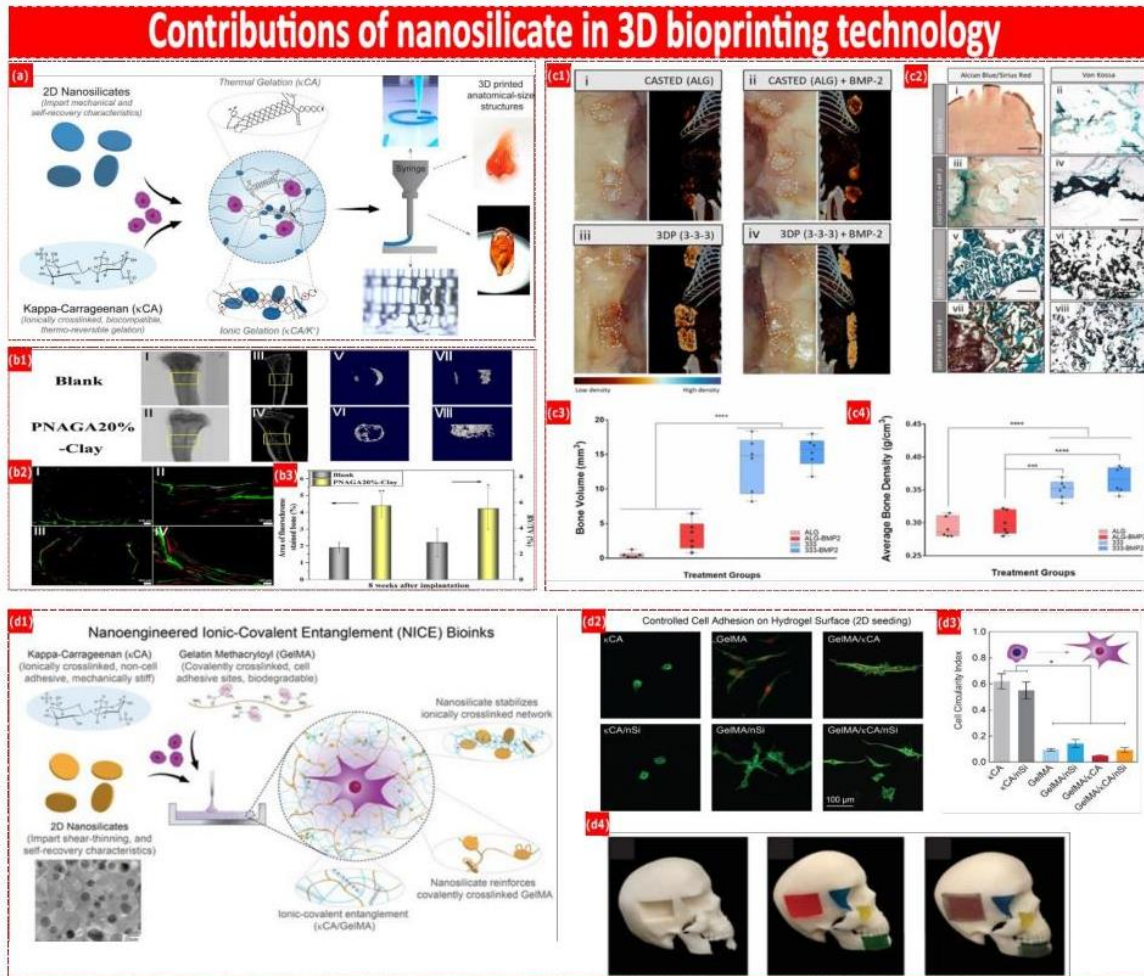
Figure 10. Contributions of nanosilicate in 3D bioprinting.(a) Improving the printability of κCA upon the adhesion of laponite. Laponite with intrinsic thixotropic behavior was introduced in the single-component κCA hydrogel to modify its rheological behavior [46a]. Reproduced with permission from ref. [46a], Copyright (2017) American Chemical Society. (b1-b3) Enhanced bone regeneration of the scaffold. Sustainable release of laponite biodegradation products improved the bone regeneration rate. (b1) Evaluation of the efficiency of the implanted blank and PNAGA20%-Clay bioink in terms of new bone formation via micro-CT (b1(I) and b1(II)), micro-CT reconstruction images (b1(III) and b1(IV)), and reconstructed 3D models (b1(V)-b1(VIII)) of the new bones. (b2) Fluorescent labeling assay of blank (b2(I) and b2(II)) and PNAGA20%-Clay (b2(III) and b2(IV)). Three different colors including yellow, red, and green

53

represent tetracycline hydrochloride, alizarin red S, and calcein labeling, respectively. (b3) Comparison of the percentage of the fluorescent labeling area of bone and new bone volume/total volume (BV/TV) ratio for blank and PNAGA20%-Clay 8 weeks after surgery [142]. Reproduced with permission from ref. [142], Copyright (2017) American Chemical Society. (c1-c4) Sustained delivery of BMP-2 molecules loaded within the scaffolds. (c1) Characterization of the *In vivo* mineralization of casted and 3D printed scaffolds 4 weeks after implantation scaffolds with and without BMP-2. (c2) Alcian Blue/Sirius Red and Von Kossa staining of casted and 3D printed scaffolds with and without BMP-2. (c3) Bone volume , and (c4) average bone density of three-dimensional constructs [116a]. Reproduced with permission from ref. [116a], Copyright (2020) IOPSCIENCE. (d1-d4) NICE bioink composed of laponite, GelMA, and κCA designed for bone tissue engineering with improved printability, bioactivity, and tuneable degradation [46b, 110a]. (d1) schematic illustration of the synthesis of cell-laden NICE bioink [110a]. (d2) Improved the cell adhesion on the NICE bioink upon addition of GelMA into the Lpaonite-κCA hydrogel [110a]. (d3) The extent of cell spreading of circularity index, showing the higher elongation of cells after addition of GelMA [110a]. Reproduced with permission from ref. [110a], Copyright (2018) American Chemical Society. (d4) The fabrication of several scaffolds for the craniomaxillofacial bone defects to showcase the capability of NICE bioinks for bone tissue engineering [46b]. Reproduced with permission from ref. [46b], Copyright (2020) American Chemical Society.

5.3. Black phosphorous-based nanocomposite inks

In 2014, BP, also known as phosphorene, was added to the 2D NMs family and since then significantly contributed to the field of biomedicine and electronics [179]. BP is made of phosphorus atoms in a honeycomb structure similar to graphene where intralayer and interlayer atoms are held by covalent bonding and van der Waals forces, respectively. BP is a

54

layered semiconductor with strong PAP bonds and unique properties including light-induced biodegradability, tunable band gaps (from 0.3 to 2.0 eV), high carrier mobility, modifiable layer numbers, and high photothermal conversion ability [8a, 180]. 2D BP exhibits an excellent NIR photothermal performance with a photo-thermal conversion efficiency of 28.4% and extinction coefficient of 14.8L $g^{-1}cm^{-1}$ at 808nm [181]. In addition, BP exhibited rapid biodegradation and inherent biocompatibility as the comprising elements of BP can react easily with water and oxygen and degrade into non-toxic compounds such as phosphates and phosphonates [124d, 181-182]. Recent studies proved that these degradation products of BP stimulate the bone regeneration process [1c, 183].

The high photothermal conversion efficiency and bioactivity of BP make it a suitable candidate for the integration of tissue regeneration and photothermal therapy [184]. Thus, according to the concept of "kill first, then repair and regenerate", the inclusion of BP nanosheets into the inks' formulation would be significantly valuable to meet both TE and PTT aims. To date, few studies have taken advantage of BP characteristics to develop bi-functional scaffolds. For example, Yang et al. [185] printed out a bi-functional scaffold by the integration of the 2D BP nanosheets into 3D printed bioglass (BG), as illustrated in **Figure 11 a**. 3D printed BP-BG implants first serve as a photothermal therapy of osteosarcoma to eliminate the cancerous cells. Following that, the scaffold provides a physical matrix for bone regeneration to restore the defected tissue. The photothermal responsive BP allows the elimination of osteosarcoma once irradiated by NIR light. The temperature of the prepared scaffold under NIR irradiation relies on the content of BP and the power of the NIR. Interestingly, the biodegradation of BP leads to the release of PO_4^{-3} and subsequent extraction of calcium from the physiological environment. This results in the enhanced formation of new calcium phosphate (CAP)

55

nanoparticles. Accordingly, BP served as a photothermal agent in the PTT strategy and then as the initiator for biomineralization performance to facilitate osseointegration. In a similar study, Wang et al. [183b] have also reported the fabrication of a multi-functional scaffold through 3D printing of water-in-oil emulsion ink in a cryogenic environment (**Figure 11 b**). The scaffold comprised of deionized (DI) water, β-TCP nanoparticles and poly(lactic-co-glycolic acid)/dichloromethane(PLGA/ DCM) solutions. Accordingly, sustained release of DOX chemo-drugs and on-demand photothermal properties of BP reduce the chance of tumor reoccurrence. Furthermore, the degradation product of BP along with the presence of β-TCP and sustainable release of peptide could provide a desirable environment for the bone regeneration.

Very recently, poly(propylene fumarate) biodegradable scaffolds were coated with two 2D NMs (BP and GO) to synergize cell osteogenesis (**Figure 11 c**) [186]. It was found that the initial cell adhesion to the scaffold surface was enhanced upon coating with GO, which is attributed to the protein absorption capacity of GO. Moreover, the slow release of phosphate from BP nanosheets can facilitate osteogenic differentiation, which is beneficial for bone regeneration. Compared to the scaffolds incorporated with only one 2D NM, the incorporation of 2D BP and GO materials have a synergistic effect on cell proliferation.

Overall, BP is another 2D NM that has been exploited in the development of new bioinks for 3D bioprinting technology [187]. This is attributed to its ability to induce photothermal property into the ink to prevent the reoccurrence of cancerous cells as well as its biodegradation byproduct in the physiological environment that contributes to biomineralization and subsequently enhanced bone formation. Although research on the

56

...

potential biomedical application of BP nanosheets is still in the infancy stage, it is expected that more BP bioinks with added functionality would be developed.
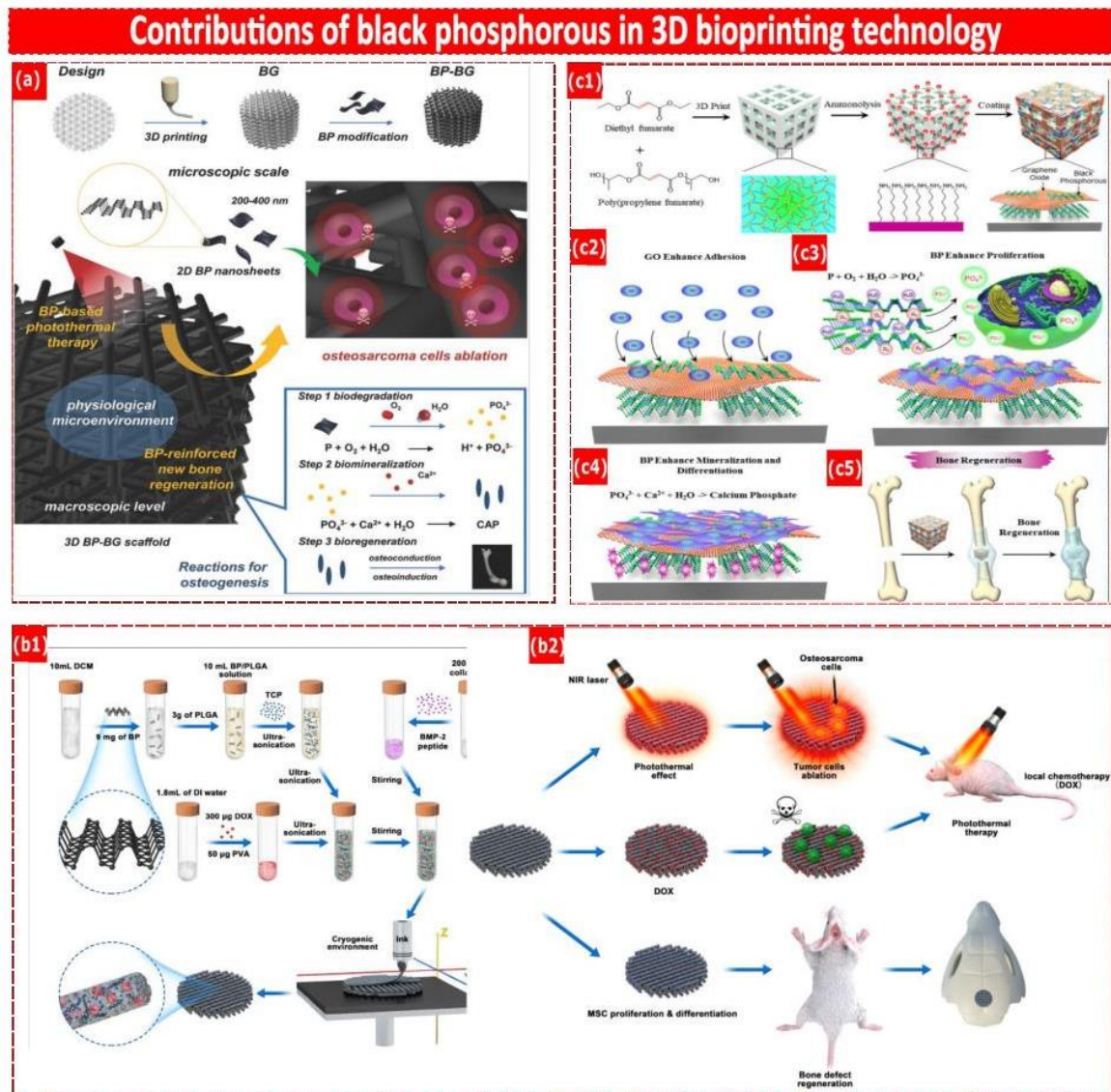
Figure 11. Contributions of BP in 3D bioprinting. (a) Endowing photothermal conversion effect into the scaffold. Modification of BG scaffold with BP nanosheets renders photothermal conversion effect to the scaffold for ablation of osteosarcoma cells followed by osteogenesis by BP-BG [185]. Reproduced with permission from ref. [185], Copyright (2018) Wiley-VCH. (b1-b2) The fabrication process of cryogenic 3D printing of multi-functional scaffold and its formulation.

57

(b2) Elimination of tumor tissue upon photothermal therapy and localized chemotherapy and regeneration of cranial bone defects of rats [183b]. Reproduced with permission from ref. [183b], Copyright (2020) IOPSCIENCE. (c1-c5) Coating of the 3D printed scaffold with a composite of graphene and BP nanosheets. (c2) Cell adhesion to the surface of the printed scaffolds was found to improve upon coating with GO. (c3, c4) On the other hand, release phosphate following by the biodegradation of BP enhance the proliferation of pre-osteoblasts and scaffold mineralization and cellular differentiation, (c5) improved bone formation due to the synergy of GO and BP nanosheets [186]. Reproduced with permission from ref. [186], Copyright (2019) American Chemical Society.

5.4. MXene-based nanocomposite inks

Ultrathin 2D MXene nanosheets have many fascinating properties including biodegradability [188], cellular endocytosis [189], photothermal conversion [190], ease of functionalization [191], excellent electrical conductivity [192] and biocompatibility [9b, 193]. MXenes' outstanding advantages over other 2D NMs include abundant reactive sites for functionalization, a hydrophilic surface which ease the solution processing, and metallic conductivity [194]. In contrast to most 2D NMs, MXene, which can be exfoliated from bulk crystals known as MAX, showed excellent conductivity [9b, 193]. The versatile chemistry of MXenes as a ceramic-based 2D NM has lured tremendous scientific interest with great potentials in biomedical applications such as antibacterial agents [195], cancer therapy [196], drug delivery [197], magnetic resonance imaging (MRI) [198], wearable technologies [199], biosensors [200], and surface coating of implants [201]. Although MXene have been widely studied in modern medicine since thier discovery, their potential applications in 3D bioprinting have remained almost untouched until recently.

58

Having favorable photothermal-conversion property coupled with biocompatibility make MXenes interesting 2D NMs in the development of multi-functional inks. In a recent study [143], 2D Ti_3C_2 MXene nanosheets integrated into BG scaffold to impart NIR-triggered photothermal-conversion performance for eradicating the potential residual bone-tumor cells (**Figure 12 a**). In addition, the biodegradation product of Ti_3C_2 MXene improved the growth of new bone tissue *in vivo*. As evidenced by both *in vitro* and *in vivo* experiments, the Ti_3C_2 MXene-integrated scaffolds can eradicate the bone cancer cells under NIR irradiation and, on the other hand, accelerate the bone tissue regeneration compared to the pristine BG scaffolds. Recently, by harnessing the high electrical conductivity of Ti_3C_2 MXene, Rastin et al. [113c] synthesized an electroconductive cell-laden bioink where Ti_3C_2 MXene nanosheets directly integrated into the hyaluronic acid/alginate hydrogels (**Figure 12 b**). Excellent printability of the bioink allows the fabrication of complex 3D constructs. It was found that the integration of Ti_3C_2 MXene results in a significant improvement in the electrical conductivity of the ink, which addresses the poor electrical conductivity of the current bioinks. Moreover, the MXene nanocomposite bioink showed high biocompatibility as evidenced by the high viability of HEK-293 cells in both bulk and printed hydrogel.

Overall, MXenes are a relatively new member of the 2D NM family, and most studies still focused on their synthesis and fundamental characteristics instead of transitional applications. However, these 2D NMs with favorable properties are expected to gain their place in 3D bioprinting applications in near future.

59

Contributions of MXene in 3D bioprinting technology

60
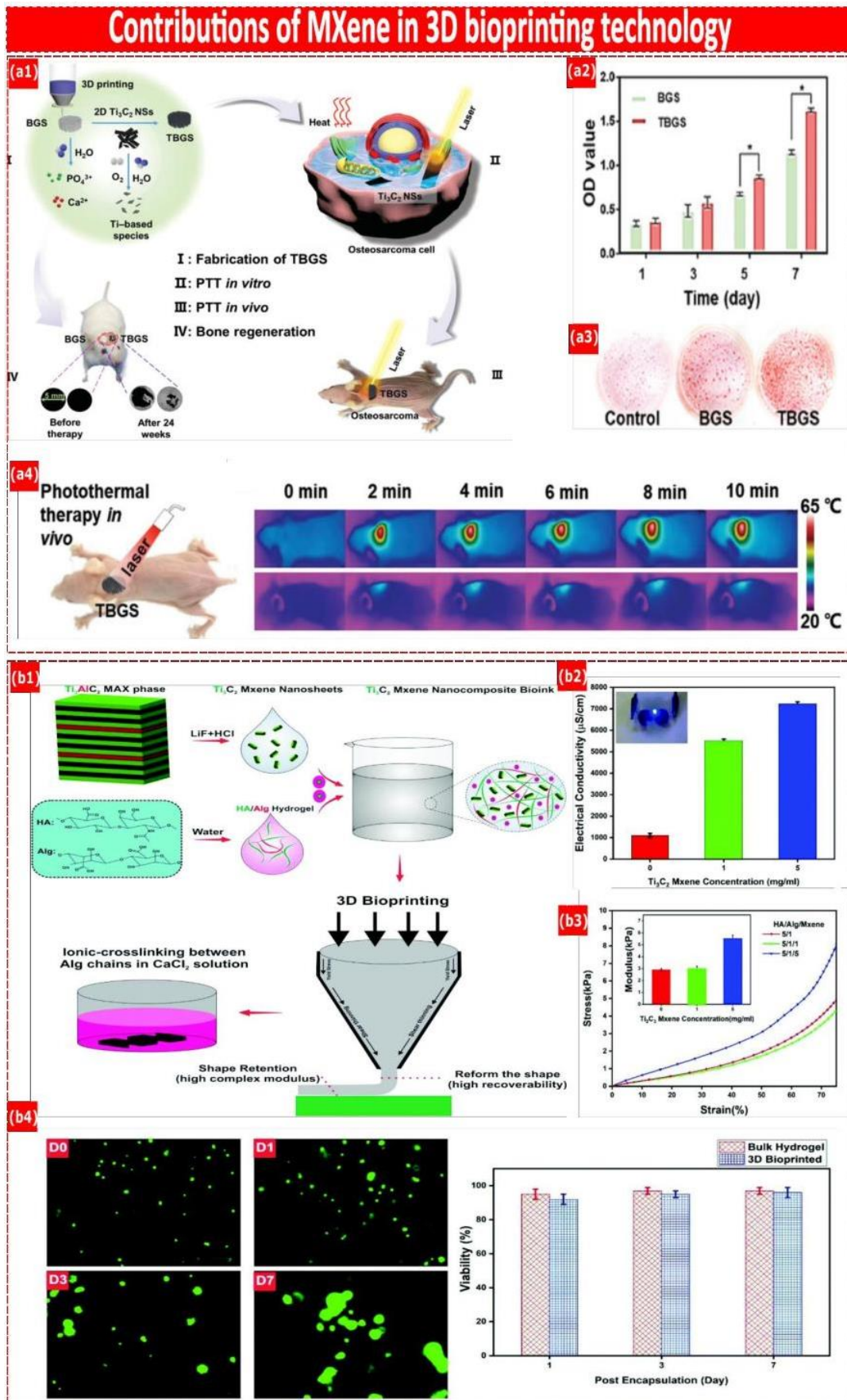
Figure 12. Contributions of MXene in 3D bioprinting. (a1) Endow photothermal effect along with improved tissue formation [143]. Reproduced with permission from ref. [143], Copyright (2020) Wiley-VCH. Synthesis of biomaterial ink composed of 2D Ti_3C_2 MXene nanosheets integrated into BG scaffold (I). The photothermal conversion property of the biomaterial ink eradicates the bone cancer *in vitro* (II) and *in vivo* (III). In addition, the biodegradation of the biomaterial ink promotes bone tissue regeneration (IV). (a2) Characterization of the *in vitro* proliferation of hBMSCs seeded on the blank and modified BGS and TBGSs over a week measured by CCK-8 assay. (a3) Alizarin red S staining of BGSs and TBGSs after three weeks. (a4) Evaluation of the photothermal conversion efficiency of BGSs (upper) and TBGS (bottom) panel. (b1-b4) Improved the electrical conductivity and mechanical strength of the bioink while maintaining cell viability [113c]. Reproduced with permission from ref. [113c], Copyright (2020) Royal Society of Chemistry. (b1) Schematic illustrations of the synthesis of electroconductive nanocomposite bioink. (b2, b3) Enhanced the electrical conductivity and mechanical strength upon inclusion of various concentrations of MXene. (b4) Viability of encapsulated HEK-293 cells within bioink over a week.

5.5. Transition metal dichalcogenides-based nanocomposite inks

TMDs are crystal-structured semiconductors of type X-M-X with M as the transition metal such as Mo, W, V, Ti, and X as a chalcogenide such as S, Se, or Te [202]. TMDs have been considered as an alternative to graphene due to their exciting properties including good biocompatibility and catalytic properties [202b, 203]. As an example of TMDs materials family, Molybdenum disulfide (MoS_2) consists of hexagonal layers with 2D S-Mo-S stack held by van der Waals' interactions [204]. MoS_2 offers a favorable combination of features such as a direct bandgap of 1.8 eV, photo-luminescence, and adjustable electrical conductivity, which are

attributed to the transition character of molybdenum coupled with high chemical activity of sulphur [14b]. MoS_2 has been investigated as a potential candidate for biomolecular sensors, drug delivery, photothermal therapy, and bioimaging [205].

Like BP and graphene, 2D MoS_2 has exhibited great capacity as an efficient photothermal agent in both *in vitro* and *in vivo* studies [206]. Several studies have investigated the photothermal performance of MoS_2 and showed its therapeutic efficiency for the ablation of cancerous cells. *Wang* et al. [207] printed out akermanite (AKT) bioceramic scaffold, followed by in situ hydrothermal process for growing the MoS_2 nanosheets on the 3D-printed bioceramic scaffolds (**Figure 13**). The uniform growth of the MoS_2 layer over the 3D-printed ceramic scaffolds (MS-AKT) endow photothermal therapeutic properties to the scaffold. The temperature of the bioceramic increases once exposed to NIR irradiation and subsequently, the viability of osteosarcoma and breast cancer cells diminished. The temperature increment of MS-AKT scaffolds upon NIR-irradiation depends on the content of the MoS_2 nanosheets and laser power density. In addition to photothermal capacity, the MS-AKT scaffolds exhibited attachment, proliferation, and osteogenic differentiation of rBMSCs and induced bone regeneration *in vivo*.

Overall, with an ever-growing interest in TMDs, these 2D NMs have been successfully used in 3D bioprinting applications owing to their excellent potential photothermal property. However, compared to other 2D NMs, TMDs have been relatively less-explored material in the 3D bioprinting field despite their favorable properties for biomedical applications.

62

Contributions of transition metal dichalcogenides in 3D bioprinting technology

(a) 3D-Printed scaffolds → H₂NCSNH₂ / MoO₄²⁻ → 180°C 24h Hydrothermal → Bifunctional scaffolds

○ MoO₄²⁻   ○ H₂NCSNH₂   ● Mo   ○ S

(b) NIR — MoS₂ — Heat → Tumor Therapy; Bioceramics → Ca²⁺, Mg²⁺, SiO₄⁴⁻, Mo⁴⁺ → Tissue Regeneration

(c) 0 min 1 min 2 min 4 min 6 min 8 min 10 min; MS-AKT; AKT; 52°C – 24°C

(d) MS-AKT+laser, AKT+laser; Temperature (°C) vs Time (s)

(e) MS-AKT+laser MS-AKT AKT+laser AKT; Overlay

(f) AKT, AKT+laser, MS-AKT, MS-AKT+laser; Relative Tumor Volume vs Time (day)

63

Figure 13. Contributions of TMDs in 3D bioprinting. (a) Endow photothermal conversion effect into the AKT scaffolds upon growing MoS_2 on the scaffold surface, (b,c) Characterization of tumor temperature under irradiation NIR at different time intervals implanted with MS-AKT and AKT scaffolds. (e,f) The whole-body fluorescence imaging of tumor at day 0 (left) and day 7 (right), and representative relative tumor volume [207]. Reproduced with permission from ref. [207], Copyright (2017) Nature.

5.6. Hexagonal boron Nitride-based nanocomposite inks

hBN, which is also called white graphene, is a 2D crystalline NM with a hexagonal structure made of boron and nitrogen atoms [208]. Owing to its special atomic arrangement, this nitrogen-based 2D material has become one of the current focuses for biomedical researches with special attention on its potential application in tissue engineering [209] and drug delivery [11, 210]. High hydrophobicity, resistance to oxidation, antioxidation capacity, high mechanical strength, thermal conductivity, high chemical stability, low toxicity, and high specific surface area are some of its favorable properties [5].

The development of printable biomaterial ink with high flexibility is highly critical for the scaffolds to be able to function in the dynamic environment of the body. Given this, Guiney et al. [211] have developed high content HBN-embedded PLGA ink where the mechanical and thermal properties of the ink were tunable upon the change in the content of HBN (**Figure 14 a**). The 3D printed structures exhibited high flexibility as can be cut, folded, or rolled immediately after printing without collapsing. The tensile testing results show that the elongation to failure of 3D printed structure increases upon increasing the hBH till 60 vol.% then experienced a significant drop (**Figure 14 a2**). In addition, evaluations of cytocompatibility of the scaffold show the high viability and proliferation of hMSCs on scaffolds over four weeks.

64

Similar enforcement effects of HBN have also been reported elsewhere that incorporated into the Polyvinyl Alcohol/Bacterial Cellulose biomaterial ink [209b]. More recently, the *in vitro* effectiveness of HBN-containing ink on bone tissue regeneration was investigated and showed that the even small addition of exfoliated HBN into PLA favored the attachment, proliferation, and differentiation of cells with osteogenic potential (**Figure 14 b**) [212]. They reported that printed PLA/hBN scaffolds have a higher rate of cell attachment and proliferation compared to pristine PLA scaffolds. In addition, the evaluation of mineralization activity of pristine PLA and PLA/hBN scaffold shows that the latter has a significantly higher amount of calcium deposition after three weeks.

65
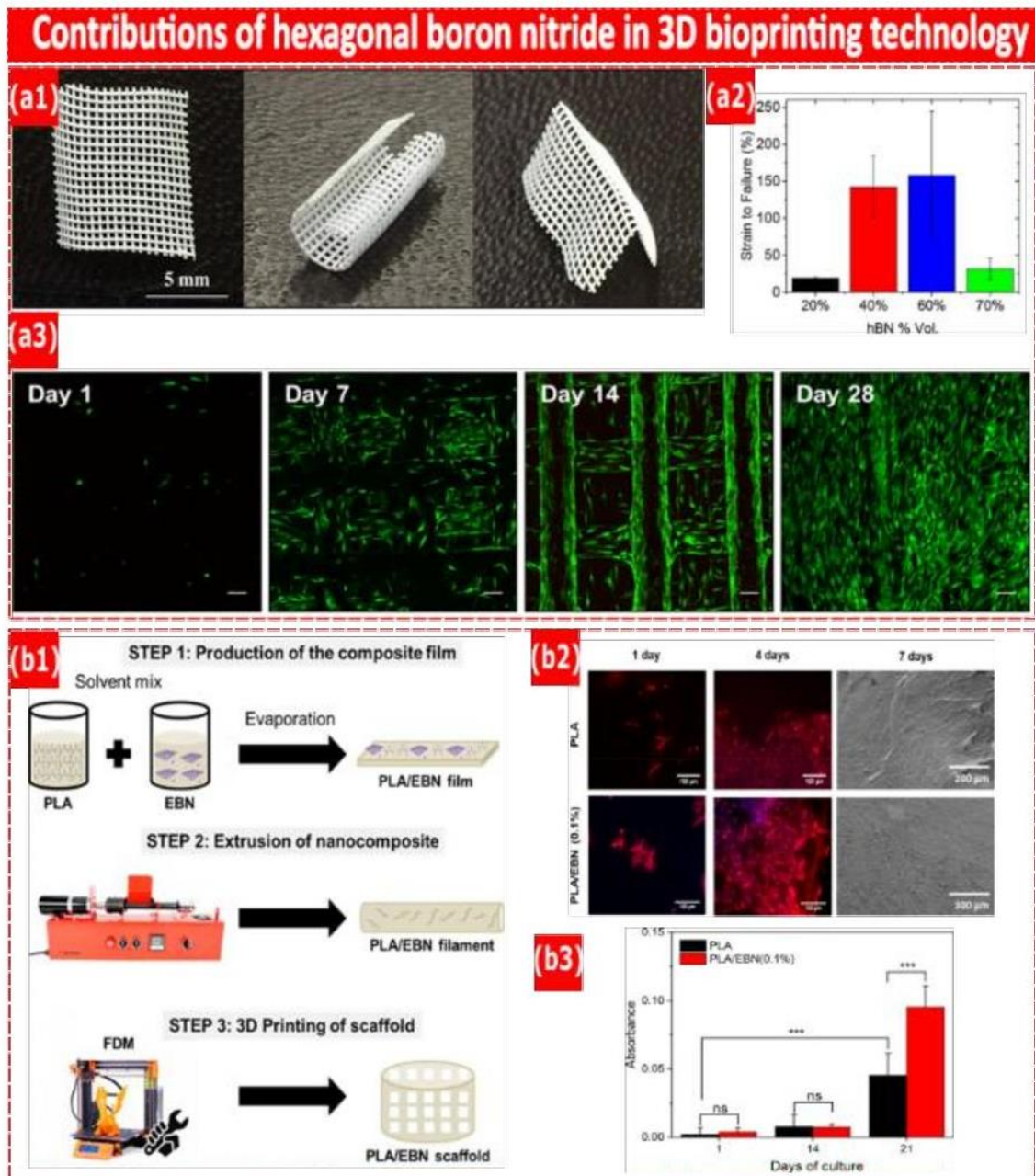
Figure 14. Contributions of hBN in 3D bioprinting. (a) Enhanced flexibility of the 3D printed biomaterial ink [211]. Reproduced with permission from ref. [211], Copyright (2018) American Chemical Society. (a1) Images taken from 3D printed 40% vol hBN. (a2) Strain to failure results of 3D printed structure with varying amounts of hBN. (a3) Cytocompatibility of hMSCs seeded on the 40% volume hBN scaffold at different time intervals. (b) Enhanced the cellular functions of 3D printed PLA scaffold upon inclusion of hBN in terms of attachment, proliferation, and

66

differentiation. (b1) Schematic illustrations of the steps involved in the production of a scaffold. (b2) Attachment and proliferation of MG-63 cells on PLA and PLA/hBN nanocomposites by immunofluorescence staining of actin (red), DNA staining (blue). (b3) Evaluation of mineralization activity of MG-63 cells cultured on PLA and PLA/hBN scaffolds over three weeks [212]. Reproduced with permission from ref. [212], Copyright (2020) American Chemical Society.

5.7. Metal-organic framework-based nanocomposite ink

MOFs are cage-like crystalline porous materials, composed of inorganic metal ions/clusters with organic ligands linked by coordination bonds, hydrogen bonding, and electrostatic interactions [213]. Adjacent layers in the MOFs layered crystal structures connected with weak van der Waals forces that can be exfoliated into individual nanosheets by a variety of methods and synthesize 2D MOFs [214]. Compared to the bulk MOFs, the 2D nanostructure of MOFs possessed several merits including ultrathin thickness, high specific surface areas, and more reachable active sites [215]. Research on the biomedical applications of 2D MOFs is a fast-growing field as it can integrate the advantages of 2D nanostructures with MOF porous structure [12b]. A set of intriguing and unique features of 2D MOFs (e.g., ordered porosity, easy functionalization, tunable chemical composition, and framework,) offer significant potential for a broad range of advanced technological applications [12b].

In a recent study [216], TCP biomaterial ink was firstly printed and then 2D MOF nanosheets (copper coordinated tetrakis (4-carboxyphenyl) porphyrin (Cu-TCPP)) were grown *in situ* on the surface of printed TCP scaffolds through a solvothermal reaction, forming Cu-TCPP-TCP scaffold for PTT and tissue engineering purposes (**Figure 15 a**). Photo-thermal conversion ability of Cu-TCCP's induced the ablation of osteosarcoma cells when irradiated by NIR *in vitro*. Results of *in vivo* tests also confirmed the successful ablation of subcutaneous bone tumor tissues on

67

the backs of naked mice after implanting Cu-TCPP-TCP scaffolds at the defect site (**Figure 15 b**). It was shown that the photothermal performance of the scaffold can be adjusted by varying the Cu-TCPP nanosheets concentration, the ambient humidity, and power density of NIR light. In addition to the photothermal conversion ability, the scaffold showed enhanced osteogenic differentiation *in vitro* and higher bone-forming bioactivity at the site of bone defects *in vivo* (**Figure 15 c**).
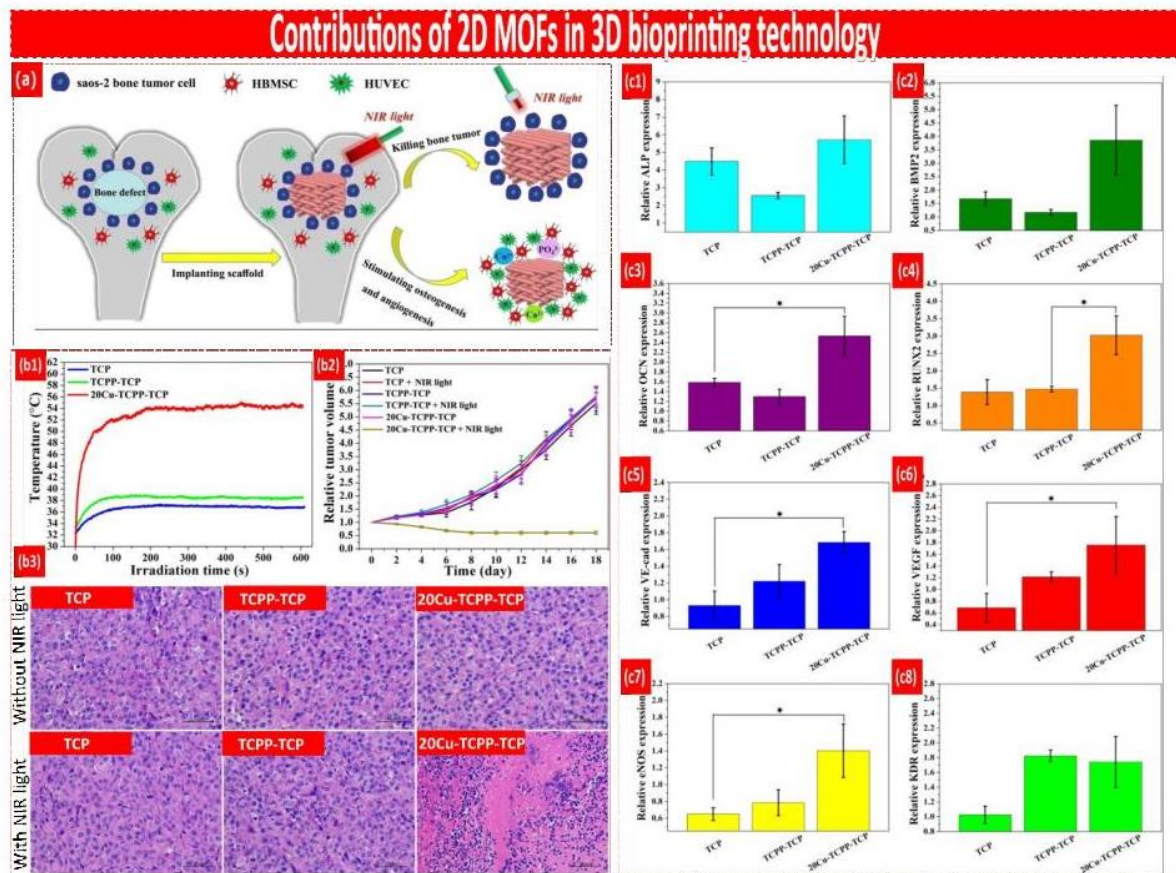
Figure 15. Contributions of 2D MOFs in 3D bioprinting. (a) Schematic illustration of 3D printed 20Cu-TCPP-TCP scaffolds. The scaffolds are designed to kill bone tumor cells through the conversion of NIR to the heat, and then stimulate the osteogenesis and angiogenesis at the bone defect site. (b1) The measured temperature of bone tumors containing TCP, TCPP-TCP, and 20Cu-TCPP-TCP scaffolds on the backs of naked mice that were irradiated by NIR light. (b2) Alteration of bone tumor volume of six groups of mice with and without NIR light over time.

Accordingly, the tumor volume stopped growth for the mice bearing 20Cu-TCPP-TCP scaffold and irradiated with NIR light. (b3) H&E staining images of bone tumor tissue bearing TCP, TCPP-TCP, and 20Cu-TCPP-TCP scaffolds with and without NIR light irradiation. Changes in the expressions level of osteogenic differentiation-related genes ALP (c1), BMP2 (c2), OCN (c3), and RUNX2 (c4) in HBMSCs and angiogenic differentiation-related genes VE-cad (c5), VEGF (c6), eNOS (c7), and KDR (c8) in HUVECs [216]. Reproduced with permission from ref. [216], Copyright (2020) IOPSCIENCE.

69

Table 1. Library of the contributions of each studied 2DNMs in 3D bioprinting found in the literature

2D NMs	Ink formulation	Contributions in the ink	Printing technology	cell type	ref
Graphene	PEGDA/GelMA/GO	Promoting chondrogenic differentiation of human bone marrow mesenchymal stem cells	Stereolithography	Human bone marrow mesenchymal stem cells	[113b]
	collagen type I/Chitosan/GO	Release of small molecule drugs (BMP7)	Extrusion	Human chondrocytes	[125a]
	Gelatin/hydroxyapatite/rGO	Improve the mechanical strength and printability	Extrusion	-	[158]
	PCL/GO	Improve the cell proliferation and differentiation of OB6	Extrusion	Murine preosteoblast cell line (OB6)	[217]
	β-TCP/Ag@GO	Impart antibacterial activity towards *E. coli*, Enhanced the osteogenic differentiation of Rabbit bone marrow stromal cells	Extrusion	Rabbit bone marrow stromal cells	[154]
	PLGA/graphene	Improve electrical conductivity and mechanical strength of the ink, Promote the adhesion, proliferation, and neurogenic differentiation of hMSC with significant upregulation of glial and neuronal genes	Extrusion	Human mesenchymal stem cell (hMSC)	[119]
	rGO/PTMC	Improve the electrical conductivity and mechanical properties, Enhanced mesenchymal stem cell attachment and proliferation	Extrusion	Mesenchymal stem cells(MSC)	[152]
	rGO or GO	The hydrothermal reduction of GO-based scaffold improved electrical conductivity, which has led to better cell alignment along the fiber axis. However, better cell attachment and proliferation were reported for GO scaffolds.	Extrusion	SH-SY5Y human neuroblastoma cell line	[151]
	β-TCP/GO	impart photothermal conversion activity, improve the new bone formation	Extrusion	Rabbit bone mesenchymal stem cells	[131b]
	graphene–polyurethane	Enhanced oxygen metabolism (2- to 4-fold increase) as well as the neural differentiation of Neural stem cells	Extrusion	Neural stem cell	[218]
	GO/alginate	Enhanced osteogenic differentiation, significantly enhanced the printing performances, improved the stability of the printed lattice over 10 days	Extrusion	Mesenchymal stem cells	[149a]
	PVA/GO	enhanced mechanical strength, improve the growth and proliferation of MG-63 cells	SLS	Human osteoblast-like MG-63 cells	[219]

70

	Tricalcium phosphate (TCP)/alginic acid (AA)/GO	Increased porosity, improved swelling profile, and better mechanical performance than TCP/AA scaffolds.	Extrusion	Human osteoblast (hOB) cells	[220]
	β-TCP/PVA/GO	significantly enhance the proliferation, alkaline phosphatase activity, and osteogenic gene expression of human bone marrow stromal cells (hBMSCs)	Extrusion	Human bone marrow stromal cells (hBMSCs)	[221]
	tricalcium phosphate/gelatin/chitosan/GO	Improve mineralization of scaffold, Enhanced wettability, and mechanical properties	Extrusion	Human osteoblast (hOB)	[222]
	β-TCP/PVA/Fe–GO	Accelerate the proliferation and the bone-related gene expression of rBMSCs	Extrusion	rabbit bone marrow stromal cells (rBMSCs)	[223]
Nanosilicate	Laponite/GelMA/κCA	formation of osteo-related mineralized extracellular matrix, Impart printability, osteoinductivity	Extrusion	Human mesenchymal stem cells (hMSCs)	[46b, 110a]
	Laponite/GelMA	Improve the printability, Promote cell viability and differentiation, Deliver proteins of interest such as vascular endothelial growth factor (VEGF)	Extrusion	Human bone marrow stromal cell (HBMSC)	[165]
	Laponite/MC/Alginate	Improved printability, increased shape fidelity and was beneficial for controlled release of biologically active agents such as growth factors	Extrusion	Human mesenchymal stem cells	[116a, 175]
	Laponite/NAGA	Promote the osteogenic differentiation of ROB cell	Extrusion	Primary rat osteoblast (ROB)	[142]
	Laponite/PEGDA	Impart printability	Extrusion	Murine preosteoblasts (NIH MC3T3)	[160c]
	Laponite/KCA	Impart printability	Extrusion	MC3T3-E1 mouse preosteoblasts	[46a]
BP and GO	PPF/BP/GO	Improve the initial cell adhesion because of the GO properties, Improve the osteogenic differentiation due to the degradation of BP	Stereolithography	MC3T3 pre-osteoblast cells	[186]
	GelMA/BP hydrogel integration with 3D printed CaP scaffold	Improve the mechanical properties, photothermal performance for ablation of cancer cells and bacteria, enhanced mineralization and bone regeneration	Extrusion	Human mesenchymal stem cells (hMSCs)	[187]
	BG/BP	Impart photothermal conversion properties, enhanced new bone regeneration	Extrusion	Saos-2 cells and Primary hBMSCs	[185]
BP	β-TCP/PLGA/ BP	Impart photothermal conversion properties, enhanced new bone regeneration	Extrusion	MG63 cells and rBMSCs	[183b]
MXene	hyaluronic acid/alginate/ Ti₃C₂ MXene	Impart electrical conductivity, Improve the mechanical properties and rheological behavior	Extrusion	HEK-293	[113c]

71

	BG/Ti$_3$C$_2$	Impart photothermal conversion property, accelerate the new growth of newborn bone	Extrusion	Primary hBMSCs	[143]
TMDs	Akermanite/MoS$_2$	Impart photothermal conversion therapy, Improve the expression of bone-related genes	Extrusion	Saos-2 cells (osteosarcoma cells) and MDA-MB-231 cells (breast cancer cells)	[207]
hBN	PLGA/hBN	Improve the mechanical strength of the scaffold	Extrusion	hMSCs	[211]
	PLA/hBN	Improved the cellular functions in terms of the attachment, proliferation, and differentiation of cells with osteogenic potential	Extrusion	MG-63 osteosarcoma and MC3T3-E1 preosteoblast cells	[212]
MOF	Cu-TCPP/TCP	Impart photothermal conversion therapy, Improve the expression of osteogenic and angiogenic differentiation-related genes	Extrusion	Human bone marrow stromal cells (HBMSCs) and human umbilical vein endothelial cells (HUVECs)	[216]

72

6. Toxicity of 2D NMs

Recent progress has demonstrated that 2D NMs can actively interact with the biological system and regulate cellular functions [224]. These interactions between 2D NMs and biological entities can benefit health or may induce adverse biological outcomes on cells and tissues [225]. For example, there are multiple reports associated with the risk of nanoscale materials in developing some chronic diseases such as asthma, dermatitis, rhinitis, pleural, interstitial lung disease, and so forth [226]. Therefore, it is imperative to question the interaction, fate, and long-term toxicity of 2D NMs when interacting with biological systems. However, knowledge about the interaction of 2D NMs and biological processes is scarce due to the relatively recent emergence of 2D NMs, even for the relatively well-characterized graphene family. The challenge in the studies of 2D NMs safety lies in the substantial inconsistency in their toxicity profile, which arises from the complex interplay of physicochemical variables that can ultimately affect the toxicity of these materials. Thus, it is highly valuable to understand how tuning the physicochemical properties of 2D NMs can enhance therapeutic use and mitigate their cytotoxicity. A full review of 2D NMs toxicity is beyond the scope of this work, therefore, interested readers can refer to the cited literature [225, 227].

6.1. Cellular uptake mechanisms of NMs

Before getting into the details of the cytotoxicity of 2D NMs, it is necessary to understand the cellular uptake mechanism because 2D NMs' fate and biological response strongly depend on their uptake mechanism [228]. For example, materials entering the cells by clathrin-mediated endocytosis generally end up undergoing lysosomal degradation, whereas materials entering the cells by caveolae-dependent endocytosis usually can escape lysosomal degradation [228c,

73

[229]. In addition, considering the growing number of analogous 2D NMs, it is worthwhile to dissect the role of 2D NMs' physicochemical properties on cellular uptake mechanism and intracellular location to maximize their therapeutic efficiency [230].

Cell membranes, also known as plasma membranes, are semi-permeable barriers that separate the interior of cells from the outer environment. Cell membranes regulate the transferring of substance between the cells and their microenvironment through diverse mechanisms [231]. Gradients of concentration between the interior and the outer cell membrane are the main driving forces for translocating nonpolar molecules such as oxygen, carbon dioxide, and water. In addition, protein pumps or ion channels allow the transferring of amino acids and ions. Another internalization mechanism is endocytosis that is dominant for the internalization of polar or charged biomolecules. Endocytosis is a vesicular internalization mechanism by which cells take up a variety of cargos into the cells via creating a pocket around them, followed by budding off from its cytoplasmic membrane [232]. Literature reveals that the 2D NMs enter the cells via endocytosis uptake machinery, which can be grouped into two broad pathways: phagocytosis (also called cell eating) and pinocytosis (also called cell drinking) [228b, 233]. The distinctions between these pathways lie in the size of the endocytic vesicle, the type of the cargo, the type of the protein coat of the engulfed vesicle, the mechanism of vesicle formation, and the fate of the cargo [234]. **Figure 16 a** presents different uptake endocytosis mechanisms of NMs by cells based on their size. As seen, each mechanism can internalize NMs with a specific size range.

Phagocytosis is a dominant internalization mechanism for relatively large particles (> 500 nm in diameter) that are mostly performed by immune system cells such as macrophages and neutrophils to destroy the infected cells, pathogens, dead cells, and debris [235]. In this process,

74

the particles bind to the receptors located on the surface of the phagocyte and then are engulfed within cup-shaped protrusions and intrude to produce a phagosome that is pinched off and released into the cytoplasm. On the other hand, pinocytosis plays a key role in the internalizations of NMs ranging from a few to several hundred nanometres [236]. Pinocytosis can be subdivided into four main mechanisms: micropinocytosis, clathrin-mediated endocytosis (CME), caveolae-mediated endocytosis, and clathrin- and caveolae-independent endocytosis [228a].

Micropinocytosis is a biological process by which cells enable to take up a large volume of extracellular fluid non-specifically [237]. During pinocytosis, extensions of plasma membrane form ruffles and enclose extracellular fluids through forming large vesicles (0.2–5 μm) called pinosomes [237a]. This leads to the accidental internalization of materials, with a size of up to 0.1 μm, when located nearby the plasma membranes. Compared to the phagocytosis pathway, this route functions non-selectively, and almost all cell types use pinocytosis. This route is preferred for the internalization of big NMs due to the formation of large vesicles [228b, 233].

Clathrin-mediated endocytosis (CME) is a vesicular transport process by which cells take up vital materials such as nutrients, plasma membrane components, and iron [228b, 238]. NMs with a size of 120–150 nm can be internalized via Clathrin-mediated endocytosis [239]. CME forms vesicles with a diameter of 100-150 nm and encloses extracellular fluid, followed by releasing the budding vesicle at its neck. CME occurs where clathrin is rich on the plasma membrane. CME mechanism can fall into two main pathways with regards to the interaction of cells and NMs: non-specific adsorptive uptake and receptor-mediated uptake [230a, 240]. The former occurs when non-specific interactions such as hydrophobic or electrostatic interactions

75

form between nanoparticles and cells, whereas the latter, internalize the material when specific ligands bind to receptors on the surface of the cell membrane [228b].

Caveolae-dependent endocytosis is essential for many biological processes, which is more pronounced in epithelial and non-epithelial cells [241]. This route is characterized with flask-shaped invaginations of the plasma membrane with a size of ~50–80 nm [242]. Caveolae-dependent endocytosis is triggered by certain caveolin proteins with contributions of other proteins, such as dynamin [230a]. Caveolin is a dimeric protein that is responsible for the formation of flask shape invaginations. Materials entered the cells by this route are likely to escape from degradation by lysosomes, which is highly valuable for gene [243] or protein delivery [244].

In addition to the above-mentioned pathways, cells are found to use a different mechanism to take up a variety of materials [245]. For example, Lipid rafts are specific solid microdomains of the cell membrane, where enriched in cholesterol and sphingolipids [246]. Lipid rafts involves several important biological processes of cells such as membrane trafficking, cell signaling, and endocytosis [247]. Lipid raft-mediated endocytosis was found to internalize modified nanoparticles with particular cell-penetrating peptides and nucleic acids [248]. It is expected that more cellular uptake pathways of NMs will be discovered in the future.

6.2. Intracellular trafficking of NMs

In addition to cellular uptake mechanisms, intracellular trafficking and ultimate localization of 2D NMs in a subcellular component are critical to their fate and therapeutic efficacy [249]. The internalized NMs are generally encapsulated within vesicular structures called endosomes, regardless of the internalization pathway (**Figure 16 b**) [250]. These endosomes create a physical

76

barrier between NMs and cytosol or cytoplasmic organelles and contains hydrolases. Endosomes can be grouped into the three main classes called early endosomes, late endosomes, and recycling endosomes [251]. The early endosome is responsible to direct endocytic vesicles' cargo to the targeted location within the cell. A portion of the cargo will be recycled to the plasma membrane, meanwhile, the rest stay in the early endosomes and then transform to late endosomes via maturation and differentiation [252]. Late endosomes can integrate with the plasma membrane and redirect the cargo to the extracellular fluid. Alternatively, late endosomes can integrate with lysosomes and form endolysosomes, where encapsulated nanoparticles undergo degradation by existing hydrolytic enzymes within the vesicles. In addition, entrapped cargo experiences pH of around 6 within endosomes and around 4.5 in lysosomes [253]. These acidic environments result in acid etching of the NMs, which will in turn release free ions and molecules from the NMs that can change the cell homeostasis and function. It is likely the entrapped NMs can escape this pathway and leak into the cytoplasm, and thereby interacting with intracellular compartments [253]. However, these NMs may be arrested via the autophagy pathway and delivered to lysosomal degradation [254].

77
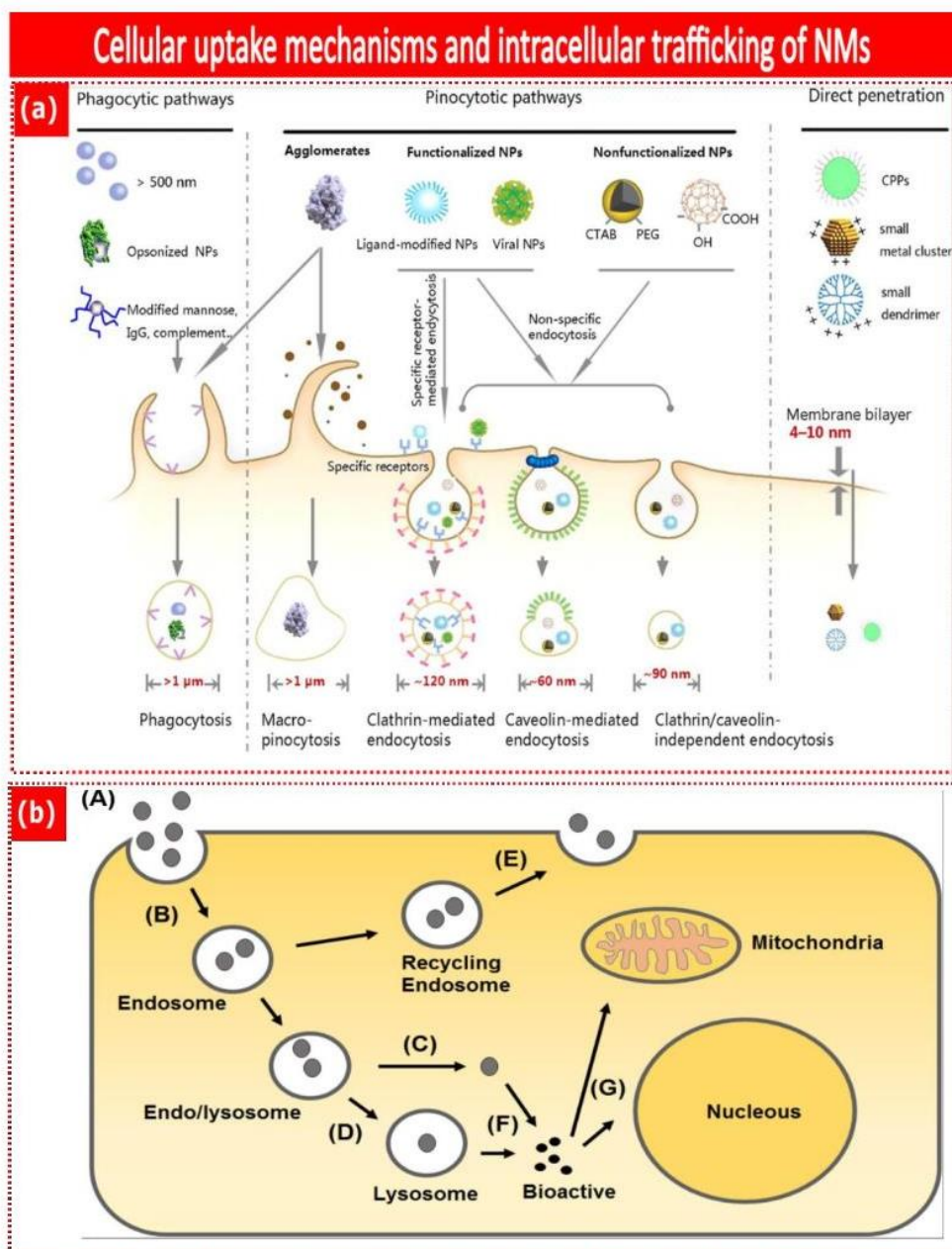
Figure 16. (a) Cellular uptake mechanism of nanomaterials by endocytosis pathways according to their size [255]. Reproduced with permission from ref. [255], Copyright (2012) American Chemical Society. (b) Intracellular location of nanomaterials [256]. Reproduced with permission from ref. [256], Copyright (2020) Elsevier. (A) Interaction of cell membrane and nanomaterial, (B) uptake of NMs by cell, (C) endosomal escape or (D) lysosomal degradation

78

of NMs, (E) redirecting of NMs into extracellular matrix by recycling endosome, (F) release of compounds into the cytoplasm, and (G) localization of bioactive compounds to the organelles.

6.3. The role of physicochemical properties of 2D NMs on the cellular uptake and intracellular location

The physicochemical properties of 2D NMs such as size, surface charge, and surface functionalization impinge on the cellular uptake efficiency and intracellular location and subsequently their potential cytotoxicity [224d, 228a, 257]. Thus, it is crucial to explore the role of physicochemical properties of 2D NM of interest on cellular uptake and intracellular location. It should be noted that an in-depth discussion of the role of physicochemical properties of 2D NMs on cellular uptake mechanism and intracellular location entails a standalone review, and thus we refer the interested readers to the following specialized review references [230a, 240, 258] and only the most important parameters will be discussed briefly.

The size of 2D NMs proved to matter the most in determining cellular uptake [231b, 255]. For example, it was shown that large coated GO by bovine serum albumin (BSA)nanosheets (>500 nm) diffused into the cell via phagocytosis mechanism, whereas clathrin-mediated endocytosis is dominant for the smaller size of GO/BSA [255] (**Figure 17 a1**). In addition to the size of NMs, surface charge plays a key role in the rate of internalization of NMs by cells and thus affects the cytotoxicity [250, 259]. Reportedly, due to the negatively charged nature of the cell membrane, positively charged NMs are internalized faster, which may lead to the loss of cell membrane integrity and trigger cell death mechanisms [240]. For example, to explore the effect of surface charges on the cellular uptake kinetics, GO nanosheets have been modified with three different polymers (PEG, BSA, PEI) [259a], as shown in **Figure 17 b**. It was shown that GO-PEI with positive charges have a higher rate of cellular uptake compared to pristine GO or

79

negatively charged GO-BSA and GO-PEG up to 10 µg/mL. Once the concentration of graphene increased further, the uptake of GO-PEI remains almost unchanged, while the internalization of GO-BSA and pristine GO increased up to the studied 40 µg/mL (**Figure 17 b4**). In addition to the kinetics of internalization, the surface charge of NMs determines the uptake mechanism of NMs by cells. For example, micropinocytosis is more dominant for uptaking positively charged NPs, while negatively charged NP mainly diffuse through clathrin-/caveolae-independent endocytosis [245b]. In another study [260], a combination of the size and surface charge of graphene on the cellular uptake mechanism was investigated (**Figure 17 c**). They observed that the graphene nanosheets larger than around 1 µm size enter the cell through the phagocytosis pathway irrespective of the surface charge. While, in the case of graphene nanosheets with ≈200 nm size, surface charge plays a key role in the determination of cellular uptake mechanism. As reported by authors, positively charged graphene nanosheets are internalized predominantly via the CME pathway, while this pathway is negligible for negatively charged graphene sheets. Cellular uptake mechanism of negatively charged graphene nanosheets occurs through phagocytosis and sulfate-receptor-mediated endocytosis, depending on their size. In addition, graphene sheets with neutral charge do not exhibit any significant uptake, regardless of their sizes.

Like cellular uptake of NMs, intracellular trafficking of NMs depends on the physicochemical properties. For example, to explore the role of surface charge on the intracellular location of graphene, two distinct branched polyethylenimine (PEI) and 6-armed polyethylene glycol (PEG) were used to functionalize GO nanosheets, which resulted in the synthesis of positively (GO-PEI) and negatively (GO-PEG) charged GO nanosheets [261]. They observed that not only positively charged GO-PEI have a higher rate of uptake by Raw264.7

80

cells, but also they can escape from degradation and release into the cytoplasm, while GO-PEG localizes only in endosomes. Same biological responses to positively and negatively charged nanomaterials have been reported for other types of nanomaterials. For example, Yue et al. [262] synthesized chitosan-based nanoparticles with three different surface charges to address the role of surface charge on cellular uptake profiles (rate and amount) and intracellular trafficking on eight different cell lines. Accordingly, positively charged chitosan NMs have higher kinetics of internalization and some of which can escape from lysosomal degradation and localize perinuclear, while neutrally and negatively charged nanoparticles are co-localized with lysosomes.
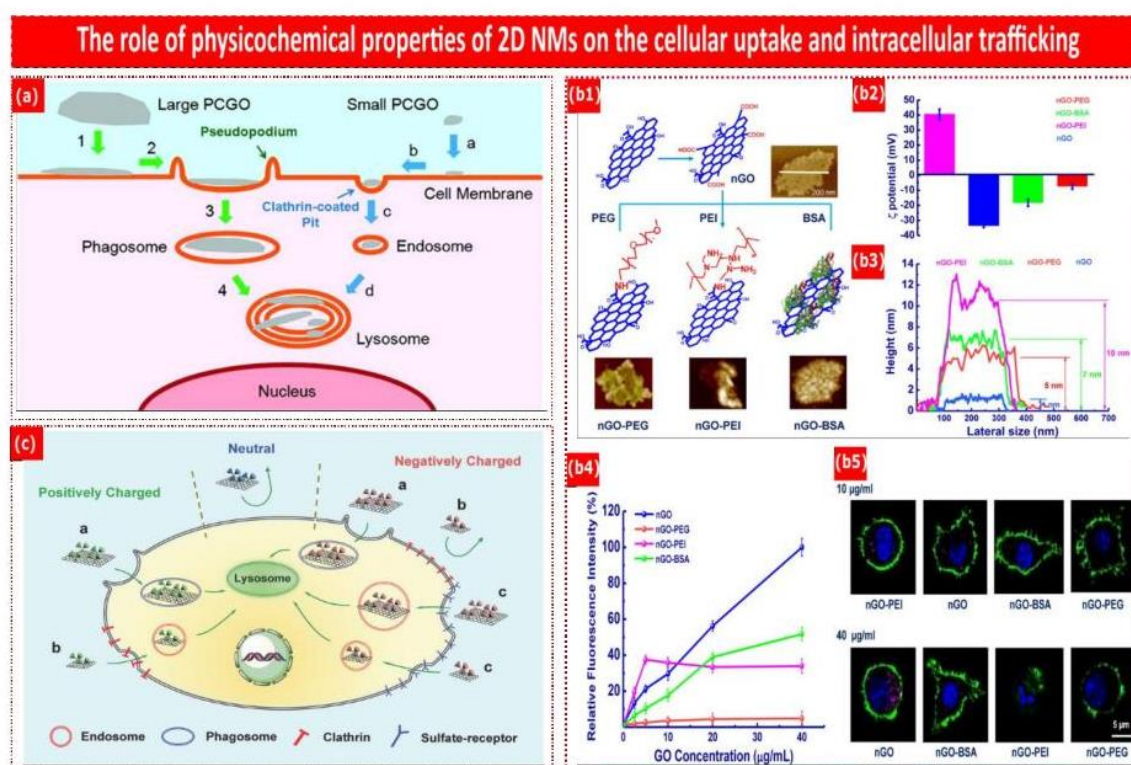
Figure 17. (a) Role of lateral size of GO on the cellular uptake mechanism. Small GO nanosheets enter the cell through CME only, while large GO nanosheets dominantly internalize by both CME and phagocytosis [255]. Reproduced with permission from ref. [255], Copyright (2012)

81

American Chemical Society. (b) Role of surface charges of GO on the cellular uptake mechanism [259a]. (b1) Modification of GO with three different polymers including PEG, BSA, and PEI. (b2, b3) Surface charges and thickness of prepared GO-PEG, GO-BSA, GO-PEI, and pristine GO. (b4) Uptake of prepared GO nanosheets by pMØs at different dosages and (b5) corresponding images at 10 and 40 µg/mL dosage, where purple dots shows nGO complexes. Reproduced with permission from ref. [259a], Copyright (2015) American Chemical Society. (c) The uptake mechanisms of graphene with varying sizes and surface charges. The cellular uptake mechanism: a) phagocytosis, b) clathrin-mediated endocytosis, and c) sulfate-receptor-mediated endocytosis [260]. Reproduced with permission from ref. [260], Copyright (2017) Wiley-VCH.

6.4. Toxicity mechanism of 2D NMs

6.4.1. Physical interactions with the cell membrane

Sharp edges proved to be one of the main origins of 2D NMs cytotoxicity that can function as nano-blade and damage the cell membrane [153c, 263]. For example, GO and rGO have shown strong antibacterial activities towards both Gram-negative and Gram-positive bacteria, due to the set of chemical and physical origins especially sharp edges of graphene nanosheets and the generations of reactive species oxygen (ROS) [153a, 263b, 264]. Like graphene, the antibacterial activity of the MXene nanosheets is ascribed to the physical destruction of bacterial membranes by sharp edges, which leads to the leakage of intracellular substances and finally cell death (**Figure 18 a**) [144]. Physical destruction of cell membranes has also been reported for other 2D NMs such as BP [263a, 265] and TMDs [266]. In addition to the nano-blade effect, the interaction of 2D NMs basal plane with cells plays a crucial role in their toxicity [267]. For example, the antibacterial activity of GO with different lateral size towards *E. coli* cells showed that the GO with larger lateral size induces higher antibacterial activity [268]. As

82

suggested by the authors, this is mainly due to the higher capability of larger GO nanosheets in wrapping bacteria membrane that can effectively isolate cells from nutrients and eventually leads to cell death.

6.4.2. Oxidative stress

Oxidative stress is proved to induce damage to the cellular macromolecules due to the excessive generations of ROS, which has been thought to be the main origin of toxicity of BP [269], graphene, MoS$_2$ [266a, 270]. ROS are oxygen-containing free radicals that function as cell signaling molecules for normal biologic processes [271]. Mitochondria are the main source of ROS generation, however, other cellular components also contribute to the generation of ROS [272]. Oxidative stress occurs when the ROS level exceeds the cellular antioxidant defense system, where the antioxidant enzymes are not able to mitigate ROS [225b]. Catalytic features of 2D NMs can generate excessive amounts of ROS, which may subsequently lead to oxidative stress, mitochondrial damage, DNA damage, the commencement of lipid peroxidation, and induction of inflammatory responses (**Figure 18 b**) [227a, 273]. For example, it was found that GO can induce apoptosis and inflammation of lung tissue caused by oxidative stress, while the unoxidization of GO significantly reduces the toxicity of GO [274]. Similar oxidative stress mechanism have been reported for BP [275], MXenes [276], and MoS$_2$ [277].

6.4.3. DNA damage

Considering the possible DNA damage induced by 2D NMs, it is necessary to carefully monitor the genotoxicity profiles of 2D NMs because even minor damage to the genes can lead to severe health problems such as induction of cancer [226c, 278]. Considering the size of NMs and high surface area, the interaction between NMs and DNA is likely to occur that may results

83

in the chromosomal fragmentation, DNA strand breakages, DNA adducts, and mutations [279]. Two mechanisms have been identified in the genotoxicity of NMs (**Figure 18 c**) [280]: (1) Primary mechanism refers to the direct or indirect interaction of NMs and genetic materials. In direct interaction, NMs physically or chemically damage the DNA strands once NMs contact with genetic materials [281]. In the indirect pathway, the toxicity is due to the oxidative stress caused by NMs that may lead to chromosomal fragmentation, DNA strand breakages, and mutations [281]. For instance, *in vitro* and *in vivo* assessments have shown that BP induces DNA damage via the generations of an excessive amount of ROS [282]. (2) The secondary mechanism is ascribed to the chronic inflammatory response of cells. It should be noticed that despite the fact that if NMs cannot diffuse into the nucleus of cells, NMs still have a chance to contact with genetic materials during mitosis once the nuclear membrane disappears [280].
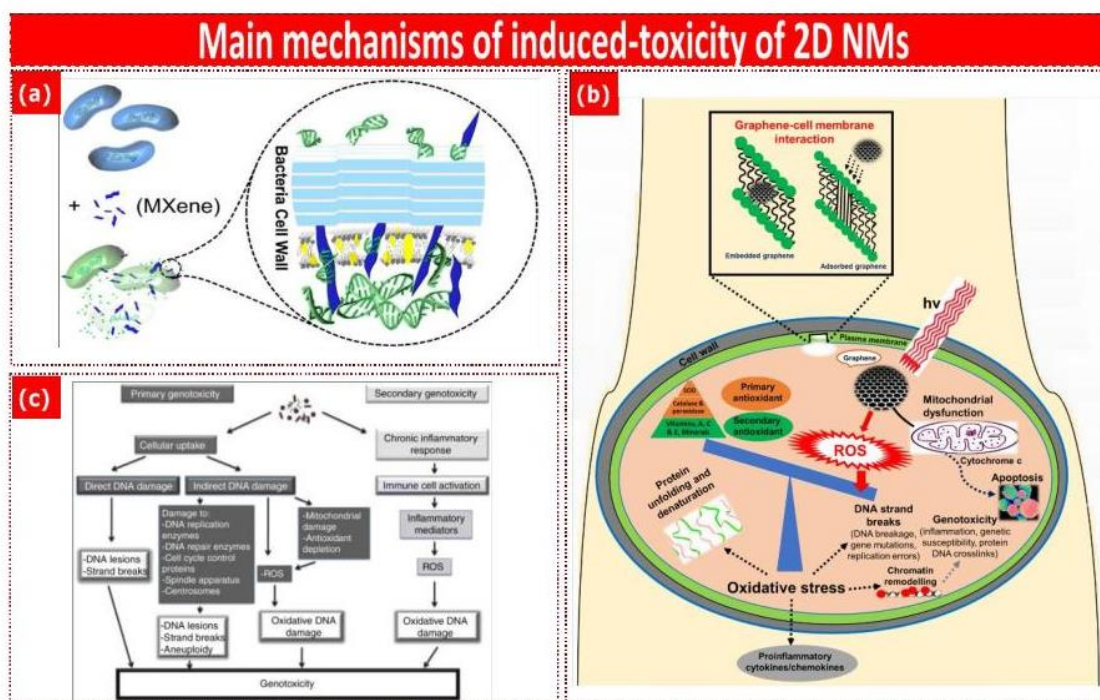
Figure 18. Main toxicity origins of 2D NMs: (a) Physical interactions [144]. Reproduced with permission from ref. [144], Copyright (2018) American Chemical Society. (b) Oxidative stress

84

resulting from excessive generation of ROS, which may damage subcellular components [283]. Reproduced with permission from ref. [283], Copyright (2018) Elsevier. (c) DNA damage through primary and secondary mechanism [284]. Reproduced with permission from ref. [284], Copyright (2017) Elsevier.

6.5. Common methodologies to analyze the toxicities of NMs

In vitro and *in vivo* assessments are two main toxicity evaluation methods to investigate the relationship between various physicochemical properties of each 2D NMs and their cytotoxic impacts on the biological system [225a].

6.5.1. *In vitro* assessment

The primary aim of *in vitro* assessment is to simulate the cellular events in the body once exposed to foreign materials. As a first stage for assessing the biocompatibility of 2D NMs, *in vitro* assessment is highly valuable for the determination of induced toxicity [285]. NMs come in contact with a variety of cell types such as red blood cells, phagocytes, and non-phagocytic cells. In this context, *in vitro* assessment provides very useful information regarding (i) hemocompatibility, (ii) inflammation responses, and (iii) cytotoxicity of 2D NMs [286]. Hemocompatibility testing is an essential investigation to monitor the potentially harmful effect of foreign materials once they come in contact with blood cells [287]. In addition, the interactions of NMs with the immune system should be considered in the design of NMs for targeted application [288]. For example, *in vitro* assessment allows to track how adsorbed corona of biomolecules on the 2D NMs surface can change the immune response towards these materials. Moreover, *In vitro* assessment allows measuring the dosage limits of exposure and track the fate of NMs [289].

85

Compared to *in vivo* approach, this study is cost-effective, quick, and does not involve any ethical issues of animal testing [290]. There are a variety of routes for *in vitro* methods such as cell membrane disintegration, oxidative stress as well as DNA damage, and they are often coupled with functional and viability assays [291]. Viability assay is an approach that examines the degree of cell death during cell exposure to 2D NMs [291]. During this assay, the membrane integrity and metabolic activity of cells are measured to determine the cytotoxicity of NMs [292]. Whereas, the functional assay is another method to determine the cytotoxicity mechanism via examination of specific cellular processes [293]. However, the *in vitro* toxicity assays should be carefully selected to avoid inconsistent, contradictive, false-positive/false-negative results [294]. For example, *in vitro* cytotoxicity of GO and rGO sheets with various size and oxygen content were monitored in red blood cells (RBCs) and human skin fibroblast cells via MTT and WST-8 viability assays [287b]. While WST-8 assay exhibited the toxicity of GO and rGO towards human skin fibroblast cells, the MTT assay failed to detect the cytotoxicity. This is ascribed to the reaction of graphene with MTT materials and generation of MTT formazan, which will in turn shows false high biocompatibility of graphene. Therefore, it is necessary to take caution once choosing *in vitro* assayS to ensure the NMs does not have any interference with the reagents. It is suggested that distinct properties of each 2D NMs along with their potential interaction with cells should be articulated to select the fast and robust assay for each 2D NMs [295].

6.5.2. *In vivo* assessment

In vivo assessments of 2D NMs provide an essential information related to the particle distribution, metabolism as well as particle absorption, which is needed to minimize the potential particle-related risk of cytotoxicity [225a]. For example, a broad variety of studies have found that graphene-related particles are mostly not toxic at low concentrations, but further

86

investigation on chronic effects of these particles still needs to be performed for the biomedical industries [296].

6.6. Deciphering the underlying physicochemical properties of 2D NMs affecting biocompatibility

Literature has revealed that the toxicity of 2DNMs is closely related to their physicochemical properties such as lateral size, the number of layers, the composition of the protein corona, type of functionalization, and surface charge [225b, 257]. Even small variations in those characteristics could significantly impact their biocompatibility and therapeutic efficacy [225b]. The knowledge of interactions between 2D NMs and the organism facilitates the development of 2D NMs for targeted application. Therefore, it is essential to tune the physicochemical properties of 2D NMs to promote the biocompatibility and subsequently their therapeutic efficacy.

Although these physicochemical factors proved to be governing the cytotoxicity of 2D NMs, very limited and inconsistent information is available that remains ambiguous over their toxicity profile. Another challenge encountered in the studies of nanotoxicity of 2D NMs is the difficulty in the determination of certain factors individually as changes in one of those physicochemical parameters can vary the other parameters. Many excellent reviews are detailing the physicochemical properties of NMs on their toxicity profile [225b, 226c, 227a, 228c, 257]. Therefore, we only attempt to highlight the most important physicochemical properties of 2D NMs to explain the relevance of these parameters to their toxicity profile.

6.6.1. Lateral size

87

The biological behavior of 2D NMs varies significantly upon a change in the lateral size [288-289, 297]. Given this, it is necessary to characterize the lateral size of 2D NMs once examining the biological response of these NMs [225b]. In this context, cellular uptake, cytotoxicity, and inflammatory responses of MoS_2 flakes with various lateral sizes (50, 117, and 177 nm) was monitored in three different cell-lines (A549, AGS, and THP-1 cell lines) after 24 hr exposure (**Figure 19 a**) [298]. Accordingly, MoS_2 did not induce any toxicity on any of the three cell lines with no signs of necrosis or apoptosis at 1 µg/mL dose, regardless of the lateral size. However, the Inflammatory response of THP-1 cells indicates that the MoS_2 flake with a smaller lateral size triggers the highest cytokine production (IL-6, IL-10, IL-13, TNF-α, and IL-1β). In addition, MoS_2 NMs were uptaken by all cell lines and located in single membrane vesicles. Of note, the incubation of 2D NMs in a cell culture media generally results in the formation of protein corona on NMs' surface, which subsequently changes their hydrodynamic size [299]. Therefore, particular consideration should be taken once determining the role of NMs size on their biological response. It is suggested measuring of NM size should be performed in the biological environment to obtain a realistic size.

6.6.2. Thickness

The extent of exfoliation proved to impact the toxicity of TMDs [300]. In an interesting research, the potential *in vitro* toxicity of MoS_2 nanosheets that were chemically exfoliated with different lithium intercalating agents (Methyllithium (Me-Li), n-butyllithium (n-Bu-Li) and tert-butyllithium (t-Bu-Li)) were evaluated towards A549 cells (**Figure 19 b**) [300]. *t*-Bu-Li and *n*-Bu-Li is more effective than Me-Li in the exfoliation of MoS_2, which led to the synthesis of MoS_2 with a lower number of layers. According to MTT and WST-8 results, higher exfoliated

88

MoS_2 induced significantly higher toxicity, which was attributed to the increased surface area and active sharp edges.

6.6.3. Chemical composition

Numerous researches have shown that the chemical composition of 2D NMs plays a key role in the toxicology profiles [227b, 301]. In addition, chemical composition governs the solubility and surface chemistry of NMs and therefore determines their cellular interactions, uptake, and biodistribution. In this context, *in vitro* cytotoxicity of three common TMDs with different chemical compositions (MoS_2, WS_2, and WSe_2) were evaluated towards the A549 cells after 24 h exposure via MTT and WST-assays (**Figure 19 c**) [301a]. Compared to MoS_2 and WS_2 nanosheets with slight cytotoxicity even up to 400 µg/mL dose, WSe_2 induced higher toxicity with a dose-dependent manner as the viability of A549 cell exposed to 400 µg/mL of WSe_2 reduced to 31.8%. This indicated that the nature of chalcogen in the chemical structure of 2D TMDs plays a key role in the toxicity profile. In a similar study [302], the cytotoxicity of group 5 transition metal ditellurides (MTe_2; M=V, Nb, Ta) was assessed in the same condition. It was found that $NbTe_2$ and $TaTe_2$ induced mild toxicities, whereas VTe_2 was highly toxic. Compared to group 6 transition metal disulphide, the ditellurides induced higher cytotoxicity except for WSe_2 that exhibited similar cytotoxicity to the ditellurides.

6.6.4. Surface functionalization

Surface functionalization of 2D NMs allows binding of NMs to the targeted cells selectively, which is called active targeting ligands [258, 303]. The most commonly used targeting ligands in nanomedicine are peptides, proteins, antibodies, and nucleic acids, which can bind to the cell surface receptors. In addition, the surface functionalization of 2D NMs significantly

89

changes the toxicological response [304]. For example, surface functionalization of GO by PEG has been reported to mitigate the cytotoxicity of GO because of the weakening of the interaction of GO with biological interfaces [305]. In addition, PEG can endow stealth properties to the graphene nanosheets, which will in turn hide them from internalization by macrophages [306]. In a recent comparative study, GO nanosheets have been functionalized with carboxyl, imidazole, and GO-polyethylene glycol and examined their toxicity towards aquatic model species *Daphnia magna*. The results exhibited that all three modifications mitigate the cytotoxicity of pristine GO, which is more pronounced in PEG (**Figure 19 d**) [307].

6.6.5. Protein corona

Protein corona is a layer of bound proteins on the NMs surface in the biological environment that endow a new identity called "biological identity" [308]. In this context, numerous studies have shown that the formation of protein corona on the NMs surface is likely to govern the subsequent biological events such as cellular recognition, uptake toxicity, biodistribution, efficacy, and immunostimulatory effects [309]. For example, a recent study examined the absorbed protein on BP surfaces via liquid chromatography tandem mass spectrometry [310]. They found that the majority of absorbed proteins on BP were immune relevant proteins, which resulted in the higher cellular uptake of BP by macrophages (**Figure 19 e**). They found that the composition of corona proteins varies significantly upon a change in the size of 2D BP NMs. In addition, the absorbed corona proteins can define the shape of ultra-small 2D NMs, while corona proteins cannot change the shape of large 2D BP NMs.

Numerous studies have revealed that the multiple factors involved in the formation of corona proteins, among which the physicochemical properties of the NM are of utmost importance in interactions at the NM–protein interface [311]. For example, it was shown that

90

the charged NMs are likely to pick up more proteins compared to neutral NMs. In addition, the NMs with the same physicochemical properties shape the different compositions of protein corona when incubated in different protein sources. For instance, the extent of absorbed protein on NMs surfaces significantly differs in mouse plasma and human plasma, which means the animal models cannot correctly mimic the biological identity of NMs. In addition, there is strong evidence that other parameters such as protein concentration [312], temperature [313], exospore time [314], and shear stress [315] also impact the protein corona formation. The formation of protein corona also can hide the ligands on the NMs surfaces and leads to the loss of targeting capacity of ligand-modified NMs [316].

The interaction at the NM–protein interface not only changes the biological response of NMs but also induce structural and functional altered corona proteins, which will in turn change their activity and functionality [224b, 317]. For example, the absorption of fibrinogen on NMs surfaces induces fibrinogen unfolding, which subsequently activates NF-κB signaling pathway and triggers cytokine secretion [318].

6.6.6. Surface charge

In a recent study [319], it was shown the surface modifications of negatively charged MXene with positively charged collagen mitigate the toxicity of MXenes on the different cell lines (MCF-7, MCF-10, HaCaT, and A375), evidenced by reduced oxidative stress (**Figure 19 f**). They reported that the zeta potential value of 2D MXenes immediately shifted from negative to positive values upon the addition of a small amount of collagen.

91
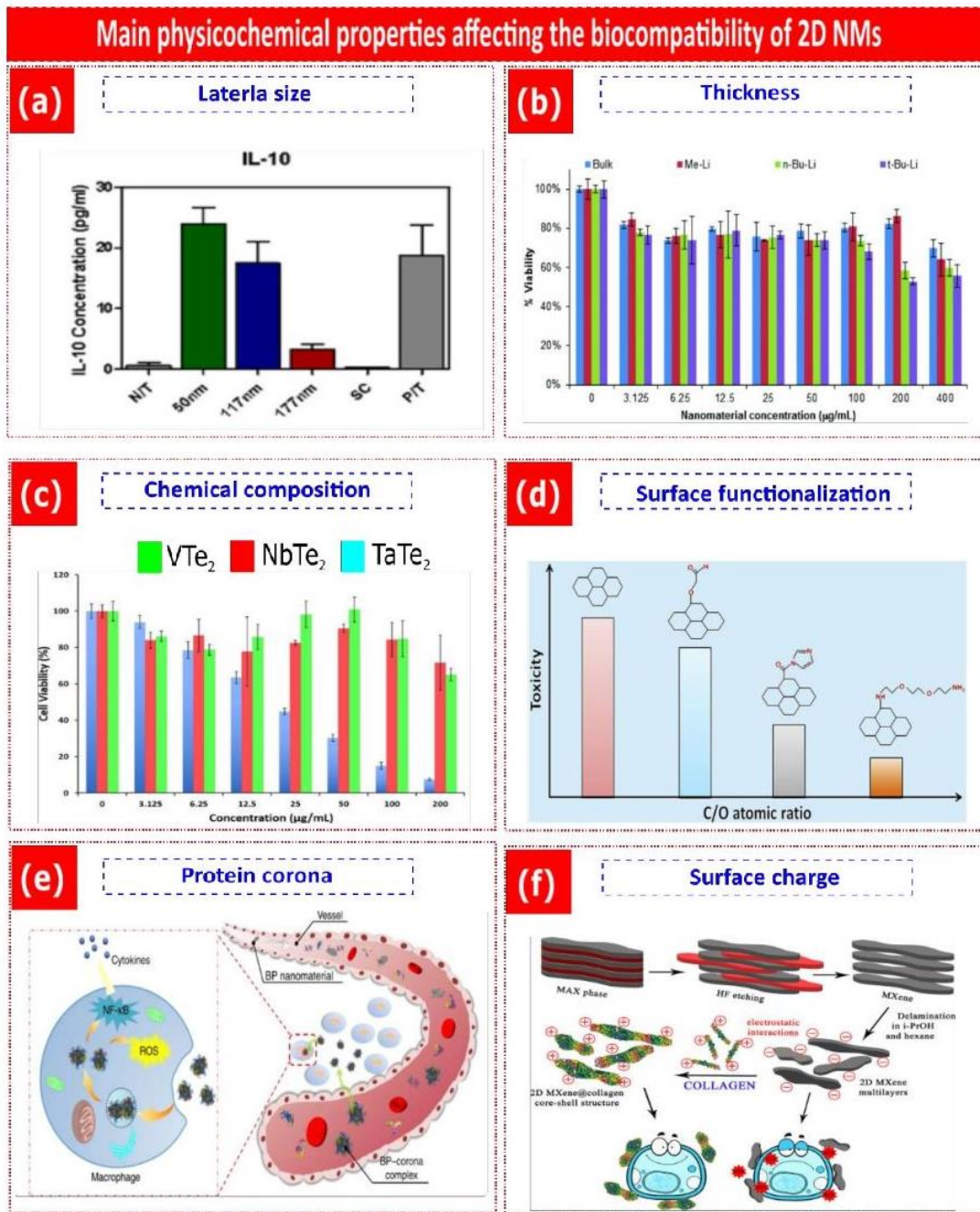
Figure 19. Main physicochemical properties that affecting the cytotoxicity of 2D NMs. (a)

Lateral size. An increase in the lateral size of MoS_2 nanosheets leads to higher cytokine

production [298]. Reproduced with permission from ref. [298], Copyright (2017) IOPSCIENCE. (b)

Thickness. A higher extent of exfoliation of MoS_2 was obtained once using t-Bu-Li and n-Bu-Li,

Which induced higher toxicity [300]. Reproduced with permission from ref. [300], Copyright (2014)

92

Royal Society of Chemistry. (c) Chemical composition. The viability of A549 cells exposed to three different TMDs nanosheets varied significantly upon a change in the chemical composition of TMDs [301a]. Reproduced with permission from ref. [301a], Copyright (2014) Wiley-VCH. (d) Surface functionalization. Evaluation of Cytotoxicity of functionalized-GO with carboxyl, imidazole, and polyethylene glycol towards *D. magna* exhibited the toxicity of pristine GO functionalization significantly were alleviated, which ascribed to the ratio of C/O atomic ratio after functionalization [307]. Reproduced with permission from ref. [307], Copyright (2018) Elsevier. (e) Protein corona. Absorbed protein on BP were immune relevant proteins, which led to the cellular uptake of BP by macrophages increase [310]. Reproduced with permission from ref. [310], Copyright (2018) Nature. (f) Surface charge. Surface modifications of negatively charged MXene nanosheets with positively charged collagen reduce the generation of ROS and subsequently mitigate the toxicity of MXenes on different cell lines (MCF-7, MCF-10, HaCaT, and A375) [319]. Reproduced with permission from ref. [319], Copyright (2020) **Elsevier**.

6.7. Toxicity of the studied 2D NMs

Based on the requirements of biosystem condition, it is firstly needed to evaluate the cytotoxicity of 2D NMs before translation into biological applications. Here, the toxicity of studied 2D NMs was summarized in **Table 2**.

6.7.1. Graphene

While the graphene family has shown significant promise in the nanomedicine, the full realization of excellent properties of graphene requires in-depth determination of the nanotoxicity profiles [227b, 320]. However, the toxicity profile of the graphene family is often

93

inconsistent and subject of discussion [321]. This is mainly due to the multiple physicochemical properties that play important roles in cytotocixity of the graphene family in contact with cells [322]. For example, in a study conducted by Akhavan et al.[279a] the cytotoxicity of GO and rGO with different lateral dimensions and distributions on hMSCs were investigated. It was found that, in the case of rGO, smaller lateral size induces lower toxicity on hMSCs. As suggested by the authors, combinations of oxidative stress and mechanical damage of membrane are the origins of rGO toxicity, while in the case of GO nanoplates oxidative stress is playing the primary role in cell destruction and resulting toxicity. In addition to the physicochemical properties of graphene, the cytotoxicity of graphene exhibits time and dose-dependent behavior. For example, Wang et al. [323] reported that the GO nanosheets are nontoxic *at* concentrations lower than 20 μg/mL towards skin fibroblasts, after which it is detrimental to cells. In addition, injection of a very high dose of GO led to chronic toxicity, following lung granuloma formation and death of mice in the experiment. Moreover, other research suggests that the graphene-based NMs can harm cells through mitochondrial depolarization or even genotoxicity when it enters the nucleus and interacts directly with DNA [324]. It can be inferred that the graphene family can be either safe or deadly to various cells and organs depending on different structural and physicochemical parameters. Therefore, for the safe application of nano-sized graphene-based material in the biomedical field, deeper knowledge and understanding of their interaction with cells are required.

6.7.2. Nanosilicate

Although the toxicity profile of laponite has not been fully characterized, significant progress has been made in the determination of its safety [325]. Like other 2D NMs, the cytotoxicity of laponite also depends on the concentration. For example, the *in vitro* toxicity

assessment of laponite towards hMSCs showed that the safe dosage of laponite in contact with hMSCs is less than 1 mg/mL, above which cytotoxicity notably increases due to the intense formation of intracellular ROS [326]. In addition, half maximal inhibitory concentration (IC_{50}) for silicate nanoplatelets was around $IC_{50} \approx 4$ mg/mL, which was ten times higher than recorded IC_{50} for silica nanoparticles and hydroxyapatite nanoparticles, indicating possible cytotoxicity of laponite only at higher concentration. Further, another study proved the time and dose-dependent toxicity of laponite towards HEK and SiHa cells, as significant toxicity was observed at concentration around 0.05 % after 24h incubation [327]. Some reports are confirming the biocompatibility of composite of laponite with other polymers such as hydroxypropylmethyl cellulose, alginate, silk fibroin towards different cell lines [172a, 328].

In vivo toxicity assessment of laponite has also revealed favorable biocompatibility due to the safe biodegradation pathway of laponite nanoparticles. For example, *In vivo* biocompatibility of laponite was investigated through intramuscular stimulation and toxicity test by assessing health parameters of rats that received an injection of 50 mL/kg laponite extract for up to seven days [329]. No significant changes in the health parameters of treated rats compared with the control group were found, confirming suitable biosafety of laponite bioceramics.

6.7.3. Black phosphorous

BP have exhibited an excellent *in vivo* biodegradability, which dissociates into the nontoxic products under a physiological environment and releases phosphates and phosphonates [330]. *In vivo* biodegradability of BP nanosheets allows the clearance of BP from the body without the need for further surface functionalization. However, more systematic biosafety assessments are required for its safe clinical translation. For instance, in a recent

study, BP nanosheets were coated with polydopamine (PDA) followed by covalently binding to chlorin e6 (Ce6) and triphenyl phosphonium (TPP), forming BP@PDA–Ce6&TPP for photothermal and photodynamic cancer therapy [184b]. *In vitro* cytotoxicity evaluation of functionalized BP nanosheets towards HeLa cells indicated a very low decrease in cell viability up to 25 μg/mL concentrations before laser illumination. However, after laser irradiation, the *in vitro* and *in vivo* results confirm the high efficacy of the prepared BP@PDA–Ce6&TPP nanosheets in eradication of cancerous cells owing to the strong absorbance of BP@PDA in the NIR region, high ROS production of Ce6, and targeting mitochondria due to the TPP moiety.

Like other 2D NMs, the toxicity profile of BP nanosheets is generally determined by physicochemical properties. For example, the cytotoxicity of BP nanosheets with different lateral size and thickness was monitored towards three different cell lines (293T, NIH 3T3, HCoEpiC) [275a]. The IC_{50} values significantly depend on the BP size and cell types as BP with largest lateral size and thickness induced more toxicity. Combinations of oxidative stress and disruption of cell membrane mechanism were proposed as the origin of toxicity of BP, however, only the latter exhibited size-dependent behavior as the larger lateral size led to more physical damage to the cell membrane. In another study, *in vitro* cytotoxicity assessment of BP nanosheets towards A549 cells revealed the cell viability decreased upon increasing the BP concentrations, as the cell viability reduced to 48% (WST-8) and 34% (MTT) at 50 μg/mL BP concentration [331]. In addition, a comparison of cytotoxicity of BP with other 2D NMs exhibited that the BP nanosheets induced intermediate toxicity between GO and exfoliated TMDs (MoS_2, WS_2, WSe_2) towards A549 cells. Elsewhere, The time and concentration-dependent cytotoxicity of BP nanosheets evaluated towards various fibroblast cells(NIH3T3, nHDF, HT1080) via CCK-8 and LDH assays [332]. The viability of cells exposed to BP nanosheets

96

decreased with increasing the dosage and exposure time, which is more pronounced in HT1080 cells. The sensitivity of studied fibroblast cells was in the order, HT1080>nHDF>NIH3T3.

6.7.4. MXene

Literature data on the application of MXene in biomedical fields indicates high biocompatibility of $Ti_3C_2T_x$ MXene [9b, 333]. For instance, in recent research evaluating the biocompatibility of Ti_3C_2 MXene on zebrafish embryo model, no adverse effect on the neuron cells was observed, which indirectly implies possible non-neurotoxic interaction of MXene with human cells [334]. Considering the locomotion and neurotoxicity assay results, Ti_3C_2 falls into the "practically nontoxic" group according to the Acute Toxicity Rating Scale by the Fish and Wildlife Service.

In an interesting study, the cytotoxicity of Ti_3C_2 MXene nanosheets have been compared towards normal (MRC-5 and HaCaT) and cancerous (A549 and A375) cell lines [335]. It was found the MXene induced higher toxicity towards cancerous cells compared to the normal cell lines. Elsewhere, it was demonstrated that the cytotoxicity of the Ti_3C_2 flakes can be tuned upon the change in the nature of the surface terminations on the Ti_3C_2 surfaces [336]. In this sense, the authors compared the cytotoxicity of three different Ti_3C_2 MXene nanosheets; as-received (AS-Ti_3C_2), probe-sonicated (SO-Ti_3C_2), and thermally oxidized (TO-Ti_3C_2) towards cancer and non-malignant ones. They found that the SO-Ti_3C_2 and TO-Ti_3C_2 induced higher toxicity towards cancer cells (A375 cells) than non-malignant ones (HaCaT), which is more pronounced for thermally oxidized Ti_3C_2 flakes. As suggested by authors, the

97

selective toxicity of Ti_3C_2 MXene nanosheets towards cancer cells is attributed to the formation of superficial titanium (III) oxide layer after oxidative post-treatment.

In this context, soybean phospholipid-modified MXene (Ti_3C_2-SP) nanosheets demonstrated negligible cytotoxicity towards breast 4T1 cancer cells and glioma U87 cancer cells [196]. Confocal laser scanning microscopy images have proved that the Ti_3C_2–SP nanosheets could successfully internalize into the cancer cells after 4 hours of incubation. In addition, Kunming mice received up to 20 mg kg^{-1} through intravenous injection and were euthanized after 30 days. Results obtained from *in vivo* toxicity assays also demonstrated no significant acute and chronic toxicity, suggesting high biocompatibility of Ti_3C_2Tx MXene. In a similar work, the cytotoxicity of SP-modified tantalum carbide nanosheets (Ta_4C_3 MXenes) was evaluated in the same conditions *in vitro* and *in vivo*, guaranteeing biocompatibility of Ta_4C_3 [189]. Elsewhere, *in vivo* toxicity of Ti_3C_2-based composite MXene (MnO_x/Ti_3C_2) was investigated by intravenous injection into healthy Kunming mice at different dosages up to 20 mg kg^{-1}. A similar result was reported with no abnormal change in the blood index, indicating high biocompatibility and low toxicity of MnO_x/Ti_3C_2 composite [198].

6.7.5. Transition metal dichalcogenides

Reportedly, TMDs induces lower cytotoxicity compared to other 2D NMs, which is highly valuable for biomedical applications [337]. However, considering the diversity of TMDs surface chemistry and their potential toxicity, it is required to carefully select the comprising elements to lower the risk of side effects *in vivo*.

One drawback of TMDs is their intrinsic poor hydrophilicity, which significantly hinders their future usage in biomedical fields. To address this issue, many efforts have been devoted

98

to modifying TMDs surfaces using a variety of materials such as polymers, proteins, or small organic molecules [338]. For example, lipoic acid conjugated PEG (LA-PEG) was used to functionalize the MoS_2, which improved the biological stability without any agglomeration in PBS and serum [339]. The *in vitro* toxicity of pristine MoS_2 and MoS_2-PEG have been monitored for 72 hrs on Hella cells. In the case of pristine MoS_2, almost all cells remain viable after 24-hour incubation, which further decreased to around 80 % and 73% after 48 and 72 hrs, respectively. While more than 90% of cell viability was observed when incubated with MoS_2-PEG nanosheets. In addition, no significant increase in the ROS level was detected in cells when incubated MoS_2-PEG or MoS2. Further, *in vivo* toxicity confirmed the biocompatibility of MoS_2-PEG without noticeable toxicity to mice. Similarly, the toxicity of albumin functionalized flower-like MoS_2 nanoparticles (MoS_2@BSA) was evaluated towards murine breast cancer cells (4T1). High cell viability (>80%) was observed after 48h incubation with MoS_2@BSA at high concentration (200 µg/mL). In addition, *in vitro* hemolysis assay on the RBCs showed negligible hemolysis phenomenon, conforming high hemocompatibility of MoS_2 hybrids [340].

6.7.6. Hexagonal boron nitride

In general, low solubility is the major problem with the application of hBN in biomedical fields as it decreases the biological integration of hBN with the biological environment. Therefore, researches on their cytotoxicity behavior have mainly focused on the modified hBN based materials and hybrids with higher water dispersibility [341]. There are some reports that the biocompatibility of hBN significantly depends on the physicochemical properties of hBN [342]. For example, the biocompatibility of hBN with different lateral sizes was examined towards the SaOS-2 cell line [343]. It was found that hBN with a diameter below 1 µm and a thickness of less than 100 nm induces more toxicity, resulting from the higher production of

99

ROS. This is ascribed to the higher surface area of small size hBN that offers a higher number of unsaturated boron atoms on the BN surface. In addition, NMs with lower size can be taken up more by cells, and subsequently generate more ROS.

In addition to the physicochemical properties of hBN, dosage and exposure time also have been reported to have a significant impact on the cytotoxicity. In this context, Singh et al. [341b] reported the synthesis of highly water dispersible nanostructured hBN at a relatively low temperature. The *in vitro* cytotoxicity of obtained dispersible nanostructured hBN exhibited dose and time-dependent toxicity behavior towards three different cell lines (MCF-7, Hela, HEK-293). According to the MTT results, cell viability declined upon increasing time exposure and dosage of hBN. Interestingly, cancerous MCF-7 and HeLa cell lines demonstrated a higher vulnerability to the hBN presence compared to normal cells. In another study, Lu et al. [344] reported the synthesis of highly dispersed water-soluble hBN nanoplates with average lateral size of 30–60 nm and 1.6 nm in thickness. It was found that the hBN (up to 100 µg/mL) did not induce noticeable toxicity towards HEK-293T and CHO cell lines after 48 hours of incubation according to the MTT and apoptosis assay results. In addition, injection of hBN nanoplates did not induce any apparent antibody response, showing the non-immunogenic nature *in vivo*.

6.7.7. Metal-organic framework

The evaluation of the cytotoxicity of MOFs is still in its infancy stage, however, it has been reported that the toxicity of MOF significantly depends on the types of cross-linkers and metals. Therefore, it is necessary to take caution when choosing the MOFs building blocks as MOFs generally show the characteristics of the comprising component once MOFs are degraded in the body [345]. For example, the in vitro cytotoxicity of 2D Cu-TCPP(Fe) MOF was

examined toward human normal lung epithelial cells (BEAS-2B) and human pulmonary carcinoma cells (A549) [346]. It was reported that 2D Cu-TCPP(Fe) MOF had minor inhibitory effects toward BEAS-2B cells up to 100 µg/mL after 48 h of treatment, while, 25.4% inhibition rate was observed for A549 cells at the maximum concentration of 100 µg/mL after 48 h. Authors suggested that the inhibitory effect attributed to the degradation of degradation Cu-TCPP(Fe) nanosheets and subsequently release of copper ions to the environment. Thus, MOFs containing toxic metals (e.g, cadmium, arsenic, lead, and chromium) might exhibit toxicity and needs to be replaced with other non-toxic metals. In another study [12a], a set of 14 MOFs were prepared and their toxicity was evaluated towards two cell lines (J774 and HeLa). The authors found that the toxicity of MOFs depends on the nature of the metal ions as the MOFs containing Fe induced lower toxicity compared to the Zr- or Zn-MOF NPs. In addition, J774 cells showed more sensitivity once exposed to the MOFs compared to the HeLa cells, which is due to the higher rate of NPs uptake in the macrophage line. Elsewhere, Zhu el al. [347] synthesized a 2D NMOFs that made by linking of Zn^{2+} and tetrakis(4-carboxyphenyl) porphyrin (TCPP), and then functionalized with PEG, forming 2D Zn-TCPP@PEG MOF nanosheets. Compared to its 1D compartment, the 2D Zn-TCPP@PEG MOF nanosheets exhibited higher drug loading capacity that is advantageous to chemotherapy and photodynamic therapy (PDT). *In vitro* cytotoxicity assessment showed no obvious toxicity 4T1, CT26 and MCF-7 cell lines up to studied 20 µg/mL, indicating the biocompatibility of synthesized 2D Zn-TCPP@PEG MOF. In addition, *in vivo* toxicity assessment also suggest the good biocompatibility of the 2D Zn-TCPP@PEG MOF without any appreciable long-term toxicity.

Taking advantage of the sustainable release of metal ions from MOFs structure into the environment and their intrinsic antibacterial activity, several MOFs suggested for antibacterial

101

therapy [348]. For example, Lu et al. [349] prepared two silver-based MOFs (Ag$_2$(O-IPA)(H$_2$O)·(H$_3$O)] and [Ag$_5$(PYDC)$_2$(OH)] and compared the antibacterial activity of the MOFs with silver nanoparticles. It was found that slow release of silver ions induces long-term antibacterial activity against both Gram-negative bacteria, *E. coli,* and Gram-positive bacteria, S. aureus. The measurement of the silver concentration in the environment by inductively coupled plasma atomic emission spectroscopy showed the slow release of Ag ions, which gives potent antibacterial activity to the prepared MOFs. In addition, the toxicity of both MOFs was evaluated toward white and red blood cells in vivo, showing the cells were not significantly changed under a concentration of 100 ppm.

102

Table 2. Some examples of *in vitro* and *in vivo* toxicity assessment of studied 2D NMs

2D NM family	type of 2D NM	Physicochemical properties	in vitro			in vivo	main results	ref
			cell line	incubation time	Dose			
Graphene	Graphene	Thickness: 3–5 nm, Zeta potential: −35.59 mV	PC12	Up to 24 hr	Up to 100 µg/mL	-	(1) Graphene exhibited lower toxicity compared to SWCNT towards PC12 cells, indicating the role of nanomaterials shape in their toxicity. (2) Oxidative stress is identified as the main toxicity mechanism of carbon nanomaterials. (3) Both apoptosis (Caspase) and necrosis markers released once exposed to graphene nanosheets	[150]
	GO with different lateral size	The average hydrodynamic diameter: m-GO (588 nm), l-GO (556 nm), and s-GO (148 nm)	A549	Up to 72 hr	Up to 200 µg/mL	-	(1) GO nanosheets could not diffuse into the A549 cells. (2) The toxicity of GO is dose and size-dependent. (3) Oxidative stress generated by GO decrease the cell viability at high concentrations.	[149a]
	GO	Thickness: 1 nm	A549	Up to 12 hr	20 and 100 µg/mL	-	Formation of protein corona composed of fetal bovine serum (FBS) around GO mitigates the cytotoxicity.	[151]
	GO with the different oxidation rate	Lateral size: 200–260 nm	MEFs	Up to 24 hr	0- 100 µg/mL	-	(1) All prepared GOs can be internalized by MEFs. (2) A lower degree of oxidation induced more toxicity towards MEFs, due to the higher amount of ROS generation	[152]
nanosilicate	Laponite	Lateral size: 25-30 nm,	hMSCs	Up to 48 hr	Up to 20 mg/mL	-	(1) Laponite did not induce any toxicity towards hMSCs up to 1 mg/mL dosage. (2) IC₅₀ for laponite was around IC₅₀ ≈ 4 mg/mL, showing the possible cytotoxicity of laponite at a higher concentration.	[126]
	Laponite-Fe₃O₄	Hydrodynamic size: LAP(113.1 ± 1.40 nm), LAP-Fe₃O₄NPs(210.2 ± 1.26)	HeLa	Up to 24 hr	Up to 100 mg/mL	Model: Two C57 mice, Dosage: LAP-Fe₃O₄NPs (930 µg/mL Fe, in 0.1 mL PBS), administration route: intravenous injection, time:	(1) The viability of HeLa cells was more than 80%, showing the safety of LAP-Fe₃O₄NPs towards HeLa cells. (2) The injected LAP-Fe₃O₄NPs were removed from the body organs after 24 h post-injection. (3) Compared to the untreated mice, no obvious	[153]

103

					Two weeks	changes in the cell morphology were observed, indicating the absence of long-term organ toxicity.	
	laponite–doxorubicin	Hydrodynamic size: Laponite (41.1 ± 0.4), Laponite–doxorubicin (112.2 ± 0.9)	MCF-7	Up to 72 hr		-	Viability of MCF-7 reduced significantly upon release of loaded Dox drug compared to the free drug laponite.	[3.54]
BP	BP@PDA-Ce6&TPP	the lateral size of around 120 nm BP:24.3 NM BPA@PDA: 49.1 nm	HeLa	Up to 24 hr	Up to 25 µg/mL	Model: The Female nude mice bearing Hela tumor, Dosage: BP@PDA-Ce6&TPP NSs (200 µL, 0.56 mg/kg), administration route: intravenous injection	The prepared BP@PDA-Ce6&TPP induced very low toxicity towards Hela cells before laser illuminations. While after laser illumination, it could kill all cancer cells, confirmed by *in vitro* and *in vivo* results.	[1.84b]
	BP	Thickness: BP-1 (91.9 ± 32.0 nm), BP-2 (27.0 ± 12.0 nm), BP-3 (17.4 ± 9.1 nm) Lateral size: BP-1 (884.0 ± 102.2 nm), BP-2 (425.5 ± 78.8 nm), BP-3 (208.5 ± 46.9 nm)	NIH 3T3, HCoEpiC, and 293T	Up to 48 hr	0–200 µg/mL		BP-1 with the largest lateral size and thickness induced more cytotoxicity towards studied cell lines. In addition, the sensitivity of cell lines towards BP are as follows 293T > NIH 3T3 > HCoEpiC.	[2.75a]
	BP	-	A549	Up to 24 hr	Up to 400 µg/mL	-	The cytotoxicity of BP is dose-dependent as cell viability reduced to 48% (WST-8) and 34% (MTT) at 50 µg/mL BP concentration	[3.31]
	BP	Thickness: 5.7–12.5 nm, hydrodynamic size: 916 ± 185 nm zeta potential:-20 ± 4 mV	NIH3T3, nHDF, and HT1080	Up to 48 hr	Up to 125 µg/mL	-	The viability of all studied fibroblast cells that were incubated with BP nanosheets decreased upon increasing the dosage and exposure time, The sensitivity of studied fibroblast cells was in the order HT1080>nHDF>NIH3T3.	[3.32]
	Ti₃C₂	Single or few-layer flakes	-	-	-	Model: the zebrafish model	It was suggested that Ti₃C₂Tx is safe and does not pose a serious threat to the zebrafish embryos or other aquatic fauna.	[3.34]
	Ti₃C₂	Thickness:6 nm	MCF-7, MCF-10,	Up to 24 hr	Up to 125 mg/mL	x	The surface modification of MXene with collagen can reduce the toxicity of MXene.	[3.19]

104

			HaCaT, and A375				
	Ti$_3$C$_2$-SP	the average lateral size of around 150 nm	4T1 and U87	Up to 48 h	Up to 400 µg/mL	Model: Kunming mice, Dosage: 5, 10, and 20 mg/kg administration route: intravenous injections of Ti$_3$C$_2$-SP time: 30 day	(1) Ti$_3$C$_2$-SP demonstrated negligible cytotoxicity towards breast 4T1 cancer cells and glioma U87 cancer cells. (2) Confocal laser scanning microscopy (CLSM) images have proved that the Ti$_3$C$_2$-SP nanosheets could successfully internalize into the cancer cells after 4 hours of incubations. (3) Results obtained from *in vivo* toxicity assays also demonstrated no significant acute and chronic pathological toxicity, suggesting high biocompatibility of Ti$_3$C$_2$-SP MXene	[196]
	Ti$_3$C$_2$	Three samples with various lateral size: 3000 ± 200 nm, 1430 ± 40 nm, 408 ± 3.4 nm	MSU1.1 and HeLa	Up to 48 h	Up to 400 µg/mL	x	(1) Incubation of cells with MAX phase with the sizes <44 µm induced toxicity. 2) Regardless of lateral size and thickness, the Ti3C2Tx nanosheets showed only slight cytotoxic behavior at the highest concentration	[355]
Mxenes	Ta$_4$C$_3$-SP	lateral size:100 nm	4T1	Up to 48 h	0–400 µg/mL	Model: Kunming mice, Dosage: 5, 10, and 20 mg/kg administration route: intravenous injections of Ti$_3$C$_2$-SP time: 30 day	(1) The *in vitro* cytotoxicity assessment shows that exposure of 4T1 cells to Ta$_4$C$_3$-SP has a negligible effect on viability, even at 400 µg mL^{-1}. (2) The results of *in vivo* experiments show that about 1.41% ID g^{-1} of Ta$_4$C$_3$-SP had accumulated into the tumor. (3) The blood circulation half-time of Ta$_4$C$_3$-SP was about 1.59 hr.	[189]
	Ti$_3$C$_2$	Thickness: 10–50 layers	RC-5 and HaCaT, A549 and A375	Up to 24 h	0–500 µg/mL	-	Ti$_3$C$_2$ induced higher toxicity towards cancerous cells compared to normal cell lines.	[335]
	AS-Ti$_3$C$_2$, SO-Ti$_3$C$_2$, and TO-Ti$_3$C$_2$	-	MCF-10A, MCF-7, HaCaT, and A375	Up to 24 h	0–500 µg/mL	-	(1) The prepared TO-Ti$_3$C$_2$ showed the highest toxicity towards cancerous cells compared to normal cell lines. (2) Oxidative post-treatment was proposed as an easy and effective way to tune the toxicity of MXene nanosheets.	[336]
	V$_2$C	Few and single-layered MXenes	HaCaT and A375	Up to 48 h	0–200 µg/mL	-	The oxidation of V$_2$C MXene led to a higher level of toxicity towards cells, which exhibited time and dose-dependent. This is due to the degradation of the toxic vanadium oxides mixture.	[276b]
	Received and ball-milled MOS$_2$	-	-	-	-	Model: embryonated eggs of Gallus gallus domesticus Dosage: 5 × 10^1, 5 × 10^{-1}, and 5 × 10^{-3} mg/mL	(1) Ball-milled MoS$_2$ resulted in the deaths at the concentration of 5 × 10^{-3} mg/mL, whereas at a lower dosage the embryos kept the embryonic development. (2) In terms of size, treated embryos	[356]

105

Category	Material	Size/Thickness	Cell line	Time	Dosage	In vivo model	Results	Ref
TMDs						Time: At different times of embryonic development up to the 19th day after incubation	with MoS_2 is smaller than untreated embryos of the same embryonic moment.	
	TiS_2-PEG	Lateral size:100 nm	4T1	Up to 24 h	Up to 0.1 mg/mL	Model: Balb/c mice bearing 4T1 tumors, Administration: intravenous injection, Dosage: 20 mg kg^{-1}, Time: up to 60 days	(1)TiS_2-PEG have shown insignificant toxicity towards 4T1 cells even at 0.1 mg.mL^{-1} dosage, signifying the good biocompatibility of TiS_2-PEG. (2) In vivo toxicity assessment also have confirmed the biocompatibility of TiS_2-PEG as no sign of toxic effect was observed within two months.	[157]
	MoS_2	Average thickness: MoS_2 (8.2 nm), graphene (five layers) average lateral size: MoS_2 (150 nm), graphene (312 nm)	M1 and M2 macrophages	Up to 24 h	Up to 50 µg/mL	-	(1) The in vitro cytotoxicity evaluation of MoS_2 and few-layered graphene shows an insignificant decrease in viability in M1 and M2 macrophages. (2) Both 2D NMs were internalized by M1 and M2 macrophages. (3) The secretion of inflammatory cytokines in M1 macrophages was increased once exposed to MoS_2 or graphene. (4) Cell activity changed in different ways when exposed to MoS_2 and few-layered graphene.	[158]
hBN	hBN	Lateral size: of 30-60 nm, Thickness: 1.6 nm	HEK-293T and CHO	Up to 24 hr	Up to 100 µg/mL	Model: KM male mice, dosage: BSA (100 µg) or BSA@BN (containing 100 µg BSA)	hBN nanoplates showed no toxicity in the range of studied dosage and time exposure towards HEK-293 and CHO.	[144]
	hBN	-	Hela, HEK-293, and MCF-7	Up to 48 h	Up to 2 mg/mL	-	cell viability declined upon increasing time exposure and dosage of hBN.	[141b]
MOF	Cu-TCPP(Fe)	Thickness: less than 10 nm	BEAS-2B, A549	Up to 48 h	Up to 100 µg/mL	-	A549 cells showed a significant inhibitory effect when incubated with 100 µg/mL of Cu-TCPP(Fe) after 48 h, while the negligible inhibitory effect was reported toward BEAS-2B cells.	[146]
	Zn-TCPP@PEG	Thickness: 2 nm	4T1, CT26, and MCF-7	-	Up to 20 µg/mL	Model: Mice bearing 4T1 tumors, administration: intravenous injection, dosage Zn-TCPP@PEG/DOX ([TCPP]: 2.4 mg/mL, [Zn2+]: 2.05 mg/mL, [DOX]: 0.5 mg/mL, 200 µL), time: 12 days	(1) No obvious toxicity toward any of the studied cell lines were reported up to 20 µg/mL. (2) In vivo studies also proved the biocompatibility of the synthesized 2D Zn-TCPP@PEG MOF.	[147]

106

7. Unsolved bottlenecks

Like 3D bioprinting technology, the exploration of 2D NMs is still at the preliminary stage. Therefore, there are some challenges once integrating 2D NMs and 3D bioprinting that needs carful considerations, as follows:

- **Preparation methods:** Effective therapeutic performance of 2D NMs lies in their intrinsic physicochemical properties such as size, shape, thickness. However, controlling these physicochemical factors proved to be challenging with current synthesis methods. Thus, developing a robust and effective method to produce 2D NMs with desired physicochemical properties remains a challenge to the biomedical field.

- **Surface functionalization:** Surface functionalization of 2D NMs appeared as an effective strategy to adjust their biocompatibility, biodistribution, and toxicity, especially for intrinsic hydrophobic 2D NMs. However, surface functionalization generally involves multiple and rigid steps that add to the complexity of the system. Therefore, there is still an urgent need to establish easy and effective functionalization methods for 2D NMs case-by-case to fully realize the remarkable properties of 2D NMs in the biomedical field.

- **Toxicity:** Although the exploration of 2D NMs is still in infancy, 2D NMs have demonstrated high clinical translation potential. However, unfortunately, a lack of knowledge on the cytotoxicity of 2D NMs has resulted in impeding their clinical development, which necessitates further researches on their cytotoxicity. There is some suggestion towards biocompatibility evaluations of 2D NMs: (i) evaluation of 2D NMs toxicity has been mainly limited to the potential short-term toxicity, while fate and long-term toxicity of 2D NMs in

107

the body have been largely overlooked. Thus, it is necessary to devote more focus to the fate and long-term toxicity of 2D NMs before any clinical translation. (ii) *In vitro* cytotoxicity of 2D NMs usually has been conducted on cell cultures grown in the form of a monolayer. However, this model cannot replicate the biological environment precisely, therefore the next frontier that must be crossed is the use of advanced 3D biological models such as spheroids or organoids. (iii) Considering the difficulty in controlling the physicochemical properties of 2D NMs with current synthesis methods, evaluation of the cytotoxicity of 2D NMs is faced with contradictive results. Therefore, it is required to fully characterize the 2D NMs once examining their biocompatibility. It is suggested to prepare a library of 2D NM of interest with varying physicochemical properties to isolate the role of specific physicochemical properties (e.g., lateral size, thickness, surface functionalization) on the biological process (e.g., protein adsorption, cellular uptake mechanism, intracellular localization, and fate).

- **The mechanism behind the extraordinary features of 2D NMs:** There are various reports that some 2D NMs can regulate cellular functions such as proliferation, differentiation, and adhesion. These 2D NMs do not share any similarity except their common 2D structures, indicating the key role of NM's shape on their interaction with cellular components. Although some studies have attempted to elucidate the mechanism behind the effect of 2D NMs on signaling pathways, many questions remain largely unanswered.

8. Conclusions and emerging future trends

Since two decades ago, 3D bioprinting has experienced rapid advances in the fabrication of functional biological structures in three dimensions. In parallel, the biomedical applications of 2D NMs have witnessed enormous expansion with remarkable outcomes in a variety of

108

biomedical areas. High controllability of the 3D bioprinting technologies and unprecedented properties of 2D NMs have led to the converging of 3D bioprinting and 2D NMs fields. This conversion has resulted in a valuable shift towards advanced nanocomposite bioinks. In a nutshell, this review highlights the recent progress in the emergence of 2D NMs in 3D bioprinting technology, with a special focus on the main identified contributions of these 2D NMs. By taking advantage of the extraordinary features of 2D NMs, conventional inks can be equipped with added functionality. Back to the theme of the review, the main contributions of 2D NMs in the design of bioink were grouped into six classes: 1) reinforcement effect, 2) delivery of bioactive molecules, 3) improved the electrical conductivity, 4) enhanced tissue formation, 5) photothermal effect, 6) and stronger antibacterial properties. It is indisputable that 2D NMs bring significant benefits to the advanced bioinks, however, we cannot deny that a variety of unresolved challenges remain in the full exploitation of 2D NMs in 3D bioprinting. Therefore, extensive research is still needed to exploit more features of 2D NMs and address these challenges in the future

No doubt, there are high demands to devote extensive interdisciplinary researches among biology, chemistry, physics, and engineering to accelerate the current exciting paradigm of 2D nanocomposite inks. It is expected that the exploitation of 2D NMs in the design of bioinks become one of the main successful trends. Here are a few main streams that are expected to be explored more in the future:

- **Adding new functionality to the ink:** Taking advantage of extraordinary features of 2D NMs to add new functionality to the conventional bioink is the current trend in the developments of 2D nanocomposite bioinks.

109

- **Composite of NMs:** Obtaining synergistic properties resulting from the combining of different NMs is another emerging trend, which is expected to grow in the future. Such synergistic properties hold great promise for enhancing the efficacy of printed functional constructs, necessitating more efforts to combine different NMs.

- **The emergence of other 2D NMs in the bioink formulation:** Since 2D NMs are at the infancy stage, only a few types of 2D NMs have been exploited in 3D bioprinting. Current researches on the 2D nanocomposite bioinks have been firmly focused on graphene and laponite NMs. However, as the family of 2D NMs is expanding, it is expected new types of 2D NMs will be exploited in the design of bioinks.

- **Enhanced biological stability of hydrophobic 2D NMs to be used in bioink formulation:** Recent 2D NMs of interest such as BP, hBN, TMDs exhibit hydrophobic behavior, appearing as a major challenge in their biomedical applications. In these cases, a surface functionalization is paramount for their biomedical application, allowing control over their biological stability of those hydrophobic 2D NMs. Therefore, it is expected that functionalized 2D NMs will draw more attention in the design of bioink formulations.

110

Abbreviations

Two-dimensional nanomaterial	2D NMs
akermanite	AKT
Atomic force microscopy	AFM
bioglass	BG
black phosphorus	BP
bovine serum albumin	BSA
calcium phosphate	CAP
chlorin e6	Ce6
Clathrin-mediated endocytosis	CME
dichloromethane	DCM
drop-on-demand	DOD
extracellular matrix	ECM
fetal bovine serum	FBS
Gelatin methacryloyl	GelMA
Graphene oxide	GO
half maximal inhibitory concentration	IC_{50}
hexagonal boron nitride	hBN
High-resolution transmission electron microscopy	HRTEM
hydrofluoric acid	HF

111

interpenetrating networks	IPNs
kappa-carrageenan	κCA
Laser-induced forward transfer	LIFT
lipoic acid	LA
Magnetic Resonance Imaging	MRI
Metal-organic framework	MOF
methylcellulose	MC
Methyllithium	Me-Li
Molybdenum disulfide	MoS_2
N-acryloyl glycinamide	NAGA
nanoengineered ionic-covalent entanglement	NICE
n-butyllithium	n-Bu-Li
near-infrared	NIR
photodynamic therapy	PDT
Photothermal therapy	PTT
Poly(ethylene glycol) diacrylate	PEGDA
poly(ethylene glycol)-dithiothreitol	PEGDTT
poly(ε-caprolactone)	PCL
poly(lactic-co-glycolic acid)	PLGA
Poly(trimethylene Carbonate)	PTMC
polydopamine	PDA
Polyethylene glycol	PEG

112

Polyethyleneimine	PEI
Polylactic acid	PLA
Polyvinyl alcohol	PVA
reactive oxygen species	ROS
reduced graphene oxide	rGO
silver	Ag
soybean phospholipid	SP
Strontium-containing hydroxyapatite	SrHA
tert-butyllithium	t-Bu-Li
tetrakis(4-carboxyphenyl) porphyrin	TCPP
Titanium disulfide	TiS_2
transition metal dichalcogenides	TMDs
triphenyl phosphonium	TPP
Tungsten disulfide	WS_2
ultraviolet	UV
vascular endothelial growth factor	VEGF
Zirconium disulfide	ZrS_2
β-tricalcium phosphate	β-TCP

113

References

[1] a) X. Wang, L. Cheng, *Nanoscale* **2019**, 11, 15685; b) B. Liu, K. Zhou, *Progress in Materials Science* **2019**, 100, 99; c) L. Cheng, X. Wang, F. Gong, T. Liu, Z. Liu, *Advanced Materials* **2020**, 32, 1902333.

[2] W. Wen, Y. Song, X. Yan, C. Zhu, D. Du, S. Wang, A. M. Asiri, Y. Lin, *Materials Today* **2018**, 21, 164.

[3] K. S. Novoselov, A. K. Geim, S. V. Morozov, D. Jiang, Y. Zhang, S. V. Dubonos, I. V. Grigorieva, A. A. Firsov, *science* **2004**, 306, 666.

[4] K. S. Novoselov, V. Fal, L. Colombo, P. Gellert, M. Schwab, K. Kim, *nature* **2012**, 490, 192.

[5] T. Hu, X. Mei, Y. Wang, X. Weng, R. Liang, M. Wei, *Science Bulletin* **2019**, 64, 1707.

[6] S. Kumar, K. Chatterjee, *ACS applied materials & interfaces* **2016**, 8, 26431.

[7] D. Chimene, D. L. Alge, A. K. Gaharwar, *Advanced Materials* **2015**, 27, 7261.

[8] a) M. Luo, T. Fan, Y. Zhou, H. Zhang, L. Mei, *Advanced Functional Materials* **2019**, 29, 1808306; b) S. Anju, J. Ashtami, P. Mohanan, *Materials Science and Engineering: C* **2019**, 97, 978.

[9] a) K. Huang, Z. Li, J. Lin, G. Han, P. Huang, *Chemical Society Reviews* **2018**, 47, 5109; b) H. Lin, Y. Chen, J. Shi, *Advanced Science* **2018**, 5, 1800518; c) A. Szuplewska, D. Kulpińska, A. Dybko, M. Chudy, A. M. Jastrzębska, A. Olszyna, Z. Brzózka, *Trends in biotechnology* **2020**, 38, 264.

[10] a) X. Li, J. Shan, W. Zhang, S. Su, L. Yuwen, L. Wang, *Small* **2017**, 13, 1602660; b) S. Zhu, L. Gong, J. Xie, Z. Gu, Y. Zhao, *Small Methods* **2017**, 1, 1700220.

[11] S. M. Sharker, *International Journal of Nanomedicine* **2019**, 14, 9983.

[12] a) C. Tamames-Tabar, D. Cunha, E. Imbuluzqueta, F. Ragon, C. Serre, M. J. Blanco-Prieto, P. Horcajada, *Journal of Materials Chemistry B* **2014**, 2, 262; b) S. Arun Kumar, B. Balasubramaniam, S. Bhunia, M. K. Jaiswal, K. Verma, Prateek, A. Khademhosseini, R. K. Gupta, A. K. Gaharwar, *WIREs Nanomedicine and Nanobiotechnology* n/a, e1674.

[13] a) B. L. Li, R. Li, H. L. Zou, K. Ariga, N. B. Li, D. T. Leong, *Materials Horizons* **2020**, 7, 455; b) F. Yin, B. Gu, Y. Lin, N. Panwar, S. C. Tjin, J. Qu, S. P. Lau, K.-T. Yong, *Coordination Chemistry Reviews* **2017**, 347, 77.

[14] a) C. Zhu, D. Du, Y. Lin, *Biosensors and Bioelectronics* **2017**, 89, 43; b) V. Yadav, S. Roy, P. Singh, Z. Khan, A. Jaiswal, *Small* **2019**, 15, 1803706.

[15] a) Y. Chen, L. Wang, J. Shi, *Nano Today* **2016**, 11, 292; b) M. Li, Z. Luo, Y. Zhao, *Science China Chemistry* **2018**, 61, 1214.

[16] a) J. Zhang, H. Chen, M. Zhao, G. Liu, J. Wu, *Nano Research* **2020**, 1; b) A. K. Gaharwar, N. A. Peppas, A. Khademhosseini, *Biotechnology and bioengineering* **2014**, 111, 441.

[17] a) M. L. Bedell, A. M. Navara, Y. Du, S. Zhang, A. G. Mikos, *Chemical Reviews* **2020**; b) H. Cui, M. Nowicki, J. P. Fisher, L. G. Zhang, *Advanced healthcare materials* **2017**, 6, 1601118.

[18] A. Su, S. J. Al'Aref, in *3D Printing Applications in Cardiovascular Medicine*, DOI: https://doi.org/10.1016/B978-0-12-803917-5.00001-8 (Eds: S. J. Al'Aref, B. Mosadegh, S. Dunham, J. K. Min), Academic Press, Boston **2018**, p. 1.

[19] a) M. Hospodiuk, M. Dey, D. Sosnoski, I. T. Ozbolat, *Biotechnology Advances* **2017**, 35, 217; b) Y. Sun, Y. You, W. Jiang, Q. Wu, B. Wang, K. Dai, *Applied Materials Today* **2020**, 18, 100469.

[20] a) F. Pati, J. Gantelius, H. A. Svahn, *Angewandte Chemie International Edition* **2016**, 55, 4650; b) A. Arslan-Yildiz, R. El Assal, P. Chen, S. Guven, F. Inci, U. Demirci, *Biofabrication* **2016**, 8, 014103.

[21] W. Peng, P. Datta, B. Ayan, V. Ozbolat, D. Sosnoski, I. T. Ozbolat, *Acta biomaterialia* **2017**, 57, 26.

[22] a) Y. Wang, W. Shi, M. Kuss, S. Mirza, D. Qi, A. Krasnoslobodtsev, J. Zeng, H. Band, V. Band, B. Duan, *ACS Biomaterials Science & Engineering* **2018**, 4, 4401; b) P. Datta, M. Dey, Z. Ataie, D. Unutmaz, I. T. Ozbolat, *NPJ Precision Oncology* **2020**, 4, 1.

[23] J. Li, C. Wu, P. K. Chu, M. Gelinsky, *Materials Science and Engineering: R: Reports* **2020**, 140, 100543.

[24] a) N. Di Marzio, D. Eglin, T. Serra, L. Moroni, *Frontiers in Bioengineering and Biotechnology* **2020**, 8; b) B. Chen, H. Xiang, S. Pan, L. Yu, T. Xu, Y. Chen, *Advanced Functional Materials* **2020**, 30, 2002621; c) G. Bouguéon, T. Kauss, B. Dessane, P. Barthélémy, S. Crauste-Manciet, *Drug discovery today* **2019**, 24, 163.

[25] X. Mei, T. Hu, Y. Wang, X. Weng, R. Liang, M. Wei, *Wiley Interdisciplinary Reviews: Nanomedicine and Nanobiotechnology* **2020**, 12, e1596.

[26] a) S. Hales, E. Tokita, R. Neupane, U. Ghosh, B. Elder, D. Wirthlin, Y. L. Kong, *Nanotechnology* **2020**, 31, 172001; b) R. Yang, J. Zhou, C. Yang, L. Qiu, H. Cheng, *Advanced Materials Technologies* **2020**, 5, 1901066; c) G. Hu, J. Kang, L. W. Ng, X. Zhu, R. C. Howe, C. G. Jones, M. C. Hersam, T. Hasan, *Chemical Society Reviews* **2018**, 47, 3265.

114

[27]   a) H. Zhao, X. Chen, G. Wang, Y. Qiu, L. Guo, *2D Materials* **2019**, 6, 032002; b) M. Zeng, Y. Zhang, *Journal of Materials Chemistry A* **2019**, 7, 23301; c) F. Yang, P. Song, M. Ruan, W. Xu, *FlatChem* **2019**, 18, 100133.

[28]   J. Groll, J. A. Burdick, D. W. Cho, B. Derby, M. Gelinsky, S. C. Heilshorn, T. Jüngst, J. Malda, V. A. Mironov, K. Nakayama, A. Ovsianikov, W. Sun, S. Takeuchi, J. J. Yoo, T. B. F. Woodfield, *Biofabrication* **2018**, 11, 013001.

[29]   K. Dubbin, Y. Hori, K. K. Lewis, S. C. Heilshorn, *Advanced Healthcare Materials* **2016**, 5, 2488.

[30]   D. Liu, W. Nie, D. Li, W. Wang, L. Zheng, J. Zhang, J. Zhang, C. Peng, X. Mo, C. He, *Chemical Engineering Journal* **2019**, 362, 269.

[31]   a) T. H. Jovic, G. Kungwengwe, A. C. Mills, I. S. Whitaker, *Frontiers in Mechanical Engineering* **2019**, 5; b) P. S. Gungor-Ozkerim, I. Inci, Y. S. Zhang, A. Khademhosseini, M. R. Dokmeci, *Biomaterials Science* **2018**, 6, 915.

[32]   Y.-J. Seol, H.-W. Kang, S. J. Lee, A. Atala, J. J. Yoo, *European Journal of Cardio-Thoracic Surgery* **2014**, 46, 342.

[33]   R. Lozano, L. Stevens, B. C. Thompson, K. J. Gilmore, R. Gorkin III, E. M. Stewart, M. in het Panhuis, M. Romero-Ortega, G. G. Wallace, *Biomaterials* **2015**, 67, 264.

[34]   a) A. M. Compaan, K. Christensen, Y. Huang, *ACS Biomaterials Science & Engineering* **2017**, 3, 1519; b) L. H. Solis, Y. Ayala, S. Portillo, A. Varela-Ramirez, R. Aguilera, T. Boland, *Biofabrication* **2019**, 11, 045005; c) C. Xu, W. Chai, Y. Huang, R. R. Markwald, *Biotechnology and Bioengineering* **2012**, 109, 3152.

[35]   a) K. Zhu, N. Chen, X. Liu, X. Mu, W. Zhang, C. Wang, Y. S. Zhang, *Macromolecular Bioscience* **2018**, 18, 1800127; b) W. Liu, Z. Zhong, N. Hu, Y. Zhou, L. Maggio, A. K. Miri, A. Fragasso, X. Jin, A. Khademhosseini, Y. S. Zhang, *Biofabrication* **2018**, 10, 024102; c) K. Markstedt, A. Mantas, I. Tournier, H. Martínez Ávila, D. Hägg, P. Gatenholm, *Biomacromolecules* **2015**, 16, 1489; d) J. Yin, M. Yan, Y. Wang, J. Fu, H. Suo, *ACS applied materials & interfaces* **2018**, 10, 6849.

[36]   a) J. A. Barron, P. Wu, H. D. Ladouceur, B. R. Ringeisen, *Biomedical Microdevices* **2004**, 6, 139; b) B. Guillotin, A. Souquet, S. Catros, M. Duocastella, B. Pippenger, S. Bellance, R. Bareille, M. Rémy, L. Bordenave, J. Amédée, *Biomaterials* **2010**, 31, 7250; c) V. Keriquel, H. Oliveira, M. Rémy, S. Ziane, S. Delmond, B. Rousseau, S. Rey, S. Catros, J. Amédée, F. Guillemot, *Scientific reports* **2017**, 7, 1.

[37]   a) Z. Wang, R. Abdulla, B. Parker, R. Samanipour, S. Ghosh, K. Kim, *Biofabrication* **2015**, 7, 045009; b) Z. Wang, H. Kumar, Z. Tian, X. Jin, J. F. Holzman, F. Menard, K. Kim, *ACS applied materials & interfaces* **2018**, 10, 26859; c) R. Raman, R. Bashir, in *Essentials of 3D Biofabrication and Translation*, Elsevier **2015**, p. 89.

[38]   J. Malda, J. Visser, F. P. Melchels, T. Jüngst, W. E. Hennink, W. J. Dhert, J. Groll, D. W. Hutmacher, *Advanced materials* **2013**, 25, 5011.

[39]   K. Hölzl, S. Lin, L. Tytgat, S. Van Vlierberghe, L. Gu, A. Ovsianikov, *Biofabrication* **2016**, 8, 032002.

[40]   W. Peng, D. Unutmaz, I. T. Ozbolat, *Trends in biotechnology* **2016**, 34, 722.

[41]   I. T. Ozbolat, M. Hospodiuk, *Biomaterials* **2016**, 76, 321.

[42]   a) C. C. Chang, E. D. Boland, S. K. Williams, J. B. Hoying, *Journal of Biomedical Materials Research Part B: Applied Biomaterials* **2011**, 98B, 160; b) K. Nair, M. Gandhi, S. Khalil, K. C. Yan, M. Marcolongo, K. Barbee, W. Sun, *Biotechnology Journal* **2009**, 4, 1168; c) F. P. Melchels, W. J. Dhert, D. W. Hutmacher, J. Malda, *Journal of Materials Chemistry B* **2014**, 2, 2282.

[43]   D. Chimene, K. K. Lennox, R. R. Kaunas, A. K. Gaharwar, *Annals of biomedical engineering* **2016**, 44, 2090.

[44]   a) P. T. Smith, A. Basu, A. Saha, A. Nelson, *Polymer* **2018**; b) N. Paxton, W. Smolan, T. Böck, F. Melchels, J. Groll, T. Jungst, *Biofabrication* **2017**, 9, 044107.

[45]   L. Ouyang, C. B. Highley, C. B. Rodell, W. Sun, J. A. Burdick, *ACS Biomaterials Science & Engineering* **2016**, 2, 1743.

[46]   a) S. A. Wilson, L. M. Cross, C. W. Peak, A. K. Gaharwar, *ACS applied materials & interfaces* **2017**, 9, 43449; b) D. Chimene, L. Miller, L. M. Cross, M. K. Jaiswal, I. Singh, A. K. Gaharwar, *ACS Applied Materials & Interfaces* **2020**, 12, 15976.

[47]   a) I. T. Ozbolat, H. Chen, Y. Yu, *Robotics and Computer-Integrated Manufacturing* **2014**, 30, 295; b) R. Attalla, E. Puersten, N. Jain, P. R. Selvaganapathy, *Biofabrication* **2018**, 11, 015012; c) L. Ruiz-Cantu, A. Gleadall, C. Faris, J. Segal, K. Shakesheff, J. Yang, *Materials Science and Engineering: C* **2020**, 109, 110578.

[48]   I. T. Ozbolat, H. Chen, Y. Yu, *Robotics and Computer-Integrated Manufacturing* **2014**, 30, 295.

[49]   W. Liu, Y. S. Zhang, M. A. Heinrich, F. De Ferrari, H. L. Jang, S. M. Bakht, M. M. Alvarez, J. Yang, Y. C. Li, G. Trujillo-de Santiago, *Advanced Materials* **2017**, 29, 1604630.

115

[50] *Tissue Engineering Part A* **2008**, 14, 41.

[51] J. Li, M. Chen, X. Fan, H. Zhou, *J Transl Med* **2016**, 14, 271.

[52] I. N. Aguilar, L. J. Smith, D. J. Olivos, T.-M. G. Chu, M. A. Kacena, D. R. Wagner, *Bioprinting* **2019**, 15, e00048.

[53] a) M. Nakamura, A. Kobayashi, F. Takagi, A. Watanabe, Y. Hiruma, K. Ohuchi, Y. Iwasaki, M. Horie, I. Morita, S. Takatani, *Tissue engineering* **2005**, 11, 1658; b) T. Boland, T. Xu, B. Damon, X. Cui, *Biotechnology Journal: Healthcare Nutrition Technology* **2006**, 1, 910.

[54] T. Xu, W. Zhao, J.-M. Zhu, M. Z. Albanna, J. J. Yoo, A. Atala, *Biomaterials* **2013**, 34, 130.

[55] R. Zimmermann, C. Hentschel, F. Schrön, D. Moedder, T. Büttner, P. Atallah, T. Wegener, T. Gehring, S. Howitz, U. Freudenberg, C. Werner, *Biofabrication* **2019**, 11, 045008.

[56] H. Gudapati, M. Dey, I. Ozbolat, *Biomaterials* **2016**, 102, 20.

[57] a) M. S. Onses, E. Sutanto, P. M. Ferreira, A. G. Alleyne, J. A. Rogers, *Small* **2015**, 11, 4237; b) S. N. Jayasinghe, A. N. Qureshi, P. A. Eagles, *Small* **2006**, 2, 216.

[58] a) Z. Zheng, D. Eglin, M. Alini, G. R. Richards, L. Qin, Y. Lai, *Engineering* **2020**, DOI: https://doi.org/10.1016/j.eng.2020.05.021; b) B. K. Gu, D. J. Choi, S. J. Park, M. S. Kim, C. M. Kang, C.-H. Kim, *Biomaterials research* **2016**, 20, 12; c) N. E. Sanjana, S. B. Fuller, *Journal of neuroscience methods* **2004**, 136, 151.

[59] a) L. Gasperini, D. Maniglio, A. Motta, C. Migliaresi, *Tissue engineering part C: Methods* **2015**, 21, 123; b) C. Xu, W. Chai, Y. Huang, R. R. Markwald, *Biotechnology and bioengineering* **2012**, 109, 3152.

[60] A. Blaeser, D. F. Duarte Campos, M. Weber, S. Neuss, B. Theek, H. Fischer, W. Jahnen-Dechent, *BioResearch open access* **2013**, 2, 374.

[61] a) *Tissue Engineering Part A* **2012**, 18, 1304; b) U. A. Gurkan, R. El Assal, S. E. Yildiz, Y. Sung, A. J. Trachtenberg, W. P. Kuo, U. Demirci, *Molecular Pharmaceutics* **2014**, 11, 2151.

[62] Y.-B. Lee, S. Polio, W. Lee, G. Dai, L. Menon, R. S. Carroll, S.-S. Yoo, *Experimental neurology* **2010**, 223, 645.

[63] A. GhavamiNejad, N. Ashammakhi, X. Y. Wu, A. Khademhosseini, *Small* **2020**, 16, 2002931.

[64] G. Gao, T. Yonezawa, K. Hubbell, G. Dai, X. Cui, *Biotechnology Journal* **2015**, 10, 1568.

[65] a) C. J. Ferris, K. J. Gilmore, S. Beirne, D. McCallum, G. G. Wallace, M. in het Panhuis, *Biomaterials Science* **2013**, 1, 224; b) M. E. Pepper, V. Seshadri, T. C. Burg, K. J. L. Burg, R. E. Groff, *Biofabrication* **2012**, 4, 011001.

[66] X. Li, B. Liu, B. Pei, J. Chen, D. Zhou, J. Peng, X. Zhang, W. Jia, T. Xu, *Chemical Reviews* **2020**, 120, 10793.

[67] T. Xu, C. A. Gregory, P. Molnar, X. Cui, S. Jalota, S. B. Bhaduri, T. Boland, *Biomaterials* **2006**, 27, 3580.

[68] a) D. J. Odde, M. J. Renn, *Trends in biotechnology* **1999**, 17, 385; b) J. A. Barron, B. R. Ringeisen, H. Kim, B. J. Spargo, D. B. Chrisey, *Thin Solid Films* **2004**, 453, 383.

[69] a) C. Mandrycky, Z. Wang, K. Kim, D.-H. Kim, *Biotechnology Advances* **2016**, 34, 422; b) F. Guillemot, A. Souquet, S. Catros, B. Guillotin, M. Lopez, M. Faucon, B. Pippenger, R. Bareille, M. Rémy, S. Bellance, P. Chabassier, J. C. Fricain, J. Amédée, *Acta Biomaterialia* **2010**, 6, 2494.

[70] S. Michael, H. Sorg, C.-T. Peck, L. Koch, A. Deiwick, B. Chichkov, P. M. Vogt, K. Reimers, *PloS one* **2013**, 8, e57741.

[71] S. Catros, B. Guillotin, M. Bačáková, J.-C. Fricain, F. Guillemot, *Applied Surface Science* **2011**, 257, 5142.

[72] F. Guillemot, A. Souquet, S. Catros, B. Guillotin, *Nanomedicine* **2010**, 5, 507.

[73] a) D. Hakobyan, C. Médina, N. Dusserre, M.-L. Stachowicz, C. Handschin, J.-C. Fricain, J. Guillermet-Guibert, H. Oliveira, *Biofabrication* **2020**, 12, 035001; b) M. Ali, E. Pages, A. Ducom, A. Fontaine, F. Guillemot, *Biofabrication* **2014**, 6, 045001.

[74] M. A. Heinrich, W. Liu, A. Jimenez, J. Yang, A. Akpek, X. Liu, Q. Pi, X. Mu, N. Hu, R. M. Schiffelers, *Small* **2019**, 15, 1805510.

[75] N. Poomathi, S. Singh, C. Prakash, V. Patil Rajkumar, P. T. Perumal, A. Barathi Veluchamy, K. Balasubramanian Kalpattu, S. Ramakrishna, N. U. Maheshwari, *Rapid Prototyping Journal* **2019**, 25, 496.

[76] J. T. Huh, J. J. Yoo, A. Atala, S. J. Lee, in *Principles of Tissue Engineering (Fifth Edition)*, DOI: https://doi.org/10.1016/B978-0-12-818422-6.00076-9 (Eds: R. Lanza, R. Langer, J. P. Vacanti, A. Atala), Academic Press **2020**, p. 1391.

[77] a) B. Hopp, T. Smausz, G. Szabó, L. Kolozsvari, A. Nogradi, D. Kafetzopoulos, C. Fotakis, *Optical Engineering* **2012**, 51, 014302; b) H. Gudapati, J. Yan, Y. Huang, D. B. Chrisey, *Biofabrication* **2014**, 6, 035022.

[78] L. Koch, S. Kuhn, H. Sorg, M. Gruene, S. Schlie, R. Gaebel, B. Polchow, K. Reimers, S. Stoelting, N. Ma, *Tissue Engineering Part C: Methods* **2010**, 16, 847.

116

[79]   a) Z. Yue, X. Liu, P. T. Coates, G. G. Wallace, *Current opinion in organ transplantation* **2016**, 21, 467; b) R. Raman, R. Bashir, in *Essentials of 3D Biofabrication and Translation*, DOI: https://doi.org/10.1016/B978-0-12-800972-7.00006-2 (Eds: A. Atala, J. J. Yoo), Academic Press, Boston **2015**, p. 89.

[80]   a) S. Zakeri, M. Vippola, E. Levänen, *Additive Manufacturing* **2020**, 35, 101177; b) F. P. Melchels, K. Bertoldi, R. Gabbrielli, A. H. Velders, J. Feijen, D. W. Grijpma, *Biomaterials* **2010**, 31, 6909.

[81]   a) J.-W. Choi, R. Wicker, S.-H. Lee, K.-H. Choi, C.-S. Ha, I. Chung, *Journal of Materials Processing Technology* **2009**, 209, 5494; b) T. Chartier, A. Badev, Y. Abouliatim, P. Lebaudy, L. Lecamp, *Journal of the European Ceramic Society* **2012**, 32, 1625.

[82]   F. P. W. Melchels, J. Feijen, D. W. Grijpma, *Biomaterials* **2010**, 31, 6121.

[83]   R. P. Sinha, D.-P. Häder, *Photochemical & Photobiological Sciences* **2002**, 1, 225.

[84]   a) A. K. Au, W. Lee, A. Folch, *Lab on a Chip* **2014**, 14, 1294; b) R. Zhang, N. B. Larsen, *Lab on a Chip* **2017**, 17, 4273.

[85]   a) S. Knowlton, B. Yenilmez, S. Tasoglu, *Trends in Biotechnology* **2016**, 34, 685; b) A. P. Kuo, N. Bhattacharjee, Y. S. Lee, K. Castro, Y. T. Kim, A. Folch, *Advanced materials technologies* **2019**, 4, 1800395.

[86]   a) R. Kurapati, K. Kostarelos, M. Prato, A. Bianco, *Adv. Mater.* **2016**, 28, 6052; b) H. Zhang, H.-M. Cheng, P. Ye, *Chemical Society Reviews* **2018**, 47, 6009.

[87]   H. Zhang, *ACS Nano* **2015**, 9, 9451.

[88]   C. Murugan, V. Sharma, R. K. Murugan, G. Malaimegu, A. Sundaramurthy, *Journal of Controlled Release* **2019**, 299, 1.

[89]   a) B. Mendoza-Sánchez, Y. Gogotsi, *Advanced Materials* **2016**, 28, 6104; b) A. Jayakumar, A. Surendranath, M. Pv, *International Journal of Pharmaceutics* **2018**, 551, 309; c) P. Karfa, K. Chandra Majhi, R. Madhuri, in *Two-Dimensional Nanostructures for Biomedical Technology*, DOI: https://doi.org/10.1016/B978-0-12-817650-4.00002-4 (Eds: R. Khan, S. Barua), Elsevier **2020**, p. 35.

[90]   a) M. Yi, Z. Shen, *Journal of Materials Chemistry A* **2015**, 3, 11700; b) H. Li, G. Lu, Y. Wang, Z. Yin, C. Cong, Q. He, L. Wang, F. Ding, T. Yu, H. Zhang, *Small* **2013**, 9, 1974; c) K. J. Koski, Y. Cui, *ACS Nano* **2013**, 7, 3739.

[91]   J. Wang, G. Li, L. Li, *Two-Dimensional Materials—Synthesis, Characterization and Potential Applications; Nayak, PK, Ed* **2016**, 1.

[92]   T. T. Tung, J. Yoo, F. K. Alotaibi, M. J. Nine, R. Karunagaran, M. Krebsz, G. T. Nguyen, D. N. H. Tran, J.-F. Feller, D. Losic, *ACS Applied Materials & Interfaces* **2016**, 8, 16521.

[93]   L. Z. Zhao, C. H. Zhou, J. Wang, D. S. Tong, W. H. Yu, H. Wang, *Soft Matter* **2015**, 11, 9229.

[94]   a) S. Yang, P. Zhang, A. S. Nia, X. Feng, *Adv. Mater.* **2020**, 32, 1907857; b) Y. Yang, H. Hou, G. Zou, W. Shi, H. Shuai, J. Li, X. Ji, *Nanoscale* **2019**, 11, 16; c) L. Magerusan, F. Pogacean, M. Coros, C. Socaci, S. Pruneanu, C. Leostean, I. O. Pana, *Electrochimica Acta* **2018**, 283, 578; d) M. Coroş, F. Pogăcean, L. Măgeruşan, C. Socaci, S. Pruneanu, *Frontiers of Materials Science* **2019**, 13, 23.

[95]   Z. Zeng, Z. Yin, X. Huang, H. Li, Q. He, G. Lu, F. Boey, H. Zhang, *Angew. Chem. Int. Ed.* **2011**, 50, 11093.

[96]   a) X. Xiao, H. Wang, P. Urbankowski, Y. Gogotsi, *Chem. Soc. Rev.* **2018**, 47, 8744; b) W. Peng, Y. Li, F. Zhang, X. Fan, *Nanoscale* **2020**.

[97]   a) M. Alhabeb, K. Maleski, T. S. Mathis, A. Sarycheva, C. B. Hatter, S. Uzun, A. Levitt, Y. Gogotsi, *Angewandte Chemie* **2018**, 130, 5542; b) J. Mei, G. A. Ayoko, C. Hu, J. M. Bell, Z. Sun, *Sustainable Materials and Technologies* **2020**, 25, e00156.

[98]   M. Naguib, V. N. Mochalin, M. W. Barsoum, Y. Gogotsi, *Advanced materials* **2014**, 26, 992.

[99]   M. Alhabeb, K. Maleski, T. S. Mathis, A. Sarycheva, C. B. Hatter, S. Uzun, A. Levitt, Y. Gogotsi, *Angew. Chem. Int. Ed.* **2018**, 57, 5444.

[100]   a) N. Zhou, R. Yang, T. Zhai, *Materials Today Nano* **2019**, 8, 100051; b) Y. M. Manawi, A. Samara, T. Al-Ansari, M. A. Atieh, *Materials* **2018**, 11, 822; c) X. He, F. Liu, P. Hu, W. Fu, X. Wang, Q. Zeng, W. Zhao, Z. Liu, *Small* **2015**, 11, 5423.

[101]   Z. Huang, X. Cui, S. Li, J. Wei, P. Li, Y. Wang, C.-S. Lee, *Nanophotonics* **2020**, 9, 2233.

[102]   J. Jeon, S. K. Jang, S. M. Jeon, G. Yoo, Y. H. Jang, J.-H. Park, S. Lee, *Nanoscale* **2015**, 7, 1688.

[103]   a) C. Tan, H. Zhang, *Nat. Commun.* **2015**, 6, 7873; b) C. Tan, H. Zhang, *Nature communications* **2015**, 6, 1; c) H. Lin, W. Qiu, J. Liu, L. Yu, S. Gao, H. Yao, Y. Chen, J. Shi, *Advanced Materials* **2019**.

[104]   W. Huang, C. Li, L. Gao, Y. Zhang, Y. Wang, Z. N. Huang, T. Chen, L. Hu, H. Zhang, *J. Mater. Chem. C* **2020**, 8, 1172.

[105]   B. Tian, B. Tian, B. Smith, M. C. Scott, Q. Lei, R. Hua, Y. Tian, Y. Liu, *Proceedings of the National Academy of Sciences* **2018**, 115, 4345.

117

[106]   a) J. M. Lee, W. Y. Yeong, *Advanced healthcare materials* **2016**, 5, 2856; b) J. M. Unagolla, A. C. Jayasuriya, *Applied Materials Today* **2020**, 18, 100479; c) H. Li, C. Tan, L. Li, *Materials & Design* **2018**, 159, 20.

[107]   a) W. Schuurman, P. A. Levett, M. W. Pot, P. R. van Weeren, W. J. Dhert, D. W. Hutmacher, F. P. Melchels, T. J. Klein, J. Malda, *Macromolecular bioscience* **2013**, 13, 551; b) J. M. Townsend, E. C. Beck, S. H. Gehrke, C. J. Berkland, M. S. Detamore, *Progress in Polymer Science* **2019**, 91, 126.

[108]   a) J. H. Chung, S. Naficy, Z. Yue, R. Kapsa, A. Quigley, S. E. Moulton, G. G. Wallace, *Biomaterials Science* **2013**, 1, 763; b) H. Rastin, R. T. Ormsby, G. J. Atkins, D. Losic, *ACS Applied Bio Materials* **2020**, 3, 1815.

[109]   Y. Zhao, Y. Li, S. Mao, W. Sun, R. Yao, *Biofabrication* **2015**, 7, 045002.

[110]   a) D. Chimene, C. W. Peak, J. L. Gentry, J. K. Carrow, L. M. Cross, E. Mondragon, G. B. Cardoso, R. Kaunas, A. K. Gaharwar, *ACS applied materials & interfaces* **2018**, 10, 9957; b) M. Mehrali, A. Thakur, C. P. Pennisi, S. Talebian, A. Arpanaei, M. Nikkhah, A. Dolatshahi-Pirouz, *Advanced Materials* **2017**, 29, 1603612.

[111]   a) S. Heid, A. R. Boccaccini, *Acta Biomaterialia* **2020**, 113, 1; b) G. Turnbull, J. Clarke, F. Picard, P. Riches, L. Jia, F. Han, B. Li, W. Shu, *Bioactive Materials* **2018**, 3, 278.

[112]   a) A. L. Rutz, E. S. Gargus, K. E. Hyland, P. L. Lewis, A. Setty, W. R. Burghardt, R. N. Shah, *Acta Biomaterialia* **2019**, 99, 121; b) J. Jang, T. G. Kim, B. S. Kim, S.-W. Kim, S.-M. Kwon, D.-W. Cho, *Acta Biomaterialia* **2016**, 33, 88.

[113]   a) D. Chimene, R. Kaunas, A. K. Gaharwar, *Advanced Materials* **2020**, 32, 1902026; b) X. Zhou, M. Nowicki, H. Cui, W. Zhu, X. Fang, S. Miao, S.-J. Lee, M. Keidar, L. G. Zhang, *Carbon* **2017**, 116, 615; c) H. Rastin, B. Zhang, A. Mazinani, K. Hassan, J. Bi, T. T. Tung, D. Losic, *Nanoscale* **2020**.

[114]   H. Rastin, B. Zhang, A. Mazinani, K. Hassan, J. Bi, T. T. Tung, D. Losic, *Nanoscale* **2020**, 12, 16069.

[115]   L. Peng, X. Mei, J. He, J. Xu, W. Zhang, R. Liang, M. Wei, D. G. Evans, X. Duan, *Advanced Materials* **2018**, 30, 1707389.

[116]   a) G. Cidonio, M. Glinka, Y.-H. Kim, J. M. Kanczler, S. A. Lanham, T. Ahlfeld, A. Lode, J. I. Dawson, M. Gelinsky, R. O. Oreffo, *Biofabrication* **2020**, 12, 035010; b) C. W. Peak, K. A. Singh, M. a. Adlouni, J. Chen, A. K. Gaharwar, *Advanced Healthcare Materials* **2019**, 8, 1801553.

[117]   a) H. Zhang, T. Fan, W. Chen, Y. Li, B. Wang, *Bioactive materials* **2020**, 5, 1071; b) X. Mei, T. Hu, Y. Wang, X. Weng, R. Liang, M. Wei, *WIREs Nanomedicine and Nanobiotechnology* **2020**, 12, e1596.

[118]   S.-J. Lee, W. Zhu, M. Nowicki, G. Lee, D. N. Heo, J. Kim, Y. Y. Zuo, L. G. Zhang, *Journal of Neural Engineering* **2018**, 15, 016018.

[119]   A. E. Jakus, E. B. Secor, A. L. Rutz, S. W. Jordan, M. C. Hersam, R. N. Shah, *ACS Nano* **2015**, 9, 4636.

[120]   a) L. Ghasemi-Mobarakeh, M. P. Prabhakaran, M. Morshed, M. H. Nasr-Esfahani, H. Baharvand, S. Kiani, S. S. Al-Deyab, S. Ramakrishna, *Journal of Tissue Engineering and Regenerative Medicine* **2011**, 5, e17; b) N. Li, Q. Zhang, S. Gao, Q. Song, R. Huang, L. Wang, L. Liu, J. Dai, M. Tang, G. Cheng, *Scientific Reports* **2013**, 3, 1604; c) B. Guo, P. X. Ma, *Biomacromolecules* **2018**, 19, 1764.

[121]   a) N. Zanjanizadeh Ezazi, M.-A. Shahbazi, Y. V. Shatalin, E. Nadal, E. Mäkilä, J. Salonen, M. Kemell, A. Correia, J. Hirvonen, H. A. Santos, *International Journal of Pharmaceutics* **2018**, 536, 241; b) G. L. Mario Cheong, K. S. Lim, A. Jakubowicz, P. J. Martens, L. A. Poole-Warren, R. A. Green, *Acta Biomaterialia* **2014**, 10, 1216.

[122]   a) K. Cysewska, J. Karczewski, P. Jasiński, *Measurement Science and Technology* **2017**, 28, 074004; b) R. Ravichandran, J. G. Martinez, E. W. H. Jager, J. Phopase, A. P. F. Turner, *ACS Applied Materials & Interfaces* **2018**, 10, 16244.

[123]   E. S. Place, J. H. George, C. K. Williams, M. M. Stevens, *Chemical Society Reviews* **2009**, 38, 1139.

[124]   a) S. Y. Park, J. Park, S. H. Sim, M. G. Sung, K. S. Kim, B. H. Hong, S. Hong, *Advanced Materials* **2011**, 23, H263; b) H. H. Yoon, S. H. Bhang, T. Kim, T. Yu, T. Hyeon, B.-S. Kim, *Advanced Functional Materials* **2014**, 24, 6455; c) R. Huang, X. Chen, Y. Dong, X. Zhang, Y. Wei, Z. Yang, W. Li, Y. Guo, J. Liu, Z. Yang, H. Wang, L. Jin, *ACS Applied Bio Materials* **2020**, 3, 2125; d) K. Huang, J. Wu, Z. Gu, *ACS applied materials & interfaces* **2018**, 11, 2908; e) A. K. Gaharwar, P. J. Schexnailder, B. P. Kline, G. Schmidt, *Acta Biomaterialia* **2011**, 7, 568.

[125]   a) Z. Cheng, B. Landish, Z. Chi, C. Nannan, D. Jingyu, L. Sen, L. Xiangjin, *Materials Science and Engineering: C* **2018**, 82, 244; b) C. Sears, E. Mondragon, Z. I. Richards, N. Sears, D. Chimene, E. P. McNeill, C. A. Gregory, A. K. Gaharwar, R. Kaunas, *Advanced Healthcare Materials* **2020**, 9, 1901580.

[126]   L. S. Elting, C. Cooksley, M. Chambers, S. B. Cantor, E. Manzullo, E. B. Rubenstein, *Cancer* **2003**, 98, 1531.

[127]   J. B. Vines, J.-H. Yoon, N.-E. Ryu, D.-J. Lim, H. Park, *Frontiers in Chemistry* **2019**, 7.

[128]   E. A. Hussein, M. M. Zagho, G. K. Nasrallah, A. A. Elzatahry, *International journal of nanomedicine* **2018**, 13, 2897.

118

[129]   a) S. Liu, X. Pan, H. Liu, *Angewandte Chemie* **2020**, 132, 5943; b) X. Li, J. Zhu, B. Wei, *Chemical Society Reviews* **2016**, 45, 3145; c) B. Peng, P. K. Ang, K. P. Loh, *Nano Today* **2015**, 10, 128.

[130]   a) H. Kim, D. Lee, J. Kim, T.-i. Kim, W. J. Kim, *ACS Nano* **2013**, 7, 6735; b) X. Zeng, M. Luo, G. Liu, X. Wang, W. Tao, Y. Lin, X. Ji, L. Nie, L. Mei, *Advanced Science* **2018**, 5, 1800510.

[131]   a) X. Wang, J. Zhang, J. Li, Y. Chen, Y. Chen, N. Kawazoe, G. Chen, *Journal of Materials Chemistry B* **2018**, 6, 7728; b) H. Ma, C. Jiang, D. Zhai, Y. Luo, Y. Chen, F. Lv, Z. Yi, Y. Deng, J. Wang, J. Chang, C. Wu, *Advanced Functional Materials* **2016**, 26, 1197; c) W. Dang, T. Li, B. Li, H. Ma, D. Zhai, X. Wang, J. Chang, Y. Xiao, J. Wang, C. Wu, *Biomaterials* **2018**, 160, 92.

[132]   H. Ma, J. Luo, Z. Sun, L. Xia, M. Shi, M. Liu, J. Chang, C. Wu, *Biomaterials* **2016**, 111, 138.

[133]   a) L. Zhao, P. K. Chu, Y. Zhang, Z. Wu, *Journal of Biomedical Materials Research Part B: Applied Biomaterials* **2009**, 91, 470; b) S. Li, S. Dong, W. Xu, S. Tu, L. Yan, C. Zhao, J. Ding, X. Chen, *Advanced science* **2018**, 5, 1700527.

[134]   J. Hoque, B. Bhattacharjee, R. G. Prakash, K. Paramanandham, J. Haldar, *Biomacromolecules* **2018**, 19, 267.

[135]   M. C. Giano, Z. Ibrahim, S. H. Medina, K. A. Sarhane, J. M. Christensen, Y. Yamada, G. Brandacher, J. P. Schneider, *Nature communications* **2014**, 5, 1.

[136]   a) S. Wang, H. Zheng, L. Zhou, F. Cheng, Z. Liu, H. Zhang, L. Wang, Q. Zhang, *Nano Letters* **2020**, 20, 5149; b) Y. Zhong, H. Xiao, F. Seidi, Y. Jin, *Biomacromolecules* **2020**, 21, 2983.

[137]   D. Campoccia, L. Montanaro, C. R. Arciola, *Biomaterials* **2006**, 27, 2331.

[138]   a) L. Mei, S. Zhu, W. Yin, C. Chen, G. Nie, Z. Gu, Y. Zhao, *Theranostics* **2020**, 10, 757; b) Q. Wu, M. Liang, S. Zhang, X. Liu, F. Wang, *Nanoscale* **2018**, 10, 10428.

[139]   a) Y. Li, X. Liu, L. Tan, Z. Cui, D. Jing, X. Yang, Y. Liang, Z. Li, S. Zhu, Y. Zheng, K. W. K. Yeung, D. Zheng, X. Wang, S. Wu, *Advanced Functional Materials* **2019**, 29, 1900946; b) N. Beyth, Y. Houri-Haddad, A. Domb, W. Khan, R. Hazan, *Evid Based Complement Alternat Med* **2015**, 2015, 246012.

[140]   J. R. Xavier, T. Thakur, P. Desai, M. K. Jaiswal, N. Sears, E. Cosgriff-Hernandez, R. Kaunas, A. K. Gaharwar, *ACS nano* **2015**, 9, 3109.

[141]   G. Lokhande, J. K. Carrow, T. Thakur, J. R. Xavier, M. Parani, K. J. Bayless, A. K. Gaharwar, *Acta Biomaterialia* **2018**, 70, 35.

[142]   X. Zhai, Y. Ma, C. Hou, F. Gao, Y. Zhang, C. Ruan, H. Pan, W. W. Lu, W. Liu, *ACS Biomaterials Science & Engineering* **2017**, 3, 1109.

[143]   S. Pan, J. Yin, L. Yu, C. Zhang, Y. Zhu, Y. Gao, Y. Chen, *Advanced Science* **2020**, 7, 1901511.

[144]   A. Arabi Shamsabadi, M. Sharifian Gh, B. Anasori, M. Soroush, *ACS Sustainable Chemistry & Engineering* **2018**, 6, 16586.

[145]   N. Lu, L. Wang, M. Lv, Z. Tang, C. Fan, *Nano Research* **2019**, 12, 247.

[146]   K. Khan, A. K. Tareen, M. Aslam, R. Wang, Y. Zhang, A. Mahmood, Z. Ouyang, H. Zhang, Z. Guo, *Journal of Materials Chemistry C* **2020**, 8, 387.

[147]   T. T. Tung, M. J. Nine, M. Krebsz, T. Pasinszki, C. J. Coghlan, D. N. H. Tran, D. Losic, *Advanced Functional Materials* **2017**, 27, 1702891.

[148]   G. M. Vlăsceanu, H. Iovu, M. Ioniță, *Composites Part B: Engineering* **2019**.

[149]   a) G. Choe, S. Oh, J. M. Seok, S. A. Park, J. Y. Lee, *Nanoscale* **2019**, 11, 23275; b) F. Olate-Moya, L. Arens, M. Wilhelm, M. A. Mateos-Timoneda, E. Engel, H. Palza, *ACS Applied Materials & Interfaces* **2020**, 12, 4343.

[150]   a) C. Gardin, A. Piattelli, B. Zavan, *Trends in Biotechnology* **2016**, 34, 435; b) S. R. Shin, Y.-C. Li, H. L. Jang, P. Khoshakhlagh, M. Akbari, A. Nasajpour, Y. S. Zhang, A. Tamayol, A. Khademhosseini, *Advanced Drug Delivery Reviews* **2016**, 105, 255.

[151]   H. Qing, Y. Ji, W. Li, G. Zhao, Q. Yang, X. Zhang, Z. Luo, T. J. Lu, G. Jin, F. Xu, *ACS Applied Materials & Interfaces* **2020**, 12, 2049.

[152]   S. Sayyar, M. Bjorninen, S. Haimi, S. Miettinen, K. Gilmore, D. Grijpma, G. Wallace, *ACS Applied Materials & Interfaces* **2016**, 8, 31916.

[153]   a) S. Liu, T. H. Zeng, M. Hofmann, E. Burcombe, J. Wei, R. Jiang, J. Kong, Y. Chen, *ACS Nano* **2011**, 5, 6971; b) X. Zou, L. Zhang, Z. Wang, Y. Luo, *Journal of the American Chemical Society* **2016**, 138, 2064; c) O. Akhavan, E. Ghaderi, *ACS Nano* **2010**, 4, 5731.

[154]   Y. Zhang, D. Zhai, M. Xu, Q. Yao, H. Zhu, J. Chang, C. Wu, *Biofabrication* **2017**, 9, 025037.

[155]   S. F. Melo, S. C. Neves, A. T. Pereira, I. Borges, P. L. Granja, F. D. Magalhães, I. C. Gonçalves, *Materials Science and Engineering: C* **2020**, 109, 110537.

[156]   O. Akhavan, E. Ghaderi, S. Aghayee, Y. Fereydooni, A. Talebi, *Journal of Materials Chemistry* **2012**, 22, 13773.

119

[157] a) S. Tarashi, H. Nazockdast, G. Sodeifian, *Polymer* **2019**, 183, 121837; b) Y. Huang, M. Zhang, W. Ruan, *Journal of Materials Chemistry A* **2014**, 2, 10508.

[158] H. Nosrati, R. S. Mamoory, D. Q. S. Le, C. E. Bünger, *Materials Chemistry and Physics* **2020**, 239, 122305.

[159] Y. Yang, A. M. Asiri, Z. Tang, D. Du, Y. Lin, *Materials Today* **2013**, 16, 365.

[160] a) S. Hong, D. Sycks, H. F. Chan, S. Lin, G. P. Lopez, F. Guilak, K. W. Leong, X. Zhao, *Advanced materials* **2015**, 27, 4035; b) T. Cebe, N. Ahuja, F. Monte, K. Awad, K. Vyavhare, P. Aswath, J. Huang, M. Brotto, V. Varanasi, *Journal of Materials Research* **2020**, 35, 58; c) C. W. Peak, J. Stein, K. A. Gold, A. K. Gaharwar, *Langmuir* **2018**, 34, 917; d) A. Nadernezhad, O. S. Caliskan, F. Topuz, F. Afghah, B. Erman, B. Koc, *ACS Applied Bio Materials* **2019**, 2, 796.

[161] a) Y. M. Joshi, G. R. K. Reddy, A. L. Kulkarni, N. Kumar, R. P. Chhabra, *Proceedings of the Royal Society A: Mathematical, Physical and Engineering Sciences* **2008**, 464, 469; b) J. L. Dávila, M. A. d'Ávila, *Carbohydrate polymers* **2017**, 157, 1.

[162] D. W. Thompson, J. T. Butterworth, *Journal of Colloid and Interface Science* **1992**, 151, 236.

[163] B. Ruzicka, E. Zaccarelli, *Soft Matter* **2011**, 7, 1268.

[164] C. B. Highley, C. B. Rodell, J. A. Burdick, *Advanced Materials* **2015**, 27, 5075.

[165] G. Cidonio, C. R. Alcala-Orozco, K. S. Lim, M. Glinka, I. Mutreja, Y.-H. Kim, J. I. Dawson, T. B. Woodfield, R. O. Oreffo, *Biofabrication* **2019**, 11, 035027.

[166] J. L. Dávila, M. A. d'Ávila, *The International Journal of Advanced Manufacturing Technology* **2019**, 101, 675.

[167] B. Liu, J. Li, X. Lei, P. Cheng, Y. Song, Y. Gao, J. Hu, C. Wang, S. Zhang, D. Li, H. Wu, H. Sang, L. Bi, G. Pei, *Materials Science and Engineering: C* **2020**, 112, 110905.

[168] Y. Chen, X. Xiong, X. Liu, R. Cui, C. Wang, G. Zhao, W. Zhi, M. Lu, K. Duan, J. Weng, S. Qu, J. Ge, *Journal of Materials Chemistry B* **2020**, 8, 5500.

[169] a) D. Su, L. Jiang, X. Chen, J. Dong, Z. Shao, *ACS Applied Materials & Interfaces* **2016**, 8, 9619; b) Y. Liu, H. Meng, S. Konst, R. Sarmiento, R. Rajachar, B. P. Lee, *ACS Applied Materials & Interfaces* **2014**, 6, 16982.

[170] H. Tomás, C. S. Alves, J. Rodrigues, *Nanomedicine: Nanotechnology, Biology and Medicine* **2018**, 14, 2407.

[171] S. Wang, R. Castro, X. An, C. Song, Y. Luo, M. Shen, H. Tomás, M. Zhu, X. Shi, *Journal of Materials Chemistry* **2012**, 22, 23357.

[172] a) C. Boyer, L. Figueiredo, R. Pace, J. Lesoeur, T. Rouillon, C. L. Visage, J.-F. Tassin, P. Weiss, J. Guicheux, G. Rethore, *Acta Biomaterialia* **2018**, 65, 112; b) X. Xie, X. Li, T. Zhou, T. Zhang, J. Liao, in *Cartilage Regeneration*, DOI: 10.1007/978-3-319-51617-2_5 (Ed: Y. Lin), Springer International Publishing, Cham **2017**, p. 77.

[173] a) G. Wang, D. Maciel, Y. Wu, J. Rodrigues, X. Shi, Y. Yuan, C. Liu, H. Tomás, Y. Li, *ACS Applied Materials & Interfaces* **2014**, 6, 16687; b) M. Ghadiri, H. Hau, W. Chrzanowski, H. Agus, R. Rohanizadeh, *RSC Advances* **2013**, 3, 20193; c) S. Wang, Y. Wu, R. Guo, Y. Huang, S. Wen, M. Shen, J. Wang, X. Shi, *Langmuir* **2013**, 29, 5030.

[174] S. S. Das, Neelam, K. Hussain, S. Singh, A. Hussain, A. Faruk, M. Tebyetekerwa, *Current Pharmaceutical Design* **2019**, 25, 424.

[175] T. Ahlfeld, G. Cidonio, D. Kilian, S. Duin, A. Akkineni, J. Dawson, S. Yang, A. Lode, R. Oreffo, M. Gelinsky, *Biofabrication* **2017**, 9, 034103.

[176] K. Yue, G. Trujillo-de Santiago, M. M. Alvarez, A. Tamayol, N. Annabi, A. Khademhosseini, *Biomaterials* **2015**, 73, 254.

[177] B. J. Klotz, D. Gawlitta, A. J. W. P. Rosenberg, J. Malda, F. P. W. Melchels, *Trends in Biotechnology* **2016**, 34, 394.

[178] W. Liu, M. A. Heinrich, Y. Zhou, A. Akpek, N. Hu, X. Liu, X. Guan, Z. Zhong, X. Jin, A. Khademhosseini, Y. S. Zhang, *Advanced Healthcare Materials* **2017**, 6, 1601451.

[179] a) R. Gusmao, Z. Sofer, M. Pumera, *Angewandte Chemie International Edition* **2017**, 56, 8052; b) H. Liu, Y. Du, Y. Deng, D. Y. Peide, *Chemical Society Reviews* **2015**, 44, 2732.

[180] A. Jayakumar, A. Surendranath, P. Mohanan, *International journal of pharmaceutics* **2018**, 551, 309.

[181] M. Qiu, A. Singh, D. Wang, J. Qu, M. Swihart, H. Zhang, P. N. Prasad, *Nano Today* **2019**, 25, 135.

[182] G. Abellán, S. Wild, V. Lloret, N. Scheuschner, R. Gillen, U. Mundloch, J. Maultzsch, M. Varela, F. Hauke, A. Hirsch, *Journal of the American Chemical Society* **2017**, 139, 10432.

[183] a) X. Liu, M. N. George, L. Li, D. Gamble, A. L. Miller Ii, B. Gaihre, B. E. Waletzki, L. Lu, *ACS Biomaterials Science & Engineering* **2020**, 6, 4653; b) C. Wang, X. Ye, Y. Zhao, L. Bai, Z. He, Q. Tong, X. Xie, H. Zhu, D. Cai, Y. Zhou, *Biofabrication* **2020**, 12, 035004.

120

[184]   a) X. Yang, G. Liu, Y. Shi, W. Huang, J. Shao, X. Dong, *Nanotechnology* **2018**, 29, 222001; b) X. Yang, D. Wang, J. Zhu, L. Xue, C. Ou, W. Wang, M. Lu, X. Song, X. Dong, *Chemical science* **2019**, 10, 3779; c) W. Pan, C. Dai, Y. Li, Y. Yin, L. Gong, J. O. a. Machuki, Y. Yang, S. Qiu, K. Guo, F. Gao, *Biomaterials* **2020**, 239, 119851.

[185]   B. Yang, J. Yin, Y. Chen, S. Pan, H. Yao, Y. Gao, J. Shi, *Advanced Materials* **2018**, 30, 1705611.

[186]   X. Liu, A. L. Miller, S. Park, M. N. George, B. E. Waletzki, H. Xu, A. Terzic, L. Lu, *ACS applied materials & interfaces* **2019**, 11, 23558.

[187]   Y. Miao, X. Shi, Q. Li, L. Hao, L. Liu, X. Liu, Y. Chen, Y. Wang, *Biomaterials science* **2019**, 7, 4046.

[188]   W. Feng, R. Wang, Y. Zhou, L. Ding, X. Gao, B. Zhou, P. Hu, Y. Chen, *Advanced Functional Materials* **2019**, 29, 1901942.

[189]   H. Lin, Y. Wang, S. Gao, Y. Chen, J. Shi, *Advanced Materials* **2018**, 30, 1703284.

[190]   a) H. Lin, S. Gao, C. Dai, Y. Chen, J. Shi, *Journal of the American Chemical Society* **2017**, 139, 16235; b) A. Szuplewska, D. Kulpińska, A. Dybko, A. M. Jastrzębska, T. Wojciechowski, A. Rozmysłowska, M. Chudy, I. Grabowska-Jadach, W. Ziemkowska, Z. Brzózka, *Materials Science and Engineering: C* **2019**, 98, 874.

[191]   H. Weng, A. Ranjbar, Y. Liang, Z. Song, M. Khazaei, S. Yunoki, M. Arai, Y. Kawazoe, Z. Fang, X. Dai, *Physical Review B* **2015**, 92, 075436.

[192]   C. Zhang, B. Anasori, A. Seral-Ascaso, S. H. Park, N. McEvoy, A. Shmeliov, G. S. Duesberg, J. N. Coleman, Y. Gogotsi, V. Nicolosi, *Advanced materials* **2017**, 29, 1702678.

[193]   a) Y.-Z. Zhang, J. K. El-Demellawi, Q. Jiang, G. Ge, H. Liang, K. Lee, X. Dong, H. N. Alshareef, *Chemical Society Reviews* **2020**; b) Q. Wang, X. Pan, X. Wang, S. Cao, L. Chen, X. Ma, L. Huang, Y. Ni, *Ceramics International* **2020**.

[194]   B. Anasori, Û. G. Gogotsi, *2D metal carbides and nitrides (MXenes)*, Springer, **2019**.

[195]   K. Rasool, M. Helal, A. Ali, C. E. Ren, Y. Gogotsi, K. A. Mahmoud, *ACS nano* **2016**, 10, 3674.

[196]   H. Lin, X. Wang, L. Yu, Y. Chen, J. Shi, *Nano letters* **2017**, 17, 384.

[197]   X. Han, J. Huang, H. Lin, Z. Wang, P. Li, Y. Chen, *Advanced healthcare materials* **2018**, 7, 1701394.

[198]   C. Dai, H. Lin, G. Xu, Z. Liu, R. Wu, Y. Chen, *Chemistry of materials* **2017**, 29, 8637.

[199]   K. Li, T. H. Chang, Z. Li, H. Yang, F. Fu, T. Li, J. S. Ho, P. Y. Chen, *Advanced Energy Materials* **2019**, 9, 1901687.

[200]   R. Rakhi, P. Nayak, C. Xia, H. N. Alshareef, *Scientific reports* **2016**, 6, 1.

[201]   M. Soleymaniha, M. A. Shahbazi, A. R. Rafieerad, A. Maleki, A. Amiri, *Advanced healthcare materials* **2019**, 8, 1801137.

[202]   a) W. Choi, N. Choudhary, G. H. Han, J. Park, D. Akinwande, Y. H. Lee, *Materials Today* **2017**, 20, 116; b) M. Chhowalla, H. S. Shin, G. Eda, L.-J. Li, K. P. Loh, H. Zhang, *Nature chemistry* **2013**, 5, 263.

[203]   M. Chhowalla, Z. Liu, H. Zhang, *Chemical Society Reviews* **2015**, 44, 2584.

[204]   a) E. Benavente, M. Santa Ana, F. Mendizábal, G. González, *Coordination chemistry reviews* **2002**, 224, 87; b) W. Zhou, X. Zou, S. Najmaei, Z. Liu, Y. Shi, J. Kong, J. Lou, P. M. Ajayan, B. I. Yakobson, J.-C. Idrobo, *Nano letters* **2013**, 13, 2615.

[205]   Z. Xu, J. Lu, X. Zheng, B. Chen, Y. Luo, M. N. Tahir, B. Huang, X. Xia, X. Pan, *Journal of Hazardous Materials* **2020**, 123057.

[206]   a) K. Wang, Q. Chen, W. Xue, S. Li, Z. Liu, *ACS Biomaterials Science & Engineering* **2017**, 3, 2325; b) S. Cai, J. Yan, H. Xiong, H. Xing, Y. Liu, S. Liu, Z. Liu, *International Journal of Pharmaceutics* **2020**, 119948; c) J. Lu, M. Chen, L. Dong, L. Cai, M. Zhao, Q. Wang, J. Li, *Colloids and Surfaces B: Biointerfaces* **2020**, 111162.

[207]   X. Wang, T. Li, H. Ma, D. Zhai, C. Jiang, J. Chang, J. Wang, C. Wu, *NPG Asia Materials* **2017**, 9, e376.

[208]   Q. Weng, X. Wang, X. Wang, Y. Bando, D. Golberg, *Chemical Society Reviews* **2016**, 45, 3989.

[209]   a) S. Nagarajan, H. Belaid, C. Pochat-Bohatier, C. Teyssier, I. Iatsunskyi, E. Coy, S. Balme, D. Cornu, P. Miele, N. S. Kalkura, *ACS applied materials & interfaces* **2017**, 9, 33695; b) D. Aki, S. Ulag, S. Unal, M. Sengor, N. Ekren, C.-C. Lin, H. Yılmazer, C. B. Ustundag, D. M. Kalaskar, O. Gunduz, *Materials & Design* **2020**, 196, 109094.

[210]   a) A. Merlo, V. R. S. S. Mokkapati, S. Pandit, I. Mijakovic, *Biomaterials science* **2018**, 6, 2298; b) F. Lu, F. Wang, L. Cao, C. Y. Kong, X. Huang, *Nanoscience and Nanotechnology Letters* **2012**, 4, 949.

[211]   L. M. Guiney, N. D. Mansukhani, A. E. Jakus, S. G. Wallace, R. N. Shah, M. C. Hersam, *Nano letters* **2018**, 18, 3488.

[212]   H. Belaid, S. Nagarajan, C. Barou, V. Huon, J. Bares, S. Balme, P. Miele, D. Cornu, V. Cavaillès, C. Teyssier, *ACS Applied Bio Materials* **2020**, 3, 1865.

[213]   S. Zhang, X. Pei, H. Gao, S. Chen, J. Wang, *Chinese Chemical Letters* **2020**, 31, 1060.

121

[214] M. T. Ulhakim, M. Rezki, K. K. Dewi, S. A. Abrori, S. Harimurti, N. L. W. Septiani, K. A. Kurnia, W. Setyaningsih, N. Darmawan, B. Yuliarto, *Journal of The Electrochemical Society* **2020**, 167, 136509.

[215] a) J. Liu, H. Yu, L. Wang, Z. Deng, A. Nazir, F. Haq, *Inorganica Chimica Acta* **2018**, 483, 550; b) M. Zhao, Q. Lu, Q. Ma, H. Zhang, *Small Methods* **2017**, 1, 1600030.

[216] W. Dang, B. Ma, B. Li, Z. Huan, N. Ma, H. Zhu, J. Chang, Y. Xiao, C. Wu, *Biofabrication* **2020**, 12, 025005.

[217] J. M. Unagolla, A. C. Jayasuriya, *Materials Science and Engineering: C* **2019**, 102, 1.

[218] C.-T. Huang, L. Kumar Shrestha, K. Ariga, S.-h. Hsu, *Journal of Materials Chemistry B* **2017**, 5, 8854.

[219] C. Shuai, P. Feng, C. Gao, X. Shuai, T. Xiao, S. Peng, *RSC Advances* **2015**, 5, 25416.

[220] J. C. Boga, S. P. Miguel, D. de Melo-Diogo, A. G. Mendonça, R. O. Louro, I. J. Correia, *Colloids and Surfaces B: Biointerfaces* **2018**, 165, 207.

[221] C. Wu, L. Xia, P. Han, M. Xu, B. Fang, J. Wang, J. Chang, Y. Xiao, *Carbon* **2015**, 93, 116.

[222] C. S. Cabral, S. P. Miguel, D. de Melo-Diogo, R. O. Louro, I. J. Correia, *Carbon* **2019**, 146, 513.

[223] Y. Zhang, D. Zhai, M. Xu, Q. Yao, J. Chang, C. Wu, *Journal of Materials Chemistry B* **2016**, 4, 2874.

[224] a) X. Cui, S. Xu, X. Wang, C. Chen, *Carbon* **2018**, 138, 436; b) G. Qu, T. Xia, W. Zhou, X. Zhang, H. Zhang, L. Hu, J. Shi, X.-F. Yu, G. Jiang, *Chemical Reviews* **2020**, 120, 2288; c) S. Keshavan, P. Calligari, L. Stella, L. Fusco, L. G. Delogu, B. Fadeel, *Cell Death & Disease* **2019**, 10, 569; d) Z. Tu, G. Guday, M. Adeli, R. Haag, *Advanced Materials* **2018**, 30, 1706709.

[225] a) M. Fojtů, W. Z. Teo, M. Pumera, *Environmental Science: Nano* **2017**, 4, 1617; b) Kenry, C. T. Lim, *ChemNanoMat* **2017**, 3, 5.

[226] a) N. Li, S. Georas, N. Alexis, P. Fritz, T. Xia, M. A. Williams, E. Horner, A. Nel, *Journal of Allergy and Clinical Immunology* **2016**, 138, 386; b) H.-Y. Liao, Y.-T. Chung, C.-H. Lai, M.-H. Lin, S.-H. Liou, *Industrial health* **2014**, 2013; c) P. Ganguly, A. Breen, S. C. Pillai, *ACS Biomaterials Science & Engineering* **2018**, 4, 2237.

[227] a) L. Ou, B. Song, H. Liang, J. Liu, X. Feng, B. Deng, T. Sun, L. Shao, *Particle and Fibre Toxicology* **2016**, 13, 57; b) E. Tan, B. L. Li, K. Ariga, C. T. Lim, S. Garaj, D. T. Leong, *Bioconjug Chem* **2019**, 30, 2287.

[228] a) F. Zhao, Y. Zhao, Y. Liu, X. Chang, C. Chen, Y. Zhao, *Small* **2011**, 7, 1322; b) S. D. Conner, S. L. Schmid, *Nature* **2003**, 422, 37; c) M. Zhu, G. Nie, H. Meng, T. Xia, A. Nel, Y. Zhao, *Accounts of Chemical Research* **2013**, 46, 622.

[229] M. Ehrlich, W. Boll, A. van Oijen, R. Hariharan, K. Chandran, M. L. Nibert, T. Kirchhausen, *Cell* **2004**, 118, 591.

[230] a) S. Behzadi, V. Serpooshan, W. Tao, M. A. Hamaly, M. Y. Alkawareek, E. C. Dreaden, D. Brown, A. M. Alkilany, O. C. Farokhzad, M. Mahmoudi, *Chemical Society Reviews* **2017**, 46, 4218; b) M. Hasanzadeh Kafshgari, F. J. Harding, N. H. Voelcker, *Current Drug Delivery* **2015**, 12, 63.

[231] a) J. Lin, A. Alexander-Katz, *ACS Nano* **2013**, 7, 10799; b) S. Zhang, H. Gao, G. Bao, *ACS Nano* **2015**, 9, 8655.

[232] a) P. Decuzzi, M. Ferrari, *Biomaterials* **2007**, 28, 2915; b) Y. Cao, Y. Gong, L. Liu, Y. Zhou, X. Fang, C. Zhang, Y. Li, J. Li, *Journal of Applied Toxicology* **2017**, 37, 1359.

[233] D. A. Kuhn, D. Vanhecke, B. Michen, F. Blank, P. Gehr, A. Petri-Fink, B. Rothen-Rutishauser, *Beilstein Journal of Nanotechnology* **2014**, 5, 1625.

[234] a) J. L. Goldstein, R. G. W. Anderson, M. S. Brown, *Nature* **1979**, 279, 679; b) N. Oh, J.-H. Park, *International journal of nanomedicine* **2014**, 9 Suppl 1, 51; c) T.-G. Iversen, T. Skotland, K. Sandvig, *Nano Today* **2011**, 6, 176.

[235] a) J. A. Swanson, *Nature Reviews Molecular Cell Biology* **2008**, 9, 639; b) A. Kunzmann, B. Andersson, T. Thurnherr, H. Krug, A. Scheynius, B. Fadeel, *Biochimica et Biophysica Acta (BBA) - General Subjects* **2011**, 1810, 361; c) M. A. Dobrovolskaia, S. E. McNeil, *Nature nanotechnology* **2007**, 2, 469.

[236] J. G. Huang, T. Leshuk, F. X. Gu, *Nano Today* **2011**, 6, 478.

[237] a) J. P. Lim, P. A. Gleeson, *Immunology & Cell Biology* **2011**, 89, 836; b) A. Musyanovych, J. Dausend, M. Dass, P. Walther, V. Mailänder, K. Landfester, *Acta Biomaterialia* **2011**, 7, 4160; c) C. Greulich, J. Diendorf, T. Simon, G. Eggeler, M. Epple, M. Köller, *Acta Biomaterialia* **2011**, 7, 347.

[238] J. Hirst, M. S. Robinson, *Biochimica et Biophysica Acta (BBA) - Molecular Cell Research* **1998**, 1404, 173.

[239] a) A. Sorkin, M. A. Puthenveedu, in *Vesicle Trafficking in Cancer*, DOI: 10.1007/978-1-4614-6528-7_1 (Eds: Y. Yarden, G. Tarcic), Springer New York, New York, NY **2013**, p. 1; b) O. Harush-Frenkel, N. Debotton, S. Benita, Y. Altschuler, *Biochemical and Biophysical Research Communications* **2007**, 353, 26.

[240] J. Zhao, M. H. Stenzel, *Polymer Chemistry* **2018**, 9, 259.

[241] a) L. Pelkmans, A. Helenius, *Traffic* **2002**, 3, 311; b) R. Mora, V. L. Bonilha, A. Marmorstein, P. E. Scherer, D. Brown, M. P. Lisanti, E. Rodriguez-Boulan, *J Biol Chem* **1999**, 274, 25708.

122

[242]   a) K. C. Partlow, G. M. Lanza, S. A. Wickline, *Biomaterials* **2008**, 29, 3367; b) T. Nishikawa, N. Iwakiri, Y. Kaneko, A. Taguchi, K. Fukushima, H. Mori, N. Morone, J.-i. Kadokawa, *Biomacromolecules* **2009**, 10, 2074.

[243]   J. Rejman, M. Conese, D. Hoekstra, *J Liposome Res* **2006**, 16, 237.

[244]   L. A. Carver, J. E. Schnitzer, *Nat Rev Cancer* **2003**, 3, 571.

[245]   a) S. Kumari, S. Mg, S. Mayor, *Cell Research* **2010**, 20, 256; b) C. Brandenberger, C. Mühlfeld, Z. Ali, A.-G. Lenz, O. Schmid, W. J. Parak, P. Gehr, B. Rothen-Rutishauser, *Small* **2010**, 6, 1669; c) J. Gilleron, W. Querbes, A. Zeigerer, A. Borodovsky, G. Marsico, U. Schubert, K. Manygoats, S. Seifert, C. Andree, M. Stöter, H. Epstein-Barash, L. Zhang, V. Koteliansky, K. Fitzgerald, E. Fava, M. Bickle, Y. Kalaidzidis, A. Akinc, M. Maier, M. Zerial, *Nature Biotechnology* **2013**, 31, 638.

[246]   a) A. El-Sayed, H. Harashima, *Molecular Therapy* **2013**, 21, 1118; b) P. Panja, N. R. Jana, *The Journal of Physical Chemistry B* **2020**, 124, 5323.

[247]   a) J. Bi, R. Wang, Y. Zhang, X. Han, K. K. Ampah, X. Liu, X. Zeng, *Molecules and cells* **2013**, 36, 507; b) A. Chakraborty, N. R. Jana, *The Journal of Physical Chemistry Letters* **2015**, 6, 3688.

[248]   a) C. Foerg, U. Ziegler, J. Fernandez-Carneado, E. Giralt, R. Rennert, A. G. Beck-Sickinger, H. P. Merkle, *Biochemistry* **2005**, 44, 72; b) S. W. Jones, R. Christison, K. Bundell, C. J. Voyce, S. M. Brockbank, P. Newham, M. A. Lindsay, *British journal of pharmacology* **2005**, 145, 1093.

[249]   a) J. P. Peñaloza, V. Márquez-Miranda, M. Cabaña-Brunod, R. Reyes-Ramírez, F. M. Llancalahuen, C. Vilos, F. Maldonado-Biermann, L. A. Velásquez, J. A. Fuentes, F. D. González-Nilo, M. Rodríguez-Díaz, C. Otero, *Journal of Nanobiotechnology* **2017**, 15, 1; b) M. S. Cartiera, K. M. Johnson, V. Rajendran, M. J. Caplan, W. M. Saltzman, *Biomaterials* **2009**, 30, 2790.

[250]   P. Foroozandeh, A. A. Aziz, *Nanoscale Research Letters* **2018**, 13, 339.

[251]   a) J. Huotari, A. Helenius, *The EMBO Journal* **2011**, 30, 3481; b) L. Y. T. Chou, K. Ming, W. C. W. Chan, *Chemical Society Reviews* **2011**, 40, 233.

[252]   B. D. Grant, J. G. Donaldson, *Nature Reviews Molecular Cell Biology* **2009**, 10, 597.

[253]   T. F. Martens, K. Remaut, J. Demeester, S. C. De Smedt, K. Braeckmans, *Nano Today* **2014**, 9, 344.

[254]   a) A. L. Anding, E. H. Baehrecke, *Developmental Cell* **2017**, 41, 10; b) X. Ma, Y. Wu, S. Jin, Y. Tian, X. Zhang, Y. Zhao, L. Yu, X.-J. Liang, *ACS Nano* **2011**, 5, 8629.

[255]   Q. Mu, G. Su, L. Li, B. O. Gilbertson, L. H. Yu, Q. Zhang, Y.-P. Sun, B. Yan, *ACS Applied Materials & Interfaces* **2012**, 4, 2259.

[256]   A. Brandelli, *Food Science and Human Wellness* **2020**, 9, 8.

[257]   Y. Chen, Y. Wu, B. Sun, S. Liu, H. Liu, *Small* **2017**, 13, 1603446.

[258]   N. D. Donahue, H. Acar, S. Wilhelm, *Advanced Drug Delivery Reviews* **2019**, 143, 68.

[259]   a) N. Luo, D. Ni, H. Yue, W. Wei, G. Ma, *ACS Applied Materials & Interfaces* **2015**, 7, 5239; b) S. Ye, P. Yang, K. Cheng, T. Zhou, Y. Wang, Z. Hou, Y. Jiang, L. Ren, *ACS Biomaterials Science & Engineering* **2016**, 2, 722.

[260]   Z. Tu, K. Achazi, A. Schulz, R. Mülhaupt, S. Thierbach, E. Rühl, M. Adeli, R. Haag, *Advanced Functional Materials* **2017**, 27, 1701837.

[261]   B. Wang, X. Su, J. Liang, L. Yang, Q. Hu, X. Shan, J. Wan, Z. Hu, *Materials Science and Engineering: C* **2018**, 90, 514.

[262]   Z.-G. Yue, W. Wei, P.-P. Lv, H. Yue, L.-Y. Wang, Z.-G. Su, G.-H. Ma, *Biomacromolecules* **2011**, 12, 2440.

[263]   a) Z. Xiong, X. Zhang, S. Zhang, L. Lei, W. Ma, D. Li, W. Wang, Q. Zhao, B. Xing, *Ecotoxicology and Environmental Safety* **2018**, 161, 507; b) W. Hu, C. Peng, W. Luo, M. Lv, X. Li, D. Li, Q. Huang, C. Fan, *ACS Nano* **2010**, 4, 4317.

[264]   J. Chen, X. Wang, H. Han, *Journal of Nanoparticle Research* **2013**, 15, 1658.

[265]   T. Guo, S. Zhuang, H. Qiu, Y. Guo, L. Wang, G. Jin, W. Lin, G. Huang, H. Yang, *Particle & Particle Systems Characterization* **2020**, 37, 2000169.

[266]   a) X. Yang, J. Li, T. Liang, C. Ma, Y. Zhang, H. Chen, N. Hanagata, H. Su, M. Xu, *Nanoscale* **2014**, 6, 10126; b) N. Wu, Y. Yu, T. Li, X. Ji, L. Jiang, J. Zong, H. Huang, *PLOS ONE* **2016**, 11, e0167245.

[267]   a) L. Hui, J.-G. Piao, J. Auletta, K. Hu, Y. Zhu, T. Meyer, H. Liu, L. Yang, *ACS Applied Materials & Interfaces* **2014**, 6, 13183; b) J. D. Mangadlao, C. M. Santos, M. J. L. Felipe, A. C. C. de Leon, D. F. Rodrigues, R. C. Advincula, *Chemical Communications* **2015**, 51, 2886.

[268]   S. Liu, M. Hu, T. H. Zeng, R. Wu, R. Jiang, J. Wei, L. Wang, J. Kong, Y. Chen, *Langmuir* **2012**, 28, 12364.

[269]   W. Liu, Y. Zhang, Y. Zhang, A. Dong, *Chemistry – A European Journal* **2020**, 26, 2478.

[270]   T. I. Kim, J. Kim, I.-J. Park, K.-O. Cho, S.-Y. Choi, *2D Materials* **2019**, 6, 025025.

[271]   T. Finkel, *Journal of Cell Biology* **2011**, 194, 7.

[272]   Michael P. Murphy, *Biochemical Journal* **2008**, 417, 1.

123

[273] a) S. Syama, P. V. Mohanan, *Nano-Micro Letters* **2019**, 11, 6; b) A. Jarosz, M. Skoda, I. Dudek, D. Szukiewicz, *Oxidative Medicine and Cellular Longevity* **2016**, 2016, 5851035.

[274] M. C. Duch, G. R. S. Budinger, Y. T. Liang, S. Soberanes, D. Urich, S. E. Chiarella, L. A. Campochiaro, A. Gonzalez, N. S. Chandel, M. C. Hersam, G. M. Mutlu, *Nano Letters* **2011**, 11, 5201.

[275] a) X. Zhang, Z. Zhang, S. Zhang, D. Li, W. Ma, C. Ma, F. Wu, Q. Zhao, Q. Yan, B. Xing, *Small* **2017**, 13, 1701210; b) N. Kong, X. Ji, J. Wang, X. Sun, G. Chen, T. Fan, W. Liang, H. Zhang, A. Xie, O. C. Farokhzad, W. Tao, *Nano Letters* **2020**, 20, 3943.

[276] a) A. Szuplewska, A. Rozmysłowska-Wojciechowska, S. Poźniak, T. Wojciechowski, M. Birowska, M. Popielski, M. Chudy, W. Ziemkowska, L. Chlubny, D. Moszczyńska, A. Olszyna, J. A. Majewski, A. M. Jastrzębska, *Journal of Nanobiotechnology* **2019**, 17, 114; b) A. M. Jastrzębska, B. Scheibe, A. Szuplewska, A. Rozmysłowska-Wojciechowska, M. Chudy, C. Aparicio, M. Scheibe, I. Janica, A. Ciesielski, M. Otyepka, M. W. Barsoum, *Materials Science and Engineering: C* **2021**, 119, 111431.

[277] S. Roy, A. Mondal, V. Yadav, A. Sarkar, R. Banerjee, P. Sanpui, A. Jaiswal, *ACS Applied Bio Materials* **2019**, 2, 2738.

[278] a) N. A. El-Yamany, F. F. Mohamed, T. A. Salaheldin, A. A. Tohamy, W. N. Abd El-Mohsen, A. S. Amin, *Experimental and Toxicologic Pathology* **2017**, 69, 383; b) C.-J. Lu, X.-F. Jiang, M. Junaid, Y.-B. Ma, P.-P. Jia, H.-B. Wang, D.-S. Pei, *Chemosphere* **2017**, 184, 795; c) J. H. Appel, D. O. Li, J. D. Podlevsky, A. Debnath, A. A. Green, Q. H. Wang, J. Chae, *ACS Biomaterials Science & Engineering* **2016**, 2, 361.

[279] a) O. Akhavan, E. Ghaderi, A. Akhavan, *Biomaterials* **2012**, 33, 8017; b) Y. Liu, Y. Luo, J. Wu, Y. Wang, X. Yang, R. Yang, B. Wang, J. Yang, N. Zhang, *Scientific reports* **2013**, 3, 3469; c) N. Chatterjee, H.-J. Eom, J. Choi, *Biomaterials* **2014**, 35, 1109.

[280] N. Golbamaki, B. Rasulev, A. Cassano, R. L. Marchese Robinson, E. Benfenati, J. Leszczynski, M. T. D. Cronin, *Nanoscale* **2015**, 7, 2154.

[281] Z. Magdolenova, A. Collins, A. Kumar, A. Dhawan, V. Stone, M. Dusinska, *Nanotoxicology* **2014**, 8, 233.

[282] X. Mu, J.-Y. Wang, X. Bai, F. Xu, H. Liu, J. Yang, Y. Jing, L. Liu, X. Xue, H. Dai, Q. Liu, Y.-M. Sun, C. Liu, X.-D. Zhang, *ACS Applied Materials & Interfaces* **2017**, 9, 20399.

[283] T. A. Tabish, S. Zhang, P. G. Winyard, *Redox biology* **2018**, 15, 34.

[284] S. H. Doak, Y. Liu, C. Chen, in *Adverse Effects of Engineered Nanomaterials*, Elsevier **2017**, p. 423.

[285] I. L. Gunsolus, C. L. Haynes, *Anal Chem* **2016**, 88, 451.

[286] S. F. Kiew, L. V. Kiew, H. B. Lee, T. Imae, L. Y. Chung, *Journal of Controlled Release* **2016**, 226, 217.

[287] a) X. Zhang, J. Yin, C. Peng, W. Hu, Z. Zhu, W. Li, C. Fan, Q. Huang, *carbon* **2011**, 49, 986; b) K.-H. Liao, Y.-S. Lin, C. W. Macosko, C. L. Haynes, *ACS Applied Materials & Interfaces* **2011**, 3, 2607.

[288] H. Yue, W. Wei, Z. Yue, B. Wang, N. Luo, Y. Gao, D. Ma, G. Ma, Z. Su, *Biomaterials* **2012**, 33, 4013.

[289] a) Y. Chang, S.-T. Yang, J.-H. Liu, E. Dong, Y. Wang, A. Cao, Y. Liu, H. Wang, *Toxicology letters* **2011**, 200, 201; b) Y. Li, Q. Wu, Y. Zhao, Y. Bai, P. Chen, T. Xia, D. Wang, *ACS Nano* **2014**, 8, 2100.

[290] S. Sharifi, S. Behzadi, S. Laurent, M. L. Forrest, P. Stroeve, M. Mahmoudi, *Chem Soc Rev* **2012**, 41, 2323.

[291] B. J. Marquis, S. A. Love, K. L. Braun, C. L. Haynes, *Analyst* **2009**, 134, 425.

[292] C. Korzeniewski, D. M. Callewaert, *Journal of Immunological Methods* **1983**, 64, 313.

[293] S. A. Love, M. A. Maurer-Jones, J. W. Thompson, Y. S. Lin, C. L. Haynes, *Annu Rev Anal Chem (Palo Alto Calif)* **2012**, 5, 181.

[294] L. Horváth, A. Magrez, M. Burghard, K. Kern, L. Forró, B. Schwaller, *Carbon* **2013**, 64, 45.

[295] A. Magrez, S. Kasas, V. Salicio, N. Pasquier, J. W. Seo, M. Celio, S. Catsicas, B. Schwaller, L. Forro, *Nano Lett* **2006**, 6, 1121.

[296] S. Y. Park, H. U. Lee, Y. C. Lee, S. Choi, D. H. Cho, H. S. Kim, S. Bang, S. Seo, S. C. Lee, J. Won, B. C. Son, M. Yang, J. Lee, *Sci Rep* **2015**, 5, 12420.

[297] P.-P. Jia, T. Sun, M. Junaid, L. Yang, Y.-B. Ma, Z.-S. Cui, D.-P. Wei, H.-F. Shi, D.-S. Pei, *Environmental Pollution* **2019**, 247, 595.

[298] C. Moore, D. Movia, R. J. Smith, D. Hanlon, F. Lebre, E. C. Lavelle, H. J. Byrne, J. N. Coleman, Y. Volkov, J. McIntyre, *2D Materials* **2017**, 4, 025065.

[299] G. Caracciolo, O. C. Farokhzad, M. Mahmoudi, *Trends in biotechnology* **2017**, 35, 257.

[300] E. L. K. Chng, Z. Sofer, M. Pumera, *Nanoscale* **2014**, 6, 14412.

[301] a) W. Z. Teo, E. L. K. Chng, Z. Sofer, M. Pumera, *Chemistry – A European Journal* **2014**, 20, 9627; b) L. M. Guiney, X. Wang, T. Xia, A. E. Nel, M. C. Hersam, *ACS Nano* **2018**, 12, 6360.

[302] H. L. Chia, N. M. Latiff, Z. Sofer, M. Pumera, *Chemistry – A European Journal* **2018**, 24, 206.

[303] N. Bertrand, J. Wu, X. Xu, N. Kamaly, O. C. Farokhzad, *Advanced Drug Delivery Reviews* **2014**, 66, 2.

[304] a) T. Kuila, S. Bose, A. K. Mishra, P. Khanra, N. H. Kim, J. H. Lee, *Progress in Materials Science* **2012**, 57, 1061; b) V. Georgakilas, J. N. Tiwari, K. C. Kemp, J. A. Perman, A. B. Bourlinos, K. S. Kim, R. Zboril,

124

Chemical Reviews **2016**, 116, 5464; c) M. Xu, J. Zhu, F. Wang, Y. Xiong, Y. Wu, Q. Wang, J. Weng, Z. Zhang, W. Chen, S. Liu, *ACS Nano* **2016**, 10, 3267; d) V. Georgakilas, M. Otyepka, A. B. Bourlinos, V. Chandra, N. Kim, K. C. Kemp, P. Hobza, R. Zboril, K. S. Kim, *Chemical Reviews* **2012**, 112, 6156.

[305]   K. Yang, J. Wan, S. Zhang, Y. Zhang, S.-T. Lee, Z. Liu, *ACS Nano* **2011**, 5, 516.

[306]   a) C. Cruje, D. B. Chithrani, *Reviews in Nanoscience and Nanotechnology* **2014**, 3, 20; b) M. Wang, O. J. R. Gustafsson, G. Siddiqui, I. Javed, H. G. Kelly, T. Blin, H. Yin, S. J. Kent, D. J. Creek, K. Kempe, P. C. Ke, T. P. Davis, *Nanoscale* **2018**, 10, 10863.

[307]   Y. Liu, W. Han, Z. Xu, W. Fan, W. Peng, S. Luo, *Environmental Pollution* **2018**, 237, 218.

[308]   a) J. Mo, Y. Xu, X. Wang, W. Wei, J. Zhao, *Nanoscale* **2020**, 12, 1742; b) D. Nierenberg, A. R. Khaled, O. Flores, *Reports of Practical Oncology & Radiotherapy* **2018**, 23, 300; c) I. Capjak, S. Š. Goreta, D. D. Jurašin, I. V. Vrček, *Archives of Industrial Hygiene and Toxicology* **2017**, 68, 245.

[309]   a) M. Rahman, S. Laurent, N. Tawil, L. H. Yahia, M. Mahmoudi, in *Protein-Nanoparticle Interactions: The Bio-Nano Interface*, DOI: 10.1007/978-3-642-37555-2_2, Springer Berlin Heidelberg, Berlin, Heidelberg **2013**, p. 21; b) K.-C. Mei, A. Ghazaryan, E. Z. Teoh, H. D. Summers, Y. Li, B. Ballesteros, A. Walters, R. C. Hider, V. Mailänder, K. T. Al-Jamal, *Advanced Materials* **2018**, 30, 1802732; c) R. Cai, C. Chen, *Advanced Materials* **2019**, 31, 1805740; d) C. D. Walkey, J. B. Olsen, F. Song, R. Liu, H. Guo, D. W. H. Olsen, Y. Cohen, A. Emili, W. C. W. Chan, *ACS Nano* **2014**, 8, 2439.

[310]   J. Mo, Q. Xie, W. Wei, J. Zhao, *Nature Communications* **2018**, 9, 2480.

[311]   a) A. Gessner, A. Lieske, B. R. Paulke, R. H. Müller, *European Journal of Pharmaceutics and Biopharmaceutics* **2002**, 54, 165; b) M. Jansch, *Die Pharmazie - An International Journal of Pharmaceutical Sciences* **2013**, 68, 27; c) L. C. Stoehr, E. Gonzalez, A. Stampfl, E. Casals, A. Duschl, V. Puntes, G. J. Oostingh, *Particle and Fibre Toxicology* **2011**, 8, 36; d) P. Jain, R. S. Pawar, R. S. Pandey, J. Madan, S. Pawar, P. K. Lakshmi, M. S. Sudheesh, *Biotechnology Advances* **2017**, 35, 889.

[312]   a) G. Maiorano, S. Sabella, B. Sorce, V. Brunetti, M. A. Malvindi, R. Cingolani, P. P. Pompa, *ACS Nano* **2010**, 4, 7481; b) M. M. Yallapu, N. Chauhan, S. F. Othman, V. Khalilzad-Sharghi, M. C. Ebeling, S. Khan, M. Jaggi, S. C. Chauhan, *Biomaterials* **2015**, 46, 1.

[313]   M. Mahmoudi, A. M. Abdelmonem, S. Behzadi, J. H. Clement, S. Dutz, M. R. Ejtehadi, R. Hartmann, K. Kantner, U. Linne, P. Maffre, S. Metzler, M. K. Moghadam, C. Pfeiffer, M. Rezaei, P. Ruiz-Lozano, V. Serpooshan, M. A. Shokrgozar, G. U. Nienhaus, W. J. Parak, *ACS Nano* **2013**, 7, 6555.

[314]   S. Tenzer, D. Docter, J. Kuharev, A. Musyanovych, V. Fetz, R. Hecht, F. Schlenk, D. Fischer, K. Kiouptsi, C. Reinhardt, K. Landfester, H. Schild, M. Maskos, S. K. Knauer, R. H. Stauber, *Nat Nanotechnol* **2013**, 8, 772.

[315]   a) S. Palchetti, V. Colapicchioni, L. Digiacomo, G. Caracciolo, D. Pozzi, A. L. Capriotti, G. La Barbera, A. Laganà, *Biochimica et Biophysica Acta (BBA) - Biomembranes* **2016**, 1858, 189; b) V. H. Nguyen, B.-J. Lee, *International journal of nanomedicine* **2017**, 12, 3137.

[316]   a) H. Zhang, T. Wu, W. Yu, S. Ruan, Q. He, H. Gao, *ACS Applied Materials & Interfaces* **2018**, 10, 9094; b) V. Mirshafiee, M. Mahmoudi, K. Lou, J. Cheng, M. L. Kraft, *Chemical Communications* **2013**, 49, 2557.

[317]   A. E. Nel, L. Mädler, D. Velegol, T. Xia, E. M. V. Hoek, P. Somasundaran, F. Klaessig, V. Castranova, M. Thompson, *Nature Materials* **2009**, 8, 543.

[318]   Z. J. Deng, M. Liang, M. Monteiro, I. Toth, R. F. Minchin, *Nature Nanotechnology* **2011**, 6, 39.

[319]   A. Rozmysłowska-Wojciechowska, A. Szuplewska, T. Wojciechowski, S. Poźniak, J. Mitrzak, M. Chudy, W. Ziemkowska, L. Chlubny, A. Olszyna, A. M. Jastrzębska, *Materials Science and Engineering: C* **2020**, 111, 110790.

[320]   K. Yang, Y. Li, X. Tan, R. Peng, Z. Liu, *Small* **2013**, 9, 1492.

[321]   C. Liao, Y. Li, S. C. Tjong, *International journal of molecular sciences* **2018**, 19, 3564.

[322]   M. Adabi, M. Naghibzadeh, M. Adabi, M. A. Zarrinfard, S. S. Esnaashari, A. M. Seifalian, R. Faridi-Majidi, H. Tanimowo Aiyelabegan, H. Ghanbari, *Artificial Cells, Nanomedicine, and Biotechnology* **2017**, 45, 833.

[323]   K. Wang, J. Ruan, H. Song, J. Zhang, Y. Wo, S. Guo, D. Cui, *Nanoscale research letters* **2011**, 6, 8.

[324]   M. Pelin, L. Fusco, C. Martín, S. Sosa, J. Frontiñán-Rubio, J. M. González-Domínguez, M. Durán-Prado, E. Vázquez, M. Prato, A. Tubaro, *Nanoscale* **2018**, 10, 11820.

[325]   M. Kryuchkova, A. Danilushkina, Y. Lvov, R. Fakhrullin, *Environmental Science: Nano* **2016**, 3, 442.

[326]   A. K. Gaharwar, S. M. Mihaila, A. Swami, A. Patel, S. Sant, R. L. Reis, A. P. Marques, M. E. Gomes, A. Khademhosseini, *Advanced Materials* **2013**, 25, 3329.

[327]   K. Rawat, S. Agarwal, A. Tyagi, A. K. Verma, H. B. Bohidar, *Applied Biochemistry and Biotechnology* **2014**, 174, 936.

[328]   a) M. Ghadiri, W. Chrzanowski, W. H. Lee, A. Fathi, F. Dehghani, R. Rohanizadeh, *Applied Clay Science* **2013**, 85, 64; b) M. Atrian, M. Kharaziha, R. Emadi, F. Alihosseini, *Applied Clay Science* **2019**, 174, 90.

125

[329]   C. Wang, S. Wang, K. Li, Y. Ju, J. Li, Y. Zhang, J. Li, X. Liu, X. Shi, Q. Zhao, *PLOS ONE* **2014**, 9, e99585.

[330]   X. Qian, Z. Gu, Y. Chen, *Materials Horizons* **2017**, 4, 800.

[331]   N. M. Latiff, W. Z. Teo, Z. Sofer, A. C. Fisher, M. Pumera, *Chemistry – A European Journal* **2015**, 21, 13991.

[332]   S.-J. Song, I. S. Raja, Y. B. Lee, M. S. Kang, H. J. Seo, H. U. Lee, D.-W. Han, *Biomaterials Research* **2019**, 23, 23.

[333]   A. M. Jastrzębska, A. Szuplewska, T. Wojciechowski, M. Chudy, W. Ziemkowska, L. Chlubny, A. Rozmysłowska, A. Olszyna, *Journal of Hazardous Materials* **2017**, 339, 1.

[334]   G. K. Nasrallah, M. Al-Asmakh, K. Rasool, K. A. Mahmoud, *Environmental Science: Nano* **2018**, 5, 1002.

[335]   A. Jastrzębska, A. Szuplewska, T. Wojciechowski, M. Chudy, W. Ziemkowska, L. Chlubny, A. Rozmysłowska, A. Olszyna, *Journal of hazardous materials* **2017**, 339, 1.

[336]   A. M. Jastrzębska, A. Szuplewska, A. Rozmysłowska-Wojciechowska, M. Chudy, A. Olszyna, M. Birowska, M. Popielski, J. A. Majewski, B. Scheibe, V. Natu, M. W. Barsoum, *2D Materials* **2020**, 7, 025018.

[337]   a) V. Agarwal, K. Chatterjee, *Nanoscale* **2018**, 10, 16365; b) Y. Chen, C. Tan, H. Zhang, L. Wang, *Chemical Society Reviews* **2015**, 44, 2681.

[338]   a) Z. Li, S. L. Wong, *Materials Science and Engineering: C* **2017**, 70, 1095; b) X. Li, J. Shan, W. Zhang, S. Su, L. Yuwen, L. Wang, *Small* **2017**, 13, 1602660.

[339]   T. Liu, C. Wang, X. Gu, H. Gong, L. Cheng, X. Shi, L. Feng, B. Sun, Z. Liu, **2014**, 26, 3433.

[340]   L. Chen, W. Feng, X. Zhou, K. Qiu, Y. Miao, Q. Zhang, M. Qin, L. Li, Y. Zhang, C. He, *RSC Advances* **2016**, 6, 13040.

[341]   a) M. Jedrzejczak-Silicka, M. Trukawka, M. Dudziak, K. Piotrowska, E. Mijowska, *Nanomaterials* **2018**, 8, 605; b) B. Singh, G. Kaur, P. Singh, K. Singh, B. Kumar, A. Vij, M. Kumar, R. Bala, R. Meena, A. Singh, A. Thakur, A. Kumar, *Scientific Reports* **2016**, 6, 35535.

[342]   M. Emanet, Ö. Sen, I. Ç. Taşkın, M. Çulha, *Frontiers in Bioengineering and Biotechnology* **2019**, 7.

[343]   S. Mateti, C. S. Wong, Z. Liu, W. Yang, Y. Li, L. H. Li, Y. Chen, *Nano Research* **2018**, 11, 334.

[344]   T. Lu, L. Wang, Y. Jiang, Q. liu, C. Huang, *Journal of Materials Chemistry B* **2016**, 4, 6103.

[345]   C. He, D. Liu, W. Lin, *Chemical Reviews* **2015**, 115, 11079.

[346]   Y. Li, Z. Gao, F. Chen, C. You, H. Wu, K. Sun, P. An, K. Cheng, C. Sun, X. Zhu, B. Sun, *ACS Applied Materials & Interfaces* **2018**, 10, 30930.

[347]   W. Zhu, Y. Yang, Q. Jin, Y. Chao, L. Tian, J. Liu, Z. Dong, Z. Liu, *Nano Research* **2019**, 12, 1307.

[348]   W. Zhao, J. Deng, Y. Ren, L. Xie, W. Li, Q. Wang, S. Li, S. Liu, *Nanotoxicology* **2020**, DOI: 10.1080/17435390.2020.18514201.

[349]   X. Lu, J. Ye, D. Zhang, R. Xie, R. F. Bogale, Y. Sun, L. Zhao, Q. Zhao, G. Ning, *Journal of inorganic biochemistry* **2014**, 138, 114.

[350]   Y. Zhang, S. F. Ali, E. Dervishi, Y. Xu, Z. Li, D. Casciano, A. S. Biris, *ACS nano* **2010**, 4, 3181.

[351]   W. Hu, C. Peng, M. Lv, X. Li, Y. Zhang, N. Chen, C. Fan, Q. Huang, *ACS nano* **2011**, 5, 3693.

[352]   W. Zhang, L. Yan, M. Li, R. Zhao, X. Yang, T. Ji, Z. Gu, J.-J. Yin, X. Gao, G. Nie, *Toxicology letters* **2015**, 237, 61.

[353]   L. Ding, Y. Hu, Y. Luo, J. Zhu, Y. Wu, Z. Yu, X. Cao, C. Peng, X. Shi, R. Guo, *Biomaterials Science* **2016**, 4, 474.

[354]   S. Xiao, R. Castro, D. Maciel, M. Gonçalves, X. Shi, J. Rodrigues, H. Tomás, *Materials Science and Engineering: C* **2016**, 60, 348.

[355]   B. Scheibe, J. K. Wychowaniec, M. Scheibe, B. Peplińska, M. Jarek, G. Nowaczyk, Ł. Przysiecka, *ACS Biomaterials Science & Engineering* **2019**, 5, 6557.

[356]   E. M. Scalisi, A. Salvaggio, F. Antoci, A. Messina, R. Pecoraro, M. Cantarella, G. Gorrasi, G. Impellizzeri, M. V. Brundo, *Ecotoxicology and Environmental Safety* **2020**, 200, 110772.

[357]   X. Qian, S. Shen, T. Liu, L. Cheng, Z. Liu, *Nanoscale* **2015**, 7, 6380.

[358]   H. Lin, D.-K. Ji, M. A. Lucherelli, G. Reina, S. Ippolito, P. Samorì, A. Bianco, *Small* **2020**, 16, 2002194.

126

[1]   a) L. G. Griffith, G. Naughton, *science* **2002**, 295, 1009; b) V. Mironov, T. Boland, T. Trusk, G. Forgacs, R. R. Markwald, *TRENDS in Biotechnology* **2003**, 21, 157.

[2]   P. Bajaj, R. M. Schweller, A. Khademhosseini, J. L. West, R. Bashir, *Annual Review of Biomedical Engineering* **2014**, 16, 247.

[3]   a) P. Sharma, P. Kumar, R. Sharma, V. D. Bhatt, P. Dhot, *Journal of medicine and life* **2019**, 12, 225; b) A. Haleem, M. Javaid, R. H. Khan, R. Suman, *Journal of clinical orthopaedics and trauma* **2020**, 11, S118.

[4]   S. Caddeo, M. Boffito, S. Sartori, *Frontiers in Bioengineering and Biotechnology* **2017**, 5.

[5]   a) K. H. Moon, I. K. Ko, J. J. Yoo, A. Atala, *Methods* **2016**, 99, 112; b) J. S. Uzarski, Y. Xia, J. C. Belmonte, J. A. Wertheim, *Current opinion in nephrology and hypertension* **2014**, 23, 399.

[6]   a) J. T. Shearn, K. R. Kinneberg, N. A. Dyment, M. T. Galloway, K. Kenter, C. Wylie, D. L. Butler, *Journal of musculoskeletal & neuronal interactions* **2011**, 11, 163; b) W. L. Lim, L. L. Liau, M. H. Ng, S. R. Chowdhury, J. X. Law, *Tissue engineering and regenerative medicine* **2019**, 16, 549.

[7]   a) R. N. Palchesko, S. D. Carrasquilla, A. W. Feinberg, *Advanced healthcare materials* **2018**, 7, 1701434; b) F. N. Syed-Picard, Y. Du, A. J. Hertsenberg, R. Palchesko, M. L. Funderburgh, A. W. Feinberg, J. L. Funderburgh, *Journal of tissue engineering and regenerative medicine* **2018**, 12, 59.

[8]   M. Baguneid, A. Seifalian, H. Salacinski, D. Murray, G. Hamilton, M. Walker, *British Journal of Surgery* **2006**, 93, 282.

[9]   J. Kluin, H. Talacua, A. I. Smits, M. Y. Emmert, M. C. Brugmans, E. S. Fioretta, P. E. Dijkman, S. H. Söntjens, R. Duijvelshoff, S. Dekker, *Biomaterials* **2017**, 125, 101.

[10]   D. P. Pacheco, N. S. Vargas, S. Visentin, P. Petrini, *Biomaterials Science* **2021**, 9, 70.

[11]   Y. K. Kurokawa, S. C. George, *Advanced drug delivery reviews* **2016**, 96, 225.

[12]   a) J. Malda, J. Visser, F. P. Melchels, T. Jüngst, W. E. Hennink, W. J. Dhert, J. Groll, D. W. Hutmacher, *Advanced materials* **2013**, 25, 5011; b) J. Groll, T. Boland, T. Blunk, J. A. Burdick, D.-W. Cho, P. D. Dalton, B. Derby, G. Forgacs, Q. Li, V. A. Mironov, *Biofabrication* **2016**, 8, 013001.

[13]   S. Ostrovidov, S. Salehi, M. Costantini, K. Suthiwanich, M. Ebrahimi, R. B. Sadeghian, T. Fujie, X. Shi, S. Cannata, C. Gargioli, *Small* **2019**, 15, 1805530.

[14]   B. K. Gu, D. J. Choi, S. J. Park, Y.-J. Kim, C.-H. Kim, *Cutting-Edge Enabling Technologies for Regenerative Medicine* **2018**, 15.

[15]   K. A. Deo, K. A. Singh, C. W. Peak, D. L. Alge, A. K. Gaharwar, *Tissue Engineering Part A* **2020**, 26, 318.

[16]   M. Varkey, D. O. Visscher, P. P. M. van Zuijlen, A. Atala, J. J. Yoo, *Burns & Trauma* **2019**, 7, 4.

[17]   J. Groll, J. A. Burdick, D. W. Cho, B. Derby, M. Gelinsky, S. C. Heilshorn, T. Jüngst, J. Malda, V. A. Mironov, K. Nakayama, A. Ovsianikov, W. Sun, S. Takeuchi, J. J. Yoo, T. B. F. Woodfield, *Biofabrication* **2018**, 11, 013001.

[18]   K. Dubbin, Y. Hori, K. K. Lewis, S. C. Heilshorn, *Advanced Healthcare Materials* **2016**, 5, 2488.

[19]   D. Liu, W. Nie, D. Li, W. Wang, L. Zheng, J. Zhang, J. Zhang, C. Peng, X. Mo, C. He, *Chemical Engineering Journal* **2019**, 362, 269.

[20]   H. Cui, M. Nowicki, J. P. Fisher, L. G. Zhang, *Advanced healthcare materials* **2017**, 6, 1601118.

[21]   a) T. H. Jovic, G. Kungwengwe, A. C. Mills, I. S. Whitaker, *Frontiers in Mechanical Engineering* **2019**, 5; b) P. S. Gungor-Ozkerim, I. Inci, Y. S. Zhang, A. Khademhosseini, M. R. Dokmeci, *Biomaterials Science* **2018**, 6, 915.

[22]   Y.-J. Seol, H.-W. Kang, S. J. Lee, A. Atala, J. J. Yoo, *European Journal of Cardio-Thoracic Surgery* **2014**, 46, 342.

[23]   R. Lozano, L. Stevens, B. C. Thompson, K. J. Gilmore, R. Gorkin III, E. M. Stewart, M. in het Panhuis, M. Romero-Ortega, G. G. Wallace, *Biomaterials* **2015**, 67, 264.

[24]   a) K. Zhu, N. Chen, X. Liu, X. Mu, W. Zhang, C. Wang, Y. S. Zhang, *Macromolecular Bioscience* **2018**, 18, 1800127; b) W. Liu, Z. Zhong, N. Hu, Y. Zhou, L. Maggio, A. K. Miri, A. Fragasso, X. Jin, A. Khademhosseini, Y. S. Zhang, *Biofabrication* **2018**, 10, 024102; c) K. Markstedt, A. Mantas, I. Tournier, H. Martínez Ávila, D. Hägg, P. Gatenholm, *Biomacromolecules* **2015**, 16, 1489; d) J. Yin, M. Yan, Y. Wang, J. Fu, H. Suo, *ACS applied materials & interfaces* **2018**, 10, 6849.

[25]   a) A. M. Compaan, K. Christensen, Y. Huang, *ACS Biomaterials Science & Engineering* **2017**, 3, 1519; b) L. H. Solis, Y. Ayala, S. Portillo, A. Varela-Ramirez, R. Aguilera, T. Boland, *Biofabrication* **2019**, 11, 045005; c) C. Xu, W. Chai, Y. Huang, R. R. Markwald, *Biotechnology and Bioengineering* **2012**, 109, 3152.

[26]   a) J. A. Barron, P. Wu, H. D. Ladouceur, B. R. Ringeisen, *Biomedical Microdevices* **2004**, 6, 139; b) B. Guillotin, A. Souquet, S. Catros, M. Duocastella, B. Pippenger, S. Bellance, R. Bareille, M. Rémy, L. Bordenave, J. Amédée, *Biomaterials* **2010**, 31, 7250; c) V. Keriquel, H. Oliveira, M. Rémy, S. Ziane, S. Delmond, B. Rousseau, S. Rey, S. Catros, J. Amédée, F. Guillemot, *Scientific reports* **2017**, 7, 1.

[27]   a) Z. Wang, R. Abdulla, B. Parker, R. Samanipour, S. Ghosh, K. Kim, *Biofabrication* **2015**, 7, 045009; b) Z. Wang, H. Kumar, Z. Tian, X. Jin, J. F. Holzman, F. Menard, K. Kim, *ACS applied materials & interfaces* **2018**, 10, 26859; c) R. Raman, R. Bashir, in *Essentials of 3D Biofabrication and Translation*, Elsevier **2015**, p. 89.

[28]   K. Hölzl, S. Lin, L. Tytgat, S. Van Vlierberghe, L. Gu, A. Ovsianikov, *Biofabrication* **2016**, 8, 032002.

[29]   W. Peng, D. Unutmaz, I. T. Ozbolat, *Trends in biotechnology* **2016**, 34, 722.

[30]   I. T. Ozbolat, M. Hospodiuk, *Biomaterials* **2016**, 76, 321.

[31]   a) C. C. Chang, E. D. Boland, S. K. Williams, J. B. Hoying, *Journal of Biomedical Materials Research Part B: Applied Biomaterials* **2011**, 98B, 160; b) K. Nair, M. Gandhi, S. Khalil, K. C. Yan, M. Marcolongo, K. Barbee, W. Sun, *Biotechnology Journal* **2009**, 4, 1168; c) F. P. Melchels, W. J. Dhert, D. W. Hutmacher, J. Malda, *Journal of Materials Chemistry B* **2014**, 2, 2282; d) M. Hospodiuk, M. Dey, D. Sosnoski, I. T. Ozbolat, *Biotechnology Advances* **2017**, 35, 217.

[32]   D. Chimene, K. K. Lennox, R. R. Kaunas, A. K. Gaharwar, *Annals of biomedical engineering* **2016**, 44, 2090.

[33]   a) P. T. Smith, A. Basu, A. Saha, A. Nelson, *Polymer* **2018**; b) N. Paxton, W. Smolan, T. Böck, F. Melchels, J. Groll, T. Jungst, *Biofabrication* **2017**, 9, 044107.

[34]   L. Ouyang, C. B. Highley, C. B. Rodell, W. Sun, J. A. Burdick, *ACS Biomaterials Science & Engineering* **2016**, 2, 1743.

[35]   a) S. A. Wilson, L. M. Cross, C. W. Peak, A. K. Gaharwar, *ACS applied materials & interfaces* **2017**, 9, 43449; b) D. Chimene, L. Miller, L. M. Cross, M. K. Jaiswal, I. Singh, A. K. Gaharwar, *ACS Applied Materials & Interfaces* **2020**, 12, 15976.

[36]   a) I. T. Ozbolat, H. Chen, Y. Yu, *Robotics and Computer-Integrated Manufacturing* **2014**, 30, 295; b) R. Attalla, E. Puersten, N. Jain, P. R. Selvaganapathy, *Biofabrication* **2018**, 11, 015012; c) L. Ruiz-Cantu, A. Gleadall, C. Faris, J. Segal, K. Shakesheff, J. Yang, *Materials Science and Engineering: C* **2020**, 109, 110578.

[37]   I. T. Ozbolat, H. Chen, Y. Yu, *Robotics and Computer-Integrated Manufacturing* **2014**, 30, 295.

[38]   W. Liu, Y. S. Zhang, M. A. Heinrich, F. De Ferrari, H. L. Jang, S. M. Bakht, M. M. Alvarez, J. Yang, Y. C. Li, G. Trujillo-de Santiago, *Advanced Materials* **2017**, 29, 1604630.

[39]   *Tissue Engineering Part A* **2008**, 14, 41.

[40]   J. Li, M. Chen, X. Fan, H. Zhou, *J Transl Med* **2016**, 14, 271.

[41]   I. N. Aguilar, L. J. Smith, D. J. Olivos, T.-M. G. Chu, M. A. Kacena, D. R. Wagner, *Bioprinting* **2019**, 15, e00048.

[42]   a) M. Nakamura, A. Kobayashi, F. Takagi, A. Watanabe, Y. Hiruma, K. Ohuchi, Y. Iwasaki, M. Horie, I. Morita, S. Takatani, *Tissue engineering* **2005**, 11, 1658; b) T. Boland, T. Xu, B. Damon, X. Cui, *Biotechnology Journal: Healthcare Nutrition Technology* **2006**, 1, 910.

[43]   T. Xu, W. Zhao, J.-M. Zhu, M. Z. Albanna, J. J. Yoo, A. Atala, *Biomaterials* **2013**, 34, 130.

[44]   R. Zimmermann, C. Hentschel, F. Schrön, D. Moedder, T. Büttner, P. Atallah, T. Wegener, T. Gehring, S. Howitz, U. Freudenberg, C. Werner, *Biofabrication* **2019**, 11, 045008.

[45]   H. Gudapati, M. Dey, I. Ozbolat, *Biomaterials* **2016**, 102, 20.

[46]   a) M. S. Onses, E. Sutanto, P. M. Ferreira, A. G. Alleyne, J. A. Rogers, *Small* **2015**, 11, 4237; b) S. N. Jayasinghe, A. N. Qureshi, P. A. Eagles, *Small* **2006**, 2, 216.

[47]   a) Z. Zheng, D. Eglin, M. Alini, G. R. Richards, L. Qin, Y. Lai, *Engineering* **2020**, DOI: https://doi.org/10.1016/j.eng.2020.05.021; b) B. K. Gu, D. J. Choi, S. J. Park, M. S. Kim, C. M. Kang, C.-H. Kim, *Biomaterials research* **2016**, 20, 12; c) N. E. Sanjana, S. B. Fuller, *Journal of neuroscience methods* **2004**, 136, 151.

[48]   a) L. Gasperini, D. Maniglio, A. Motta, C. Migliaresi, *Tissue engineering part C: Methods* **2015**, 21, 123; b) C. Xu, W. Chai, Y. Huang, R. R. Markwald, *Biotechnology and bioengineering* **2012**, 109, 3152.

[49]   A. Blaeser, D. F. Duarte Campos, M. Weber, S. Neuss, B. Theek, H. Fischer, W. Jahnen-Dechent, *BioResearch open access* **2013**, 2, 374.

[50]   a) *Tissue Engineering Part A* **2012**, 18, 1304; b) U. A. Gurkan, R. El Assal, S. E. Yildiz, Y. Sung, A. J. Trachtenberg, W. P. Kuo, U. Demirci, *Molecular Pharmaceutics* **2014**, 11, 2151.

[51]   Y.-B. Lee, S. Polio, W. Lee, G. Dai, L. Menon, R. S. Carroll, S.-S. Yoo, *Experimental Neurology* **2010**, 223, 645.

[52]   A. GhavamiNejad, N. Ashammakhi, X. Y. Wu, A. Khademhosseini, *Small* **2020**, 16, 2002931.

[53]   G. Gao, T. Yonezawa, K. Hubbell, G. Dai, X. Cui, *Biotechnology Journal* **2015**, 10, 1568.

[54]   a) C. J. Ferris, K. J. Gilmore, S. Beirne, D. McCallum, G. G. Wallace, M. in het Panhuis, *Biomaterials Science* **2013**, 1, 224; b) M. E. Pepper, V. Seshadri, T. C. Burg, K. J. L. Burg, R. E. Groff, *Biofabrication* **2012**, 4, 011001.

[55]   X. Li, B. Liu, B. Pei, J. Chen, D. Zhou, J. Peng, X. Zhang, W. Jia, T. Xu, *Chemical Reviews* **2020**, 120, 10793.

[56]   T. Xu, C. A. Gregory, P. Molnar, X. Cui, S. Jalota, S. B. Bhaduri, T. Boland, *Biomaterials* **2006**, 27, 3580.

[57]   a) D. J. Odde, M. J. Renn, *Trends in biotechnology* **1999**, 17, 385; b) J. A. Barron, B. R. Ringeisen, H. Kim, B. J. Spargo, D. B. Chrisey, *Thin Solid Films* **2004**, 453, 383.

[58]   a) C. Mandrycky, Z. Wang, K. Kim, D.-H. Kim, *Biotechnology Advances* **2016**, 34, 422; b) F. Guillemot, A. Souquet, S. Catros, B. Guillotin, J. Lopez, M. Faucon, B. Pippenger, R. Bareille, M. Rémy, S. Bellance, P. Chabassier, J. C. Fricain, J. Amédée, *Acta Biomaterialia* **2010**, 6, 2494.

[59]   S. Michael, H. Sorg, C.-T. Peck, L. Koch, A. Deiwick, B. Chichkov, P. M. Vogt, K. Reimers, *PloS one* **2013**, 8, e57741.

[60]   S. Catros, B. Guillotin, M. Bačáková, J.-C. Fricain, F. Guillemot, *Applied Surface Science* **2011**, 257, 5142.

[61]   F. Guillemot, A. Souquet, S. Catros, B. Guillotin, *Nanomedicine* **2010**, 5, 507.

[62]   a) D. Hakobyan, C. Médina, N. Dusserre, M.-L. Stachowicz, C. Handschin, J.-C. Fricain, J. Guillermet-Guibert, H. Oliveira, *Biofabrication* **2020**, 12, 035001; b) M. Ali, E. Pages, A. Ducom, A. Fontaine, F. Guillemot, *Biofabrication* **2014**, 6, 045001.

[63]   M. A. Heinrich, W. Liu, A. Jimenez, J. Yang, A. Akpek, X. Liu, Q. Pi, X. Mu, N. Hu, R. M. Schiffelers, *Small* **2019**, 15, 1805510.

[64]   N. Poomathi, S. Singh, C. Prakash, V. Patil Rajkumar, P. T. Perumal, A. Barathi Veluchamy, K. Balasubramanian Kalpattu, S. Ramakrishna, N. U. Maheshwari, *Rapid Prototyping Journal* **2019**, 25, 496.

[65]   J. T. Huh, J. J. Yoo, A. Atala, S. J. Lee, in *Principles of Tissue Engineering (Fifth Edition)*, DOI: https://doi.org/10.1016/B978-0-12-818422-6.00076-9 (Eds: R. Lanza, R. Langer, J. P. Vacanti, A. Atala), Academic Press **2020**, p. 1391.

[66]   a) B. Hopp, T. Smausz, G. Szabó, L. Kolozsvari, A. Nogradi, D. Kafetzopoulos, C. Fotakis, *Optical Engineering* **2012**, 51, 014302; b) H. Gudapati, J. Yan, Y. Huang, D. B. Chrisey, *Biofabrication* **2014**, 6, 035022.

[67]   L. Koch, S. Kuhn, H. Sorg, M. Gruene, S. Schlie, R. Gaebel, B. Polchow, K. Reimers, S. Stoelting, N. Ma, *Tissue Engineering Part C: Methods* **2010**, 16, 847.

[68]   a) Z. Yue, X. Liu, P. T. Coates, G. G. Wallace, *Current opinion in organ transplantation* **2016**, 21, 467; b) R. Raman, R. Bashir, in *Essentials of 3D Biofabrication and Translation*, DOI: https://doi.org/10.1016/B978-0-12-800972-7.00006-2 (Eds: A. Atala, J. J. Yoo), Academic Press, Boston **2015**, p. 89.

[69]   a) S. Zakeri, M. Vippola, E. Levänen, *Additive Manufacturing* **2020**, 35, 101177; b) F. P. Melchels, K. Bertoldi, R. Gabbrielli, A. H. Velders, J. Feijen, D. W. Grijpma, *Biomaterials* **2010**, 31, 6909.

[70]   a) J.-W. Choi, R. Wicker, S.-H. Lee, K.-H. Choi, C.-S. Ha, I. Chung, *Journal of Materials Processing Technology* **2009**, 209, 5494; b) T. Chartier, A. Badev, Y. Abouliatim, P. Lebaudy, L. Lecamp, *Journal of the European Ceramic Society* **2012**, 32, 1625.

[71]   F. P. W. Melchels, J. Feijen, D. W. Grijpma, *Biomaterials* **2010**, 31, 6121.

[72]   R. P. Sinha, D.-P. Häder, *Photochemical & Photobiological Sciences* **2002**, 1, 225.

[73]   a) A. K. Au, W. Lee, A. Folch, *Lab on a Chip* **2014**, 14, 1294; b) R. Zhang, N. B. Larsen, *Lab on a Chip* **2017**, 17, 4273.

[74]   a) S. Knowlton, B. Yenilmez, S. Tasoglu, *Trends in Biotechnology* **2016**, 34, 685; b) A. P. Kuo, N. Bhattacharjee, Y. S. Lee, K. Castro, Y. T. Kim, A. Folch, *Advanced materials technologies* **2019**, 4, 1800395.

[75]   Y. S. Zhang, A. Khademhosseini, *Science* **2017**, 356.

[76]   H. Li, C. Tan, L. Li, *Materials & Design* **2018**, 159, 20.

[77]   J. M. Unagolla, A. C. Jayasuriya, *Applied Materials Today* **2020**, 18, 100479.

[78]   S. Heid, A. R. Boccaccini, *Acta Biomaterialia* **2020**, 113, 1.

[79]   K. Varaprasad, G. M. Raghavendra, T. Jayaramudu, M. M. Yallapu, R. Sadiku, *Materials Science and Engineering: C* **2017**, 79, 958.

[80]   W. Hu, Z. Wang, Y. Xiao, S. Zhang, J. Wang, *Biomaterials science* **2019**, 7, 843.

[81]   M. Mahinroosta, Z. J. Farsangi, A. Allahverdi, Z. Shakoori, *Materials today chemistry* **2018**, 8, 42.

[82]   E. Caló, V. V. Khutoryanskiy, *European Polymer Journal* **2015**, 65, 252.

[83]   M. C. Catoira, L. Fusaro, D. Di Francesco, M. Ramella, F. Boccafoschi, *Journal of Materials Science: Materials in Medicine* **2019**, 30, 115.

[84]   J. Li, C. Wu, P. K. Chu, M. Gelinsky, *Materials Science and Engineering: R: Reports* **2020**, 140, 100543.

[85]   P. Jaipan, A. Nguyen, R. J. Narayan, *MRS Communications* **2017**, 7, 416.

[86]   K. Su, C. Wang, *Biotechnology letters* **2015**, 37, 2139.

[87]   A. I. Van Den Bulcke, B. Bogdanov, N. De Rooze, E. H. Schacht, M. Cornelissen, H. Berghmans, *Biomacromolecules* **2000**, 1, 31.

[88]   K. Yue, G. Trujillo-de Santiago, M. M. Alvarez, A. Tamayol, N. Annabi, A. Khademhosseini, *Biomaterials* **2015**, 73, 254.

[89]   Z. Dong, Q. Yuan, K. Huang, W. Xu, G. Liu, Z. Gu, *RSC Advances* **2019**, 9, 17737.

[90]   a) F. E. Freeman, D. J. Kelly, *Scientific Reports* **2017**, 7, 17042; b) E. Axpe, M. L. Oyen, *International journal of molecular sciences* **2016**, 17, 1976; c) M. D. Giuseppe, N. Law, B. Webb, R. A. Macrae, L. J. Liew, T. B. Sercombe, R. J. Dilley, B. J. Doyle, *Journal of the Mechanical Behavior of Biomedical Materials* **2018**, 79, 150.

[91]   a) J. Lewicki, J. Bergman, C. Kerins, O. Hermanson, *Bioprinting* **2019**, 16, e00053; b) M. Alruwaili, J. A. Lopez, K. McCarthy, E. G. Reynaud, B. J. Rodriguez, *Bio-Design and Manufacturing* **2019**, 2, 172.

[92]   M. L. Bedell, A. M. Navara, Y. Du, S. Zhang, A. G. Mikos, *Chemical Reviews* **2020**.

[93]   N. Contessi, L. Altomare, A. Filipponi, S. Farè, *Materials Letters* **2017**, 207, 157.

[94]   C. Chang, L. Zhang, *Carbohydrate polymers* **2011**, 84, 40.

[95]   N. Contessi Negrini, L. Bonetti, L. Contili, S. Farè, *Bioprinting* **2018**, 10, e00024.

[96]   K. Schütz, A. M. Placht, B. Paul, S. Brüggemeier, M. Gelinsky, A. Lode, *Journal of tissue engineering and regenerative medicine* **2017**, 11, 1574.

[97]   a) S. Liu, L. Li, *ACS applied materials & interfaces* **2016**, 8, 29749; b) Y. Yuguchi, H. Urakawa, K. Kajiwara, *Food Hydrocolloids* **2003**, 17, 481.

[98]   a) S. Liu, W. L. Chan, L. Li, *Macromolecules* **2015**, 48, 7649; b) S. M. Mihaila, A. K. Gaharwar, R. L. Reis, A. P. Marques, M. E. Gomes, A. Khademhosseini, *Advanced healthcare materials* **2013**, 2, 895.

[99]   a) S. Liu, S. Huang, L. Li, *Journal of Rheology* **2016**, 60, 203; b) D. Chimene, C. W. Peak, J. L. Gentry, J. K. Carrow, L. M. Cross, E. Mondragon, G. B. Cardoso, R. Kaunas, A. K. Gaharwar, *ACS applied materials & interfaces* **2018**, 10, 9957.

[100]   a) S. H. Park, J. Y. Seo, J. Y. Park, Y. B. Ji, K. Kim, H. S. Choi, S. Choi, J. H. Kim, B. H. Min, M. S. Kim, *NPG Asia Materials* **2019**, 11, 1; b) M. F. Graça, S. P. Miguel, C. S. Cabral, I. J. Correia, *Carbohydrate Polymers* **2020**, 116364.

[101]   a) M. T. Poldervaart, B. Goversen, M. De Ruijter, A. Abbadessa, F. P. Melchels, F. C. Öner, W. J. Dhert, T. Vermonden, J. Alblas, *PLoS One* **2017**, 12, e0177628; b) I. Noh, N. Kim, H. N. Tran, J. Lee, C. Lee, *Biomaterials research* **2019**, 23, 1.

[102]   H. Si, T. Xing, Y. Ding, H. Zhang, R. Yin, W. Zhang, *Polymers* **2019**, 11, 1584.

[103]   I. Donderwinkel, J. C. M. van Hest, N. R. Cameron, *Polymer Chemistry* **2017**, 8, 4451.

[104]   L. Valot, J. Martinez, A. Mehdi, G. Subra, *Chemical Society Reviews* **2019**, 48, 4049.

[105]   a) W. Schuurman, P. A. Levett, M. W. Pot, P. R. van Weeren, W. J. Dhert, D. W. Hutmacher, F. P. Melchels, T. J. Klein, J. Malda, *Macromolecular bioscience* **2013**, 13, 551; b) J. M. Townsend, E. C. Beck, S. H. Gehrke, C. J. Berkland, M. S. Detamore, *Progress in Polymer Science* **2019**, 91, 126.

[106]   a) M. Chopin-Doroteo, E. A. Mandujano-Tinoco, E. Krötzsch, *Biochimica et Biophysica Acta (BBA) - General Subjects* **2021**, 1865, 129782; b) O. Chaudhuri, L. Gu, D. Klumpers, M. Darnell, S. A. Bencherif, J. C. Weaver, N. Huebsch, H.-p. Lee, E. Lippens, G. N. Duda, D. J. Mooney, *Nature Materials* **2016**, 15, 326.

[107] a) Y. Chen, X. Xiong, X. Liu, R. Cui, C. Wang, G. Zhao, W. Zhi, M. Lu, K. Duan, J. Weng, *Journal of Materials Chemistry B* **2020**, 8, 5500; b) A. Parak, P. Pradeep, L. C. du Toit, P. Kumar, Y. E. Choonara, V. Pillay, *Drug discovery today* **2019**, 24, 198.

[108] a) J. H. Chung, S. Naficy, Z. Yue, R. Kapsa, A. Quigley, S. E. Moulton, G. G. Wallace, *Biomaterials Science* **2013**, 1, 763; b) H. Rastin, R. T. Ormsby, G. J. Atkins, D. Losic, *ACS Applied Bio Materials* **2020**, 3, 1815.

[109] Y. Zhao, Y. Li, S. Mao, W. Sun, R. Yao, *Biofabrication* **2015**, 7, 045002.

[110] M. Mehrali, A. Thakur, C. P. Pennisi, S. Talebian, A. Arpanaei, M. Nikkhah, A. Dolatshahi-Pirouz, *Advanced Materials* **2017**, 29, 1603612.

[111] P. A. Amorim, M. A. d'Ávila, R. Anand, P. Moldenaers, P. Van Puyvelde, V. Bloemen, *Bioprinting* **2021**, 22, e00129.

[112] J. L. Dávila, M. A. d'Ávila, *The International Journal of Advanced Manufacturing Technology* **2019**, 101, 675.

[113] E. A. Kiyotake, A. W. Douglas, E. E. Thomas, S. L. Nimmo, M. S. Detamore, *Acta Biomaterialia* **2019**, 95, 176.

[114] a) L. Ghasemi-Mobarakeh, M. P. Prabhakaran, M. Morshed, M. H. Nasr-Esfahani, H. Baharvand, S. Kiani, S. S. Al-Deyab, S. Ramakrishna, *Journal of Tissue Engineering and Regenerative Medicine* **2011**, 5, e17; b) N. Li, Q. Zhang, S. Gao, Q. Song, R. Huang, L. Wang, L. Liu, J. Dai, M. Tang, G. Cheng, *Scientific Reports* **2013**, 3, 1604; c) B. Guo, P. X. Ma, *Biomacromolecules* **2018**, 19, 1764.

[115] a) N. Zanjanizadeh Ezazi, M.-A. Shahbazi, Y. V. Shatalin, E. Nadal, E. Mäkilä, J. Salonen, M. Kemell, A. Correia, J. Hirvonen, H. A. Santos, *International Journal of Pharmaceutics* **2018**, 536, 241; b) G. L. Mario Cheong, K. S. Lim, A. Jakubowicz, P. J. Martens, L. A. Poole-Warren, R. A. Green, *Acta Biomaterialia* **2014**, 10, 1216.

[116] a) K. Cysewska, J. Karczewski, P. Jasiński, *Measurement Science and Technology* **2017**, 28, 074004; b) R. Ravichandran, J. G. Martinez, E. W. H. Jager, J. Phopase, A. P. F. Turner, *ACS Applied Materials & Interfaces* **2018**, 10, 16244.

[117] a) H. Rastin, B. Zhang, A. Mazinani, K. Hassan, J. Bi, T. T. Tung, D. Losic, *Nanoscale* **2020**; b) A. E. Jakus, E. B. Secor, A. L. Rutz, S. W. Jordan, M. C. Hersam, R. N. Shah, *ACS Nano* **2015**, 9, 4636.

[118] S.-J. Lee, W. Zhu, M. Nowicki, G. Lee, D. N. Heo, J. Kim, Y. Y. Zuo, L. G. Zhang, *Journal of Neural Engineering* **2018**, 15, 016018.

[119] a) T. Distler, A. R. Boccaccini, *Acta biomaterialia* **2020**, 101, 1; b) S. S. Athukorala, T. S. Tran, R. Balu, V. K. Truong, J. Chapman, N. K. Dutta, N. Roy Choudhury, *Polymers* **2021**, 13, 474.

[120] H. Qing, Y. Ji, W. Li, G. Zhao, Q. Yang, X. Zhang, Z. Luo, T. J. Lu, G. Jin, F. Xu, *ACS Applied Materials & Interfaces* **2020**, 12, 2049.

[121] S. Sayyar, M. Bjorninen, S. Haimi, S. Miettinen, K. Gilmore, D. Grijpma, G. Wallace, *ACS Applied Materials & Interfaces* **2016**, 8, 31916.

[122] a) L. Zhao, P. K. Chu, Y. Zhang, Z. Wu, *Journal of Biomedical Materials Research Part B: Applied Biomaterials* **2009**, 91, 470; b) S. Li, S. Dong, W. Xu, S. Tu, L. Yan, C. Zhao, J. Ding, X. Chen, *Advanced science* **2018**, 5, 1700527.

[123] J. Hoque, B. Bhattacharjee, R. G. Prakash, K. Paramanandham, J. Haldar, *Biomacromolecules* **2018**, 19, 267.

[124] M. C. Giano, Z. Ibrahim, S. H. Medina, K. A. Sarhane, J. M. Christensen, Y. Yamada, G. Brandacher, J. P. Schneider, *Nature communications* **2014**, 5, 1.

[125] a) S. Wang, H. Zheng, L. Zhou, F. Cheng, Z. Liu, H. Zhang, L. Wang, Q. Zhang, *Nano Letters* **2020**, 20, 5149; b) Y. Zhong, H. Xiao, F. Seidi, Y. Jin, *Biomacromolecules* **2020**, 21, 2983.

[126] D. Campoccia, L. Montanaro, C. R. Arciola, *Biomaterials* **2006**, 27, 2331.

[127] a) L. Mei, S. Zhu, W. Yin, C. Chen, G. Nie, Z. Gu, Y. Zhao, *Theranostics* **2020**, 10, 757; b) Q. Wu, M. Liang, S. Zhang, X. Liu, F. Wang, *Nanoscale* **2018**, 10, 10428.

[128] Y. Zhang, D. Zhai, M. Xu, Q. Yao, H. Zhu, J. Chang, C. Wu, *Biofabrication* **2017**, 9, 025037.

[129] S. F. Melo, S. C. Neves, A. T. Pereira, I. Borges, P. L. Granja, F. D. Magalhães, I. C. Gonçalves, *Materials Science and Engineering: C* **2020**, 109, 110537.

[130] E. S. Place, J. H. George, C. K. Williams, M. M. Stevens, *Chemical Society Reviews* **2009**, 38, 1139.

[131] a) C. Gardin, A. Piattelli, B. Zavan, *Trends in Biotechnology* **2016**, 34, 435; b) S. R. Shin, Y.-C. Li, H. L. Jang, P. Khoshakhlagh, M. Akbari, A. Nasajpour, Y. S. Zhang, A. Tamayol, A. Khademhosseini, *Advanced Drug Delivery Reviews* **2016**, 105, 255; c) S. Kumar, K. Chatterjee, *ACS applied materials & interfaces* **2016**, 8, 26431.

[132] X. Zhou, M. Nowicki, H. Cui, W. Zhu, X. Fang, S. Miao, S.-J. Lee, M. Keidar, L. G. Zhang, *Carbon* **2017**, 116, 615.

[133] Z. Cheng, B. Landish, Z. Chi, C. Nannan, D. Jingyu, L. Sen, L. Xiangjin, *Materials Science and Engineering: C* **2018**, 82, 244.

[134] G. Choe, S. Oh, J. M. Seok, S. A. Park, J. Y. Lee, *Nanoscale* **2019**, 11, 23275.

[135] a) A. L. Rutz, E. S. Gargus, K. E. Hyland, P. L. Lewis, A. Setty, W. R. Burghardt, R. N. Shah, *Acta Biomaterialia* **2019**, 99, 121; b) J. Jang, T. G. Kim, B. S. Kim, S.-W. Kim, S.-M. Kwon, D.-W. Cho, *Acta Biomaterialia* **2016**, 33, 88.

[136] L. M. Guiney, N. D. Mansukhani, A. E. Jakus, S. G. Wallace, R. N. Shah, M. C. Hersam, *Nano letters* **2018**, 18, 3488.

[137] D. Aki, S. Ulag, S. Unal, M. Sengor, N. Ekren, C.-C. Lin, H. Yılmazer, C. B. Ustundag, D. M. Kalaskar, O. Gunduz, *Materials & Design* **2020**, 196, 109094.

[138] H. Belaid, S. Nagarajan, C. Barou, V. Huon, J. Bares, S. Balme, P. Miele, D. Cornu, V. Cavaillès, C. Teyssier, *ACS Applied Bio Materials* **2020**, 3, 1865.

[139] G. Turnbull, J. Clarke, F. Picard, P. Riches, L. Jia, F. Han, B. Li, W. Shu, *Bioactive Materials* **2018**, 3, 278.

[140] D. Petta, A. Armiento, D. Grijpma, M. Alini, D. Eglin, M. D'Este, *Biofabrication* **2018**, 10, 044104.

[141] L. Ouyang, *Study on Microextrusion-based 3D Bioprinting and Bioink Crosslinking Mechanisms*, Springer, **2019**.

[142] J. Y. Shin, Y. H. Yeo, J. E. Jeong, S. A. Park, W. H. Park, *Carbohydrate polymers* **2020**, 238, 116192.

[143] H. Rastin, M. Ramezanpour, K. Hassan, A. Mazinani, T. T. Tung, S. Vreugde, D. Losic, *Carbohydrate Polymers* **2021**, DOI: https://doi.org/10.1016/j.carbpol.2021.117989117989.

[144] J. Koffler, W. Zhu, X. Qu, O. Platoshyn, J. N. Dulin, J. Brock, L. Graham, P. Lu, J. Sakamoto, M. Marsala, S. Chen, M. H. Tuszynski, *Nature Medicine* **2019**, 25, 263.

[145] L. E. Bertassoni, J. C. Cardoso, V. Manoharan, A. L. Cristino, N. S. Bhise, W. A. Araujo, P. Zorlutuna, N. E. Vrana, A. M. Ghaemmaghami, M. R. Dokmeci, A. Khademhosseini, *Biofabrication* **2014**, 6, 024105.

[146] I. Noshadi, S. Hong, K. E. Sullivan, E. S. Sani, R. Portillo-Lara, A. Tamayol, S. R. Shin, A. E. Gao, W. L. Stoppel, L. D. Black III, *Biomaterials science* **2017**, 5, 2093.

[147] S. V. Murphy, A. Atala, *Nature biotechnology* **2014**, 32, 773.

[148] a) A. J. Engler, S. Sen, H. L. Sweeney, D. E. Discher, *Cell* **2006**, 126, 677; b) F. Guilak, D. M. Cohen, B. T. Estes, J. M. Gimble, W. Liedtke, C. S. Chen, *Cell Stem Cell* **2009**, 5, 17.

[149] Z. Zhang, Y. Jin, J. Yin, C. Xu, R. Xiong, K. Christensen, B. R. Ringeisen, D. B. Chrisey, Y. Huang, *Applied Physics Reviews* **2018**, 5, 041304.

[150] G. Gillispie, P. Prim, J. Copus, J. Fisher, A. G. Mikos, J. J. Yoo, A. Atala, S. J. Lee, *Biofabrication* **2020**, 12, 022003.

[151] A. Schwab, R. Levato, M. D'Este, S. Piluso, D. Eglin, J. Malda, *Chemical Reviews* **2020**, 120, 11028.

[152] *Tissue Engineering Part A* **2020**, 26, 318.

[153] a) A. Blaeser, D. F. Duarte Campos, U. Puster, W. Richtering, M. M. Stevens, H. Fischer, *Advanced healthcare materials* **2016**, 5, 326; b) W. Sun, B. Starly, A. C. Daly, J. A. Burdick, J. Groll, G. Skeldon, W. Shu, Y. Sakai, M. Shinohara, M. Nishikawa, J. Jang, D.-W. Cho, M. Nie, S. Takeuchi, S. Ostrovidov, A. Khademhosseini, R. D. Kamm, V. Mironov, L. Moroni, I. T. Ozbolat, *Biofabrication* **2020**, 12, 022002.

[154] R. L. Smith, D. R. Carter, D. J. Schurman, *Clinical Orthopaedics and Related Research (1976-2007)* **2004**, 427, S89.

[155] F. Zhao, R. Chella, T. Ma, *Biotechnology and bioengineering* **2007**, 96, 584.

[156] D. E. Discher, P. Janmey, Y.-l. Wang, *Science* **2005**, 310, 1139.

[157] M. Li, X. Tian, D. J. Schreyer, X. Chen, *Biotechnology Progress* **2011**, 27, 1777.

[158] P. Bianchi, G. Petit, J.-C. M. Monbaliu, *Reaction Chemistry & Engineering* **2020**, 5, 1224.

[159] a) K. Jakab, C. Norotte, F. Marga, K. Murphy, G. Vunjak-Novakovic, G. Forgacs, *Biofabrication* **2010**, 2, 022001; b) A. L. Rutz, K. E. Hyland, A. E. Jakus, W. R. Burghardt, R. N. Shah, *Advanced Materials* **2015**, 27, 1607; c) H.-W. Kang, S. J. Lee, I. K. Ko, C. Kengla, J. J. Yoo, A. Atala, *Nature Biotechnology* **2016**, 34, 312.

[160] J. A. Rowley, G. Madlambayan, D. J. Mooney, *Biomaterials* **1999**, 20, 45.

[161] B. Duan, E. Kapetanovic, L. A. Hockaday, J. T. Butcher, *Acta Biomaterialia* **2014**, 10, 1836.

[162] C. Sears, E. Mondragon, Z. I. Richards, N. Sears, D. Chimene, E. P. McNeill, C. A. Gregory, A. K. Gaharwar, R. Kaunas, *Advanced Healthcare Materials* **2020**, 9, 1901580.

[163] J. M. Lee, W. Y. Yeong, *Advanced healthcare materials* **2016**, 5, 2856.

[164] a) S. Hong, D. Sycks, H. F. Chan, S. Lin, G. P. Lopez, F. Guilak, K. W. Leong, X. Zhao, *Advanced materials* **2015**, 27, 4035; b) T. Cebe, N. Ahuja, F. Monte, K. Awad, K. Vyavhare, P. Aswath, J. Huang, M. Brotto, V. Varanasi, *Journal of Materials Research* **2020**, 35, 58; c) C. W. Peak, J. Stein, K. A. Gold, A. K. Gaharwar, *Langmuir* **2018**, 34, 917; d) A. Nadernezhad, O. S. Caliskan, F. Topuz, F. Afghah, B. Erman, B. Koc, *ACS Applied Bio Materials* **2019**, 2, 796.

[165] a) Y. M. Joshi, G. R. K. Reddy, A. L. Kulkarni, N. Kumar, R. P. Chhabra, *Proceedings of the Royal Society A: Mathematical, Physical and Engineering Sciences* **2008**, 464, 469; b) J. L. Dávila, M. A. d'Ávila, *Carbohydrate polymers* **2017**, 157, 1.

[166] D. W. Thompson, J. T. Butterworth, *Journal of Colloid and Interface Science* **1992**, 151, 236.

[167] B. Ruzicka, E. Zaccarelli, *Soft Matter* **2011**, 7, 1268.

[168] C. B. Highley, C. B. Rodell, J. A. Burdick, *Advanced Materials* **2015**, 27, 5075.

[169] G. Cidonio, C. R. Alcala-Orozco, K. S. Lim, M. Glinka, I. Mutreja, Y.-H. Kim, J. I. Dawson, T. B. Woodfield, R. O. Oreffo, *Biofabrication* **2019**, 11, 035027.

[170] G. Lokhande, J. K. Carrow, T. Thakur, J. R. Xavier, M. Parani, K. J. Bayless, A. K. Gaharwar, *Acta Biomaterialia* **2018**, 70, 35.

[171] B. Liu, J. Li, X. Lei, P. Cheng, Y. Song, Y. Gao, J. Hu, C. Wang, S. Zhang, D. Li, H. Wu, H. Sang, L. Bi, G. Pei, *Materials Science and Engineering: C* **2020**, 112, 110905.

[172] Y. Chen, X. Xiong, X. Liu, R. Cui, C. Wang, G. Zhao, W. Zhi, M. Lu, K. Duan, J. Weng, S. Qu, J. Ge, *Journal of Materials Chemistry B* **2020**, 8, 5500.

[173]   a) D. Su, L. Jiang, X. Chen, J. Dong, Z. Shao, *ACS Applied Materials & Interfaces* **2016**, 8, 9619; b) Y. Liu, H. Meng, S. Konst, R. Sarmiento, R. Rajachar, B. P. Lee, *ACS Applied Materials & Interfaces* **2014**, 6, 16982; c) A. K. Gaharwar, P. J. Schexnailder, B. P. Kline, G. Schmidt, *Acta Biomaterialia* **2011**, 7, 568.

[174]   a) H. Tomás, C. S. Alves, J. Rodrigues, *Nanomedicine: Nanotechnology, Biology and Medicine* **2018**, 14, 2407; b) D. Chimene, D. L. Alge, A. K. Gaharwar, *Advanced Materials* **2015**, 27, 7261.

[175]   S. Wang, R. Castro, X. An, C. Song, Y. Luo, M. Shen, H. Tomás, M. Zhu, X. Shi, *Journal of Materials Chemistry* **2012**, 22, 23357.

[176]   a) C. Boyer, L. Figueiredo, R. Pace, J. Lesoeur, T. Rouillon, C. L. Visage, J.-F. Tassin, P. Weiss, J. Guicheux, G. Rethore, *Acta Biomaterialia* **2018**, 65, 112; b) X. Xie, X. Li, T. Zhou, T. Zhang, J. Liao, in *Cartilage Regeneration*, DOI: 10.1007/978-3-319-51617-2_5 (Ed: Y. Lin), Springer International Publishing, Cham **2017**, p. 77.

[177]   X. Zhai, Y. Ma, C. Hou, F. Gao, Y. Zhang, C. Ruan, H. Pan, W. W. Lu, W. Liu, *ACS Biomaterials Science & Engineering* **2017**, 3, 1109.

[178]   H. Jian, M. Wang, Q. Dong, J. Li, A. Wang, X. Li, P. Ren, S. Bai, *ACS applied materials & interfaces* **2019**, 11, 46419.

[179]   C. B. Highley, C. B. Rodell, J. A. Burdick, *Advanced Materials* **2015**, 27, 5075.

[180]   M. M. Stanton, J. Samitier, S. Sánchez, *Lab on a Chip* **2015**, 15, 3111.

[181]   J. Müller, A. C. Jäkel, D. Schwarz, L. Aufinger, F. C. Simmel, *Small* **2020**, 16, 2001815.

[182]   C. Li, A. Faulkner-Jones, A. R. Dun, J. Jin, P. Chen, Y. Xing, Z. Yang, Z. Li, W. Shu, D. Liu, R. R. Duncan, *Angewandte Chemie International Edition* **2015**, 54, 3957.

[1]   a) L. G. Griffith, G. Naughton, *science* **2002**, 295, 1009; b) V. Mironov, T. Boland, T. Trusk, G. Forgacs, R. R. Markwald, *TRENDS in Biotechnology* **2003**, 21, 157.

[2]   P. Bajaj, R. M. Schweller, A. Khademhosseini, J. L. West, R. Bashir, *Annual Review of Biomedical Engineering* **2014**, 16, 247.

[3]   a) P. Sharma, P. Kumar, R. Sharma, V. D. Bhatt, P. Dhot, *Journal of medicine and life* **2019**, 12, 225; b) A. Haleem, M. Javaid, R. H. Khan, R. Suman, *Journal of clinical orthopaedics and trauma* **2020**, 11, S118.

[4]   S. Caddeo, M. Boffito, S. Sartori, *Frontiers in Bioengineering and Biotechnology* **2017**, 5.

[5]   a) K. H. Moon, I. K. Ko, J. J. Yoo, A. Atala, *Methods* **2016**, 99, 112; b) J. S. Uzarski, Y. Xia, J. C. Belmonte, J. A. Wertheim, *Current opinion in nephrology and hypertension* **2014**, 23, 399.

[6]   a) J. T. Shearn, K. R. Kinneberg, N. A. Dyment, M. T. Galloway, K. Kenter, C. Wylie, D. L. Butler, *Journal of musculoskeletal & neuronal interactions* **2011**, 11, 163; b) W. L. Lim, L. L. Liau, M. H. Ng, S. R. Chowdhury, J. X. Law, *Tissue engineering and regenerative medicine* **2019**, 16, 549.

[7]   a) R. N. Palchesko, S. D. Carrasquilla, A. W. Feinberg, *Advanced healthcare materials* **2018**, 7, 1701434; b) F. N. Syed-Picard, Y. Du, A. J. Hertsenberg, R. Palchesko, M. L. Funderburgh, A. W. Feinberg, J. L. Funderburgh, *Journal of tissue engineering and regenerative medicine* **2018**, 12, 59.

[8]   M. Baguneid, A. Seifalian, H. Salacinski, D. Murray, G. Hamilton, M. Walker, *British Journal of Surgery* **2006**, 93, 282.

[9]   J. Kluin, H. Talacua, A. I. Smits, M. Y. Emmert, M. C. Brugmans, E. S. Fioretta, P. E. Dijkman, S. H. Söntjens, R. Duijvelshoff, S. Dekker, *Biomaterials* **2017**, 125, 101.

[10]   D. P. Pacheco, N. S. Vargas, S. Visentin, P. Petrini, *Biomaterials Science* **2021**, 9, 70.

[11]   Y. K. Kurokawa, S. C. George, *Advanced drug delivery reviews* **2016**, 96, 225.

[12]   a) J. Malda, J. Visser, F. P. Melchels, T. Jüngst, W. E. Hennink, W. J. Dhert, J. Groll, D. W. Hutmacher, *Advanced materials* **2013**, 25, 5011; b) J. Groll, T. Boland, T. Blunk, J. A. Burdick, D.-W. Cho, P. D. Dalton, B. Derby, G. Forgacs, Q. Li, V. A. Mironov, *Biofabrication* **2016**, 8, 013001.

[13]   S. Ostrovidov, S. Salehi, M. Costantini, K. Suthiwanich, M. Ebrahimi, R. B. Sadeghian, T. Fujie, X. Shi, S. Cannata, C. Gargioli, *Small* **2019**, 15, 1805530.

[14]   B. K. Gu, D. J. Choi, S. J. Park, Y.-J. Kim, C.-H. Kim, *Cutting-Edge Enabling Technologies for Regenerative Medicine* **2018**, 15.

[15]   K. A. Deo, K. A. Singh, C. W. Peak, D. L. Alge, A. K. Gaharwar, *Tissue Engineering Part A* **2020**, 26, 318.

[16]   M. Varkey, D. O. Visscher, P. P. M. van Zuijlen, A. Atala, J. J. Yoo, *Burns & Trauma* **2019**, 7, 4.

[17]   J. Groll, J. A. Burdick, D. W. Cho, B. Derby, M. Gelinsky, S. C. Heilshorn, T. Jüngst, J. Malda, V. A. Mironov, K. Nakayama, A. Ovsianikov, W. Sun, S. Takeuchi, J. J. Yoo, T. B. F. Woodfield, *Biofabrication* **2018**, 11, 013001.

[18]   K. Dubbin, Y. Hori, K. K. Lewis, S. C. Heilshorn, *Advanced Healthcare Materials* **2016**, 5, 2488.

[19]   D. Liu, W. Nie, D. Li, W. Wang, L. Zheng, J. Zhang, J. Zhang, C. Peng, X. Mo, C. He, *Chemical Engineering Journal* **2019**, 362, 269.

[20]   H. Cui, M. Nowicki, J. P. Fisher, L. G. Zhang, *Advanced healthcare materials* **2017**, 6, 1601118.

[21]   a) T. H. Jovic, G. Kungwengwe, A. C. Mills, I. S. Whitaker, *Frontiers in Mechanical Engineering* **2019**, 5; b) P. S. Gungor-Ozkerim, I. Inci, Y. S. Zhang, A. Khademhosseini, M. R. Dokmeci, *Biomaterials Science* **2018**, 6, 915.

[22]   Y.-J. Seol, H.-W. Kang, S. J. Lee, A. Atala, J. J. Yoo, *European Journal of Cardio-Thoracic Surgery* **2014**, 46, 342.

[23]   R. Lozano, L. Stevens, B. C. Thompson, K. J. Gilmore, R. Gorkin III, E. M. Stewart, M. in het Panhuis, M. Romero-Ortega, G. G. Wallace, *Biomaterials* **2015**, 67, 264.

[24]   a) K. Zhu, N. Chen, X. Liu, X. Mu, W. Zhang, C. Wang, Y. S. Zhang, *Macromolecular Bioscience* **2018**, 18, 1800127; b) W. Liu, Z. Zhong, N. Hu, Y. Zhou, L. Maggio, A. K. Miri, A. Fragasso, X. Jin, A. Khademhosseini, Y. S. Zhang, *Biofabrication* **2018**, 10, 024102; c) K. Markstedt, A. Mantas, I. Tournier, H. Martínez Ávila, D. Hägg, P. Gatenholm, *Biomacromolecules* **2015**, 16, 1489; d) J. Yin, M. Yan, Y. Wang, J. Fu, H. Suo, *ACS applied materials & interfaces* **2018**, 10, 6849.

[25]   a) A. M. Compaan, K. Christensen, Y. Huang, *ACS Biomaterials Science & Engineering* **2017**, 3, 1519; b) L. H. Solis, Y. Ayala, S. Portillo, A. Varela-Ramirez, R. Aguilera, T. Boland, *Biofabrication* **2019**, 11, 045005; c) C. Xu, W. Chai, Y. Huang, R. R. Markwald, *Biotechnology and Bioengineering* **2012**, 109, 3152.

[26]   a) J. A. Barron, P. Wu, H. D. Ladouceur, B. R. Ringeisen, *Biomedical Microdevices* **2004**, 6, 139; b) B. Guillotin, A. Souquet, S. Catros, M. Duocastella, B. Pippenger, S. Bellance, R. Bareille, M. Rémy, L. Bordenave, J. Amédée, *Biomaterials* **2010**, 31, 7250; c) V. Keriquel, H. Oliveira, M. Rémy, S. Ziane, S. Delmond, B. Rousseau, S. Rey, S. Catros, J. Amédée, F. Guillemot, *Scientific reports* **2017**, 7, 1.

[27]   a) Z. Wang, R. Abdulla, B. Parker, R. Samanipour, S. Ghosh, K. Kim, *Biofabrication* **2015**, 7, 045009; b) Z. Wang, H. Kumar, Z. Tian, X. Jin, J. F. Holzman, F. Menard, K. Kim, *ACS applied materials & interfaces* **2018**, 10, 26859; c) R. Raman, R. Bashir, in *Essentials of 3D Biofabrication and Translation*, Elsevier **2015**, p. 89.

[28]   K. Hölzl, S. Lin, L. Tytgat, S. Van Vlierberghe, L. Gu, A. Ovsianikov, *Biofabrication* **2016**, 8, 032002.

[29]   W. Peng, D. Unutmaz, I. T. Ozbolat, *Trends in biotechnology* **2016**, 34, 722.

[30] I. T. Ozbolat, M. Hospodiuk, *Biomaterials* **2016**, 76, 321.

[31] a) C. C. Chang, E. D. Boland, S. K. Williams, J. B. Hoying, *Journal of Biomedical Materials Research Part B: Applied Biomaterials* **2011**, 98B, 160; b) K. Nair, M. Gandhi, S. Khalil, K. C. Yan, M. Marcolongo, K. Barbee, W. Sun, *Biotechnology Journal* **2009**, 4, 1168; c) F. P. Melchels, W. J. Dhert, D. W. Hutmacher, J. Malda, *Journal of Materials Chemistry B* **2014**, 2, 2282; d) M. Hospodiuk, M. Dey, D. Sosnoski, I. T. Ozbolat, *Biotechnology Advances* **2017**, 35, 217.

[32] D. Chimene, K. K. Lennox, R. R. Kaunas, A. K. Gaharwar, *Annals of biomedical engineering* **2016**, 44, 2090.

[33] a) P. T. Smith, A. Basu, A. Saha, A. Nelson, *Polymer* **2018**; b) N. Paxton, W. Smolan, T. Böck, F. Melchels, J. Groll, T. Jungst, *Biofabrication* **2017**, 9, 044107.

[34] L. Ouyang, C. B. Highley, C. B. Rodell, W. Sun, J. A. Burdick, *ACS Biomaterials Science & Engineering* **2016**, 2, 1743.

[35] a) S. A. Wilson, L. M. Cross, C. W. Peak, A. K. Gaharwar, *ACS applied materials & interfaces* **2017**, 9, 43449; b) D. Chimene, L. Miller, L. M. Cross, M. K. Jaiswal, I. Singh, A. K. Gaharwar, *ACS Applied Materials & Interfaces* **2020**, 12, 15976.

[36] a) I. T. Ozbolat, H. Chen, Y. Yu, *Robotics and Computer-Integrated Manufacturing* **2014**, 30, 295; b) R. Attalla, E. Puersten, N. Jain, P. R. Selvaganapathy, *Biofabrication* **2018**, 11, 015012; c) L. Ruiz-Cantu, A. Gleadall, C. Faris, J. Segal, K. Shakesheff, J. Yang, *Materials Science and Engineering: C* **2020**, 109, 110578.

[37] I. T. Ozbolat, H. Chen, Y. Yu, *Robotics and Computer-Integrated Manufacturing* **2014**, 30, 295.

[38] W. Liu, Y. S. Zhang, M. A. Heinrich, F. De Ferrari, H. L. Jang, S. M. Bakht, M. M. Alvarez, J. Yang, Y. C. Li, G. Trujillo-de Santiago, *Advanced Materials* **2017**, 29, 1604630.

[39] *Tissue Engineering Part A* **2008**, 14, 41.

[40] J. Li, M. Chen, X. Fan, H. Zhou, *J Transl Med* **2016**, 14, 271.

[41] I. N. Aguilar, L. J. Smith, D. J. Olivos, T.-M. G. Chu, M. A. Kacena, D. R. Wagner, *Bioprinting* **2019**, 15, e00048.

[42] a) M. Nakamura, A. Kobayashi, F. Takagi, A. Watanabe, Y. Hiruma, K. Ohuchi, Y. Iwasaki, M. Horie, I. Morita, S. Takatani, *Tissue engineering* **2005**, 11, 1658; b) T. Boland, T. Xu, B. Damon, X. Cui, *Biotechnology Journal: Healthcare Nutrition Technology* **2006**, 1, 910.

[43] T. Xu, W. Zhao, J.-M. Zhu, M. Z. Albanna, J. J. Yoo, A. Atala, *Biomaterials* **2013**, 34, 130.

[44] R. Zimmermann, C. Hentschel, F. Schrön, D. Moedder, T. Büttner, P. Atallah, T. Wegener, T. Gehring, S. Howitz, U. Freudenberg, C. Werner, *Biofabrication* **2019**, 11, 045008.

[45] H. Gudapati, M. Dey, I. Ozbolat, *Biomaterials* **2016**, 102, 20.

[46] a) M. S. Onses, E. Sutanto, P. M. Ferreira, A. G. Alleyne, J. A. Rogers, *Small* **2015**, 11, 4237; b) S. N. Jayasinghe, A. N. Qureshi, P. A. Eagles, *Small* **2006**, 2, 216.

[47] a) Z. Zheng, D. Eglin, M. Alini, G. R. Richards, L. Qin, Y. Lai, *Engineering* **2020**, DOI: https://doi.org/10.1016/j.eng.2020.05.021; b) B. K. Gu, D. J. Choi, S. J. Park, M. S. Kim, C. M. Kang, C.-H. Kim, *Biomaterials research* **2016**, 20, 12; c) N. E. Sanjana, S. B. Fuller, *Journal of neuroscience methods* **2004**, 136, 151.

[48] a) L. Gasperini, D. Maniglio, A. Motta, C. Migliaresi, *Tissue engineering part C: Methods* **2015**, 21, 123; b) C. Xu, W. Chai, Y. Huang, R. R. Markwald, *Biotechnology and bioengineering* **2012**, 109, 3152.

[49] A. Blaeser, D. F. Duarte Campos, M. Weber, S. Neuss, B. Theek, H. Fischer, W. Jahnen-Dechent, *BioResearch open access* **2013**, 2, 374.

[50]   a) *Tissue Engineering Part A* **2012**, 18, 1304; b) U. A. Gurkan, R. El Assal, S. E. Yildiz, Y. Sung, A. J. Trachtenberg, W. P. Kuo, U. Demirci, *Molecular Pharmaceutics* **2014**, 11, 2151.

[51]   Y.-B. Lee, S. Polio, W. Lee, G. Dai, L. Menon, R. S. Carroll, S.-S. Yoo, *Experimental neurology* **2010**, 223, 645.

[52]   A. GhavamiNejad, N. Ashammakhi, X. Y. Wu, A. Khademhosseini, *Small* **2020**, 16, 2002931.

[53]   G. Gao, T. Yonezawa, K. Hubbell, G. Dai, X. Cui, *Biotechnology Journal* **2015**, 10, 1568.

[54]   a) C. J. Ferris, K. J. Gilmore, S. Beirne, D. McCallum, G. G. Wallace, M. in het Panhuis, *Biomaterials Science* **2013**, 1, 224; b) M. E. Pepper, V. Seshadri, T. C. Burg, K. J. L. Burg, R. E. Groff, *Biofabrication* **2012**, 4, 011001.

[55]   X. Li, B. Liu, B. Pei, J. Chen, D. Zhou, J. Peng, X. Zhang, W. Jia, T. Xu, *Chemical Reviews* **2020**, 120, 10793.

[56]   T. Xu, C. A. Gregory, P. Molnar, X. Cui, S. Jalota, S. B. Bhaduri, T. Boland, *Biomaterials* **2006**, 27, 3580.

[57]   a) D. J. Odde, M. J. Renn, *Trends in biotechnology* **1999**, 17, 385; b) J. A. Barron, B. R. Ringeisen, H. Kim, B. J. Spargo, D. B. Chrisey, *Thin Solid Films* **2004**, 453, 383.

[58]   a) C. Mandrycky, Z. Wang, K. Kim, D.-H. Kim, *Biotechnology Advances* **2016**, 34, 422; b) F. Guillemot, A. Souquet, S. Catros, B. Guillotin, J. Lopez, M. Faucon, B. Pippenger, R. Bareille, M. Rémy, S. Bellance, P. Chabassier, J. C. Fricain, J. Amédée, *Acta Biomaterialia* **2010**, 6, 2494.

[59]   S. Michael, H. Sorg, C.-T. Peck, L. Koch, A. Deiwick, B. Chichkov, P. M. Vogt, K. Reimers, *PloS one* **2013**, 8, e57741.

[60]   S. Catros, B. Guillotin, M. Bačáková, J.-C. Fricain, F. Guillemot, *Applied Surface Science* **2011**, 257, 5142.

[61]   F. Guillemot, A. Souquet, S. Catros, B. Guillotin, *Nanomedicine* **2010**, 5, 507.

[62]   a) D. Hakobyan, C. Médina, N. Dusserre, M.-L. Stachowicz, C. Handschin, J.-C. Fricain, J. Guillermet-Guibert, H. Oliveira, *Biofabrication* **2020**, 12, 035001; b) M. Ali, E. Pages, A. Ducom, A. Fontaine, F. Guillemot, *Biofabrication* **2014**, 6, 045001.

[63]   M. A. Heinrich, W. Liu, A. Jimenez, J. Yang, A. Akpek, X. Liu, Q. Pi, X. Mu, N. Hu, R. M. Schiffelers, *Small* **2019**, 15, 1805510.

[64]   N. Poomathi, S. Singh, C. Prakash, V. Patil Rajkumar, P. T. Perumal, A. Barathi Veluchamy, K. Balasubramanian Kalpattu, S. Ramakrishna, N. U. Maheshwari, *Rapid Prototyping Journal* **2019**, 25, 496.

[65]   J. T. Huh, J. J. Yoo, A. Atala, S. J. Lee, in *Principles of Tissue Engineering (Fifth Edition)*, DOI: https://doi.org/10.1016/B978-0-12-818422-6.00076-9 (Eds: R. Lanza, R. Langer, J. P. Vacanti, A. Atala), Academic Press **2020**, p. 1391.

[66]   a) B. Hopp, T. Smausz, G. Szabó, L. Kolozsvari, A. Nogradi, D. Kafetzopoulos, C. Fotakis, *Optical Engineering* **2012**, 51, 014302; b) H. Gudapati, J. Yan, Y. Huang, D. B. Chrisey, *Biofabrication* **2014**, 6, 035022.

[67]   L. Koch, S. Kuhn, H. Sorg, M. Gruene, S. Schlie, R. Gaebel, B. Polchow, K. Reimers, S. Stoelting, N. Ma, *Tissue Engineering Part C: Methods* **2010**, 16, 847.

[68]   a) Z. Yue, X. Liu, P. T. Coates, G. G. Wallace, *Current opinion in organ transplantation* **2016**, 21, 467; b) R. Raman, R. Bashir, in *Essentials of 3D Biofabrication and Translation*, DOI: https://doi.org/10.1016/B978-0-12-800972-7.00006-2 (Eds: A. Atala, J. J. Yoo), Academic Press, Boston **2015**, p. 89.

[69]   a) S. Zakeri, M. Vippola, E. Levänen, *Additive Manufacturing* **2020**, 35, 101177; b) F. P. Melchels, K. Bertoldi, R. Gabbrielli, A. H. Velders, J. Feijen, D. W. Grijpma, *Biomaterials* **2010**, 31, 6909.

[70]   a) J.-W. Choi, R. Wicker, S.-H. Lee, K.-H. Choi, C.-S. Ha, I. Chung, *Journal of Materials Processing Technology* **2009**, 209, 5494; b) T. Chartier, A. Badev, Y. Abouliatim, P. Lebaudy, L. Lecamp, *Journal of the European Ceramic Society* **2012**, 32, 1625.

[71]   F. P. W. Melchels, J. Feijen, D. W. Grijpma, *Biomaterials* **2010**, 31, 6121.

[72]   R. P. Sinha, D.-P. Häder, *Photochemical & Photobiological Sciences* **2002**, 1, 225.

[73]   a) A. K. Au, W. Lee, A. Folch, *Lab on a Chip* **2014**, 14, 1294; b) R. Zhang, N. B. Larsen, *Lab on a Chip* **2017**, 17, 4273.

[74]   a) S. Knowlton, B. Yenilmez, S. Tasoglu, *Trends in Biotechnology* **2016**, 34, 685; b) A. P. Kuo, N. Bhattacharjee, Y. S. Lee, K. Castro, Y. T. Kim, A. Folch, *Advanced materials technologies* **2019**, 4, 1800395.

[75]   S. Boularaoui, G. Al Hussein, K. A. Khan, N. Christoforou, C. Stefanini, *Bioprinting* **2020**, 20, e00093.

[76]   a) W. Schuurman, P. A. Levett, M. W. Pot, P. R. van Weeren, W. J. Dhert, D. W. Hutmacher, F. P. Melchels, T. J. Klein, J. Malda, *Macromolecular bioscience* **2013**, 13, 551; b) J. M. Townsend, E. C. Beck, S. H. Gehrke, C. J. Berkland, M. S. Detamore, *Progress in Polymer Science* **2019**, 91, 126.

[77]   a) M. Chopin-Doroteo, E. A. Mandujano-Tinoco, E. Krötzsch, *Biochimica et Biophysica Acta (BBA) - General Subjects* **2021**, 1865, 129782; b) O. Chaudhuri, L. Gu, D. Klumpers, M. Darnell, S. A. Bencherif, J. C. Weaver, N. Huebsch, H.-p. Lee, E. Lippens, G. N. Duda, D. J. Mooney, *Nature Materials* **2016**, 15, 326.

[78]   a) Y. Chen, X. Xiong, X. Liu, R. Cui, C. Wang, G. Zhao, W. Zhi, M. Lu, K. Duan, J. Weng, *Journal of Materials Chemistry B* **2020**, 8, 5500; b) A. Parak, P. Pradeep, L. C. du Toit, P. Kumar, Y. E. Choonara, V. Pillay, *Drug discovery today* **2019**, 24, 198.

[79]   P. A. Amorim, M. A. d'Ávila, R. Anand, P. Moldenaers, P. Van Puyvelde, V. Bloemen, *Bioprinting* **2021**, 22, e00129.

[80]   J. L. Dávila, M. A. d'Ávila, *The International Journal of Advanced Manufacturing Technology* **2019**, 101, 675.

[81]   E. A. Kiyotake, A. W. Douglas, E. E. Thomas, S. L. Nimmo, M. S. Detamore, *Acta Biomaterialia* **2019**, 95, 176.

[82]   Z. Liu, B. Bhandari, S. Prakash, S. Mantihal, M. Zhang, *Food Hydrocolloids* **2019**, 87, 413.

[83]   Y. S. Zhang, A. Khademhosseini, *Science* **2017**, 356.

[84]   H. Li, C. Tan, L. Li, *Materials & Design* **2018**, 159, 20.

[85]   J. M. Unagolla, A. C. Jayasuriya, *Applied Materials Today* **2020**, 18, 100479.

[86]   S. Heid, A. R. Boccaccini, *Acta Biomaterialia* **2020**, 113, 1.

[87]   K. Varaprasad, G. M. Raghavendra, T. Jayaramudu, M. M. Yallapu, R. Sadiku, *Materials Science and Engineering: C* **2017**, 79, 958.

[88]   W. Hu, Z. Wang, Y. Xiao, S. Zhang, J. Wang, *Biomaterials science* **2019**, 7, 843.

[89]   M. Mahinroosta, Z. J. Farsangi, A. Allahverdi, Z. Shakoori, *Materials today chemistry* **2018**, 8, 42.

[90]   E. Caló, V. V. Khutoryanskiy, *European Polymer Journal* **2015**, 65, 252.

[91]   M. C. Catoira, L. Fusaro, D. Di Francesco, M. Ramella, F. Boccafoschi, *Journal of Materials Science: Materials in Medicine* **2019**, 30, 115.

[92]   J. Li, C. Wu, P. K. Chu, M. Gelinsky, *Materials Science and Engineering: R: Reports* **2020**, 140, 100543.

[93]   P. Jaipan, A. Nguyen, R. J. Narayan, *MRS Communications* **2017**, 7, 416.

[94]   K. Su, C. Wang, *Biotechnology letters* **2015**, 37, 2139.

[95]   A. I. Van Den Bulcke, B. Bogdanov, N. De Rooze, E. H. Schacht, M. Cornelissen, H. Berghmans, *Biomacromolecules* **2000**, 1, 31.

[96] K. Yue, G. Trujillo-de Santiago, M. M. Alvarez, A. Tamayol, N. Annabi, A. Khademhosseini, *Biomaterials* **2015**, 73, 254.

[97] Z. Dong, Q. Yuan, K. Huang, W. Xu, G. Liu, Z. Gu, *RSC Advances* **2019**, 9, 17737.

[98] a) F. E. Freeman, D. J. Kelly, *Scientific Reports* **2017**, 7, 17042; b) E. Axpe, M. L. Oyen, *International journal of molecular sciences* **2016**, 17, 1976; c) M. D. Giuseppe, N. Law, B. Webb, R. A. Macrae, L. J. Liew, T. B. Sercombe, R. J. Dilley, B. J. Doyle, *Journal of the Mechanical Behavior of Biomedical Materials* **2018**, 79, 150.

[99] a) J. Lewicki, J. Bergman, C. Kerins, O. Hermanson, *Bioprinting* **2019**, 16, e00053; b) M. Alruwaili, J. A. Lopez, K. McCarthy, E. G. Reynaud, B. J. Rodriguez, *Bio-Design and Manufacturing* **2019**, 2, 172.

[100] M. L. Bedell, A. M. Navara, Y. Du, S. Zhang, A. G. Mikos, *Chemical Reviews* **2020**.

[101] N. Contessi, L. Altomare, A. Filipponi, S. Farè, *Materials Letters* **2017**, 207, 157.

[102] C. Chang, L. Zhang, *Carbohydrate polymers* **2011**, 84, 40.

[103] N. Contessi Negrini, L. Bonetti, L. Contili, S. Farè, *Bioprinting* **2018**, 10, e00024.

[104] K. Schütz, A. M. Placht, B. Paul, S. Brüggemeier, M. Gelinsky, A. Lode, *Journal of tissue engineering and regenerative medicine* **2017**, 11, 1574.

[105] a) S. Liu, L. Li, *ACS applied materials & interfaces* **2016**, 8, 29749; b) Y. Yuguchi, H. Urakawa, K. Kajiwara, *Food Hydrocolloids* **2003**, 17, 481.

[106] a) S. Liu, W. L. Chan, L. Li, *Macromolecules* **2015**, 48, 7649; b) S. M. Mihaila, A. K. Gaharwar, R. L. Reis, A. P. Marques, M. E. Gomes, A. Khademhosseini, *Advanced healthcare materials* **2013**, 2, 895.

[107] a) S. Liu, S. Huang, L. Li, *Journal of Rheology* **2016**, 60, 203; b) D. Chimene, C. W. Peak, J. L. Gentry, J. K. Carrow, L. M. Cross, E. Mondragon, G. B. Cardoso, R. Kaunas, A. K. Gaharwar, *ACS applied materials & interfaces* **2018**, 10, 9957.

[108] a) S. H. Park, J. Y. Seo, J. Y. Park, Y. B. Ji, K. Kim, H. S. Choi, S. Choi, J. H. Kim, B. H. Min, M. S. Kim, *NPG Asia Materials* **2019**, 11, 1; b) M. F. Graça, S. P. Miguel, C. S. Cabral, I. J. Correia, *Carbohydrate Polymers* **2020**, 116364.

[109] a) M. T. Poldervaart, B. Goversen, M. De Ruijter, A. Abbadessa, F. P. Melchels, F. C. Öner, W. J. Dhert, T. Vermonden, J. Alblas, *PLoS One* **2017**, 12, e0177628; b) I. Noh, N. Kim, H. N. Tran, J. Lee, C. Lee, *Biomaterials research* **2019**, 23, 1.

[110] H. Si, T. Xing, Y. Ding, H. Zhang, R. Yin, W. Zhang, *Polymers* **2019**, 11, 1584.

[111] I. Donderwinkel, J. C. M. van Hest, N. R. Cameron, *Polymer Chemistry* **2017**, 8, 4451.

[112] L. Valot, J. Martinez, A. Mehdi, G. Subra, *Chemical Society Reviews* **2019**, 48, 4049.

[113] a) J. H. Chung, S. Naficy, Z. Yue, R. Kapsa, A. Quigley, S. E. Moulton, G. G. Wallace, *Biomaterials Science* **2013**, 1, 763; b) H. Rastin, R. T. Ormsby, G. J. Atkins, D. Losic, *ACS Applied Bio Materials* **2020**, 3, 1815.

[114] Y. Zhao, Y. Li, S. Mao, W. Sun, R. Yao, *Biofabrication* **2015**, 7, 045002.

[115] M. Mehrali, A. Thakur, C. P. Pennisi, S. Talebian, A. Arpanaei, M. Nikkhah, A. Dolatshahi-Pirouz, *Advanced Materials* **2017**, 29, 1603612.

[116] a) L. Ghasemi-Mobarakeh, M. P. Prabhakaran, M. Morshed, M. H. Nasr-Esfahani, H. Baharvand, S. Kiani, S. S. Al-Deyab, S. Ramakrishna, *Journal of Tissue Engineering and Regenerative Medicine* **2011**, 5, e17; b) N. Li, Q. Zhang, S. Gao, Q. Song, R. Huang, L. Wang, L. Liu, J. Dai, M. Tang, G. Cheng, *Scientific Reports* **2013**, 3, 1604; c) B. Guo, P. X. Ma, *Biomacromolecules* **2018**, 19, 1764.

[117] a) N. Zanjanizadeh Ezazi, M.-A. Shahbazi, Y. V. Shatalin, E. Nadal, E. Mäkilä, J. Salonen, M. Kemell, A. Correia, J. Hirvonen, H. A. Santos, *International Journal of Pharmaceutics* **2018**, 536, 241; b) G. L. Mario Cheong, K. S. Lim, A. Jakubowicz, P. J. Martens, L. A. Poole-Warren, R. A. Green, *Acta Biomaterialia* **2014**, 10, 1216.

[118] a) K. Cysewska, J. Karczewski, P. Jasiński, *Measurement Science and Technology* **2017**, 28, 074004; b) R. Ravichandran, J. G. Martinez, E. W. H. Jager, J. Phopase, A. P. F. Turner, *ACS Applied Materials & Interfaces* **2018**, 10, 16244.

[119] a) H. Rastin, B. Zhang, A. Mazinani, K. Hassan, J. Bi, T. T. Tung, D. Losic, *Nanoscale* **2020**; b) A. E. Jakus, E. B. Secor, A. L. Rutz, S. W. Jordan, M. C. Hersam, R. N. Shah, *ACS Nano* **2015**, 9, 4636.

[120] S.-J. Lee, W. Zhu, M. Nowicki, G. Lee, D. N. Heo, J. Kim, Y. Y. Zuo, L. G. Zhang, *Journal of Neural Engineering* **2018**, 15, 016018.

[121] a) T. Distler, A. R. Boccaccini, *Acta biomaterialia* **2020**, 101, 1; b) S. S. Athukorala, T. S. Tran, R. Balu, V. K. Truong, J. Chapman, N. K. Dutta, N. Roy Choudhury, *Polymers* **2021**, 13, 474.

[122] H. Qing, Y. Ji, W. Li, G. Zhao, Q. Yang, X. Zhang, Z. Luo, T. J. Lu, G. Jin, F. Xu, *ACS Applied Materials & Interfaces* **2020**, 12, 2049.

[123] S. Sayyar, M. Bjorninen, S. Haimi, S. Miettinen, K. Gilmore, D. Grijpma, G. Wallace, *ACS Applied Materials & Interfaces* **2016**, 8, 31916.

[124] a) L. Zhao, P. K. Chu, Y. Zhang, Z. Wu, *Journal of Biomedical Materials Research Part B: Applied Biomaterials* **2009**, 91, 470; b) S. Li, S. Dong, W. Xu, S. Tu, L. Yan, C. Zhao, J. Ding, X. Chen, *Advanced science* **2018**, 5, 1700527.

[125] J. Hoque, B. Bhattacharjee, R. G. Prakash, K. Paramanandham, J. Haldar, *Biomacromolecules* **2018**, 19, 267.

[126] M. C. Giano, Z. Ibrahim, S. H. Medina, K. A. Sarhane, J. M. Christensen, Y. Yamada, G. Brandacher, J. P. Schneider, *Nature communications* **2014**, 5, 1.

[127] a) S. Wang, H. Zheng, L. Zhou, F. Cheng, Z. Liu, H. Zhang, L. Wang, Q. Zhang, *Nano Letters* **2020**, 20, 5149; b) Y. Zhong, H. Xiao, F. Seidi, Y. Jin, *Biomacromolecules* **2020**, 21, 2983.

[128] D. Campoccia, L. Montanaro, C. R. Arciola, *Biomaterials* **2006**, 27, 2331.

[129] a) L. Mei, S. Zhu, W. Yin, C. Chen, G. Nie, Z. Gu, Y. Zhao, *Theranostics* **2020**, 10, 757; b) Q. Wu, M. Liang, S. Zhang, X. Liu, F. Wang, *Nanoscale* **2018**, 10, 10428.

[130] Y. Zhang, D. Zhai, M. Xu, Q. Yao, H. Zhu, J. Chang, C. Wu, *Biofabrication* **2017**, 9, 025037.

[131] S. F. Melo, S. C. Neves, A. T. Pereira, I. Borges, P. L. Granja, F. D. Magalhães, I. C. Gonçalves, *Materials Science and Engineering: C* **2020**, 109, 110537.

[132] E. S. Place, J. H. George, C. K. Williams, M. M. Stevens, *Chemical Society Reviews* **2009**, 38, 1139.

[133] a) C. Gardin, A. Piattelli, B. Zavan, *Trends in Biotechnology* **2016**, 34, 435; b) S. R. Shin, Y.-C. Li, H. L. Jang, P. Khoshakhlagh, M. Akbari, A. Nasajpour, Y. S. Zhang, A. Tamayol, A. Khademhosseini, *Advanced Drug Delivery Reviews* **2016**, 105, 255; c) S. Kumar, K. Chatterjee, *ACS applied materials & interfaces* **2016**, 8, 26431.

[134] X. Zhou, M. Nowicki, H. Cui, W. Zhu, X. Fang, S. Miao, S.-J. Lee, M. Keidar, L. G. Zhang, *Carbon* **2017**, 116, 615.

[135] Z. Cheng, B. Landish, Z. Chi, C. Nannan, D. Jingyu, L. Sen, L. Xiangjin, *Materials Science and Engineering: C* **2018**, 82, 244.

[136] G. Choe, S. Oh, J. M. Seok, S. A. Park, J. Y. Lee, *Nanoscale* **2019**, 11, 23275.

[137] G. Turnbull, J. Clarke, F. Picard, P. Riches, L. Jia, F. Han, B. Li, W. Shu, *Bioactive Materials* **2018**, 3, 278.

[138] a) A. L. Rutz, E. S. Gargus, K. E. Hyland, P. L. Lewis, A. Setty, W. R. Burghardt, R. N. Shah, *Acta Biomaterialia* **2019**, 99, 121; b) J. Jang, T. G. Kim, B. S. Kim, S.-W. Kim, S.-M. Kwon, D.-W. Cho, *Acta Biomaterialia* **2016**, 33, 88.

[139] L. M. Guiney, N. D. Mansukhani, A. E. Jakus, S. G. Wallace, R. N. Shah, M. C. Hersam, *Nano letters* **2018**, 18, 3488.

[140] D. Aki, S. Ulag, S. Unal, M. Sengor, N. Ekren, C.-C. Lin, H. Yılmazer, C. B. Ustundag, D. M. Kalaskar, O. Gunduz, *Materials & Design* **2020**, 196, 109094.

[141] H. Belaid, S. Nagarajan, C. Barou, V. Huon, J. Bares, S. Balme, P. Miele, D. Cornu, V. Cavaillès, C. Teyssier, *ACS Applied Bio Materials* **2020**, 3, 1865.

[142] S. V. Murphy, A. Atala, *Nature biotechnology* **2014**, 32, 773.

[143] a) A. J. Engler, S. Sen, H. L. Sweeney, D. E. Discher, *Cell* **2006**, 126, 677; b) F. Guilak, D. M. Cohen, B. T. Estes, J. M. Gimble, W. Liedtke, C. S. Chen, *Cell Stem Cell* **2009**, 5, 17.

[144] a) K. Jakab, C. Norotte, F. Marga, K. Murphy, G. Vunjak-Novakovic, G. Forgacs, *Biofabrication* **2010**, 2, 022001; b) A. L. Rutz, K. E. Hyland, A. E. Jakus, W. R. Burghardt, R. N. Shah, *Advanced Materials* **2015**, 27, 1607; c) H.-W. Kang, S. J. Lee, I. K. Ko, C. Kengla, J. J. Yoo, A. Atala, *Nature Biotechnology* **2016**, 34, 312.

[145] J. A. Rowley, G. Madlambayan, D. J. Mooney, *Biomaterials* **1999**, 20, 45.

[146] B. Duan, E. Kapetanovic, L. A. Hockaday, J. T. Butcher, *Acta Biomaterialia* **2014**, 10, 1836.

[147] C. Sears, E. Mondragon, Z. I. Richards, N. Sears, D. Chimene, E. P. McNeill, C. A. Gregory, A. K. Gaharwar, R. Kaunas, *Advanced Healthcare Materials* **2020**, 9, 1901580.

[148] J. M. Lee, W. Y. Yeong, *Advanced healthcare materials* **2016**, 5, 2856.

[149] a) S. Hong, D. Sycks, H. F. Chan, S. Lin, G. P. Lopez, F. Guilak, K. W. Leong, X. Zhao, *Advanced materials* **2015**, 27, 4035; b) T. Cebe, N. Ahuja, F. Monte, K. Awad, K. Vyavhare, P. Aswath, J. Huang, M. Brotto, V. Varanasi, *Journal of Materials Research* **2020**, 35, 58; c) C. W. Peak, J. Stein, K. A. Gold, A. K. Gaharwar, *Langmuir* **2018**, 34, 917; d) A. Nadernezhad, O. S. Caliskan, F. Topuz, F. Afghah, B. Erman, B. Koc, *ACS Applied Bio Materials* **2019**, 2, 796.

[150] a) Y. M. Joshi, G. R. K. Reddy, A. L. Kulkarni, N. Kumar, R. P. Chhabra, *Proceedings of the Royal Society A: Mathematical, Physical and Engineering Sciences* **2008**, 464, 469; b) J. L. Dávila, M. A. d'Ávila, *Carbohydrate polymers* **2017**, 157, 1.

[151] D. W. Thompson, J. T. Butterworth, *Journal of Colloid and Interface Science* **1992**, 151, 236.

[152] B. Ruzicka, E. Zaccarelli, *Soft Matter* **2011**, 7, 1268.

[153] C. B. Highley, C. B. Rodell, J. A. Burdick, *Advanced Materials* **2015**, 27, 5075.

[154] G. Cidonio, C. R. Alcala-Orozco, K. S. Lim, M. Glinka, I. Mutreja, Y.-H. Kim, J. I. Dawson, T. B. Woodfield, R. O. Oreffo, *Biofabrication* **2019**, 11, 035027.

[155] G. Lokhande, J. K. Carrow, T. Thakur, J. R. Xavier, M. Parani, K. J. Bayless, A. K. Gaharwar, *Acta Biomaterialia* **2018**, 70, 35.

[156] B. Liu, J. Li, X. Lei, P. Cheng, Y. Song, Y. Gao, J. Hu, C. Wang, S. Zhang, D. Li, H. Wu, H. Sang, L. Bi, G. Pei, *Materials Science and Engineering: C* **2020**, 112, 110905.

[157] Y. Chen, X. Xiong, X. Liu, R. Cui, C. Wang, G. Zhao, W. Zhi, M. Lu, K. Duan, J. Weng, S. Qu, J. Ge, *Journal of Materials Chemistry B* **2020**, 8, 5500.

[158] a) D. Su, L. Jiang, X. Chen, J. Dong, Z. Shao, *ACS Applied Materials & Interfaces* **2016**, 8, 9619; b) Y. Liu, H. Meng, S. Konst, R. Sarmiento, R. Rajachar, B. P. Lee, *ACS Applied Materials & Interfaces* **2014**, 6, 16982; c) A. K. Gaharwar, P. J. Schexnailder, B. P. Kline, G. Schmidt, *Acta Biomaterialia* **2011**, 7, 568.

[159] a) H. Tomás, C. S. Alves, J. Rodrigues, *Nanomedicine: Nanotechnology, Biology and Medicine* **2018**, 14, 2407; b) D. Chimene, D. L. Alge, A. K. Gaharwar, *Advanced Materials* **2015**, 27, 7261.

[160] S. Wang, R. Castro, X. An, C. Song, Y. Luo, M. Shen, H. Tomás, M. Zhu, X. Shi, *Journal of Materials Chemistry* **2012**, 22, 23357.

[161]   a) C. Boyer, L. Figueiredo, R. Pace, J. Lesoeur, T. Rouillon, C. L. Visage, J.-F. Tassin, P. Weiss, J. Guicheux, G. Rethore, *Acta Biomaterialia* **2018**, 65, 112; b) X. Xie, X. Li, T. Zhou, T. Zhang, J. Liao, in *Cartilage Regeneration*, DOI: 10.1007/978-3-319-51617-2_5 (Ed: Y. Lin), Springer International Publishing, Cham **2017**, p. 77.

[162]   X. Zhai, Y. Ma, C. Hou, F. Gao, Y. Zhang, C. Ruan, H. Pan, W. W. Lu, W. Liu, *ACS Biomaterials Science & Engineering* **2017**, 3, 1109.

[163]   H. Jian, M. Wang, Q. Dong, J. Li, A. Wang, X. Li, P. Ren, S. Bai, *ACS applied materials & interfaces* **2019**, 11, 46419.

[164]   C. B. Highley, C. B. Rodell, J. A. Burdick, *Advanced Materials* **2015**, 27, 5075.

[165]   M. M. Stanton, J. Samitier, S. Sánchez, *Lab on a Chip* **2015**, 15, 3111.

[166]   J. Müller, A. C. Jäkel, D. Schwarz, L. Aufinger, F. C. Simmel, *Small* **2020**, 16, 2001815.

[167]   C. Li, A. Faulkner-Jones, A. R. Dun, J. Jin, P. Chen, Y. Xing, Z. Yang, Z. Li, W. Shu, D. Liu, R. R. Duncan, *Angewandte Chemie International Edition* **2015**, 54, 3957.

Chapter 3

Development of a bioink with high stability

I n this chapter, a novel bioink based on Methylcellulose/gelatin methacryloyl (MC/GelMA) has been introduced in which GelMA stabilizes the 3D printed structure once exposed to UV irradiation. The bioink exhibited long-term stability in the biological condition without significant dissociation. Compared to pristine MC, the MC/GelMA bioink demonstrated better printability as evidenced by higher shape integrity and better shear-thinning behaviour. In addition, encapsulated human primary osteoblast cells remains viable within the MC/GelMA bioink with no significant differences with the bulk hydrogel.

This chapter has been published as

"Rastin H, Ormsby RT, Atkins GJ, Losic D. 3D Bioprinting of Methylcellulose/Gelatin-Methacryloyl (MC/GelMA) Bioink with High Shape Integrity. ACS Applied Bio Materials. 2020;3(3):1815-1826."

Statement of Authorship

Title of Paper	3D Bioprinting of Methylcellulose/Gelatin-Methacryloyl (MC/GelMA) Bioink with High Shape Integrity
Publication Status	☑ Published ☐ Accepted for Publication ☐ Submitted for Publication ☐ Unpublished and Unsubmitted work written in manuscript style
Publication Details	Rastin H, Ormsby RT, Atkins GJ, Losic D. 3D Bioprinting of Methylcellulose/Gelatin-Methacryloyl (MC/GelMA) Bioink with High Shape Integrity. ACS Applied Bio Materials. 2020;3(3):1815-1826.

Principal Author

Name of Principal Author (Candidate)	Hadi Rastin
Contribution to the Paper	Conceptualization, Investigation, Methodology, data processing, Original Draft.
Overall percentage (%)	70%
Certification:	This paper reports on original research I conducted during the period of my Higher Degree by Research candidature and is not subject to any obligations or contractual agreements with a third party that would constrain its inclusion in this thesis. I am the primary author of this paper.
Signature		Date	07/04/2021

Co-Author Contributions

By signing the Statement of Authorship, each author certifies that:

i.   the candidate's stated contribution to the publication is accurate (as detailed above);

ii. permission is granted for the candidate in include the publication in the thesis; and

iii. the sum of all co-author contributions is equal to 100% less the candidate's stated contribution.

Name of Co-Author	Prof. Dusan Losic
Contribution to the Paper	Conceptualization, Resources, Funding Acquisition, Re-view&Editing, Supervision, submission
Signature		Date	15/04/21

Name of Co-Author	Prof. Gerald J. Atkins
Contribution to the Paper	Resouces, Review&Editing.
Signature		Date	15/04/2021

Please cut and paste additional co-author panels here as required.

Name of Co-Author	Renee T. Ormsby		
Contribution to the Paper	selected investigation, Methodology, Review & Editing.		
Signature			Date	20/04/2021

3D Bioprinting of Methylcellulose/Gelatin-Methacryloyl (MC/GelMA) Bioink with High Shape Integrity

Hadi Rastin, Renee T. Ormsby, Gerald J. Atkins, and Dusan Losic*

ACCESS | Metrics & More | Article Recommendations | Supporting Information

ABSTRACT: The advent of three-dimensional (3D) bioprinting offers a feasible approach to construct complex structures suitable for tissue regeneration, during which cell-laden materials are dispensed on a substrate according to a predesigned structure. However, the lack of ideal printable bioinks with high shape fidelity and improved biological stability remains a major challenge. In this study, methylcellulose/gelatin-methacryloyl (MC/GelMA) bioink with high shape integrity is presented, which takes advantage of the printability of MC and the permanent photo-cross-linking of GelMA under UV irradiation. Although MC demonstrates good printability at room temperature, the lack of cross-linking ability causes distortion and finally dissociation of printed MC in biological media within a few days. However, UV-cross-linked MC/GelMA bioink remains stable in biological media over a period of several months. The shape integrity of MC/GelMA was systematically characterized in terms of yield stress and complex modulus. Unlike pure MC ink, the MC/GelMA ink demonstrated self-supporting behavior once printed due to the higher complex modulus and yield stress induced by GelMA in the system. Shape integrity of MC/GelMA ink resulted in higher resolution and printability which are evaluated by the successful printing of various 1D, 2D, and 3D constructs. Moreover, human primary osteoblasts encapsulated within the MC/GelMA hydrogel show cell viability of >95%. Overall, this work introduces MC/GelMA bioink with high shape integrity and improved biological stability and highlights the importance of rheological properties and post-cross-linking for fabrication of physiologically scaled tissue implants.

KEYWORDS: *GelMA, methylcellulose, shear-thinning, 3D bioprinting, shape integrity*
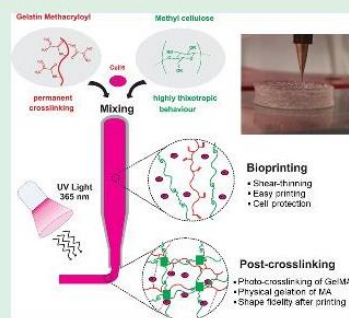
1. INTRODUCTION

Bioprinting is defined as the use of computer-aided processes for the fabrication of living bioengineered structures according to a predesigned pattern.[1] 3D printing can be subcategorized into three main classes; laser-based 3D printing, inkjet-based 3D printing, and nozzle-based 3D printing. The latter has attracted more attention because of its capability to print high viscosity bioink along with high cell density.[2−4] Although considerable improvements have been made in 3D printing technology in terms of resolution and printing speed, the lack of suitable and versatile bioinks with essential characteristics remains a serious challenge. Generally, properties that improve the biofabrication process negatively impact the biological requirements, which has resulted in the limited clinical use of 3D printed materials.[5,6]

Hydrogels are popular bioinks in 3D bioprinting due to their ability to replicate the tissue environment and to regulate cell fate.[7,8] From a printability point of view, a hydrogel should have five main properties: (i) shear-thinning behavior to shield cells from high shear stress during extrusion and consequently improve cell viability.[9] Shear-thinning properties cause the viscosity drop when bioink is extruded along a nozzle, which facilitates the bioprinting process;[10,11] (ii) high recoverability,

which enables bioink to recover the initial viscosity once printed;[12] (iii) high self-supporting behavior to hinder the spreading of printed bioink on a surface and support the weight of top printed layers;[9] (iv) hydrogels and their byproduct degradation should be biocompatible with minimal toxicity; (v) cross-linking ability to provide stability in biological media. Two significant strategies to impart a permanent network are photo[13,14] and ionic cross-linking.[10]

It is undeniable that single-component hydrogels cannot satisfy all of the above-mentioned requirements at the same time because most single-component hydrogels suffer from the lack of sufficient mechanical strength and unsuitable degradation rate compared to native tissues.[12] Therefore, there is a demand to develop bioinks with high shear-thinning behavior and recoverability, superior shape fidelity, biocompatibility, and post-cross-linking ability. Accordingly, hydrogel
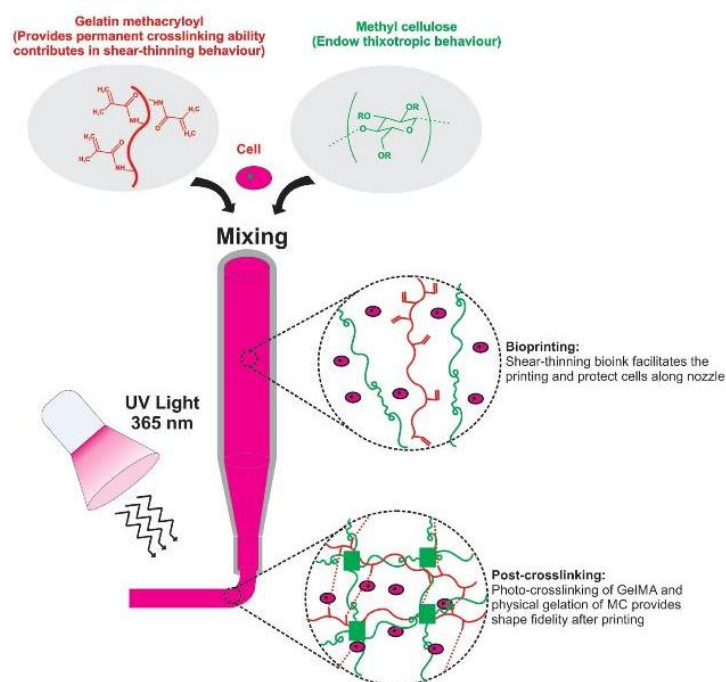
Figure 1. Schematic illustration of 3D bioprinting of cell-laden MC/GelMA bioink. Shear-thinning behavior of the ink shields cells from high shear stress during extrusion. Once printed, photo-cross-linking of the ink forms a permanent 3D network that secures the stability of printed constructs in biological media.

composites seem a powerful strategy to endow different functionalities into a bioink.

Methylcellulose (MC) is a water-soluble biopolymer isolated from cellulose by partial substitution of hydroxyl groups with methoxy groups[15] and shows sol−gel transition around 37 °C, which is related to the change from a hydrophilic to a hydrophobic nature.[16] It was shown that single-component MC hydrogel could be easily printed at 21 °C with more than 80% cell viability, whereas rough strands containing voids were observed at lower or higher temperatures.[17] Despite the suitable properties of MC for 3D bioprinting, the lack of a post-cross-linking ability causes dissociation of MC in biological media. Given this, MC has been used as a printable component in combination with other polymers, which act as viscosity-enhancing agents. In the multicomponent MC-based hydrogel for a 3D bioprinting application, a blend of alginate/MC bioink has been introduced, in which alginate serves as a post-cross-linking agent in the presence of calcium chloride solution.[18] Moreover, treatment of alginate/MC with triso-dium citrate as a chelating agent improved the adhesion between printed layers resulting in better stackability. However, alginate could not sustain its structure in the biological medium and rapidly dissociated due to ionic exchange in body fluids.[12,19] Moreover, alginate is a bioinert polysaccharide without cell-adhesion sites.

Gelatin-methacryloyl (GelMA) is able to form a chemically cross-linked hydrogel under UV-irradiation.[20,21] This is also biodegradable, biocompatible, and has an integrin recognition RGD motif along its backbone, which is essential for the effective interaction of biomaterials with cells.[22−24] However, direct bioprinting of GelMA still remains a challenging matter due to the inadequate shear-thinning behavior and low viscosity at body temperature.[25] To address this issue, Liu et al.[26] took advantage of the physical gelation of GelMA at low temperatures, which occurs due to the coil-helix transition. Direct bioprinting of GelMA physical gel enable followed by photo-cross-linking under UV light enables the fabrication of complex 3D constructs. However, GelMA physical gel showed poor printing resolution. In this sense, the printability of GelMA was improved through blending with other biopol-ymers such as gelatin,[21] alginate,[27] hyaluronic acid,[28] and gellan gum,[14] which allows the adjustment of the rheological behavior of GelMA.

Here, we aimed to introduce methylcellulose/gelatin-methacryloyl (MC/GelMA) bioink, in which GelMA works as a permanent macromolecular cross-linker when exposed to UV irradiation and MC provides printability properties. Figure 1 visualizes the principle behind the proposed bioink used in this work. In brief, a photo-cross-linked MC/GelMA hydrogel was developed to address the lack of printability of GelMA as well as the quick degradation of MC in biological media. In addition, GelMA intensifies the thixotropic behavior of MC, which is advantageous in the printing process. Accordingly, a mixture of MC and GelMA was prepared and printed using a 3D printer to fabricate 3D constructs, which were then exposed to UV light. In the first step the degradation kinetics, the swelling ratio (SR), mechanical behavior, and morpho-logical features of prepared MC/GelMA hydrogel were characterized. Following this, the characterization of the rheological properties of bioink in terms of shear-thinning, self-healing, yield stress, time, and temperature sweep was performed to gain more insight into the material behavior before, during and after the bioprinting process. Influential printing parameters including applied pressure, print speed and

nozzle height were optimized to obtain the best resolution of MC-based hydrogels and print a series of 3D structures. Finally, the viability of human primary osteoblasts encapsulated within the MC/GelMA hydrogel was evaluated to confirm the biocompatibility of prepared bioinks and its ability to be used for practical 3D bioprinting applications.

2. EXPERIMENTAL SECTION

2.1. Synthesis and Fabrication of Bioink. Gelatin from porcine skin with a gel strength of 175 g bloom, methylcellulose with an approximate viscosity of 1500 cp at 2 wt %, methacrylic anhydride, and 2-hydroxy-1-(4-(hydroxyethoxy)phenyl)-2-methyl-1-propanone as a common photoinitiator were supplied by Sigma-Aldrich.

Gelatin was modified as reported previously, with slight changes.[20,29] Gelatin (10 g) was added to carbonate buffer (100 mL, 1 M, pH = 9.4) under vigorous stirring for 1 h at 60 °C. Next, 1.2 mL of methacrylic anhydride was divided into six equal volumes and each part was added dropwise to the solution every 30 min at 50 °C and pH was readjusted to 9−9.5 by the addition of 5 M sodium hydroxide before the addition of methacrylic anhydride. After completion of the reaction, the resulting solution was centrifuged for 10 min at 4200 rpm to remove unreacted methacrylic anhydride from the sediment. Then, 100 mL of preheated deionized water was added to the solution and the pH was adjusted to pH 7.0 by the dropwise addition of 6 M hydrochloric acid. Following this, the resulting modified gelatin was dialyzed against deionized water for 5 days at 45 °C with 12−14 kDa molecular weight cutoff and then lyophilized in a freeze-dryer for 2 days. ^{1}H NMR measurement (Bruker AVANCE II 500 MHz) was used to confirm the successful functionalization of gelatin in which 20 mg/mL of GelMA was dissolved in deuterated water (Figure S1). To prepare MC/GelMA hydrogel, lyophilized GelMA (5 and 10 wt %) and a photoinitiator (0.75 wt %) were dissolved in Na$_2$SO$_4$ 0.05 M at 70 °C for 10 min. Next, MC powder was gradually added to the resulting solution at 50 °C under stirring for 30 min to achieve homogenous dispersion of MC. The resulting solution was kept at 4 °C for 24 h to ensure full hydration. To compare the MC/GelMA hydrogel with MC, three different concentrations of MC (4, 6, 8 wt %) were prepared, in which MC powder was dispersed in Na$_2$SO$_4$ 0.05 M. Table 1 summarized the different formulation of prepared MC/GelMA inks. Samples were coded as MCx/GelMAy where x and y denote the weight concentrations of MC and GelMA, respectively.

Table 1. Formulation of Prepared MC/GelMA Inks in 4 mL 0.05 M Na$_2$SO$_4$ Solution

sample code	MC (mg)	GelMA (mg)	photoinitiator (mg)
MC4	160	0	0
MC6	240	0	0
MC8	320	0	0
GelMA5	0	200	30
GelMA10	0	400	30
MC8/GelMA5	320	200	30
MC8/GelMA10	320	400	30

2.2. Rheological Analysis. Rheological characteristics of hydrogels were measured by means of a Physica MCR301 rheometer (Anton Paar, Ostfildern, Germany) equipped with cone-plate accessories (50 mm diameter with a gap of 49 μm). Frequency sweep was performed over the range of 0.01−100 Hz in the oscillation mode. Shear-thinning behavior of the prepared samples was investigated over the shear rate ramp from 0.01 to 1000 s^{-1}. Yield stress of the samples was measured in the oscillation mode by ramping the shear stress from 0.01 to 10,000 Pa at 1 Hz frequency and cross-section point of storage and loss modulus considered as the yield point. Recoverability of samples was measured by applying repetitive low strain of 1% for 1 min, followed by a high strain of

100% (or 1000%) for another minute at 1 Hz frequency. Moreover, recoverability was also examined by measuring viscosity variation during three steps; (i) low shear rate (0.1 s^{-1}) for 1 min, (ii) high shear rate (100 or 500 s^{-1}) for 5 s as the residence time in which bioink passes through the needle, and finally, (iii) low shear rate (0.1 s^{-1}) for 2 min to trace the extent of recovery. Temperature ramp experiments were recorded over 20−60 °C with 2 °C/min heating rate at 1 Hz frequency. Finally, a time sweep experiment was carried out at 37 °C for 600 s. The samples were left at room temperature for 10 min to reach equilibrium prior to testing. To determine the linear viscoelastic region, the strain was swept between 0.01 and 100% (Figure S2).

2.3. Morphological Features. To evaluate the morphological features of prepared hydrogels, GelMA and MC/GelMA hydrogels were cross-linked under UV-irradiation for 60 s (UV light intensity is 150 mW/cm^2) and then immersed in deionized water for 24 h, achieving the equilibrium state. Next, hydrogels were frozen at −80 °C and lyophilized for 2 days in a freeze dryer. Afterward, hydrogels were coated by 10 nm Pt and the cross-section of samples was observed by means of a scanning electron microscope (SEM; model S4700, Hitachi, Japan).

2.4. Dynamic Mechanical Analysis. Cylindrical samples with 10 mm thickness and 15 mm diameter were prepared and cross-linked under UV-irradiation for 1 min prior to testing. Mechanical properties of prepared hydrogels were measured using a Q800 dynamic mechanical analyzer. Testing was implemented by applying uniaxial compression with 0.1 N steps at 25 °C. Compressive modulus was calculated from the slope of the stress−strain curve in the 10% strain range.

2.5. Swelling ratio of the Hydrogel. Presolution (125 μL) was added between two glass slides and then thin films of hydrogel were prepared under UV-irradiation for 60 s. The swelling ratios (SRs) of GelMA and MC/GelMA were measured for 6, 12, and 24 h in deionized water at 37 °C. The SR of the hydrogel is calculated based on the equation

$$SR = \frac{W(swell) - W(dry)}{W(dry)} \qquad (1)$$

where $W(swell)$ and $W(dry)$ denote hydrogel weight at the swollen and dry state. Three trials were performed for each sample.

2.6. Degradation of Hydrogel. To measure the degradation of hydrogel, three samples of MC/GelMA (20 mm diameter and 10 mm height) were prepared and cured under UV-irradiation for 60 s and soaked in deionized water for 60 days. After certain intervals, samples were taken out and weighted. Degradation of samples was calculated as follows

$$DP \% = \frac{W(t) - W(0)}{W(0)} \times 100 \qquad (2)$$

where $W(0)$ is the weight of the sample before immersing in deionized water and $W(t)$ is the weight of the sample at a predetermined time.

2.7. FTIR and XRD Measurements. To investigate the interaction between MC and GelMA, Infrared [Fourier transform infrared (FTIR)] spectrometry was performed by means of a Nicolet 6700 (Thermo-Fisher) in the wavelength range of 4000−600 cm^{-1}. X-ray diffraction (XRD) analysis was also carried out by means of Rigaku MiniFlex 600 (Japan) under predefined condition (40 kV and 15 mA, $2\theta = 5-75°$).

2.8. Printability Test. Fiber formation of MC/GelMA hydrogel at the needle tip was viewed using a contact angle camera. In this way, 3 mL of hydrogel was loaded into a 10 mL syringe with a 225 μm blunt-tipped stainless steel needle and extruded by a syringe pump with a 0.5 mL/h flow rate in a horizontal direction.

2.9. Printing. 3D printing was conducted in an Allevi 2 printer (Allevi, PA, USA) through the layer-by-layer deposition of hydrogel onto a glass slide. 3D constructs were designed in an Autodesk fusion 360 and converted into Gcode by Slic3r software and then uploaded into Allevi software. Bioink was loaded into a syringe with a blunt-
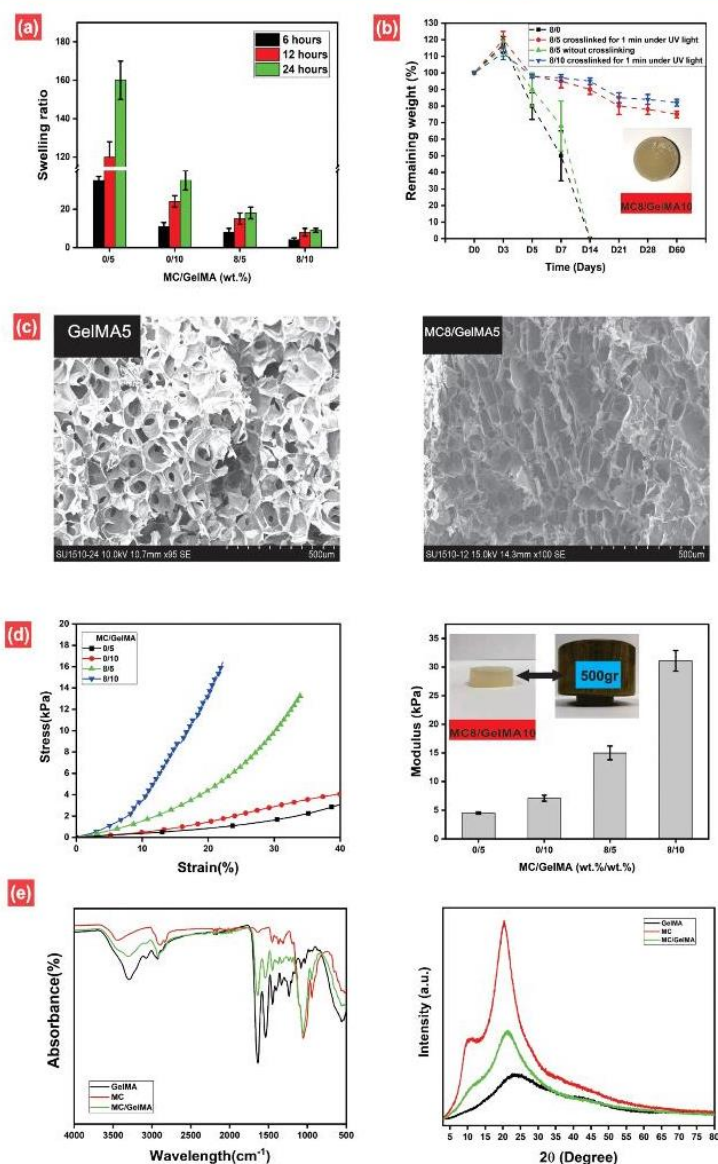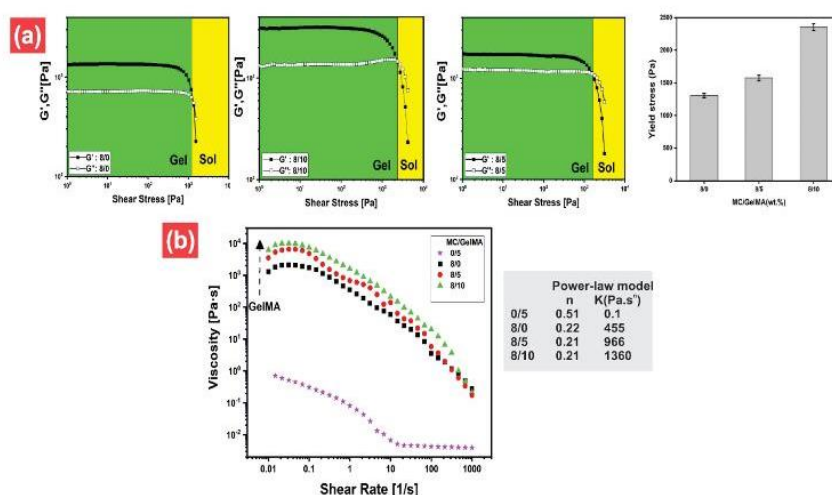
Figure 2. Characterization of MC/GelMA hydrogels; (a) SR of MC/GelMA hydrogel at 3 different times. It was observed that the introduction of MC lead to a decrease in SR capacity. In addition, the SR drops as GelMA concentration increases. (b) Effect of GelMA on the degradation behavior of MC in deionized water at 37 °C. Pure MC and uncured MC/GelMA hydrogel fully dissociated in two weeks. (c) Effect of MC on the morphological features of GelMA. SEM micrograph of GelMA5 and MC8/GelMA5 hydrogel shows an interconnected porous structure with roughly the same pore size. (d) Effect of MC on the compression strength of MC/GelMA hydrogels. The compressive modulus was calculated from the initial linear region. Compressive modulus directly related to the GelMA concentration and addition of MC improved the mechanical properties. (e) FTIR and XRD pattern of MC/GelMA hydrogels.

tipped stainless steel needle (225 μm) at room temperature and left for 15 min to reach equilibrium prior to printing. To optimize the printing parameters, prepared hydrogels were printed at different deposition speeds (1, 2, 4, 6, 8 mm/s), pressures, and nozzle heights (0.2, 0.3, 0.4 mm), and the widths of printed lines were imaged using a stereomicroscope. For visualization, 3D constructs were colored by the addition of food dye and imaged using a stereomicroscope. Printed objects were cross-linked under UV light for 1 min after completion of printing.

2.10. Cell Viability and Bioprinting. To assess the cell viability of prepared bioink, human primary osteoblasts derived from adult cancellous bone[30] were cultured in alpha-modified minimal essential medium containing 10% fetal bovine serum in an incubator with humidified atmosphere and 5% of CO_2 for 1 week at 37 °C. Next, cells were removed by collagenase/trypsin digestion and encapsulated in the MC8/GelMA5 hydrogel. For the control sample, the cells were added to the culture media instead of mixing with hydrogel. A live/dead cell assay was performed to evaluate the extent of cell viability over time, in which live cells were stained with calcein AM (green) and dead cells with were stained ethidium homodimer-3 (red). The stained cells were incubated for 10 min and then placed under an inverted fluorescence microscope. Images were obtained from a z-stack probe using EZC1 software. The number of live (green) and dead (red) cells were counted after 1, 24, and 48 h. Three samples of

Figure 3. Characterization of rheological behavior of MC/GelMA hydrogel dominating in the extrusion stage. (a) Monitoring of the G' and G'' values over shear stress sweep, revealing higher yield stress of MC/GelMA compared to pure MC. (b) Variation of viscosity over the shear rate sweep. For all cases, shear-thinning behavior was observed.

MC8/GelMA5 ink were examined for cell viability testing. Moreover, the cell-laden bioink was then transferred into the syringe and a lattice structure was printed into a culture well using a 27G needle with a printing speed of 8 mm/s and then cured under UV-irradiation for 1 min and imaged under an inverted fluorescence microscope.

3. RESULTS AND DISCUSSION

3.1. Characterization of Prepared Bioink. The SR plays an important role in biological applications and determines the water uptake capacity; a higher value of SR indicates greater retention of water, which better mimics native tissue.[31] Moreover, the rate of diffusion and removal of waste are also governed by the SR.[28,32] Because GelMA is a well-known hydrophilic biopolymer, it was expected that GelMA would display a high SR. As can be seen in Figure 2a, the SR exceeded ~160 for GelMA. However, this was diminished fourfold upon increasing the GelMA concentration to 10 wt %, which shows that the SR strongly depends on the cross-linking density of 3D network; higher cross-linking density causes segments between joint points to become smaller and prevents swelling.[33] SR also closely related to the diffusion coefficient, which is discussed in Supporting Information (Figure S3). Overall, the SR of GelMA significantly declined upon the addition of MC hydrogel. This behavior is explained by the fact that the addition of another biopolymer component to GelMA fills the existing free volumes and limits water diffusion in the GelMA matrix.[32]

In tissue engineering, the biodegradability of hydrogels is an advantage for a scaffold as there is no need for further surgery to remove implanted material. However, it should be noted that the degradation rate of a hydrogel scaffold should ideally match that of tissue regeneration. To explore the effect of GelMA on the degradation of MC, the remaining weights of MC-based hydrogels were traced for 2 months in deionized water at 37 °C (Figure 2b). It was observed that pure MC and uncured MC8/GelMA5 hydrogels rapidly dissociated within two weeks due to the lack of permanent cross-linking. However, in the case of cured MC8/GelMA5 and MC8/GelMA10, stable hydrogels were observed without any deformation, as reflected in the representative image of

MC8/GelMA10. To quantify the degradation kinetics of MC/GelMA hydrogel, experimental results were fitted with $\left(\frac{W(t)}{w(0)}\right)^{0.5} = 1 - K_{d}t$ equation,[34] where K_{d} is the degradation coefficient (Figure S4). Accordingly, the K_{d} for cured MC/GelMA hydrogels ($0.4-0.7 \times 10^{-2}$ day^{-1}) is significantly lower than pure MC8 (10×10^{-2} day^{-1}) and uncured MC8/GelMA5 (9.6×10^{-2} day^{-1}), indicating a lower degradation rate of MC/GelMA hydrogel. The slow degradation rate of MC/GelMA hydrogel preserves its mechanical properties, thus cells and newly forming tissue would remain supported during the regenerative process.

Scaffolds with interconnected porous structures promote cell adhesion and proliferation because this provides a pathway to discard waste and transfer oxygen and nutrition to encapsulated cells.[22] Given this, to explore the effect of MC on GelMA microstructure, the cross-sectional morphologies of GelMA before and after addition of MC were compared. As seen in Figure 2c, GelMA5 forms a honeycomb-like interconnected porous structure as reported elsewhere.[23] The introduction of MC does not disrupt the morphological features of GelMA significantly and only causes the formation of pores with wrinkled walls. In addition, the pore size distribution drops from 82 ± 35 μm for GelMA5 to 69 ± 22 μm for MC8/GelMA5 hydrogel, which is attributed to the higher polymer content in MC8/GelMA5 hydrogel. A porous structure with this pore size distribution is predicted to be suitable for use as a scaffold material in tissue engineering.[35]

The mechanical strength of hydrogels is dominantly governed by the nature of the polymer and cross-linking density, which can behave as a physical cue for the regulation of cell behavior.[36,37] The compressive stress−strain curves of MC/GelMA hydrogel are shown in Figure 2d. As can be seen, the introduction of MC resulted in curves shifted toward higher strains, as the compressive modulus for GelMA5 is 4.5 ± 0.2 kPa, whereas it improved 3 times and reached $15 + 1.2$ kPa for MC8/GelMA5. Compared to that of MC9/Alginate3 hydrogel with a reported compressive modulus of 11.1 kPa,[19] the compressive stiffness of MC8/GelMA10 hydrogel is almost 3 times higher. In addition, an increase in the GelMA loading
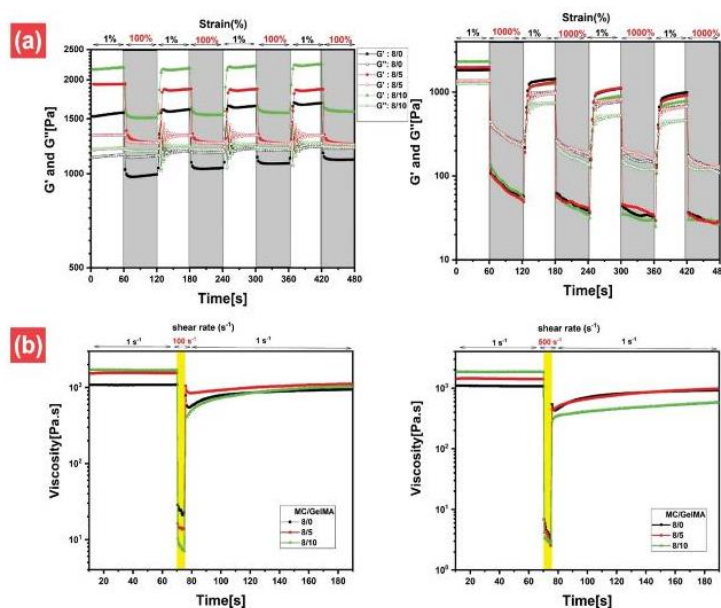
Figure 4. Characterization of rheological behavior of the MC/GelMA hydrogel dominating in the recovery stage. Self-healing properties of MC/GelMA over alternative low and high (a) strain and (b) shear rates. Storage modulus sharply decreases at high strain and recover quickly after removing strain. Viscosity of the studied MC/GelMA hydrogels quickly recovered after removing the high shear rate.

improved the compressive modulus, reflected in pure GelMA and MC/GelMA hydrogel. This trend has been reported in other studies. For example, Camci-Unal et al.[33] found that mechanical stiffness of GelMA/hyaluronic acid improved upon increasing polymer concentrations. Overall, the mechanical properties of MC/GelMA appears adequate for supporting cell growth in tissue engineering.[33]

Interaction between GelMA and MC biopolymers was investigated by means of FTIR and XRD measurements (Figure 2e). In the FTIR spectra, MC shows a characteristic peak centered at 2882 cm^{-1} (C−H stretch in methyl ether), which appeared at the same wavelength in the MC/GelMA spectra. In addition, MC and GelMA present broad peaks at around 3438 and 3302 cm^{-1} (OH stretch) respectively, which does not shift in the MC/GelMA spectra. FTIR results suggests that physical blending of MC to GelMA does not change chemical composition of corresponding biopolymers. The XRD pattern of MC displays diffraction peaks at following 2θ angles: 10.5 and 20.2°, which the former proves the modification of cellulose and substitution of methyl groups along the MC backbone and the latter related to the partial crystalline structure of MC.[38] Moreover, GelMA displays one broad peak at $2\theta = 23.5°$, as reported in previous works.[39] The MC/GelMA hydrogel shows the same diffraction peaks at $2\theta = 11$ and 21.2°, indicating that the crystalline structure of MC and GelMA is not disrupted upon physical blending.

3.2. Rheological Evaluation. *3.2.1. Flow Initiation and Shear-Thinning Characteristics of MC/GelMA Ink.* Rheological analysis gives a deep insight into the flow behavior of bioink when it is subjected to shear stress during the 3D printing process.[40] Printing of ink can be classified into three main stages. In the first stage, ink should pass through a thin nozzle, which generally characterized by yield stress and shear-thinning behavior. Yield stress reflects the minimum force required for initiation of flow. Figure 3a presents the G' and G''

values obtained from shear stress sweep analysis of the MC/GelMA hydrogels with different formulations. Bioink shows yield where applied shear stress overcomes the attraction force between polymer chains and is defined as the crossover point of G' and G''.[41] Accordingly, in the gel state at lower shear stress, the G'' value is lower than the G' for all studied MC/GelMA hydrogel. Transition from gel-like behavior ($G' > G''$) to solution-like behavior ($G' < G''$) occurs once $G' = G''$, indicating the flow initiation of ink.[42] The introduction of GelMA into MC cause crossover point between G' and G'' shifted toward higher shear stress. In addition, when the concentration of GelMA increases, a progressive increase in yield stress is observed for MC8/GelMA5 (1356 ± 42 Pa) and MC8/GelMA10 (2354 ± 53 Pa) hydrogel, corroborating to the physical interaction between MC and GelMA as well as the physical gelation of GelMA at room temperature. Higher yield stress enables the printed filament to behave as a solid and sustain its structure without cross-linking.[14] As a result, the MC/GelMA bioink needs higher pressure for dispensing and could provide better shape integrity after printing.[6]

Once pneumatic pressure behind the syringe reaches the yield stress, bioink starts flowing along the nozzle, where shear-thinning behavior is critical to conserve encapsulated cells from high shear stress.[11,43] Shear-thinning behavior, defined as a non-Newtonian behavior, causes the bioink experiences lower shear stress during the extrusion stage because of the drop in the viscosity value at high shear rates.[8] The shear-thinning behavior of MC/GelMA hydrogels was traced over a shear rate of 0.01−1000 s^{-1} (Figure 3b). The shear-thinning behavior of pure MC with different concentrations is discussed in the Supporting Information (Figure S5). The flow curves of the MC/GelMA hydrogel followed that of the MC8 hydrogel, showing a shoulder at the low shear rate, which is attributed to the yield stress. Following that, the viscosity of MC/GelMA ink plunged at higher shear rates, which is typical shear-
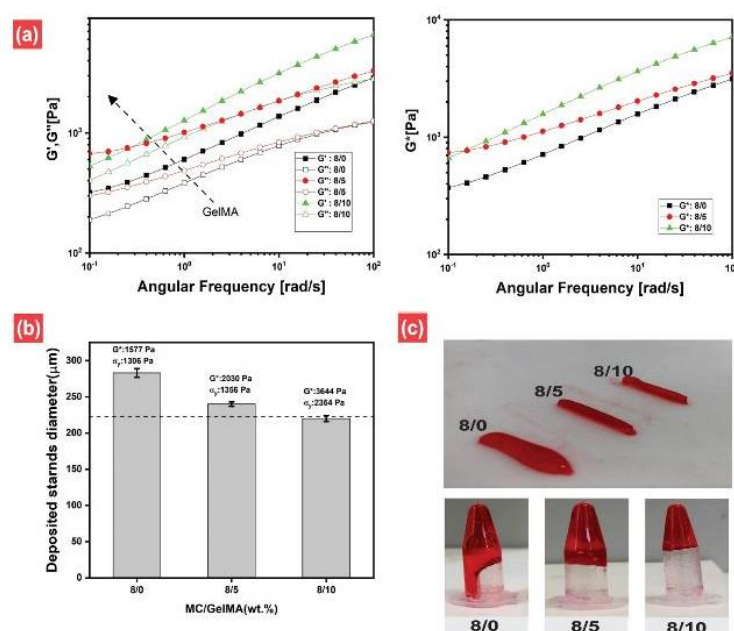
Figure 5. Characterization of rheological behavior of MC/GelMA hydrogel dominating in the shape integrity stage. (a) Variation of the G', G'' and G^* values over frequency sweep before cross-linking, (b) printed strands diameter for MC/GelMA inks, (c) the effect of self-supporting behavior on the integrity of printed strands (top) and tube inversion of formed MC/GelMA hydrogel (bottom).

thinning behavior. The shear-thinning behavior of MC is associated with the dynamic hydrophobic interactions between methoxy groups, which undergo breakdown under shear stress and reassemble once shear stress is removed.[44] The power-law model has been frequently employed to quantify the shear-thinning behavior of hydrogels as follows

$$\eta = K\dot{\gamma}^{1-n} \qquad (3)$$

where η is viscosity, $\dot{\gamma}$ is the shear rate, K is the consistency index, and n is the power-law index. The consistency index indicates the viscosity value at low shear rates and the power-law index is an indicator of the non-Newtonian behavior. For a Newtonian fluid, n is equal to one, whereas $n < 1$ or $n > 1$ are attributed to the shear-thinning and shear-thickening behaviors, respectively.[10] The power-law indexes for the MC8/GelMA5 and the MC8/GelMA10 are around 0.21, similar to the MC8, showing that viscosity and shear-thinning behavior of MC/GelMA is governed by the MC component and shear-thinning behavior of MC was not disrupted by the addition of GelMA. Moreover, the viscosity of the MC/GelMA hydrogel at low shear rates increased with an increased in the GelMA concentration, as reflected in the calculated K value. In general, higher values of K benefit shape fidelity of printed constructs after printing. It should be highlighted that, although GelMA5 shows shear-thinning behavior, the low viscosity of GelMA causes the lack of printability of pure GelMA bioink. However, further addition of 8 wt % MC to the GelMA5 solution causes the viscosity of GelMA to shift toward higher values by 3−4 orders of magnitude at a low shear rate. It can be concluded that MC/GelMA bioink demonstrates shear-thinning behavior with a higher viscosity than pure MC and GelMA at lower shear rates, which provide higher shape fidelity after printing.

3.2.2. Recoverability of MC/GelMA Ink. In the second stage of printing, once the ink is extruded from the nozzle tip, it is relieved from the high shear stress and should have the ability

to quickly recover to its initial state. The recoverability of the MC8, MC8/GelMA5, and MC8/GelMA10 hydrogels was investigated by applying alternating low and high strain (Figure 4a). The G' values of MC8, MC8/GelMA5, and MC8/GelMA10 plunged suddenly when subjected to high strain and recovered quickly in both high strain levels. For each cycle, hydrogels changed from gel-like behavior to sol-like behavior at high strain ($G'' > G'$) and rebound to gel-like behavior after removing the strain. Recoverability of hydrogels differs slightly between cycles, revealing that the MC/GelMA hydrogel is able to reassemble its physical structure quickly. Self-healing kinetic is another important concern, which determines the rate of recovery after extrusion; low self-healing kinetic causes a printed strand leaked to a neighboring area. As observed, for all cases, G' recovered in less than 10 s. However, the degree of recoverability is influenced by the applied strain level. For example, when strain is 100%, MC/GelMA could fully recover to its initial state, while once strain increased to 1000%, recoverability declined to 70−80%. Moreover, recoverability just slightly decreased with increasing GelMA concentration, which shows that MC controls the recovery properties of MC/GelMA hydrogel. It should be noticed that even though MC/GelMA could not recover completely at 1000% strain, the G' value of MC/GelMA can recover to >800 Pa which is enough for fiber formation after extrusion. In addition, recoverability of MC6 and MC4 is shown in Figure S6.

To further characterize the recoverability, viscosity values of the MC/GelMA inks were measured over three steps (Figure 4b): (i) subjecting low shear rate similar to the extrusion sate in syringe, (ii) application of high shear rate for a short time simulating the nozzle part, and (iii) returning to the low shear rate once ink extruded out from needle tip. As can be seen, the viscosity of MC/GelMA hydrogels with different formulations were ~1000−1200 Pa·s at low shear rates, dropping suddenly to ~10 Pa·s at high shear rate(100 s^{-1}) and recovered quickly
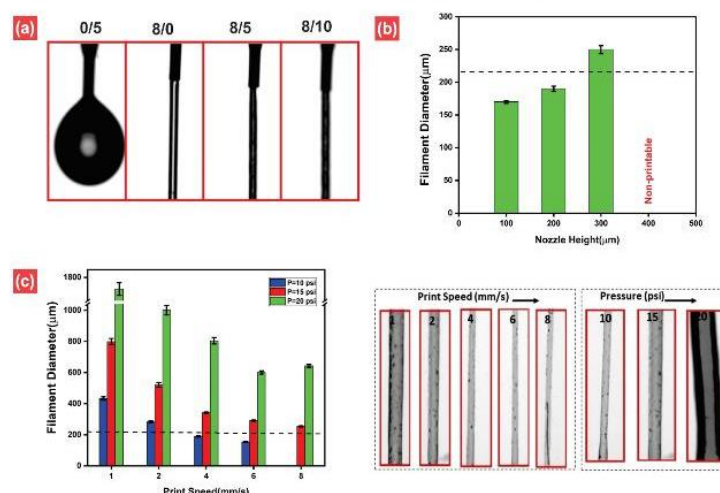
Figure 6. Fiber characterization of MC/GelMA bioink. (a) Fiber formation of MC/GelMA with different concentrations. GelMA5 formed droplet at the needle tip, while the addition of MC cause it changed to filament shape. (b) Filament resolution in terms of nozzle height and (c) print speed.

at a low shear rate. However, the extent of recovery for viscosity is inversely related to the applied shear rate and GelMA concentration, as expected from recoverability of storage and loss modulus at different strains. It can be concluded that the MC/GelMA hydrogel can recover quickly even using a printing needle with a very narrow aperture causing bioink to experience high strain and the incorporation of GelMA does not hinder recoverability.

3.2.3. Shape Integrity Characteristics of MC/GelMA Inks. In the third stage of printing, gravity force and weight of top layers place pressure on the printed strands, that might adversely affect the print resolution; therefore, ink should have enough mechanical strength once deposited on the surface to support the integrity of printed construct. Apart from the role of yield stress in the determination of mechanical resistance of ink underneath top layers, the G' and complex modulus ($G*$) also reflects the shape integrity of the construct before permanent cross-linking. In this way, Figure 5a provides the evolution of G', G'', and $G*$ over the frequency sweep for MC/GelMA inks before the cross-linking. As observed, all the G', G'' and $G*$ are frequency-dependent and show downward trend upon decline in the frequency values. Frequency sweep test shows the G' values for MC-based hydrogels are always over respective the G'' value with no crossover point in the entire studied range of frequency, confirming the gel behavior of MC8 and MC8/GelMA5 and MC8/GelMA10 hydrogels. Moreover, it is observed that the addition of GelMA increases the value of the G' and $G*$ over the whole frequency sweep, similar to the yield stress results. This is mainly due to the lower free volume for water movement when GelMA is mixed with MC. Similar behavior was reported for a MC/Xanthan Gum blend.[44] To find the link between the resolution of printed strands and $G*$ and σ_y, the diameter of printed strands on the surface was compared with the nozzle diameter (Figure 5b). Accordingly, significant differences were observed between strand and nozzle diameter for pure MC hydrogel due to the spreading of pure MC on the surface. However, the strand diameters are consistent with the needle diameter at a higher concentration of GelMA due to the higher complex modulus and yield stress of MC/GelMA compared to MC

hydrogel. Surface tension defined as the tendency of fluid to minimize the possible surface area when is in contact with other substance, which arises from the strong attraction of fluid molecules to each other compared to other molecules in other substances. Given this, it is expected that high surface tension avoids flow-induced distortion of printed strands on the surface. Accordingly, it is observed that pure MC spreads on the surface, whereas the MC/GelMA inks sustain the integrity of printed strands (Figure 5C, top). For further illustration of the role of surface tension on the mechanical strength of the MC/GelMA inks, inks were inserted into a 1.5 mL reaction tube and inverted for 30 min (Figure 5C, bottom). Accordingly, pure MC flows after 30 min, whereas the MC8/GelMA5 and MC8/GelMA10 remain motionless. Printed structures cross-linked under UV irradiation and were placed at 37 °C. Therefore, the thermo-responsive behavior of the MC and MC/GelMA was shown in Figures S7 and S8, respectively. In general, MC is expected to achieve higher resolution once mixed with GelMA due to the higher shape integrity of MC/GelMA inks compared to single-component MC.

3.3. Printability of MC/GelMA Bioink. Printable bioink needs to form a cylindrical fiber rather than a droplet at the tip of needle during extrusion, as an indication of sufficient shape fidelity.[6,9] Prepared MC/GelMA hydrogels were evaluated in terms of fiber formation by dispensing bioink with a constant volume rate (Figure 6a). GelMA5 displayed droplet formation at the needle tip and the addition of MC to GelMA leads to consistent fiber formation because of an increase in the viscosity value by almost 1000-fold. It is interesting to note that, although pure MC formed a continuous cylindrical filament instead of a droplet at the needle tip, MC4 and MC6 hydrogels continued to extrude after eliminating load from the syringe, which indicates that they are inappropriate for printing (not shown here). This simple screening test revealed that MC/GelMA could be successfully extruded into a fiber shape from the needle, which is a prerequisite for bioink.

Next, to assess the resolution of prepared MC-based hydrogels, it is crucial to find the best operating parameters for the 3D printing process. Hereafter, according to the results
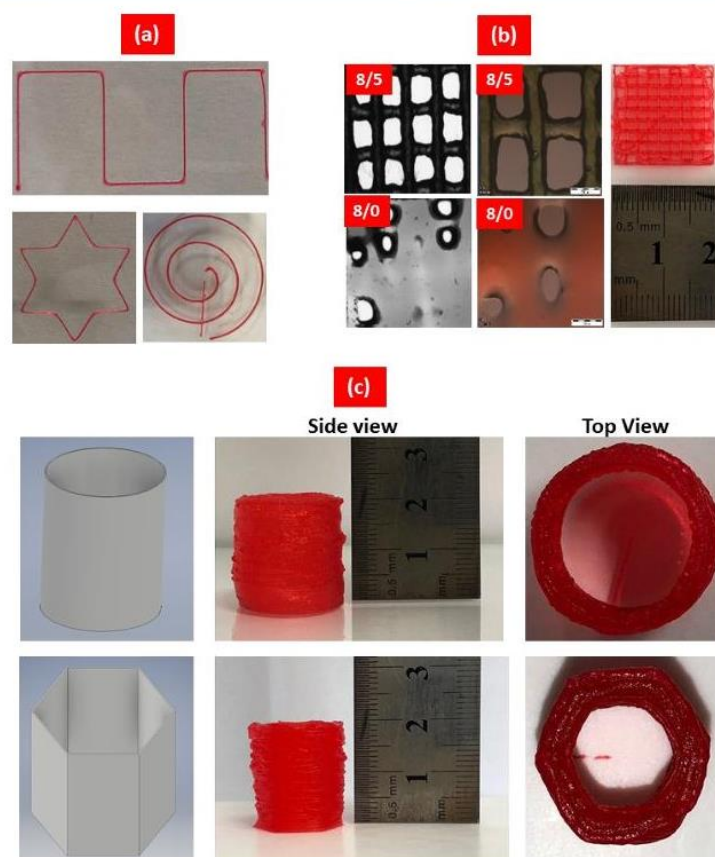
Figure 7. Assess the printability of the MC8/GelMA5 ink in (a) 1D, (b) 2D, and (c) 3D constructs.

obtained from the shape integrity of MC/GelMA inks, we selected the 8/5 formulation for further characterization. The nozzle height is determining factor, which allows us to print 3D constructs. To optimize the nozzle height, we tested four different levels (0.1, 0.2, 0.3, 0.4 mm), as shown in Figure 6b. It was found that when the distance between the needle tip and platform is 0.4 mm, the extruded material is not able to attach to the surface consistently because it is too far from the platform and materials twist around the needle tip. When the distance is 0.3 mm, the strand diameter ($250 \pm 6 \ \mu m$) is larger than the needle size ($225 \ \mu m$). On the other hand, when the nozzle height is too low ($100 \ \mu m$), the strand diameter is less than the needle size ($195 \pm 4 \ \mu m$). Consequently, it is perceived that when nozzle height ($200 \ \mu m$) is close to the nozzle diameter ($225 \ \mu m$), the best resolution is achieved, whereas if the nozzle height set too far from platform, printed layers cannot attach, and if it is too close, the needle tip will disturb the bottom layer when it is moving to print the next. Similar results were reported by Wilson et al.[10] who reported that the nozzle height should be adjusted to the needle diameter to attain a better resolution of bioink. Furthermore, print speed and air pressure not only have a significant impact on the resolution of printed strands but also determine the time bioink resides inside the needle; less residence time in the needle is likely to improve viability of cells within the bioink. Given this, the effects of air pressure (10, 15, 20 psi) and print speed (1, 2, 4, 6, 8 mm/s) on strand diameter were investigated for the MC8/GelMA5 hydrogel (Figure 6c). It

was observed that, for all print speeds, the strand diameter increased upon the increase in the air pressure. On the other hand, the strand diameter steadily declined as print speed increased. It is noteworthy that once the print speed and air pressure are 8 mm/s and 10 psi, respectively, MC8/GelMA5 formed discontinuous strands. To attain higher resolution, we chose to set nozzle height at 200 μm from the platform, the print speed at 8 mm/s and the air pressure at 15 psi for the MC8/GelMA5 formulation.

To systematically assess the printability of the ink, first, the MC8/GelMA5 printed one-dimensional single-layer structures (Figure 7a). Accordingly, MC8/GelMA5 printed straight lines matched with needle size. Further, star shape with different angles were printed without overlapped area, showing the ability of ink to print constructs with sharp angles. Next, a single-layer spiral with round edges was printed without spreading on the surface. Overall, the high yield stress and G^* lead to high shape integrity behavior.

Next, four-layers lattice structure was printed and evaluated in terms of accuracy and shape fidelity (Figure 7b). As seen, the MC8/GelMA5 ink can maintain shape integrity without spreading on the surface. However, the MC8 hydrogel spread on the surface and compromised the lattice porosity. This is due to the lower G^* and yield stress value of the MC8 compared to the MC8/GelMA5 ink. Printability (Pr) of ink can be defined according to the following equation[45]
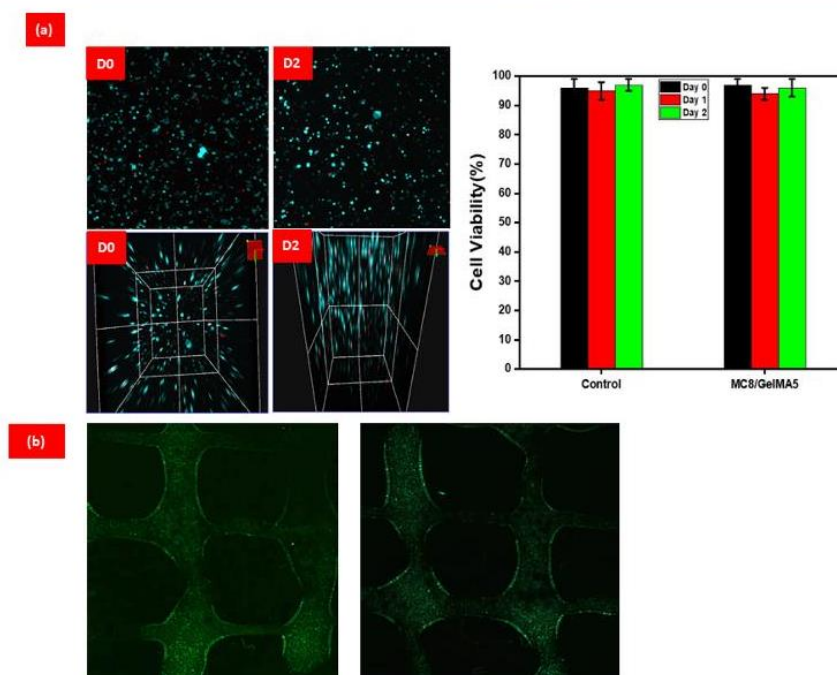
Figure 8. Fluorescent images of cell-laden MC8/GelMA5 hydrogel stained with calcein−AM and ethidium homodimer-3. (a) Bulk MC8/GelMA5 bioink over 48 h (b) Bioprinted lattice.

$$Pr = \frac{L^2}{16A} \tag{4}$$

where L is the perimeter and A is the area. Pr = 1 means that the channels with regular square shapes are formed during printing. The smaller value of Pr indicates the spreading of ink to the neighboring area. The Pr values are 0.2 and 0.94 for the MC8 and MC8/GelMA5 hydrogels, suggesting the high printability of MC8/GelMA5 ink.

Finally, MC/GelMA hydrogel printed 3D constructs including 100-layer cylindrical and hexagonal structures (Figure 7c). As can be viewed, the printed objects are able to withstand the load from the multiple printed layers without collapsing. This is due to the high shape integrity behavior of MC8/GelMA5 ink, which provides enough strength for bearing load. These 3D printed structures demonstrate that the MC/GelMA ink is able to print complex multi-layered structures with round or sharp edges.

3.4. 3D Bioprinting of MC/GelMA Ink. Single-component GelMA hydrogel proved to be a promising scaffold for bone tissue regeneration due to the tunable mechanical strength and good biocompatibility.[46] In research conducted by Weitz et al.,[47] it was found that GelMA microgel promotes osteogenesis after injection into a bone lesion site. Moreover, GelMA has been combined with other natural or synthetic polymers such as alginate,[48] hyaluronic acid,[39] and poly ethylene glycol diacrylate[49] to be used for bone tissue engineering. On the other hand, MC hydrogel incorporated with calcium phosphate nanoparticles shows high bone formation, in which MC provides interparticular space for bone ingrowth.[50] Given this, human primary osteoblasts were encapsulated within the MC8/GelMA5 hydrogel and viability of the cells was monitored in the thin film (bulk hydrogel) and 3D bioprinted structure. Figure 8 provides the fluorescence

images taken from a thin film and 3D bioprinted lattice of cell-laden MC8/GelMA5 hydrogel stained with calcein−AM (green) and ethidium homodimer-1 (red). In the thin film, the viability of encapsulated human osteoblastic cells in the control sample and MC8/GelMA5 hydrogel are almost identical and above 90% (Figure 8a). Moreover, as seen from 3D images, cells are distributed in the hydrogel homogenously and without noticeable clustering of cells. Next, cell-laden MC8/GelMA5 hydrogel transferred to the syringe was printed into a lattice structure, and cells remained viable during bioprinting similar to the thin film (Figure 8b). This is likely due to the shear-thinning behavior of MC8/GelMA5 bioink, which facilitates the injection of hydrogel along nozzle through a drop in the viscosity value. Overall, MC/GelMA bioink proved to be a promising bioink in terms of cell viability, with above 90% survival.

4. CONCLUSIONS

In summary, new photo-cross-linkable MC/GelMA bioink with highly thixotropic behavior was developed in which GelMA is used as permanent macromolecular cross-linker and MC to provides printability requirements. MC shows degradation within two weeks, whereas the addition of GelMA imparts biological stability to MC as it remained almost intact for up to 2 months. This is attributed to the photo-cross-linking ability of GelMA, as uncured MC/GelMA also dissociates within two weeks. Moreover, it was found that compressive modulus for GelMA5 (4.5 ± 0.2 kPa) improved threefold for MC8/GelMA5 as a result of physical polymer−polymer interaction of MC/GelMA. The rheological properties of pure MC and MC/GelMA at different concentrations were evaluated during three different stages of printing including extrusion, recovery, and shape integrity. It was found that viscosity of MC/GelMA plunges from ~1200 Pa·s at low shear

rate to ~10 Pa·s at 100 s^{-1}, which eases the extrusion during the printing process. In addition, MC/GelMA bioink shows full recoverability at 100% strain. Yield stress of MC8 was also improved upon the addition of GelMA, which provides more shape fidelity after deposition. Polymer−polymer interactions between GelMA and MC improved yield stress and complex modulus of the MC/GelMA ink, resulting in better printability. Taking into consideration rheological properties, hydration, biological stability, shape fidelity, and printability of different formulations, MC8/GelMA5 was selected as the optimal compound. Different 1D, 2D, and 3D structures were successfully printed, showing that the ink provides high shape fidelity without spreading on the surface or collapsing under loading of multiple layers and therefore can be used for 3D printing of complex biological structures. Finally, the cell viability of human primary osteoblasts encapsulated within the MC8/GelMA5 ink was evaluated and confirmed the biocompatibility of prepared bioinks in both bulk hydrogel and 3D bioprinted structures.

ASSOCIATED CONTENT

Supporting Information

The Supporting Information is available free of charge at https://pubs.acs.org/doi/10.1021/acsabm.0c00169.

H NMR spectra of pure gelatin and GelMA, strain-sweep of MC/GelMA hydrogel with different weight ratio to find linear viscoelastic region, linear regression of SR against time to determine SR kinetics, linear regression of $(W(t)/W(0))^{0.5}$ against time for MC/GelMA to determine degradation kinetics, shear-thinning behavior of pure MC hydrogels, recoverability of pure MC with different concentrations, thermo-responsive behavior of pure MC at 23 and 37 °C, and thermo-responsive behavior of MC/GelMA over time and temperature sweep (PDF)

AUTHOR INFORMATION

Corresponding Author
Dusan Losic − *School of Chemical Engineering and Advanced Materials, The University of Adelaide, Adelaide, South Australia 5005, Australia;* orcid.org/0000-0002-1930-072X; Email: dusan.losic@adelaide.edu.au

Authors
Hadi Rastin − *School of Chemical Engineering and Advanced Materials, The University of Adelaide, Adelaide, South Australia 5005, Australia*
Renee T. Ormsby − *Biomedical Orthopaedic Research Group, Centre for Orthopaedic & Trauma Research, The University of Adelaide, Adelaide, South Australia 5000, Australia*
Gerald J. Atkins − *Biomedical Orthopaedic Research Group, Centre for Orthopaedic & Trauma Research, The University of Adelaide, Adelaide, South Australia 5000, Australia*

Complete contact information is available at:
https://pubs.acs.org/10.1021/acsabm.0c00169

Notes
The authors declare no competing financial interest.

ACKNOWLEDGMENTS

REFERENCES

(1) Chimene, D.; Kaunas, R.; Gaharwar, A. K. Hydrogel Bioink Reinforcement for Additive Manufacturing: A Focused Review of Emerging Strategies. *Adv. Mater.* **2020**, *32*, 1902026.
(2) Hölzl, K.; Lin, S.; Tytgat, L.; Van Vlierberghe, S.; Gu, L.; Ovsianikov, A. Bioink properties before, during and after 3D bioprinting. *Biofabrication* **2016**, *8*, 032002.
(3) Chung, J. H. Y.; Naficy, S.; Yue, Z.; Kapsa, R.; Quigley, A.; Moulton, S. E.; Wallace, G. G. Bio-ink properties and printability for extrusion printing living cells. *Biomater. Sci.* **2013**, *1*, 763−773.
(4) Lee, J. M.; Yeong, W. Y. Design and printing strategies in 3D bioprinting of cell-hydrogels: A review. *Adv. Healthcare Mater.* **2016**, *5*, 2856−2865.
(5) Guvendiren, M.; Molde, J.; Soares, R. M. D.; Kohn, J. Designing biomaterials for 3D printing. *ACS Biomater. Sci. Eng.* **2016**, *2*, 1679−1693.
(6) Malda, J.; Visser, J.; Melchels, F. P.; Jüngst, T.; Hennink, W. E.; Dhert, W. J. A.; Groll, J.; Hutmacher, D. W. 25th anniversary article: engineering hydrogels for biofabrication. *Adv. Mater.* **2013**, *25*, 5011−5028.
(7) Stanton, M. M.; Samitier, J.; Sánchez, S. Bioprinting of 3D hydrogels. *Lab Chip* **2015**, *15*, 3111−3115.
(8) Guvendiren, M.; Lu, H. D.; Burdick, J. A. Shear-thinning hydrogels for biomedical applications. *Soft Matter* **2012**, *8*, 260−272.
(9) Paxton, N.; Smolan, W.; Böck, T.; Melchels, F.; Groll, J.; Jungst, T. Proposal to assess printability of bioinks for extrusion-based bioprinting and evaluation of rheological properties governing bioprintability. *Biofabrication* **2017**, *9*, 044107.
(10) Wilson, S. A.; Cross, L. M.; Peak, C. W.; Gaharwar, A. K. Shear-thinning and thermo-reversible nanoengineered inks for 3D bioprinting. *ACS Appl. Mater. Interfaces* **2017**, *9*, 43449−43458.
(11) Smith, P. T.; Basu, A.; Saha, A.; Nelson, A. Chemical modification and printability of shear-thinning hydrogel inks for direct-write 3D printing. *Polymer* **2018**, *152*, 42−50.
(12) Chimene, D.; Lennox, K. K.; Kaunas, R. R.; Gaharwar, A. K. Advanced bioinks for 3D printing: a materials science perspective. *Ann. Biomed. Eng.* **2016**, *44*, 2090−2102.
(13) Kolesky, D. B.; Truby, R. L.; Gladman, A. S.; Busbee, T. A.; Homan, K. A.; Lewis, J. A. 3D bioprinting of vascularized, heterogeneous cell-laden tissue constructs. *Adv. Mater.* **2014**, *26*, 3124−3130.
(14) Melchels, F. P. W.; Dhert, W. J. A.; Hutmacher, D. W.; Malda, J. Development and characterisation of a new bioink for additive tissue manufacturing. *J. Mater. Chem. B* **2014**, *2*, 2282−2289.
(15) Contessi, N.; Altomare, L.; Filipponi, A.; Farè, S. Thermo-responsive properties of methylcellulose hydrogels for cell sheet engineering. *Mater. Lett.* **2017**, *207*, 157−160.
(16) Chang, C.; Zhang, L. Cellulose-based hydrogels: present status and application prospects. *Carbohydr. Polym.* **2011**, *84*, 40−53.
(17) Negrini, N. C.; Bonetti, L.; Contili, L.; Farè, S. 3D printing of methylcellulose-based hydrogels. *Bioprinting* **2018**, *10*, No. e00024.
(18) Schütz, K.; Placht, A.-M.; Paul, B.; Brüggemeier, M.; Gelinsky, M.; Lode, A. Three-dimensional plotting of a cell-laden alginate/methylcellulose blend: towards biofabrication of tissue engineering constructs with clinically relevant dimensions. *J. Tissue Eng. Regener. Med.* **2017**, *11*, 1574−1587.
(19) Li, H.; Tan, Y. J.; Leong, K. F.; Li, L. 3D bioprinting of highly thixotropic alginate/methylcellulose hydrogel with strong interface bonding. *ACS Appl. Mater. Interfaces* **2017**, *9*, 20086−20097.
(20) Lee, B. H.; Shirahama, H.; Cho, N.-J.; Tan, L. P. Efficient and controllable synthesis of highly substituted gelatin methacrylamide for mechanically stiff hydrogels. *RSC Adv.* **2015**, *5*, 106094−106097.

(21) Yin, J.; Yan, M.; Wang, Y.; Fu, J.; Suo, H. 3D bioprinting of low-concentration cell-laden gelatin methacrylate (GelMA) bioinks with a two-step cross-linking strategy. *ACS Appl. Mater. Interfaces* **2018**, *10*, 6849–6857.

(22) Nichol, J. W.; Koshy, S. T.; Bae, H.; Hwang, C. M.; Yamanlar, S.; Khademhosseini, A. Cell-laden microengineered gelatin methacrylate hydrogels. *Biomaterials* **2010**, *31*, 5536–5544.

(23) Chen, Y.-C.; Lin, R.-Z.; Qi, H.; Yang, Y.; Bae, H.; Melero-Martin, J. M.; Khademhosseini, A. Functional human vascular network generated in photocrosslinkable gelatin methacrylate hydrogels. *Adv. Funct. Mater.* **2012**, *22*, 2027–2039.

(24) Spencer, A. R.; Shirzaei Sani, E.; Soucy, J. R.; Corbet, C. C.; Primbetova, A.; Koppes, R. A.; Annabi, N. Bioprinting of a Cell-Laden Conductive Hydrogel Composite. *ACS Appl. Mater. Interfaces* **2019**, *11*, 30518–30533.

(25) Bertassoni, L. E.; Cardoso, J. C.; Manoharan, V.; Cristino, A. L.; Bhise, N. S.; Araujo, W. A.; Zorlutuna, P.; Vrana, N. E.; Ghaemmaghami, A. M.; Dokmeci, M. R.; Khademhosseini, A. Direct-write bioprinting of cell-laden methacrylated gelatin hydrogels. *Biofabrication* **2014**, *6*, 024105.

(26) Liu, W.; Heinrich, M. A.; Zhou, Y.; Akpek, A.; Hu, N.; Liu, X.; Guan, X.; Zhong, Z.; Jin, X.; Khademhosseini, A.; Zhang, Y. S. Extrusion bioprinting of shear-thinning gelatin methacryloyl bioinks. *Adv. Healthcare Mater.* **2017**, *6*, 1601451.

(27) Colosi, C.; Shin, S. R.; Manoharan, V.; Massa, S.; Costantini, M.; Barbetta, A.; Dokmeci, M. R.; Dentini, M.; Khademhosseini, A. Microfluidic bioprinting of heterogeneous 3D tissue constructs using low-viscosity bioink. *Adv. Mater.* **2016**, *28*, 677–684.

(28) Schuurman, W.; Levett, P. A.; Pot, M. W.; van Weeren, P. R.; Dhert, W. J. A.; Hutmacher, D. W.; Melchels, F. P. W.; Klein, T. J.; Malda, J. Gelatin-Methacrylamide Hydrogels as Potential Biomaterials for Fabrication of Tissue-Engineered Cartilage Constructs. *Macromol. Biosci.* **2013**, *13*, 551–561.

(29) Shirahama, H.; Lee, B. H.; Tan, L. P.; Cho, N.-J. Precise tuning of facile one-pot gelatin methacryloyl (GelMA) synthesis. *Sci. Rep.* **2016**, *6*, 31036.

(30) Ormsby, R. T.; Solomon, L. B.; Yang, D.; Crotti, T. N.; Haynes, D. R.; Findlay, D. M.; Atkins, G. J. Osteocytes respond to particles of clinically-relevant conventional and cross-linked polyethylene and metal alloys by up-regulation of resorptive and inflammatory pathways. *Acta Biomater.* **2019**, *87*, 296–306.

(31) Okay, O. General properties of hydrogels. *Hydrogel Sensors and Actuators*; Springer, 2009; pp 1–14.

(32) Gaharwar, A. K.; Rivera, C.; Wu, C.-J.; Chan, B. K.; Schmidt, G. Photocrosslinked nanocomposite hydrogels from PEG and silica nanospheres: structural, mechanical and cell adhesion characteristics. *Mater. Sci. Eng. C* **2013**, *33*, 1800–1807.

(33) Camci-Unal, G.; Cuttica, D.; Annabi, N.; Demarchi, D.; Khademhosseini, A. Synthesis and characterization of hybrid hyaluronic acid-gelatin hydrogels. *Biomacromolecules* **2013**, *14*, 1085–1092.

(34) Cha, C.; Shin, S. R.; Gao, X.; Annabi, N.; Dokmeci, M. R.; Tang, X. S.; Khademhosseini, A. Controlling mechanical properties of cell-laden hydrogels by covalent incorporation of graphene oxide. *Small* **2014**, *10*, 514–523.

(35) Li, C.; Mu, C.; Lin, W. Novel hemocompatible nanocomposite hydrogels crosslinked with methacrylated gelatin. *RSC Adv.* **2016**, *6*, 43663–43671.

(36) Shi, J.; Xing, M. M. Q.; Zhong, W. Development of hydrogels and biomimetic regulators as tissue engineering scaffolds. *Membranes* **2012**, *2*, 70–90.

(37) Geiger, B.; Spatz, J. P.; Bershadsky, A. D. Environmental sensing through focal adhesions. *Nat. Rev. Mol. Cell Biol.* **2009**, *10*, 21.

(38) Filho, G. R.; de Assunção, R. M. N.; Vieira, J. G.; Meireles, C. d. S.; Cerqueira, D. A.; da Silva Barud, H.; Ribeiro, S. J. L.; Messaddeq, Y. Characterization of methylcellulose produced from sugar cane bagasse cellulose: Crystallinity and thermal properties. *Polym. Degrad. Stab.* **2007**, *92*, 205–210.

(39) Zuo, Y.; Liu, X.; Wei, D.; Sun, J.; Xiao, W.; Zhao, H.; Guo, L.; Wei, Q.; Fan, H.; Zhang, X. Photo-cross-linkable methacrylated gelatin and hydroxyapatite hybrid hydrogel for modularly engineering biomimetic osteon. *ACS Appl. Mater. Interfaces* **2015**, *7*, 10386–10394.

(40) Rutz, A. L.; Hyland, K. E.; Jakus, A. E.; Burghardt, W. R.; Shah, R. N. A multimaterial bioink method for 3D printing tunable, cell-compatible hydrogels. *Adv. Mater.* **2015**, *27*, 1607–1614.

(41) Ouyang, L.; Highley, C. B.; Rodell, C. B.; Sun, W.; Burdick, J. A. 3D printing of shear-thinning hyaluronic acid hydrogels with secondary cross-linking. *ACS Biomater. Sci. Eng.* **2016**, *2*, 1743–1751.

(42) Mouser, V. H. M.; Melchels, F. P. W.; Visser, J.; Dhert, W. J. A.; Gawlitta, D.; Malda, J. Yield stress determines bioprintability of hydrogels based on gelatin-methacryloyl and gellan gum for cartilage bioprinting. *Biofabrication* **2016**, *8*, 035003.

(43) Gupta, D.; Tator, C. H.; Shoichet, M. S. Fast-gelling injectable blend of hyaluronan and methylcellulose for intrathecal, localized delivery to the injured spinal cord. *Biomaterials* **2006**, *27*, 2370–2379.

(44) Liu, Z.; Yao, P. Injectable thermo-responsive hydrogel composed of xanthan gum and methylcellulose double networks with shear-thinning property. *Carbohydr. Polym.* **2015**, *132*, 490–498.

(45) Ouyang, L.; Yao, R.; Zhao, Y.; Sun, W. Effect of bioink properties on printability and cell viability for 3D bioplotting of embryonic stem cells. *Biofabrication* **2016**, *8*, 035020.

(46) Dong, Z.; Yuan, Q.; Huang, K.; Xu, W.; Liu, G.; Gu, Z. Gelatin methacryloyl (GelMA)-based biomaterials for bone regeneration. *RSC Adv.* **2019**, *9*, 17737–17744.

(47) Zhao, X.; Liu, S.; Yildirimer, L.; Zhao, H.; Ding, R.; Wang, H.; Cui, W.; Weitz, D. Injectable stem cell-laden photocrosslinkable microspheres fabricated using microfluidics for rapid generation of osteogenic tissue constructs. *Adv. Funct. Mater.* **2016**, *26*, 2809–2819.

(48) Zuo, Y.; He, X.; Yang, Y.; Wei, D.; Sun, J.; Zhong, M.; Xie, R.; Fan, H.; Zhang, X. Microfluidic-based generation of functional microfibers for biomimetic complex tissue construction. *Acta Biomater.* **2016**, *38*, 153–162.

(49) Wang, Y.; Ma, M.; Wang, J.; Zhang, W.; Lu, W.; Gao, Y.; Zhang, B.; Guo, Y. Development of a photo-crosslinking, biodegradable GelMA/PEGDA hydrogel for guided bone regeneration materials. *Materials* **2018**, *11*, 1345.

(50) Kim, M. H.; Kim, B. S.; Park, H.; Lee, J.; Park, W. H. Injectable methylcellulose hydrogel containing calcium phosphate nanoparticles for bone regeneration. *Int. J. Biol. Macromol.* **2018**, *109*, 57–64.

Supplementary information:

3D Bioprinting of Methylcellulose/Gelatin-Methacryloyl (MC/GelMA)

Bioink with High Shape Integrity

Hadi Rastin[1], Renee T Ormsby[2], Gerald J Atkins[2], Dusan Losic[1,*]

[1]School of Chemical Engineering and Advanced Materials, The University of Adelaide, Adelaide, SA 5005, Australia

[2]Biomedical Orthopaedic Research Group, Centre for Orthopaedic & Trauma Research, The University of Adelaide, Adelaide, SA 5000, Australia

Corresponding author: E-mail address: dusan.losic@adelaide.edu.au (D. Losic)

S1

1. HNMR characterization of GelMA and gelatin

To confirm the successful modification of gelatin by methacrylic anhydride, we carried out **HNMR** analysis before and after modification of gelatin with methacrylic anhydride (**Figure S1**). As seen, two new peaks appeared around δ=5.5-6 ppm related to the vinyl groups of the methacrylate (=CH$_2$).
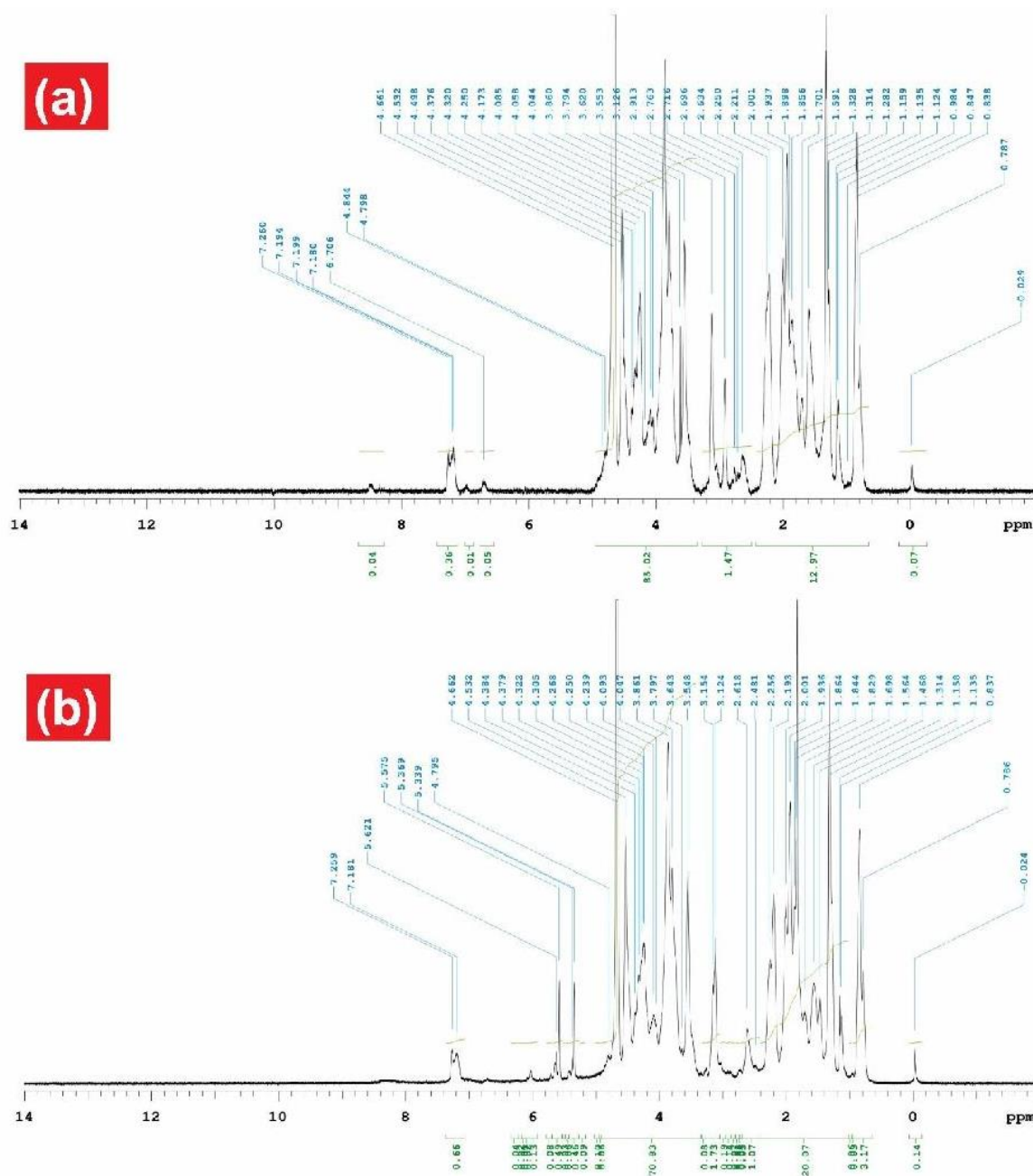
Figure S1: HNMR spectra of gelatin(a) and GelMA(b)

S2

2.   Determination of linear viscoelastic region OFMC/GelMA ink

To determine the linear viscoelastic region of MC/GelMA hydrogels, we track the variation of G' and G'' over strain sweep at 10 Hz frequency (**Figure S2**). Accordingly, all samples are in linear region once strain is lower than 1 %. Therefore, all rheological test performed in 1% strain.
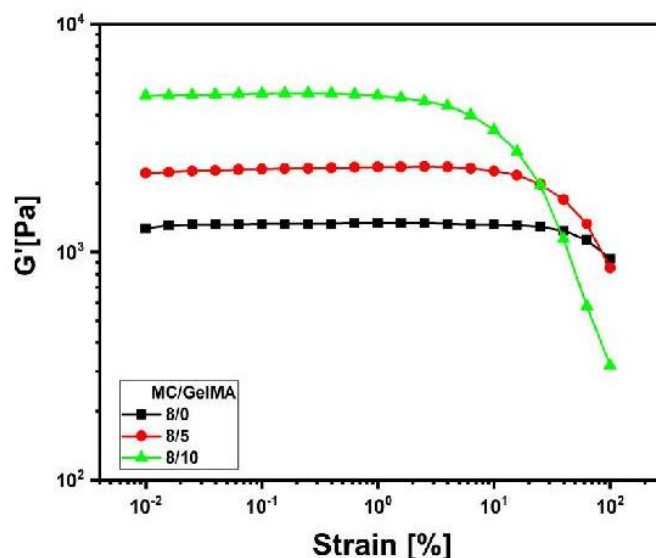
Figure S2: Strain-sweep of MC/GelMA hydrogel with different weight ratio

3.   Kinetics of degradation and swelling ratio

Diffusion coefficient shows the amount of certain substance that diffuse across the unit of area in unit of time, which closely related to the swelling ratio kinetics. To determine the swelling ratio kinetics, results of swelling ratio fitted with following equation [2S]:

$$SR = kt^n \quad (S1)$$

Where k is swelling constant and n is swelling exponent. Diffusion coefficient (D) is directly related to the swelling ratio constant (k). **Figure S3** shows the experimental results of swelling ratio and calculated values of k and n. Accordingly, the k value drop upon increasing the concentration of MC, showing the lower diffusion coefficient at higher concentration of MC and GelMA.

S3
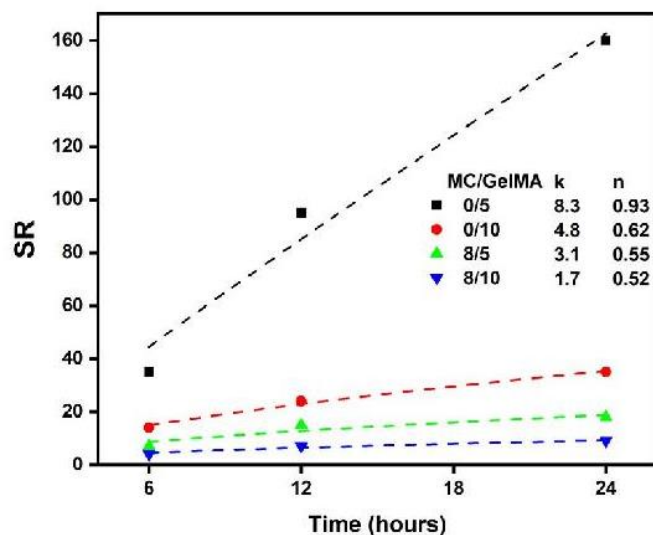
Figure S3: Linear regression of SR against time for MC/GelMA according to equation S1

To quantify the degradation kinetics of MC/GelMA hydrogels before and after curing under UV-irradiation experimental results matched with $\left(\frac{W(t)}{w(0)}\right)^{0.5} = 1 - K_d t$ equation. **Figure S4** presents the linear regression of $(w(t)/w(0))^{0.5}$ against time. As seen, cured MC/GelMA follow the same trend, showing the stability in biological media.
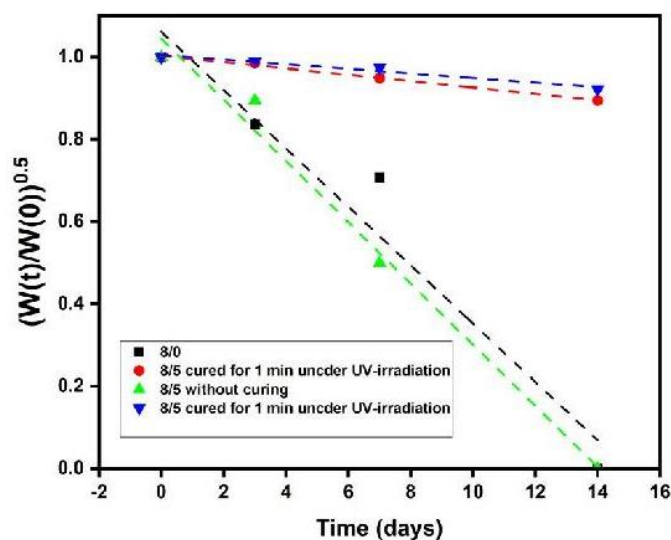
Figure S4: Linear regression of $(w(t)/w(0))^{0.5}$ against time for MC/GelMA

S4

4. Determination of shear rate and Reynold's number

Dimensionless Reynold's number (Re) defines as the ratio of inertial force to viscose force, which can be calculated as follows:

$$Re = \frac{\rho V_p D}{\eta} \quad (S2)$$

Where ρ denotes fluid density, V_p is printing speed, D is nozzle diameter, and η is the viscosity at applied shear rate. Shear rate ($\dot{\gamma}$) at certain redial (r) can be calculated from following equation [1]:

$$\dot{\gamma}^n = r \left[\frac{VR^2}{\left(\frac{n}{3n+1}\right) R^{\left(\frac{3n+1}{n}\right)}} \right]^n \quad (S3)$$

Where V is the flow rate of extruded ink, R is the radius of nozzle and n is power-law index. Flow rate of extruded ink can be obtained from the volumetric flow rate as $Q = \pi R^2 V$. Volumetric flow rate (Q) is 0.32 mm³/s for MC8/GelMA5 formulation, which calculated from the amount of bioink volume extruded in a certain perid of time under optimized pressure. Accordingly, maximum shear rate is 570 s⁻¹ for MC8/GelMA5 ink in the vicinity of wall. According to **Figure 3b**, viscosity of MC8/GelMA5 inks are about 1 Pa.s. Therefore, Reynolds number is 0.00180, showing the laminar behavior of fluid along the nozzle.

5. Shear-thinning behaviour of pure MC

Figure S5 provides the flow curve of pure MC at different concentrations. As seen, flow curve shift to higher values upon increasing MC concentration due the more condensed hydrophobic interaction.

S5
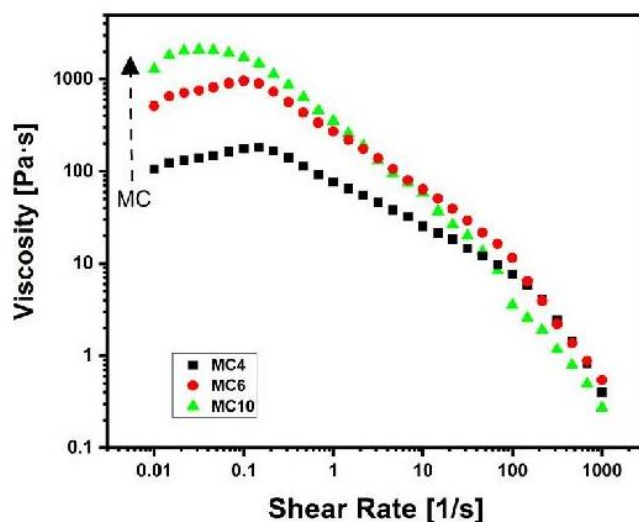
Figure S5: Variation of viscosity in terms of shear rate for pure MC hydrogels

6. Recoverability of pure MC

Figure S6 provides the variation of G' and G'' over repetitive change of strain between 1 % and 100 % to investigate the recoverability of pure MC hydrogels. Accordingly, G'' is over G' for MC4 and MC6, showing the sol state over low and high strain. It should be mentioned that G' and G'' recover to the initial values after removing the strain.
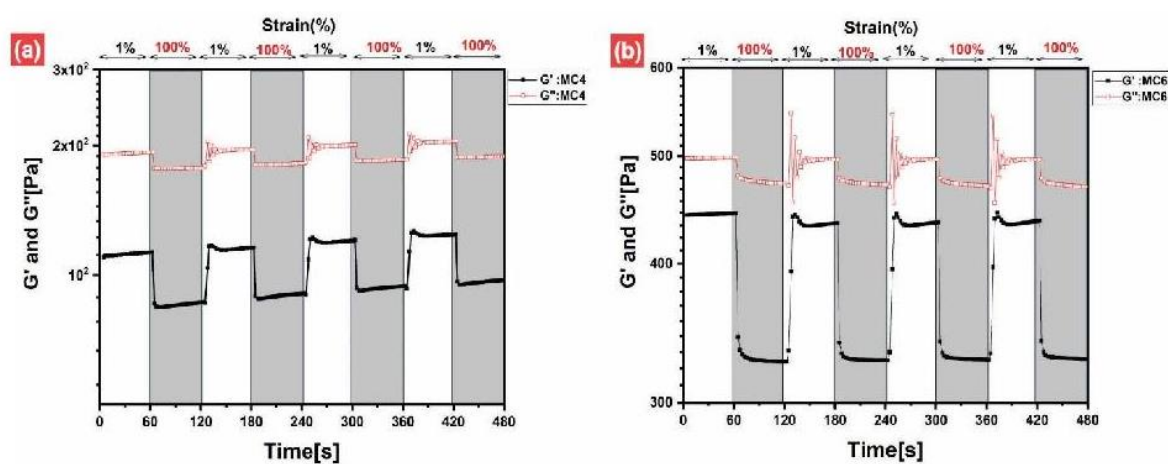
Figure S6: Recoverability of MC4 (a) and MC6 (b)

7. Thermo-responsive characterization of MC/GelMA inks

The role of temperature on the rheological behaviour of pure MC hydrogel were assessed over

frequency sweep at 23 °C and 37 °C (**Figure S7**). Accordingly, G'' is greater than G' for MC4

and MC6 at 23 °C, showing the solution state of MC. However, G' is over G'' for MC at 4, 6,

and 8 wt.% once temperature set at 37 °C,
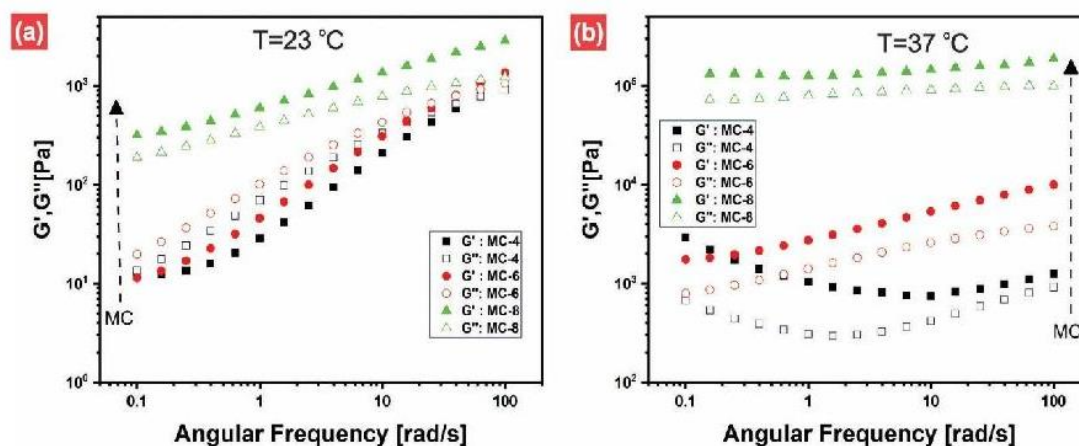
Figure S7: Frequency sweep of MC at different concentration at 23 °C (a) and 37 °C (b),

To further characterize the temperature-response of MC hydrogels, variation of G' and G''

were traced over temperature ramp (**Figure S8 a**). As seen, MC8 shows upward trend when

temperature reached around 35 °C and surge to higher values upon increasing temperature.

However, for MC/GelMA hydrogel, G' and G'' drop at around 40 °C due to the gel-sol

transition of GelMA component. Residence time of hydrogel at certain temperature is another

deciding factor in rheological behaviour of MC. In this way, variation of G' and G'' traced for

10 min at 37 °C for MC hydrogel (**Figure S8 b**). As seen, G' and G'' continuously shows

upward trend respect to time.

S7
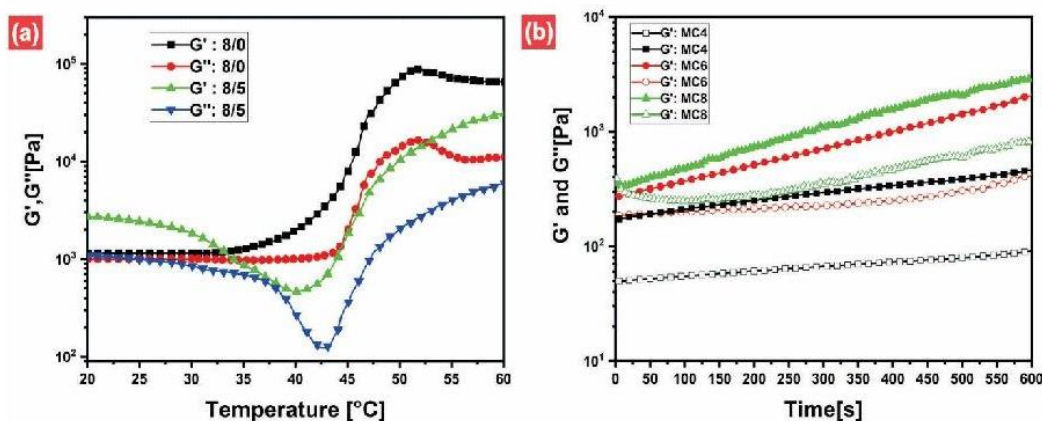
Figure S8: Variation of G' and G'' over (a) Temperature and (b) time sweep

References

(1) Li, H.; Tan, Y. J.; Leong, K. F.; Li, L. 3D bioprinting of highly thixotropic alginate/methylcellulose hydrogel with strong interface bonding. *ACS applied materials & interfaces* **2017,** *9* (23), 20086-20097.

(2) Boztepe, C.; Solener, M.; Yuceer, M.; Kunkul, A.; Kabasakal, O. S. Modeling of swelling behaviors of acrylamide-based polymeric hydrogels by intelligent system. *Journal of Dispersion Science and Technology* **2015,** *36* (11), 1647-1656.

S8

Chapter 4

Employing MXene nanosheets in the 3D bioprinting

In this chapter, the potential application of MXene nanosheets in the design of bioink was investigated in which MXene homogenously dispersed within hyaluronic acid/alginate (HA/Alg) hydrogels. The bioink exhibited excellent printability with adjustable electrical conductivity by varying the MXene dosage. In addition, the developed MXene nanocomposite ink have demonstrated high biocompatibility as evidenced by the high viability of encapsulated cell within both bulk hydrogel and 3D bioprinted structures. These results suggests the potential application of the developed MXene nanocomposite bioink in tissue engineering.

This chapter has been published as

" Rastin H, Zhang B, Mazinani A, Hassan K, Bi J, Tung TT, et al. 3D bioprinting of cell-laden electroconductive MXene nanocomposite bioinks. Nanoscale. 2020;12(30):16069-16080."

Statement of Authorship

Title of Paper	3D bioprinting of cell-laden electroconductive MXene nanocomposite bioinks
Publication Status	☑ Published ☐ Accepted for Publication ☐ Submitted for Publication ☐ Unpublished and Unsubmitted work written in manuscript style
Publication Details	Rastin H, Zhang B, Mazinani A, Hassan K, Bi J, Tung TTLosic D,. 3D bioprinting of cell-laden electroconductive MXene nanocomposite bioinks. Nanoscale. 2020;12(30):16069-16080.

Principal Author

Name of Principal Author (Candidate)	Hadi Rastin
Contribution to the Paper	Conceptualization, Investigation, Methodology, data processing, Original Draft.
Overall percentage (%)	70%
Certification:	This paper reports on original research I conducted during the period of my Higher Degree by Research candidature and is not subject to any obligations or contractual agreements with a third party that would constrain its inclusion in this thesis. I am the primary author of this paper.
Signature		Date	07/04/2021

Co-Author Contributions

By signing the Statement of Authorship, each author certifies that:

     i.   the candidate's stated contribution to the publication is accurate (as detailed above);

     ii.   permission is granted for the candidate in include the publication in the thesis; and

     iii.   the sum of all co-author contributions is equal to 100% less the candidate's stated contribution.

Name of Co-Author	Prof. Dusan Losic
Contribution to the Paper	Conceptualization, Resources, Funding Acquisition, Re-view&Editing, Supervision, submission
Signature		Date	15/04/71

Name of Co-Author	Dr. Tran Thanh Tung
Contribution to the Paper	C-supervision, Review & Editing.
Signature		Date	14/4/2021

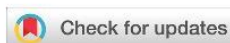Please cut and paste additional co-author panels here as required.

Name of Co-Author	Arash Mazinani		
Contribution to the Paper	selected investigation, Methodology, Review & Editing.		
Signature		Date	15.04.2021

Name of Co-Author	Kamrul Hassan		
Contribution to the Paper	selected investigation, Methodology, Review & Editing.		
Signature		Date	16.04.2021

Name of Co-Author	Jingxiu Bi		
Contribution to the Paper	Resources, Review&Editing.		
Signature		Date	15/04/2021

Name of Co-Author	Bingyang Zhang		
Contribution to the Paper	selected investigation, Methodology, Review & Editing.		
Signature		Date	15/04/2021

3D bioprinting of cell-laden electroconductive MXene nanocomposite bioinks†

Hadi Rastin, Bingyang Zhang, Arash Mazinani, Kamrul Hassan, Jingxiu Bi, Tran Thanh Tung [ID] and Dusan Losic [ID] *

MXenes, a new family of burgeoning two-dimensional (2D) transition metal carbides/nitrides, have been extensively explored in recent years owing to their outstanding properties such as a large specific surface area, high electrical conductivity, low toxicity, and biodegradability. Numerous efforts have been devoted to exploring MXenes for various biomedical applications such as cancer therapy, bioimaging, biosensing, and drug delivery. However, the potential application of MXene nanosheets in tissue engineering has been almost overlooked despite their excellent performance in other biomedical applications. The over-arching goal of this paper is to demonstrate the potential of MXene cell-laden bioinks for tissue engineering and their ability to assemble functional scaffolds to regenerate damaged tissue *via* 3D bioprinting. We formulate a new electroconductive cell-laden bioink composed of Ti_3C_2 MXene nanosheets dispersed homogeneously within hyaluronic acid/alginate (HA/Alg) hydrogels and showed its performance for extrusion-based 3D bioprinting. The prepared hydrogel bioinks with MXenes display excellent rheological properties, which allows the fabrication of multilayered 3D structures with high resolution and shape retention. Moreover, the introduction of Ti_3C_2 MXene nanosheets within the HA/Alg hydrogel introduces electrical conductivity to the ink, addressing the poor electrical conductivity of the current bioinks that mismatch with the physico-chemical properties of tissue. In addition, the MXene nanocomposite ink with encapsulated Human Embryonic Kidney 293 (HEK-293) cells displayed high cell viability (>95%) in both bulk hydrogel and 3D bioprinted structures. These results suggest that MXene nanocomposite bioinks and their 3D bioprinting with high electrical conductivity, biocompatibility and degradability can synergize some new applications for tissue and neural engineering.

1. Introduction

MXenes were discovered in 2011 by Gogotsi and co-workers as a new class of 2D transition metal carbide nanomaterials.[1] MXene nanosheets are mostly derived by selective chemical etching of an A layer from the 3D MAX phase with the structural formula of $M_{n+1}AX_n$ (M represents transition metals such as Sc, Ti, Zr, Hf, V and Ta, X is C and/or N elements, and A denotes the elements of groups 13 and 14 of the periodic table, *e.g.* Al).[2] Various terminal functional groups such as –OH, –F, and –O appear on the MXene nanosheets upon removal of A layers using an F-containing etching agent (HF or *in situ* HF), which provides hydrophilic surface properties and thus easy dispersion in aqueous solution.[3] MXenes have

attracted considerable attention for exploring their potential capability in a broad range of applications such as energy storage devices,[4] chemical sensors,[5,6] and water purification.[7] Recently, significant efforts have been focused on the biomedical capability of MXenes including photothermal conversion,[8] cellular imaging,[9] antimicrobial performance,[10] biosensing,[11] and drug delivery.[12] This is related to their outstanding characteristics such as a large specific surface area, high electrical conductivity, low toxicity, and biodegradability.[2] In addition, existing oxygen-containing groups within the structure of MXenes offer a facile modification of the MXene surface to be suited for the target application.[1] Although to date, MXenes have been exploited in many biomedical applications due to their versatile unique properties, the capability of MXenes in tissue engineering has been almost overlooked, especially in soft tissue engineering.

The primary goal of tissue engineering is to regenerate damaged tissue by incorporating cells and growth factors within porous scaffold biomaterials.[13] To realize this goal, various biofabrication methods have been developed, among which three-dimensional (3D) bioprinting has attracted signifi-

School of Chemical Engineering and Advanced Materials, The University of Adelaide, Adelaide, SA 5005, Australia. E-mail: dusan.losic@adelaide.edu.au

†Electronic supplementary information (ESI) available: Fig. S1 shows the biocompatibility of MXene nanosheets in 2D cell culture. Fig. S2 presents the homogenous distribution of encapsulated cells within the hydrogel. See DOI: 10.1039/d0nr02581j

Paper   Nanoscale

cant attention. 3D bioprinting revolutionizes the fabrication method in tissue engineering, which allows the construction of tissue-like structures with the ability to pattern multiple cell types at the desired location.[14,15] 3D bioprinting aims to fabricate physiologically scaled tissues, matching the complexity of native tissues and can thus be considered as a promising approach for easing the organ shortage crisis.[16] In the past, printing was used to form 3D structures without cells, which needs further cell seeding procedures.[17] However, post cell seeding proved to be challenging due to the poor cell adhesion and inability to deposit different cells at the desired location.[18] Currently, cell-laden bioprinting employs hydrogels to deposit biomaterials and cells together according to the pre-designed structures. In this sense, various biomaterial inks composed of synthetic polymers (pluronic, polylactic acid, polyethylene glycol) and natural polymers (i.e., gelatin, alginate, methylcellulose, hyaluronic acid) have been investigated by researchers.[19–23] An ideal cell-laden bioink should be engineered to meet both the printing process and biological requirements, which are often in contrast to each other.[18] The properties of biomaterial inks determine the type of printing technology that can be employed.[24] Despite the significant advances in the 3D bioprinting technology, the mismatch between the native tissue environment and the designed bioink properties remains a challenging aspect.[25]

The electrical conductivity of hydrogels has been proved to be advantageous for the improvement of signalling between cells.[26] However, the current biomaterial inks which are mostly composed of polymeric biomaterials suffer from poor electrical conductivity due to their inherent chemical structures.[27] Previous studies have shown that the incorporation of electrically conductive materials (metal nanoparticles, carbon-based nanomaterials, and conductive polymers) within the hydrogel bioink could enhance the conductivity of the bulk bioink, which enables the propagation of electrical signals evenly to the cells.[28–30] For example, Zhu et al. developed a cell-laden bioink composed of gold nanorod (GNR)-incorporated gelatin methacryloyl (GelMA) and alginate.[17] It was shown that the electrical impedance of the bioink reduced with an increase in the GNR content. Moreover, the adhesion and proliferation of encapsulated cells improved in the GNR nanocomposite bioink compared to the pure GelMA/alginate bioink.[17] In other works, electroconductive nanocomposite biomaterial inks were synthesized from polyurethane (PU) and graphene in which PU provides the required rheological characteristics for the printing process and graphene provided conductivity to the hydrogel.[31] An improved neural stem cell differentiation at a very low concentration of graphene loading (25 ppm) was observed. In a recent study, a conducting polymer complex, poly(3,4-ethylenedioxythiophene):poly(styrenesulfonate) (PEDOT:PSS), was physically blended with gelatin methacryloyl (GelMA) to generate a cell-laden bioink.[25] Primary ionic crosslinking of PEDOT:PSS with calcium ions followed by photocrosslinking of GelMA stabilizes the constructs. Most of these developments of conductive bioinks were based on the combination of bio and conductive polymers with very limited studies to introduce

other conductive materials such as 2D materials that could provide new properties and advantages.

MXenes' advantages over carbon or metallic nanomaterials stem from their versatile chemistry.[32] M and X sites in the MXene structure can be replaced by several elements, which can be tuned and expand the usage territory of MXene nanosheets. In addition, surface termination of MXene nanosheets equips researchers to design the hydrophilicity of MXene nanosheets. Graphene is the most important member of the carbon nanomaterial family, which provides a large surface area for decorating various functional groups. However, the electrical conductivity of graphene oxide significantly diminished upon oxidation and further reduction of GO leads to poor dispersion in water.[33]

Here, for the first time, we have exploited MXene nanosheets in the 3D bioprinting application. Easy dispersion of MXene nanosheets in aqueous solution and high electrical conductivity make MXene appropriate nanomaterials to be used in 3D bioprinting applications. In this study, we present the development of a cell-laden electroconductive bioink composed of 2D Ti_3C_2 MXene nanosheets dispersed within the hyaluronic acid/alginate (HA/Alg) hydrogel for extrusion-based 3D bioprinting (Fig. 1). The bioink properties are specifically formulated to achieve the synergistic effect between HA/Alg and 2D Ti_3C_2 MXene nanosheets, in which highly thixotropic behavior of HA/Alg provides excellent printability and Ti_3C_2 MXene nanosheets induce the electrical conductivity. Herein, we first evaluate the effect of MXene dosages on the key properties of the prepared MXene HA/Alg bioink. Next, the printability of the optimized bioink was fully investigated using rheological measurements followed by the printing of multi-layered complex 3D structures to demonstrate its printing performance. Finally, the in vitro biocompatibility of the MXene nanocomposite ink was characterized by the live/dead cell assay in the bulk and bioprinted structures.

2. Experimental section

2.1. Synthesis of Ti_3C_2 MXene nanosheets

Ti_3C_2 MXene nanosheets were synthesized by selective etching of the aluminum layers from the Ti_3AlC_2 MAX-phase as reported previously.[3] Briefly, the etchant solution was first prepared by dissolving 1 gr LiF in 20 ml 9 M HCl under mild stirring at room temperature for 10 min. Next, Ti_3AlC_2 MAX-phase carbide fine powder (1 gr, Carbon-Ukraine) was added gradually to the etchant solution at 35 °C and left to react overnight. Following this, the prepared product was washed several times with deionized (DI) water by centrifugation until the pH of the supernatant reached around 6. Finally, the multilayered Ti_3C_2 MXene sediment was sonicated for 1 h and then centrifuged (3500 rpm) for another hour to obtain Ti_3C_2 MXene nanosheets.

2.2. Characterization of Ti_3C_2 MXene nanosheets

Transmission Electron Microscopy (TEM), X-ray powder diffraction (XRD) and Raman spectroscopy were used to charac-

Nanoscale   Paper
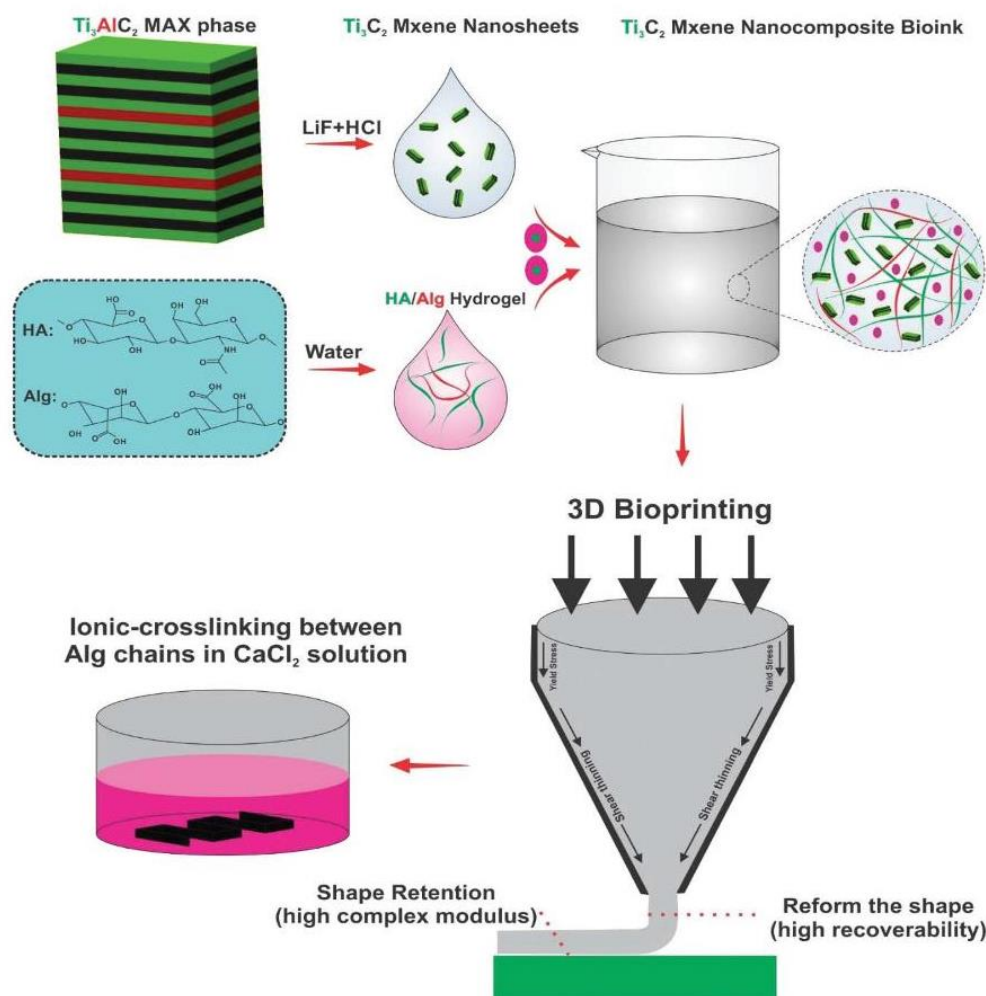
Fig. 1 Schematic representation of the synthesis of MXene-based nanocomposite bioink. The Al layer from the Ti_3AlC_2 MAX-phase removed in the etching solution (*in situ* HF) to produce few-layered Ti_3C_2 MXene nanosheets. HA and alginate hydrogels were mixed with the prepared MXene nanosheets and loaded into an extrusion-based 3D printer for fabrication of multilayer structures.

terize the obtained Ti_3C_2 MXene nanosheets. TEM was carried out on a Titan Themis microscope (Adelaide Microscopes) operated at 200 kV. XRD analysis was performed using a Rigaku MiniFlex 600 (Japan) from $2\theta = 5$–$80°$ under 40 kV and 15 mA conditions. Raman spectra of samples were recorded using WITEC Alpha300 (Ulm, Germany) in the range of 0–2000 cm^{-1} with an excitation wavelength of 532 nm.

2.3. Synthesis of the Ti_3C_2 MXene nanocomposite bioink

MXene solution, HA powder, and Alg powder were placed under UV-irradiation for one hour before mixing with sterilized DI water. The Ti_3C_2 MXene nanocomposite ink was prepared by adding Ti_3C_2 MXene solution to DI water to reach the final concentrations of 1 mg ml^{-1} and 5 mg ml^{-1}. MXene

nanosheets at higher concentrations tend to agglomerate which subsequently blocks the nozzle during printing. Therefore, only 1 mg ml^{-1} and 5 mg ml^{-1} were selected and characterized in this work. The solution was subsequently sonicated for 5 min to ensure homogeneous dispersion of Ti_3C_2 MXene nanosheets. Next, 1 wt% sodium alginate (Sigma Aldrich, USA) was added to the solution and mixed for 4 hours at room temperature. Finally, 5 wt% HA powder (1000–1500 kDa, Lotioncrafter, Australia) was mixed with the solution and kept in a fridge for 2 hours to ensure complete hydration. The samples were referred to as HA-*x*/Alg-*y*/MXene-*z*, where *x*, *y*, and *z* denote the content of the corresponding components. It should be noted that the bioink crosslinked just after printing by immersion in $CaCl_2$ solution.

Paper   Nanoscale

2.4. Characterization of the Ti$_3$C$_2$ MXene-based nano-composite bioink

2.4.1. Swelling ratio. The Ti$_3$C$_2$ MXene nanocomposite hydrogels were crosslinked by immersion in 5 wt% CaCl$_2$ solution for 10 min. Following this, a disk with a 10 mm radius of each sample was punched and further soaked in DI water at 37 °C. The swollen samples were weighed at different time intervals and then lyophilized in a freeze dryer for two days and weighed again. The swelling ratio of each sample was obtained from the weight ratio of the swollen to the lyophilized sample.

2.4.2. Morphology. Hydrogels were prepared as described above and then submerged in DI water for 24 h at 37 °C. Next, the samples were lyophilized in a freeze dryer for two days. A Quanta 450 scanning electron microscope (Hillsboro, OR, USA) equipped with an EDX analysis device was utilized to observe the morphology of samples.

2.4.3. Electrical conductivity. The electrical conductivity of the inks with different formulations was determined using a capacitively coupled contactless conductivity detection C^{4}D instrument, equipped with a capillary head stage that fits a 660 μm fused silica capillary.[34,35] Accordingly, emitter and receiver electrodes are separated by a gap and the studied sample transferred into a capillary tube to isolate from the electrodes. Applying an AC-voltage to the emitter electrode and measuring the current value in the receiver electrode make it possible to calculate the conductivity of the sample. Since a thick insulating layer isolates electrodes and electrolytes, the capacitances are less than 1 pF and therefore it is required to apply a high frequency of 300 kHz.

2.4.4. Mechanical strength. Compression testing was conducted using a Q800 dynamic mechanical analyser (TA Instruments LLC, Delaware, USA) with a load cell capacity of 10 N. The samples were crosslinked in CaCl$_2$ solution and then soaked in DI water for 12 h to reach the equilibrium state before testing. Testing was performed with 0.1 N steps at room temperature. The compression modulus of the prepared hydrogels was calculated from the slope of the curves in the initial linear region.

2.4.5. Rheological measurements. A Physica MCR301 rheometer (Anton Paar, Ostfildern, Germany) fitted with a cone and plate (diameter of 50 mm, a gap of 49 μm) was used to explore the printability of the prepared ink. Samples were prepared as described in section 2.2 and then mounted on a Peltier module and left for 10 min before testing to remove the history of tension. All rheological measurements were carried out at 20 °C, unless otherwise stated. The linear viscoelastic region of samples was determined from the oscillatory strain sweep test from 0.01% to 100% sat 10 Hz. To evaluate the yield stress of the prepared inks, shear stress sweep test was performed from 1 to 10 000 Pa at 1 Hz frequency and the crossover point of the loss modulus and storage modulus was considered as the yield point. Shear-thinning behavior of the inks was determined from the evolution of viscosity over shear rate sweep from 0.01 s^{-1} to 1000 s^{-1}. Oscillatory time sweep was

carried out by alternating 1% and 100% strain at 1 Hz frequency to explore the recoverability of the prepared inks. Moreover, the recovery of viscosity was measured upon applying a high shear rate (100 s^{-1}) for 5 s. Finally, the frequency sweep tests were performed from 100 Hz to 0.01 Hz.

2.5. 3D printing

The printable MXene Ti$_3$C$_2$ nanocomposite was transferred into a 10 ml syringe fitted with a plastic conical nozzle tip. A commercial Allevi 2 bioprinter (Philadelphia, United States) was used to print the prepared bioink according to the programed structures by application of air pressure behind the syringe. Slic3r software was employed to convert STL files designed in Autodesk fusion 360 software to Gcode. The air pressure, print speed, and nozzle distance from the substrate were optimized according to the difference between the nozzle diameter and printed strands. After printing, the samples were directly soaked in 5 wt% CaCl$_2$ solution for 10 min.

2.6. 2D cell culture

The Human Embryonic Kidney 293 (HEK-293) cells were seeded and cultured in a T25 flask (25 cm^2) in modified Eagle's medium (MEM, Gibco™) supplemented with 10% fetal bovine serum (Gibco™) in an incubator (5% of CO$_2$ at 37 °C). Next, when the T-flask is about 90% confluent, the adherent HEK-293 cells were resuspended using the culture medium and then centrifuged at 5000 rpm for 5 minutes to remove the culture medium. Next, the cytotoxicity of MXene nanosheets was measured from the HEK-293 cell's viability after being mixed with two different concentrations of MXene nanosheets over a week. HEK-293 cells were seeded at the density of 5 × 10^4 cells per ml in each well. The cell culture without MXene nanosheets was considered as the control sample.

2.6.1. Cell viability in the bulk and 3D bioprinted structures. The HA-5/Alg-1/MXene-1 ink was prepared as described earlier by using sterilized culture media instead of DI water solution. Next, the cell pellet was mixed with the prepared precursor solution in culture medium to reach the final cell density of 5 × 10^4 cells per ml. Part of the prepared bioink was poured into the 4-well imaging cell slide to form a thin layer of hydrogel. The remaining part of the bioink was transferred into the 10 ml syringe and few-layer spiral and polyline structures were printed using a 27 G tapered plastic tip with the optimized operating printing parameters. The 3D bioprinter and all involved accessories were disinfected with 70% w/v ethanol solution before use. Live/dead cell assay was conducted using a LIVE/DEAD™ Viability/Cytotoxicity Kit (calcein AM, green fluorescence for live cells and ethidium homodimer-1, red fluorescence for dead cells, Invitrogen™) following the instructions of the kit. The viability of the encapsulated HEK-293 cells within the ink in both bulk hydrogel and 3D bioprinted structures was monitored 1, 3, and 7 days after encapsulation. For the control sample, HEK-293 cells were added to the culture media and were imaged at the same time intervals. The viability of cells was reported as the ratio of viable cells to the sum of viable and dead cells.

3. Results and discussion

3.1. Characterization of the Ti_3C_2 MXene nanocomposite ink

The 2D Ti_3C_2 MXene nanosheets prepared by selective etching of the Al layer from the MAX phase Ti_3AlC_2 using an *in situ* HF etchant were characterized by XRD, Raman spectroscopy, and TEM (Fig. 2a). The XRD spectra of MAX phase Ti_3AlC_2 display a sharp diffraction peak at $2\theta = 9.9°$, indicating the crystalline structure of the MAX phase.[36] However, etching and exfoliation of the MAX phase resulted in the broadening and shifting of the characteristic peak to $2\theta = 8.5°$, as indicated by the blue line in the curve. This is correlated with the structural expansion of the MAX phase during the etching process and removal of Al from the structure by intercalation of water and the etching products.[37] In addition, the weakening of peaks at $2\theta = 39°$, $41°$ and $60.3°$ reflects the successful removal of the Al
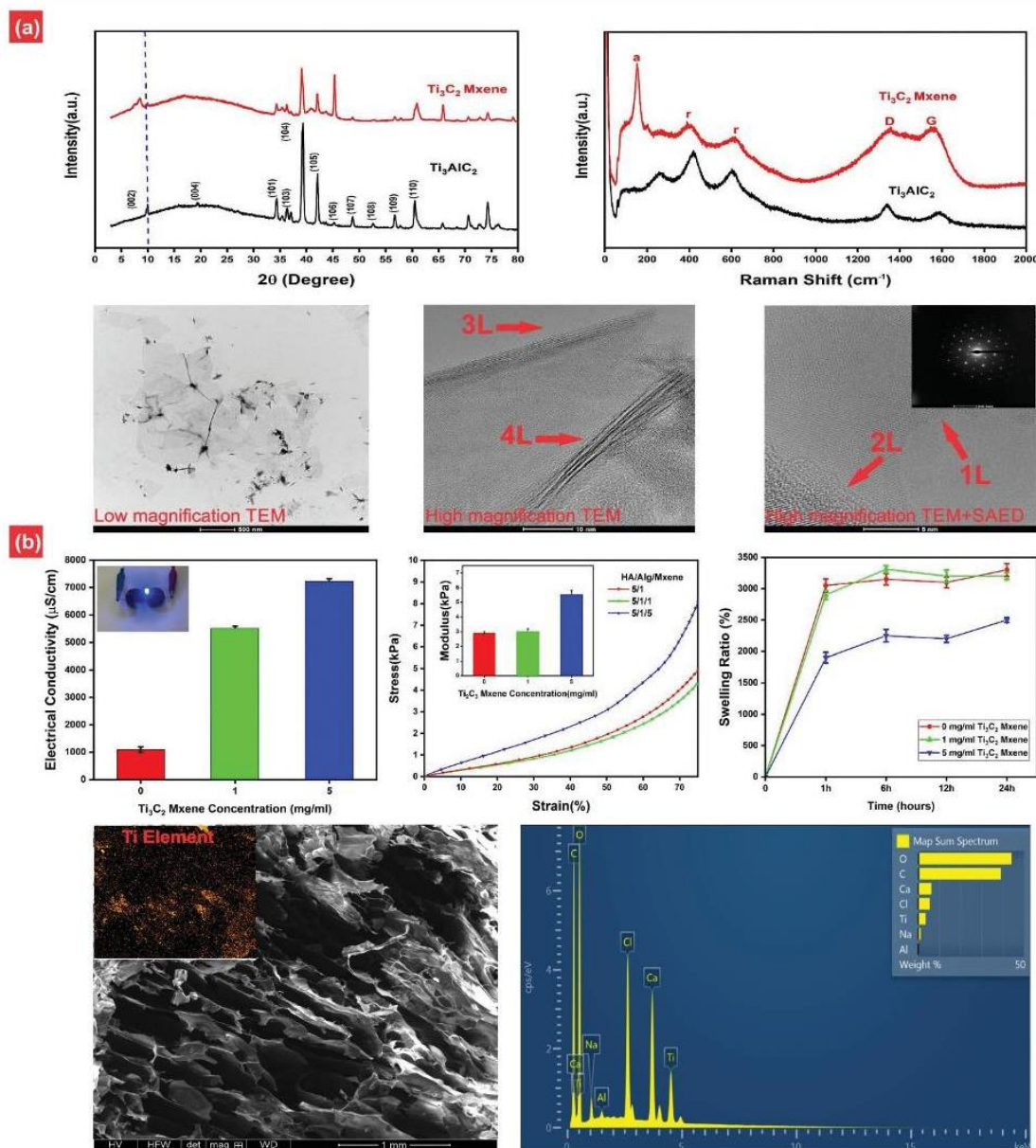
Fig. 2 (a) Characterization of Ti_3C_2 MXene nanosheets in terms of XRD, Raman spectroscopy, and TEM observations. These results suggest the successful synthesis of Ti_3C_2 MXene nanosheets by selective etching of the Al layer. (b) Characterization of MXene nanocomposite ink in terms of electrical conductivity, compression strength, swelling ratio, morphology, and EDX analysis.

Paper
                                                    Nanoscale

layer from MAX phase Ti_3AlC_2.[1] For further characterization, the Raman spectroscopy results of MAX phase Ti_3AlC_2 and Ti_3C_2 MXene were compared, which is in agreement with the XRD results. The formation of titanium dioxides is evidenced by the presence of rutile peaks at 398 cm^{-1} and 612 cm^{-1} and the anatase phase peak at 149 cm^{-1}.[38] Furthermore, the appearance of D and G bands at 1359 cm^{-1} and 1557 cm^{-1}, respectively, shows the disordered graphite and corresponding defects in the structure.[38] The calculated intensity ratio I_D/I_G for MXenes and MAX phases is 0.99 and 1.14, respectively, which demonstrates the presence of amorphous carbon in the MAX phase. Additionally, noticeable depletion of the characteristic peak at 262 cm^{-1} is related to the removal of Al from the MAX structure and thus the appearance of surface terminal groups, which is consistent with the reported XRD result.[39] The sound-exfoliated structure of Ti_3C_2 MXene nanosheets is also proved by the TEM observation. As can be seen, the TEM image with low magnification clearly displays the ultra-thin layers of Ti_3C_2 MXene nanosheets. It can be observed in the higher-resolution TEM images that Ti_3C_2 MXene nanosheets form a single or few-layered structure. Accordingly, the lateral size of MXenes is in the range of 1 to 4 μm as can be observed in the low magnification TEM image (Fig. 2a). The thickness depends on the number of MXene layers; a selective TEM image can find a single layer (1L ~ 1 nm) of MXenes or double layer (~2 nm), however a dominant area of 3–4 layers (3–4 nm). This is consistent with the AFM measurement (data not shown) with a typical thickness of 3.5 nm. In addition, the SAED pattern confirms the crystalline nature of the obtained Ti_3C_2 MXene nanosheets, while keeping the identical hexagonal symmetry of the precursor MAX phase Ti_3AlC_2. Overall, these results promise the successful synthesis of Ti_3C_2 MXene nanosheets from MAX phase Ti_3AlC_2.

After the synthesis of Ti_3C_2 MXene nanosheets, MXene nanocomposite inks were prepared by the dispersion of different contents of MXene nanosheets within the HA/Alg hydrogel and characterized in terms of electrical conductivity, mechanical strength, swelling ratio, and morphology. Electroconductive hydrogels have been widely explored in biomedical applications such as bioactuators,[40,41] biosensing,[42,43] and tissue engineering.[44,45] However, electroconductive hydrogels often suffer from poor biocompatibility, which hampers their application as biomaterials.[27] Here, the electrical conductivities of MXene nanocomposite inks were evaluated in terms of MXene content (Fig. 2b). Accordingly, the electrical conductivity of inks containing 1 mg ml^{-1} and 5 mg ml^{-1} of MXene nanosheets was 5500 ± 85 μs cm^{-1} and 7200 ± 126 μs cm^{-1}, respectively, where the conductivity of the ink before the addition of MXene is 1103 ± 93 μs cm^{-1}. This is due to the inherent electrical conductivity of Ti_3C_2 MXene nanosheets that renders a high electrical conductivity to the system. According to the literature,[46] the electrical conductivity of the excitable tissues such as the heart, spinal cord, and skin ranges around 0.4–0.9 S m^{-1}, which matched well with the electrical conductivity of the MXene nanocomposite ink. In addition, the inset picture shows that MXene nanocomposite

ink is able to illuminate a LED by the completion of a circuit. These results clearly indicate that the electrical conductivity of the ink was improved upon the incorporation of MXene nanosheets, which can be tuned by changing the MXene content.

The compression strength of the MXene nanocomposite inks with various formulations was studied to infer the effect of MXene on the ultimate mechanical properties. The stress–strain curves of the prepared inks are shown in Fig. 2b with calculated compression modulus in the inset picture. As can be seen, the incorporation of MXene nanosheets with 5 mg ml^{-1} concentration resulted in the improvement of the mechanical strength compared to the pristine HA/Alg hydrogel, while the addition of 1 mg ml^{-1} MXene nanosheets has no significant effect on the compressive modulus. This is probably related to the higher molecular interactions between MXene and hydrophilic polymers upon the addition of 5 mg ml^{-1} MXene nanosheets. In addition, abundant functional groups on the MXene nanosheets can react with functional groups along the HA or alginate backbone, which can contribute to the enhancement of mechanical strength.[47] To support this hypothesis, the swelling ratio of MXene nanocomposite inks was measured, as it reflects the molecular interactions between MXene and hydrophilic polymers (Fig. 2b).[25] In agreement with the mechanical results, the addition of 5 mg ml^{-1} MXene nanosheets to HA/Alg hydrogel causes a decrease in the swelling ratio as an indicator of higher molecular interactions between MXene and hydrophilic polymers.[48]

The SEM images of the crosslinked MXene nanocomposite ink suggest a porous morphology (Fig. 2b). There were no significant differences between the morphology of different formulations of the inks (data not shown). Interestingly, aggregation of MXene nanosheets within the HA/Alg matrix was not observed, which could be due to the highly hydrophilic nature of the obtained MXene nanosheets. In addition, elemental analysis of the ink by EDX shows that almost all Al layers were removed and the EDX mapping (inset image) reveals the homogenous distribution of MXene nanosheets within the HA/Alg hydrogel.

3.2. Printability of MXene-based nanocomposite inks

Although preliminary testing such as fiber formation and layer stacking can provide some insight into the printability of the ink, further modification in the ink formulation needs more accurate testing. Rheology measurements provide a powerful tool for the assessment of ink's behavior during the printing process. An ideal printable bioink should possess specific rheological properties. The close relationship between the printability and rheological behavior of a biomaterial ink has been previously established in the literature.[49–51] In this regard, we explore the printability of the MXene nanocomposite bioink by means of rheological characteristics over three stages as shown in Fig. 3. In the first stage of the printing process, the ink initiates flowing along a thin nozzle. The force required for flow initiation is closely related to the yield stress.[52] It is determined from the crossover point of the G'
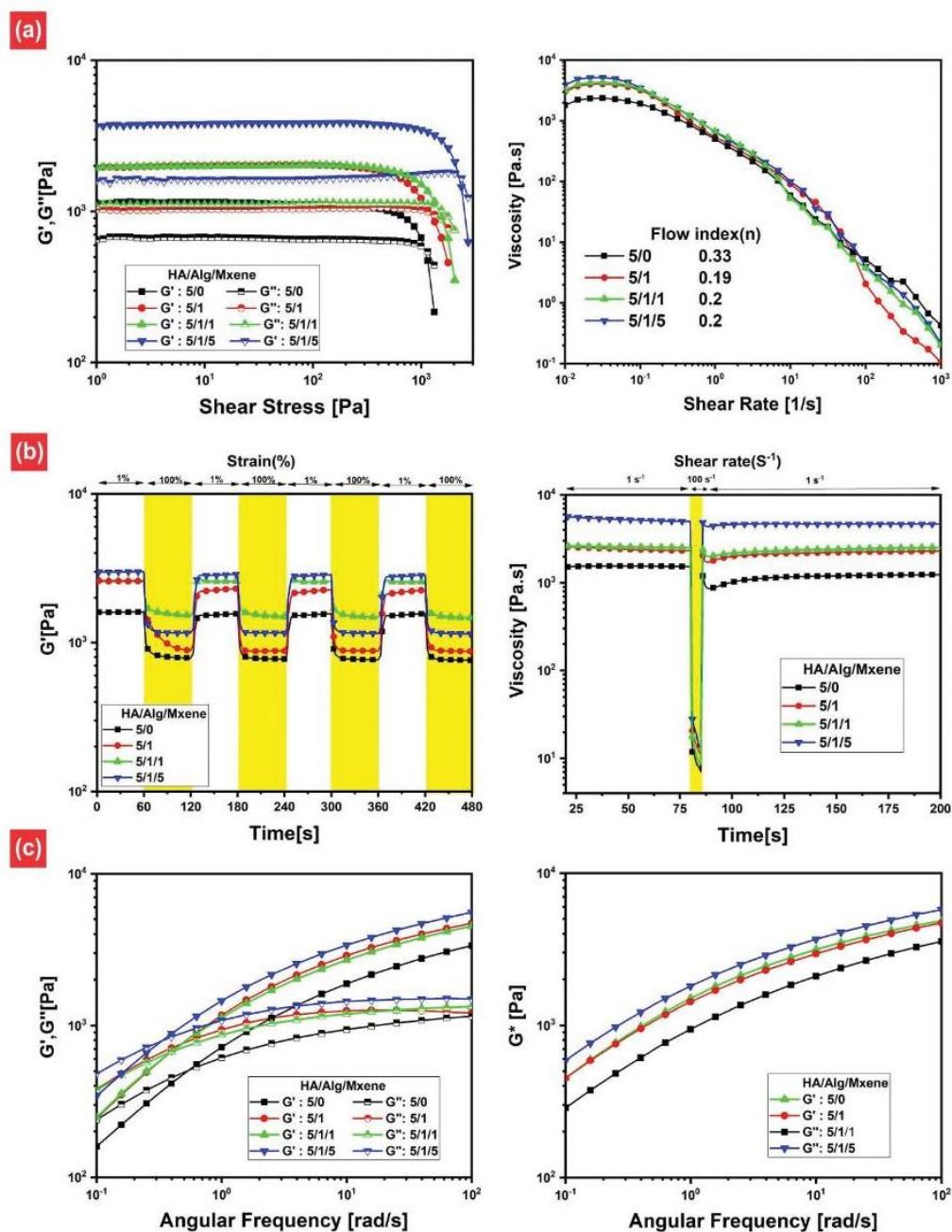
Fig. 3 Rheological characterization of the MXene nanocomposite ink. (a) Extrusion stage. Shear stress sweep test allows determining the yield stress, where the solid-to-liquid transition occurs. Shear rate sweep reveals the shear-thinning behavior of the ink. (b) Recovery stage. Recoverability of the prepared inks was monitored after removing the applied strain and shear rate. (c) Shape retention stage. The frequency sweep test gives deep insight into the solid-like behavior of the ink.

and G'' curves in the shear stress sweep test, where the gel-to-sol transition occurs (Fig. 3a). As can be seen, the viscoelastic properties of the inks demonstrate solid-like behavior at low shear stress, where the G' values are greater than the G'' values

at low shear stress. Following this, the liquid-like behavior is observed once the shear stress reaches the yield stress value, allowing the ink to flow through the nozzle. The magnitude of yield stress increased upon the addition of alginate into the

pure HA hydrogel due to more entanglement between polymer chains. In addition, the G' value and yield stress of the HA-5/Alg-1 hydrogel shifted toward higher values with increased MXene loading, suitable for extrusion-based printing. Higher G' value and yield stress are indicatives of the higher shape retention of the ink once printed.

Bioinks with low viscosity have poor shape retention once printed, thus highly viscous inks with shear-thinning behavior are advantageous for 3D bioprinting for easy extrusion of ink through the nozzle.[53,54] The flow curves of the studied samples demonstrate that an increase of shear rate causes a significant drop in the viscosity of all samples, indicating shear-thinning behavior (Fig. 3a). Although MXene nanocomposite inks display higher viscosity than the HA/Alg hydrogel at a low shear rate, the flow curve of the prepared samples almost overlap at a high shear rate close to the applied shear rate in the 3D bioprinting process. The extent of shear-thinning behavior can be quantified by fitting the flow curve results with the power-law model ($\eta = K\dot{\gamma}^{n-1}$), where η represents the viscosity, $\dot{\gamma}$ denotes the shear rate, n is the flow index and K is the consistency index.[55] The value of flow index (n) provides useful information regarding the material's behavior as $n < 1$ characterized fluids with shear-thinning properties. The addition of alginate intensifies the shear-thinning ability of HA, as evident from the flow index value of 0.33 and 0.19 for HA and HA/Alg hydrogels, respectively. In addition, the similarity of the flow index value of MXene nanocomposites and HA/Alg means that the shear-thinning ability of the HA/Alg hydrogel has not been disrupted after impregnation with MXene nanosheets. Shear-thinning behavior indicates the plug-like flow of the ink once it passes through the nozzle, which shows that the velocity of the ink is constant over the cross-section of the nozzle.[50] It was reported that the cell viability reduced at higher shear stress, which eliminated in the shear-thinning hydrogels.[56] Higher shear-thinning behavior also means a higher mass flow rate, which lowers the pressure required for extrusion and eases the printing.

In the second stage of printing, the printable ink should have the ability to recover immediately to its initial stage.[52,57] In order to explore the recoverability of the prepared ink, alternating low (1%) and high (100%) strain was applied at 60 s intervals (Fig. 3b). The ink experiences high strain while passing through the nozzle and should have the ability to reshape after extrusion. It is observed that the G' values for all studied formulations suddenly dropped when they were subjected to high strain and then almost fully recovered after removing the applying strain. The recovery of the inks remains unchanged after different cycles. The incorporation of MXene into the HA/Alg hydrogel has no effect on the extent of recovery and only change the G' value. This indicates that HA/Alg controls the rheological behavior of the ink. Interestingly, the inks showed full recovery in 10 s after eliminating the high strain for all studied formulations, which is critical for high-resolution printing. In further characterization, the recoverability of the inks was measured upon applying and removing a high shear rate (100 s^{-1}) as shown in Fig. 3b. Accordingly, the vis-

cosity of the inks shows a significant reduction upon the application of a high shear rate followed by recovering to the initial stage. Interestingly, viscosity values for all samples are similar at a high shear rate, as observed in the flow curve, which shields the cells from disruption along the nozzle. Overall, the high recoverability of the MXene nanocomposite ink indicates the potential application of the ink for extrusion-based bioprinting.

In the next stage, the ink should exhibit self-supporting behavior to sustain the integrity of the structure after deposition, which was determined by the complex modulus ($G*$) and yield stress.[52] Higher values of $G*$ and yield stress reflect higher mechanical strength, which benefits the self-supporting behavior of the ink.[49,52] As seen in Fig. 3c, the G' value is greater than the G'' value at higher frequencies for all studied formulations, indicating the solid-like behavior. However, G'' surpassed the G' at lower frequencies, showing the solution behavior. Interestingly, the crossover of G' and G'' shifted toward lower frequencies upon the addition of alginate or MXene nanosheets as well as the magnitude of G' and G'' jumps to higher values. In addition, the $G*$ value for the prepared MXene nanocomposite ink with a higher content of MXene is higher, consistent with the G' curve. These results along with that of the yield stress show that a higher loading of alginate and MXene benefits the self-supporting behavior of the ink, which would help to construct high-resolution structures.

One of the main objectives of 3D bioprinting is the ability to construct complex 3D structures with high resolution and shape fidelity. Therefore, it is required to find the best operating parameters for the 3D printing process to obtain the best match between the nozzle diameter and deposited strands (Fig. 4a). For example in the case of HA-5/Alg-1/MXene-1 ink, the increase of the air pressure causes an increase of the diameter of the deposited strands because more material is extruded out of the nozzle at the higher air pressure, whereas the strand diameter reduces with an increase in the printing speed. The best match between the nozzle (outlined by the blue line) and strand diameter occurs at an air pressure of ≈ 5 psi and a print speed of ≈ 6 mm s^{-1}. In the next step, the diameter of the deposited strands was compared with the nozzle diameter using different formulations of MXene nanocomposite inks (Fig. 4a). Accordingly, the strand diameter corresponding to the pure HA hydrogel differs significantly with the nozzle diameter, which aroused from the low yield stress and complex modulus values. However, other formulations approximately match with the target accuracy. The 3D printed lattice structure demonstrates that HA/Alg can print delicate pores without compromising the porous structure, while pure HA cannot sustain the integrity of the printed structure and disrupt the lattice pores.

To demonstrate the printability of the MXene nanocomposite ink, multilayered lattice and cylindrical constructs were printed with optimized printing parameters (air pressure: 15 psi and printing speed: 6 mm s^{-1}), as shown in Fig. 4b. As seen from different views, a lattice with delicate porosity was formed, confirming the high self-supporting behavior of the
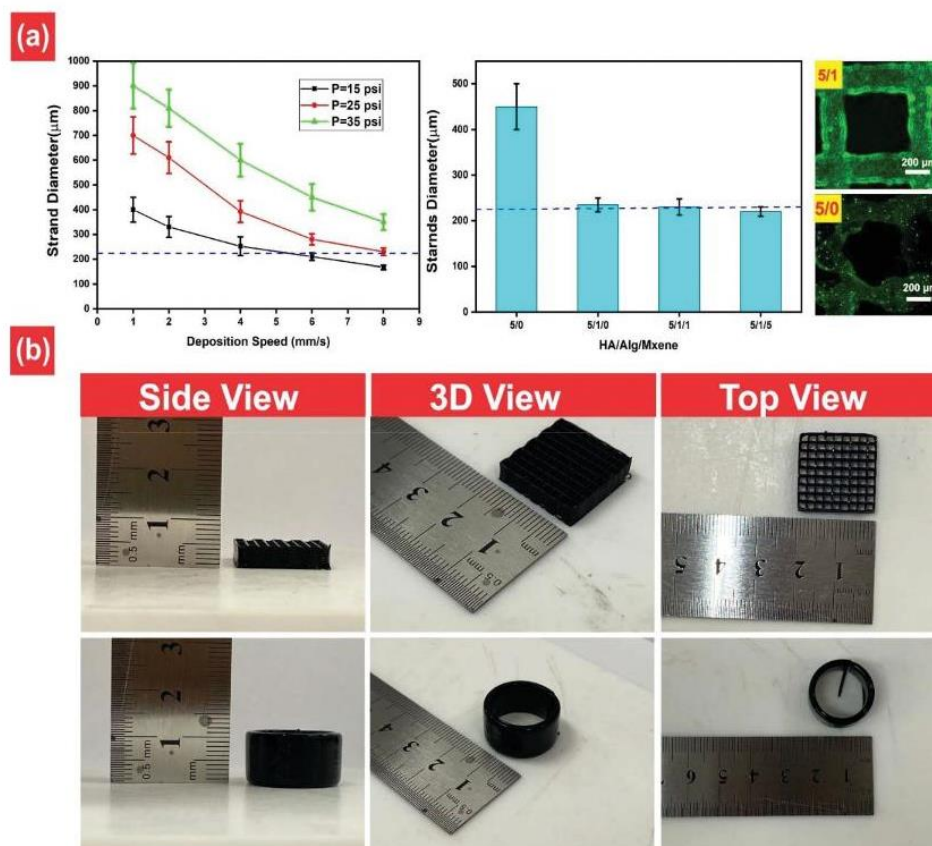
Nanoscale   Paper

Fig. 4 Evaluation of the printability of MXene nanocomposite ink. (a) Finding the optimized operating parameters for extrusion-based 3D printing. (b) Pictures of 3D printed structures fabricated using the MXene nanocomposite ink containing 1 mg ml^{-1} Ti$_3$C$_2$ MXene nanosheets.

ink due to the high G' and yield stress values. In further printing, the ink successfully printed cylindrical structures (50 stacking layers) without collapsing or spreading on the platform, showing the ability of the ink in the fabrication of complex structures with round edges. Overall, these results clearly demonstrate that the MXene nanocomposite ink has the ability to fabricate complex multi-layered structures with high shape retention and resolution.

3.3. 3D bioprinting of the MXene nanocomposite ink

Recent studies have demonstrated the potential applications of MXene nanosheets in versatile biomedical applications such as cancer theranostics, diagnostic imaging, and biosensing.[58,59] Although MXene nanosheets have exhibited excellent biocompatibility for different cell types such as preosteoblasts, neurons, and brain cells in 2D cell culture,[60,61] very little is known about the *in vitro* cytotoxicity of MXene nanosheets to encapsulated cells in 3D hydrogel networks. 2D cell culture with MXene nanosheets reflects higher cell growth upon mixing with 1 mg ml^{-1} MXene nanosheets (Fig. S1†). Given this, 1 mg ml^{-1} MXene nanosheets were selected as the optimal concentration for 3D bioprinting. Here, the viability of

the encapsulated HEK-293 cells within the MXene nanocomposite ink was traced to evaluate the *in vitro* cytotoxicity of the ink over a week. Fig. 5 presents the fluorescence images taken from the bulk hydrogel (unprinted ink) and 3D bioprinted structures, stained with calcein-AM (green) and ethidium homodimer-1 (red). Although it is often challenging to mix cells with highly viscous bioinks, here, encapsulated cells were distributed homogenously within the ink due to the shear-thinning behavior of the HA/Alg hydrogel (Fig. S2†). In the case of the bulk hydrogel, the encapsulated HEK-293 cells remained viable (>95%) after a week without a noticeable change in the cell viability percentage, showing the biocompatibility of the MXene nanocomposite ink (Fig. 5a). In addition, it is observed that the intensity of green fluorescence amplified over time, which indicates the growth of the cells. In the 3D bioprinted structure, the cell-laden MXene nanocomposite ink printed spiral and polyline structures with 27G tapered plastic tips (Fig. 5b). No significant difference was observed in the viability of the encapsulated cell between the bulk hydrogel and bioprinted structures. This is due to the shear-thinning behavior of the ink that shields cells from high shear stress during extrusion. Overall, the cell-laden MXene nanocomposite ink
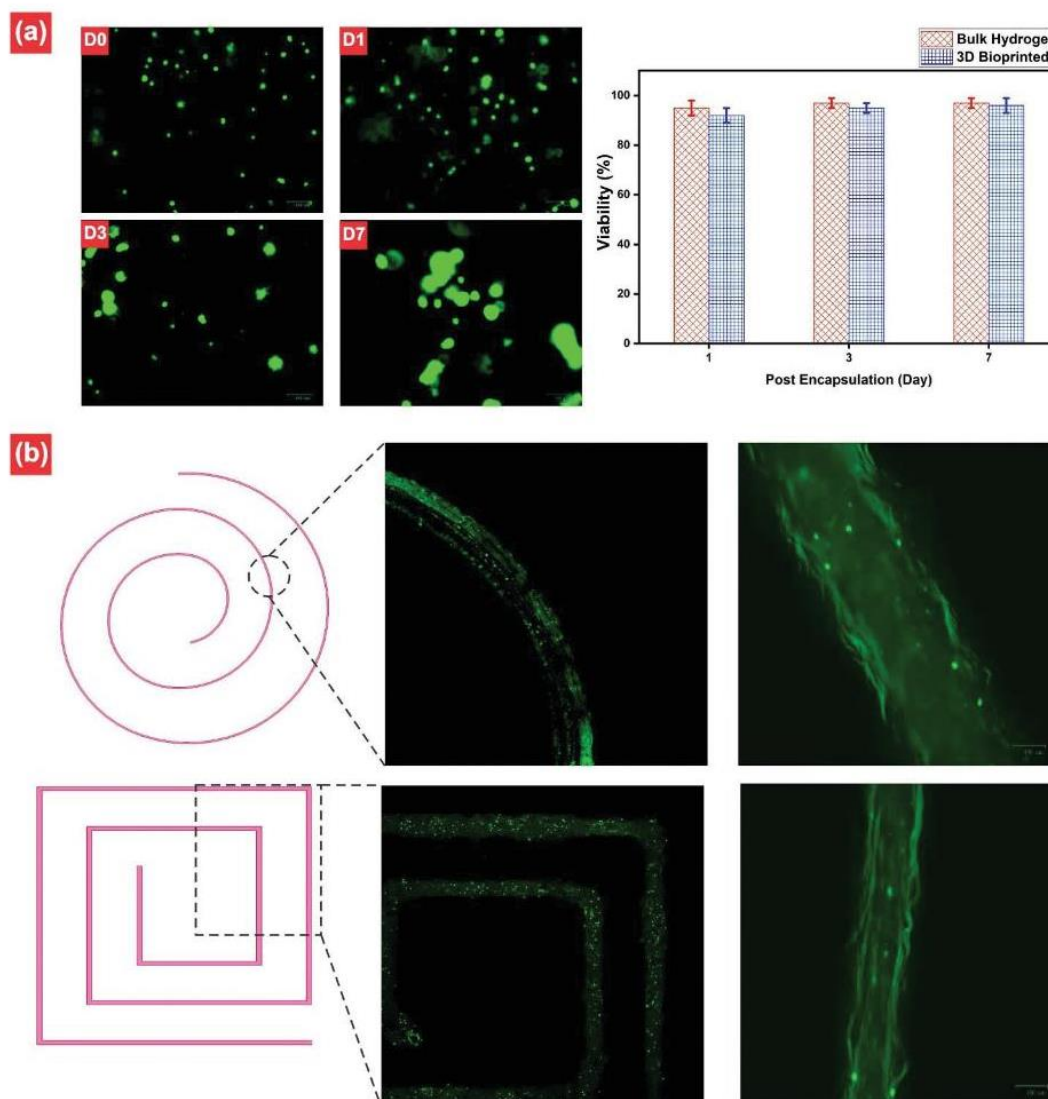
Fig. 5 Evaluation of the *in vitro* cytotoxicity of cell-laden MXene nanocomposite ink by live/dead cell assay in the (a) bulk hydrogel and (b) 3D bio-printed structures. Cells stained with calcein-AM (green) and ethidium homodimer-1 (red).

demonstrated high cell viability over a week, confirming the biocompatibility of the prepared ink.

4.   Conclusions

In summary, herein, we demonstrated the use of Ti_3C_2 MXene nanosheets for 3D bioprinting application, which addresses the poor electrical conductivity of most current bioinks. New hybrid bioinks composed of Ti_3C_2 nanosheets within HA/Alg hydrogels are formulated, showing the excellent printability with high shape retention and resolution. It was found that the electrical conductivity of the nanocomposite bioink con-

taining 1 mg ml^{-1} and 5 mg ml^{-1} MXene nanosheets was 5500 ± 85 μs cm^{-1} and 7200 ± 126 μs cm^{-1}, respectively, which are significantly higher than that of the pure hydrogel. In addition, MXene nanocomposite ink showed enhanced mechanical properties due to the higher molecular inter-actions between MXene and hydrophilic polymers that is not achievable with PEDOT:PSS conductive inks. The rheological behavior of the bioink with different formulations was fully characterized in the extrusion, recovery, and shape retention stages. The viscosity of the bioink dropped significantly at a high shear rate, which can protect cells during extrusion. It was found that the bioinks can recover in a very short time to the initial status after removing the shear stress. The introduc-

Nanoscale   Paper

tion of 1 wt% Alg within the HA hydrogel caused an increase in the yield stress and complex modulus, which provides adequate mechanical strength after printing on the platform. The MXene nanocomposite bioinks printed multilayered complex 3D structures, showing high shape fidelity and resolution. Finally, *in vitro* cytotoxicity of the cell-laden ink *via* live/dead cell assay showed high cell viability (>95%) in both thin film and bioprinted structures over a week. There were no significant differences in the viability of the encapsulated HEK-293 cells between the bulk hydrogel and 3D bioprinted structure due to the shear-thinning behavior of the ink, which shields cells during extrusion. These results suggest the promising potential of MXene bioinks for 3D bioprinting in neural tissue engineering and other biomedical applications.

Conflicts of interest

There are no conflicts to declare.

Acknowledgements

Notes and references

1 M. Naguib, M. Kurtoglu, V. Presser, J. Lu, J. Niu, M. Heon, L. Hultman, Y. Gogotsi and M. W. Barsoum, *Adv. Mater.*, 2011, **23**, 4248–4253.

2 M. Soleymaniha, M. A. Shahbazi, A. R. Rafieerad, A. Maleki and A. Amiri, *Adv. Healthcare Mater.*, 2019, **8**, 1801137.

3 M. Alhabeb, K. Maleski, B. Anasori, P. Lelyukh, L. Clark, S. Sin and Y. Gogotsi, *Chem. Mater.*, 2017, **29**, 7633–7644.

4 B. Anasori, M. R. Lukatskaya and Y. Gogotsi, *Nat. Rev. Mater.*, 2017, **2**, 1–17.

5 S. J. Kim, H.-J. Koh, C. E. Ren, O. Kwon, K. Maleski, S.-Y. Cho, B. Anasori, C.-K. Kim, Y.-K. Choi and J. Kim, *ACS Nano*, 2018, **12**, 986–993.

6 Y. Ma, Y. Yue, H. Zhang, F. Cheng, W. Zhao, J. Rao, S. Luo, J. Wang, X. Jiang and Z. Liu, *ACS Nano*, 2018, **12**, 3209–3216.

7 Q. Zhang, J. Teng, G. Zou, Q. Peng, Q. Du, T. Jiao and J. Xiang, *Nanoscale*, 2016, **8**, 7085–7093.

8 H. Lin, X. Wang, L. Yu, Y. Chen and J. Shi, *Nano Lett.*, 2017, **17**, 384–391.

9 Q. Xue, H. Zhang, M. Zhu, Z. Pei, H. Li, Z. Wang, Y. Huang, Y. Huang, Q. Deng and J. Zhou, *Adv. Mater.*, 2017, **29**, 1604847.

10 F. Alimohammadi, M. Sharifian Gh, N. H. Attanayake, A. C. Thenuwara, Y. Gogotsi, B. Anasori and D. R. Strongin, *Langmuir*, 2018, **34**, 7192–7200.

11 A. Sinha, H. Zhao, Y. Huang, X. Lu, J. Chen and R. Jain, *TrAC, Trends Anal. Chem.*, 2018, **105**, 424–435.

12 X. Han, J. Huang, H. Lin, Z. Wang, P. Li and Y. Chen, *Adv. Healthcare Mater.*, 2018, **7**, 1701394.

13 T. D. Stocco, N. J. Bassous, S. Zhao, A. E. Granato, T. J. Webster and A. O. Lobo, *Nanoscale*, 2018, **10**, 12228–12255.

14 C. Mandrycky, Z. Wang, K. Kim and D.-H. Kim, *Biotechnol. Adv.*, 2016, **34**, 422–434.

15 B. Duan, *Ann. Biomed. Eng.*, 2017, **45**, 195–209.

16 K. Zhang, S. Wang, C. Zhou, L. Cheng, X. Gao, X. Xie, J. Sun, H. Wang, M. D. Weir, M. A. Reynolds, N. Zhang, Y. Bai and H. H. K. Xu, *Bone Res.*, 2018, **6**, 31.

17 K. Zhu, S. R. Shin, T. van Kempen, Y. C. Li, V. Ponraj, A. Nasajpour, S. Mandla, N. Hu, X. Liu and J. Leijten, *Adv. Funct. Mater.*, 2017, **27**, 1605352.

18 K. Hölzl, S. Lin, L. Tytgat, S. Van Vlierberghe, L. Gu and A. Ovsianikov, *Biofabrication*, 2016, **8**, 032002.

19 D. Chimene, K. K. Lennox, R. R. Kaunas and A. K. Gaharwar, *Ann. Biomed. Eng.*, 2016, **44**, 2090–2102.

20 J. Malda, J. Visser, F. P. Melchels, T. Jüngst, W. E. Hennink, W. J. Dhert, J. Groll and D. W. Hutmacher, *Adv. Mater.*, 2013, **25**, 5011–5028.

21 G. Choe, S. Oh, J. M. Seok, S. A. Park and J. Y. Lee, *Nanoscale*, 2019, **11**, 23275–23285.

22 F. V. Ferreira, L. P. Souza, T. M. Martins, J. H. Lopes, B. D. Mattos, M. Mariano, I. F. Pinheiro, T. M. Valverde, S. Livi and J. A. Camilli, *Nanoscale*, 2019, **11**, 19842–19849.

23 D. N. Heo, N. J. Castro, S.-J. Lee, H. Noh, W. Zhu and L. G. Zhang, *Nanoscale*, 2017, **9**, 5055–5062.

24 S. Kyle, Z. M. Jessop, A. Al-Sabah and I. S. Whitaker, *Adv. Healthcare Mater.*, 2017, **6**, 1700264.

25 A. R. Spencer, E. Shirzaei Sani, J. R. Soucy, C. C. Corbet, A. Primbetova, R. A. Koppes and N. Annabi, *ACS Appl. Mater. Interfaces*, 2019, **11**, 30518–30533.

26 M. Mehrali, A. Thakur, C. P. Pennisi, S. Talebian, A. Arpanaei, M. Nikkhah and A. Dolatshahi-Pirouz, *Adv. Mater.*, 2017, **29**, 1603612.

27 A. R. Spencer, A. Primbetova, A. N. Koppes, R. A. Koppes, H. Fenniri and N. Annabi, *ACS Biomater. Sci. Eng.*, 2018, **4**, 1558–1567.

28 S. H. Ku, S. H. Lee and C. B. Park, *Biomaterials*, 2012, **33**, 6098–6104.

29 A. S. Rowlands and J. J. Cooper-White, *Biomaterials*, 2008, **29**, 4510–4520.

30 W. Zhu, T. Ye, S.-J. Lee, H. Cui, S. Miao, X. Zhou, D. Shuai and L. G. Zhang, *Nanomedicine*, 2018, **14**, 2485–2494.

31 C.-T. Huang, L. K. Shrestha, K. Ariga and S.-h. Hsu, *J. Mater. Chem. B*, 2017, **5**, 8854–8864.

32 H. Lin, Y. Chen and J. Shi, *Adv. Sci.*, 2018, **5**, 1800518.

Paper

Nanoscale

33 S. Pei and H.-M. Cheng, *Carbon*, 2012, **50**, 3210–3228.

34 J. M. Cabot, E. Duffy, S. Currivan, A. Ruland, R. Jalili, A. J. Mozer, P. C. Innis, G. G. Wallace, M. Breadmore and B. Paull, *Analyst*, 2016, **141**, 2774–2782.

35 A. Ruland, R. Jalili, A. J. Mozer and G. G. Wallace, *Analyst*, 2018, **143**, 215–223.

36 C. Zhao, Q. Wang, H. Zhang, S. Passerini and X. Qian, *ACS Appl. Mater. Interfaces*, 2016, **8**, 15661–15667.

37 A. Pazniak, P. Bazhin, N. Shplis, E. Kolesnikov, I. Shchetinin, A. Komissarov, J. Polcak, A. Stolin and D. Kuznetsov, *Mater. Des.*, 2019, **183**, 108143.

38 X. Li, X. Yin, M. Han, C. Song, H. Xu, Z. Hou, L. Zhang and L. Cheng, *J. Mater. Chem. C*, 2017, **5**, 4068–4074.

39 K. Raagulan, R. Braveenth, B. M. Kim, K. J. Lim, S. B. Lee, M. Kim and K. Y. Chai, *RSC Adv.*, 2020, **10**, 1613–1633.

40 A. Zolfagharian, A. Z. Kouzani, S. Y. Khoo, B. Nasri-Nasrabadi and A. Kaynak, *Sens. Actuators, A*, 2017, **265**, 94–101.

41 Q. Shi, H. Liu, D. Tang, Y. Li, X. Li and F. Xu, *NPG Asia Mater.*, 2019, **11**, 1–21.

42 A. Guiseppi-Elie, *Biomaterials*, 2010, **31**, 2701–2716.

43 L. Li, Y. Shi, L. Pan, Y. Shi and G. Yu, *J. Mater. Chem. B*, 2015, **3**, 2920–2930.

44 P. Baei, S. Jalili-Firoozinezhad, S. Rajabi-Zeleti, M. Tafazzoli-Shadpour, H. Baharvand and N. Aghdami, *Mater. Sci. Eng., C*, 2016, **63**, 131–141.

45 S. Sayyar, E. Murray, B. Thompson, J. Chung, D. L. Officer, S. Gambhir, G. M. Spinks and G. G. Wallace, *J. Mater. Chem. B*, 2015, **3**, 481–490.

46 J. Jin, F. Liu, E. Weber and S. Crozier, *Phys. Med. Biol.*, 2012, **57**, 8153.

47 W. T. Cao, C. Ma, D. S. Mao, J. Zhang, M. G. Ma and F. Chen, *Adv. Funct. Mater.*, 2019, **29**, 1905898.

48 H. Rastin, R. T. Ormsby, G. J. Atkins and D. Losic, *Mol. Syst. Des. Eng.*, 2020, **3**, 1815–1826.

49 N. Paxton, W. Smolan, T. Böck, F. Melchels, J. Groll and T. Jungst, *Biofabrication*, 2017, **9**, 044107.

50 J. Emmermacher, D. Spura, J. Cziommer, D. Kilian, T. Wollborn, U. Fritsching, J. Steingroewer, T. Walther, M. Gelinsky and A. Lode, *Biofabrication*, 2020, **12**, 025022.

51 A. Shafiee, E. Ghadiri, H. Ramesh, C. Kengla, J. Kassis, P. Calvert, D. Williams, A. Khademhosseini, R. Narayan and G. Forgacs, *Appl. Phys. Rev.*, 2019, **6**, 021315.

52 Z. Liu, B. Bhandari, S. Prakash, S. Mantihal and M. Zhang, *Food Hydrocolloids*, 2019, **87**, 413–424.

53 S. A. Wilson, L. M. Cross, C. W. Peak and A. K. Gaharwar, *ACS Appl. Mater. Interfaces*, 2017, **9**, 43449–43458.

54 A. Thakur, M. K. Jaiswal, C. W. Peak, J. K. Carrow, J. Gentry, A. Dolatshahi-Pirouz and A. K. Gaharwar, *Nanoscale*, 2016, **8**, 12362–12372.

55 H. Li, Y. J. Tan, K. F. Leong and L. Li, *ACS Appl. Mater. Interfaces*, 2017, **9**, 20086–20097.

56 L. Ouyang, R. Yao, Y. Zhao and W. Sun, *Biofabrication*, 2016, **8**, 035020.

57 W. Yang, J. Yang, J. J. Byun, F. P. Moissinac, J. Xu, S. J. Haigh, M. Domingos, M. A. Bissett, R. A. Dryfe and S. Barg, *Adv. Mater.*, 2019, **31**, 1902725.

58 K. Huang, Z. Li, J. Lin, G. Han and P. Huang, *Chem. Soc. Rev.*, 2018, **47**, 5109–5124.

59 M. Naguib, V. N. Mochalin, M. W. Barsoum and Y. Gogotsi, *Adv. Mater.*, 2014, **26**, 992–1005.

60 N. Driscoll, A. G. Richardson, K. Maleski, B. Anasori, O. Adewole, P. Lelyukh, L. Escobedo, D. K. Cullen, T. H. Lucas, Y. Gogotsi and F. Vitale, *ACS Nano*, 2018, **12**, 10419–10429.

61 A. M. Jastrzębska, A. Szuplewska, T. Wojciechowski, M. Chudy, W. Ziemkowska, L. Chlubny, A. Rozmysłowska and A. Olszyna, *J. Hazard. Mater.*, 2017, **339**, 1–8.

Page 243

3D Bioprinting of Cell-Laden Electroconductive MXene Nanocomposite Bioinks

Hadi Rastin, Bingyang Zhang, Arash Mazinani, Kamrul Hassan, Jingxiu Bi, Tran Tung,
Dusan Losic*

School of Chemical Engineering and Advanced Materials, The University of Adelaide,
Adelaide, SA 5005, Australia

Corresponding author: Professor Dusan Losic
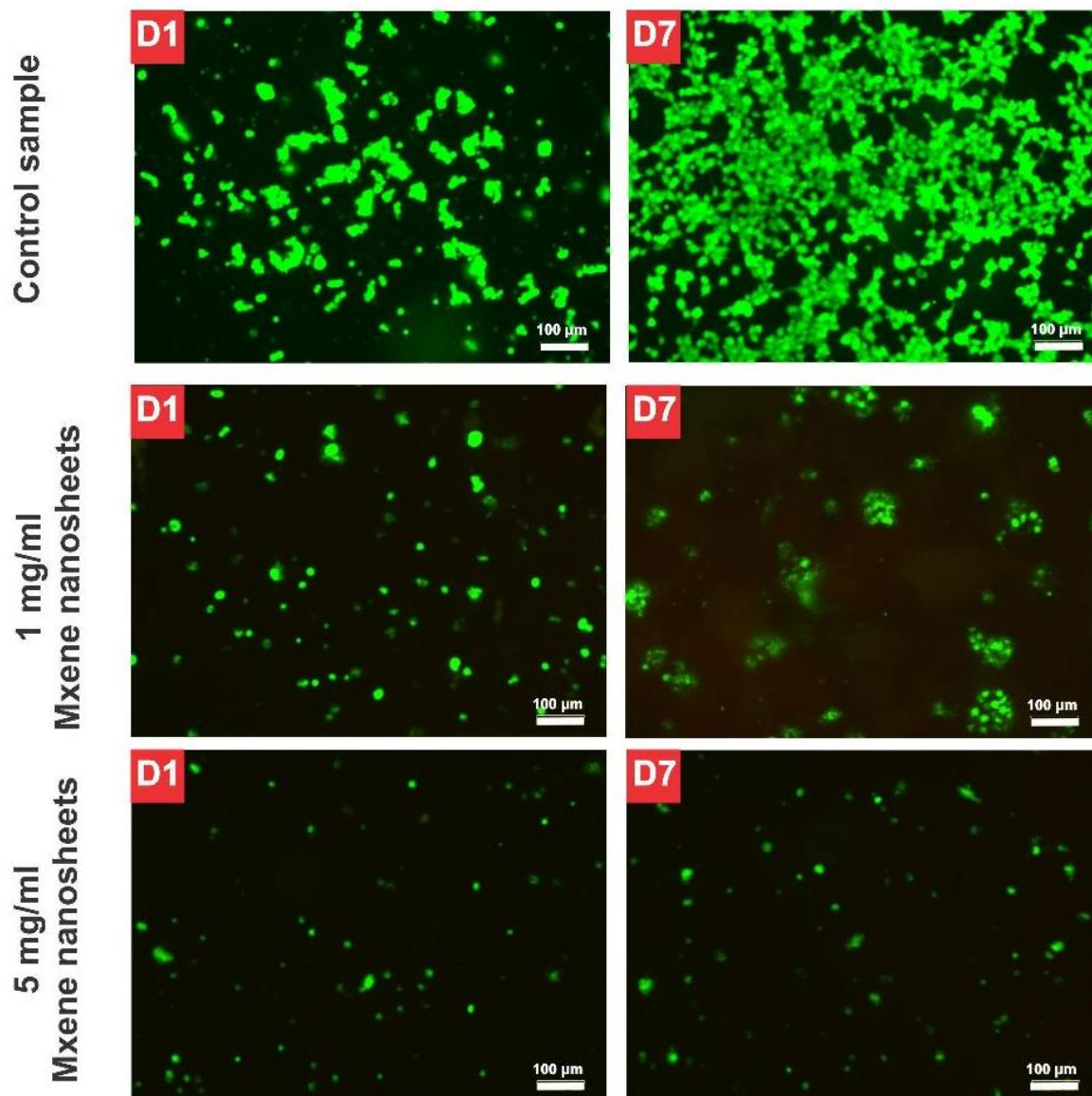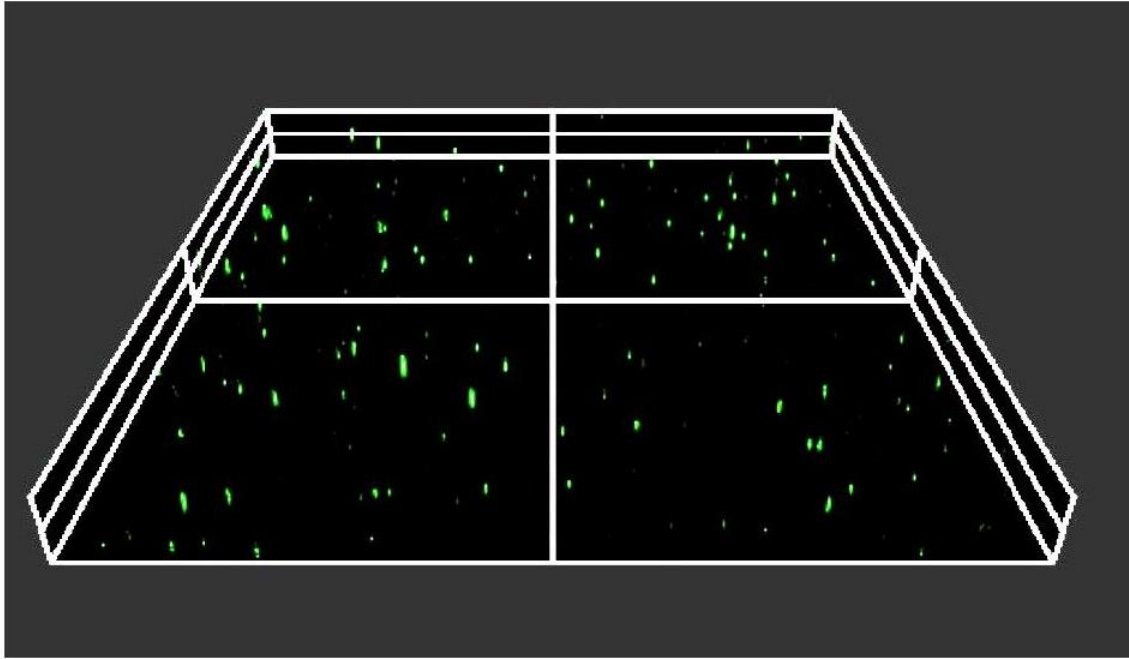E-mail address: dusan.losic@adelaide.edu.au

1

Figure S1: Fluorescent images of stained HEK-293 cells taken from 2D cell culture with different MXene nanosheets content after 1 and 7 days of culture. Cells stained with calcein-AM (green) and ethidium homodimer-1 (red)

2

Figure S2: 3D Fluoresce images taken from cell-laden HA-5/Alg-1/MXene-1 ink, stained with calcein-AM (green) and ethidium homodimer-1 (red)

3

Chapter 5

Development of an electroconductive bioink

I n this chapter, to overcome the challenges associated with poor electrical conductivity of current bioinks, a bioink with tunable electrical conductivity is introduced. The bioink is composed of thixotropic methylcellulose/kappa-carrageenan (MC/κCA) hydrogels filled with poly(3,4-ethylenedioxythiophene):poly(styrenesulfonate) (PEDOT:PSS) conducting polymers. In this chapter, the printability of the MC/κCA hydrogel was characterized comprehensively to obtain the optimal printing parameters. To showcase the successful printability of the bioink, a variety of multi-layered 3D structures were printed, confirming the excellent performance of the bioink in terms of shape fidelity and printing resolution. Harnessing the high electrical conductivity of PEDOT:PSS allows adjusting the conductivity to the ink. In terms of biocompatibility, encapsulated HEK-293 cells remain viable within the ink without noticeable changes before and after the printing process.

This chapter has been published as:

"Rastin H, Zhang B, Bi J, Hassan K, Tung TT, Losic D. 3D printing of cell-laden electroconductive bioinks for tissue engineering applications. Journal of Materials Chemistry B. 2020;8(27):5862-5876."

Statement of Authorship

Title of Paper	3D printing of cell-laden electroconductive bioinks for tissue engineering applications
Publication Status	☑ Published ☐ Accepted for Publication ☐ Submitted for Publication ☐ Unpublished and Unsubmitted work written in manuscript style
Publication Details	Rastin H, Zhang B, Bi J, Hassan K, Tung TT, Losic D. 3D printing of cell-laden electroconductive bioinks for tissue engineering applications. Journal of Materials Chemistry B. 2020;8(27):5862-5876.

Principal Author

Name of Principal Author (Candidate)	Hadi Rastin		
Contribution to the Paper	Conceptualization, Investigation, Methodology, data processing, Original Draft.		
Overall percentage (%)	70%		
Certification:	This paper reports on original research I conducted during the period of my Higher Degree by Research candidature and is not subject to any obligations or contractual agreements with a third party that would constrain its inclusion in this thesis. I am the primary author of this paper.		
Signature		Date	07/04/2021

Co-Author Contributions

By signing the Statement of Authorship, each author certifies that:

   i.   the candidate's stated contribution to the publication is accurate (as detailed above);

   ii. permission is granted for the candidate in include the publication in the thesis; and

   iii. the sum of all co-author contributions is equal to 100% less the candidate's stated contribution.

Name of Co-Author	Prof. Dusan Losic		
Contribution to the Paper	Conceptualization, Resources, Funding Acquisition, Re-view&Editing, Supervision, submission		
Signature		Date	15/04/21

Name of Co-Author	Dr. Tran Thanh Tung		
Contribution to the Paper	C-supervision, Review & Editing.		
Signature		Date	14/4/2021

Please cut and paste additional co-author panels here as required.

Name of Co-Author	Jingxiu Bi			
Contribution to the Paper	Resources, Review&Editing.			
Signature			Date	15/04/2021

Name of Co-Author	Bingyang Zhang			
Contribution to the Paper	selected investigation, Methodology, Review & Editing.			
Signature			Date	15/04/2021

Name of Co-Author	Kamrul Hassan			
Contribution to the Paper	selected investigation, Methodology, Review & Editing.			
Signature			Date	15/04/2021

PAPER

Check for updates

3D printing of cell-laden electroconductive bioinks for tissue engineering applications†

Hadi Rastin, Bingyang Zhang, Jingxiu Bi, Kamrul Hassan, Tran Thanh Tung [ID] and Dusan Losic [ID] *

Bioprinting is an emerging powerful fabrication method, which enables the rapid assembly of 3D bioconstructs with dispensing cell-laden bioinks in pre-designed locations. However, to translate this technology into real applications, there are still a number of challenges that need to be addressed. First, the current inks are generally composed of polymeric materials with poor electrical conductivity that mismatches with the native tissue environment. The second challenge associated with the 3D bioprinting of hydrogel-based bioinks is the fabrication of anatomical-size constructs without any loss of shape fidelity and resolution. To address these challenges, in this work, we introduced a biocompatible bioink associated with current 3D bioprinting by combining methylcellulose and kappa-carrageenan (MC/κCA) hydrogels with poly(3,4-ethylenedioxythiophene):poly(styrenesulfonate) (PEDOT:PSS) conducting polymers. The prepared ink exhibited highly thixotropic behaviour, which could be tuned *via* changing the concentration of MC and κCA to obtain easy printing with high shape fidelity. The ink was able to fabricate physiological-scale constructs without requiring a secondary support bath. In addition, varying the concentration of PEDOT:PSS could control the electrical conductivity of the ink. Moreover, the encapsulated human embryonic kidney 293 (HEK-293) cells in bulk hydrogels and 3D bioprinted structures maintained high cell viability (>96%) over a week, confirming the *in vitro* biocompatibility of the ink. Overall, these findings indicate that the MC/κCA/PEDOT:PSS bioink can be promising in biomedical applications, which improved the electroconductivity of bioinks and can exploit the advantage of conductive polymers in the 3D bioprinting technology.

1. Introduction

3D bioprinting allows for the rapid assembly of constructs in which a cell-laden hydrogel is dispensed in a pre-designed location *via* layer-by-layer stacking.[1,2] Based on the required properties of bioinks, the 3D bioprinting process can be categorized into three main classes, namely, orifice-free bioprinting, inkjet bioprinting, and extrusion bioprinting.[3] The latter has drawn more attention due to its ability to dispense highly viscous bioinks with high cell density.[4] In extrusion-based bioprinters, the bioink is drawn into a syringe and extruded *via* the nozzle by

applying a pneumatic or mechanical force.[5] However, despite considerable advances in the 3D bioprinting technology nowadays, the design and development of novel bioinks with required characteristics to print high-resolution constructs remain challenging in the 3D bioprinting of biological-scale tissues.[3,6,7]

The first challenge in the development of the 3D bioprinting method is the limitation of biomaterials suitable for the 3D bioprinting process because usually, biomaterials that show promising cellular responses are not printable.[3] In this sense, shear-thinning hydrogels as rheology modifiers can impart printability to the existing biomaterials. These hydrogels are promising biomaterials to be used in 3D bioprinting owing to their ability to shield living cells from high shear forces during extrusion, self-healing behaviour once printed, and similarity to the extracellular matrix.[8] Methylcellulose (MC) is a class of natural polysaccharides with high shear-thinning behaviour.[9,10] Moreover, MC exhibits a reversible sol-to-gel transition upon heating due to the strong intermolecular interactions at high temperatures.[11] Although single-component MC hydrogels can be printed solely with high cell viability, they have poor shape retention and suffer from the lack of post-crosslinking ability, which leads to the fast degradation of printed structures in biological media.[12] Considering this, MC has been mixed with

Paper   Journal of Materials Chemistry B

other polymers such as alginate[13,14] or hyaluronic acid.[15] Kappa-carrageenan (κCA) is a negatively charged sulfonated polysaccharide obtained from red algae, and it is widely used as a thickening agent in the pharmaceutical and food industries.[16,17] It exhibits stiff gel behaviour once it undergoes gelation in the presence of potassium ions, which offers enough mechanical strength for supporting cells.[18,19] Moreover, from the rheological point of view, κCA possesses shear-thinning behaviour and can be a promising candidate for 3D bioprinting applications.[20–22]

The second challenge associated with 3D bioprinting relates to the poor electrical conductivity of most current bioinks due to the inherent properties of polymers used in bioinks.[23] Conductive hydrogels allow providing uniform electrical cues to living cells within 3D constructs to mediate the growth and differentiation of various cells.[24–26] Recent research regarding the development of conductive bioinks revealed that the incorporation of metallic or carbon-based conductive nanomaterials could impart conductivity within the printed constructs.[27] Gold nanoparticles (AuNPs) are typical examples of metallic conductive materials, which present high stability, biocompatibility and tunability in terms of shape and size.[28] For instance, a bioink composed of the blend of gold nanorod (GNR)-incorporated gelatin methacryloyl (GelMA) and alginate was developed, in which coaxial extrusion with calcium chloride enables 3D printing of constructs.[27] It was found that the incorporation of GNRs imparts conductivity within pristine GelMA/alginate bioinks, which improved cell adhesion and electrical signal propagation between cardiac cells. However, it was also reported that gold nanoparticles show a tendency to produce reactive oxygen species, which might damage proteins, lipids, and DNA at high concentrations.[29,30] Another drawback of the AuNPs is the small size that enables them to diffuse into the cell membrane and affect cellular activities.[30] In the case of carbon-based conductive nanomaterials, carbon nanotubes (CNTs) are rolled-up sheets of honeycomb carbon, which have been widely used in tissue engineering thanks to their high conductivity, stability, and unique mechanical properties.[31] For example, an electroconductive scaffold composed of poly(ethylene glycol)diacrylate (PEGDA) and amine-functionalized multi-walled carbon nanotubes (MWCNTs) was fabricated by a stereolithographic 3D printing process.[32] It revealed that the electrical conductivity of PEGDA/MWCNT scaffolds promotes neuronal differentiation and proliferation. However, the cytotoxicity of CNTs caused by the disruption of intracellular metabolic pathways, membrane damage, and the generation of reactive oxygen species (ROS) restricts the real application of CNTs.[33] Recently, graphene, a single layer of carbon atoms arranged in a hexagonal honeycomb lattice,[34] have drawn significant attention due to its unique electrical and mechanical properties.[35] Huang et al.[36] reported a nano-composite bioink composed of thermo-sensitive waterborne polyurethane and graphene for neural stem cell (NSC) printing. They found that the incorporation of fewer amounts of graphene (25 ppm) enhances neural differentiation. However, the cytotoxic effects of graphene and its derivatives remain a challenge, which depends on the concentration, size, charge, and functional groups of the graphene surface.[37] Thus, it is a critical demand to design new conductive bioinks to meet both the printability and biological requirements.

Conductive polymers have been considered as alternative candidates for metallic or carbon-based conductive nanomaterials, which offer improved biocompatibility for the fabrication of electroconductive hydrogels.[38,39] Poly(3,4-ethylenedioxythiophene):poly(styrene-sulfonate) (PEDOT:PSS) is characterized with its inherent electrical conductivity, biocompatibility, cost-effectiveness, electrochemical stability under physiological conditions, and easy dispersion in aqueous solutions.[40,41] In an aqueous dispersion of PEDOT:PSS complex polymers, PEDOT nanoparticles were wrapped and stabilized by PSS chains.[42] In a recent study, a conductive bioink composed of gelatin methacryloyl (GelMA) and PEDOT:PSS hydrogels was prepared for extrusion-based 3D bioprinting.[43] However, on the one hand, photo-crosslinking of GelMA might induce endogenous oxidative damage to DNA or change DNA causing immunosuppression in vivo.[44] On the other hand, it is reported that cell viability deteriorates upon prolonged exposure to light.[45] In addition, incorporation of PEDOT:PSS within the GelMA matrix blocks a fraction of light and causes crosslinking density decline.[42] More importantly, since GelMA/PEDOT:PSS is not printable, a microgel support bath provides temporary mechanical strength to improve the fidelity of printed structures, which adds more complexity to the printing process.

In this study, to address these key challenges in developing advanced cell-laden electroconductive bioinks for soft 3D printing and tissue engineering, we introduce an electroconductive bioink composed of conductive polymer PEDOT:PSS dispersed homogeneously within highly thixotropic bio-hydrogels (Fig. 1). We proposed that the rheological behaviour of the MC/κCA hydrogel will enable excellent printability for the fabrication of 3D constructs, while the PEDOT:PSS conducting polymer will provide electrical conductivity to the bioink. We specifically introduced κCA to play dual roles in the ink; first, providing ionic-crosslinking ability to stabilize printed structures after printing by immersion in potassium chloride solution (37 °C, 5 min) and, second, contributing to the thixotropic behaviour of the bioink by the synergistic interaction of MC and κCA. The concentration of PEDOT:PSS was tailored to induce the required electrical conductivity within the ink. Herein, first, we characterized MC/κCA bioink in terms of water uptake capacity, degradation kinetics and mechanical properties. Then, we investigated on the rheological behaviour of the ink before, during, and after the 3D printing process. Furthermore, to evaluate the in vitro cytotoxicity of the ink, the viability of encapsulated Human Embryonic Kidney 293 (HEK-293) cells within the ink was monitored by a live/dead cell assay in both bulk and printed 3D bioconstructs. Finally, to demonstrate the ability of the ink, multilayered 3D structures were printed without the need for a secondary support bath showing robust fabrication of physiological-scale structures by the 3D printing process.

2. Experimental section

2.1. Materials

Kappa-carrageenan, methylcellulose with approximate viscosity of 1500 cp at 2 wt%, PEDOT:PSS with 1.3 wt% dispersion in
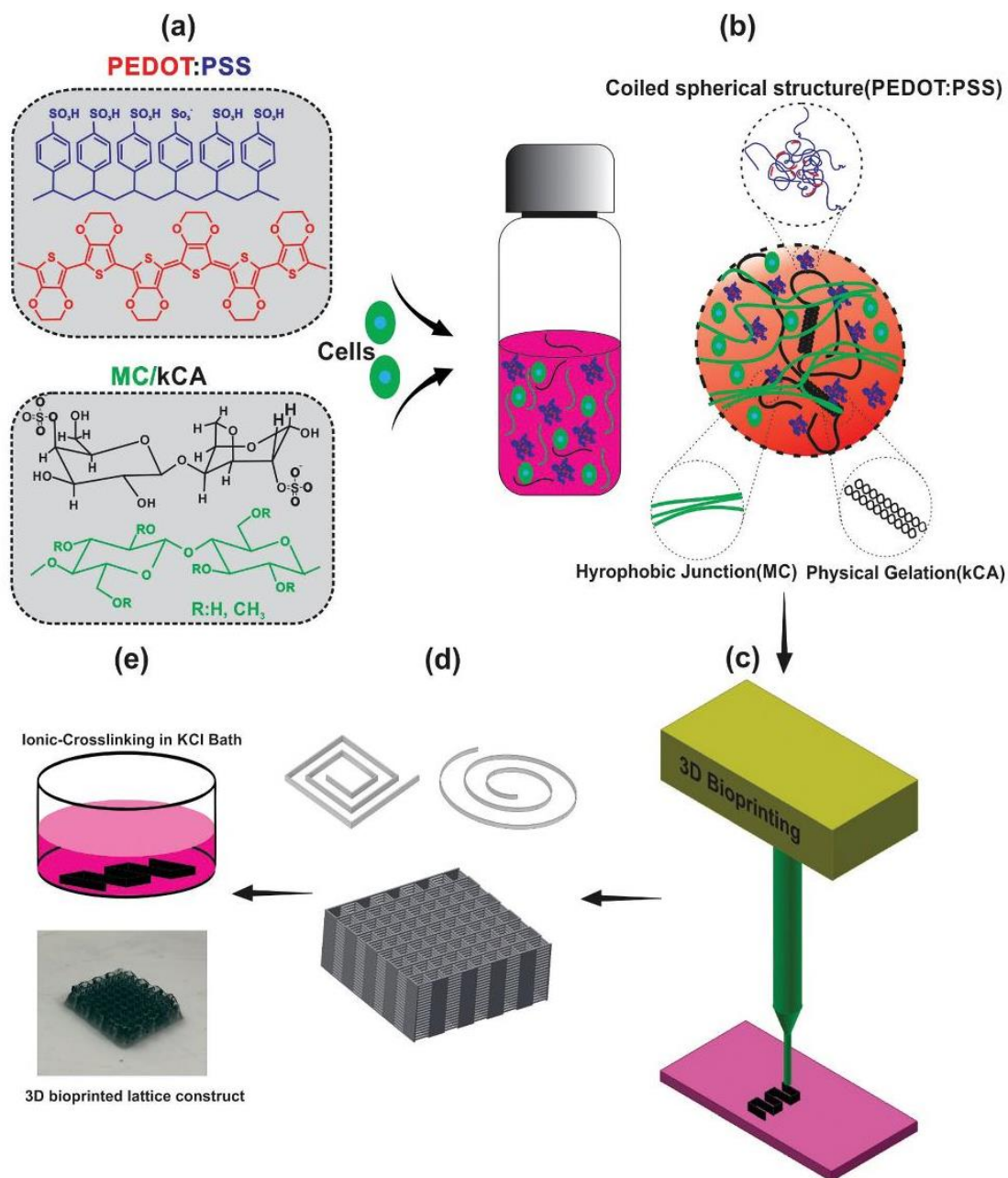
Fig. 1 Schematic of an electroconductive bioink synthesized from the MC/κCA hydrogel and PEDOT:PSS conducting polymer. (a) Chemical structures of MC, κCA and PEDOT:PSS mixed with the cells. (b) Schematic showing the coiled spherical structures of PEDOT:PSS dispersed within the MC/κCA hydrogel. The thermo-responsive behaviour of the κCA allows the physical gelation of κCA due to the formation of coaxial double helix under salt-free conditions. MC demonstrates sol–gel transition upon heating due to the change from hydrophilic nature in the sol state to hydrophobic nature in the gel state. (c) Construct is built via layer-by-layer deposition of ink according to the pre-fabricated design. (d) Pictures of 3D bioprinted structures by MC/κCA/PEDOT:PSS. (e) Stabilization of printed structures in KCl bath after printing.

water and sodium sulfate were purchased from Sigma-Aldrich. Calcein AM and ethidium homodimer-1 were supplied by Invitrogen (Carlsbad, CA) for the live/dead cell assay.

2.2. Fabrication of MC/κCA/PEDOT:PSS bioinks

To prepare the MC/κCA/PEDOT:PSS hydrogel, first, we dissolved κCA powder (1 and 1.5 wt%) in Na_2SO_4 0.05 M solution

at 80 °C for 10 min. Then, PEDOT:PSS solution was added to the κCA solution to reach final concentrations of 0.1 and 0.3 wt%. It should be noticed that the PEDOT:PSS solution was sonicated for 20 min in an ice bath to breakdown large particle aggregates before mixing with the κCA solution. Finally, MC (4, 6 and 8 wt%) was added to the κCA/PEDOT:PSS solution for an additional 10 min to obtain a homogenous dispersion of MC and stored in a fridge at 4 °C for 24 h. Table S1 (ESI†) summarizes the recipe of the prepared hydrogels in detail. For convenience, the prepared hydrogel samples were designated as MC-x/κCA-y/PEDOT:PSS-z, where x, y, and z indicate the weight concentrations of MC, κCA, and PEDOT:PSS, respectively.

2.3. Characterization of MC/κCA/PEDOT:PSS hydrogels

2.3.1. Swelling ratio. The swelling ratio (SR) of the prepared hydrogels was measured in deionised (DI) water at 37 °C for 24 h. The prepared hydrogels were soaked in PBS and weighed carefully after removal from the solution. They were then lyophilized in a freeze dryer for two days. The SR was calculated according to the following equation:

$$SR = \frac{W(\text{swell}) - W(\text{dry})}{W(\text{dry})} \quad (1)$$

where $W(\text{swell})$ and $W(\text{dry})$ denote the hydrogel weight at the swollen and dry states. At least three samples for each formulation were used to measure the swelling ratio and average values were reported.

2.3.2. Degradation kinetics. The degradation kinetics of the prepared hydrogels was determined for three weeks in DI water at 37 °C. The samples were removed from the DI solution at certain time intervals and weighed. The remaining weight of the samples was calculated using the following equation:

$$\text{Remaining weight } \% = \frac{W(t) - W(0)}{W(0)} \times 100 \quad (2)$$

where $W(0)$ is the weight of the sample before immersion in DI water and $W(t)$ is the weight of the sample at a predetermined time.

2.3.3. Dynamic mechanical analysis. The uniaxial compression strength of the prepared inks was measured using a Q800 Dynamic mechanical analyser (TA Instruments LLC, Delaware, USA) equipped with a load cell capacity of 10 N. Testing was performed with 0.1 N steps at room temperature. The samples were first crosslinked in 5 wt% KCl solution for 5 min, swollen in deionized water for 24 hours and then cut into cylindrical shapes ($D = 15$ mm, $H = 10$ mm). The stress–strain curve of the prepared samples was plotted and the corresponding compressive modulus was calculated from the slope of the curves in the initial linear region.

2.3.4. FTIR and XRD spectra. The interaction between MC and κCA was investigated using a Nicolet 6700 Thermo Fisher Fourier transform infrared (FTIR) spectrometer over the wavelength range of 4000–600 cm^{-1}. XRD analysis was also carried out using a Rigaku MiniFlex 600, Japan under predefined conditions (40 kV and 15 mA, $2\theta = 5°$–$80°$).

2.3.5. Rheological measurements. The viscoelastic behaviour of the prepared inks was characterized using a Physica MCR301 rheometer (Anton Paar, Ostfildern, Germany). Stainless steel plates with the geometry of cones and plates (diameter of 50 mm, gap of 49 μm) were used for all measurements. For all cases, the samples were loaded on the plate and surrounded by silicon oil to avoid evaporation of water. First, oscillatory strain sweep tests were performed by increasing the strain from 0.01% to 100% at 10 Hz to determine the linear region of viscoelastic behaviour. The frequency sweep test was carried out by logarithmically decreasing the frequency from 100 Hz to 0.01 Hz at room temperature. The shear-viscosity tests were performed over a shear rate sweep from 0.01 s^{-1} to 1000 s^{-1} at room temperature. The yield stress of the prepared inks was measured in an oscillation stress sweep ranging from 1 to 10 000 Pa at 1 Hz frequency. The yield stress is defined as the crossover point of storage (G') and loss modulus (G''). The recoverability of inks was characterized in both oscillatory and shear modes. In the oscillation mode, the prepared hydrogels repetitively underwent low strain of 1% for 1 min, followed by a high strain of 100% (or 500%) at 1 Hz frequency. In the shear mode, the viscosity of samples was traced first at a low shear rate of 0.1 s^{-1} for 60 s, then at a high shear rate of 100 s^{-1} (or 500 s^{-1}) for 5 s, and finally at 0.1 s^{-1} for another 2 minutes. The temperature sweep was also performed at a heating rate of 2 °C min^{-1} over the range of 20–50 °C at 1 Hz frequency. In addition, rheological properties of the prepared hydrogels were measured at a constant temperature of 37 °C for 600 s.

2.3.6. Electrical conductivity. The conductivity of the prepared hydrogels was measured in a contactless mode using a C4D instrument at room temperature. The contactless conductivity measurements are possible as the external electrodes form double layer capacitances, as known from electrochemistry, with the electrolyte (hydrogels) inside the fluidic channel. Probing the solution conductance is carried out by applying an AC-voltage to one electrode and measuring the resulting current at the other electrode. As the electrodes and electrolytes are separated by a relatively thick insulating barrier, the capacitances are small (less than 1 pF) and thus relatively high frequency (300 kHz) are supplied. The electrical impedance of hydrogels was measured on an electrochemical station in the frequency range of 0.1 Hz–10^4 Hz at room temperature with an AC amplitude of 10 mV. Hydrogels were first swollen in ultrapure water for 12 hours to remove the ions from the samples and then sandwiched between two copper electrodes.

2.4. The 3D Printing technology

2.4.1. Initial screening of printing. As an initial screening of printability, the prepared inks with different formulations were extruded through a 225 μm blunt-tipped stainless steel needle with constant pressure, and the roughness of fibers was imaged using a contact angle's camera.

2.4.2. The 3D printing technology. 3D printing was performed using an Allevi 2 (Philadelphia, United States) extrusion-based bioprinter equipped with an adjustable air pressure supplier *via* layer-by-layer dispensing of hydrogels on the surface.

Autodesk fusion 360 was employed to design structures and export STL files, followed by conversion into Gcode using the Slic3r software. For printing, the prepared inks were drawn into a 10 ml syringe and extruded through the nozzle upon application of air pressure. Optimized operating parameters for 3D printing were identified through a systematic change of air pressure (10, 15, and 20 psi), print speed (1, 2, 4, 6, and 8 mm s^{-1}), and nozzle height (0.2, 0.3, and 0.4 mm). For all experiments, a conical needle with an inner diameter of 225 µm was used to print at room temperature. The ink prints various objects including lattice (L = 2 cm, W = 2 cm, H = 0.5 cm), cylindrical (D = 2 cm, H = 2 cm) and hexagonal (D = 2 cm, H = 2 cm) shapes.

2.5. The 3D bioprinting technology and cell viability

2.5.1. Cell culture.
The seeding of Human Embryonic Kidney 293 (HEK-293) cells was cultured in a T25 flask (25 cm^2) containing modified Eagle's medium (MEM, Gibco™) supplemented with 10% fetal bovine serum (Gibco™) as the cell culture medium in an incubator with a humidified atmosphere and 5% CO$_2$ at 37 °C. Then, when the cell growth in the T-flask reached about 90% confluence, the adherent HEK-293 cells were resuspended using a culture medium and then centrifuged at 5000 rpm for 5 min to remove the culture medium.

2.5.2. The 3D bioprinting technology.
An MC-8/κCA-1/PEDOT:PSS-0.1 precursor solution was first prepared as described earlier using sterilized culture media instead of DI water solution. Then, the cell pellet was mixed with the prepared precursor solution in a culture medium to reach a final cell density of 5 × 10^4 cells per ml. Part of the prepared bioink was poured into the 4-well imaging cell slide to form a thin layer of hydrogel. The remaining part of bioink was drawn into a 10 ml syringe and few layer lattice and polyline structures were printed using a 27 G tapered plastic tip with optimized operating printing parameters (print speed: 240 mm min^{-1}; air pressure: 15 psi; and nozzle height: 0.2 mm). All the 3D bioprinted structures were immersed in 5 wt% KCl solution for 5 min. The 3D bioprinter and all involved accessories were disinfected with 70% w/v ethanol solution before use. A live/dead cell assay was conducted using the LIVE/DEAD™ Viability/Cytotoxicity Kit (calcein AM, green fluorescent for live cells and ethidium homodimer-1, red fluorescent for dead cells, Invitrogen™) following the instructions mentioned in the kit. The viability of the encapsulated HEK-293 cells within the ink in both bulk hydrogels and 3D bioprinted structures were monitored on day 1, 3, and 7 of culture after encapsulation. For the control sample, HEK-293 cells were added to the culture media without any hydrogel ink and were imaged at the same time intervals. The viability of cells was reported as the ratio of viable cells to the sum of viable and dead cells.

2.5.3. MTT assay.
The methylthiazolyldiphenyl-tetrazolium bromide (MTT) assay was employed to examine the metabolic activity of the cells on days 1, 3, and 5. Accordingly, hydrogels were transferred to a 96 well-plate and 1 × 10^4 HEK-293 cells were seeded on the hydrogel surface in a Minimum Essential Medium (MEM) supplemented with 10% fetal bovine serum (FBS). Samples were incubated at 37 °C in 5% CO$_2$ atmosphere for five days. Then, 200 µl of cell samples were transferred to the 96-well plate, and MTT in PBS buffer was added to each well plate (final concentration: 0.5 mg ml^{-1}). The cells were further incubated at 37 °C in 5% CO$_2$ atmosphere for further 4 h. To each well, 100 µl of dimethyl sulfoxide (DMSO) was added to ensure the complete solubilization of formazan products. Finally, the absorbance was determined using a Biotek Microplate Reader (Biotek, USA) at a wavelength of 595 nm.

2.5.4. Cell count.
To monitor the proliferation rate of the cells, hydrogels were transferred to a 24-well plate followed by seeding 5 × 10^4 HEK-293 cells on the hydrogel surface in each well. The cells were maintained in a MEM supplemented with 10% fetal bovine serum in an incubator with a humidified atmosphere and 5% CO$_2$ at 37 °C. Cell numbers of each sample were counted every day for 5 days using a glass cell counting plate.

3. Results and discussion

To develop a printable conductive bioink, the MC/κCA hydrogel was combined with the PEDOT:PSS conductive polymer, in which the MC/κCA hydrogel serves to provide the rheological requirements for the 3D bioprinting process, while the PEDOT:PSS conductive polymer imparts conductivity to the system. The hydrophobic interaction between methoxyl groups along the MC backbone leads to the gelation of MC; however, the fast degradation of MC in biological media limits its application. Given this, MC has been generally mixed with other components such as xanthan,[46] chitosan,[47] and Pluronic.[48] Herein, κCA was selected to be blended with MC, which renders the ionic crosslinking ability to the system. In addition, κCA can intensify the thixotropic behaviour of MC that benefits the printability of the system. Mixing of κCA and MC does not disrupt the hydrophobic interaction of MC as well as the helical junction zone of κCA. In addition, the PEDOT:PSS conductive polymer dispersed and formed coiled spherical structures within the hydrogel. Accordingly, we first characterized the MC/κCA hydrogels with different formulations in detail to determine the optimized ratio for obtaining high shape fidelity and resolution. Following that, the effect of the PEDOT:PSS conductive polymer on the electrical conductivity and printability of the hydrogel was investigated.

3.1. Characterization of MC/κCA hydrogels

The high swelling ratio is advantageous for hydrogels in regenerative medicine due to the similarity to the tissue microenvironment.[49,50] In addition, the scaffolds should be removed in a controlled manner from the lesion site after it has served its purpose.[51] Given this, the swelling ratio and degradation kinetics of different formulations of MC/κCA hydrogels were evaluated (Fig. 2a). Considering the κCA concentration constant, the swelling ratio of MC/κCA hydrogels falls progressively upon increasing the MC concentration due to the more compact polymer entanglement.[46] In addition, MC/κCA hydrogels with a higher content of κCA display a lower swelling ratio because of the formation of more double helix structures at higher concentrations of κCA.
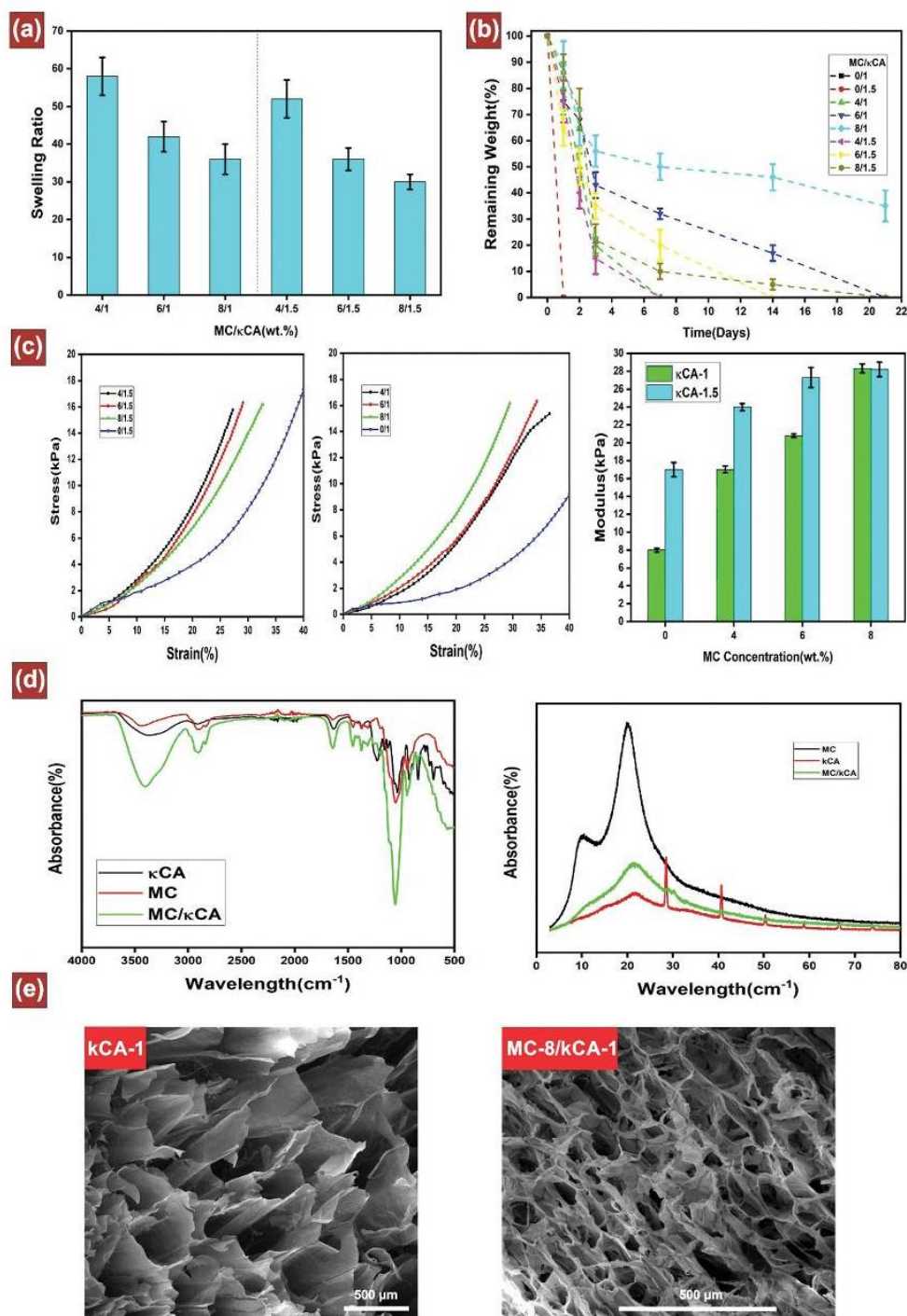
Paper

Fig. 2 Characterization of MC/κCA hydrogels in terms of (a) swelling ratio, (b) degradation rate, (c) mechanical strength under applying compression force, (d) FTIR and XRD spectra, and (e) SEM micrographs of the κCA-1 and the MC-8/κCA-1 hydrogels.

These results indicated that the swelling ratio of MC/κCA can be adjusted by varying the polymer content. The degradation kinetics of the prepared MC/κCA hydrogels has been studied by monitoring the weight loss of the hydrogels in DI water at 37 °C over time (Fig. 2b). Accordingly, both 1 and 1.5 wt% pure κCA hydrogels demonstrate full dissociation after 24 h,

presumably due to the collapse of ionic interactions between the double helix structure of κCA and K$^+$ ions as well as strong binding of κCA and water.[19] In addition, maintaining the concentration of MC to be constant, higher κCA contents in the MC/κCA hydrogel lead to more weight loss, indicating the high affinity of κCA and water. However, the introduction of MC into the κCA hydrogel improves the stability of the hydrogel as MC-8/κCA-1 shows approximately 50% weight loss after 21 days. The hydrophobic interactions along MC chains are responsible for the slower degradation profile of the MC/κCA hydrogel,[52] which has been reported for MC/hyaluronic acid[53] and MC/xanthan gum[46] systems.

MC and κCA are characterized with their thermo-gelation and thickening behaviours, which have been exploited previously in tissue engineering and drug delivery.[54,55] Liu *et al.*[46] synthesized an injectable hydrogel composed of MC and xanthan gum that disappeared from the injection site after 36 days of administration without any inflammatory response, indicating the biodegradability of the hydrogel. Elsewhere, a blend of MC/Pluronic F127 was used as an injectable hydrogel for the local delivery of docetaxel, showing that MC diminished from the injection site after three weeks.[48] In the case of *in vivo* biodegradability of κCA, it was stated that the κCA hydrogel does not form any toxic by-products once degraded and causes only minor inflammatory responses.[56] In another study, a blend of κCA and gellan gum has been used for ophthalmic topical drug delivery.[57] Accordingly, no changes or adverse effects on the corneal thickness were observed even after 3 months of administration of the hydrogel in rats. Overall, MC and κCA hydrogels have been proved to be biodegradable, and hence, they can be considered for tissue engineering and drug delivery.

The mechanical strength of the scaffold plays a key role in regulating the cell's fate in tissue engineering, which is mainly determined by the crosslinking density and nature of polymers.[58,59] In this way, the mechanical strength of the MC/κCA hydrogels subjected to compression force has been investigated, as shown in Fig. 2c. Accordingly, at a constant concentration of κCA, the compressive modulus of MC/κCA hydrogels go progressively upward upon increasing the concentration of MC, mainly due to the formation of more hydrophobic interaction of MC chains. Moreover, higher concentrations of κCA form stronger hydrogels in all studied formulations due to the more ionic interaction between K$^+$ and κCA chains, as reported in other works.[19] Overall, the mechanical properties of MC/κCA hydrogels are high enough to provide strong support to encapsulated cells.[60]

Fig. 2d provides the FTIR and XRD patterns of MC/κCA hydrogels and their components. Accordingly, the characteristic peak of MC at 2882 cm^{-1}, which was attributed to the C–H stretching vibration of methyl ether, does not change upon the introduction of κCA.[61] In addition, both MC and κCA components show broad peaks centered at 3438 cm^{-1} and 3356 cm^{-1} respectively, assigned to the OH stretching vibration. This peak appeared at 3401 cm^{-1} for the MC/κCA hydrogel, which is an average of its building components. In the case of XRD patterns, MC shows two characteristic diffraction peaks at $2\theta = 10.5°$ and

20.2°, which were related to the successful modification of cellulose and partial crystalline structure of MC, as illustrated elsewhere previously.[62] In addition, the XRD pattern of κCA presents broad peaks centered at $2\theta = 21.8°$, showing the semicrystalline nature of κCA. The prepared MC/κCA hydrogel displayed peaks at diffraction angles of $2\theta = 10.5°$ and 21.3°, closely similar to its building components. The FTIR and XRD spectra indicated that the physical blending of MC and κCA does not change the chemical composition and crystalline structure of the corresponding biopolymers.

The SEM micrographs of the κCA-1 and the MC-8/κCA-1 hydrogels are demonstrated in Fig. 2e. As shown, both hydrogels present an interconnected porous structure, which is critical for carrying nutrition in and waste out of the scaffold. The incorporation of 8 wt% MC caused the pore size decline significantly from 450 ± 45 μm for the pure κCA-1 hydrogel to 112 ± 34 μm. In fact, an increase in the polymer content causes the polymer network to be filled tightly, which is reflected in the pore size and swelling ratio.

3.2. Rheological characterization

3.2.1. Extrusion stage.
Rheological studies offer a powerful tool to understand the response of bioinks at different stages of 3D printing.[63] Generally, three steps are involved in the 3D printing process, namely, extrusion stage, recovery stage, and shape retention stage.[64] In the extrusion stage, applied pneumatic pressure should surpass minimum forces required for flow initiation of ink along nozzle, which is defined as yield stress.[64] The yield stress can be obtained from the crossover point of the G' and G'' curves in the shear stress sweep test, as shown in Fig. 3a. Of note, all oscillatory rheological experiments were performed in the linear viscoelastic region otherwise stated,
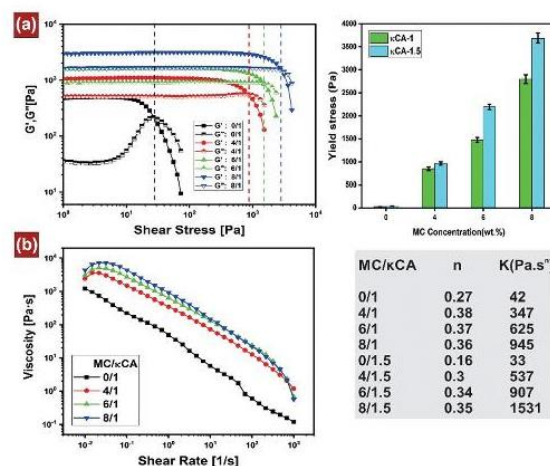

Fig. 3 Rheological characterization of MC/κCA hydrogels in the extrusion stage. (a) Monitoring the change in the G' and G'' value over shear stress sweep at 1 Hz. Yield stress defined as crossover point of G' and G'' curves. (b) Viscosity measurements ranging from 0.01 to 1000 s^{-1} shear rate. The power-law model was employed to quantify the shear-thinning behaviour of the studied hydrogel.

which were detected for all studied MC/κCA formulations (Fig. S1, ESI†). As viewed, the G' and G'' values are both stable at low shear stress and $G' > G''$ for all studied MC/κCA hydrogels, characterized by gel-like behaviour. Once shear stress exceeds the linear region, the G' and G'' curves started to fall and meet each other at the yield point, where gel-to-sol transition occurs. The yield stress is very low for pure κCA hydrogels (27 Pa for κCA-1 and 42 Pa for κCA-1.5), which surged three orders upon the addition of MC. This is because of the newly formed hydrogel bonds between polymer chains and lower free volume for the movement of water molecules. In addition, the crossover points of G' and G'' shift to higher shear stress upon increasing the concentration of MC, due to the more compact hydrophobic interaction of methoxy groups in MC chains. Furthermore, the increase in the κCA concentration from 1 to 1.5 wt% causes hydrogels to show yields at higher stress (Fig. S2, ESI†). Although the bioink with lower yield stress needs lower pressure to be extruded, it cannot sustain its structure once printed. This means that the printed construct is more stable and robust at higher concentrations of MC.

Once the ink started to flow, the cell-containing hydrogel passes along a very thin needle and experiences high shear stress, which adversely affects the cell viability. Loss of cell viability can be compensated by using a bigger needle, but this deteriorates the resolution of the printed construct.[7] The shear-thinning behaviour of hydrogels is advantageous for inks to save cells from the application of high shear stress. This feature causes the viscosity of bioink decline at high shear stress along the nozzle and saves cells from high stress. To examine the extent of shear-thinning behaviour of the prepared MC/κCA hydrogel, the variation in viscosity was measured over shear rate sweep (Fig. 3b). The viscosity of the MC/κCA hydrogel remains almost stable at low shear rates, which are related to the yield stress of the hydrogel, followed by a continuous drop with the increase in shear rate known as shear-thinning behaviour. This is related to the breakdown of hydrophobic interactions between methoxy groups along the MC backbone once shear stress is applied.[46] In addition, the flow curve of MC/κCA hydrogels shifted toward higher values once MC or κCA concentration increased as expected. The flow curve of MC/κCA with 1.5 wt% κCA is illustrated in Fig. S2 (ESI†). Compared to the MC/κCA hydrogel, pure κCA only shows shear-thinning behaviour without any plateau region, which implies very low yield stress as shown before. To address the shear-thinning behaviour of the bioink, the power-law model can be utilized as follows:

$$\eta = K\dot{\gamma}^{1-n} \qquad (3)$$

where η is the viscosity, $\dot{\gamma}$ is the shear rate, K is the consistency index, and n is the power-law index. For a Newtonian fluid, $n = 1$, while $n > 1$ and $n < 1$ imply shear-thickening and shear-thinning fluids, respectively. The K value also refers to the viscosity at a low shear rate, which contributes for the shape retention of the printed construct after printing.[65,66] Accordingly, power-law indexes are less than 1 for all cases, as indicative of the shear-thinning behaviour. The extent of shear-thinning behaviour
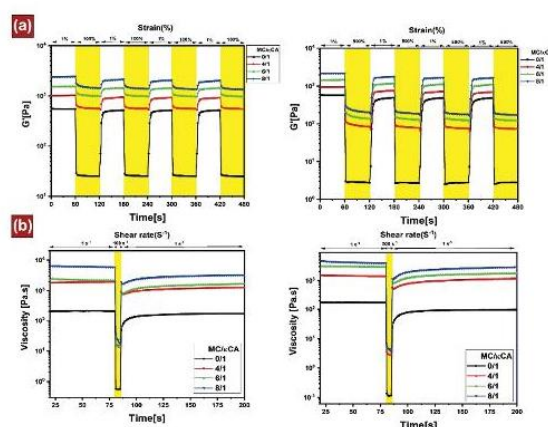

Fig. 4 Rheological characterization of MC/κCA hydrogels in the recovery stage. (a) Change in G' upon applying repetitive low (1%) and high strains (100% left panel, 500% right panel) and (b) variation of visosity over low (1 s^{-1}) and high shear rates (100 s^{-1} left panel, 500 s^{-1} right panel).

is getting more pronounced when the MC or κCA concentration increased, evident by lower n values.

3.2.2. Recovery stage. In the second stage, when bioink passes through the nozzle, it undergoes high strain and shear rate. Quick recovery of the bioink to the initial state could significantly determine the printing accuracy once it exits the nozzle.[64] Given this, for further rheological characterization of the bioink, the recoverability of MC/κCA was evaluated by applying repetitive low and high strain, as shown in Fig. 4a. Accordingly, for pure κCA hydrogel, the G' falls rapidly once it undergoes high strain and then recovers to the initial value immediately after eliminating the applied strain in a very short time (<5 s). This behaviour is observed with slight differences for all cycles. Moreover, when MC was mixed with κCA, the extent of recovery progressively decreased with the cycles because of the disruption of polymer–polymer interactions. While comparing 100% and 500% strain, it is observed that G' drop more and recover less at higher strain. It is interesting to note that the κCA concentration does not influence the extent of recovery and only controls the G' value (Fig. S3, ESI†). The recovery of viscosity was also traced at high and low shear rates to simulate the change in the value of viscosity before, during, and after printing (Fig. 4b). As can be seen, the viscosity of MC/κCA inks with different formulations quickly plummet some orders at the high shear rate and recover after removing stress. The drop in the viscosity protects cells from high shear as well as easy printing. Moreover, the viscosity of MC/κCA inks drops more in 500 s^{-1} compared to 100 s^{-1}, which is expected from the flow curve and recoverability in the oscillation mode. Overall, the MC/κCA ink displays high recoverability at high strain and shear rate, which enables it to return to its initial stage after extrusion.

3.2.3. Shape retention stage. In the third stage, the ink should possess sufficient mechanical strength to be capable of supporting its integrity after finishing the deposition on the platform. The higher value of complex modulus (G^*) and yield
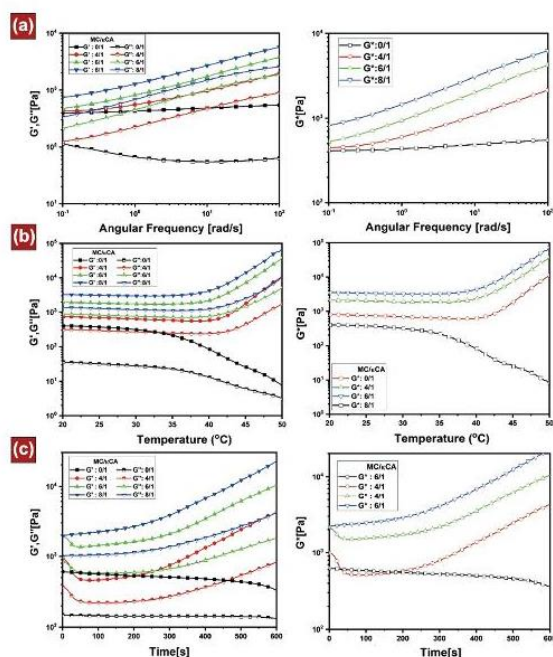
Fig. 5 Rheological characterization of MC/κCA hydrogels in the shape retention stage. Change in G', G'', and G^* over (a) frequency sweep from 0.1 Hz to 100 Hz, (b) temperature ramp from 20 °C to 50 °C, and (c) time sweep for 10 min.

stress are advantageous for shape retention behaviour of an ink.[64] Fig. 5a demonstrates the changes in the G', G'', and G^* values over frequency sweep at room temperature. Although the G' and G'' display frequency-dependent behaviours, the G' value is higher than the G'' value over the entire studied frequency, indicating the gel behaviour of the MC/κCA hydrogel with different formulations. In addition, increased amounts of MC cause the G^* values shift to higher values due to the higher hydrophobic interaction of MC chains. Previous studies on MC/xanthan gum,[46] MC/alginate,[13,14] and MC/hyaluronic acid[15] also reported that the addition of complementary components to MC hydrogels improves the storage modulus. Therefore, it is expected that MC-8/κCA-1 with a higher value of G^* shows higher shape retention after printing. This behaviour agrees well with the yield stress trend (Fig. 2a). In addition, shape retention behaviour of MC/κCA-1.5 hydrogels is shown in Fig. S4 (ESI†).

After finishing the printing process, the printed structure was kept at 37 °C. Therefore, it is crucial to comprehend the thermo-responsive behaviour of MC/κCA hydrogel. The change in the G', G'', and G^* values of MC/κCA inks was traced over the temperature in the range of 20–50 °C (Fig. 5b). As can be seen, the G', G'', and G^* values corresponding to pure κCA remain initially stable from 20 °C to 35 °C, following which it sharply drops due to the transformation of the aggregated helix to random coil structure.[19] In the case of MC/κCA hydrogels, G', G'', and G^* experienced a stable trend between 20 and 40 °C, followed by rising continuously to higher values due to the

thermo-responsive behaviour of MC.[46] It is interesting to note that an increase in the MC content causes the onset temperature, where G' and G'' start surging, shift to lower temperatures. In a further experiment, any change in the value of the G', G'', and G^* for different formulations of MC/κCA was examined at a constant temperature of 37 °C over time (Fig. 5c). Accordingly, the G', G'', and G^* values for pure κCA decline slowly, showing the weakening of the gel behaviour over time. However, MC/κCA inks experience a decline for a short period, followed by a progressive rise over time due to the formation of more hydrophobic interactions between methyl groups of MC components. Overall, the thermo-responsive behaviour of the MC/κCA ink causes G^* value grow over temperature and time ramp, which promise to prevent the collapse of printed structures after printing.

3.3. Conductivity characterization

The electrical conductivity of the MC/κCA/PEDOT:PSS hydrogels was measured *versus* different concentrations of PEDOT:PSS (Fig. 6a). As expected, the increase in the content of PEDOT:PSS complex within the system causes the electrical conductivity of the hydrogel to progressively increase. In addition, compared to pure MC, the incorporation of κCA improves the electrical conductivity from 250 ± 32 μs cm^{-1} for MC-8 to 1210 ± 120 μs cm^{-1} for MC-8/κCA-1 due to the ionic nature of κCA hydrogels. To further characterize the electrical properties of the prepared inks, the electrical impedance of MC-8/κCA-1 hydrogels with different contents of PEDOT:PSS was measured in the frequency range of 0.1 Hz–10^4 Hz (Fig. 6b). Accordingly, the electrical impedance of MC-8/κCA-1 hydrogels containing PEDOT:PSS is significantly lower than that of the hydrogel without PEDOT:PSS (≈ 12 kΩ) component. In addition, the electrical impedance of MC-8/κCA-1/PEDOT:PSS-0.1 obtained ≈ 6 kΩ at low frequency drop with an increase in the concentration of PEDOT:PSS conducting polymer complexes. Furthermore, MC-8/κCA-1/PEDOT:PSS-0.1 connected to a complete circuit
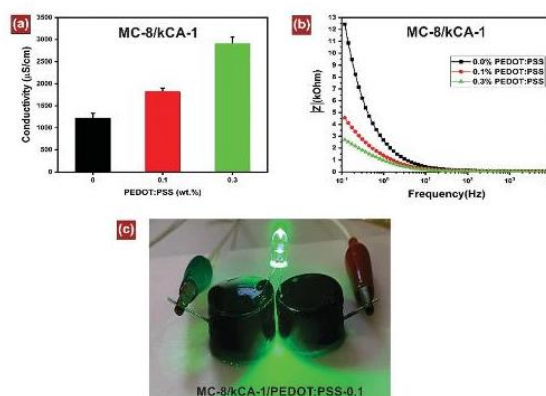

Fig. 6 Electrical characterization of MC-8/κCA-1/PEDOT:PSS hydrogel. (a) Conductivity of the ink with different contents of PEDOT:PSS conducting polymers, (b) electrochemical impedance spectroscopy spectra of the ink with different amounts of PEDOT:PSS, (c) illumination of LED connected to MC-8/κCA-1/PEDOT:PSS-0.1 hydrogel.

can illuminate an LED, showing the electrical conductivity of the hydrogel (Fig. 6c). The electrical impedance of the printed lattice structure and bulk hydrogels containing 0.1 wt% PEDOT:PSS was compared in Fig. S5 (ESI†). Accordingly, no significant differences were observed between printed and bulk hydrogels, indicating that the printing process did not disrupt the PEDOT:PSS conductive polymer structure. Overall, these results indicated that the electrical conductivity of the ink can be adjusted by tuning the PEDOT:PSS content.

3.4. Finding the optimized printing parameters

Printable ink displays smooth continuous filaments at the needle tip once extruded out.[65,67] Fig. 7a illustrates the extrudability of the MC/κCA ink with different formulations at a constant flow rate. Irregular wavy filaments have been formed at the needle tip once the pure κCA hydrogel extrudes through the nozzle. However, filaments were converted into smooth cylindrical figures after the addition of 6–8 wt% MC component due to
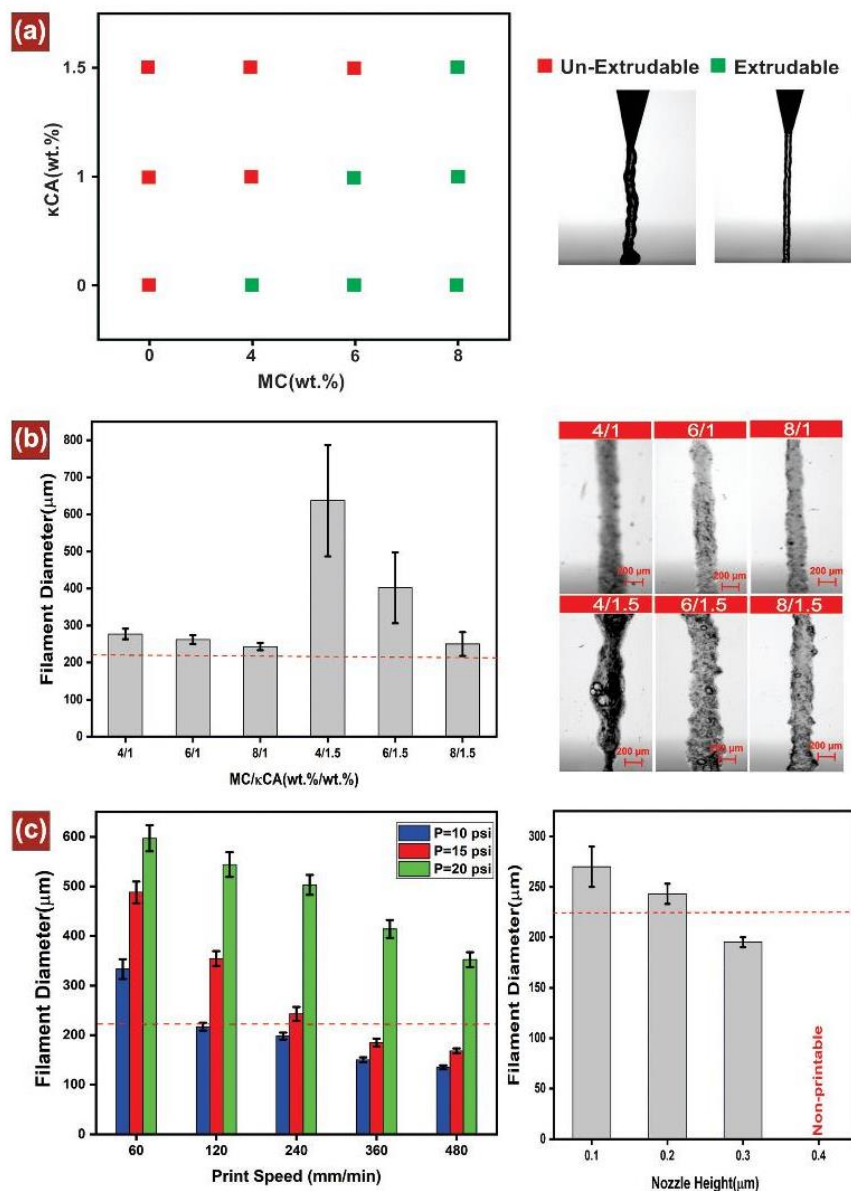

Fig. 7 (a) Window of extrudability of MC/κCA bioink, (b) strand diameter of MC/κCA bioink with different concentrations, and (c) effect of the nozzle height from the surface, print speed and pressure on the filament diameter.

Journal of Materials Chemistry B   Paper

the higher shape retention behaviour of MC/κCA bioinks. The fibre formation test suggests that non-extrudability of the κCA bioink can be eliminated upon the addition of MC to achieve a printed structure with high shape fidelity and accuracy. In a further characterization of printed filaments, the strand diameter of the MC/κCA ink with different formulations was measured after its deposition on the platform (Fig. 7b). Accordingly, the strand diameter differs largely with the nozzle diameter once the κCA concentration is 1.5 wt%, which is caused by the wavy fibre formation of κCA at the nozzle tip. However, the inconsistency between the printed strand and nozzle diameters is lower when the MC concentration reached up to 8 wt% due to the higher viscosity and yield stress value. However, at 1 wt% of κCA concentration, the dimension of the printed strand and nozzle diameters matched well, especially at higher concentrations of the MC component. In this way, we choose MC-8/κCA-1 formulation for further experiments.

In addition to the ink properties, printing parameters such as applied pressure, nozzle height, and print speed strongly determine the resolution of the printed structure. Given this, Fig. 7c compares the dimension of the printed strand and nozzle diameters at different print speeds (60, 120, 240, 360,

and 480 mm min^{-1}) and applied pressures (10, 15, and 20 psi) for MC-8/κCA-1 bioink. Expectedly, increased pressure causes the strand diameter to progressively increase, regardless of print speed because a higher pressure means more material comes out of the nozzle. However, the print speed has converse relations with the strand diameter. The best match for the MC-8/κCA-1 bioink is obtained when the pressure is 15 psi and print speed is 240 mm min^{-1}. For other formulations, the same way was followed to find the best operating parameter of the bioprinter. In the case of nozzle height, the nozzle tip should be adjusted to the optimal distance from the platform to get the closest strand diameter with respect to the nozzle diameter, as shown in Fig. 7c. It is observed that when the nozzle diameter was set at 0.4 mm, the bioink could not touch the platform easily and an inconsistent strand was obtained. However, when the nozzle height was 0.1 mm, the nozzle was too close to the platform and it delaminated the bottom layers, which caused it to spread on the surface. The best match between the strand and nozzle diameter was obtained when the distance from the platform was set at 0.2 mm. Overall, taking into consideration the rheological properties and the best match between the printed strand and nozzle diameters, MC-8/κCA-1 was selected

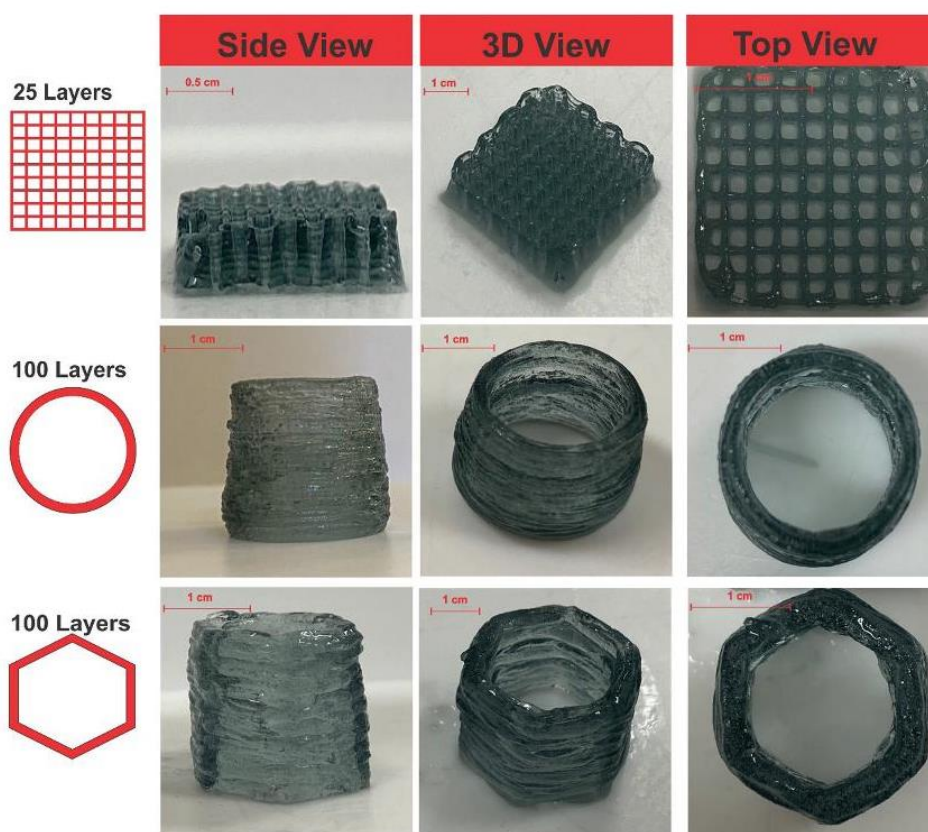

Fig. 8 Pictures of 3D-printed constructs including lattice, hexagonal and cylindrical objects from top, side and 3D views by MC-8/κCA-1/PEDOT:PSS-0.1 inks.

Paper   **Journal of Materials Chemistry B**

as the optimized formulation with optimized printing parameters of 15 psi pressure, 240 mm min^{-1} print speed, and 0.2 mm nozzle height.

Furthermore, it was found that incorporation of PEDOT:PSS within the MC/κCA hydrogel has negligible effects on the rheological properties and printing resolution (not shown here), which stand in contrast with the previous work.[43] In other words, PEDOT:PSS only serves to induce electrical conductivity to the ink, while MC/κCA provides the printability requirements. It might be because of the low concentration of conductive polymers.

3.5. The 3D printing technology of complex structures by MC/κCA/PEDOT:PSS inks

The 3D bioprinting technology aims to construct complex anatomical-size structures. However, most of the current inks

suffer from poor mechanical strength, which resulted in the collapse of 3D printed objects after a few layers of deposition. In this way, to demonstrate the ability of the ink in the fabrication of different constructs with high shape fidelity, MC-8/κCA-1/PEDOT:PSS-0.1 inks printed a variety of 3D designs. Fig. 8 presents the pictures of 3D printed constructs including lattice, cylindrical, and hexagonal constructs from different views. The thickness of each layer was set to be 0.2 mm. Herein, lattice structures with delicate meshes were printed without compromising the internal lattice porosity and showing the high resolution of MC-8/κCA-1/PEDOT:PSS-0.1 inks. In addition, the ink can print rounded edges with high shape retention, as evident by printing of cylindrical shape (2 cm height) even under the weight of 100 layers. High $G*$ and yield stress values of the MC-8/κCA-1 ink allow for the fabrication of multilayer constructs without collapsing. Furthermore, hexagonal shapes with obtuse
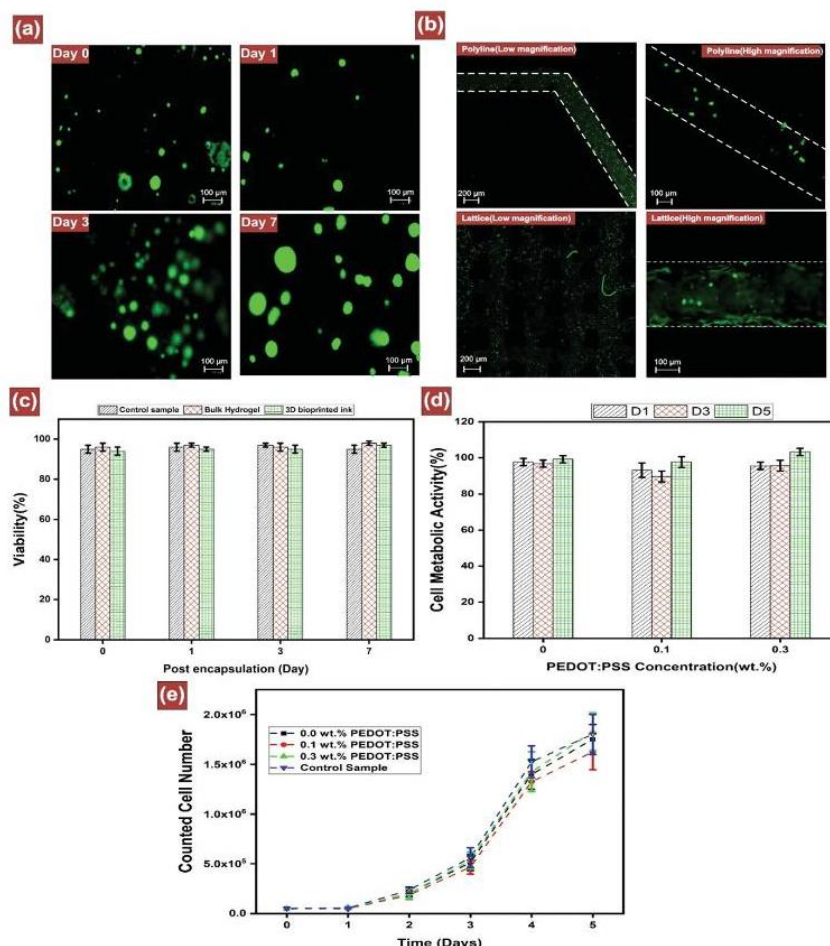
Fig. 9   Fluorescence images taken from the cell-laden MC-8/κCA-1/PEDOT:PSS-0.1 hydrogel stained with calcein-AM and ethidium homodimer-3 and cell survival over a week in (a) bulk hydrogel and (b) 3D bioprinted structures. (c) Percentage of cell viability over a week, which was calculated as the ratio of viable cells to sum of viable and dead cells. (d) MTT assay showing the metabolic activity of seeded cells on the hydrogel surface on day 1, 3, and 5. (e) Proliferation rate of the seeded HEK-293 cells on the hydrogel surface.

angles were printed to demonstrate the ability of the ink in patterning objects with angles. This printed hexagonal shape with 2 cm height and 100 layers reveals high shape retention and resolution of the ink. In contrast, the printing of cylindrical and hexagonal shapes by MC-8 inks resulted in structural collapse after a few layers of deposition due to the inadequate shape retention characteristics (Fig. S6, ESI†). Furthermore, the effect of swelling on the shape integrity and resolution of the 3D printed lattice was investigated (Fig. S7, ESI†). Accordingly, although the printed lattice remained stable and retained the shape integrity, the resolution of printed structure diminished after swelling. On the one hand, a higher swelling ratio is appropriate for tissue regeneration, on the other hand, a high swelling ratio leads to the loss of the resolution of printed structures. Therefore, a hydrogel with a low swelling ratio and high porosity is promising for the 3D bioprinting application.

These results indicated that MC-8/κCA-1/PEDOT:PSS-0.1 can print multi-layered constructs with high shape retention and resolution, whose computer-designed structures and printed structures nicely matched.

3.6. The 3D bioprinting technology and cell viability

Recent studies have revealed that incorporation of PEDOT:PSS conducting polymers at high concentrations (>0.1 wt%) causes cell viability decline.[40,41] Given this, here, we monitored the *in vitro* cytotoxicity of the MC-8/κCA-1/PEDOT:PSS-0.1 ink by a live/dead cell assay for a week. Fig. 9 presents the viability of encapsulated HEK-293 cells, as a model cell, within the MC-8/κCA-1/PEDOT:PSS-0.1 bulk hydrogel and 3D bioprinted structure after 1, 3 and 7 days of cell encapsulation, in which live and dead cells determined by two-colour fluorescence: live cells in green and dead cells in red. Cell-laden bioinks printed lattice and polyline structures with 27 G tapered plastic tips. Accordingly, MC-8/κCA-1/PEDOT:PSS-0.1 demonstrates high cell viability over a week ($>96\%$), similar to that of 2D control samples. The viabilities of encapsulated HEK-293 cells in bulk hydrogels and 3D bioprinted structures are almost similar, showing the protection of cells over extrusion due to the shear-thinning behaviour of the hydrogel (Fig. 9c). More importantly, the fluorescence intensity increased after a week, indicating the growth of cells in the matrix. The MTT assay was performed to further examine the biocompatibility of the hydrogel (Fig. 9d). Accordingly, the average metabolic activity of the seeded cells on the hydrogel remained stable at 1, 3, and 5 days with no significant differences between the prepared formulations, which proved the biocompatibility of the hydrogel. Furthermore, to examine the proliferation of seeded cells, hydrogels were transferred to a well plate followed by seeding of cells on the hydrogel surface at a density of 5×10^4 HEK-293 cells per well. Accordingly, cells' number grew over time similarly for all hydrogels without significant differences with the control sample (Fig. 9e). Overall, the encapsulated and seeded cells remained viable and kept growing similar to the control sample, indicating the biocompatibility of the prepared hydrogels.

4. Conclusion

In this work, we presented the development of a biocompatible ink to address two main challenges associated with the current 3D bioprinting technology: poor electrical conductivity and fabrication of multi-layered complex constructs. These challenges were fulfilled by the simple physical blending of highly thixotropic MC/κCA hydrogels with PEDOT:PSS conducting polymers. Rheological characteristics of the MC/κCA hydrogel were characterized in detail over the whole three stages of printing to find the optimized MC/κCA formulations. The shear-thinning behaviour of the MC/κCA hydrogel was approved by tracing the drop in the viscosity as it fell from ≈ 5000 Pa at a low shear rate of about 10 Pa at $100\ \mathrm{s}^{-1}$, which helps protect the loaded cells from high shear stress and death. Moreover, the recovery test indicates that the MC/κCA bioink could recover in a very short time after removing the shear stress, which assists the bioink to form stable filaments upon release from the nozzle. In addition, high complex viscosity and yield stress of the MC/κCA ink resulted in high shape fidelity and printing resolution. Exploiting the electrical conductivity of PEDOT:PSS enables us to impart conductivity to the ink. The optimized ratio of MC and κCA was found to be MC-8/κCA-1 according to the rheological properties and the best match between the dimensions of the printed strand and nozzle diameters. The feasibility of the MC/κCA/PEDOT:PSS ink for the fabrication of multi-layered structures was demonstrated by 3D printing of several structures with high shape retention and resolution. In addition, the encapsulated HEK-293 cells within the ink demonstrated high viability over a week ($>96\%$) in both bulk and 3D bioprinted structures. We envision that MC/κCA/PEDOT:PSS with tunable electrical conductivity is able to print 3D stable multilayered structures with high shape fidelity and resolution without the need for added complexity of support baths or UV radiation.

Conflicts of interest

There are no conflicts to declare.

Acknowledgements

References

1 H. N. Chia and B. M. Wu, *J. Biol. Eng.*, 2015, **9**, 4.
2 B. K. Gu, D. J. Choi, S. J. Park, M. S. Kim, C. M. Kang and C.-H. Kim, *Biomater. Res.*, 2016, **20**, 12.
3 K. Hölzl, S. Lin, L. Tytgat, S. Van Vlierberghe, L. Gu and A. Ovsianikov, *Biofabrication*, 2016, **8**, 032002.

4 C. C. Chang, E. D. Boland, S. K. Williams and J. B. Hoying, *J. Biomed. Mater. Res., Part B*, 2011, **98**, 160–170.

5 C. Mandrycky, Z. Wang, K. Kim and D.-H. Kim, *Biotechnol. Adv.*, 2016, **34**, 422–434.

6 J. H. Chung, S. Naficy, Z. Yue, R. Kapsa, A. Quigley, S. E. Moulton and G. G. Wallace, *Biomater. Sci.*, 2013, **1**, 763–773.

7 J. M. Lee and W. Y. Yeong, *Adv. Healthcare Mater.*, 2016, **5**, 2856–2865.

8 M. Guvendiren, H. D. Lu and J. A. Burdick, *Soft Matter*, 2012, **8**, 260–272.

9 S. Morozova, P. W. Schmidt, A. Metaxas, F. S. Bates, T. P. Lodge and C. S. Dutcher, *ACS Macro Lett.*, 2018, **7**, 347–352.

10 T. Ahlfeld, G. Cidonio, D. Kilian, S. Duin, A. Akkineni, J. Dawson, S. Yang, A. Lode, R. Oreffo and M. Gelinsky, *Biofabrication*, 2017, **9**, 034103.

11 N. Contessi, L. Altomare, A. Filipponi and S. Farè, *Mater. Lett.*, 2017, **207**, 157–160.

12 N. C. Negrini, L. Bonetti, L. Contili and S. Farè, *Bioprinting*, 2018, **10**, e00024.

13 K. Schütz, A. M. Placht, B. Paul, S. Brüggemeier, M. Gelinsky and A. Lode, *J. Tissue Eng. Regener. Med.*, 2017, **11**, 1574–1587.

14 H. Li, Y. J. Tan, K. F. Leong and L. Li, *ACS Appl. Mater. Interfaces*, 2017, **9**, 20086–20097.

15 N. Law, B. Doney, H. Glover, Y. Qin, Z. M. Aman, T. B. Sercombe, L. J. Liew, R. J. Dilley and B. J. Doyle, *J. Mech. Behav. Biomed. Mater.*, 2018, **77**, 389–399.

16 S. Liu and L. Li, *ACS Appl. Mater. Interfaces*, 2016, **8**, 29749–29758.

17 Y. Yuguchi, H. Urakawa and K. Kajiwara, *Food Hydrocolloids*, 2003, **17**, 481–485.

18 S. Liu, W. L. Chan and L. Li, *Macromolecules*, 2015, **48**, 7649–7657.

19 S. M. Mihaila, A. K. Gaharwar, R. L. Reis, A. P. Marques, M. E. Gomes and A. Khademhosseini, *Adv. Healthcare Mater.*, 2013, **2**, 895–907.

20 S. Liu, S. Huang and L. Li, *J. Rheol.*, 2016, **60**, 203–214.

21 S. A. Wilson, L. M. Cross, C. W. Peak and A. K. Gaharwar, *ACS Appl. Mater. Interfaces*, 2017, **9**, 43449–43458.

22 D. Chimene, C. W. Peak, J. L. Gentry, J. K. Carrow, L. M. Cross, E. Mondragon, G. B. Cardoso, R. Kaunas and A. K. Gaharwar, *ACS Appl. Mater. Interfaces*, 2018, **10**, 9957–9968.

23 M. Izadifar, D. Chapman, P. Babyn, X. Chen and M. E. Kelly, *Tissue Eng., Part C*, 2018, **24**, 74–88.

24 S. H. Ku, S. H. Lee and C. B. Park, *Biomaterials*, 2012, **33**, 6098–6104.

25 A. S. Rowlands and J. J. Cooper-White, *Biomaterials*, 2008, **29**, 4510–4520.

26 W. Zhu, T. Ye, S.-J. Lee, H. Cui, S. Miao, X. Zhou, D. Shuai and L. G. Zhang, *Nanomedicine*, 2018, **14**, 2485–2494.

27 K. Zhu, S. R. Shin, T. van Kempen, Y. C. Li, V. Ponraj, A. Nasajpour, S. Mandla, N. Hu, X. Liu and J. Leijten, *Adv. Funct. Mater.*, 2017, **27**, 1605352.

28 K. P. Steckiewicz, E. Barcinska, A. Malankowska, A. Zauszkiewicz-Pawlak, G. Nowaczyk, A. Zaleska-Medynska and I. Inkielewicz-Stepniak, *J. Mater. Sci.: Mater. Med.*, 2019, **30**, 22.

29 S. J. Soenen, B. Manshian, J. M. Montenegro, F. Amin, B. Meermann, T. Thiron, M. Cornelissen, F. Vanhaecke, S. Doak and W. J. Parak, *ACS Nano*, 2012, **6**, 5767–5783.

30 D. Kumar, I. Mutreja, K. Chitcholtan and P. Sykes, *Nanotechnology*, 2017, **28**, 475101.

31 X. Li, Y. Fan and F. Watari, *Biomed. Mater.*, 2010, **5**, 022001.

32 S.-J. Lee, W. Zhu, M. Nowicki, G. Lee, D. N. Heo, J. Kim, Y. Y. Zuo and L. G. Zhang, *J. Neural Eng.*, 2018, **15**, 016018.

33 M. Hussain, M. Kabir and A. Sood, *Curr. Sci.*, 2009, **96**, 664–673.

34 M. J. Allen, V. C. Tung and R. B. Kaner, *Chem. Rev.*, 2010, **110**, 132–145.

35 T. P. D. Shareena, D. McShan, A. K. Dasmahapatra and P. B. Tchounwou, *Nano-Micro Lett.*, 2018, **10**, 53.

36 C.-T. Huang, L. K. Shrestha, K. Ariga and S.-h. Hsu, *J. Mater. Chem. B*, 2017, **5**, 8854–8864.

37 R. Zhou and H. Gao, *Wiley Interdiscip. Rev.: Nanomed. Nanobiotechnol.*, 2014, **6**, 452–474.

38 H. Liu, Q. Li, S. Zhang, R. Yin, X. Liu, Y. He, K. Dai, C. Shan, J. Guo and C. Liu, *J. Mater. Chem. C*, 2018, **6**, 12121–12141.

39 T. Nezakati, A. Seifalian, A. Tan and A. M. Seifalian, *Chem. Rev.*, 2018, **118**, 6766–6843.

40 A. R. Spencer, A. Primbetova, A. N. Koppes, R. A. Koppes, H. Fenniri and N. Annabi, *ACS Biomater. Sci. Eng.*, 2018, **4**, 1558–1567.

41 R. Balint, N. J. Cassidy and S. H. Cartmell, *Acta Biomater.*, 2014, **10**, 2341–2353.

42 L. Yan, X. Gao, J. P. Thomas, J. Ngai, H. Altounian, K. T. Leung, Y. Meng and Y. Li, *Sustainable Energy Fuels*, 2018, **2**, 1574–1581.

43 A. R. Spencer, E. Shirzaei Sani, J. R. Soucy, C. C. Corbet, A. Primbetova, R. A. Koppes and N. Annabi, *ACS Appl. Mater. Interfaces*, 2019, **11**, 30518–30533.

44 I. Noshadi, S. Hong, K. E. Sullivan, E. S. Sani, R. Portillo-Lara, A. Tamayol, S. R. Shin, A. E. Gao, W. L. Stoppel and L. D. Black III, *Biomater. Sci.*, 2017, **5**, 2093–2105.

45 N. E. Fedorovich, M. H. Oudshoorn, D. van Geemen, W. E. Hennink, J. Alblas and W. J. Dhert, *Biomaterials*, 2009, **30**, 344–353.

46 Z. Liu and P. Yao, *Carbohydr. Polym.*, 2015, **132**, 490–498.

47 Y. Zhang, C. Gao, X. Li, C. Xu, Y. Zhang, Z. Sun, Y. Liu and J. Gao, *Carbohydr. Polym.*, 2014, **101**, 171–178.

48 J. K. Kim, Y.-W. Won, K. S. Lim and Y.-H. Kim, *Pharm. Res.*, 2012, **29**, 525–534.

49 O. Okay, *Hydrogel sensors and actuators*, Springer, 2009, pp. 1–14.

50 J. Zhu and R. E. Marchant, *Expert Rev. Med. Devices*, 2011, **8**, 607–626.

51 C. D. Spicer, *Polym. Chem.*, 2020, **11**, 184–219.

52 M. C. Tate, D. A. Shear, S. W. Hoffman, D. G. Stein and M. C. LaPlaca, *Biomaterials*, 2001, **22**, 1113–1123.

53 D. Gupta, C. H. Tator and M. S. Shoichet, *Biomaterials*, 2006, **27**, 2370–2379.

54 T. Ahlfeld, V. Guduric, S. Duin, A. Akkineni, K. Schütz, D. Kilian, J. Emmermacher, N. Cubo-Mateo, S. Dani and M. v. Witzleben, *Biomater. Sci.*, 2020, **8**, 2102–2110.

55 J. Liu, X. Zhan, J. Wan, Y. Wang and C. Wang, *Carbohydr. Polym.*, 2015, **121**, 27–36.

Journal of Materials Chemistry B

Paper

56 E. G. Popa, P. P. Carvalho, A. F. Dias, T. C. Santos, V. E. Santo, A. P. Marques, C. A. Viegas, I. R. Dias, M. E. Gomes and R. L. Reis, *J. Biomed. Mater. Res., Part A*, 2014, **102**, 4087–4097.

57 A. Fernández-Ferreiro, M. G. Barcia, M. Gil-Martínez, A. Vieites-Prado, I. Lema, B. Argibay, J. B. Méndez, M. J. Lamas and F. J. Otero-Espinar, *Eur. J. Pharm. Biopharm.*, 2015, **94**, 342–351.

58 J. Shi, M. M. Xing and W. Zhong, *Membranes*, 2012, **2**, 70–90.

59 B. Geiger, J. P. Spatz and A. D. Bershadsky, *Nat. Rev. Mol. Cell Biol.*, 2009, **10**, 21.

60 G. Camci-Unal, D. Cuttica, N. Annabi, D. Demarchi and A. Khademhosseini, *Biomacromolecules*, 2013, **14**, 1085–1092.

61 R. L. Oliveira, J. G. Vieira, H. S. Barud, R. Assunção, G. R. Filho, S. J. Ribeiro and Y. Messadeqq, *J. Braz. Chem. Soc.*, 2015, **26**, 1861–1870.

62 G. R. Filho, R. M. N. de Assunção, J. G. Vieira, C. d. S. Meireles, D. A. Cerqueira, H. da Silva Barud, S. J. L. Ribeiro and Y. Messaddeq, *Polym. Degrad. Stab.*, 2007, **92**, 205–210.

63 A. L. Rutz, K. E. Hyland, A. E. Jakus, W. R. Burghardt and R. N. Shah, *Adv. Mater.*, 2015, **27**, 1607–1614.

64 Z. Liu, B. Bhandari, S. Prakash, S. Mantihal and M. Zhang, *Food Hydrocolloids*, 2019, **87**, 413–424.

65 J. Malda, J. Visser, F. P. Melchels, T. Jüngst, W. E. Hennink, W. J. Dhert, J. Groll and D. W. Hutmacher, *Adv. Mater.*, 2013, **25**, 5011–5028.

66 J. Guo, R. Zhang, L. Zhang and X. Cao, *ACS Macro Lett.*, 2018, 7, 442–446.

67 N. Paxton, W. Smolan, T. Böck, F. Melchels, J. Groll and T. Jungst, *Biofabrication*, 2017, **9**, 044107.

Supporting information:

3D Printing of Cell-Laden Electroconductive Bioink for Tissue Engineering Application

Hadi Rastin, Bingyang Zhang, Jingxiu Bi, Kamrul Hasan, Tran Tung, Dusan Losic[*]

School of Chemical Engineering & Advanced Materials, The University of Adelaide, Adelaide, SA 5005, Australia

Corresponding author: Prof Dusan Losic
E-mail address: dusan.losic@adelaide.edu.au

1

1. Formulation of the bioink

Table S1 summarized the prepared formulation of MC/κCA/PEDOT:PSS inks in total 4 ml solution.

Table S1: Formulation of prepared MC/κCA/PEDOT:PSS inks in total 4 ml solution

Sample code	MC(mg)	κCA(mg)	PEDOT:PSS(μl)
MC-4/κCA-1	160	40	0
MC-6/κCA-1	240	40	0
MC-8/κCA-1	320	40	0
MC-4/κCA-1.5	160	60	0
MC-6/κCA-1.5	240	60	0
MC-8/κCA-1.5	320	60	0
MC-8/κCA-1/PEDOT:PSS-0.1	320	60	307
MC-8/κCA-1/PEDOT:PSS-0.3	320	60	923

2. Linear viscoelastic region of MC/κCA hydrogel

Figure S1 presents the evolution of the G' value over frequency range 0.01-100% to determine the linear viscoelastic regions. As seen, the G' value remain unchanged up to 1% strain followed by continuous fall. Accordingly, all oscillatory rheological experiments were conducted in 1 % stain.
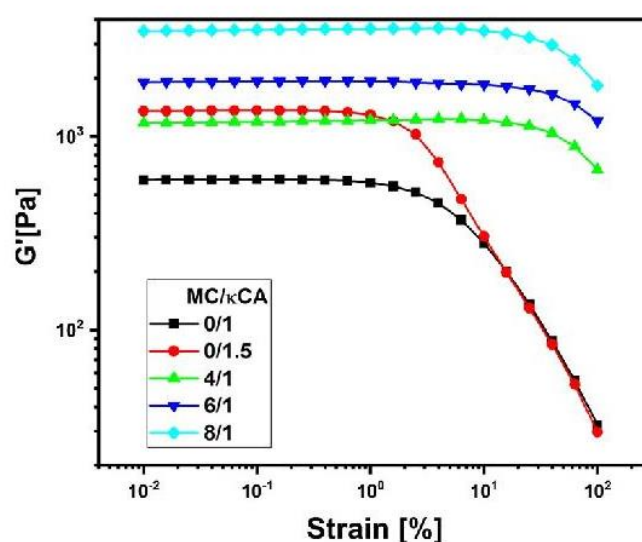
Figure S1: Change in the G' value over strain sweep from 0.01 % to 100 %

3.   Rheological measurements of MC/κCA-1.5 in extrusion stage

Figure S2 provide the evolution of the G' and G'' over shear stress sweep and flow curve of MC/κCA with 1.5 wt.% κCA component. As seen, an increase in the MC concentration cause yield stress shift toward higher values. In addition, flow curves jump to higher values upon increase in the MC content.
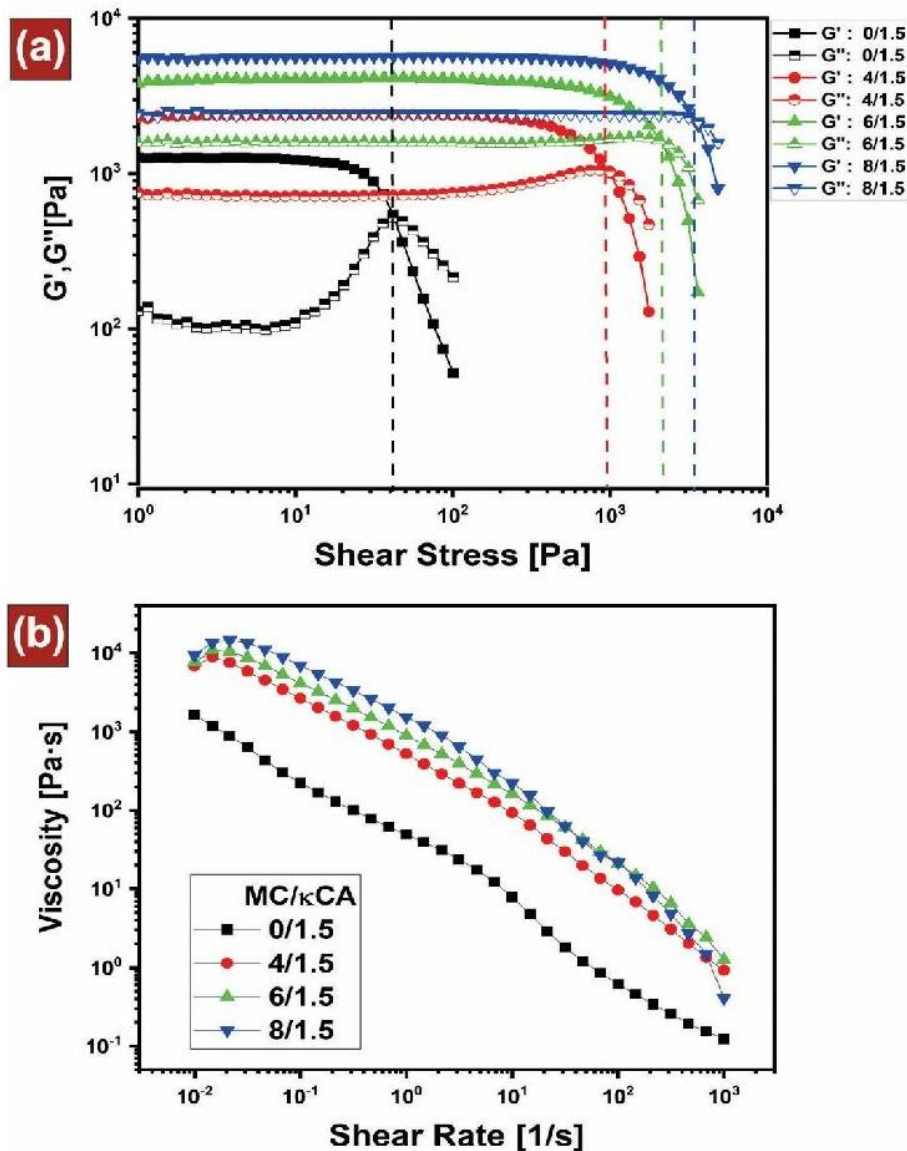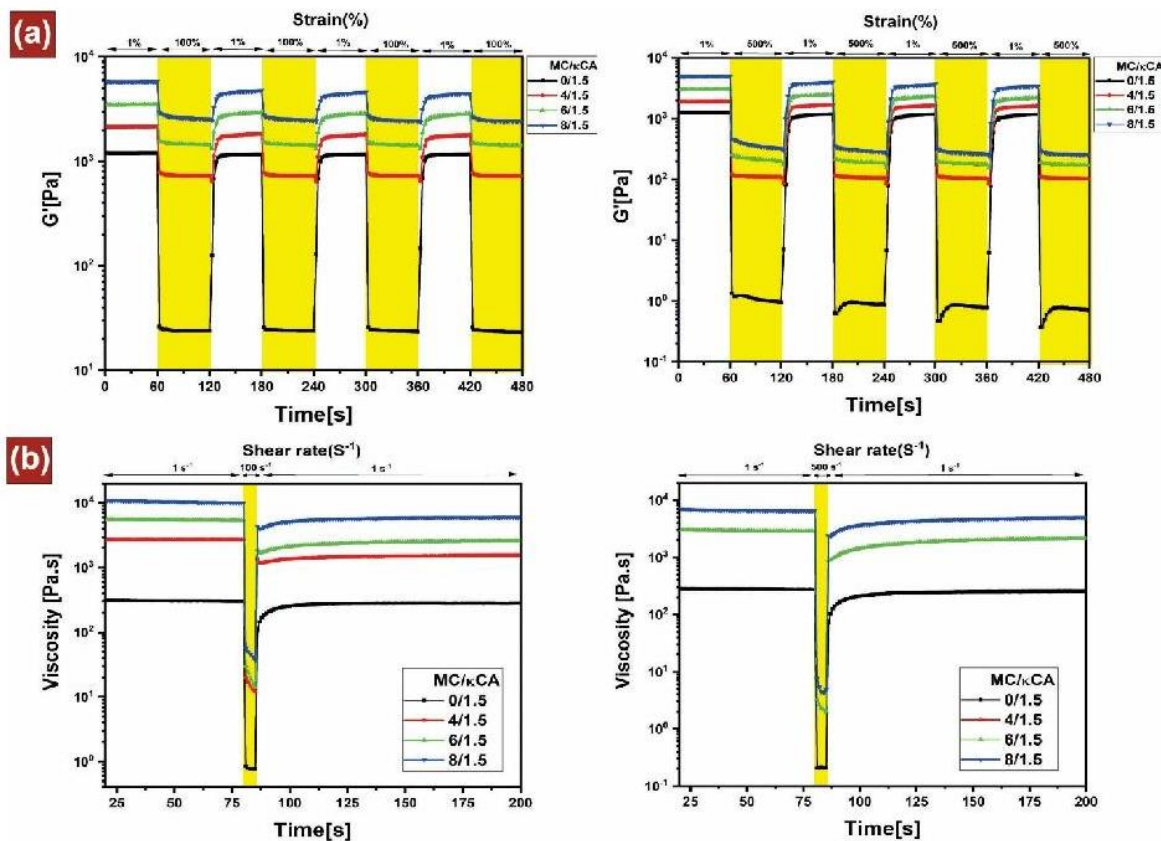

Figure S2. Rheological characterization of MC/κCA with 1.5 wt.% κCA in extrusion stage.

(a) yield stress determination (b) flow curve

3

4. Rheological measurements of MC/κCA-1.5 in recovery stage

Figure S3 provides the recoverability of MC/κCA hydrogel with 1.5 wt.% κCA component by applying alternating low and high strain and shear rate. As seen, almost full recovery occurs for all prepared MC/κCA-1.5 hydrogels after removing of high strain (**Figure S3 a**). In addition, viscosity of MC/κCA-1.5 hydrogels declined significantly immediately after application of high shear rate and then recovered in a short time (**Figure S3 b**).

Figure S3. Rheological characterization of MC/κCA with 1.5 wt.% κCA in recovery stage. (a) change of G' upon applying repetetive low (1%) and high strains (100% left panel, 500 % right panel) and (b) Variation of visosity over low (1 s^{-1}) and high shear rate (100 s^{-1} left panel, 500 s^{-1} right panel)

5. Rheological measurements of MC/κCA-1.5 in shape retention stage

4
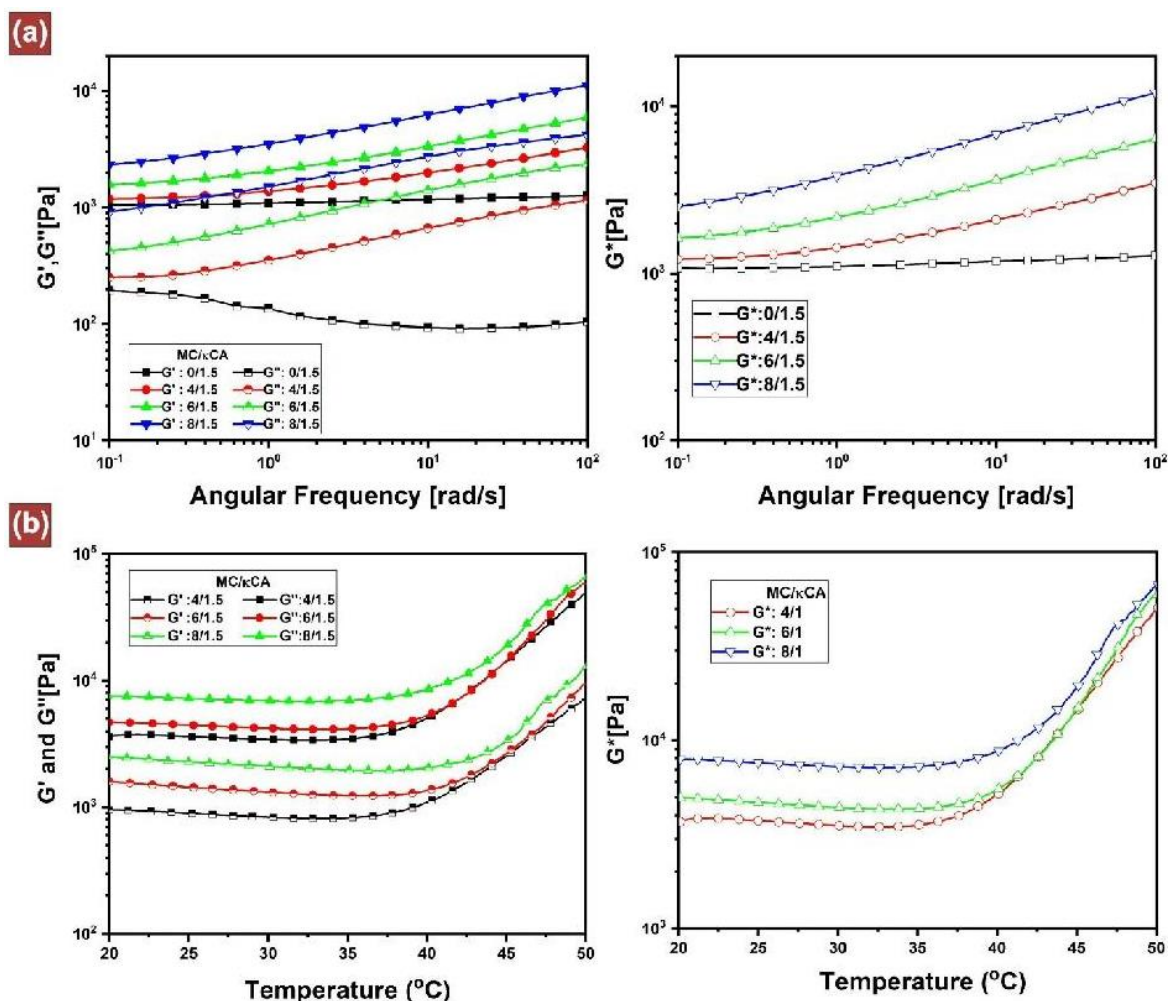
Figure S4. Rheological characterization of MC/κCA with 1.5 wt.% κCA in shape retention stage. Change of G',G'', and G* over (a) frequency sweep from 0.1 Hz to 100 Hz , and (b) tempeartuire ramp from 20 °C to 50 °C,

6. Electrical conductivity of the printed and bulk hydrogel

5
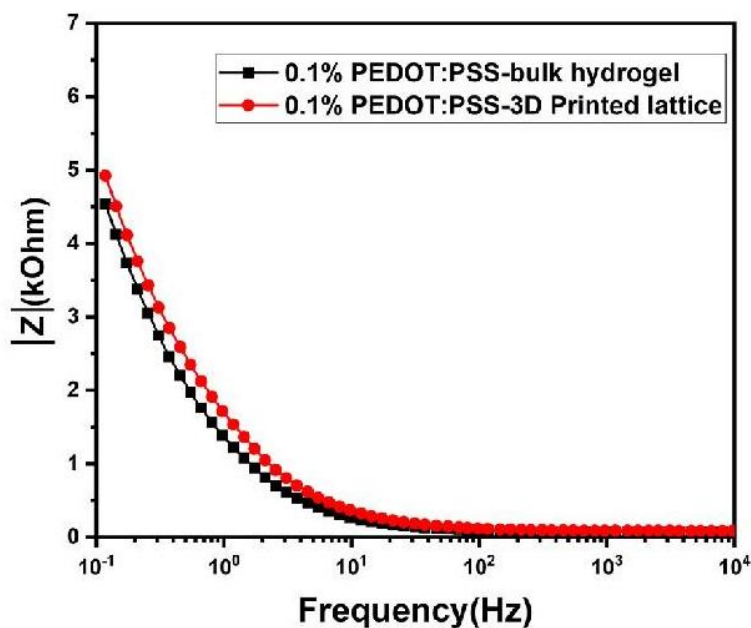
Figure S5: Electrical conductivity of the printed and bulk hydrogel containing 0.1 wt.% PEDOT:PSS conductive polymer

7. Collapse of 3D printed structurs by MC-8 hydrogel

Figure S6 presnts the hexagonal and circular shapes printed by MC-8 hysfogel. As seen, these strustures collapsed after few layer of deposition due to the low shape-retention behaviour.
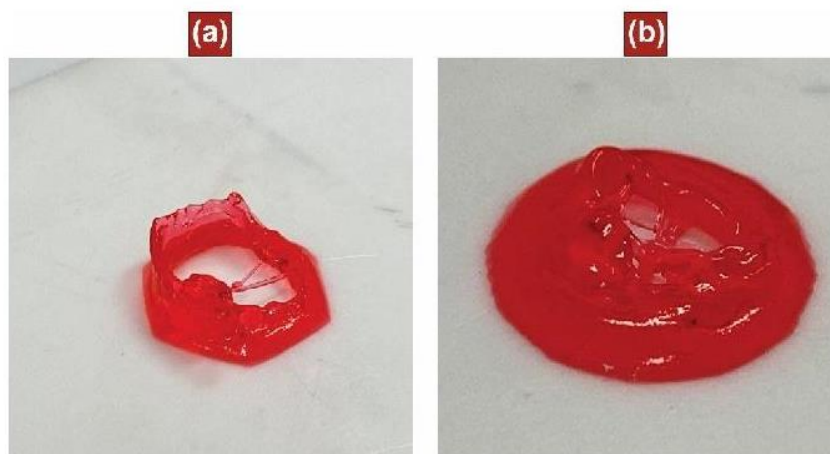
Figure S6. Pictures of 3D printed constructs with MC-8, which collapsed after few layers of deposition. (a) Hexagonal shape, (b) circular shape

6

8. Swelling of the 3D printed lattice construct
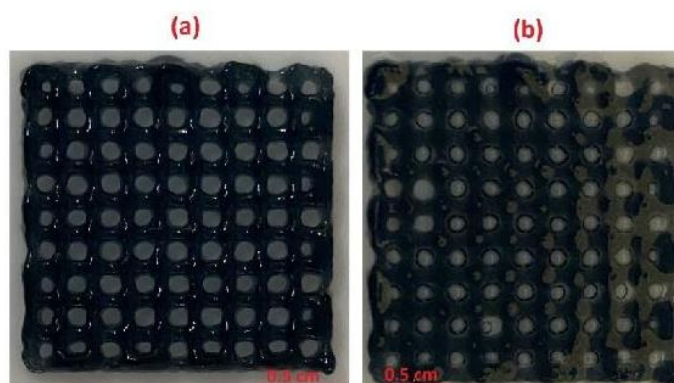
Figure S7: Pictures of 3D printed lattice construct by MC-8/κCA-1/PEDOT:PSS-0.1 ink (a) before and (b) after swelling

7

Chapter 6

Development of an antibacterial bioink

I n this chapter, a cell-laden antibacterial bioink based on Methylcellulose/Alginate (MC/Alg) hydrogel was developed to address the challenges associated with a bacterial infection in skin tissue engineering. This chapter first characterized the bioink in terms of printability, followed by the antibacterial performance of the bioink. The results have demonstrated the potent antibacterial activity toward both Gram-positive (Staphylococcus aureus) and Gram-negative (Pseudomonas aeruginosa) bacteria with a bactericidal rate of 99.99%. Next, the biocompatibility of gallium- and calcium-crosslinked hydrogel were compared, showing no significant differences between these two crosslinker in terms of cell viability and metabolic activity of fibroblast cells. These results suggests that gallium-crosslinked bioink supports encapsulated fibroblast cellular functions while eliminating the bacterial infection risk simultaneously.

This chapter has been published as

" Rastin H, Ramezanpour M, Hassan K, Mazinani A, Tung TT, Vreugde S, et al. 3D Bioprinting of a Cell-laden Antibacterial Polysaccharide Hydrogel Composite. Carbohydrate Polymers. 2021:117989."

Statement of Authorship

Title of Paper	3D bioprinting of a cell-laden antibacterial polysaccharide hydrogel composite
Publication Status	☑ Published ☐ Accepted for Publication ☐ Submitted for Publication ☐ Unpublished and Unsubmitted work written in manuscript style
Publication Details	Rastin H, Ramezanpour M, Hassan K, Mazinani A, Tung TT, Vreugde S, Losic D. 3D Bioprinting of a Cell-laden Antibacterial Polysaccharide Hydrogel Composite. Carbohydrate Polymers. 2021:117989.

Principal Author

Name of Principal Author (Candidate)	Hadi Rastin
Contribution to the Paper	Conceptualization, Investigation, Methodology, data processing, Original Draft.
Overall percentage (%)	70%
Certification:	This paper reports on original research I conducted during the period of my Higher Degree by Research candidature and is not subject to any obligations or contractual agreements with a third party that would constrain its inclusion in this thesis. I am the primary author of this paper.
Signature	Date 7/04/2021

Co-Author Contributions

By signing the Statement of Authorship, each author certifies that:

i. the candidate's stated contribution to the publication is accurate (as detailed above);

ii. permission is granted for the candidate in include the publication in the thesis; and

iii. the sum of all co-author contributions is equal to 100% less the candidate's stated contribution.

Name of Co-Author	Prof. Dusan Losic
Contribution to the Paper	Conceptualization, Resources, Funding Acquisition, Re-view&Editing, Supervision, submission
Signature	Date 15/04/21

Name of Co-Author	Dr. Tran Thanh Tung
Contribution to the Paper	C-supervision, Review & Editing.
Signature	Date 19/4/2021

Please cut and paste additional co-author panels here as required.

Name of Co-Author	Sarah Vreugde		
Contribution to the Paper	Resouces, Review&Editing.		
Signature		Date	15/04/2021

Name of Co-Author	Mahnaz Ramezanpour		
Contribution to the Paper	selected investigation, Methodology, Review & Editing.		
Signature		Date	15/04/2021

Name of Co-Author	Kamrul Hassan		
Contribution to the Paper	selected investigation, Methodology, Review & Editing.		
Signature		Date	16.04.2021

Name of Co-Author	Arash Mazinani		
Contribution to the Paper	selected investigation, Methodology, Review & Editing.		
Signature		Date	15.04.2021

3D bioprinting of a cell-laden antibacterial polysaccharide hydrogel composite

Hadi Rastin [a,b], Mahnaz Ramezanpour [c], Kamrul Hassan [a,b], Arash Mazinani [a,b], Tran Thanh Tung [a,b], Sarah Vreugde [c], Dusan Losic [a,b,*]

[a] School of Chemical Engineering and Advanced Materials, The University of Adelaide, South Australia, 5005, Australia
[b] ARC Research Hub for Graphene Enabled Industry Transformation, The University of Adelaide, South Australia, 5005, Australia
[c] Department of Surgery-Otolaryngology Head and Neck Surgery, The University of Adelaide, Woodville South, Australia

ARTICLE INFO

ABSTRACT

Bioink with inherent antibacterial activity is of particular interest for tissue engineering application due to the growing number of bacterial infections associated with impaired wound healing or bone implants. However, the development of cell-laden bioink with potent antibacterial activity while supporting tissue regeneration proved to be challenging. Here, we introduced a cell-laden antibacterial bioink based on Methylcellulose/Alginate (MC/Alg) hydrogel for skin tissue engineering *via* elimination of the risks associated with a bacterial infection. The key feature of the bioink is the use of gallium (Ga^{+3}) in the design of bioink formulation with dual functions. First, Ga^{+3} stabilized the hydrogel bioink by the formation of ionic crosslinking with Alg chains. Second, the gallium-crosslinked bioink exhibited potent antibacterial activity toward both Gram-positive (*Staphylococcus aureus*) and Gram-negative (*Pseudomonas aeruginosa*) bacteria with a bactericidal rate of 99.99 %. In addition, it was found that the developed bioink supported encapsulated fibroblast cellular functions.

1. Introduction

Skin is the largest human tissue in the body that functions as the outermost protective layer toward external threats (Jeong, Park, & Lee, 2017; Talikowska, Fu, & Lisak, 2019). However, the skin is susceptible to damage from surgery, accidents, and burns that may fail to heal by itself and need skin tissue substitute (Yan et al., 2018). To regenerate the skin tissue after injury and to promote the wound-healing process, autografts are shaved from the own-patients donor sites and then put on the wound site (Carter & Holmes, 2016; Vig et al., 2017). However, this method is limited for large or severe wounds due to the limited availability of autografts (Andreassi, Bilenchi, Biagioli, & D'Aniello, 2005; Loss, Wedler, Künzi, Meuli-Simmen, & Meyer, 2000). In addition, the use of allografts is associated with the risk of immune rejection. In response to these limitations, tissue-engineered skin substitutes offer a promising alternative in substituting donor skin grafts (Hu & Xu, 2020; Yu et al., 2019). Various conventional fabrication methods (*e.g.*, manual dispensing, electrospinning, freeze-drying, and porogen leaching) have been developed for the regeneration of skin tissue. However, these methods generally suffer from serious limitations such as poor control

over the fabrication of complex three-dimensional (3D) structures and the lack of ability to construct 3D structures using multiple cell types (Castilho et al., 2020; Zhao et al., 2018). Among a variety of biofabrication methods, special attention has been paid to 3D bioprinting technologies that emerged as an evolutionary approach in straightforward patterning functional 3D tissue-like scaffolds for skin tissue engineering (Cubo, Garcia, del Cañizo, Velasco, & Jorcano, 2016; Murphy & Atala, 2014; Zennifer, Senthilvelan, Sethuraman, & Sundaramurthi, 2020). 3D bioprinting technology allows the deposition of various cells or biomaterials at the desired location to mimic the native skin tissue microenvironment (Askari et al., 2021; Lee, Hong, Kim, & Kim, 2020; Shen et al., 2020). Hydrogels are highlighted as the mainstream materials in the design of bioinks, especially for skin tissue engineering due to their ability to closely mimic the extracellular matrix, high water uptake capacity, flexible structure, desirable biocompatibility, and biodegradability (Donderwinkel, van Hest, & Cameron, 2017; Mancha Sánchez et al., 2020; Unagolla & Jayasuriya, 2020).

Despite significant progress of tissue-engineered scaffold with potential skin tissue regeneration capability, the risk of bacterial infection at the lesion site remains a life-threatening challenge (Ahmed, Zhai, &

Gao, 2019; Johnson & García, 2015; Sun et al., 2020). The development of bioinks with potent antimicrobial activity, while serving as a physical scaffold for improving cellular functions, is highly valuable to prevent the infections associated with impaired wound healing or bone implants (Afghah et al., 2020; Melo et al., 2020; Ramesh, Kovelakuntla, Meyer, & Rivero, 2020; Zhang et al., 2017). However, current bioinks that are composed of hydrogels generally exhibit poor antibacterial activity because the highly hydrated environment provided by hydrogels also facilitates microbial infection (Muthukrishnan, 2021; Veiga & Schneider, 2013; Zhong, Xiao, Seidi, & Jin, 2020). Given this, a variety of antibacterial agents have been introduced to render antibacterial activity to the hydrogels (Giano et al., 2014). Currently, the use of antibiotics (*e.g.*, penicillin, vancomycin, and gentamicin) is the standard in bacterial infection management. However, extensive misuse and prescription of antibiotics have led to the emergence of antibiotic-resistant strains of pathogenic bacteria, which impose severe clinical threats. In addition, antibiotic treatments exhibit narrow-spectrum bactericidal efficacy, high cytotoxicity, and slow wound healing (Veiga & Schneider, 2013; Zhong et al., 2020). Thus, there is a special focus on suitable alternatives for conventional antibiotics (Cao et al., 2021; Mohandas, Deepthi, Biswas, & Jayakumar, 2018; Prasher et al., 2020).

In response to these demands, several strategies have been employed by researchers (Gutierrez et al., 2019; Melo et al., 2020; Wu & Hong, 2019; Zhang et al., 2017). In an interesting work, Wu & Hong (2019) synthesized an antibacterial wound dressing by the inclusion of silver nanoparticles (AgNPs) in the polyacrylamide (PAM)/hydroxypropyl methylcellulose (HPMC) matrix. AgNPs play dual functions in the prepared hydrogel; First, AgNPs impart potent antibacterial activity toward both Gram-positive and Gram-negative bacteria to the hydrogel, second, the chemical interaction between AgNPs and ethylene groups of N, N′-methylenebisacrylamide (MBAM) allows the crosslinking of PAM. This resulted in the slow release of AgNPs from the hydrogel structure to attain long-term antibacterial activity. To attain a porous dressing structure, poly lactic acid (PLA) template was first printed and then hydrogel precursors cast in the porous PLA templates. Once the AgNP-PAM/HPMC hydrogel crosslinking was finished, the PLA template was washed by soaking it into dichloromethane. In another study (Gutierrez et al., 2019), 3D printed alginate/bacterial-cellulose hydrogels were crosslinked with copper ions, followed by in-situ synthesizing of copper nanoparticles. To crosslink the hydrogel, two distinct methods were applied; (i) crosslinking with calcium ions and then ion exchange with copper ions (method A) and (ii) solely crosslinking with copper ions (method B). It was found that the hydrogels crosslinked with method A were more stable than method B. In addition, after in-situ synthesizing of copper nanoparticles, the 3D printed hydrogels induced higher antibacterial activity against *Escherichia coli* and *Staphylococcus aureus* strains. Elsewhere, 3D printed β-tricalcium phosphate (β-TCP) scaffolds was coated with Ag/graphene oxide (GO) particles to endow the scaffold with antibacterial activity (Zhang et al., 2017). It was demonstrated that the scaffold induces excellent antibacterial performance toward *E. coli* owing to the sustained release of silver ions. Moreover, the scaffolds found to accelerate the osteogenic differentiation of rabbit bone marrow stromal cells benefit from the presence of GO nanosheets on the scaffold. In a recent study (Melo et al., 2020), GO with varying concentrations was mixed with poly(ε-caprolactone) (PCL) biomaterials ink. It was shown that the antibacterial performance of pristine PLA has been significantly improved upon the addition of GO in a concentration and time-dependent manner.

Alginate (Alg) is a well-known linear polysaccharide, which is broadly used in the formulation of bioink owing to a set of favorable features such as biocompatibility, biodegradability, tuneable characteristics, hydrophilicity, porosity, and ionic crosslinking (Axpe & Oyen, 2016; Freeman & Kelly, 2017; Giuseppe et al., 2018). It is composed of mannuronic acid (M) and L-guluronic acid (G) units in different ratios, forming brittle hydrogel once exposed to multivalent ions (*e.g.*, Ca^{2+}, Mg^{2+}, Ba^{2+}, Sr^{2+}, Ga^{3+}) as a result of physical crosslinking of G blocks of

Alg with ions (Alruwaili, Lopez, McCarthy, Reynaud, & Rodriguez, 2019; Lewicki, Bergman, Kerins, & Hermanson, 2019). The selection of ionic crosslinker has been found to significantly affect the ultimate properties of the hydrogel (Iskandar, Rojo, Di Silvio, & Deb, 2019). For example, Zhou et al. (2018). compared the effect of four different divalent ions crosslinker (Cu^{+2}, Sr^{+2}, Zn^{+2}, and Ca^{+2}) on the Alg-polyacrylamide hydrogels for wound healing applications. It was found that the mechanical properties of the hydrogel differ significantly by varying the crosslinker type as the hydrogels crosslinked by Cu exhibited the highest breaking strength. In terms of cytotoxicity, the hydrogels crosslinked by Sr have the highest cell viability compared to Zn, Ca, and Cu crosslinkers. However, the hydrogels crosslinked by Zn and Cu induced better antibacterial activity, while others did not show antibacterial activity. In addition to those crosslinkers, gallium was found to form ionic interactions with Alg chains and form a brittle hydrogel (Mouriño et al., 2011). Gallium-based compounds (e.g., gallium nitrate) have demonstrated potent antibacterial activity toward a broad range of Gram-negative and Gram-positive bacteria (Hentze, Muckenthaler, Galy, & Camaschella, 2010; Hijazi et al., 2018). The mechanism behind the antibacterial activity of gallium is based on the disruption of iron-dependent metabolic pathways as bacterial cells cannot distinguish Ga^{3+} and Fe^{3+} due to their chemical similarity (Chitambar, 2016; Lemire, Harrison, & Turner, 2013). In addition, gallium-based compounds exhibit therapeutic potential in cancer therapy towards bladder cancer and non-Hodgkin's lymphoma *via* inhibition of iron-dependent cellular function, while demonstrating acceptable toxicity toward normal cells. This is because malignant cells show higher needs for iron than normal cells, which might result in the higher expression of proteins responsible for transferring iron into the cell (Chitambar, 2012).

Herein, we aim to report the design of a cell-laden bioink for skin tissue engineering *via* the elimination of the risks associated with a bacterial infection while supporting cellular functions. Briefly, MC/Alg hydrogel printed out 3D structures, followed by immersion in the gallium solution to crosslink Alg chains, as shown in Fig. 1. Our hypothesis and the key feature of the bioink is the use of gallium in the formulation of bioink to achieve two goals. Accordingly, gallium functions as the crosslinker of Alg chains while inducing excellent bactericidal activities toward both gram-negative and gram-positive bacteria with a bactericidal rate of 99.999 % and insignificant cytotoxicity to foreskin fibroblast cells with cell viability of 95.6 ± 1.8 %. In addition, the viability and metabolic activity of cells encapsulated in the gallium-crosslinked hydrogel reveal that the hydrogel can support cellular functions. Overall, having antibacterial activity while supporting cellular functions is significantly advantageous to the bioink for skin tissue regeneration that makes it a promising candidate for skin tissue engineering.

2. Experimental section

2.1. Materials

Methylcellulose (average molecular weight = 6.3×10^4 g/mol, degree of substitution of methoxy = 1.50–1.90, and viscosity = 1500 cp at 2 wt. % in water), sodium alginate (average molecular weight = 250000−500000 g/mol, G/M ratio 1.05, and viscosity 5.0–40.0 cp at 1 wt. %,), and gallium nitrate hydrate were purchased from Sigma–Aldrich (St Louis, MO, USA). The structural information of methylcellulose and sodium alginate was obtained from the supplier's specification sheet and literature (He, 2019), respectively. The chemical structure of the pristine methylcellulose and sodium alginate was also investigated using a Nicolet 6700 Thermo Fisher Fourier transform infrared (FTIR) spectrometer over the wavelength range of 4000–600 cm^{-1}, as shown in Fig. S1. Dulbecco's Modified Eagle Medium (DMEM) was obtained from Life technologies corporation (Grand Island, NY, USA). LIVE/DEAD cell viability kit containing ethidium homodimer-1 (EthD-1) and Calcein AM and the alamarBlue viability assays were

2
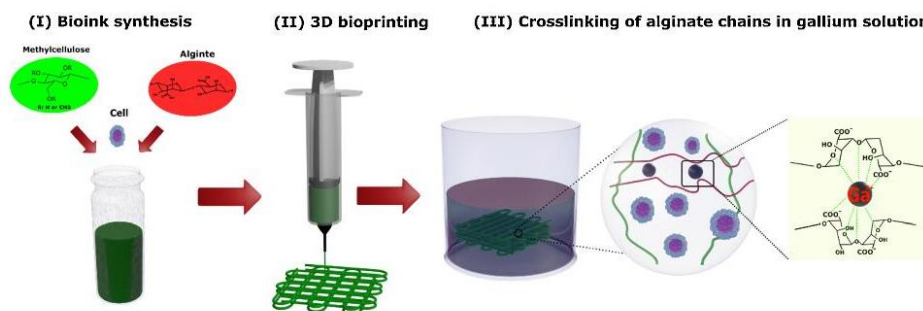
Fig. 1. (I) Schematic illustration of the synthesis of an cell-laden antibacterial bioink based on MC/Alg hydrogels. (II) The highly thixotropic behavior of the bioink allows the fabrication of multi-layered structures with high printing resolution. (III) After printing, the ionic crosslinking of Alg chains and gallium cations form a long-term stable structure. In addition, gallium imparts strong antibacterial activity toward both Gram-negative and Gram-positive bacteria.

purchased from Invitrogen (CA, USA).

2.2. Synthesis of the hydrogel composite

The bioink was prepared simply by the physical blending of MC and alginate to reach the final concentrations according to Table S1. For instance, to prepare 4 mL of MC-8/Alg-2 formulation, alginate powder (80 mg) was gradually added to 1 × PBS and heated to 50 °C for one hour. Next, MC powder (320 g) was mixed with the obtained solution at 50 °C and allowed to hydrate at 4 °C for 20 min. Prepared hydrogels were then crosslinked by immersion in 0.5 wt.% gallium nitrate solution for 10 min. The prepared hydrogels were coded as MC-x/Alg-y, where x and y imply the concentrations of the comprising components.

2.3. In vitro swelling behavior

To measure the swelling ratios, hydrogels were first crosslinked in gallium nitrate for 10 min and then immersed in 1 × PBS solution for 24 h at 37 °C to reach the swollen state of the hydrogel. Samples were retrieved, weighted, and then lyophilized over two days. Swelling ratios of the hydrogels were calculated according to the weight changes before and after lyophilization as follows:

$$\frac{W(swell) - W(dry)}{W(dry)} \times 100 \tag{1}$$

where W(swell) and W(dry) indicate the hydrogel weight in the swell and dry state.

2.4. In vitro degradation

To monitor the degradation rate, crosslinked hydrogels were soaked in 1 × PBS solution for four weeks. Samples were retrieved and weighted at various time points. The degradation rate of samples was calculated based on weight loss as follows:

$$\frac{W(t) - W(0)}{W(0)} \times 100 \tag{2}$$

where W(0) and W(t) are the weight of the sample before soaking in the PBS solution and at a predetermined time.

2.5. Mechanical strength

To measure the mechanical strength, crosslinked hydrogels (D = 10 mm, H = 2 mm) were tested on a dynamic mechanical analyzer (DMA, Q800, TA Instruments, New Castle, USA) with 0.1 N steps. The compressive modulus of the samples was calculated from the slope of the

stress-strain curve in the range of 0.05–0.15 strain.

2.6. Morphology

Morphological features of the prepared hydrogel were examined by scanning electronic microscopy (Hitachi Model S4700, Japan). Prepared hydrogels (D = 10 mm, H = 2 mm) were first crosslinked in 0.5 wt.% gallium nitrate solution for 10 min and then swollen at 37 °C for 24 h to reach the equilibrium in saline. Next, samples were lyophilized in a freeze dryer for two days and then coated by 10 nm Pt using a Cressington 108 Auto sputter coater (Cressington Scientific Instruments Ltd., Watford, England).

2.7. Rheology

Rheological properties of the hydrogel were tested using Physica MCR301 rheometer (Anton Paar, Ostfildern, Germany) that fitted with a cone-plate accessory (diameter of 50 mm, a gap of 49 μm). Hydrogels were prepared as explained in Section 2.2 and then placed on the Peltier module and allowed to rest for 15 min. First, the oscillatory strain sweep test was conducted from 0.01 %–100 % strain at 10 Hz to determine the linear viscoelastic region of samples. Next, the oscillatory frequency sweep test was conducted over a range of 0.01−10 Hz at 1 % strain to monitor the alteration in storage modulus (G') and loss modulus (G''). The viscosity of the hydrogels was measured over a shear rate ramp from 0.01–$1000\ s^{-1}$. To determine the yield stress, changes in the G' and G'' were monitored by increasing the shear stress from 1 to 10000 Pa and the cross-section of G' and G'' defined as the yield point. To evaluate the recoverability of the hydrogels, changes in the G' and G'' values were monitored over the two repetitive steps; first, samples were subjected to 1 % strain for 1 min and then 100 % strain for another minute. Application of alternate low and high strains was repeated for 3 cycles. In addition, to simulate the extrusion stage of the printing process, hydrogels were subjected to a shear rate of $100\ s^{-1}$ for 5 s. The changes in the viscosity of hydrogels were measured during and after removing the high shear rate.

2.8. Antibacterial tests

2.8.1. Bacteria and culture condition

The local institutional Human Research Ethics Committee approved the use of clinical isolates for this study (HREC/15/TQEH/132). *Staphylococcus aureus* ATCC 25923 was obtained from American Type Culture Collection (Manassas, VA, USA). *Pseudomonas aeruginosa* (clinical isolate from a chronic rhinosinusitis patient) was obtained from Adelaide Pathology Partners (Mile End, Australia). Both bacterial stocks were stored

3

at −80 °C in frozen glycerol broth. To culture bacteria, a small amount of the *S. aureus* and *P. aeruginosa* bacterial stock was plated on Tryptone Soy Agar (TSA) and Nutrient Agar (NA) plates, respectively, and grown overnight at 37 °C under static conditions.

2.8.2. Minimum inhibitory concentration (MIC)

The minimum inhibitory concentration (MIC) of gallium nitrate was determined against planktonic forms of *S. aureus* and *P. aeruginosa* using the microdilution method as described by the Clinical and Laboratory Standard Institute (CLSI) (Clinical & Institute, 2006). First, two-fold serial dilutions of gallium nitrate were prepared in Tryptic Soy Broth (TSB) for *S. aureus* and Nutrient Broth (NB) for *P. aeruginosa*. Following that, 100 µl of each dilution was transferred into a 96-well plate (Costar, Corning Incorporated, Corning, U.S.). Next, a single colony of bacteria was resuspended in broth medium to reach 0.5 MacFarland Unit (approximately 1.5×10^8 colony forming units (CFU)/mL). The suspension of *S. aureus* and *P. aeruginosa* was subsequently diluted 1:100 in TSB and NA, respectively. Following this, 100 µl of the resulting bacterial suspension was added to the 96-well plate containing gallium and allowed to incubate at 37 °C for 24 h. Untreated control bacteria (100 % bacterial growth) and the broth medium are considered as the negative and positive controls, respectively. Finally, the optical density (OD) of the bacterial suspension at 595 nm was recorded with a FLUOstar OP-TIMA plate reader (BMG Labtech, Ortenberg, Germany). To quantify the antibacterial activity of the gallium nitrate, the following equation was employed:

$$Antibacterial\ activity\ \% = 100 - \left(\frac{A_T}{A_C} \times 100\%\right) \quad (3)$$

Where A_C and A_T denote the OD of the untreated control bacteria (100 % bacterial growth) and the treated bacteria, respectively. To ensure the reliability of obtained data, each experiment was conducted three times with three biological replicates for each gallium nitrate dosage.

2.8.3. The minimum biofilm eradication concentration (MBEC)

The anti-biofilm performance of gallium nitrate against *S. aureus* and *P. aeruginosa* bacteria was determined as described elsewhere (Richter et al., 2017). Briefly, a single colony of the bacteria was suspended in 0.9 wt.% saline to reach 1.0 ± 0.1 McFarland units (approximately 3×10^8 CFU/mL), followed by 1:15 dilution in the appropriate broth (TSB for *S. aureus* and NA for *P. aeruginosa*). Next, 150 µl of bacterial suspension were transferred to a black 96-well plate and incubated on a rotating stage (3D Gyratory Mixer, Ratek Instruments, Boronia, Australia) at 70 rpm and 5 wt.% CO_2 for 48 h. Then, the formed biofilm on the bottom of the well-plate was washed twice with $1 \times$ PBS. Afterward, two-fold serial dilutions of gallium nitrate in the appropriate broth were prepared and added to the formed biofilm in the well-plate and incubated on a rotating platform for another 24 h. Finally, biofilm was washed twice with $1 \times$ PBS and the viability of the biofilm was measured by ala-marBlue assay. In brief, 100 µL fresh PBS media containing a 10 % v/v alamarBlue reagent was added into each well. Following this, the plate was incubated in the dark at 37 °C for 3 h. Then, 100 µL of incubated alamarBlue medium in each well were transferred to another black 96-well plate and the optical density (OD) at 570 and 600 nm was measured with a FLUOstar OPTIMA plate reader (BMG Labtech, Ortenberg, Germany).

2.8.4. Surface antibacterial activity

The surface antibacterial performance of hydrogels crosslinked with different concentrations of gallium nitrate was tested against both bacteria as described elsewhere (Pan et al., 2019; Zhao et al., 2017). In brief, 150 µL of hydrogels was crosslinked and then transferred to a 24-well microplate. Next, bacterial suspension (10 µL in broth medium, 10^4 CFU mL^{-1}) was added onto the hydrogel's surface and then incubated at 37 °C. After 2 and 4 h of incubation, 990 µL of sterilized saline were

added onto the hydrogel surface and repeatedly resuspended the bacterial cells. Following this, an aliquot of 50 µL bacterial suspension of each sample was inoculated onto agar plates (TSA for *S. aureus* and Cetrimide agar for *P. aeruginosa*) using the smearing method and left in an incubator for 24 h at 37 °C. Afterward, the CFU's counted on each plate. As a control sample, 10 µL of bacterial suspension was resuspended in 990 µL sterilized saline.

2.9. In vitrocytocompatibility

2.9.1. Cell culture

Human Foreskin fibroblast cells were seeded and cultured in a T25 flask (25 cm^2) in DMEM supplemented with 10 % (v/v) FBS and 1 % (v/v) penicillin/streptomycin with 10 % fetal bovine serum in an incubator (5 % CO_2 at 37 °C). Next, when the confluence reached 80–90 %, the adherent cells were digested with 0.25 % trypsinase. Following this, detached cells were resuspended in DMEM and centrifuged at 5000 rpm for 5 min to obtain cell pellets that will be used for the following experiments.

2.9.2. In vitro cytotoxicity of gallium nitrate only

The *in vitro* cytotoxicity of gallium nitrate was evaluated quantitatively using alamarBlue assay. In brief, 100 µL DMEM media containing 2.6×10^4 foreskin fibroblast cells were transferred to a 96-well plate and then incubated for 24 h at 37 °C. Then, culture media were removed and 100 µL DMEM media containing different amounts of gallium nitrate were added to each well. After a certain incubation time (2, 24, and 48 h), the culture media was removed and viability of the seeded cells was measured by alamarBlue assay, as described in Section 2.8.3.

2.9.3. In vitro cytocompatibility of the developed hydrogels

The biocompatibility of the developed hydrogel was evaluated using a direct contact method between hydrogels and foreskin fibroblast cells, as described elsewhere in detail (Qu et al., 2018). In brief, foreskin fibroblast cells were first seeded in a 96-well plate for 24 h (2.6 × 10^4 cell/well). Next, the gallium-crosslinked hydrogel was transferred to each well. The cytotoxicity of the hydrogel was evaluated using ala-marBlue assay after 2, 24, and 48 h, as described in Section 2.8.3. In addition, cell viability was evaluated using LIVE/DEAD cell assay. To do so, first, the culture media in each well were removed and washed twice with $1 \times$ PBS. Following this, $1 \times$ PBS solution containing calcein-AM (green fluorescence for live cells) and ethidium homodimer-1 (red fluorescence for dead cells) were added to the well-plate and left for 15 min at room temperature. Then, the cells were imaged using an LSM700 Confocal Laser Scanning Microscope (Zeiss Microscopy, Oberkochen, Germany).

2.10. 3D printing

To evaluate the printability of the developed hydrogel, 5 mL of which was transferred into a 10 mL syringe fitted with a plastic conical nozzle tip. Then, the operating printing factors (air pressure and print speed) were optimized by comparing the printed strands diameter and the nozzle diameter. A commercial extrusion-based Allevi 2 bioprinter (Philadelphia, USA) was employed in this study for the fabrication of 3D-printed structures including lattice and disk shape through applying air pressure. Autodesk fusion 360 software was used to create G-code files and then converted into STL file using Slic3r software. Food color was added to the ink to improve the visibility of the bioink.

2.11. 3D bioprinting

MC-8/Alg-2 formulation was selected for the 3D bioprinting process. To encapsulate the foreskin fibroblast cells within the bioink, MC-8/Alg-2 hydrogel was prepared first as described in Section 2.2 in DMEM and mixed gently with cells to obtain the final cell density of 6×10^5 cells/

4

mL. Prior to bioprinting, the 3D bioprinter and all accessories were sanitized using 70 % ethanol and left for 1 h under UV irradiation. The bioink printed 5 layer lattice structure using 225 μm tapered plastic tip with a printing speed of 6 mm/s and air pressure of 20 psi. Next, the printed structure was crosslinked in 0.5 wt.% gallium solution for 10 min and then incubated for 7 days. After 1, 3, and 7 days of cell encapsulation, the culture media was removed from each well and replaced with 1 × PBS containing LIVE/DEAD reagents and then observed using a confocal laser scanning microscope. Hydrogel cross-linked with calcium chloride was considered as the control sample. To further characterize the biocompatibility of the hydrogel, alamarBlue assay was used to compare the metabolic activity of the gallium-crosslinked hydrogel with the control sample according to the procedure described previously in Section 2.8.3.

2.12. Statistical analysis

All statistical analyses were performed by at least three independent tests. Mean values and standard deviations of obtained data were calculated. One-way analysis of variance (ANOVA) followed by Dunnett's test was employed for statistical analysis of obtained *in vitro* results in GraphPad Prism version 7.00 (La Jolla, USA). Statistical significance was assessed evaluated at the 95 % confidence level.

3. Results and discussion

3.1. Synthesis of bioprintable hydrogel

The printability of ink is closely attributed to the rheological behavior of ink. In this sense, the rheological studies were conducted to examine the viscoelastic properties of the prepared hydrogel at different stages of the 3D printing process. In general terms, the extrusion-based 3D printing process can be classified into three distinct stages; extrusion stage, recovery stage, and shape retention stage, as shown in Fig. 2a.

3.1.1. Extrusion stage

In the extrusion stage, the bioink sitting in the syringe starts flowing along the nozzle upon applying pressure behind the syringe. Once pressure behind the syringe overcomes the yield stress of the hydrogel, the cell-laden bioink passes through a nozzle and experiences high shear stress. Shear-thinning behavior allows the smooth extrusion of ink along the nozzle where viscosity drops at a high shear rate. This shear-thinning behavior shield encapsulated cells from high shear stress and subsequently prevents loss of cell viability (Rastin, Zhang, Mazinani et al., 2020). To characterize the shear-thinning behavior, the viscosity of the hydrogel was monitored over shear rate sweep (Fig. 2b). At a low shear rate, the viscosity of the MC/Alg hydrogel remains almost unchanged and forms a plateau region, which can be attributed to the yield stress of the hydrogel (Rastin, Ormsby, Atkins, & Losic, 2020). Further increase of the shear rate resulted in the continuous drop of the viscosity of all studied formulations from approximately 1000 Pa.s to 1 Pa.s, suggesting the shear-thinning behavior. Moreover, the hydrogels containing a higher content of Alg exhibited a higher value of viscosity at a low shear rate, which can be attributed to the lower free volume for the mobility of polymer chains. This shear-thinning behavior is due to the dissociation of hydrophobic interactions between methoxy groups along the MC chains once subjected to a high shear rate, as reported elsewhere (Contessi Negrini, Bonetti, Contili, & Farè, 2018; Li, Tan, Leong, & Li, 2017; Rastin, Ormsby et al., 2020).

The formation of continuous hydrogel filament at the nozzle tip is
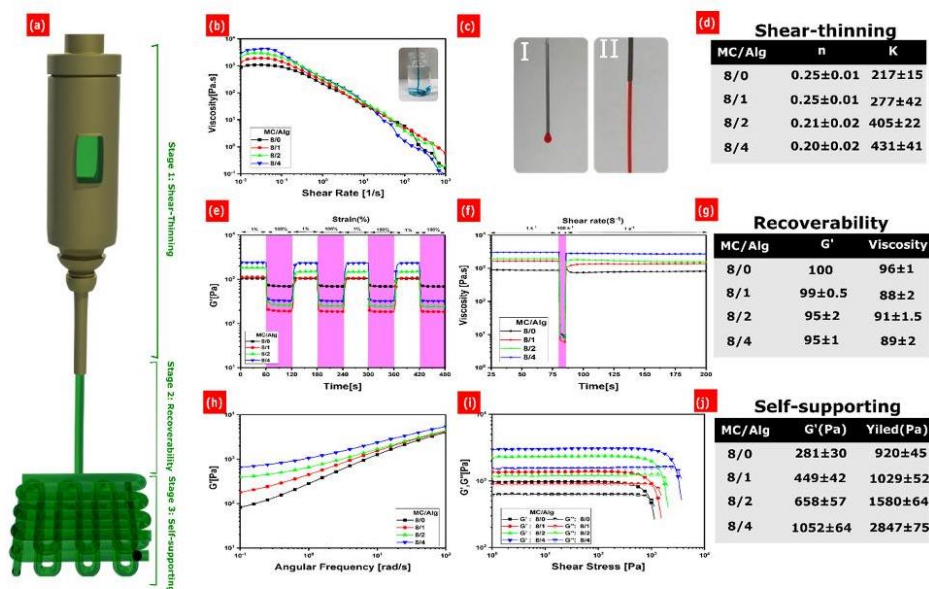
Fig. 2. (a) Schematic illustration of the 3D bioprinting process and corresponding stages. (b) Shear viscosity over the shear rate ramp. The viscosity dropped upon increasing the shear rate, showing the shear-thinning behavior. The inset image demonstrates the injection of the ink into water. (b) Examine the ability of the pure Alg-2(I) and MC-8/Alg-2(II) hydrogel to form a continuous filament shape once exiting the nozzle. (c) The calculated value of n and K from the power-law model. (e) Monitoring the changes of G' over applying alternate low (1%) and high strains (100 %). The G' quickly returns to its initial stage after removing the high strain for all cases. (f) The changes of the viscosity over applying a high shear rate. The viscosity of the developed hydrogels showed quick recovery. (g) The calculated extent of recoverability of G' and viscosity. (h) Variation of G' over frequency seep test. The addition of Alg causes an increase in the G' value. (i) Shear sweep test to determine the yield stress. (j) The obtained amount of G' (1 Hz) and yield stress, confirming the improved shape-supporting behavior at higher Alg conventions.

5

necessary to fabricate a construct matched with a pre-designed structure (Rastin, Zhang, Bi et al., 2020). The inset image in Fig. 2b shows that the MC/Alg from continuous regular filament once injected in the aqueous solution. Although MC/Alg can form a continuous filament shape once exiting the nozzle, Alg alone hydrogel form a discrete droplet at the nozzle tip (Fig. 2c), showing the failure of Alg hydrogel solely for 3D printing. To quantify the extent of shear-thinning behavior of hydrogel, the power-law model was employed as the most common model ($\eta = K\dot{\gamma}^{n-1}$), where η, $\dot{\gamma}$, n and K are viscosity, shear rate, flow index, and consistency index, respectively. The flow index (n) value determines the fluid behavior, where n<1 denotes shear-thinning behavior. According to the power-law model, MC/Alg hydrogel exhibited shear-thinning behavior, as evidenced by the flow index value lower than one (Fig. 2d). It is interesting to note that the flow index value decreased upon increasing the Alg concentration, showing that the addition of the higher amount of Alg intensified the shear-thinning behavior of the MC/Alg. Overall, these results revealed the shear-thinning behavior of the MC/Alg hydrogel that can be tuned by changing the ratio of corresponding components.

3.1.2. Recovery stage
Once bioink expels from the nozzle, the self-healing behavior of bioink allows the recovery of bioink to its initial state to avoid spreading on the surface. To explore the self-healing behavior of the hydrogel, G' and G'' values were monitored upon switching the strain between low (1 %) and high (100 %) magnitude over three cyclic strain tests (Fig. 2e). At low strain (1 %), the G' values are greater than G'' values, demonstrating the gel-like behavior (G'' data not shown here). Herein, the G' values drop suddenly upon applying high strain 100 %, followed by recovering their initial G' values at the low strain in a short time. In addition, there is an insignificant difference between different cycles, confirming the high recoverability of the MC/Alg network. In addition, the addition of Alg into MC only increases the G' values without disrupting the self-healing behavior of the hydrogel significantly. This shows that MC controls the self-healing behavior of the hydrogel. To further explore the self-healing behavior of the hydrogel, the viscosity of the ink was monitored before, during, and after applying a high shear rate (Fig. 2f). Accordingly, the viscosity of inks plunge suddenly from 1000−3000 Pa.s to about 10 Pa.s upon application of high shear rate and then quickly return to its initial state. the extent of recoverability of the G' and viscosity over applying high strain and viscosity were summarized in Fig. 2g. As seen, the recoverability of G' and viscosity for MC/Alg depends mostly on the MC component and the addition of Alg only had a minor effect. Overall, these results promise high recoverability of the ink once subjected to high strain or shear rate, which is critical for achieving high resolution in the 3D printing process.

3.1.3. Shape retention stage
Once ink deposits on the printing stage, the self-supporting behavior of hydrogel allows keeping the integrity of the printed structure to avoid collapse or spreading to the neighboring area. The ability of the hydrogel to sustain the integrity of the hydrogel was determined by G' and yield stress values as higher G' and yield stress means better shape-supporting behavior. According to the angular frequency sweep test (Fig. 2h), the G' value is over G'' value in the range of 0.1–100 rad s^{-1} (G'' data not shown here), indicating the gel-like behavior. In addition, the G' value of MC/Alg hydrogel surges considerably upon the increasing concentration of Alg. Further, the shear stress sweep test was conducted to measure the yield stress of the prepared hydrogel (Fig. 2i). Yield stress is described as the minimum stress required for materials to initiate flow. It can be obtained from the shear stress sweep test where G'=G''. At low shear stress, both the G' and G'' profiles remain unchanged. Herein, the G' value is greater than G'' for all studied formulations. Further increase of shear stress leads to the crossover of G' and G'' at yield point, where the transition of the hydrogel from a gel form to

a solution state occurs and fluid starts flowing. As viewed, the hydrogel shows higher yield stress and G' at higher concentrations of Alg hydrogel (Fig. 2j). Taking together both G' and yield values, it is expected that the higher content of Alg reflects higher shape retention after printing, which will in turn allows the fabrication of high-resolution structures.

3.2. Stability of gallium-crosslinked hydrogels
The printed 3D structure remains stable during the printing process due to the excellent shape retention behavior of the hydrogel precursor as evidenced in the G' and yield stress results. However, after the printing process, the 3D structure should be stabilized to prevent the collapse of the structure in the biological media. Therefore, the 3D printed structure was ionically crosslinked in the gallium solution for 10 min. Herein, we have characterized the stability of the developed hydrogel after crosslinking with a varying dosage of gallium (Fig. 3).
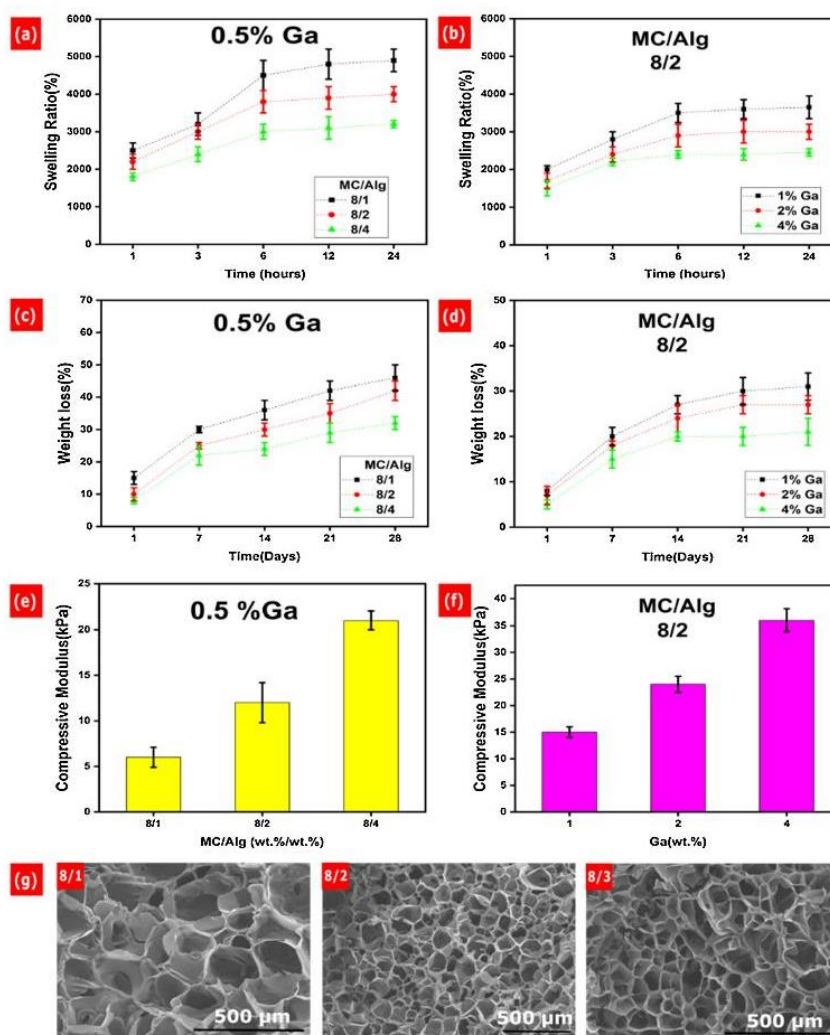
3.2.1. Swelling ratio
Hydrogels are generally characterized by their high swelling ratio, indicating the ability of hydrogels to absorb and retain a high amount of water (Li, Wu, Chu, & Gelinsky, 2020; Namazi, Hasani, & Yadollahi, 2019; Zhu et al., 2017). The high swelling ratio of a hydrogel is advantageous to the tissue-engineered scaffold to closely mimic the native tissue microenvironment (Dorishetty, Dutta, & Choudhury, 2020). It was shown that the swelling ratio of hydrogels significantly depends on the nature of polymers, crosslinking method, and polymer content (Jovic, Kungwengwe, Mills, & Whitaker, 2019). Given this, the swelling ratio of the hydrogels was monitored by varying the concentration of gallium and Alg under physiological conditions in PBS at 37 °C. Immersion of the hydrogel in gallium nitrate solution allows the ionic cross-linking of Alg chains with gallium cations. By keeping the concentration of gallium constant at 0.5 wt.% (Fig. 3a), the swelling ratio was decreased once the Alg concentration increases. This is attributed to the higher crosslinking density of hydrogel at a higher concentration of Alg, which subsequently hampers the mobility of a hydrogel network to the expansion of the polymeric network (Davidovich-Pinhas & Bianco-Peled, 2010; Dodero et al., 2019). On the other hand, the hydrogels crosslinked in a higher concentration of gallium exhibited a lower swelling ratio due to the formation of high crosslinking density (Fig. 3b). Overall, these data suggest that the swelling ratio of the hydrogel can be tuned by varying the concentration of Alg and gallium.

3.2.2. Degradation
Adjusting the degradation properties of hydrogel allows matching the degradation rate of hydrogel with the rate at which native ECM is produced (Lee, Bouhadir, & Mooney, 2004; Zhu & Marchant, 2011). To evaluate the stability of the crosslinked hydrogel in physiological conditions, changes in the weight of crosslinked hydrogels were measured over 28 days. As seen, lower Alg concentration resulted in higher weight loss over time, which is attributed to the lower crosslinking density of the network (Fig. 3c). In addition, the gallium-crosslinked hydrogel was more stable when crosslinked with a higher amount of gallium with no sign of the disintegration of the hydrogel network (Fig. 3d). It can be concluded that the ionic interaction of Alg chains with gallium cations renders a stable hydrogel that cannot be disrupted by ionic exchange and interaction with proteins present in the culture media.

3.2.3. Compressive properties
The mechanical properties of hydrogels are of utmost importance for a tissue engineering application as scaffolds serve not only as mechanical support but also as a biophysical cue for stimulating cellular functions (Kim & Choi, 2019; Shi, Xing, & Zhong, 2012). The compressive mechanical properties of the hydrogel were measured by applying uniaxial compression force on crosslinked Alg with varying concentrations of gallium nitrate. Holding the gallium concentration constant, the

6

Fig. 3. Characterization of MC/Alg hydrogel crosslinked with varying concentration of Alg and gallium in terms of (a, b) Swelling ratio, (c, d) the extent of weight loss, (e, f) the compressive modulus, and (g) SEM micrographs. The effect of Alg concentration was evaluated in (a, c, e), while the effect of gallium dosage was monitored in (b, d, f).

higher Alg content enabled the formation of a network with higher compressive modulus values, in agreement with decreased swelling ratios (Fig. 3e). It was observed that increase in the gallium concentration results in the formation of alginate hydrogel with higher compressive modulus values, which is due to a high degree of crosslinking between polymeric chains (Fig. 3f). These findings are in agreement with the results of the swelling ratio behavior of cross-linked Alg. In summary, the mechanical performance of ionic-crosslinked Alg hydrogel showed direct relation with gallium and Alg concentrations.

3.2.4. Morphology

Further, we have investigated the microstructure of the developed hydrogels, as shown in Fig. 3g. As seen, the hydrogel contains a regular interconnected porous structure, which is critical for successfully transferring the waste and nutrient between the scaffold and environment. This porous microstructure of the MC/Alg hydrogel has been previously reported elsewhere (Li et al., 2017). In addition, the hydrogel with a higher Alg concentration contains a lower pore size, as expected,

due to the higher polymer content and crosslinking density. Overall, the observation of the morphology of the gallium-crosslinked hydrogel reveals an interconnected porous structure, suitable for tissue engineering application (Li, Mu, & Lin, 2016).

3.3. Antibacterial performance of the hydrogel

Having antibacterial activity is an advantage to the ideal scaffold for skin tissue engineering and wound dressing applications as it reduces the risk of bacterial infection at the site of the damage. Prior to testing the surface antibacterial activity of the developed hydrogels, the minimum inhibitory concentrations (MIC) and the minimum biofilm eradication concentration (MBEC) of gallium nitrate solution were evaluated against *S. aureus* and *P. aeruginosa* to find the optimal content of gallium, as reported in Table S2. Accordingly, 0.5 wt.% dosage is the concentration at which gallium nitrate could kill both *S. aureus* and *P. aeruginosa* in biofilm and planktonic forms. Next, the surface antibacterial activity of prepared hydrogels was assessed after challenging with 10^4 CFU/mL of

7

S. aureus and *P. aeruginosa* for 2 h and 4 h (Fig. 4a and b). As seen, the antibacterial activity of the gallium-crosslinked hydrogel exhibited time and dose-dependent behavior toward both selected bacterial species. Accordingly, around 99 % of *S. aureus* and *P. aeruginosa* seeded on the gallium-crosslinked hydrogel surface were killed after 4 h, even at 0.5 wt.% gallium ($p < 0.05$). The mechanism of antibacterial performance of the gallium-crosslinked hydrogel is attributed to the chemical similarity between Ga^{3+} and Fe^{3+} cations (Chitambar, 2016; Lemire et al., 2013). This allows the easy binding of gallium to certain iron-binding proteins and subsequently disrupt the iron-dependent metabolic pathways of bacteria. Overall, the hydrogels crosslinked with gallium above 0.5 wt.% concentrations exhibited potent antibacterial performance

toward both *S. aureus* and *P. aeruginosa* without further need to introduce antibiotics. These results demonstrate that the hydrogel has the potential to efficiently eliminate the risk of common pathogenic infection at the lesion site for skin tissue engineering applications.

An ideal antibacterial bioink should exhibit antibacterial activity toward bacteria while retaining the viability of the mammalian cell. In this way, as a preliminary evaluation, we first examined the cytocompatibility of the gallium nitrate-only when exposed to the mammalian cells by monitoring the metabolic activity of mammalian cells. For this purpose, foreskin fibroblast cells were treated with a varying dosage of gallium nitrate, and then their metabolic activity was measured by alamarBlue assay after 2, 24, and 48 h (Fig. S2). The cells
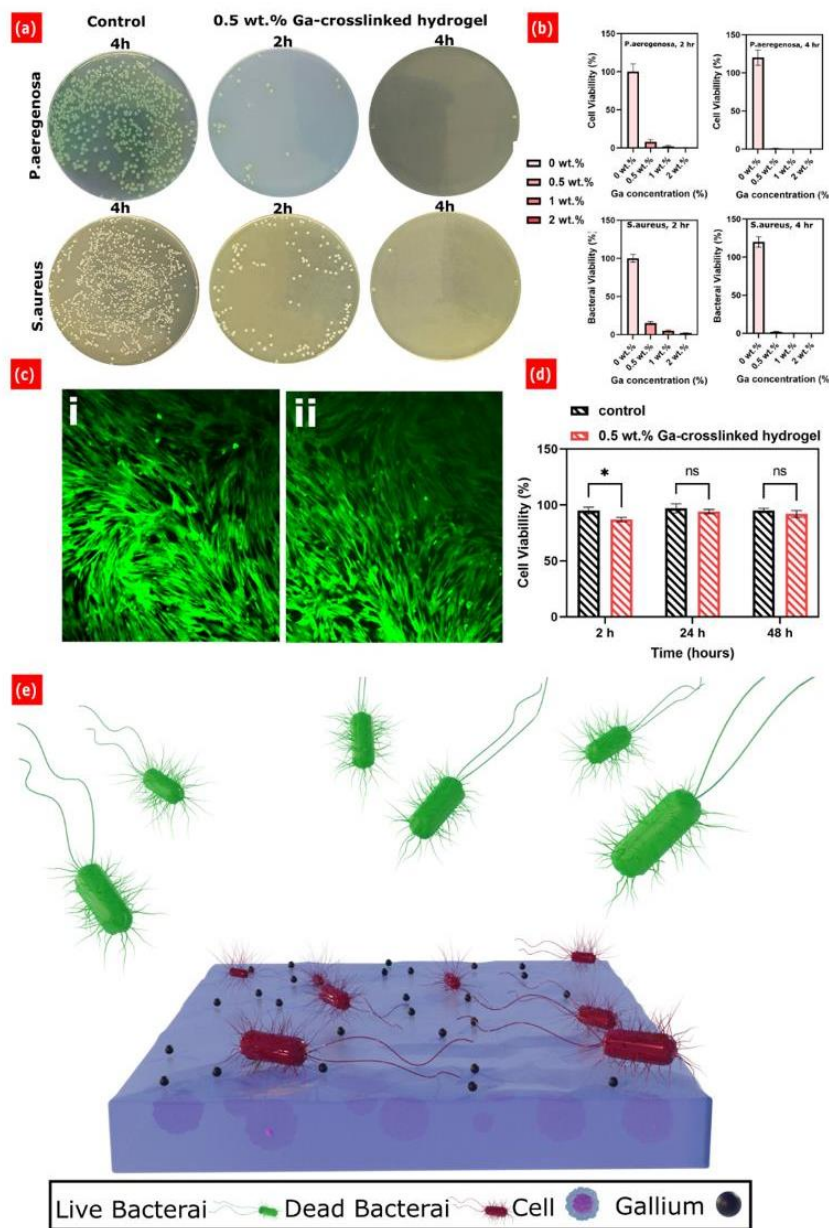
Fig. 4. Surface antibacterial activity of the hydrogel toward *S. aureus* and *P. aeruginosa* bacteria. (a) Surviving *S. aureus* and *P. aeruginosa* colonies on agar plates after contacting with 0.5 wt.% gallium-crosslinked hydrogels. The gallium-crosslinked hydrogel enables killing almost all bacteria contacted with the hydrogel surface. (b) Calculated antibacterial performance of the hydrogel against *S. aureus* and *P. aeruginosa* bacteria after 2 h and 4 h. (c) LIVE/DEAD fluorescence images of fibroblast cells contacted with the developed hydrogel after 48 h. Cells remain viable when treated with gallium-crosslinked hydrogel. (d) Results of cell viability were obtained from alamarBlue assay after 2, 24, and 48 h. Data are demonstrated as mean ± Standard deviation ($p < 0.05$: *, $p < 0.01$: **, $p < 0.001$: ***, and $p < 0.0001$: ****, $n \geq 3$). (e) Schematic illustration of the antibacterial activity of the gallium-crosslinked hydrogel. Accordingly, the antibacterial activity of the hydrogel stems from the presence of gallium cations on the hydrogel surface.

treated with culture media only were used as the control. The results obtained from the alamarBlue assay show that there are no significant differences between the control sample and cells treated with gallium nitrate below 0.5 wt.% dosages in terms of metabolic activity over 48 h, which confirms the biocompatibility of the gallium nitrate toward mammalian cells at low concentration. However, a significant decrease was observed for the cells treated with gallium nitrate above 0.75 wt.% dosages, indicating the toxic effect of gallium at high concentrations. As hydrogels crosslinked with 0.5 wt.% gallium exhibited high antibacterial activity without noticeable toxicity effect, we selected 0.5 % wt.% gallium as the optimum concentration. Next, we monitored the cytocompatibility of the gallium-crosslinked hydrogels by using the direct contacting method. Accordingly, LIVE/DEAD assay was used to observe the loss of viability of the seeded cells after direct contact with developed hydrogels (Fig. 4c). As seen, the seeded cells remain viable when exposed to gallium-crosslinked hydrogel after 48 h without noticeable changes in the viability of the cells compared to the control. To further characterize the cytotoxicity of the gallium-crosslinked hydrogels, alamarBlue assay was used to compare the metabolic activity of seeded

cells treated with gallium-crosslinked hydrogels with the control sample (Fig. 4d). Accordingly, no significant differences were observed in the metabolic activity of cells treated with the gallium-crosslinked hydrogel and the control sample over 48 h. Fig. 4e provides a schematic illustration of the antibacterial activity of the gallium-crosslinked hydrogel. Accordingly, the contacted bacteria end up dying on the hydrogel surface due to the presence of gallium cations. These results are in agreement with that of the LIVE/DEAD assay. Overall, these results suggest developed hydrogel crosslinked with 0.5 wt.% gallium had excellent antibacterial activity and biocompatibility as a promising candidate for skin tissue engineering.

3.4. 3D printing

A key feature of an ideal bioink is to print strands on the stage that matches with nozzle diameter. Therefore, we have optimized the operating printing parameter to achieve the best match between the printed stand and nozzle diameter (Fig. 5a). Printing speed and air pressure behind the syringe are two main factors that need to be carefully
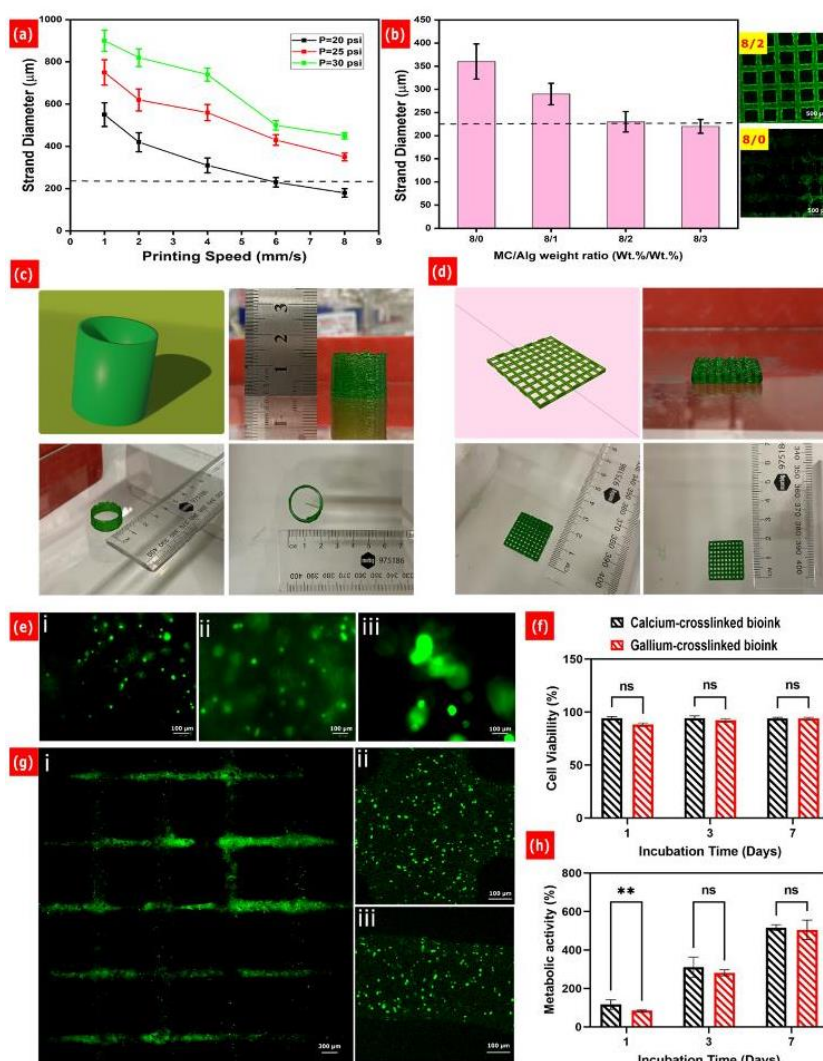
Fig. 5. 3D bioprinting of the gallium-crosslinked hydrogel to pattern cell-laden lattice. (a) Finding the optimal operating parameter of 3D printing in terms of printing speed and air pressure. The best matched between nozzle diameter and printed strands diameter obtained at printing speed of 6 mm/s and air pressure of 20 psi for MC-8/Alg-2 formulation. (b) Comparing the diameter of the printed strand of MC/Alg hydrogel with different formulations. An increase in the Alg concentration leads to a better match between nozzle diameter and printed strands diameter. (c, d) Images of 3D printed disk (Height: 13 mm) and lattice (Height: 4 mm) structure from different views along with designed CAD model using MC-8/Alg-2 at optimized operating printing parameter. (e) Representative LIVE/DEAD fluorescence images of fibroblast cells encapsulated within the gallium-crosslinked hydrogel after 1 (i), 3 (ii), and 7 (iii) days. Encapsulated cells remain viable within the matrix over time. (f) The extent of cell viability over a week that calculated as the ratio of observed viable cells to the sum of all viable and dead cells. (g, h) Representative LIVE/DEAD fluorescence images of fibroblast cells encapsulated within the printed bioink and corresponding metabolic activity over a week. Data are demonstrated as mean ± Standard deviation ($p < 0.05$: *, $p < 0.01$: **, $p < 0.001$: ***, and $p < 0.0001$: ****, $n \geq 3$).

adjusted. In general, as the printing pressure was increased, the size of the deposited strands became larger due to the higher amount of expelled materials out of the nozzle. While thinner printing strands were obtained at higher printing speed. Accordingly, we set the printing speed and air pressure at 6 mm/s and 20 psi, respectively, for MC-8/Alg-2 formulation. For other formulations, the same procedure was followed to obtain the best operating printing parameters. Next, we found the best match between printed stand and nozzle diameter by changing the Alg concentration (Fig. 5a). Accordingly, the printed strands by pure MC were not able to fit with the nozzle diameter as the lattice structure misses the porous shape. This is attributed to the low self-supporting behavior of pure MC as evidenced by the low yield stress and storage modulus (Fig. 2h and i). With an introduction and increase in the Alg concentration, the diameter of the printed strand was nearing the nozzle diameter, as the best match was found at MC-8/Alg-2 ratio. These results are in agreement with the rheological analysis of MC/Alg hydrogel in the self-supporting stage.

To evaluate the printability of the bioink, two different multi-layered structures including a disk with rounded edges (Height: 13 mm) and lattice with sharp edges (Height: 4 mm) were printed using optimized parameters (air pressure: 20 psi, print speed: 6 mm/s), as shown in Fig. 5c and d. As observed from different views, MC-8/Alg-2 printed out disk shape with excellent resolution while retaining the shape integrity. In addition, the printed lattice structure also demonstrates a delicate porous structure without a sign of leaking of the materials to the neighboring area. This excellent printability of the hydrogel precursor is due to the combination of suitable rheological characteristics including shear-thinning behavior, high recoverability, and excellent self-supporting behaviors that allow keeping the integrity of the printed structure during printing. It should be noticed that the Alg-only hydrogel cannot keep the integrity of the printed architecture and spread on the platform after printing (not shown here). Overall, MC/Alg hydrogel has shown excellent ability to print multi-layered 3D structures with high shape integrity and resolution.

Next, the viability of the encapsulated fibroblast cells within the gallium-crosslinked hydrogel was monitored over seven days using a LIVE/DEAD fluorescence staining assay (Fig. 5e). The hydrogel cross-linked with calcium chloride was considered as the control sample. Accordingly, the viability of the encapsulated fibroblast cells within the gallium-crosslinked hydrogel remains stable over 90 % during 7 days, with no significant differences with the control sample (Fig. 5f). Moreover, cells' fluorescence intensified over time, showing the cell growth encapsulated within the hydrogel matrix. Next, cell-laden bioink printed out lattice structure using optimized printing parameter, followed by crosslinking in the 0.5 wt.% gallium solution (Fig. 5g). According to the fluorescence images taken from encapsulated cells within the hydrogel, cells remain viable with no significant differences with the bulk hydrogel. This is attributed to the shear-thinning behavior of the hydrogel that allows the smooth extrusion along the nozzle during direct-write printing. This shear-thinning behavior shields the encapsulated cells from the application of a high shear rate. To further characterize the biological interaction of the printed structures, the alamarBlue assay was used to evaluate the metabolic activity of the encapsulated fibroblast cells within the bioink over a week (Fig. 5h). Accordingly, continuous increases were observed in the metabolic activity of the encapsulated fibroblast cells within the bioink, regardless of the crosslinker type. Interestingly, except the first day, the metabolic activity of the encapsulated cells within gallium-crosslinked hydrogel was comparable with the control sample, indicating the high biocompatibility of the gallium-crosslinked hydrogels. The differences between the metabolic activity of the gallium-crosslinked hydrogel and the control sample on the first day might be attributed to the burst release of the gallium. Overall, these results demonstrate the gallium-crosslinked bioink not only exhibited potent antibacterial activity toward both *S. aureus* and *P. aeruginosa* but also support the cellular functions in terms of viability and metabolic activity.

4. Conclusion

Herein, we have engineered a cell-laden bioink with potent antibacterial activity for skin tissue engineering applications to address the challenges associated with a bacterial infection. This challenging matter has been fulfilled by the use of gallium in the formulation of the bioink that plays dual functions. (i) First, it stabilizes the hydrogel network through the formation of ionic crosslinking with Alg chains. (ii) Second, it endows the hydrogel with potent antibacterial activity toward both Gram-negative and Gram-positive bacteria. The printability of the developed bioink was characterized comprehensively over three different stages; extrusion, recovery, and self-supporting. In the extrusion stage, the viscosity of the developed hydrogel falls from approximately 1000 Pa.s at a low shear rate to around 1 Pa.s at a high shear rate, confirming the shear-thinning behavior of the MC/Alg hydrogel. The high recoverability of the hydrogel reveals that the hydrogel can return to its initial stage in a short time (<5 s) after removing the shear stress. In addition, the self-supporting behavior of the hydrogel was supported by the results of yield stress and storage modulus. The developed bioink printed out multi-layered 3D structures with high resolution and shape integrity, supporting the obtained results from the rheological study. The optimized bioink formulation was found to be MC-8/Alg-2 that were crosslinked with 0.5 wt.% gallium nitrate after printing. As an interesting result, the optimized gallium-crosslinking displayed excellent antibacterial activity toward both *S. aureus* and *P. aeruginosa* with a bactericidal rate of 99.99 %. Finally, the ability of the gallium-crosslinked bioink in supporting the fibroblast cellular functions in both bulk and printed structure was investigated. Accordingly, the gallium-crosslinked bioink exhibited almost similar cell viability and metabolic activity compared to the calcium-crosslinked bioink, confirming the high biocompatibility of the developed bioink. Taken together the excellent printability, potent antibacterial activity, and high cytocompatibility makes it a potential candidate for skin regenerative medicine.

CRediT authorship contribution statement

Hadi Rastin: Conceptualization, Investigation, Methodology, data processing, Original Draft. **Mahnaz Ramezanpour:** selected investigation, Methodology, Review & Editing. **Kamrul Hassan:** selected investigation, Data processing, Review & Editing. **Arash Mazinani :** selected investigation, Data processing, Review & Editing. **Tran Thanh Tung:** C–supervision, Review & Editing. **Sarah Vreugde :** Resources, Review&Editing. **Dusan Losic;** Conceptualization, Resources, Funding Acquisition, Re-view&Editing, Supervision, submission

Acknowledgement

References

Afghah, F., Ullah, M., Seyyed Monfared Zanjani, J., Akkuş Süt, P., Sen, O., Emanet, M., et al. (2020). 3D printing of silver-doped polycaprolactone-poly propylene succinate composite scaffolds for skin tissue engineering. *Biomedical Materials*.

Ahmed, W., Zhai, Z., & Gao, C. (2019). Adaptive antibacterial biomaterial surfaces and their applications. *Materials Today Bio, 2*, Article 100017.

Alruwaili, M., Lopez, J. A., McCarthy, K., Reynaud, E. G., & Rodriguez, B. J. (2019). Liquid-phase 3D bioprinting of gelatin alginate hydrogels: Influence of printing parameters on hydrogel line width and layer height. *Bio-Design and Manufacturing, 2* (3), 172–180.

10

Andreassi, A., Bilenchi, R., Biagioli, M., & D'Aniello, C. (2005). Classification and pathophysiology of skin grafts. *Clinics in Dermatology, 23*(4), 332–337.

Askari, M., Afzali Naniz, M., Kouhi, M., Saberi, A., Zolfagharian, A., & Bodaghi, M. (2021). Recent progress in extrusion 3D bioprinting of hydrogel biomaterials for tissue regeneration: a comprehensive review with focus on advanced fabrication techniques. *Biomaterials Science*.

Axpe, E., & Oyen, M. L. (2016). Applications of alginate-based bioinks in 3D bioprinting. *International Journal of Molecular Sciences, 17*(12), 1976.

Cao, Z., Luo, Y., Li, Z., Tan, L., Liu, X., Li, C., et al. (2021). Antibacterial hybrid hydrogels. *Macromolecular Bioscience, 21*(1), Article 2000252.

Carter, J. E., & Holmes, J. H. (2016). Chapter 14 - The surgical management of burn wounds. In M. Z. Albanna & J. H. Holmes Iv (Eds.), *Skin tissue engineering and regenerative medicine* (pp. 289–298). Boston: Academic Press.

Castilho, M., de Ruijter, M., Beirne, S., Villette, C. C., Ito, K., Wallace, G. G., et al. (2020). Multitechnology biofabrication: A new approach for the manufacturing of functional tissue structures? *Trends in Biotechnology, 38*(12), 1316–1328.

Chitambar, C. R. (2012). Gallium-containing anticancer compounds. *Future Medicinal Chemistry, 4*(10), 1257–1272.

Chitambar, C. R. (2016). Gallium and its competing roles with iron in biological systems. *Biochimica et Biophysica Acta (BBA) - Molecular Cell Research, 1863*(8), 2044–2053.

Clinical, & Institute, L. S. (2006). *Methods for dilution antimicrobial susceptibility tests for bacteria that grow aerobically*. PA: Clinical and Laboratory Standards Institute Wayne.

Contessi Negrini, N., Bonetti, L., Contili, L., & Farè, S. (2018). 3D printing of methylcellulose-based hydrogels. *Bioprinting, 10*, Article e00024.

Cubo, N., Garcia, M., del Cañizo, J. F., Velasco, D., & Jorcano, J. L. (2016). 3D bioprinting of functional human skin: production and in vivo analysis. *Biofabrication, 9*(1), Article 015006.

Davidovich-Pinhas, M., & Bianco-Peled, H. (2010). A quantitative analysis of alginate swelling. *Carbohydrate Polymers, 79*(4), 1020–1027.

Dodero, A., Pianella, L., Vicini, S., Alloisio, M., Ottonelli, M., & Castellano, M. (2019). Alginate-based hydrogels prepared via ionic gelation: An experimental design approach to predict the crosslinking degree. *European Polymer Journal, 118*, 586–594.

Donderwinkel, I., van Hest, J. C. M., & Cameron, N. R. (2017). Bio-inks for 3D bioprinting: recent advances and future prospects. *Polymer Chemistry, 8*(31), 4451–4471.

Dorishetty, P., Dutta, N. K., & Choudhury, N. R. (2020). Bioprintable tough hydrogels for tissue engineering applications. *Advances in Colloid and Interface Science, 281*, Article 102163.

Freeman, F. E., & Kelly, D. J. (2017). Tuning alginate bioink stiffness and composition for controlled growth factor delivery and to spatially direct MSC fate within bioprinted tissues. *Scientific Reports, 7*(1), 17042.

Giano, M. C., Ibrahim, Z., Medina, S. H., Sarhane, K. A., Christensen, J. M., Yamada, Y., et al. (2014). Injectable bioadhesive hydrogels with innate antibacterial properties. *Nature Communications, 5*(1), 1–9.

Giuseppe, M. D., Law, N., Webb, B., Macrae, R. A., Liew, L. J., Sercombe, T. B., et al. (2018). Mechanical behaviour of alginate-gelatin hydrogels for 3D bioprinting. *Journal of the Mechanical Behavior of Biomedical Materials, 79*, 150–157.

Gutierrez, E., Burdiles, P. A., Quero, F., Palma, P., Olate-Moya, F., & Palza, H. (2019). 3D printing of antimicrobial Alginate/Bacterial-Cellulose composite hydrogels by incorporating copper nanostructures. *ACS Biomaterials Science & Engineering, 5*(11), 6290–6299.

He, Z. (2019). *Significant impacts of different types of alginate on the encapsulation stability of fish oil*. Flinders University, College of Medicine and Public Health.

Hentze, M. W., Muckenthaler, M. U., Galy, B., & Camaschella, C. (2010). Two to tango: Regulation of mammalian iron metabolism. *Cell, 142*(1), 24–38.

Hijazi, S., Visaggio, D., Pirolo, M., Frangipani, E., Bernstein, L., & Visca, P. (2018). Antimicrobial activity of gallium compounds on ESKAPE pathogens. *Frontiers in Cellular and Infection Microbiology, 8*, 316.

Hu, H., & Xu, F.-J. (2020). Rational design and latest advances of polysaccharide-based hydrogels for wound healing. *Biomaterials Science, 8*(8), 2084–2101.

Iskandar, L., Rojo, L., Di Silvio, L., & Deb, S. (2019). The effect of chelation of sodium alginate with osteogenic ions, calcium, zinc, and strontium. *Journal of Biomaterials Applications, 34*(4), 573–584.

Jeong, K.-H., Park, D., & Lee, Y.-C. (2017). Polymer-based hydrogel scaffolds for skin tissue engineering applications: A mini-review. *Journal of Polymer Research, 24*(7), 112.

Johnson, C. T., & García, A. J. (2015). Scaffold-based anti-infection strategies in bone repair. *Annals of Biomedical Engineering, 43*(3), 515–528.

Jovic, T. H., Kungwengwe, G., Mills, A. C., & Whitaker, I. S. (2019). Plant-derived biomaterials: A review of 3D bioprinting and biomedical applications. *Frontiers of Mechanical Engineering, 5*(19).

Kim, H. N., & Choi, N. (2019). Consideration of the mechanical properties of hydrogels for brain tissue engineering and brain-on-a-chip. *Biochip Journal, 13*(1), 8–19.

Lee, J., Hong, J., Kim, W., & Kim, G. H. (2020). Bone-derived dECM/alginate bioink for fabricating a 3D cell-laden mesh structure for bone tissue engineering. *Carbohydrate Polymers, 250*, Article 116914.

Lee, K. Y., Bouhadir, K. H., & Mooney, D. J. (2004). Controlled degradation of hydrogels using multi-functional cross-linking molecules. *Biomaterials, 25*(13), 2461–2466.

Lemire, J. A., Harrison, J., & Turner, R. J. (2013). Antimicrobial activity of metals: Mechanisms, molecular targets and applications. *Nature Reviews Microbiology, 11*(6), 371–384.

Lewicki, J., Bergman, J., Kerins, C., & Hermanson, O. (2019). Optimization of 3D bioprinting of human neuroblastoma cells using sodium alginate hydrogel. *Bioprinting, 16*, Article e00053.

Li, C., Mu, C., & Lin, W. (2016). Novel hemocompatible nanocomposite hydrogels crosslinked with methacrylated gelatin. *RSC Advances, 6*(49), 43663–43671.

Li, H., Tan, Y. J., Leong, K. F., & Li, L. (2017). 3D bioprinting of highly thixotropic alginate/methylcellulose hydrogel with strong interface bonding. *ACS Applied Materials & Interfaces, 9*(23), 20086–20097.

Li, J., Wu, C., Chu, P. K., & Gelinsky, M. (2020). 3D printing of hydrogels: Rational design strategies and emerging biomedical applications. *Materials Science and Engineering R Reports, 140*, Article 100543.

Loss, M., Wedler, V., Künzi, W., Meuli-Simmen, C., & Meyer, V. E. (2000). Artificial skin, split-thickness autograft and cultured autologous keratinocytes combined to treat a severe burn injury of 93% of TBSA. *Burns, 26*(7), 644–652.

Mancha Sánchez, E., Gómez-Blanco, J. C., López Nieto, E., Casado, J. G., Macías-García, A., Díaz Díez, M. A., et al. (2020). Hydrogels for bioprinting: a systematic review of hydrogels synthesis, bioprinting parameters, and bioprinted structures behavior. *Frontiers in Bioengineering and Biotechnology, 8*(776).

Melo, S. F., Neves, S. C., Pereira, A. T., Borges, I., Granja, P. L., Magalhães, F. D., et al. (2020). Incorporation of graphene oxide into poly(ε-caprolactone) 3D printed fibrous scaffolds improves their antimicrobial properties. *Materials Science and Engineering C, 109*, Article 110537.

Mohandas, A., Deepthi, S., Biswas, R., & Jayakumar, R. (2018). Chitosan based metallic nanocomposite scaffolds as antimicrobial wound dressings. *Bioactive Materials, 3*(3), 267–277.

Mouriño, V., Newby, P., Pishbin, F., Cattalini, J. P., Lucangioli, S., & Boccaccini, A. R. (2011). Physicochemical, biological and drug-release properties of gallium crosslinked alginate/nanoparticulate bioactive glass composite films. *Soft Matter, 7*(14), 6705–6712.

Murphy, S. V., & Atala, A. (2014). 3D bioprinting of tissues and organs. *Nature Biotechnology, 32*(8), 773–785.

Muthukrishnan, L. (2021). Imminent antimicrobial bioink deploying cellulose, alginate, EPS and synthetic polymers for 3D bioprinting of tissue constructs. *Carbohydrate Polymers, 260*, Article 117774.

Namazi, H., Hasani, M., & Yadollahi, M. (2019). Antibacterial oxidized starch/ZnO nanocomposite hydrogel: Synthesis and evaluation of its swelling behaviours in various pHs and salt solutions. *International Journal of Biological Macromolecules, 126*, 578–584.

Pan, J., Jin, Y., Lai, S., Shi, L., Fan, W., & Shen, Y. (2019). An antibacterial hydrogel with desirable mechanical, self-healing and recyclable properties based on triple-physical crosslinking. *Chemical Engineering Journal, 370*, 1228–1238.

Prasher, P., Sharma, M., Mudila, H., Gupta, G., Sharma, A. K., Kumar, D., et al. (2020). Emerging trends in clinical implications of bio-conjugated silver nanoparticles in drug delivery. *Colloid and Interface Science Communications, 35*, Article 100244.

Qu, J., Zhao, X., Liang, Y., Zhang, T., Ma, P. X., & Guo, B. (2018). Antibacterial adhesive injectable hydrogels with rapid self-healing, extensibility and compressibility as wound dressing for joints skin wound healing. *Biomaterials, 183*, 185–199.

Ramesh, S., Kovelakuntla, V., Meyer, A. S., & Rivero, I. V. (2020). Three-dimensional printing of stimuli-responsive hydrogel with antibacterial activity. *Bioprinting*, Article e00106.

Rastin, H., Ormsby, R. T., Atkins, G. J., & Losic, D. (2020). 3D bioprinting of methylcellulose/gelatin-methacryloyl (MC/GelMA) bioink with high shape integrity. *ACS Applied Bio Materials, 3*(3), 1815–1826.

Rastin, H., Zhang, B., Bi, J., Hassan, K., Tung, T. T., & Losic, D. (2020). 3D printing of cell-laden electroconductive bioink for tissue engineering application. *Journal of Materials Chemistry B*.

Rastin, H., Zhang, B., Mazinani, A., Hassan, K., Bi, J., Tung, T. T., et al. (2020). 3D bioprinting of cell-laden electroconductive MXene nanocomposite bioinks. *Nanoscale*.

Richter, K., Thomas, N., Zhang, G., Prestidge, C. A., Coenye, T., Wormald, P.-J., et al. (2017). Deferiprone and gallium-protoporphyrin have the capacity to potentiate the activity of antibiotics in staphylococcus aureus small colony variants. *Frontiers in Cellular and Infection Microbiology, 7*(280).

Shen, Y., Tang, H., Huang, X., Hang, R., Zhang, X., Wang, Y., et al. (2020). DLP printing photocurable chitosan to build bio-constructs for tissue engineering. *Carbohydrate Polymers, 235*, Article 115970.

Shi, J., Xing, M. M., & Zhong, W. (2012). Development of hydrogels and biomimetic regulators as tissue engineering scaffolds. *Membranes, 2*(1), 70–90.

Sun, A., He, X., Li, L., Li, T., Liu, Q., Zhou, X., et al. (2020). An injectable photopolymerized hydrogel with antimicrobial and biocompatible properties for infected skin regeneration. *NPG Asia Materials, 12*(1), 25.

Talikowska, M., Fu, X., & Lisak, G. (2019). Application of conducting polymers to wound care and skin tissue engineering: A review. *Biosensors & Bioelectronics, 135*, 50–63.

Unagolla, J. M., & Jayasuriya, A. C. (2020). Hydrogel-based 3D bioprinting: A comprehensive review on cell-laden hydrogels, bioink formulations, and future perspectives. *Applied Materials Today, 18*, Article 100479.

Veiga, A. S., & Schneider, J. P. (2013). Antimicrobial hydrogels for the treatment of infection. *Biopolymers, 100*(6), 637–644.

Vig, K., Chaudhari, A., Tripathi, S., Dixit, S., Sahu, R., Pillai, S., et al. (2017). Advances in skin regeneration using tissue engineering. *International Journal of Molecular Sciences, 18*(4), 789.

Wu, Z., & Hong, Y. (2019). Combination of the silver–ethylene interaction and 3D printing to develop antibacterial superporous hydrogels for wound management. *ACS Applied Materials & Interfaces, 11*(37), 33734–33747.

Yan, W.-C., Davoodi, P., Vijayavenkataraman, S., Tian, Y., Ng, W. C., Fuh, J. Y. H., et al. (2018). 3D bioprinting of skin tissue: From pre-processing to final product evaluation. *Advanced Drug Delivery Reviews, 132*, 270–295.

Yu, J. R., Navarro, J., Coburn, J. C., Mahadik, B., Molnar, J., Holmes Iv, J. H., et al. (2019). Current and future perspectives on skin tissue engineering: Key features of

11

biomedical research, translational assessment, and clinical application. *Advanced Healthcare Materials, 8*(5), Article 1801471.

Zennifer, A., Senthilvelan, P., Sethuraman, S., & Sundaramurthi, D. (2020). Key advances of carboxymethyl cellulose in tissue engineering & 3D bioprinting applications. *Carbohydrate Polymers*, Article 117561.

Zhang, Y., Zhai, D., Xu, M., Yao, Q., Zhu, H., Chang, J., et al. (2017). 3D-printed bioceramic scaffolds with antibacterial and osteogenic activity. *Biofabrication, 9*(2), Article 025037.

Zhao, P., Gu, H., Mi, H., Rao, C., Fu, J., & Turng, L.-s. (2018). Fabrication of scaffolds in tissue engineering: A review. *Frontiers of Mechanical Engineering, 13*(1), 107–119.

Zhao, X., Wu, H., Guo, B., Dong, R., Qiu, Y., & Ma, P. X. (2017). Antibacterial anti-oxidant electroactive injectable hydrogel as self-healing wound dressing with hemostasis and adhesiveness for cutaneous wound healing. *Biomaterials, 122*, 34–47.

Zhong, Y., Xiao, H., Seidi, F., & Jin, Y. (2020). Natural polymer-based antimicrobial hydrogels without synthetic antibiotics as wound dressings. *Biomacromolecules, 21*(8), 2983–3006.

Zhou, Q., Kang, H., Bielec, M., Wu, X., Cheng, Q., Wei, W., et al. (2018). Influence of different divalent ions cross-linking sodium alginate-polyacrylamide hydrogels on antibacterial properties and wound healing. *Carbohydrate Polymers, 197*, 292–304.

Zhu, J., & Marchant, R. E. (2011). Design properties of hydrogel tissue-engineering scaffolds. *Expert Review of Medical Devices, 8*(5), 607–626.

Zhu, S., Wang, J., Yan, H., Wang, Y., Zhao, Y., Feng, B., et al. (2017). An injectable supramolecular self-healing bio-hydrogel with high stretchability, extensibility and ductility, and a high swelling ratio. *Journal of Materials Chemistry B, 5*(34), 7021–7034.

12

Chapter 7

Conclusion and future directions

I n this chapter, the main findings of this Ph.D. thesis are summarized. This includes the summary of the conducted experiments, contributions of each chapter, and conclusions of the researches carried out in this project. In addition, the recommendation for future work is provided in this chapter

7.1 Conclusion

There has been a growing demand for engineered tissue due to the unbalanced number of donors and receivers of organs. Engineered tissues must possess precise geometries with the ability to mimic the native tissue. Since two decades ago, 3D bioprinting has experienced rapid advances in the fabrication of functional biological structures in three dimensions owing to the high controllability of the 3D bioprinting technologies. Inkjet, orifice-free, stereolithography, and extrusion bioprinting are four main classes of bioprinting methods with specific limitations and strength. Latter is the most common printing technique, which can print high viscose inks with high cell density. Despite rapid development in printing accuracy and speed, ideal bioinks with suitable characteristics are lacking and appeared as the main barrier in this field. This is mainly because high viscose bioinks favor printing, whereas lower-viscosity inks are more suitable for maintaining cell viability and function.

Hydrogels have been widely explored in the design of bioink due to a set of favorable features such as high water uptake capacity, low toxicity, and similarity to ECM environments. Bioink used in extrusion-based 3D bioprinting should meet the number of requirements for 3D printing. First, bioink should provide a cell-friendly environment to ensure high cell viability within the fabricated bioconstructs. Second, bioink should possess specific rheological behavior to shield encapsulated cells from high shear stress during printing and enable the printer to deposit strands with pre-designed resolution. Cell-laden hydrogels expose to high shear stress during printing where bioink passes through a thin nozzle, which proved to be impairing the cell viability. The use of a nozzle with a bigger diameter saves cells from high shear stress, however, it adversely affects the resolution of fabricated constructs. Given this, shear-thinning hydrogels are of interest for extrusion-based bioprinting because their viscosity drops at high shear stress which secures cells along the nozzle without losing the resolution. Third, hydrogel gelation should be mechanically strong enough to preserve the construct once printed. Recently, hydrogels derived from natural resources draw more attention to be used in 3D bioprinting applications such as gelatin, alginate, chitosan, and agarose. However, they all have their intrinsic advantages and drawbacks. For example, gelatin as a natural polymer benefits from cell adhesion sites along its backbone, but it suffers from poor mechanical properties and lack of printability. Thus, the need to design and development of multi-component hydrogels with shear-thinning behavior is of critical importance to address the limitation of single-component hydrogels in terms of printability and biological requirements.

In this research, four different novel bioinks with desirable properties have developed that will be discussed below.

7.2 Contributions and conclusions

This Ph.D. thesis attempted to address the challenges in the design of bioink for extrusion-based 3D bioprinting through developing some advanced bioinks. The main findings of this research are outlined below:

➢ Chapter 3 describes a novel photo-crosslinkable MC/GelMA bioink in which GelMA serves as a permanent macromolecular crosslinker while MC provides printability requirements. The MC/GelMA bioink overcomes the quick dissociation of MC-based hydrogel in the biological media as a result of GelMA crosslinking under UV irradiation. Following are the main findings of this chapter:

- Compared to the pristine MC hydrogel, the MC-8/GelMA-5 bioink has exhibited enhanced compressive modulus, which is attributed to the physical interaction of MC and GelMA chains.

- The rheological characterization of the bioink reflects the high thixotropic behavior, suitable for the 3D bioprinting process.

- To showcase the biocompatibility of the developed bioink, the viability of encapsulated human primary osteoblasts within the MC-8/GelMA-5 ink was evaluated using LIVE/DEAD cell assay. It was observed that the cells remain viable after printing without noticeable changes compared to the bulk hydrogel.

- The main significance of this chapter is to fabricate physiologically scaled tissue implants with long-term stability in the biological media that can be used for bone tissue engineering for large non-healing fractures. Despite the favorable features of MC-based bioinks, the lack of a post-cross-linking ability leads to the dissociation of MC in biological media. This remained the main challenging issue in the 3D bioprinting of MC-based hydrogels. This chapter addresses the challenges associated with the quick dissociation of pristine MC-based bioinks. The developed bioink not only have exhibited better stability but also printed 3D structures with better printability and resolution.

➢ The development of new bioinks with desirable properties has been restricted due to the limited selection of materials used in 3D bioprinting. Each material brings a different quality to the bioink, thus it is required to the extent the library of biomaterials in 3D bioprinting. In chapter 4, MXene, a new class of 2D nanomaterials, was exploited in the design

of bioink owing to its remarkable properties. The bioink is composed of HA/Alg that is filled with Ti_3C_2 Mxene nanosheets. Following are the main findings of this chapter:

- The addition of MXene was found to improve the mechanical, rheological, and electrical properties of the bioink that can be tuned upon varying the concentration of MXene.

- Evaluation of the biocompatibility of the bioink confirmed high cell viability (>95%) in both thin-film and bioprinted structures over a week with no significant differences.

- These results promise the application of MXene nanocomposite bioinks in neural tissue engineering and other biomedical applications.

- The main significance of this chapter is to explore the potential of MXene nanocomposite bioinks for tissue engineering application. This bioink can be employed in neural tissue engineering and the design of medical devices due to its high electrical conductivity. This bioink could positively guide neural stem cell to grow and proliferate in the prepared 3D scaffold. In addition, bone tissue engineering is another promising application of this bioink due to the degradation products of MXene that promote bone tissue formation.

➢   In addition to the rheological and biological requirements, the electroconductivity of bioink is also critical to successfully replicate the properties of native tissue. However, most current bioinks deal with poor electrical conductivity due to the inherent properties of polymers. Chapter 5 introduces an electroconductive bioink composed of highly thixotropic MC/κCA hydrogels filled with PEDOT:PSS conducting polymers. Conductive polymers have been extensively investigated in biomedical applications due to the high electrical conductivity and biocompatibility. Following are the main findings of this chapter:

- It has been found that the incorporation of PEDOT:PSS impart electrical conductivity to the hydrogels.

- The bioink exhibited appropriate rheological properties, suitable for the 3D bioprinting process.

- MC/κCA/PEDOT:PSS bioink printed several multi-layered structures, confirming the excellent printability of the bioink with high shape retention and resolution.

- The encapsulated HEK-293 cells remain viable within both bulk and 3D bioprinted structures and grow over time, indicating the high biocompatibility of the bioink.

- The main significance of this chapter is to overcome the poor electrical conductivity of current bioinks for neural tissue engineering applications. This bioink enables the

transferring of electrical stimulations that can be used to promote cellular behavior. In addition, this bioink allows the printing of physiological-scale constructs without requiring a secondary support bath.

➢   Chapter 6 describes the synthesis and characterization of a bioink with potent antibacterial activity to address the challenges associated with a bacterial infection through employing gallium in the bioink formulation. The bioink is composed of MC/Alg that crosslinked with 0.5 wt.% gallium nitrate. Following are the main findings of this chapter:

- The mechanical, swelling ratio and degradation kinetics of the MC/Alg strongly depends on the concentration of comprising polymers and gallium. It was found that the higher gallium concentration leads to the higher crosslinking density and subsequently higher mechanical strength and slower degradation kinetics.

- It was found that the sustainable release of gallium from the bioink network imparts antibacterial activity to the bioink toward both gram-negative and gram-positive bacteria.

- The gallium-crosslinked bioink supported the fibroblast cellular functions with no significant differences compared to the calcium-crosslinked bioink. This confirms the high biocompatibility of the developed gallium-crosslinked bioink.

- The main significance of this chapter is to eliminate the risks of bacterial infection at the lesion site. Skin is the largest tissue in the body that is susceptible to bacterial infection once damaged. This chapter introduced a bioink with potent antibacterial activity without significant negative effects on cellular functions. This bioink opened a new frontier in the design of multi-function bioink for the treatment of bacterial infections. Excellent printability, potent antibacterial activity, and high cytocompatibility of this bioink make it a potential candidate for skin regenerative medicine.

7.3 Limitations of this thesis

Like other studies, this thesis also has several limitations as outlined below.

Chapter 3 aims to develop a Methylcellulose/gelatin methacryloyl (MC/GelMA) bioink with high shape integrity and high stability through combining the advantages of each of the printability of the MC and the permeant cross linking of the GelMA. The limitation of this reported studies includes:

- ✓ High viscosity of the bioink that limit the migration of cells.
- ✓ Use of UV-irradiation that proved to have detrimental effect on cellular viability.

✓ Limited biological studies have conducted in this study. Therefore, further studies are required to assess the function of encapsulated cells within the bioink.

Chapter 4 aims to impart exploit the extraordinary properties of MXene nanosheets in the design of bioink that would potentially encourage cell adhesion and growth. The limitation of this reported studies includes:

✓ Lack of comprehensive biological studies such as cellular adhesion, proliferation and differentiation.

✓ Lack of study on the effect of MXene nanosheets on the bioactivity of Bioink thoroughly.

✓ Lack of detailed nanotoxicity of Mxene nanosheets.

Chapter 5 aims to impart electrical conductivity within the bioink through integrating the thixotropic kappa-carrageenan with methylcellulose (MC/κCA) hydrogels filled with conducting polymers (PEDOT:PSS). The limitation of this reported studies includes:

✓ Lack of implementation of electrical signals to the bioink to monitor the cellular behaviour to the electrical cues.

✓ This work include HEK-293 cells within the hydrogel, while it is recommended to include neural cells with high sensitivity to the electrical cues.

Chapter 6 concentrated on developing a bioink with antimicrobial properties by using gallium in the formulation of bioink. The limitation of this reported studies includes:

✓ The long-term cytotoxicity of gallium nitrate on the encapsulated have not addressed in this work.

✓ Lack of comprehensive comparison of gallium-crosslinked hydrogel with calcium-crosslinked hydrogel in terms of mechanical behaviour.

7.4 Recommendations for Future work

This Ph.D. thesis made a significant contribution to the 3D bioprinting field with novel discoveries that highlight the development of advanced bioinks for tissue engineering application through employing different polymers and nanomaterials. This work opened new frontiers that deserved further research in the future. Thus, several recommendations and

pathways are highlighted here for future work to fully realize the potential of developed bioinks:

1. **Design of different nanocomposite bioinks through employing other types of 2D nanomaterials and their hybrids:** Since 2D nanomaterials are at the infancy stage, only a few types of 2D nanomaterials have been exploited in the design of bioink. Thus, as the family of 2D nanomaterials is expanding, it is expected new types of 2D nanomaterials will be exploited in the design of bioinks. In addition, obtaining synergistic properties resulting from the combining of different nanomaterials is another emerging trend, which is expected to grow in the future. Such synergistic properties hold great promise for enhancing the efficacy of printed functional constructs, necessitating more efforts to combine different nanomaterials. Taking advantage of the extraordinary features of 2D nanomaterials to add new functionality to the conventional bioink is the current trend in the developments of 2D nanocomposite bioinks.

2. **Integration of machine learning and 3D bioprinting technology to obtain more reliable results:** Considerable attention has been devoted to the significant promise and benefits of machine learning in industrialized 3D printing technologies. In generic terms, machine learning techniques aim to convert input data into outputs by employing training data. The converging of 3D printing and machine learning is due to the complexities involved in the 3D printing process. Despite the widespread potential of machine learning in 3D printing, machine learning is relatively unexplored in the 3D bioprinting field for biomedical applications that deserved further researches. The current bioprinting workflow initiates from medical image processing, followed by optimization of printing parameters and finally alterations during post-printing tissue maturation. Machine learning can be utilized to better digitalize current workflow and enhance biological performance. Machine learning can provide generalized modeling of complex processes that allow experts to optimize the affecting parameters in multiple-stages 3D bioprinting processes. For example, the current approach in 3D bioprinting is to select materials from experiments, where machine learning can build a model to reach the best material selection according to the desired properties. It is expected that 3D bioprinting will become more digital and in silico in near future by employing machine learning to unlock the bioprinting promise.

3. **Exploration of the performance of the MXene nanocomposite bioink for bone tissue engineering:** MXenes have demonstrated remarkable features such as large surface area, high biocompatibility, substantial electrical conductivity, potent antibacterial activity, and easy dispersion in aqueous solutions, Moreover, MXene degrades into components that accelerate bone formation, that makes it a prime candidate for bone tissue engineering. In general, the regeneration of bone defects requires a scaffold supporting cellular functions such as adhesion, proliferation, migration, differentiation, and maturation over bone formation. In this sense, exploration of the performance of the developed MXene nanocomposite bioink for bone tissue engineering is highly recommended.

4. **Investigating the effect of applied electrical stimulation on the cellular behavior encapsulated within the developed electroconductive bioink:** Electrical stimulation has been employed to promote large non-healing bone fractures and has recently been used to stimulate cells for better tissue formation performance. Electroconductive scaffolds can replicate the electrical properties of the target tissue, enabling the transferring of electrical signals to all cells within the scaffold. The positive effect of electrical stimulation on cellular function is related to the activation of many intracellular signaling pathways after the application of electrical stimulations. The integration of electrical stimulation and ideal tissue-engineered scaffolds have an advantage of both and are of interest for the field of regenerative medicine. In this sense, it is recommended to investigate the effect of electrical stimulation on the cellular behavior encapsulated within the developed electroconductive bioink in this thesis.

5. **Design of an antibacterial bioink by employing poly-lysin within the bioink network:** Antimicrobial hydrogels have been attracted significant attention for wound healing applications due to eliminations of bacterial infection at the lesion site. Poly-l-lysine is an emerging candidate with inherent antibacterial activity toward a broad range of bacteria and fungi. Aside from its antibacterial activity, poly-l-lysine has demonstrated a set of favorable features such as high biocompatibility, biodegradability, and nontoxicity toward mammalian cells that makes it a promising candidate for tissue engineering application. In this sense, it is recommended to design an antibacterial bioink based on Poly-l-lysine to eliminate the risks associated with bacterial infections. For example, poly-l-lysine can be modified easily with methacrylate that makes it photo-crosslinkable under UV

irradiation. Physical mixing of GelMA and methacrylated poly-l-lysine seems to be a sensible bioink formulations.

6. **Design of a nanocomposite bioink with sustainable drug delivery:** High surface area, high rate of cellular uptake, and low cytotoxicity of 2D nanomaterials offer an attractive platform to be used as a carrier for drugs and therapeutic macromolecules. For example, graphene has been widely exploited as a therapeutic delivery vehicle. In this sense, it is suggested to design a graphene-containing bioink with sustainable drug release to deliver loaded substance in a prolonged manner to cells, which can be used to regulate the cell's behavior.